Forschungszentrum Karlsruhe
in der Helmholtz-Gemeinschaft

Wissenschaftliche Berichte

FZKA 7461

4th Annual Workshop Proceedings of the Integrated Project "Fundamental Processes of Radionuclide Migration" (6th EC FP IP FUNMIG)

G. Buckau, L. Duro, B. Kienzler, V. Montoya, A. Delos

Institut für Nukleare Entsorgung
Amphos 21

Juli 2009

Forschungszentrum Karlsruhe

in der Helmholtz-Gemeinschaft

Wissenschaftliche Berichte

FZKA 7461

EURATOM
EC 6th Framework Program

Integrated Project

"Fundamental Processes of Radionuclide Migration" (FUNMIG)

4th Annual Workshop Proceedings

Gunnar Buckau (FZK-INE)
Lara Duro (Amphos 21)
Bernhard Kienzler (FZK-INE)
Vanessa Montoya (Amphos 21)
Anne Delos (Amphos 21)

Forschungszentrum Karlsruhe GmbH, Karlsruhe

2009

Forschungszentrum Karlsruhe GmbH
Postfach 3640, 76021 Karlsruhe

Mitglied der Hermann von Helmholtz-Gemeinschaft
Deutscher Forschungszentren (HGF)

ISSN 0947-8620

urn:nbn:de:0005-074618

FOREWORD

These are the proceedings of the 4th and Final Annual Workshop of the Euratom FP6 Integrated Project FUNMIG (FUNdamental processes of radionuclide MIGration). The 4th Annual Workshop of the project was hosted by FZK-INE, and held in Karlsruhe 24-27 November 2008. The project started 2005 and has had a duration of 4 years. 51 contractors and 29 Associated Groups. The kick-off meeting was hosted by Amphos, and held January 26-28 in Barcelona (Spain); the 1st annual workshop was hosted by CEA, and held 28 November - 1 December 2005 in Saclay (France). The proceedings of that workshop are published as CEA-R-6122 report. The second annual workshop was hosted by SKB, and held 21-23 November 2006 in Stockholm (Sweden). The proceedings of that workshop are published as SKB Technical report TR-07-05. The third annual workshop was hosted by NDA and held 26-29 November 2007 in Edinburgh (UK). The proceedings of that workshop are published as NDA report 2008.

The present proceedings serve different objectives, mainly for documentation purposes. They contain Scientific and Technical contributions submitted by the partners, additional contributions made available to the project through the last annual workshop.

Further information about the project can be requested from the organizations taking part of the coordination team: FZK-INE and Amphos 21, through their representatives in the project:

Coordinator gunnar.buckau@ine.fzk.de

Technical secretariat lara.duro@amphos21.com

TABLE OF CONTENTS


FUNMIG

RTD COMPONENT ACTIVITY OVERVIEWS


FUNMIG

RTD COMPONENT 1

Pascal Reiller
CEA, Centre d'Etude Nucléaire de Saclay
DEN/DANS/DPC/SECR
Laboratoire de Spéciation des Radionucléides et des Molécules
Bâtiment 391, pc 33
F-91191 Gif-sur-Yvette CEDEX, France
pascal.reiller@cea.fr

Introduction

The main objective of this component is to provide fundamental process knowledge and the required data for processes with comparably well established conceptual understanding. The overall impact of natural organic coatings is included. Processes studied are fundamental and applicable to all types of host rocks and the proper parameters are derived for the relevant migration systems. The outcome is the fundamental understanding and quantification of the processes studied. The models are developed at the research model level.

Thereafter, the finalization of the research during the last year of the project is summarised.

Advances within workpackages

WP1.1 - Ionic species/speciation, processes determining physico-chemical conditions and generation of missing thermodynamic data

The work is focused on the determination of missing key thermodynamic data. The work is not only focused on the acquisition of free energies (formation constants), but also on enthalpies and entropies in order to properly account for temperature dependencies.

CEA has investigated the interactions of Eu(III) with silicate anions by time-resolved laser-induced fluorescence spectroscopy (TRLFS) and electrospray ionisation mass spectrometry (ESI-MS). Under the experimental conditions, *i.e.*, pH < 7 and 0.1 mM < [Si] < 2 mM, Eu(III) is expected either to hydrolyse to $Eu(OH)_n^{3-n}$ or to form a silicate complex by interaction with the monomeric silicate, which should be the only aqueous species of silica. However, the presence of silica oligomers was observed under some conditions. At low Si concentrations (0.1-1 mM), the Eu(III) fluorescence measured by TRLFS changed with time, suggesting slow formation of colloidal particles and

molecular complexes in the solutions (Figure 1). More information can be found in Vercouter *et al.* (this volume)

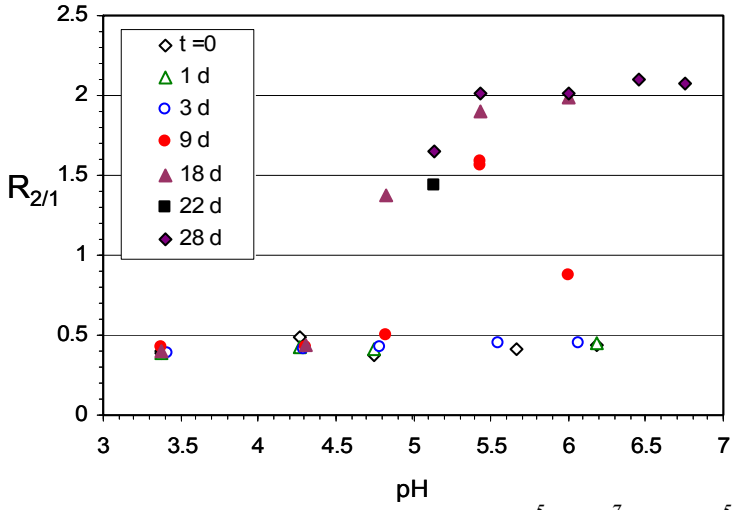

***Figure 1**: Evolution of the intensity ratio (R2/1) of the $^5D_0 \rightarrow {}^7F_2$ and $^5D_0 \rightarrow {}^7F_1$ Eu(III) bands for 0.1 mmol$_{Si}$/L solutions as a function of pH and time (in days)*

Gas-phase oligomers were detected by ESI-MS in solutions at pH 4 to 6 (Figure 2), as could be expected according to oligomerization reaction pathways. While ESI-MS had already been used for the detection of such species in concentrated silica solutions, it also succeeded here for the detection of oligomeric silicates in dilute solutions. This result suggests that silica oligomers can easily be formed even in acidic or near-neutral conditions, and are other potential ligands of metal ions.

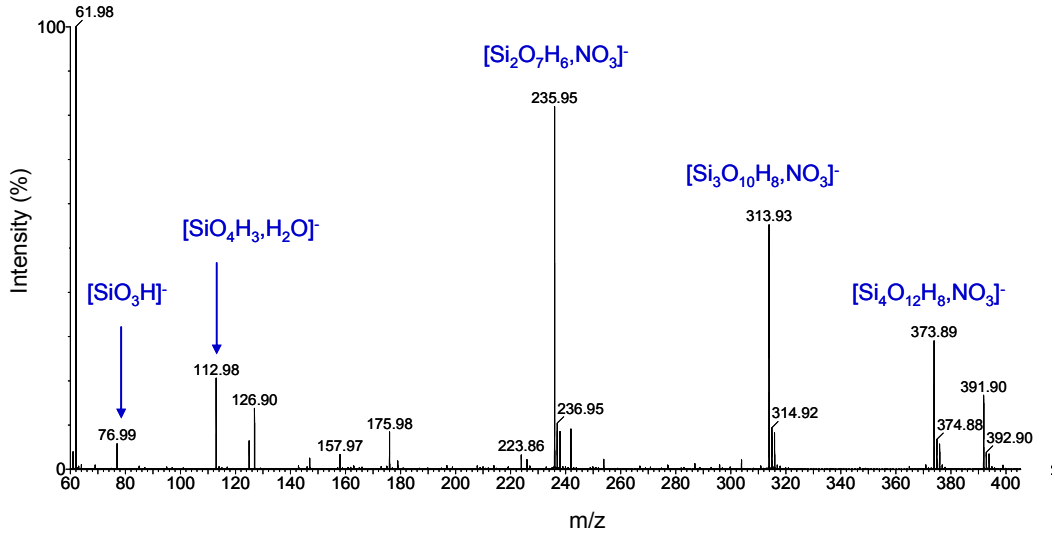

***Figure 2:** ESI mass spectrum of a 1 mM silicate solution at pH 5.*

CTH investigated the complexation of actinides (An), namely Am(III) and Th(IV), by orthosilicic acid and phosphate by using the well-known AKUFVE liquid-liquid extraction technique (Rydberg, 1969), as well as small volume batch experiments performed manually and looking at the distribution of species between the different

phases as a function of various silicate and phosphate concentrations in the aqueous phase.

The first stability constant obtained for complexation of An with silicates

$$An^{z+} + OSi(OH)_3^- \rightleftarrows AnOSi(OH)_3^{z-1}$$

has tentatively, for Am(III) a value of $\log_{10}\beta_1 = 4.7 \pm 0.1$ ($I = 1.0$ M) (Figure 3a). There are possibly indications of higher orders of complexation, but the presently collected extraction data could not verify this.

The stability constants $\log_{10}\beta_{m,q}$ for the thorium-silicate complexes are tentatively determined, from combined AKUFVE and batch experiments, to be $\log_{10}\beta_{1,1} = 5.2 \pm 0.1$, $\log_{10}\beta_{1,2} = 12.0 + 0.2$, $\log_{10}\beta_{1,3} = 18.5 + 0.3$ and $\log_{10}\beta_{1,4} = 25.1 \pm 1.9$ (Figure 3b).

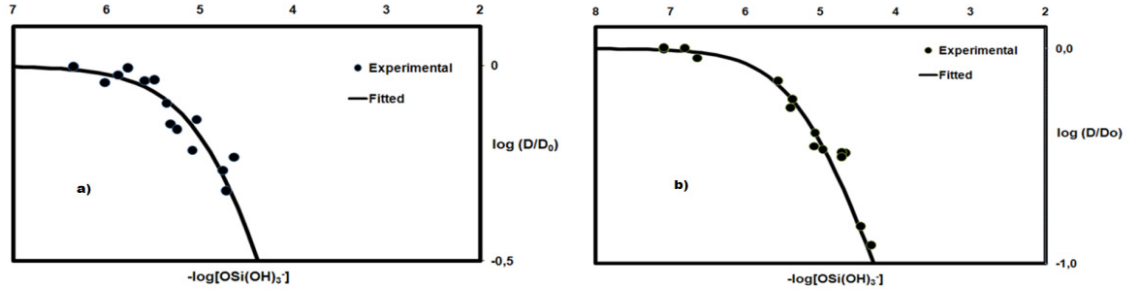

***Figure 3**: Extraction curves for a) Am (pH 6.5) and b) Th (pH 7.5) at 25 °C, I = 1.0 M with [$M^{3/4+}$] < 10^{-7} M.*

The thorium-phosphate complexation study presented in the former proceedings (Ekberg *et al.*, 2008), has been finalized and the results are ready for publication. The system has been studied at different temperatures (15, 25 and 35 °C) and varying pH of 7, 8 and 8.7 (Figure 4). Stability constants of the 1:1, 1:2 and 1:3 complexes formed were evaluated at $I = 1$ M, and from them, enthalpies and entropies of the formation reaction have been determined for the reactions:

$$m\mathrm{Th}^{4+} + q\mathrm{HPO}_4^{2-} \rightleftarrows \mathrm{Th}(\mathrm{HPO}_4)_q^{4m-2q}$$

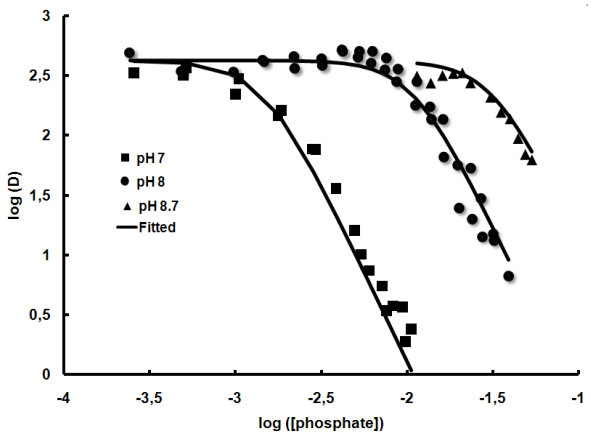

***Figure 4**: Extraction curves for the thorium-phosphate system at 25 °C.*

CEA and **CTH** have collaborated for the study of the speciation of Th(IV) with silicate in order to detect the possible formation of colloidal particles in the course of the liquid-liquid extraction experiments. The AKUFVE technique was set up in Saclay for a two-week period. The aqueous phases containing Th(IV) and silicates were sampled for analysis using Photon Correlation Spectroscopy (PCS). Particles were detected in some of the samples with a size distribution between 100 and 250 nm. The chemical nature of these particles could not be determined, and could be Th or Si colloids as well as mixed Th-Si colloids.

WP1.2 - Ion exchange and surface complexation

The work is focussed on the assessment of thermodynamic sorption models using surface complexation and ionic exchange models. Assessment is done on the laboratory systems up to real systems. Verification of the species involved is done by spectroscopic studies.

CEA Sorption models build on the ground of IXT2 (Ion-Exchangers Thermodynamic theory) may have an extended prediction capability if true constants are involved in the mass law expressions for sorption equilibria. This has been assessed in the case of a clay mineral, illite du Puy. Results from batch experiments conducted in potassium salts solutions (up to 2 M, variable pH) with illite, under potassic form, and mono-(Cs), di-(Sr) or trivalent (Am) at trace level confirm the constancy of corrected selectivity coefficients independently of aqueous phase composition. This means that the exchanging sorbed species activity coefficients have an ideal thermodynamic behaviour. To test further this conclusion in the case of sorbed elements at higher concentrations, predictions of sodium, potassium, calcium and magnesium sorbed amounts onto illite equilibrated with chloride-rich brines, simulating sea and estuarine waters (according to Millero's recipes), have been compared to measurements. Figure 5 indicates that an excellent accord is obtained. To perform this final study, thermodynamic database for potassium, calcium and magnesium sorption equilibria on illite du Puy has been beforehand completed.

Regarding the cross-evaluation of the predictive capacity of SCM and IXT2 in the case of sorption on gibbsite, the experimental benchmark failed because of very high perturbations afforded by the presence of kinetically stable soluble polynuclear forms of aluminium (keggin Al_{13}).

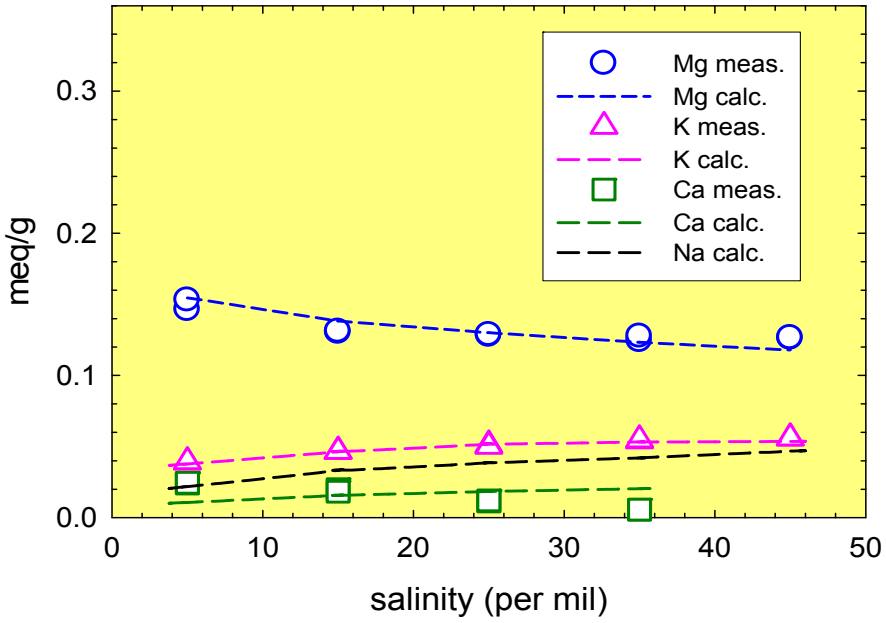

Figure 5: *Sorption of major cations on illite du Puy equilibrated with salt brines.*

CEA has characterized the interaction of Ce(III) and Ce(IV) with clay minerals such as hectorite and montmorillonite. The purpose of this study was to understand how clay minerals can catalyze the oxydo-reduction reaction for this solid. To this end, X-ray absorption fine structure was performed first on self-supporting films of the two minerals reacted with Ce(III) and Ce(IV) solids to identify the sorption mechanism of Ce at two distinct oxidation states on the solids. However, this goal was hampered by unexpected reaction of Ce with clay minerals. Indeed, X-ray absorption near edge spectroscopy (XANES) revealed that Ce(III) contacted with hectorite readily oxidized to Ce(IV), whereas a reduction of Ce(IV) to Ce(III) was observed on montmorillonite. Measurement of the suspensions electrochemical potentials E' in an H2-glove box showed that the (pH,E') conditions for the montmorillonite suspension (pH = 4,8; E'= 130 mV/NHE) coincided in a Pourbaix diagram with the equilibrium field of Ce(III); whereas, those measured in the hectorite suspension (pH = 5,9; E'= 300 mV/NHE) coincided with the equilibrium field of Ce(IV). Further examination of the XAFS spectra suggested that both Ce(III) and Ce(IV) were forming surface complexes on the clay sorbent phases instead of solution precipitates, thereby establishing a direct link between their oxidation state and the surface properties of clay minerals.

The results obtained for cerium-hectorite corroborates the finding of the ongoing programs, i.e., that specific interactions between layer edges of clay minerals (montmorillonite, hectorite) and lanthanides and actinides (Figure 6). The detailed structure of these complexes changes, presumably a consequence of distinct edge structures. Our unexpected observations of surface-related redox reactions in equilibrated clay require additional characterizations under well-controlled conditions. Overall, however, the importance of the edge reactivity of clay minerals has been substantiated and needs to be taken into account for robust modelling of radionuclide-interaction.

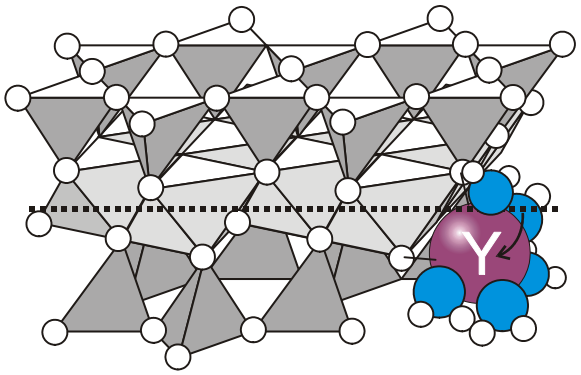

***Figure 6**: Illustration of the mechanism of lanthanide and actinide retention at the edges of clay minerals.*

Sorption experiments of europium onto purified Na-smectite and Na-illite (obtained form FEBEX bentonite and Illite du Puy, respectively) were completed by **CIEMAT** and data obtained in both systems were modelled. Europium adsorption exhibited no dependence on pH for values lower than 4, but a significant dependence with ionic strength, indicating the importance of ionic exchange processes. At higher pH, inner sphere surface complexation predominated.

Results were satisfactorily interpreted using a model which combines surface complexation and ionic exchange processes. The mean selectivity coefficient determined for the Na-Eu exchange was ($\log {}^{Eu}_{Na}K_{SEL} = 2.00 \pm 0.32$) but the effect of competitive ions in solution, coming from partial dissolution of the clay, had to be accounted for to satisfactorily explain the anomalies in the ionic strength experimentally observed. Eu(III) speciation was affected by the presence of carbonate species. Sorption by surface complexation was explained by a non electrostatic model with the formation of the following complexes: $\equiv SOEu^{2+}$, $\equiv SOEuCO_3$ and $\equiv SOEu(OH)_2$ with 1 weak ($\equiv S_WOH$) and 1 strong ($\equiv S_SOH$) surface sites. The model fits smectite and illite data and also those obtained onto two different mixtures (different proportions) of illite and smectite. Figure 7 shows an example of the modelling obtained with the sorption edges onto the Na-smectite (Figure 7a) and onto illite and smectite mixtures (Figure 7b). More information can be found in Missana *et al.* (this volume)

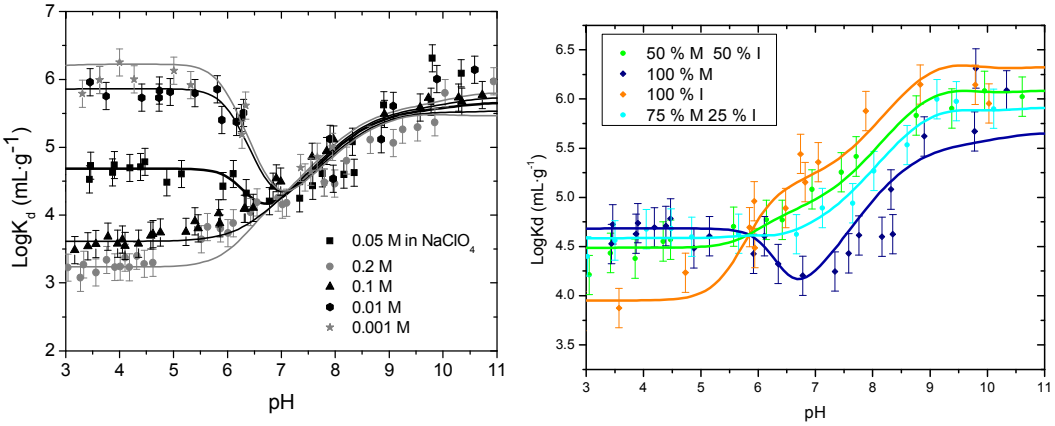

***Figure** 7: (Left) Sorption edges of [Eu] = 9.9 10^{-9} M at different ionic strength fixed by $NaClO_4$, S= 0.5 g·L^{-1} and onto FEBEX Na-smectite (a), and onto illite and smectite mixtures (b). Plain lines correspond to the adjustment of data.*

Sorption edge and isotherms for Eu(III) on purified Na-Illite du Puy (IdP) in the absence of inorganic carbon had been measured and modelled using the 2 site protolysis non electrostatic surface complexation / cation exchange (2SPNE SC/CE) sorption model in **PSI** (Bradbury & Baeyens, 1997) (red symbols and solid line in Figure 8). The influence of inorganic carbon on Na-IdP has been studied and the effect is shown by the blue symbols in Figure 8. An important outcome from the modelling was that the sorption data in the presence of inorganic carbon (pCO_2 = $10^{-3.5}$ bar) could only be quantitatively described if ternary Eu(III) carbonate surface complexes (≡SOEuCO$_3^0$ and ≡SOEuOHCO$_3^-$) were included in the modelling (solid blue line).

A sorption isotherm at Eu(III) equilibrium concentrations between 10^{-10} and 10^{-7} M was determined in a synthetic pore water at pH 8 on an Opalinus clay sample from Mont Terri. Figure 9 shows the experimental data together with the modelling (solid red line). Clearly, the predicted sorption data agreed very well with the measured data. In this "bottom-up" exercise the modelling was carried out under the assumption that the illite present in the Opalinus clay is the main sorbate and that ternary Eu(III) carbonate complexes are formed on the edge sites of illite.

The successful modelling of sorption isotherms on Opalinus clay for Eu(III) (trivalent actinide analogue) together with the previous results for Ni(II), Co(II) and U(VI) using the 2SPNE SC/CE sorption model are strong indicators that the approach used here can be applied for calculating sorption values in performance assessment.

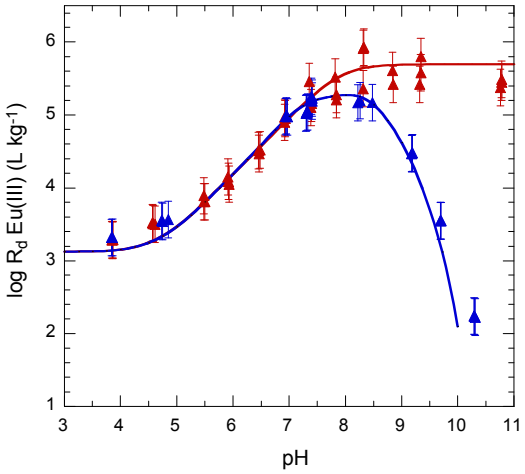

Figure 8: *Sorption edge of Eu(III) on Na-IdP in the absence (▲) and presence (▲) of inorganic carbon. Experimental and modelling.*

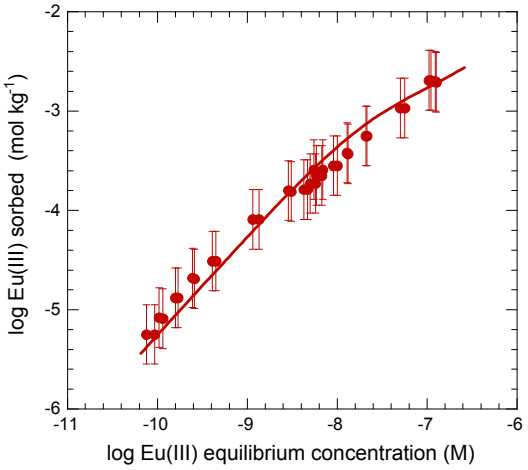

Figure 9: *Sorption isotherm of Eu(III) on Opalinus clay in a synthetic porewater (pH 8). Experimental and modelling.*

From a spectroscopic point of view, sorption of trivalent Cm(III) and Eu(III) onto aluminium oxides, namely gibbsite, bayerite and α-Al_2O_3 powder, was investigated in **FZK-INE** by batch experiments and time-resolved laser fluorescence spectroscopy (TRLFS). The pH dependent sorption was followed at constant ionic strength of 0.1 M $NaClO_4$ under argon atmosphere in a pH range between 4 and 11. Eu(III) sorption onto α-Al_2O_3 powder starts at pH > 4, indicating inner sphere surface complexation.

As the contribution of the edge faces to the overall surface area is higher in case of bayerite compared to gibbsite, and since bayerite has a lower isoelectric point than gibbsite, the adsorption edge for bayerite is shifted to lower pH values.

From the TRLFS emission spectra for Cm(III) sorption onto α-Al_2O_3 powder and bayerite, the presence of at least two different Cm(III) surface species can be derived. For spectra evaluation a detailed peak deconvolution is in progress.

The pH dependent dissolution and precipitation of gibbsite significantly affects the speciation of sorbed Cm(III). Equilibration of a gibbsite suspension in the solubility minimum and increasing or decreasing the pH inhibits the formation of an “incorporated” Cm(III) species and leads to two Cm(III) surface sorbed species with emission peak maxima at *approx.* 603 nm and 605 nm (Figure 10).

An important outcome of the study using gibbsite is that not only inner sphere surface complexation could be detected but also precipitation/incorporation of metal ions. This observation was only possible by using spectroscopic methods.

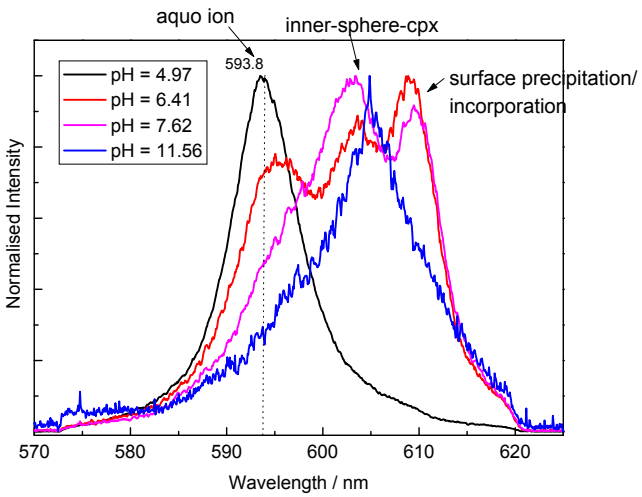

***Figure 10**: TRLFS spectra of the Cm(III) sorption onto gibbsite (0.5 gl/ gibbsite, 2 10^{-7} M Cm(III), 0.1 M $NaClO_4$)*

The interaction of Am(III), Co(II) and Cs(I) with natural apatite and quartz minerals, analyzed by BET, SEM and XRD, ICP-MS/OES for trace impurities and solubility, by sorption experiments in **CTH**. Since the ability to bind metal ions depends both on the structure of the mineral as well as its chemical composition the interpretation of results from sorption studies on in this case especially apatites, can be complicated since they can contain different anionic and cationic substituent as well as small traces of other minerals. The specific surface area however, can in most cases be considered to be the main factor affecting the sorption properties of the apatites. The aim with the work was to provide relevant reference data for work in RTDC-2 on sorption at simulated repository conditions of radionuclides on in-situ grown biofilms on apatite and quartz minerals slides with dimensions 60 × 24 × 0.9 mm. Since sorption can take place via many different mechanisms in this system reference studies on the mineral without presence of biofilm and with better control of specific surface area helps improving the knowledge of this otherwise complex system present in the natural repository environment. Other sorption studies preformed on granite slides from Äspö which contains approximately 25 % quartz and 0.5 % apatite could also be better understood with a better understanding of relevant rock properties obtained from sorption experiments with crushed and sieved pure minerals with different specific surface areas. Titrations using an automatic system monitored by a homemade software, with a combinated Ag/AgCl – glass electrode were performed either by successive additions of acid or base in a suspension of crushed and sieved mineral powders, or with varying specific surface area. Batch sorption experiments on minerals with varying surface and with a synthetic ground water with a composition based on that of a borehole in Äspö 450 m below sea level. The sorption was also checked with batch equilibrium experiments. The system has been studied at 25 °C and all experiments have been performed in a glovebox with controlled atmosphere.

Am(III) is able to form stable complexes in aqueous solution and in near-neutral pH, and it has been proven to readily sorb to soil, mineral, crushed mineral along with colloid and humic substances. Of the investigated radionuclides, ^{241}Am(III), ^{60}Co(II)

and $^{134}Cs(I)$, the distribution values for crushed minerals with different specific surface areas with synthetic groundwater, only Am(III) shows a clear dependence and a variation with specific surface area. It is proven difficult to directly correlate values measured by the batch sorption method for crushed minerals to an intact mineral slide owing to mainly the accessibility of minerals to the aqueous phase, but it may make the obtained data more comparable.

Concerning the selenium retention on clays, **KUL** laid the emphasis on the collection of three additional short term sorption edges on Na illite du Puy and further refining of the modelling. The 2SPNE SC/CE was slightly modified (log K_{wb} = 8.2 instead of 9.0) to describe the titration behaviour. The selenite pH edges and the sorption isotherm could be adequately described using the sorption of $HSeO_3^-$ and H_2SeO_3 on a combination of four sites: strongly and weakly sorbing sites of the weak basic ($\equiv S_{wb}$) and weak acid ($\equiv S_{wa}$) surface sites.

A sorption kinetics study of Se(IV) adsorption on pure illite (Montana), pyrite, and on complex systems, *i.e.*, mixtures of illite/FeS_2, and illite/FeS. The latter were investigated as a possible route (bottom up approach) to understand the complex host rock, *i.e.*, Boom Clay. The results are shown in Figure 11.

In pure Montana illite the rapid adsorption of Se(IV) is followed by a slow unknown process. A similar process occurs in Illite du Puy.

In pure FeS_2 a sorption/reduction process lead to the formation of Se(0), advanced as the final solubility controlling phase in presence of FeS_2 (Breynaert *et al.*, 2008).

In the mixed systems (illite/FeS_2) the kinetics of reduction of Se(IV) by FeS_2 are decreased and metastable plateau concentrations of Se in solution are observed. Solution speciation using SEC, IC, UF (30 kDa) indicated the presence of Se(IV) as major selenium species in solution.

FeS in mixtures of illite/FeS proves to be a more efficient reductant than FeS_2. FeSe is advanced as the solubility controlling phase in presence of FeS (Breynaert *et al.*, 2008). An independent study within RTDC 2.3 leads to the identification by XAS of Se(0) formation in presence of FeS_2 and FeSe formation in presence of FeS.

The results confirm the two competing adsorption processes, which were invoked to explain the selenite reduction in Boom Clay (Bruggeman *et al.*, 2005): (1) A rapid adsorption onto illite and/or FeS_2 is followed by (2) a slow reduction onto FeS_2. The long term Se speciation in Boom Clay is expected to be governed by the presence of reduced Se phases, due to interaction with reducing minerals such as, *e.g.*, pyrite. However the exact nature of the phases formed in real Boom Clay needs to be confirmed experimentally.

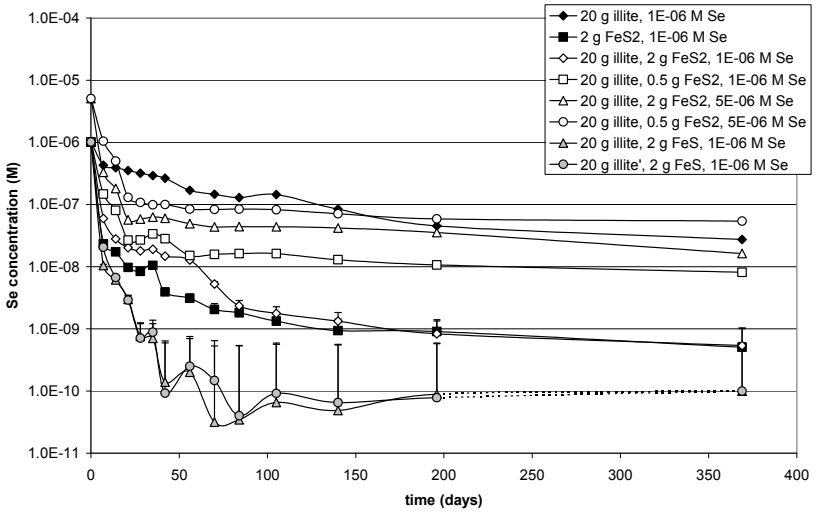

***Figure 11**: Sorption kinetics study of Se(IV) adsorption on pure illite (Montana) and pyrite and on complex systems (Mixtures of Illite / FeS_2 and Illite/FeS).*

Also in the framework of the Boom Clay formation, **SCK-CEN** aims to produce sorption datasets onto this host rock determined under variable geochemical conditions in order to set up a thermodynamic sorption model (TSM), which provides confidence for the selection of radionuclide retention parameters for PA for both non-disturbed and disturbed conditions.

The planned work constitutes of 4 parts for which some are linked or subject of different RTD components in FUNMIG.

1. Acquire site-specific sorption data sets for Am and Th. Interpretation using TSM-GC approach;
2. Identifying, and if possible quantifying, the role of mobile natural organic matter (NOM) on the sorption of Eu, as model for trivalent RN onto Illite, as model component for Boom Clay – (Liu *et al.*, this volume).
3. Upscaling from sorption data obtained on dispersed natural clay systems to confined systems: Relationship K_d – retardation (interlaboratory collaboration). Here is a link between RTDC1 and RTDC3.

Sorption isotherms for both Am(III) and Th(IV) onto Boom Clay (S/L ratio of ~0.01 g/ml) under "normal" in-situ pH and pCO_2 (pH~8.3 and anaerobic conditions with 0.4 % CO_2 atmosphere) conditions were measured in Real and Synthetic Boom Clay water to assess the influence of the dissolved organic matter present in the Real BC water (~100 ppm C). Because colloid formation was given special attention, concentrations were determined for non-filtered (high-speed centrifugation only) and UF (30 kD MWCO) samples.

Current modelling attempts follow the 2SPNE SC/CE approach and are based on Am(III) and Th(IV) sorption data on montmorillonite and illite as model component for Boom Clay. Am and Th sorption edges were measured on montmorillonite and illite to obtain more specific sorption data for refining of the modelling. For the interaction with NOM, a 1:1 RN-NOM surface complexation reaction was currently used, and the NOM

was described by 3 functional groups. The above simple model was not able to describe the available sorption isotherms and needs further refinement.

In order to get answers to the question: "Are sorption data derived from batch tests on dispersed material compatible with those deduced from diffusion experiments on intact rock" (interlaboratory collaboration), sorption and diffusion tests with Cs, Sr and Am were performed. At first instance, sorption of Cs and Sr on dispersed systems was compared to sorption on intact clay disks in order to see if compaction affects the availability of sorption sites. Compaction of the Boom Clay did not have a marked difference on the Cs and Sr sorption and the sorption of Cs and Sr can be described in a mechanistic way using a simple cation exchange model on illite as model component for Boom Clay.

Migration experiments with Cs and Sr of different types resulted in reproducible D_a values and a trustworthy value can be obtained. However, retrieving trustworthy retention parameters was more difficult. Despite these difficulties, the obtained retention values for Cs and Sr from migration experiments were comparable to the data from batch sorption experiments.

As such, the relationship between R and K_d (under the approximation that at low concentrations sorption is a linear and reversible process), seems valid for these elements. For transport modelling purposes, one can therefore introduce experimental measured sorption values or the mechanistic sorption model to simulate the transport without having to change sorption site densities.

However, combining the $D_e/D_p(HTO)$ and sorption data will not result in correct D_a values for ion-exchangeable RN.

As observed on the different clay host rocks, D_e/D_p values are always higher than $D_e/D_p(HTO)$ which is attributed to a "surface diffusion" kind of mechanism.

Am retention in Boom Clay is influenced by the presence of NOM and the migration of Am in Boom Clay is further governed by colloid filtration aspects. First steps in describing the sorption processes of Am onto clay systems in presence of NOM were done but still need further efforts.

Nothing can yet be concluded from these experiments with respect to transferability of batch sorption K_d to migration retardation.

UPC investigated the interaction of thorium(IV) with oxy-hydroxy iron minerals, such as magnetite (Fe_3O_4) and ferrihydrite ($Fe(OH)_3$), through sorption studies and spectroscopic techniques.

Sorption edge for Th(IV) on pure ferrihydrite and magnetite minerals had already been measured in $NaClO_4$ solutions as a function of ionic strength under oxic conditions. Results showed that sorption onto both solids increases with pH while it is independent on ionic strength (Figure 12). The sorption capacity of both solids was very high, the maximum sorption, almost 100 % of Th(IV), occurs at pH higher than 3.5 for ferrihydrite, and higher than 3.0 for magnetite.

In an attempt to model the sorption edges the FITEQL 4.0 code was used and three different models included in the program were tested: non electrostatic model, constant capacitance model, and the diffuse-double layer model. For both minerals, a

very good fitting to the experimental data has been obtained considering a single bidentate complex, which would to coincide with the surface complex postulated on these solids surface in previous spectroscopic EXAFS measurements performed within the project.

The studies performed combining EXAFS spectroscopic techniques with solution chemistry contribute to improve the knowledge of the sorption processes involved in the migration of thorium in minerals potentially presents in the environment.

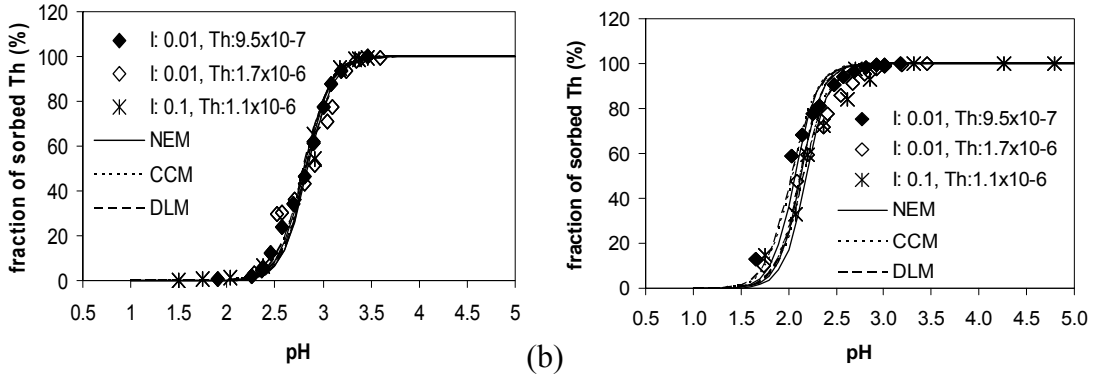

Figure 12. *Sorption of thorium as a function of pH at sorbing concentration of 10 g·L^{-1}. ionic strength in $NaClO_4$ (M) and initial thorium concentration (M) are indicated inside the graphic. Lines: optimized fits using a $(\equiv FeO)_2Th^{2+}$ species and NEM, CCM and DLM models. (a) ferrihydrite, (b) magnetite.*

A mechanistic sorption model for nickel and europium on common gneissic rock types at the coastal regions of the Baltic Sea was developed by **HU** and **VTT**. The most important mineral for sorption on the non-weathered rock types was identified by autoradiographic studies to be biotite. The sorption of nickel and europium on biotite samples and on crushed rocks was determined by **HU** in pH 3 to pH 9 buffered 0.05 M and 0.5 M $NaClO_4$ solutions and in two groundwater simulates. The sorption of Ni on the separated biotite was parallel to the crushed rock, while for europium the sorption on biotite was larger than on rock (Figure 13).

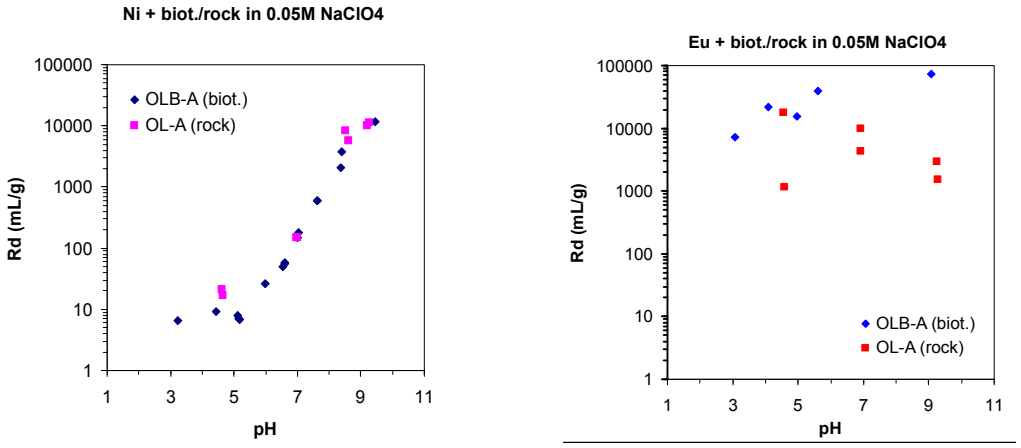

Figure 13: *Sorption of nickel and europium on biotite (OLB-A) and on crushed rock (OL-A, granodiorite) in 0.05 M $NaClO_4$ solution. The R_d values of the rock were calculated according to the biotite content of the rock.*

The modelling of the former results, performed at **VTT** (Figures 14 and 15), while sorption on crushed rock is still under work, and the results will be published later – in the beginning of the year 2009. Modelling consisted of: i) traditional mechanistic sorption modelling by FITEQL: surface complexation and cation exchange sites in 1-pK modelling scheme, mainly by diffuse layer model for surface potential; ii) modern molecular level modelling to support mechanistic sorption modelling and bring deeper info about biotite surface (Puukko *et al.*, 2008). More information can be found in Olin *et al.* (this volume)

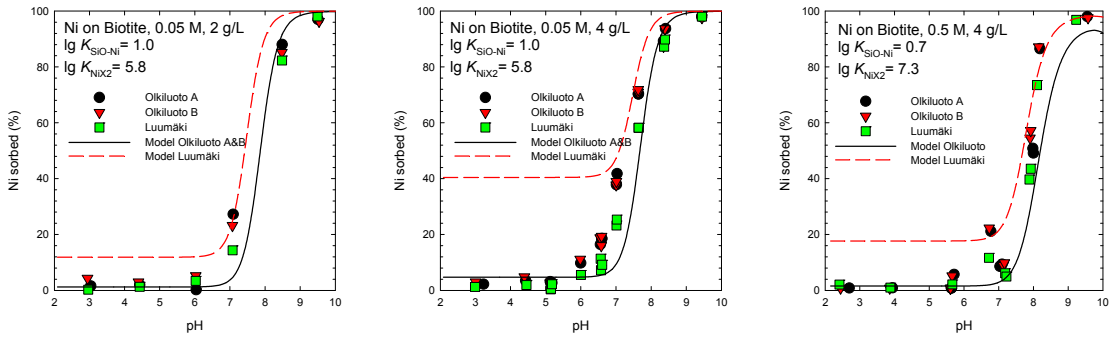

Figure 14*: Adsorption of nickel (% sorbed) on the Luumäki and Olkiluoto biotite. Symbols: experimental, lines: model fits.*

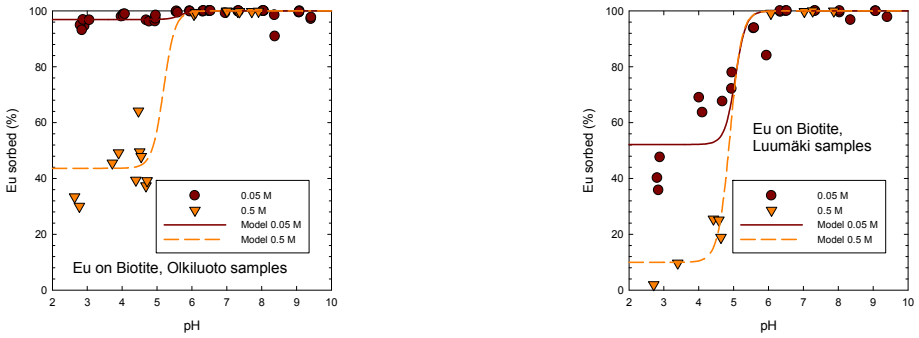

Figure 15. *Eu on biotite: % sorbed; symbols: experimental, lines: model fits.*

WP1.3 - Influence of organics on the retention of radionuclides by minerals

The work is focussed on the understanding of the influence of different organic matter/substances on the retention of radionuclides by mineral surfaces.

The work conducted by **INE**, on the establishment of organic coating, was focused *inter alia* on the characterization sedimentary organic matter in Opalinus clay sample, with synchrotron based Scanning Transmission X-Ray Microspectroscopy (STXM), at the carbon K-edge, and µFT-IR (National Synchrotron Light Source; NSLS, Brookhaven National Laboratories; BNL). As already done on rock microtome sections from the Callovo- Oxfordian argillite (Schäfer *et al.*, in press), residual organic matter in diagenetically overprinted shales or argillites of marine/terrestrial origin still shows some extractable hydrophilic compounds. The Opalinus Clay (OPA) sample (579.19-579.45m) of the borehole Benken was provided by NAGRA. The total organic carbon (TOC) concentration in the clay fraction of the Opalinus clay is < 0.4 wt. %. The untreated rock sample and the clay fraction were embedded in sulfur and ultramicrotomed. An aliquot of the OPA clay fraction was alkaline extracted and yielded ~1.1 wt. % extractable organic material of the TOC pool. Analysis of the OPA microtome section revealed organic matter in regions, where also significant K and Ca absorption indicative for illite/ mixed layer minerals (MLM) intergrown with nanocrystalline carbonate appears (Figure 16). Both clusters identified are very similar and show a low aromaticity with a very low amount of phenol-type functional groups and a high aliphaticity. From the target spectra map the illite/MLM region can be identified with a high certainty ($\sigma = 0.0195$) as most probable source for the alkaline extracted organics. The significant difference in the carboxyl-type groups for the alkaline extracted organic material indicates a higher overall hydrophilicity. The IR spectra extracted from the clay-rich region of the OPA microtome revealed lattice hydroxyl groups of kaolinite and smectite group minerals, a weak OH-stretching feature of trioctrahedral chlorites (3666 cm^{-1}), Si-O or Al-OH vibrations of quartz and/or alumosilicates (1076 cm^{-1}, 1039 cm^{-1}) and carbonates (asymmetrical stretch of CO_3^{2-} around 1426 cm^{-1}). The band at 1163 cm^{-1} can be assigned to the C-C bond in aliphatics and polymeric substances or to a Si-O-C bond, which might indicate an organic linkage to the clay Si-O groups. Characteristic features for organic components include a broad band of phenols, alcohols and carboxylic OH, aromatic CH groups and aliphatic CH_2 and CH_3 bands. Striking is furthermore the rather high transmittance in the carboxylic band region of ketones, acids or

esters indicating a loss of oxygen containing functional groups. Based on these spectroscopic in-situ observations a significant metal complexation capacity of SOC is not expected.

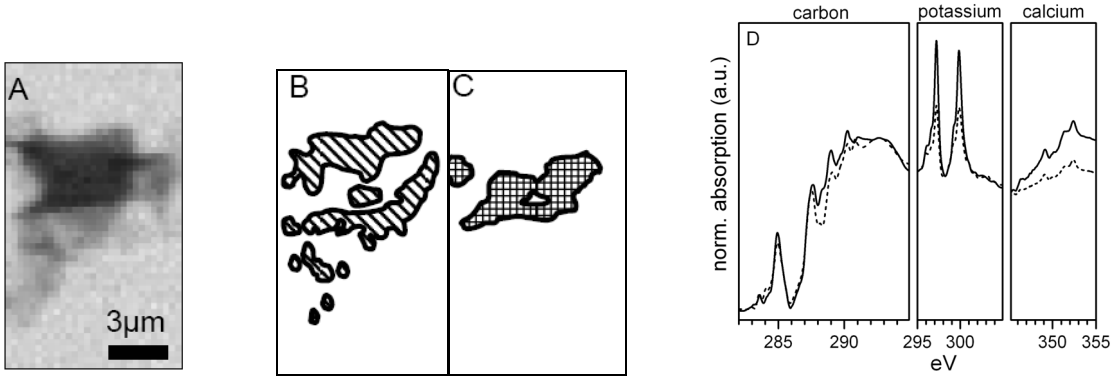

Figure 16. *STXM analysis of the OPA microtome. (A) Absorption image at 280 eV, (B, C) The two cluster regions identified, (D) Spectra of the clusters found (cluster B solid line, cluster C dashed line),*

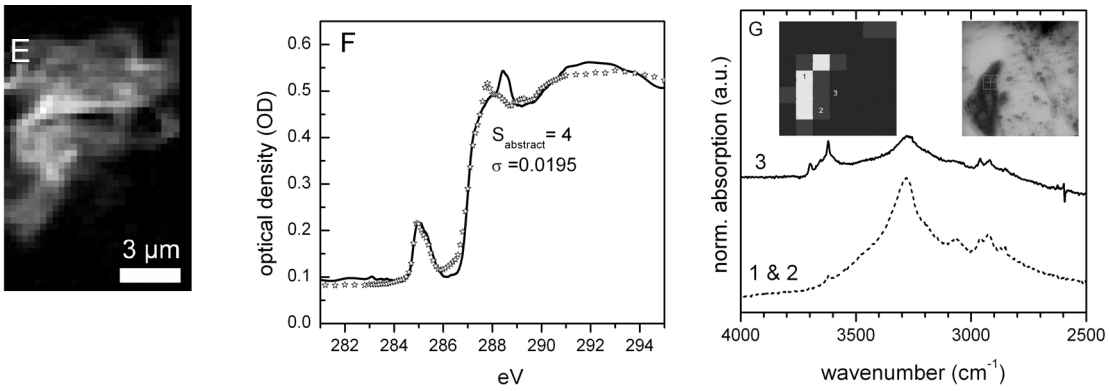

Figure 16*. continued. STXM analysis of the OPA microtome (E) Target spectra map of the STXM data (light grey colors indicate good correlation), (F) Isolated FA target spectra (solid line) and the fit using the first four significant principle components $S_{abstract}$ out of the PCA analysis (open stars), (G) µFT-IR average spectra of the three clusters found by k-mean clustering (visible microscope image and cluster regions inserted; square size 10×10µm).*

UNILOUGH have completed the data gathering and modelling of the interactions of the Fe^{2+} ion with humic acid and kaolinite, montmorillonite and goethite in the ternary systems, in conjunction with **UNIMANCH**.

Binary 'simple' organic ligand systems using EDTA, NTA, ISA, gluconic acid and picolinic acid with Eu^{3+}, Ni^{2+} and Cs^{+} have been completed. The mixed ligand (HA with either ISA, picolinate or EDTA) ternary systems have been completed with Eu^{3+} and Ni^{2+} on all three minerals. In terms of PA, simple organics show interactions with mineral surfaces and radionuclides. These interactions vary considerably from organic to organic and from radionuclide to radionuclide, making predictive modelling difficult.

***Figure 17**: Structure of Picolinic (left) and Gluconic (right) acid.*

The modelling of the humic acid systems using the Linear Additive Model (LAM) and a new quadratic development of the LAM have been completed. In general, the LAM has proved successful in modelling ternary systems when the strength of binding of the radionuclide to the natural organic matter has been strong, *e.g.*, Eu^{3+}, but much less so when the binding is relatively weak, *e.g.*, Cs^{+}. The linear additive model has been used to model systems where sorption of the 'simple' organic to mineral surface has occurred. The 'quadratic' version of the model has been more successful in these scenarios, but there is still work to be done to improve the models, if they are to be used successfully in predictive scenarios. More information can be found in Warwick *et al.* (this volume).

The Ligand Charge Distribution (LCD) model is applied by **WU** to describe the effects of the presence of FA on Ca or Cu adsorption to goethite to overcome the limitation of LAM. Adsorption of Ca to goethite in the presence of FA deviates greatly from the simple sum, whereas for Cu the deviation is much smaller. The LCD model can give good description of the data. Results show that for Ca, the electrostatic interactions are the most important to explain the effects of FA. For Cu, both the electrostatic interactions and formation of cation-bridging type ternary complexes (goethite-Cu-FA) are important. Because there is more spatial charge overlap between Ca and FA than between Cu and FA, the effects of FA on Ca adsorption are stronger than for Cu. Presence of HA and FA decreased both phosphate and arsenate adsorption to goethite. This leads to a strong increase of solution concentration of phosphate or arsenate. Effects of the relatively small FA particles are much stronger than the relatively big HA particles. The LCD model can predict this difference. The stronger effects of FA are ascribed to the closer location of FA to the surface than HA, which leads to stronger interactions with phosphate or arsenate ions adsorbed (see Figure 18). More information can be found in Weng *et al.* (2008; 2007).

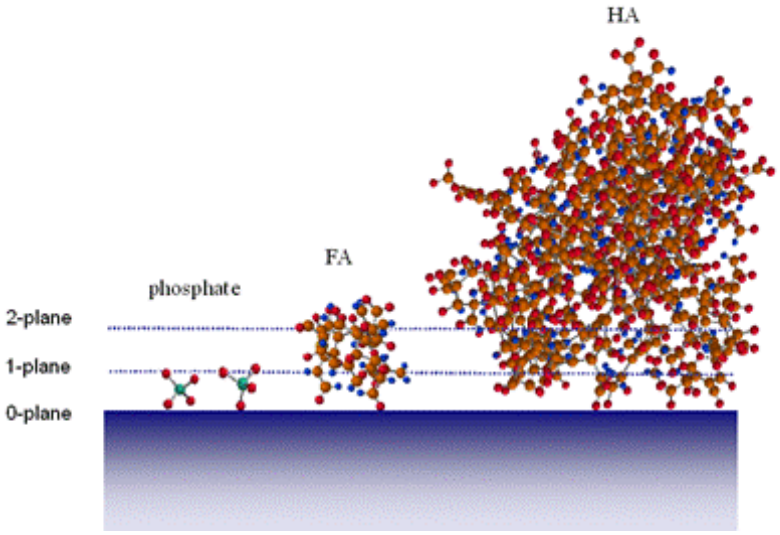

***Figure 18**: Differences in the location of small oxyions, FA and HA at the surface.*

UNIMANCH has continued to study the behaviour of radionuclides (RN) in humic (HA) ternary systems (HA/RN/mineral). The experimental work has been extended to include the clay phases montmorillonite and bentonite. On the whole, kinetic effects appear to be less important in these systems with apparent equilibrium established within a few days. However, as for the other phases that have been studied, there is multi-component behaviour. The ternary system speciation model has been applied successfully to these systems.

The work with ^{237}U and ^{237}Pu tracers (in collaboration with Dubna), allowing low RN concentrations to be studied ($<10^{-10}$ M), has been extended to the bentonite ternary system. Comparison with higher U concentration systems has shown differences at high pH, due to carbonate/U ratio, but there appears to be no significant effect of U concentration on the U-HA interactions in the ternary system, suggesting that data determined at higher U concentrations may be used to predict the effect of HA on U behaviour in the environment at low concentrations for this system at least.

The ternary system work over the last 4 years has shown that for all mineral systems there is multi-component behaviour, which has a significant effect upon RN solid/solution partition. Therefore, the mechanisms responsible for these effects have been studied by Asymmetric Flow Field Flow Fractionation (AFFF). For all systems (quartz sand, iron oxides and clays), there is evidence of significant mass fractionation of the humic. There is initial, rapid sorption of low molecular weight aromatic components (with material of mass less than 2000 Da preferentially sorbed), which results in a shift of humic average mass to higher values. Subsequently, there is slower sorption of more aliphatic material with larger masses, which causes the average mass to shift back to lower values. Comparison of the behaviour of humic and RN in ternary batch experiments with the AFFF data strongly suggest that their sorption is directly related to this mass fractionation (Figure 19).

Given that mass fractionation seems to be important, size fractions have been prepared by ultrafiltration, and the effect on sorption in the ternary systems studied. The

size fraction does appear to have an effect upon the equilibrium solid/solution partition of the RN, but not on the non-exchangeable dissociation rate constant, which is the critical parameter for RN transport. Finally, we have used AFFF to study the changes in size distribution with time for the size fractions. Although there are no significant changes in size distribution over a few weeks, there are after 6 months. More information can be found in Pitois *et al.* (this volume)

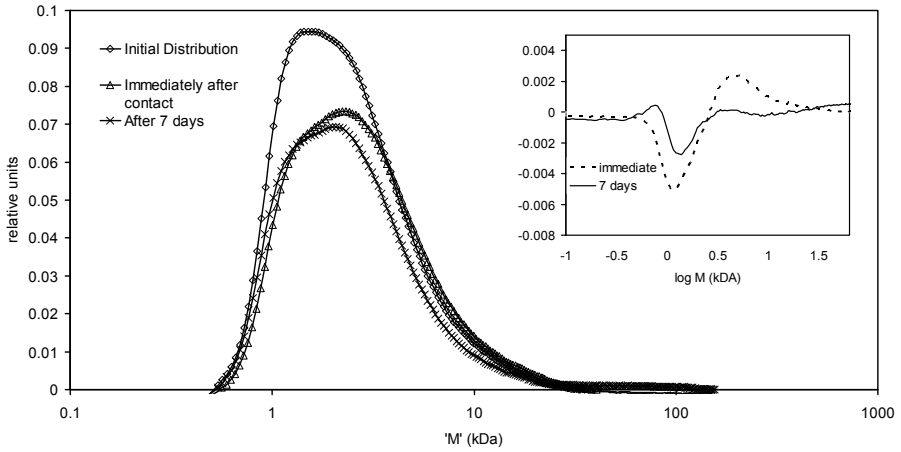

Figure 19*: Fractionation of humic acid on sorption to montmorillonite: mass distributions determined by AFFF before sorption, immediately afterwards and following 1 week, and relative change in distribution (inset: plot above 0 = preferentially left in solution). Initially, smaller molecules are preferentially adsorbed, but with time there is a shift in fractionation as larger species are sorbed.*

WP1.4 - Formation of solid solutions and secondary phases, including retardation of anions

The work is focussed on the thermodynamic definition of the standard state of solid solution and on experimental characterization of solid solution and secondary phases formation.

Pyrite (FeS_2) is a mineral phase often present as inclusions in clay or crystalline rock formations. Moreover, it turns out to be a sorption/co-precipitation sink for certain radionuclides in deep geological disposals. Se(-II) sorption onto pyrite was performed at **ARMINES** under controlled conditions (Eh, pH). A sorption process was first observed, which was then followed by a surface redox reaction leading to Se(0) (Figure 20). Selenium(0) is therefore the main species to consider in the modelling.

ARMINES also aimed to provide sorption data for high solid-to-liquid ratios to assess the effect of compaction (580-1400 kg/m^3) on the sorption properties of clay minerals for Se(IV). Two model clay minerals have been studied: illite du Puy and a synthetic Na-montmorillonite. Experiments were performed as a function of the pH, selenite loading and solution composition. We propose a simple model describing selenite retention by clay materials. No compaction effect was observed within this range of mass to solid ratios (Figure 21). More information can be found in Montavon *et al.* (2009).

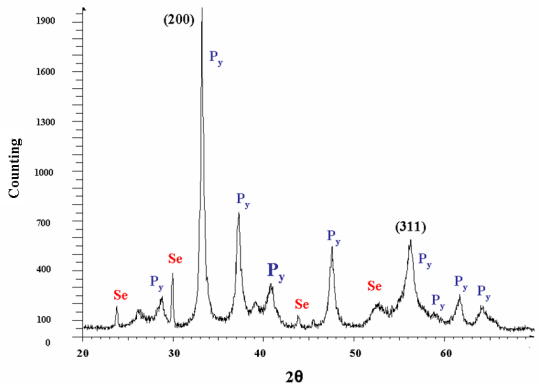

***Figure 20**: XRD pattern of Se-reacted pyrite (Py) and Se for elemental selenium. Experimental conditions: [Se/FeS_2] = 0.1 mmol/g, pH 6.6 and under -360 mV for 8h.*

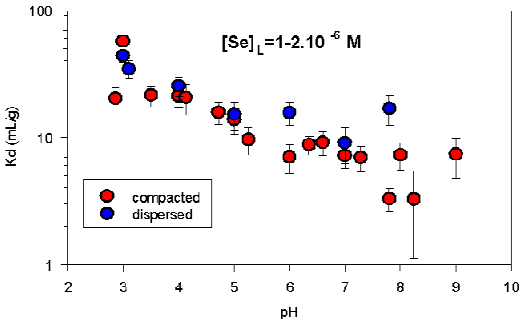

***Figure 21:** Comparison between K_d values obtained in dispersed and compacted states.*

INE attempts to calculate thermodynamic parameters for the neptunium(V) uptake by calcite show that it is crucial to precisely know the substitution mechanism. To gain more knowledge about this issue further structural investigations have been conducted. Neptunium(V) doped single crystals have been synthesized and investigated by NIR spectroscopy and polarization dependent EXAFS spectroscopy. First X-ray standing wave measurements have been performed at the INE-Beamline for actinide research.

NIR spectra show that neptunyl incorporated into calcite shows an absorption peak at 1008 nm. The molar extinction coefficient could be estimated to be 60 M^{-1} cm^{-1}. This indicates that the equatorial surrounding of neptunyl in calcite is not perfectly centrosymmetric. Polarization dependent EXAFS measurements in five different measurement geometries indicate that neptunyl coprecipitated with calcite at a calcite 104 face might show a preferential orientation and that the coordination polyhedron is a distorted tetragonal bipyramid. X-ray standing wave measurements at the INE-Beamline at ANKA on calcite reference samples show that elemental positions relative to the calcite unit cell can be determined. But the neptunyl doped samples investigated so far turned out to not be suitable for these kinds of measurements.

References

Bradbury M.H., Baeyens B. (1997): A mechanistic description of Ni and Zn sorption on Na-montmorillonite.2. Modelling, *Journal of Contaminant Hydrology*, **27**, 223.

Breynaert E., Bruggeman C., Maes A. (2008): XANES-EXAFS analysis of Se solid phase reaction products formed upon contacting Se(IV) with FeS_2 and FeS, *Environmental Science and Technology*, **42**, 3595.

Bruggeman C., Maes A., Vancluysen J., Vandermussele P. (2005): Selenite reduction in Boom Clay: effect of FeS_2, clay minerals and dissolved organic matter, *Environmental Pollution*, **137**, 209.

Ekberg C., Knutsson A., Brown P.L. (2008): Studies of the complexation behaviour of thorium with phosphates. In *3rd Annual Workshop Proceedings- 6th EC FP-FUNMIG IP, NDA Report* (G. Buckau, B. Kienzler, L. Duro, V. Montoya, & A. Delos Eds.), p. 299. Nuclear Decommissioning Authority.

Liu D.J., Bruggeman C., Salah S., Maes N. (submitted): Influence of Boom Clay organic matter on the adsorption of Eu^{3+} by illite. In *Final Annual Workshop Proceedings- 6th EC FP-FUNMIG IP, Forschungszentrum Karlsruhe Report* (G. Buckau, B. Kienzler, & L. Duro Eds.), p.

Missana T., Alonso U., García-Gutiérrez M., Albarran N., López T. (submitted): Europium adsorption onto FEBEX smectite. In *Final Annual Workshop Proceedings- 6th EC FP-FUNMIG IP, Forschungszentrum Karlsruhe Report* (G. Buckau, B. Kienzler, & L. Duro Eds.), p.

Montavon G., Guo Z., Lützenkirchen J., Alhajji E., Kedziorek M.A.M., Bourg A.C.M., Grambow B. (2009): Interaction of selenite with MX-80 bentonite: Effect of minor phases, pH, selenite loading, solution composition and compaction, *Colloids and Surfaces A: Physicochemical and Engineering Aspects*, **332**, 71.

Olin M., Puukko E., Puhakka E., Hakanen M., Lindberg A., Lehikoinen J. (submitted): Sorption on biotite. In *Final Annual Workshop Proceedings- 6th EC FP-FUNMIG IP, Forschungszentrum Karlsruhe Report* (G. Buckau, B. Kienzler, & L. Duro Eds.), p.

Pitois A., Abrahamsen L.G., Ivanov P., Bryan N.D. (submitted): Humic Acid Fractionation Studied by Asymmetric Flow Field Flow Fractionation. In *Final Annual Workshop Proceedings- 6th EC FP-FUNMIG IP, Forschungszentrum Karlsruhe Report* (G. Buckau, B. Kienzler, & L. Duro Eds.), p.

Puukko E., Olin M., Puhakka E., Hakanen M., Lindberg A., Lehikoinen J. (2008): Sorption of nickel and europium on biotite. In *3rd Annual Workshop Proceedings- 6th EC FP-FUNMIG IP, NDA Report* (G. Buckau, B. Kienzler, L. Duro, V. Montoya, & A. Delos Eds.), p. 265. Nuclear Decommissioning Authority.

Rydberg J. (1969): Solvent Extraction Studies by Akufve Method.1. Principle and General Problems, *Acta Chemica Scandinavica*, **23**, 647.

Schäfer T., Michel P., Claret F., Beetz T., Wirick S., Jacobsen C. Radiation sensitivity of natural organic matter: Clay mineral association effects in the Callovo-Oxfordian argillite, *Journal of Electron Spectroscopy and Related Phenomena*, In Press, Corrected Proof.

Vercouter T., Casanova F., Calvo A., Amekraz B., Moulin C. (submitted): Influence of silicate ions on Eu(III) aqueous speciation. In *Final Annual Workshop Proceedings- 6th EC FP-FUNMIG IP, Forschungszentrum Karlsruhe Report* (G. Buckau, B. Kienzler, & L. Duro Eds.), p.

Warwick P., Lewis T., Evans N., Bryan N.D. (submitted): Effects of EDTA on Sorption of Eu(III) and Ni(II) to Some Minerals at pH 6. In *Final Annual Workshop Proceed-*

ings- 6th EC FP-FUNMIG IP, Forschungszentrum Karlsruhe Report (G. Buckau, B. Kienzler, & L. Duro Eds.), p.

Weng L., Van Riemsdijk W.H., Hiemstra T. (2008): Cu^{2+} and Ca^{2+} adsorption to goethite in the presence of fulvic acids, *Geochimica et Cosmochimica Acta*, **72**, 5857.

Weng L.P., Van Riemsdijk W.H., Hiemstra T. (2007): Adsorption of humic acids onto goethite: Effects of molar mass, pH and ionic strength, *Journal of Colloid and Interface Science*, **314**, 107.

RTD COMPONENT 2

Thorsten Schäfer
Institut für Nukleare Entsorgung (INE), Forschungszentrum Karlsruhe, P.O. Box 3640, 76021 Karlsruhe, Germany
schaefer@ine.fzk.de

Introduction

The overall objective of RTD Component 2 is to improve our knowledge on radionuclide retention processes which are currently not well understood in order to judge if they have to be considered for predictive analysis of the far field of geological repositories. The main topics dealt with in RTD Component 2 are the effect of the presence of inorganic/organic colloids, mineral redox processes and several aspects of microbiologically mediated processes on the transport of radionuclide. Knowledge gained in RTDC-2 will be transferred as direct input parameters for the host rock specific RTDC's 3-5. Scientific work in the nanometer resolution range with trace radionuclide concentrations expected to be found in far-field environments are a big analytical challenge and progress of scientific process understanding therefore relies *inter alia* on further development of analytical methods as well as on molecular modeling approaches. RTD Component 2 has been structured in 4 work packages and results obtained in the last project year are briefly summarized for each WP.

After four years of IP FUNMIG a huge experimental work program focused on the less well established process of (1) inorganic/organic colloids, (2) redox processes and (3) microbiological processes. The interesting question to be addressed is, if a couple of key questions regarding these above mentioned processes have been answered with the gained knowledge in and outside of IP FUNMIG or in other words if we have moved part of the less-established processes in well established processes.

Concerning the colloid issue, if we ask the question of the presence of colloids in natural far-field environments of potential repository sides, clearly in crystalline rocks as well as in plastic clay formations colloids have been found. The work within FUNMIG reduced the uncertainty concerning the maximum natural colloid concentration found in crystalline environments by additional site investigations and optimization of the sampling procedure to exclude artifacts. The results show that in all sites investigated so far the upper colloid concentration limit ranges around 1 $mg \cdot L^{-1}$ (laser-induced breakdown detection; LIBD detectable colloid fraction). In clay formations the colloids are dominated by organics and in indurated clays a significant fraction of dissolved organic carbon (DOC) belongs to low molecular weight compounds and not colloids with a molecular size < 500Da. For plastic clays (Boom Clay formation) comparison between batch-type studies bringing the whole organic inventory in suspension and the pore water sampled in the HADES underground laboratory gives indications that the pore-size cut-off is ~300 kD.

Concerning additional colloid sources from the near-field it has clearly demonstrated in crystalline host rocks environments that higher colloid concentrations can occur through bentonite erosion. A large parameter screening has been performed within FUNMIG concerning pH, ionic strength, contact aperture, bentonite type and exchangeable cation composition on the erosion rate. However, implementation into a model is still pending and was not developed within FUNMIG.

Furthermore, we could ask the very fundamental question, if colloids are stable in far field environments and which parameters are affecting inorganic colloid stability and filtration of colloids in a crystalline host rock.

Colloids can be stable in groundwater systems of crystalline rocks, but their stability is a direct function of the divalent cation concentration. There is a consensus that for $[M^{2+}]$ > 1mmol bentonite colloid aggregation independent of the pH value is expected. Experiments on the effect of fulvic acids have shown that near the critical coagulation concentration (CCC) of 1-3 mmol $[M^{2+}]$ bentonite colloid stability could be increased. For purely monovalent background electrolytes a strong pH dependent colloid stability could be observed and in monovalent dominated systems with $[M^{2+}]$ > 1mmol cation exchange processes seems to trigger the colloid stability. Modeling of cation exchange processes with contact water and composition of exchangeable cations on the bentonite seems to be a route to model bentonite erosion.

The next question one could address is if colloids are mobile and which are the main factors controlling their mobility in far-field environments.

Even after four years of FUNMIG this questions is not easy to answer. In crystalline host rocks migration experiments have shown that colloids can be mobile, but their mobility strongly depends on parameters like shear zone structure/heterogeneity, surface area/roughness, surface charge heterogeneity, residence time and colloid size. A clear answer which processes are the dominant ones might be available after the data sets of FUNMIG have been thoroughly evaluated and checked for consistency. The current colloid transport models available in the scientific community have implemented filter theory, attachment/detachment rates based on measured batch-type data or from DLVO-theory predictions. New models for colloid transport have not been developed within FUNMIG, but this would have been also premature as the colloid mobility controlling processes have not clearly been identified. For claystone formations (indurated or plastic) recent pore water colloid size distribution is assumed to reflect the mobile fraction. A direct connection of the measured colloid size cut-off via porewater analysis to the connected porosity of the clay stone formation (indurated, plastic or compacted bentonite buffer/backfill) might be realized in the near-future with the development of high spatial resolution nano- tomography methods coming up.

The last key question that should be mentioned here is if radionuclides are interacting with colloidal species and if this radionuclide uptake is irreversible.

FUNMIG has contributed with a huge dataset of metal complexation on organic matter (humic and fulvic acids), but it has also been shown that for some site investigation programs colloid size dependent (and site specific) complexation constants are needed (Boom Clay). For this question we can also directly take credit of the work performed in RTDC-1. Concerning the reversibility aspect metal desorption kinetics are observed for both organic and inorganic colloids. Natural REE-HA associates for example show

significantly slower desorption kinetics than REE added to humic substances in the laboratory, the mechanistic understanding pending; modeling approaches sometimes use a irreversible bond fraction for the observation period. Reversibility kinetics have also been seen for bentonite colloid associated radionuclides. Reasons for strongly kinetic hindrance in the case of tetravalent actinides has to be investigated by new spectromicroscopic techniques to unravel the underlying process. Desorption kinetics have been implemented in various transport codes based on laboratory batch-type derived desorption data.

Comparable key questions can be addressed for the redox processes investigated under WP 2.3 and biogeochemical processes investigated in WP2.4, *inter alia*:

Which processes actually govern redox changes in the far-field (and near field), are redox processes kinetically hindered for Se species? Which is the actual redox state of radionuclides when they leave the near-field? Is it possible to map the expected microbial activity in the future environment of a repository?

Some of the key questions will be addressed in the Special Issue manuscripts of Applied Geochemistry and extended abstract are given in this proceedings volume.

The aim of this chapter is to summarize the contributions of the different research organizations involved in RTDC-2 for the work carried out in the final year of FUNMIG on the basis of the work package structure.

Advances within the work packages

WP2.1 - Activities in 2008

In **WP 2.1** the formation, migration and transport processes of inorganic colloids are investigated under near-natural conditions. Objective is a detailed process understanding and the determination of the fundamental thermodynamic parameters for the quantification of mineral surface interaction mechanisms and actinide sorption/desorption kinetics of inorganic colloids in relevant far-field systems. In the fourth project year only partner **FZK-INE** performed active work in this work package.

The scenario referred to in this particular study of WP 2.1 is described in detail in SKB (2006)[1] chapter 10. Summarizing SKB (2006) a failure mechanism that cannot be ruled out given the reference evolution of the repository is the case were the buffer erodes and subsequent enhanced canister erosion due to advective conditions takes place. In this failure mode both the canister and buffer are by-passed. As this failure mode only will occur in deposition holes with high flow rates, it will additionally correlate to low geosphere retention. Two contributions to the outward radionuclide transport can be distinguished (a) an instantaneously accessible fraction of radionuclides that is assumed to be rapidly dissolved in the water void volume and subsequently flushed out of the canister and (b) contribution from the fuel dissolution, where flow rates are in general sufficiently high to flush out all congruently released radionuclides (concentration limit become not effective). Under the given scenario described above a mass loss of 1,200 kg buffer to a fracture intersecting the deposition hole was calculated leading to conditions where advective flow in the buffer must be considered (SKB, 2006). Ac-

cording to Neretnieks (2006)[2] (chapter 4.2) a mixing zone between the diffusion controlled unaltered buffer and the advective controlled flow in the fracture of the buffer will establish and the canister corrosion products including radionuclides will be influenced by this "mixing zone". Therefore, the studies of **FZK-INE** conducted within WP 2.1 directly explore the consequences of the advection/corrosion failure mode on radionuclide speciation.[3]

In the fourth project year experimental work on colloid generation by erosion of compacted bentonite under different geochemical conditions, the interaction of colloids with mineral surfaces and radionuclide bentonite sorption reversibility studies in the presence of fracture filling material were finalized. Bentonite colloid generation was investigated for mono- and divalent electrolytes (Na^+, Ca^{2+}) with various ionic strengths, pH and filter pore sizes (2 µm, 10 µm, 100 µm). For ionic strengths lower than the critical coagulation concentration (CCC) a colloid generation can be confirmed. The strong pH dependency of colloid stability in the sodium system previously investigated in coagulation experiments was confirmed in the colloid generation experiments presented in this study. A filter pore size dependent colloid generation mechanism could not be observed in the course of this study. In all experiments the colloid concentration reaches with time a plateau value. Contact water exchange leads to a rapid neo- formation of colloids reaching again a plateau value.[4] Interaction of colloids (carboxylated latex spheres as model colloids) with several mineral surfaces (Quartz, Muscovite, Feldspar and Apatite) has been studied with AFM colloid probe technique.[5] The experiments are carried out by varying the pH from 2-10 at constant ionic strength. Relatively strong attractive forces are measured at pH values close to or below the expected pH_{pzc} of the mineral surface. In addition, the influence of Eu(III) and Ca(II) on the colloid-mineral surface interaction is investigated (see Fig. 1). Depending on pH and mineral surface, an increase of attractive forces is observed in presence of Eu(III) and Ca(II). Results show that the interaction of colloids with mineral surfaces is mainly determined by electrostatic interactions.

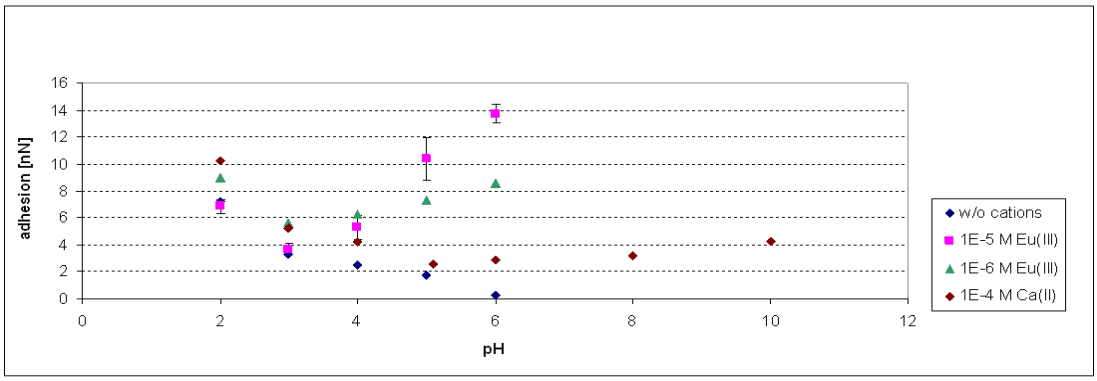

Figure 1. *Measured adhesion forces of carboxylated latex spheres on muscovite using AFM colloid probe technique*

Beside the work mentioned above also advances in colloid analysis techniques were obtained and the LIBD s-curve method was successfully applied to resolve size dispersion effects during the migration of Febex bentonite colloids (<200 nm) in column experiments.[6]

WP2.2 - Work package 2.2 activities within the year 2008

In **WP 2.2** the formation, migration and transport processes of organic/humic colloids are investigated. The main objective of this work is to provide process understanding and a fundamental thermodynamic basis for the interaction of humic colloids with radionuclides. This includes understanding of the kinetically behavior of complexation. The work described here is aimed at obtaining a thermodynamically sound description of the metal ion humic matter interaction process and an evaluation of the interactions between organic colloids and radionuclides.

The interactions of actinide ions with humic substances are of great interest to answer questions concerning the mobility and speciation of actinide ions in the natural environment. But, the nature of complexes formed between humic substances and actinide ions is still in focus of ongoing investigations. The heterogeneity of humic substances makes it very often difficult to get reliable data from applying known analytical tools. Therefore, a fundamental understanding of humic substances (HS) is needed. A promising approach to address certain properties of HS is to use suitable compounds to model the behavior of humic substances.

During the last year of FUNMIG partner **UPPC** used polymer substances as ligands to model the polyelectrolyte behavior of HS. As model polymers poly (acrylic acid) (PAA), poly (4-styrene sulfonic acid) (PSSA) and poly (4-styrene sulfonic acid co maleic acid) (PSSACMA) were used. With these types of polymers the whole range of polymers consisting of aliphatic subunits (PAA), of aromatic subunits (PSSA) and a polymer build up of both, aliphatic and aromatic subunits (PSSACMA) could be spread. Lanthanide ions (Eu^{3+} and Tb^{3+}) have unique luminescence properties in aquatic solutions and were used as luminescence probes.

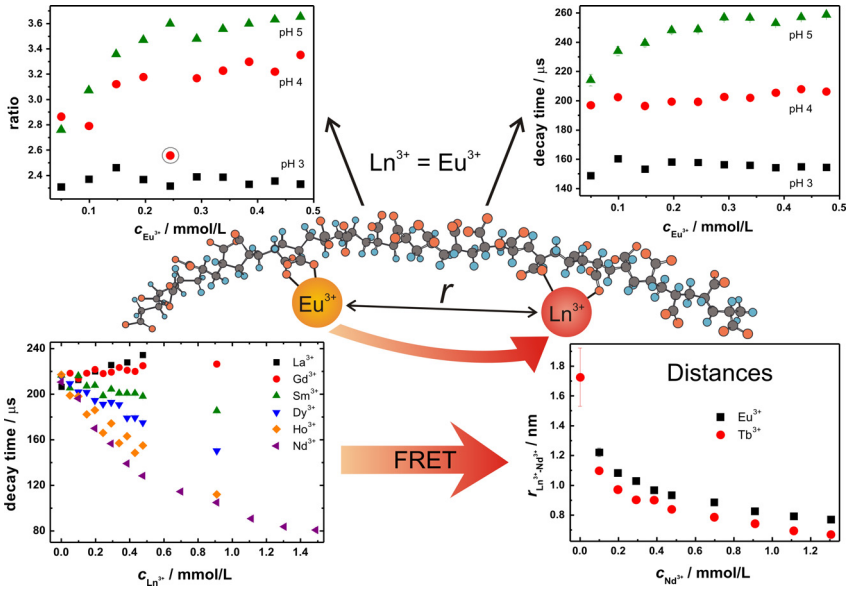

Figure. 2. *Schematic illustration of the spectroscopic approach used by partner* ***UPPC*** *as detailed in the text.*

In one set of experiments **UPPC** had a look on the interactions between different lanthanide ions complexed to the same polymer. From these lanthanide-lanthanide interactions one can deduce distances between these lanthanide ions complexed to a polymer chain making use of the intra-lanthanide energy transfer and applying the Förster resonance energy transfer (FRET) approach. First, Eu^{3+} and Tb^{3+} were added to a solution of PAA, respectively. To these solutions of the Eu^{3+}/Tb^{3+} PAA complexes, different lanthanide ions (from Lanthanum to Holmium) were added. As a result, the luminescence decay time of luminescence probes (Eu^{3+} or Tb^{3+}) were decreased. The decrease in luminescence decay time due to the inter-lanthanide energy transfer was used to calculate distances between Eu^{3+} and Tb^{3+} bound to the polymer.

In a further set of experiments the impact of metal loading and pH change on the macromolecular structure of the polymers was the aim of our studies. Here, PAA solutions at different pH were prepared. Eu^{3+} was added to these solutions and the time-resolved luminescence emission of Eu^{3+} was measured. Based on these data, the binding of the Eu^{3+} and the subsequent effects on the conformation of the polyelectrolyte could be monitored. As PAA at a high degree of ionization (pH 5) has a more stretched form because of the intra-molecular repulsion of the negative charges, the intra-molecular repulsion decreases as the pH decreases by neutralizing the anionic charges. Hence, the conformation changes from a stretched to a more folded form. This neutralization of deprotonated carboxylic groups can also be achieved by metal ions like lanthanide ions. Contrary to protons, lanthanide ions possess the possibility to act as bridging unities. This bridging can occur intra-molecular by linking spatially near parts of the same polymer chain or inter-molecular by linking different polymer chains. These changes in binding environments become accessible by measuring the luminescence decay time or calculating the intensity ratio r (quotient of the intensity of the $5D_0 \rightarrow 7F_2$ to the intensity of the $5D_0 \rightarrow 7F_1$ transition). As a result, differences between binding of protons and

lanthanide ions on the macromolecular conformation, e.g., intra- and inter-molecular bridging and association reactions were found.

The work of **SAS-IIC** has focused throughout the FUNMIG project on the quantum chemical prediction and interpretation of NMR spectra of lanthanide/actinide complexes. New theoretical methods for relativistic calculations of NMR chemical shifts and nuclear indirect spin-spin couplings at the four-component Dirac-Kohn-Sham level were developed, programmed and tested.[7,8] These methods are based on the use of restricted magnetically balanced basis sets and they provide a state-of-the-art approach for calculation of NMR parameters of heavy element compounds. In parallel, SAS-IIC continued to apply the developed previously techniques to study structure of lanthanide-humic acids complexes in solution.

Since the experimental NMR spectroscopic data for lanthanide complexes with humic acids are very scarce and incomplete, we switched our efforts to model complexes. Experimental work was devoted to ^{1}H and ^{13}C paramagnetic NMR chemical shifts (D_2O, 25°C, pH=5.5) in lanthanide $Ln(SSA)_3^{3-}$ complexes (Ln = Dy, Ho, Er, Tm, Yb), where SSA = 5-sulfosalicylic acid. The lanthanide induced shifts (LIS), as obtained in PNMR study, were surprisingly small (up to 8 ppm on ^{1}H and 59 ppm on ^{13}C for Dy complexes). That made the major goal – to extract the information about complexation of lanthanides/actinides with humic acids from NMR spectra with the help of quantum-chemical calculations more problematic. Further experimental studies with the enriched ^{17}O and ^{13}C nuclei of carboxylate groups of the salicylic and humic acids are desirable but lie outside of the partner SAS-IIC capacity. To judge about the accuracy of new theoretical approaches for calculations of NMR parameters of lanthanide complexes, better suited (more rigid) compounds were required. Higher affinitity of alkylated 2,6-di(1,2,4-triazin-3-yl)pyridines (BTP) towards trivalent actinides An(III) over lanthanides Ln(III) plays an important role in nuclear waste reprocessing. Why BTP is so effective compared to other aza-aromatic ligands, such as terpyridine, is nevertheless still unclear. Recently, joint activities of SAS-iic, Laboratory of NMR spectroscopy in Bratislava and INE-FZK resulted in combined experimental and theoretical studies of lanthanide complexes with soft and hard organic ligands. The theoretical results[9] clearly indicated that NMR shifts of ^{15}N nuclei in BTP, bounded to the diamagnetic metal center (Y^{III}, La^{III}, Lu^{III}, Ac^{III}), give the most characteristic signals. Furthermore, SAS-IIC found out that the Fermi contribution to the paramagnetic ^{1}H-NMR shifts in complexes of BTP with "isoelectronic" Gd(III) and Cm(III) is considerably larger in $[Cm(BTP)_3]^{3+}$, thus revealing more covalent character of Cm(III)-N bonds compared to the Gd(III)-N, although bond lenghts are almost identical in these complexes. The predicted changes in ^{15}N-NMR shifts in BTP ligand upon complexation with Y(III), La(III) and Lu(III) were experimentally proved and demonstrated rather high sensitivity of those shifts to the nature of central metal ion. An excellent accord between theoretical and experimental results showed a legitimacy of used quantum-chemical methods for prediction/interpretation of NMR shifts on ligand atoms in lanthanide/actinide complexes.

The fractionation of humic substances (HS) on mineral surface has often precluded the interpretation of radionuclides' sorption results in ternary systems, *i.e.*, metal-humic-mineral. In most cases the additivity rule of the systems does not work. This phenomenon is thought to be the consequence of preferential sorption of certain classes of molecules from the humic mixture, most certainly aromatic molecules, leav-

ing other classes in solution.[10] It has also recently been shown by partner **CEA** that the chemical neighbouring of Eu(III), probed by time-resolved laser induced luminescence, was different in pristine HS and with samples previously contacted with a mineral surface.[11] This change in the composition and maybe of structure of the Eu(III) complexing sites might be a clue to understand the difficulties in interpreting the ternary systems.

The aim of **CEA** in this project year was to particularly look on the structure of the Eu(III) luminescence spectra, in pristine HS and in sample which was previously submitted to sorption on α-alumina. Clear modifications of the chemical environment of Eu(III) was evidenced in humic extracts which was submitted to sorption on α-Al_2O_3. These modifications revealed a change in the interaction intensity and in the symmetry around the Eu(III) ion. These changes could be a clue to better understand the deviation from the additivity rule of binary systems for the study of ternary systems metal-humic-mineral.

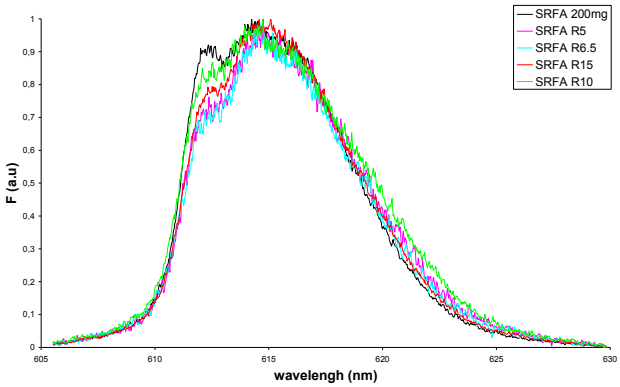

Figure. 3. *$^5D_0 \rightarrow {}^7F_2$ luminescence spectra of Eu(III) in SRFA (10^{-5} mol_{Eu}/L, 200 mg_{SRFA}/L, pH=5, I=0,1 M) and in four supernatants after sorption on α-alumina ($pH_{sorption}$=6, pH_{TRLS}=5); for every spectrum 5 × 10^{-3} mol_{Eu}/g_{HS}.*

A study of the luminescence properties of the Eu(III) implied in HS complexes at pH=5 was undertaken. Seven different extracts were contacted with Eu(III). It is shown that terrestrial extract on one hand, and aquatic extracts on the other hand, do seem to induce inner coherent luminescent properties of Eu(III) within each group.

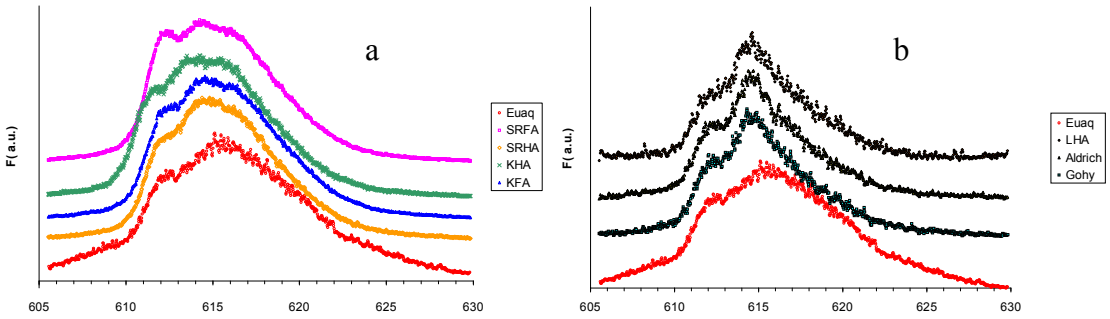

Figure 4. *Eu(III) $^5D_0 \rightarrow {}^7F_2$ transitions in 0.1 M $NaClO_4$ at pH=5, λ_{exc} = 394 nm, D=10 µs, W=300 µs, , 1800 lines mm^{-1} grating of aqueous 10^{-5} mol/L Eu^{3+} (○), Eu (III) in SRFA (□), SRHA (◇) (a) KHA (×), KFA (△) (a),GohyHA (■), PAHA (▲), LHA (◆) (b).*

In this work, it can be seen that even if humic extracts are diverse in essence, similarities can be found for the chemical environment of Eu(III)-HS complexes. The loss of symmetry compared to Eu^{3+} seem comparable for all the sample, nevertheless differences between two group of HS samples can be distinguished from the widths of

the transition and from shoulders reflecting the ligand splitting. It seems that 'terrestrial' extracts, do provide a similar chemical environment for the complexation of Eu(III) in term of crystal ligand splitting. Aquatic extracts do provide a different but also inner consistent chemical environment which can be slightly less symmetric compared to 'terrestrial' samples.[12]

The partner **NRI-REZ** has used the MALDI-TOF MS (Matrix Assisted Laser Desorption/Ionization – time of flight mass spectrometry; Masaryk University Brno) method to identify the distribution of molecular weights and molecular size for different humic acids (HA) from the Ruprechtov natural analogue site. The results showed that natural HA extracted using alkaline extraction was formed by predominantly small independent molecules with lower molecular weight. All spectra were dominated by lower molecular weight peaks, confirming low molecular compounds with a number of peaks about 400 – 600 Da and about 800 Da. High molecular weight compounds were presented to a lesser extent.

Comparing MALDI-TOF MS spectra of the extracted natural HA (borehole NA-12 [36.44-36.9 m]) with the spectra of leachates from organic matter degradation experiment (NA-12/4 leachate [38.9 m]) and the groundwater spectra (NA-12 groundwater [36.5-39.3 m filter horizon]) a noticeable fingerprint can be found: the most similar peaks can be identified around 125-145 Da, 250 Da, 353-381 Da, 413 Da, 492-500 Da, 590-600 Da for all three samples (see Fig 5). This might be interpreted as a signature for dissolved organic matter in groundwater originating from sedimentary organic matter (SOM) of the clay/lignite horizon, being formed by SOM natural degradation (oxidation, leaching by groundwater). The released fraction in groundwater is almost identical to natural humic acid that was extracted using alkaline extraction method from SOM in laboratory.

Complexation experiments with U(VI) and natural humic acid (HA-12/3), which was extracted from non-mobile organic matter, were performed. Dependence of U complexation with HA on increasing HA concentration was studied in 0.01M $NaClO_4$ at pH 6. The cation exchange technique, which is based on the measurement of the total U distribution between the solution phase and cation exchange resin in the presence and absence of a HA, was used. The concentration range investigated was from 1 to 40 mg/l for the HA and 1×10^{-4} M for the U(VI) as $UO_2(NO_3)_2$ labeled with ^{233}U. Concentration of ^{233}U was analyzed using liquid scintillation counting (LSC).

The results were evaluated by means of modified Charge Neutralization Model (CNM) in cooperation with Czech Technical University. Two slightly different approaches were used for stability constant determination: A) only uranyl ion (UO_2^{2+}) was considered for complexation, B) two uranium species were considered, namely UO_2^{2+} and $(UO_2)_3(OH)_5^{+}$. The average stability constants of U(VI) humate complexes were determined: A) log K_{cnm} (log ß) = 4.98 ± 0.619 and for the case B) log K_{cnm} (log ß) = 4.58 ± 0.645. Generally, increasing content of HA increases the complexed fraction of U and decreases loading capacity (LC), but does not influence significantly K_{cnm} value. Determined stability constants K_{cnm} are lower than the literature values and probably indicate lower U(VI) complexing potential of this natural humic acid.

The aim of the **FZD** contribution within this work package was the complexation of Pu(III) with humic substances and its reversibility, which is a continuation of

FZD's former work on the structural parameter determination for the near-neighbors surrounding of Pu(III) in complexes with humic and fulvic acids at pH 1 by means of EXAFS.[13] Before the start of FUNMIG, there was no comprehensive description of the Pu(III) complexation by humic substances and only recently a paper on Pu(III) Aldrich humic acid complexation has been published.[14]

For the study of the complexation of redox-sensitive radionuclides such as plutonium, synthetic humic acid model substances with distinct redox properties can be applied, which were developed by Sachs et al..[15] These humic acid model substances were synthesized by oxidation of diphenolic compounds in the presence of amino acids in alkaline solution. The most promising synthetic humic acids (HA) with distinct redox properties are the HA type Cat-Gly, an oxidation product of catechol synthesized in the presence of glycine, and the HA type Hyd-Glu, an oxidation product of hydroquinone synthesized in the presence of glutamic acid. The Fe(III) reducing capacities determined for HA type Cat-Gly and Hyd-Glu amount to 10.7 ± 0.2 and 14.5 ± 1.6 meq/g HA at pH 3.0 and to 33.6 ± 4.0 and 36.9 ± 0.2 meq/g HA at pH 9.2, respectively.

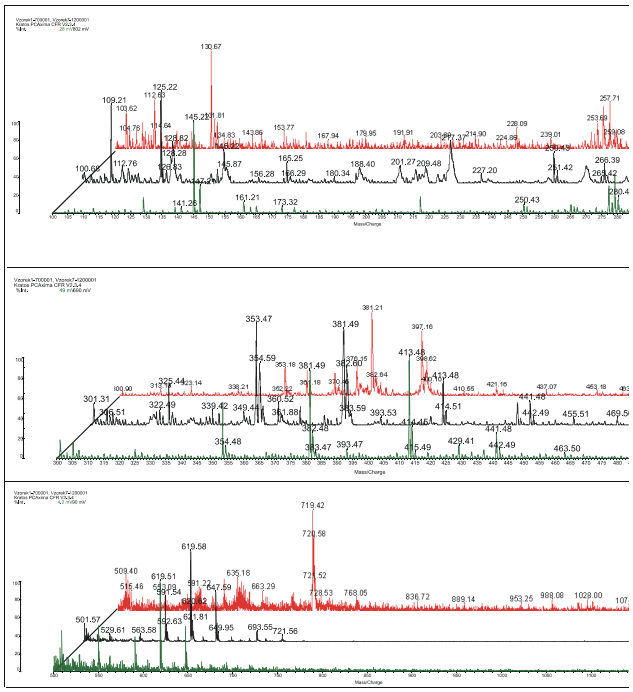

Figure 5. *(left) Comparison of MALDI-TOF MS spectra: green – extracted HA (NA-12 [36.44-36.9 m]), black – NA-12/4 leachate [38.9 m], red – NA-12 groundwater [36.5-39.3 m filter horizon]. (DOC concentration in groundwater at Ruprechtov site was 5 – 10 mg/l).*

These are significantly higher than those determined for natural Aldrich HA with 1.2 ± 0.1 and 7.2 ± 1.9 meq/g HA at pH 3.0 and 9.2, respectively. The formal redox potentials of HA type Cat-Gly and Hyd-Glu amount to 517 ± 12 and 565 ± 12 mV, decreasing with pH by -57 ± 12 and –64 ± 12 mV/pH, respectively. The reducing capability of these humic acid model substances with distinct redox properties towards Np(V) and U(VI) was already studied under anaerobic conditions and compared to that of natural humic substances.[16,17] It was found that both humic acid model substances show higher reducing capacities than natural humic substances. Exemplary for HA type Hyd-

Glu, it was shown that these humic acid model substances exhibit the capability to stabilize neptunium in the tetravalent oxidation state. The Pu(III) complexation study is performed in a glove box under nitrogen atmosphere. Applying HA type Cat-Gly as specific humic acid model substance, the low oxidation state of plutonium can be stabilized. The plutonium species are monitored by UV-Vis spectroscopy and liquid-liquid extraction.

NRIRR has been evaluated a silica/humic acid composite as a model substrate for naturally occurring humate-coated minerals that are likely to be present in the vicinity of the repositories. The binding of Pu(IV), the highly likely oxidation state, by the silica/humic substrate was examined at pH 4 in the range 0.02 to 3.00 M $NaClO_4$ by titration method. Pu(IV)-humate conditional stability constants have been evaluated from data obtained through these experiments by using non-linear regression of binding isotherms. The results have been interpreted in terms of complexes of 1:1 stoichiometry. Analysis of the complex formation dependency with ionic strength shows that the effect of ionic strength on humate complexation of Pu(IV) is not dramatically pronounced. The complexation constants are evaluated for the humate interaction with Pu^{4+} and $Pu(OH)_3^+$ at pH 4. The complexation constants are found, respectively, to be log ${}^{HA}\beta^0(Pu^{4+})$ = 16.6 ± 0.3 and log $\beta^0_{1.3.1}$ = 46.6 ± 2.3. The estimations through analogy from previous results are in agreement with these new experimental data. The effect of ionic strength on maximal binding capacity (B_{max}) appears to be significant. The B_{max} decreases gradually with increasing ionic strength.

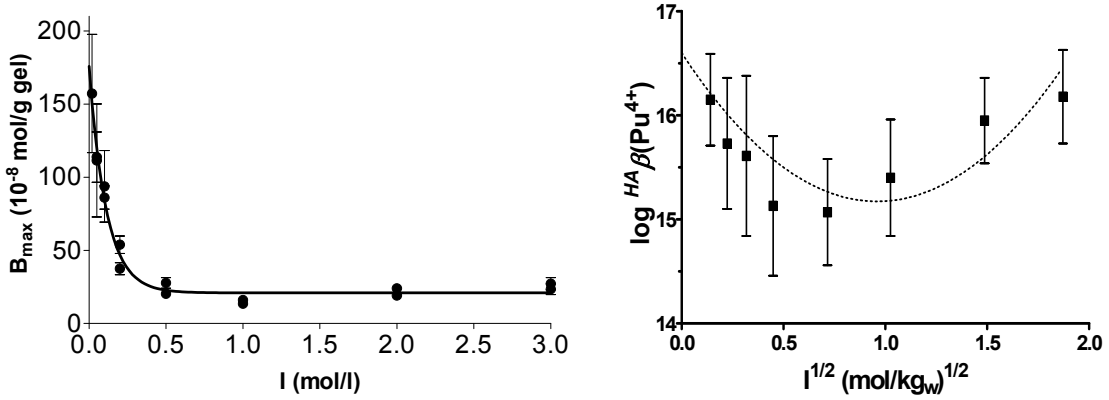

Figure. 6. *(left) Effect of ionic strength on the maximal binding capacity (B_{max}) of SiO_2-HA, (right) Effect of ionic strength on the calculated conditional stability constant log ${}^{HA}\beta(Pu^{4+})$.*

The associated group **CTU** studied complexation of Th(IV) with Aldrich humic acid in aqueous solutions of pH 2-11 using free-liquid electrophoresis. Electrophoretic mobility u of thorium labelled with ^{234}Th was measured as a function of pH and composition of solution. The mobility depends on the abundance and charge of thorium species present and thus enables to characterize the species. It was found that addition of HA to the solution caused decrease in the mobility $_{+}u$ of thorium towards cathode and increase in its mobility towards anode $_{-}u$ due to the formation of negatively charged humate complexes (ThHA). The changes were used for calculation of the abundance (*%ThHA*) and the mean mobility ($_{-}u_{ThHA}$) of the complexes. In the absence of added carbonates, *%ThHA* approached 100 in the solutions containing ≤ 10^{-9} M Th and 0.1 –

10 mg/L HA, indicating predominance of ThHA complexes. An increase in the concentration of Th brought about a decrease in the abundance of ThHA at pH 2 and 3, when the ratio [Th]/[HA] exceeded 10^{-7} mol/mg. However, at the ratio equal to 10^{-6} mol/mg Th bonding by HA significantly exceeded proton exchange capacity of dissociated carboxyl groups of the HA. Moreover, complete charge neutralization of ThHA complexes was not found even in cases, when these complexes were formed from large excess of positively charged Th ions over the dissociated carboxyl groups. This suggests that the complexation proceeds at least partially by displacement of hydrogen ions from the nondissociated groups.

Both this finding and the generally negative charge of ThHA complexes cast doubts on the common interpretation of the complexation solely by neutralization of charge of the dissociated carboxyl groups, reflected in the formulation of stability constant of ThHA using formula

$$\beta_1 = [ThHA^{3+}].[Th^{4+}]^{-1}.[HA^-]_{free}^{-1},$$

where $[HA^-]_{free}$ is the concentration of non- occupied dissociated carboxyl groups.

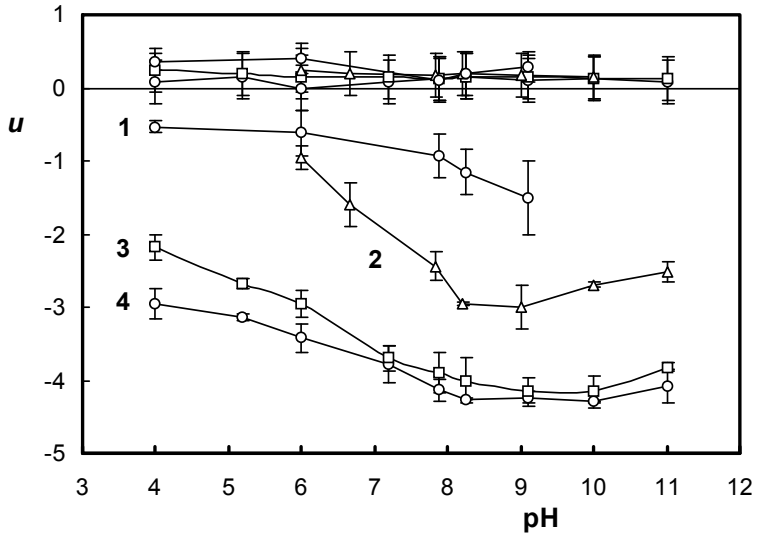

Figure 7. *Electrophoretic mobility of ^{234}Th (in 10^{-4} $cm^2s^{-1}V^{-1}$, at [Th] ≤10^{-9} M) as a function of pH and solution composition: 1) 0.01 M $NaClO_4$ + NaOH, 2) as 1 + 0.001 M $NaHCO_3$, 3) as 1 + 1 mg/l HA, 4) as 1 + 10 mg/l HA.*

More probably, negatively charged complexes are formed between hydrolyzed thorium species and multi-charged molecules HA^{y-} at pH>2. The attempt to calculate a stability constant for pH 2 – 4 was complicated by the large value of *%ThHA* and its uncertainty so that only the minimum possible value of log β_1 = 9.59 could be determined, which is lower than that published for pH 4. The mean electrophoretic mobility of the complexes formed at [Th] ≤ 10^{-9} M and absence of carbonates was found to increase with [HA] (0.1-10 mg/L) and with pH up to pH 7 (see Fig. X). The first effect must be due to the association of HA molecules. The complexes formed at the higher [HA] are larger and have higher negative charge, also due to the relatively lower neutralisation of the charge of HA by cationic forms of thorium. The increase in $-u_{ThHA}$ with increasing pH can be explained by the increasing dissociation of carboxyl groups of HA

and by the decreasing neutralisation of the charge of HA molecules with the increasing hydrolysis of thorium. Both this and the previous effects cease above pH 8 where inorganic thorium exists in solution predominantly as $Th(OH)_4$. The practically constant value of $-u_{ThHA}$ found at pH 8 – 11 and [HA] = 1 – 10 mg/L corroborates the existence of mixed complex $Th(OH)_4HA^{y-}$, previously only assumed to exist. Stability constant of this complex

$$\beta_{1,4,1} = [Th(OH)_4HA^{y-}].\ [Th^{4+}]^{-1}.[OH^-]^{-4}.[HA^-]_{free}{}^{-1}$$

calculated from the mobilities $-u$ of thorium in solutions containing carbonates and HA, considering the known stability constants of thorium carbonates, is $\log \beta^0_{1,4,1} = 45.13 \pm 0.15$ (for I = 0).[18]

The partner **FZK-INE** studied in collaboration with Lomonosov Moscow State University the Np(V) reduction by 9,10-anthrahydroquinone-2,6-disulfonate (AH_2DS). Humic substances (HS) significantly affect redox sensitive actinides (e.g. U, Np and Pu) speciation. It is generally assumed that hydroquinone/quinone moieties are important electron-donating/accepting groups and can be responsible for the redox properties of HS.[19] Authors reported a value for the apparent redox potential of HS of about +0.5 V at zero pH, that should be enough for Np(V) reduction. Previous Np experiments within the framework of FUNMIG showed that an increase of hydroquinone moieties in humic derivatives magnifies the reducing capacity of HS.[20] In order to simplify the system, the Np(V) reduction with a low molecular weight reductant as a model for the reducing entities of humic substances was studied. 9,10-anthrahydroquinone-2,6-disulfonate (AH_2DS) was used as a electron donor for Np(V) reduction. Various amounts of AH_2DS were formed by redox titration of anthraquinone (AQDS) with sodium dithionite at pH 7 and 11. For all used ratios of $AH_2DS/S_2O_4^{2-}$ rather low redox potentials between –0.1 and –0.57 V were measured. Strong dependence of Np(V) reduction kinetics from redox potential was demonstrated: no reduction at +0.4 V, slow incomplete reduction in the system with concentration ratios of dithionite to AQDS (R(Q)) of 0.4 and complete reduction at R(Q) 1.5 within 6 days. In this Eh range the redox potential is controlled by AQDS-AH_2DS couple and reduction kinetics obey first order reaction kinetics with respect to NpO_2^+. Details can be found in a S&T contribution (this volume).[21]

Partner **SCK·CEN** has quantified the influence of dissolved natural organic matter on the Th solubility in Synthetic Boom Clay Water electrolyte (SBCW, ~ 0.014 $mol \cdot L^{-1}$ $NaHCO_3$), approached from the undersaturation direction starting from crystalline ThO_2. Depending on the separation method (and associated cut-off) of dissolved species and particulates (filtration at 0.45 µm, ultrafiltration at 300 kDa and 30 kDa), different Th and organic matter concentrations were obtained. This indicates that both Th and NOM are present in a colloidal form with large size range distribution. At low NOM concentrations and for all cut-offs, an increase of the Th concentration with increasing NOM content is observed. This feature could be modelled with a complexation-type mechanism using Tipping's Humic Ion-binding model VI with generic humic acid parameters.

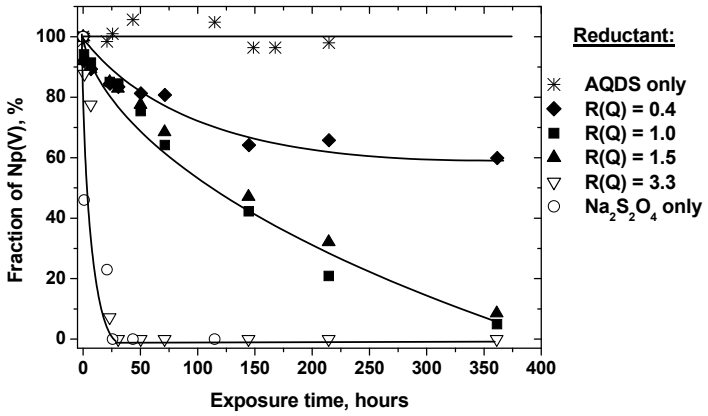

Figure. 8. *Np(V) reduction in the AH_2DS/AQDS system at different values of redox potential in 0.1 M NaCl solution;*
$C_{tot}(Np)=5\cdot10^{-5}M$,
$C_{tot}(AQDS) = 2\cdot10^{-4}$ M,
pH 7 ($1\cdot10^{-3}$M PIPES buffer); $R(Q)= C_0(Na_2S_2O_4)$ to $C_0(AQDS)$ ratio.

The influence of Boom Clay kerogen (extracted and purified from Boom Clay host rock done by IFP using HCl/HF treatment) on the uptake of trivalent lanthanides and actinides was also investigated by **SCK·CEN** through a series of experiments: (1) acid-base titrations and backtitrations of the kerogen at different ionic strengths (0.01 and 0.1 M $NaClO_4$) in the pH region of 3 to 10; (2) sorption edge at trace Eu(III) concentration as a function of pH at different ionic strenghts; (3) sorption isotherm in SBCW in a range of Eu(III) concentrations below the solubility of $EuOHCO_3$(s). The interpretation and geochemical modelling is hindered because of the presence of FeS_2 (~ 50 w%) and trace amounts of TiO_2 in the kerogen, evidenced with electron microprobe analysis (Tab. 1). However, the results clearly show that this "unpure" extracted kerogen acts as a major sink for Eu(III) in Boom Clay host rock. These data, together with results gathered within RTDC1, would suggest that the solid-liquid distribution of trivalent lanthanides and actinides in the Boom Clay formation, is dependent on the competition between solid-phase uptake by clay minerals and the kerogen fraction, and complexation with the functional groups present on dissolved humic substances.

Table. 1. *Elemental analysis of extracted Boom Clay kerogen showing inorganic impurities.*

Batches	CHN (wt%)			EMPA (wt%)						total
	C	H	N	C	O	Al	Ti	S	Fe	
LDJ	26.32	2.59	1.06		7.72	0.11	0.65	25.53	23.43	87.41
AN	36.27	2.97	1.36		7.01	0.09	0.27	22.31	19.22	89.5

WP2.3 - Work package 2.3 activities within the year 2008

In **WP 2.3** the impact of electron transfer processes at inorganic mineral surfaces on the retention of radionuclides is analyzed. The main systems investigated are Fe(II)-bearing minerals commonly found in granitic and in clay environments using advanced redox sensitive surfaces spectroscopy and microscopy.

Partner **KU** has used surface sensitive techniques in combination with bulk methods to investigate the redox behaviour in the green rust (GR) system.[22] Surface sensitive techniques such as atomic force microscopy (AFM) and X-ray photoelectron spectroscopy (XPS) were applied to investigate the formation, the existence in nature, the stability, the oxidation and reduction of GR, and the interaction of GR with several redox-sensitive elements. Complementary use of bulk measurements such as X-ray diffraction and solution chemistry demonstrated that green rust is present in natural systems and because of its behaviour, data describing it should be included in geochemical speciation models for simulating groundwater systems.

Initially, the **KU** group developed a simple and novel method to test for GR in groundwater systems by means of XRD. GR could be identified without doubt in groundwater systems on Bornholm, Denmark, and Äspö, Sweden, both places where the composition of the groundwater and thermodynamic constants indicated it should be present. XRD results, combined with chemical composition of the waters, indicated that the GR type was the carbonate containing (GR_{CO3}). Establishing the type of GR present makes it possible to incorporate the right GR type in future geochemical models.[23] In sulphate-rich systems, the formation of GR is dependent of the monovalent cation present in the formation solution. XRD and chemical composition showed that GR could be produces with Li^+, Na^+ and K^+ as part of the crystal structure, as $GR_{X,SO4}$. The structure of $GR_{Na,SO4}$ was resolved; composition, formula and crystallographic parameters are: $NaFe(II)_6Fe(III)_3(SO_4)_2(OH)_{18}\cdot 12H_2O$, space group P-3, a = 9.528(6) Å, c = 10.968(8) Å and Z = 1. This implies that the monovalent cation can be of importance when putting exchange-dependent redox reactions in the $GR_{X,SO4}$ system.[24] In the studies of $GR_{Na,SO4}$ interaction with two radioactive ions, Se and Np, AFM, XRD and XPS were applied to samples. Together with solution and solid composition data, the studies showed that when $GR_{Na,SO4}$ interacted with the SeO_3^{2-} and SeO_4^{2-}, GR was able to reduce them. The reaction mechanism was, however, different. In the case of SeO_3^{2-}, the reaction took place along the edge of the $GR_{Na,SO4}$ particles whereas with SeO_4^{2-} the reaction involved exchange or incorporation in the GR interlayer. For both selenite and selenate, the resulting compound was elemental Se and goethite; no indication of incorporation of Se into the goethite structure was observed. Incorporation into the GR structure was observed in the Np experiment. We tested how NpO_2^+ interacted with $GR_{Na,SO4}$. The edges of the GR particles were observed with AFM and seen to expand. XPS showed that 75% of the initial Np^{5+} was reduced to Np^{4+}. When the solid was allowed to oxidise in air, appr. 50% of the initial Np was still present in the tetravalent state. It was not possible to resolve whether the Np was present as a discrete phase or incorporated in the resulting Fe-oxide, goethite. Based on the new structural and compositional data for $GR_{Na,SO4}$ the thermodynamic constants have been calculated using a titration approach, with activities determined and measured concentrations compared using PHREEQ and the MINTEQ database. The dissolution reaction constants were calculated with log K = 54.5 ± 3 for experiments producing magnetite and 42.5 ± 3.7 for those producing goethite. Based on the reaction constants and values of free energy of formation, the free energy of formation for $GR_{Na,SO4}$ ($NaFe(II)_6Fe(III)_3(OH)_{18}(SO_4)_{2(s)}$) is –6366±18 kJ/mol, omitting structural water in the interlayer. Such a free energy of formation means that the sulphate form of GR (unlike the CO_3 form) is unlikely to have a wide spread natural occurrence, but may be generated in the rust layers that form when metallic Fe corrodes.

The attachment ability of green rust (sulphate) to various soil and fracture mineral surfaces was investigated using atomic force microscopy (AFM). To survey general colloid behaviour, we examined green rust attachment to muscovite, biotite, chlorite, feldspar, quartz and glass, calcite, gypsum, corundum, hematite, and graphite). Green rust colloids adhered well to all substrates except gypsum. The stickiness of green rust, regardless of surface charge, suggests that it also serves as a substrate for other colloids and dissolved species. This might have an implications for colloidal transport of radionuclides.

Redox reactions on mineral surfaces may significantly contribute to the immobilisation of actinides under Boom Clay conditions. Therefore, the role of redox controlling, Fe(II)-bearing minerals on the retention of U (as a major component of Spent Fuel) is studied by **SCK·CEN**, with a focus on the understanding of mineral surface reaction kinetics. The major redox-controlling minerals in Boom Clay are considered to be pyrite, FeS_2 (1-5 w%), and siderite, $FeCO_3$ (0-1w%). As a conclusion of the work conducted in FUNMIG it can be stated that in the U-FeS_2 systems, at least partial reduction of U(VI) to U(IV) occurs, forming a uraninite-like structure and possibly UO_2 nanocolloids, similar to the observations made for the reduction of U(VI) by green rust.[25] In fact, in all samples, both U(VI) (probably sorbed onto Fe-containing functional groups) and U(IV) structures were detected. The amount of U(IV) was the highest in systems with SBCW (absence of DOC) background electrolyte, and increased with increasing equilibration time. These observations clearly point to a kinetically-driven reduction process, which seems to be somewhat inhibited by the presence of DOC. [26] In contrast, no reduction of U(VI) was observed in the U-$FeCO_3$ systems, and uptake of U is probably dominated by sorption of U(VI) onto Fe-containing functional groups.

Sorption experiments with Se(IV) on two complex systems (mixtures of illite(Montana)/FeS_2 and illite(Montana)/FeS) were performed by partner **KULEUVEN** as a possible route (bottom up approach) to understand the complex host rock (Boom Clay). The motivation was to demonstrate the relative importance of the different mechanisms identified for Se(IV) interaction with illite (surface complex formation) in RTDC1 and with pyrite (Se(0) precipitation) and Troilite (FeSe precipitation) in RTDC2. For details see summary of RTDC-1.

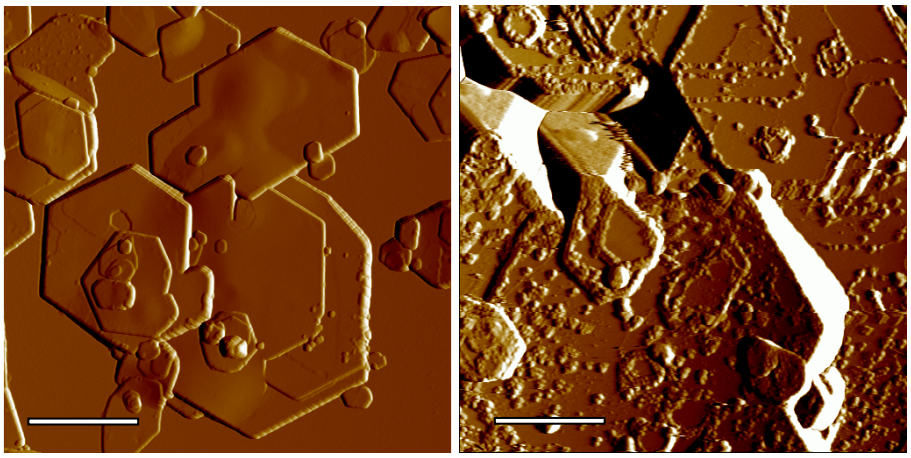

Figure. 9. *AFM deflection images, scale bar is 1 µm. The image on the left shows unreacted $GR_{Na,SO4}$ particles with step edges (terraces); the image on the right shows $GR_{Na,SO4}$ that is reacting with SeO_3^{2-}. The small particles are elemental Se(0) aligning along the former terraces of the $GR_{Na,SO4}$ particles.*

WP2.4 - Work package 2.4 activities within the year 2008

In **WP 2.4** the role and extent of microbiological mediated processes affecting radionuclide migration in the far-field of a repository will be investigated. The focus is on the identification of radionuclide interaction with detached microorganisms, retention through interaction with biofilm material, including microbiologically mediated reduction, and change in the geochemical environment generated by microbial metabolism, including the generation and influence of various chelating compounds.

CTH performed sorption studies of ^{234}Th(IV), ^{241}Am(III), ^{60}Co(II) and ^{134}Cs(I) on in-situ grown biofilm and none biofilm covered apatite and quartz slides and reference glass slides. The experiments are divided into two sets; one with biofilm grown on the slides placed in special reactors in-situ at the Äspö hard Rock Laboratory; one without biofilm. Epifluorescence microscopy gives an impression of the biofilm density on the different mineral slides (see Figure 10). The amount of biofilm on the surfaces was approximately the same on the different minerals 1.25 ±0.13 million cells cm^{-2}.

The sorption experiments on the mineral- and glass slides are performed in a N_2/H_2 (97/3) atmosphere glove-box. The slides have been placed in sterile 50 mL polypropylene tubes filled with synthetic groundwater. 300-500 µL radionuclide stock solution was added. Isotherm titrations of ground and sieved mineral slides have been performed. This work is also part of sorption studies under RTDC-1 (WP 1.2). Material used has been characterized for surface area by means of BET and ESEM/EDX for particle size determination after sieving and mineral composition. Changes in the synthetic groundwater and possible dissolution of minerals during the batch sorption experiments as well as titration experiments have been investigated by ICP/OES. Time dependent sampling and analysis of the activity has been made to investigate possible sorption kinetics. Autoradiographic analysis enables us to verify sorption of activity, and to localize were on the mineral slides the activity is sorbed, possibly relating the sorption to specific structures/compositions of the mineral slides, see Fig. 11.

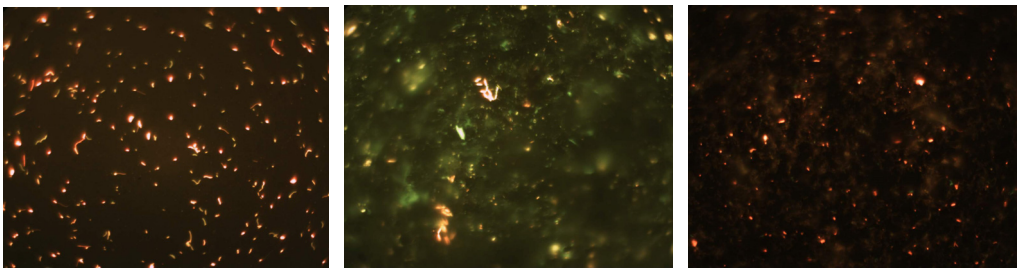

Figure 10. *Epifluorescence microscopy images of acridine orange stained biofilms on mineral surfaces. (left) glass (centre) apatite and (right) quartz.*

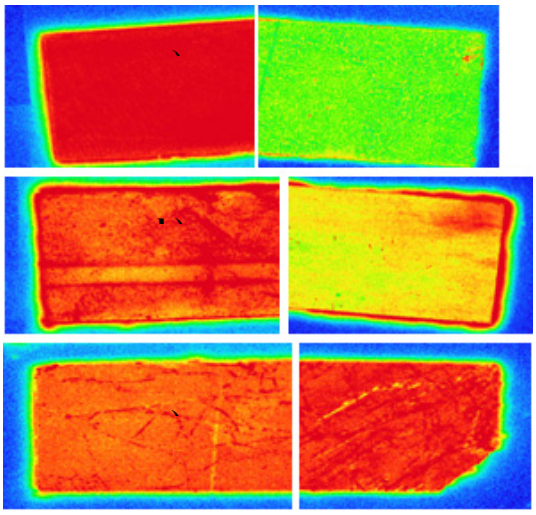

Figure 11. *Autoradiography images of biofilm vs. non biofilm covered mineral slides (BAS IP-SR 2025 Imaging Plate) a) Biofilm on glass – glass b) Biofilm on quartz – quartz c) Biofilm on apatite – apatite(C). It is interesting to see that the sorption onto glass is very much lower than on quartz, where most of the activity is on the edges of the cutted mineral slide, and apatite where activity is sorbed onto the surface following the observed surface roughness.*

FZD investigated the extracellular polymeric substance (EPS) of biofilms, which is made of polysaccharides, proteins, lipoproteins and glycoproteins. The EPS plays an important role in the immobilization of radionuclides (uranium). In contrast to studies carried out on planktonic bacteria suspensions, where U accumulates mainly at the cell surface, FZD studied the interac-tions of U with biofilms, and observed that U immobilizations are associated with EPS components and not with cell membranes or in bacterial cells.

Fluorescent U(V) and U(VI) particles were simultaneously observed for the first time in vivo by a combined laser fluorescence spectroscopy and confocal laser scanning microscopy approach in the EPS of a living multispecies biofilm grown on biotite plates. These particles ranged between 1 and 7 µm in width and up to 20 µm in length and were located at the bottom and at the edges of biofilms colonies. Laser fluorescence spectroscopy was used to identify these particles. The particles showed either a charac-teristic fluorescence spectrum in the wavelength range of 415-475 nm, indicative for U(V), or in the range of 480-560 nm, which is typical for U(VI). These uranium parti-cles were attributed for U(VI) to biologically mediated precipitation and for U(V) to redox processes taking place within the biofilm. [27]

Electrochemical microsensor studies of the O_2 concentrations within the biofilm identified depleted zones closer to the biofilm/air interface which may trigger uranium redox processes. The microsensor profile measurements in the stable multispecies

biofilms exposed to uranium in ecologically relevant concentrations ($1x10^{-5}$ and $1x10^{-6}$ M) showed that the O_2 concentration decreased faster with increasing biofilm depth compared to the uranium free biofilms. In the uranium containing biofilms, the O_2 consumption, calculated from the steady-state microprofiles, showed high consumption rates of up to 61.7 nmol cm^{-3} s^{-1} in the top layer (0–70 μm) and much lower consumption rates in the lower zone of the biofilms. Staining experiments with 5-cyano-2,3-ditolyl tetrazolium chloride (CTC) and 4,6-diamidino-2-phenylindole (DAPI) confirmed the high respiratory activities of the bacteria in the upper layer by confocal laser fluorescence microscopy (CLSM). The fast decrease in the oxygen concentrations in the biofilm profiles showed that the bacteria in the top region of the biofilms, i.e., the metabolically most active biofilm zone, battle the toxic effects of aqueous uranium with an increased respiratory activity. This increased respiratory activity results in O_2 depleted zones closer to the biofilm/air interface which may trigger uranium redox processes, since suitable redox partners, e.g., extracellular polymeric substance (EPS) and other organics (e.g., metabolites), are sufficiently available in the biofilm porewaters. Such redox reactions may lead to precipitation of uranium (IV) solids and consequently to a removal of uranium from the aqueous phase.[28]

Partner UNIUTRECH focused on the role of iron oxides in retarding U transport by acting as a sorbent for uranyl. Reductive dissolution of iron oxides by S(-II), the product of microbial sulfate reduction, can cause the mobilization of adsorbed uranium. However, reduction of U(VI) by S(-II) could counteract this effect due to the formation of U(IV) and subsequent precipitation of UO2. UNIUTRECH experimentally investigated the possibility of the release of adsorbed U(VI) from iron oxides upon reductive dissolution by S(-II) and evaluated whether U(VI) can be concomitantly reduced with the iron oxide. The activity of sulfate reducing bacteria was mimicked in the study by adding incrementally S(-II) to a lepidocrocite (FeOOH) suspension with pre-adsorbed U(VI). The main purpose was to detect changes in the phase distribution of uranium during reduction and to relate these changes to modifications of the solid phase or reduction of U(VI). Batch experiments were performed in an O2-free glove box, at a steady pH 8 and ionic strength of 0.1M. Regularly, samples were collected for analyzing the solution and characterizing the solids. In the experiments the amount of added S(-II) and the initial U/Fe ratio were varied. U-LIII edge X-ray absorption spectroscopy was used in order to determine the redox state of U and to characterize its coordination environment. The results can be summarized as follows: (a) reaction of lepidocrocite and S(-II) was a relatively fast process and completed within less than one hour. The consumption of S(-II) was predominantly coupled to the production of Fe(II). A notable increase in Fe(II) concentrations in both solution and solid was observed. (b) Prior to sulfide addition to the system the concentration of dissolved uranium (U(aq)) was virtually zero. After the instantaneous increase in U(aq) concentration, induced by S(-II) addition, the concentration decreased and approached a level significantly higher (up to about 5% of the added U) than before S(-II) addition. (c) The elevated uranium concentrations remaining in solution upon S(-II) addition can be explained by a decrease of the affinity of U for the transformed iron solids due to the replacement of hydroxyl by thiol groups at the mineral surfaces or the competition with Fe2+ for reactive surface sites. (d) XAFS analysis reveals a decrease of the coordination number of axial oxygens within a time scale of hours, indicating successive reduction of U(VI). Formation of a U containing precipitate is indicated by the appearance of U-U interactions in the EXAFS

spectra, especially in suspensions reacted with higher amounts of S(-II). The formation of the precipitate seems not to occur instantaneously upon U(IV) formation but to be a slower process than U(VI) reduction. In conclusion the results of this study show that the emergence of S(-II) in subsurface environments can lead to the mobilization of U(VI) adsorbed to iron oxides. Details on the results and possible reasons for the mobilization can be found in a separate S&T contribution.[29]

References

[1] SKB, 2006. Long-term safety for KBS-3 repositories at Forsmark and Laxemar - a first evaluation; Main report of the SR-Can project. Technical report TR-06-09, Svensk Kärnbränslehantering AB, Stockholm, Sweden.

[2] Neretnieks, I., 2006. Flow and transport through a damaged buffer - exploration of the impact of a cemented and an eroded buffer. SKB Technical Report 06-33, Svensk Kärnbränslehantering AG, Stockholm, Sweden.

[3] Kunze, P., Seher, H., Hauser, W., Panak, P.J., Geckeis, H., Fanghänel, T., Schäfer, T., (2008) The influence of colloid formation in a granite groundwater bentonite pore water mixing zone on radionuclide speciation. Journal of Contaminant Hydrology, 102, 263-272.

[4] Seher H., Albarran N., Hauser W., Götz R., Missana T., Geckeis H., Fanghänel T., Schäfer T. (2009) Colloid generation by erosion of compacted bentonite under different geochemical conditions. (S&T contribution; this issue).

[5] Filby, A., Plaschke, M., Geckeis, H., Fanghänel, T., (2008) Interaction of latex colloids with mineral surfaces and Grimsel granodiorite. Journal of Contaminant Hydrology, 102(3-4), 273-284.

[6] Delos, A. Walther, C., Schäfer, T., Büchner, S. (2008): Submicron-Colloid Size Dispersion and Colloid Mediated Radionuclide Transport in a Synthetic Porous Media. J. Colloid Interface Science 324: 212-215.

[7] S. Komorovský, M. Repiský, O. L. Malkina, V. G. Malkin, I. Malkin-Ondik, M. Kaupp, J. Chem. Phys. **128**, 104101 (2008).

[8] M. Repiský, S. Komorovský, O. L. Malkina, V. G. Malkin, Chem. Phys., in press (2008); available online: doi:10.1016/j.chemphys.2008.10.037.

[9] P. Hrobárik, R. Reviakine, A. V. Arbuznikov, O. L. Malkina, V. G. Malkin, F. H. Köhler, M. Kaupp, J. Chem. Phys. **126**, 024107 (2007).

[10] Reiller, P., Amekraz, B., Moulin, C., (2006) Sorption of Aldrich humic acid onto hematite: Insights into fractionation phenomena by electrospray ionization with quadrupole time-of-flight mass spectrometry. ES&T, 40(7), 2235-2241.

[11] Claret, F., Schäfer, T., Brevet, J., Reiller, P.E., (2008) Fractionation of Suwannee River Fulvic Acid and Aldrich Humic Acid on α-Al2O3: Spectroscopic Evidence. ES&T, 42(23), 8809-8815.

[12] Reiller P.E. & Brevet, J. (2009) Change of the chemical environment of Eu(III) during sorption experiments in the ternary system Eu(III)/humic substances/α-Al_2O_3.(S&T contribution; this issue).

[13] Schmeide, K., Reich, T., Sachs, S., Bernhard, G.: Plutonium(III) complexation by humic substances studied by X-ray absorption fine structure spectroscopy. Inorg. Chim. Acta **359**, 237-242 (2006).

[14] Buda, R.A., Banik, N.L., Kratz, J.V., Trautmann, N.: Studies of the ternary systems humic substances-kaolinite-Pu(III) and Pu(IV). Radiochim. Acta 96, 667- 665 (2008).

[15] Sachs, S., Schmeide, K., Brendler, V., Křepelová, A., Mibus, J., Geipel, G., Heise, K.H., Bernhard, G. (2004) Investigation of the complexation and the migration of actinides and non-radioactive substances with humic acids under geogenic conditions. Complexation of humic acids with actinides in the oxidation state IV Th, U, Np. Wissenschaftlich-Technische Berichte, Forschungszentrum Rossendorf, FZR- 399, Dresden.

[16] Sachs, S., Geipel, G., Bernhard, G.: Study of the redox stability of uranium(VI) in presence of humic substances. In: FZKA 7070, Wissenschaftliche Berichte (G. Buckau, ed.). Forschungszentrum Karlsruhe, Karlsruhe, 2005, p. 9-18.

[17] Schmeide, K., Geipel, G., Bernhard, G.: Study of the neptunium(V) reduction by various natural and synthetic humic substances. In: FZKA 7070, Wissenschaftliche Berichte (G. Buckau, ed.). Forschungszentrum Karlsruhe, Karlsruhe, 2005, p.19-31.

[18] P. Beneš (2009, in press): Radiotracer study of thorium complexation with humic acid at pH 2-11 using free-liquid electrophoresis. Radiochim. Acta.

[19] Osterberg, R., Shirshova, L. (1997): Oscillating, Nonequilibrium Properties of Humic Acids. Geochim. Cosmochim. Acta, **61**, 4599-4604.

[20] Kalmykov, S., Schäfer, T., Claret, F., Khasanova, A., Shcherbina, N., Perminova, I., Teterin, Y., (2008) Sorption of neptunium onto goethite in the presence of humic acids with different hydroquinone group content. Radiochimica Acta, 96(9-11), 685-691.

[21] Shcherbina, N.S., Banik, N.L. Marquardt, C.M., Kalmykov, S.N. (2009) Np(V) redox interaction by anthraquinone used as a model redox compound for humic substances. (S&T contribution; this issue).

[22] Christiansen, B.C., Stipp, S.L.S., Hansen, H.C.B. (2009, accepted) Green rust – a review, Chemical Reviews.

[23] Christiansen, B.C., Stipp, S.L.S., Balic-Zunic, T. (2009) Identification of Green Rust in Groundwater, ES&T (in press).

[24] Christiansen, B.C., Balic-Zunic, T., Petit, P-O., Frandsen, C., Geckeis, H. Mørup, S., Katerinopoulou, A., Stipp, S.L.S. (2009, in review) Composition and structure of an iron-bearing, layered double hydroxide (LDH) – Green rust sodium sulphate, GCA.

[25] O'Loughlin E.J., Kelly S.D., Cook R.E., Csencsits R., Kemner K.M. (2003) Reduction of uranium(VI) by mixed iron(II)/iron(III) hydroxide (green rust): formation of UO_2 nanoparticles, ES&T, **37**, 721-727.

[26] Bruggeman, C. & Maes, N. (2009) Aqueous uptake of U(VI) by pyrite under Boom Clay conditions. (S&T contribution; this issue).

[27] K.Großmann, T. Arnold, E. Krawczyk-Bärsch, S. Diessner, A. Wobus, G. Bernhard, R. Krawietz (2007) Identification of Fluorescent U(V) and U(VI) Microparticles in a Multispecies Biofilm by Confocal Laser Scanning Microscopy and Fluorescence. Spectroscopy. *Environ. Sci. Technol.*, **41**, 6498-6504.

[28] Evelyn Krawczyk-Bärsch, Kay Großmann, Thuro Arnold, Axel Wobus, Susann Hofmann (2008) Influence of uranium (VI) on the metabolic activity of a stable multispecies biofilms studied by oxygen microsensors and fluorescence microscopy. *Geochimica et Cosmochimica Acta* **72***,* 5251-5265.

[29] Alexandratos V. G., Behrends T., Van Capellen P., (2009) Effect of S(-II) driven conversion of iron oxides to FeS on uranium mobility. (S&T contribution; this issue).

RTD COMPONENT 3

Scott Altmann
Andra Agence Nationale pour la gestion des Déchets Radioactifs.
1/7 rue Jean Monnet
F-92298 Chatenary Malabry CEDEX, France
Scott.altmann@andra.fr

Introduction

Deep underground disposal in low permeability 'clayrock' formations has been put forward by Belgium, Switzerland and France as the most appropriate solution for managing the high and intermediate level, long half life radioactive wastes generated by their respective nuclear energy programs. These concepts rely on various favourable characteristics of the host rock formation to insure that release of radio nuclides (RN) to the biosphere will always remain at levels well below those capable of potentially affecting human health. Stakeholder confidence in these projects is based in large part on the capacity of the corresponding waste management organizations (WMO: i.e. ONDRAF/NIRAS (BE), Nagra (CH), Andra (FR)) to demonstrate that the models used to predict radionuclide migration through the respective clayrock formations (Boom Clay, Opalinus Clay, Callovo-Oxfordian (COx)) are based on a scientifically sound understanding of all contributing phenomena. WMO publish 'Safety Case' (SC) reports (1, 2, 3) describing, among many other aspects, the state of knowledge regarding RN migration phenomena in the geological barrier (GB, i.e. the host rock formation) and the results of Performance Assessment (PA) simulations of RN migration towards the biosphere. While each of these SC has its own specificities, they reveal many common points concerning the state of knowledge, and remaining questions, regarding understanding and modelling RN migration in the respective GB. RTDC3 was conceived based on the state of knowledge in 2004 regarding RN migration in clayrocks and analogous compacted clay mineral materials, the essential aspects of which are presented in the three SC. This state-of-knowledge led to formulation of several 'key questions':

- Do we have a sound theoretical basis for describing RN speciation in the porosity of highly-compacted clay materials and clayrocks, in particular the distribution of total RN mass between dissolved and sorbed species?
- Do we have a coherent conceptual model describing diffusion-driven transport of anionic and cationic RN in clayrocks?
- Do we have credible strategies / methods for carrying out the up-scaling needed to obtain representative parameter values usable for performance assessment simula-

tions of a clayrock geological barrier system, in particular taking into account the effects of spatial heterogeneity of rock physical-chemical properties.

The goal of RTDC3 was to improve our capacity to provide positive answers to these questions for use in upcoming clayrock safety cases.

At the most simplistic level, most of the research carried out in RTDC3 can be structured around conceptual models based on (i) Fick's first and second laws for diffusive driven transport, adapted to take into account the effect of reversible sorption of RN on clayrock surfaces, and (ii) consideration of whether or not the same set of Fick's law parameter values can be used to represent RN migration at all space-time scales considered in clayrock safety cases (< 10^{-3} m to > 10^{2} m).

- *Fick's first law (for steady state RN flux):* $J = -D_e \frac{dC}{dx}$ with $D_e = D_0 \left(\frac{\delta}{\tau^2}\right) \omega = D_p \omega$ where J: flux (mol·s^{-1}·m^{-2}); D_e, D_0, D_p: 'effective', 'free solution', 'pore' diffusion coefficients (m^2·s^{-1}) respectively; C: concentration (mol·m^{-3}); x: distance (m); δ/τ^2: term representing the effects of pore space geometry on RN diffusion (dimensionless); ω: porosity accessible for RN diffusion (dimensionless).
- *Fick's second law (time dependence of RN mass transfer):* $\frac{\partial C}{\partial t} = D_a \frac{\partial^2 C}{\partial x^2}$ with $D_a = \frac{D_e}{(\omega + \rho K_d)}$ where D_a: 'apparent' diffusion coefficient (m^2·s^{-1}); ρ: rock density (kg·m^{-3}) and K_d: coefficient representing the partitioning of total RN mass present at position x between mobile dissolved species and immobilized sorbed species (m^3·kg).

Most of the work carried out in RTDC3 was focused on improving conceptual models for diffusion driven transport for two classes of RN of key importance for SC:

- *Non or very weakly sorbing RN*, principally those which are anions ($^{36}Cl^-$, $^{129}I^-$…). Here the objective was to improve understanding of terms in Fick's 1st law (porosity organization, anion exclusion and mobility in clay domains, effects of mineral composition on porosity…). These aspects are discussed below in sections §2 and §3;
- *Moderately and highly sorbing RN*, principally in cationic form ($^{135}Cs^+$, actinides, analogue elements,…). Here the focus was on the partitioning term in Fick's 2nd law, but interesting information concerning mass transport was also obtained. Sections §2 and §4 describe these aspects.

RTDC3 involved the collaborative and complementary efforts of research teams from 24 different organizations (ANDRA(FR), ARMINES(FR), BRGM(FR), CEA(FR), CIEMAT(ES), ERM(FR), FZK-INE(DE), GRS(DE), II-CRC(HU), NAGRA(CH), ONDRAF/NIRAS(BE), PSI(CH), SCK·CEN(BE), UDC(ES), UNIV-BERNE(CH), UJF(FR), LPEC(FR), LMM(FR), AIED(FR)) including research institutes, laboratories, SME, national radwaste management agencies and four Associated Groups (Hydr'asa(FR), La Trobe University(AUS), CEREGE(FR), UnivAvignon(FR)).

Advances within workpackages

Characterizing and understanding clayrock properties influencing RN migration

Clayrock composition and structure largely govern the migration characteristics for any given RN species. This rather blunt affirmation is in fact the working hypothesis for a significant part of the research carried out in RTDC3, which is why it merits explanation, in particular in relation to the two situations studied in detail in RTDC3: diffusion-driven transport of anionic RN species and retardation-by-sorption of cationic RN species. First, what do we mean by composition and structure? Composition includes both the inorganic (mineralogical) and organic compounds and phases making up the rock solid matrix and, most importantly, the speciation of the pore solution and contacting mineral surfaces. Pore solution and mineral surface speciation will largely determine RN dissolved speciation (e.g. predominance of anionic or cationic forms), solid-solution partitioning of RN mass (K_d) and the intensity of electrostatic field effects on the solution volume accessible to anionic RN. As for structure, it refers to the organization, geometry and dimensions of the connected porosity of a given clayrock, and its relation to contacting minerals. Porosity structure, taken together with the electrostatic field effects on anions mentioned above, will determine the accessible porosity and diffusion path 'tortuosity' for cationic and anionic RN species. In addition, since current knowledge indicates that the permanently negatively charged swelling clay minerals present in clayrocks play a key role in determining RN migration behaviour, the structure and composition of the porosity associated with the clay mineral fraction is expected to be of prime importance. In addition, clayrock formation databases (1, 2, 3) generally show that values measured for a given composition or structure parameter vary for rock samples taken from different positions within the formation, i.e. the formation is not an homogeneous entity as regards parameters which might affect RN migration.

Research carried out in RTDC3 focused on enhancing understanding of clayrock structure and composition at the various scales and spatial resolutions which will be needed for interpreting, integrating and up-scaling the results of studies on RN diffusion and sorption described in subsequent sections, i.e.

- at the formation, i.e. Geological Barrier System (GBS), scale (~10^2 m) with a resolution of ~10^{-1} m,
- at the 'macroscopic' scale (10^{-1} to 10^{-2} m), typical of that associated with lab and in-situ determinations of RN K_d (or R) and D_e parameters, with resolutions ranging down to ~ 10^{-5} m,
- at the 'mesoscopic' scale (~ 10^{-3} to 10^{-4} m), characteristic of that of diffusion profiles for high K_d RN (cf. §4.2), with resolutions down to 10^{-6} m.

All scales were studied on the COx formation in order to provide a common 'safety case' context for inter-relating and up-scaling study results. Clayrock samples from all four clayrock formations (Opalinus Clay, Boom Clay, Callovo-Oxfordian, Boda Claystone (HU)) were also characterized in terms of mineralogy, structure, porewater composition and water states at the *macroscopic scale* in order to identify key common characteristics and essential differences likely to impact RN migration (*CIEMAT, ERM*).

Geological formation scale (10^2 – 10^3 m) results

Clayrock safety cases generally present a detailed geological model of the host formation emphasizing its stratigraphic organization and corresponding (vertical) variability in mineralogy. On the other hand, the PA calculations carried out in these same safety cases generally assume that the entire formation has uniform characteristics as regards RN migration, i.e. single values for D_e, K_d, etc. selected based on the results of measurements on many rock samples taken throughout the formation. While this process is robust from a PA standpoint, as demonstrated by an analysis carried out by *SCK•CEN* (cf. §3.4), safety case confidence could be enhanced if a method (tool) existed for evaluating the effect of formation-scale geological variability on the GBS representation in Performance Assessment. The first step in this process was achieved by research carried out by Andra which used signal profiles obtained by high resolution electrical logging of three boreholes traversing the COx to generate profiles of rock carbonate mineral concentrations with sub-cm scale resolution. Geostatistical methods were then used to divide the formation profile into three mineralogical classes based on carbonate content (which is inversely correlated with clay mineral content and porosity). This information was subsequently used to define the meshing of a RN transport model, each class being assigned different values for RN migration parameters (D_e, K_d) based on the results of measurements on representative samples of differing carbonate content (cf. §3.4 and §4.2 for further details). Another RTDC3 action along this same line, i.e. being able to link information concerning the spatial variability of rock characteristics at the formation scale with possible effects on RN migration, was development of a database for the COx formation containing all data regarding parameters likely to influence directly or indirectly RN migration (*BRGM*).

Macroscopic scale (mm-dm) results

The vast majority of the RN migration-related data (rock composition, structure, K_d, D_e, etc.) presented in safety cases are based on measurements made on cm-dm scale rock volumes. There are excellent reasons for this, among which are practical upper limitations on the sample dimensions which can be accommodated in the space-time framework laboratory experiments and lower limits imposed by the need to make measurements on volumes of rock of sufficient size to guarantee that the values measured are sufficiently representative of 'real rock' complexity to be credible for safety case use. Field experiments in underground laboratories complement such measurement. They apply to similar or slightly larger scales and allow a verification of laboratory results under chemically and mechanically more representative in-situ conditions. Several actions in RTDC3 were devoted to enhancing understanding of clayrock composition and structure at this important scale:

- A detailed analysis (*CIEMAT*) of main clayrock characteristics and properties likely to have a significant effect on RN mobility for the above mentioned four different clayrocks led to development of a conceptual model for the distribution and composition of the different types of water (external and internal water) present in highly compacted clayrocks, main inputs needed for constructing models for water-rock interaction, RN speciation and solute transport. The resulting comparative database (cf. Annexe) clearly illustrates the main commonalities and differences of the four rock types (cf. example in Figure 1).

- Investigation of processes controlling the redox state of COx clayrock pore waters (*BRGM, LPEC, La Trobe University*) show that the upper limit of dissolved Fe(II) in pore water must be less than 1/100 of the Ca concentration (< 10^{-4} mol/L). This concentration is certainly linked to the solubility of an identified siderite like mineral (sideroplesite) whose solubility has been estimated. At last clay-associated Fe(II) has been proved to be a highly reactive, redox determining component in the COX, a result in line with the demonstrated reactivity of Fe(II) sorbed onto clay minerals in laboratory systems (see below).
- Macroscopic-scale clayrock volumes can exhibit significant internal variability in terms of structure, mineral composition and porosity, all of which are capable of affecting RN migration. Samples from the four clayrock formations were characterized (*ERM, Hydr'asa, CEA*) using a wide range of methods in order to visualize and map (2D, 3D) the spatial distribution of porosity, mineralogy and structural discontinuities (pyrite inclusions…) with resolutions reaching down to the µm scale. The results of the most complete characterization, that carried out on a single dm-sized COx clayrock sample taken from a diffusion experiment carried out in the Bure URL, were used along with results of studies at the formation scale, mesoscopic and microscopic scales, as the basis for the conceptual model used to integrate and upscale many of the research results of RTDC3.
- Results from a field experiment in the Mont Terri underground research laboratory were used to validate laboratory results for mobile and sorbing tracers.

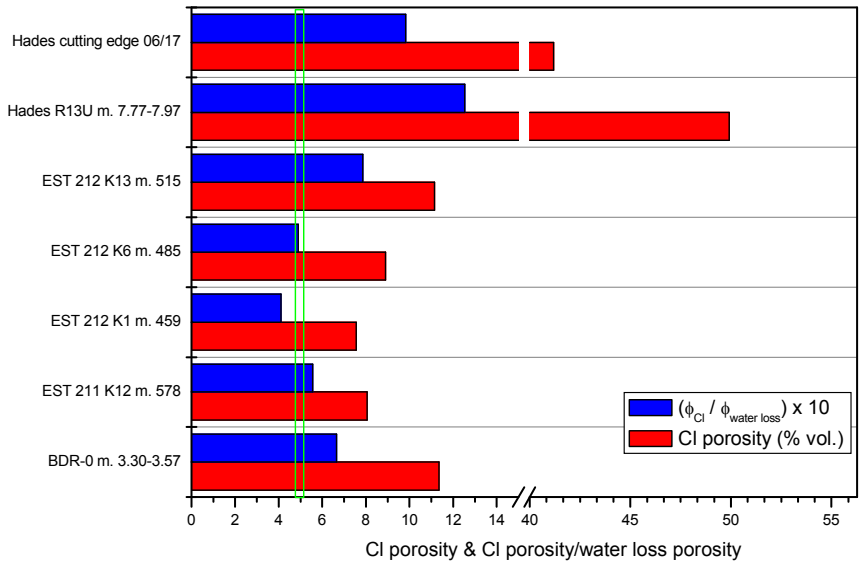

***Figure 22**: Chloride porosity and $\phi_{Cl}/\phi_{water\ loss}$ porosity ratio in core samples from the Boom Clay, Callovo-Oxfordian and Opalinus Clay formations*

Mesoscopic scale (< mm) results

An important objective of RTDC3 research was to improve understanding of how clayrock composition and structure influence RN diffusion (mainly for anions) and retention by sorption (mainly for cations). If we set aside the possible effects of discontinuities (pyrite inclusions, fissures…) on RN transport measurements carried out at the macroscopic scale, and if we assume the clay mineral fraction and its associated poros-

ity to be of prime importance, it seems reasonable to expect that a detailed understanding of the latter's organization and connectivity could help in reaching this objective. A major effort was consecrated by *Hydr'asa, ERM, Andra* and *CEA* on developing and applying methods for quantifying and analyzing the form and organization of clay, quartz, carbonate and other mineral grains in sub-mm volumes of clayrock with sub μm resolution (cf. Figure 2). Two main results were achieved:

- The results of measurements and statistical analysis of the form factors (length to width ratio) and orientations relative to the sedimentation plane of non porous quartz and carbonate mineral grains which show that both grain populations have elongated form factors, are preferentially oriented parallel to the sedimentation plane and that adjacent grains are always separated by the clay matrix. Taken together, these results show that the COx clayrock exhibits two domains of mineral particle organization: 1) the spatial arrangement of clay particles, at the μm scale, inside the clay matrix and 2) the spatial organization of the contiguous clay matrix, at the <mm scale, determined mainly by the organization of the non porous carbonate and quartz grains.
- The building of 3D representations of the pore space and mineral organization in the rock samples used for diffusion and retention experiments. These representations are the basis for defining the meshing, and associated apparent diffusivity values, for the numerical model used to predict and interpret diffusion/retention experimental results (cf. §3.3 and 4.2).

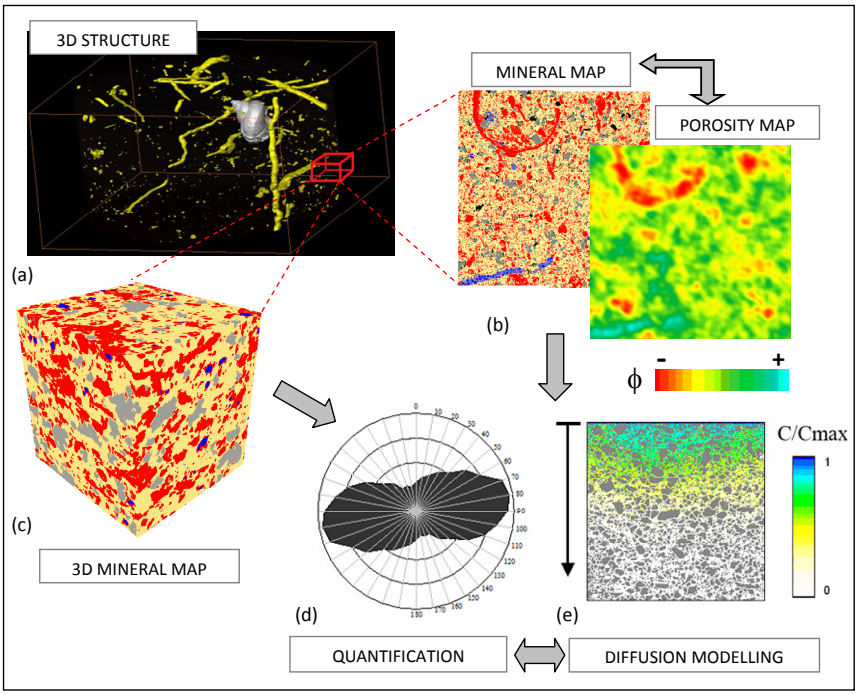

Figure 2: *Methodology used to characterize clayrocks at macroscopic and mesoscopic scales (a) 3D spatial distribution of structure (yellow : pyrite inclusions, white : fossil) acquired for a cm³ scale sample by X-ray tomography (b) comparison between porosity (³H-MMA method) and mineral (SEM) maps (c) 3D mineral spatial distribution (red: carbonates, grey: quartz, blue: pyrite, yellow: clay matrix) acquired for a sub mm scale sample by synchrotron X-ray tomography (d) statistical analysis of mineral distributions (ex: orientation rose of carbonate grains) (e) diffusion modelling computed from 2D/ 3D mineral and porosity distribution using TDD method.*

Diffusion of 'non-sorbing' RN in clayrocks

The overall objective of RTDC3 research in this domain is to develop a coherent conceptual model for diffusion of non-sorbing tracers (^{36}Cl, ^{129}I, HTO...) in clayrocks at all space-time scales. Very extensive databases have been developed (1, 2, 3) regarding anion and HTO diffusion in intact rock samples at the ~cm scale in order to provide the safety case with a sound basis for evaluating anionic RN diffusion in the GBS. The important role played by this scale in safety cases, and its potential utility in developing links between the geological model of mineralogical variability and diffusion, were the impetus for several studies carried out in RTDC3. The majority of RTC3's efforts were, however, focused on improving understanding of diffusion-governing phenomena operating at under- and over-lying scales.

Diffusion in 'clay mineral domains'

All of the clayrocks studied in Funmig contain significant amounts of permanently negatively charged illitic- and illite/smectite mixed layer type clay minerals. It is known that electrostatic repulsion results in total exclusion of anions from the volume contained within the clay layer stacks, and reduces their concentration in the pore solution

near external clay surfaces. As a result, anions can diffuse only in the connected porosity outside the clay interlayer volume, and it is expected that anion repulsion will also affect the amount and 'geometry' of this 'external' porosity accessible for anion diffusion. Cations and neutral species (HTO), on the other hand, are able to access and diffuse in, all of the pore volume. RTDC3 consecrated a significant effort toward increasing understanding and modelling equilibrium mass distribution (accessible porosities) and mobility (diffusion) of anions, HTO (and cations) in *clay mineral domains at the microscopic-scale (~μm)*, and testing the models against experimental data measured on a compacted pure clay mineral (montmorillonite) synthesized and characterized specifically for project needs (*LMPC*).

From a theoretical and modelling perspective, the challenge is to describe and model, in a scientifically rigorous fashion, diffusion of anions, cations and HTO molecules in compacted clay materials as a function of material density (which affects the pore size distribution) and solution composition (cation charge, ionic strength…). The main outcomes and advances in understanding along this line are summarized below:

- Results of molecular dynamics simulations of a montmorillonite in contact with a NaCl solution (*BRGM*, AIED) were used to estimate reasonable bounds for the anion exclusion volume, distance of water structuring and cation partitioning between the diffuse layer and the sorbed plane in the system. Molecular dynamics results on anion exclusion compares well with experimental data obtained on Na-montmorillonite suspensions, enabling to calibrate a macroscopic model for anion exclusion. This model has been extended to compacted systems showing that it is possible to predict anion exclusion volume and anion diffusion coefficients from montmorillonite partial dry density and ionic strength only for experiments carried out in NaCl salts background (Figure 3). Moreover, the H_2O data were consistent with ^{1}H-NMR measurements (*LAIEM*) on the synthetic clay mineral. It is then possible to build a dual porosity model reproducing transport properties of water and anions. The calculated ion distributions were then used to 'calibrate' the electrical double layer parameters of a surface complexation model contained in a code capable of coupling geochemical speciation and diffusion (PHREEQC2 v2.14). This code was then used to calculate diffusion of HTO, anions and cations through compacted montmorillonite under different conditions (density, solution composition). Comparison of model results with existing data sets show that it is able to simulate the principal observed characteristics. This model must be extended to divalent cation salt backgrounds in order tosimulate the experimental data obtained in Funmig (see below).
- Two new theoretical (and corresponding numerical) models of anion, cation and HTO diffusion in compacted clay domains were developed respectively by *Armines* and *CEA*. The distinctive feature of the *Armine* model is that it proposes that the hydration water associated with cations present in clay interlayers be treated as part of the solid phase, i.e. not as a constitutive part of overall porosity. This paradigm change allows a single value to be used for the porosity accessible for anion, cation and HTO diffusion, with only the latter two molecules being able to exchange mass with the pools of cation and hydration water present in the interlayer (solid). This model, which has many similarities with that developed by *BRGM*, is able to satisfactorily model data sets of anion, cation and HTO diffusion over a wide range of degree of compaction of the clayey material (dry densities).

The model developed by *CEA* takes a completely different approach, representing the compacted clay in terms of an ordered arrangement of charged, non porous, several nanometre-thick rectangular entities, immersed in a continuous dielectric medium (the pore solution). The rectangles represent the external surfaces (basal and edge) of real clay particles, i.e. the interlayer volume is not considered. Changes in pore size distribution as a function of density is taken into consideration by changing the particle population spacing. It is worth noting that this is the only model approach, at this scale, which yields different values for D_e perpendicular or parallel to particle orientation, i.e. this model allows introduction of diffusion anisotropy in the clay domains. Model simulation results are generally coherent with experimental observations of diffusion in compacted clays; e.g. D_e and accessible porosity values for anions decrease with ionic strength, D_e for the alkaline elements increase from Na to Cs. Effective diffusion coefficients for monovalent and divalent anions measured in illite compacted to different densitiesand for various ionic strengths (from 0.01 to 0.3 M NaCl or $KClO_4$) are in good agreement with those calculated using the model.

- Experimental data sets, for comparison with the blind predictions made using the theoretical models described above, are being generated by carrying out diffusion experiments with an anion (^{36}Cl), HTO and mono and divalent cations (^{22}Na, ^{45}Ca) on compacted synthetic montmorillonite samples, as a function of ionic strength (*CEA*). While these measurements are not completely finished at this time, initial results show for example that, as expected, (i) anion exclusion increases with decreasing ionic strength and there is no impact of ionic strength on HTO diffusion and (ii) ^{45}Ca diffusion is enhanced by and strongly depends on ionic strength (due to reduced Ca^{2+} sorption due to competition of Mg^{2+} for ion exchange sites).

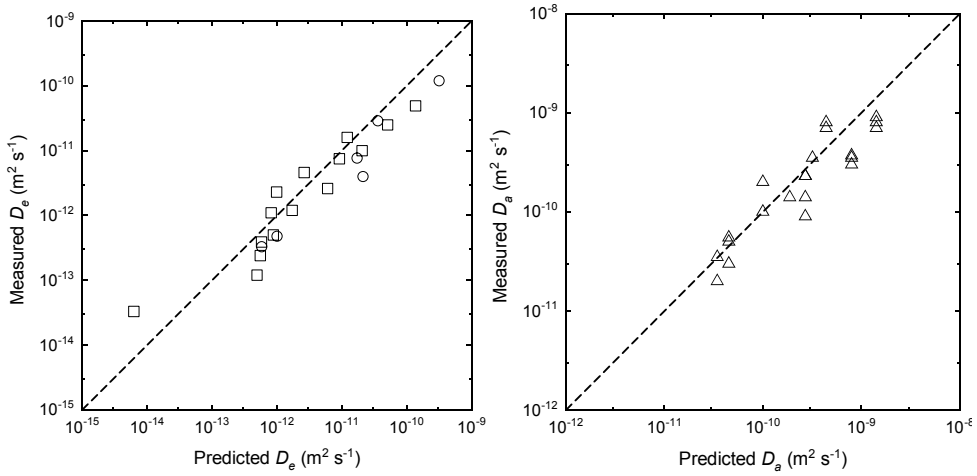

Figure 3. *Comparison of the predicted and experimental effective diffusive coefficients (left figure. Circles: data from Van Loon et al., 2007; squares: data from Muurinen et al., 1989) or apparent diffusion coefficient (right figure. Triangles: data from Molera et al., 2003). The dashed line represents the 1:1 relationship.*

Diffusion in mesoscopic scale (~mm) clayrock volumes

Considerable effort was invested in improving understanding of how clayrock mineral-porosity organization can affect diffusion of mobile (non sorbing) RN since this

seems to be a highly promising approach for establishing links between diffusion properties and observed variations in rock mineralogy. The working hypothesis, based on the observations presented in §2.3 (figure 2), was that the spatial organization of the contiguous clay matrix porosity could affect (i) the value of the apparent diffusion coefficient (D_a) for non sorbing tracers by modifying diffusion path tortuosity and (ii) the anisotropy of D_a values measured in directions perpendicular or parallel to the sedimentation planes. The study, carried out by Hydr'asa/Andra, was based on simulations of anion diffusion in numerical models of the 2D and 3D mineral-porosity distributions quantified in §2.3. These simulations were carried out using the Time Domain Diffusion (TDD) method which simulates diffusion by tracking the 'random walk' of anion particles in the 2D or 3D pixel grids based on the digitized images of mineral grain organization. Each grid pixel is characterized by its porosity (a constant value for all clay pixels, null for all others) and an isotropic D_a value (for the clay pixels). The effects of grain organization were quantified by performing simulations of diffusion, in rock volumes having different compositions, in directions parallel and perpendicular to the sedimentation surface plane. The results show that (i) D_a perpendicular to the sedimentation surface decreases with increasing fraction of non porous minerals and (ii) that the elongated shape of carbonate and quartz grains and their orientation relative to the sedimentation surface introduce geometrical anisotropy in the organization of the connected porosity at the mesoscopic scale, which in turn induces diffusion anisotropy at a larger scale. The anisotropy of diffusion, which is observed experimentally, probably has two components: inside and outside the clay matrix. The global diffusion coefficient is related to the clay matrix diffusion coefficient by a geometric factor G_m which is specific to the clay matrix geometry. The clay matrix diffusion coefficient is itself related to free diffusion of solute and a geometric factor G_{cp} related to clay particles (as described by the models presented in §3.1).

Diffusion at the macroscopic scale (cm-dm)

Several premises are behind diffusion measurements made at the ~cm scale, among the most important being that (i) they are made on samples representative of the 'average' properties (mineralogical composition, porosity characteristics, etc.) of the rock unit from which they were taken and (ii) the measured parameter values (D_e, D_a(perpendicular to bedding); D_e, D_a(parallel), accessible porosity, mineralogy, etc.) integrate, in a representative fashion, the effects on these parameters of local variations in rock properties at smaller scales. One of the working hypotheses guiding the RTDC3 experimental program at this scale was that the major characteristics of anion diffusion should be coherent with, and explainable by, phenomena which were studied and modelled at the smaller, mesoscopic scale (§3.2), in particular the role of non porous mineral grain organization in determining diffusion anisotropy, i.e. D_a(bedding parallel) > D_a(bedding perpendicular), and the reduction in D_e with increasing proportion of non porous minerals. RTDC3 efforts were therefore focused on (i) improving the capacity to measure, model and quantify the effects of rock heterogeneity and bedding on diffusion at the cm scale and (ii) evaluating the effect of rock mineralogy on diffusion, in part by comparing diffusion in samples from different clayrock formations.

Detailed analyses of HTO diffusion in dm-scale volumes of Opalinus Clay and Callovo-Oxfordian clayrock were carried out by *CIEMAT* using a novel technique con-

sisting of placing a solid source of radioactive anionic and HTO tracers at the centre of a pluri-dm sized clayrock cylinder. 3D tracer distribution maps were obtained at the end of the experiment by coring. Numerical modelling by *UDC* using a code capable of considering bedding plane relative anisotropy was used to (i) carry out sensitivity analyses to identify relevant diffusion and retention parameters and (ii) determine best estimates for parameter values by solving the inverse problem. Results for the Callovo-Oxfordian clayrock give lowest error values of $4 \cdot 10^{-11}$ $m^2 \cdot s^{-1}$ and $2.23 \cdot 10^{-11}$ $m^2 \cdot s^{-1}$ for D_e(bedding parallel) and D_e(bedding perpendicular) respectively, which leads to a diffusion anisotropy ratio of 1.8 (Figure 4). This value is of the same order, but greater than, that calculated by the TDD method (§3.2) which could be due to the fact that the TDD model does not consider possible anisotropy within the clay domains, i.e. at the scale of the models presented in §3.1. Results for HTO diffusion in the Opalinus Clay give higher anisotropy ratios, of the order of 5, which might indicate a higher degree of preferential orientation of clay particles than for the Callovo-Oxfordian formation.

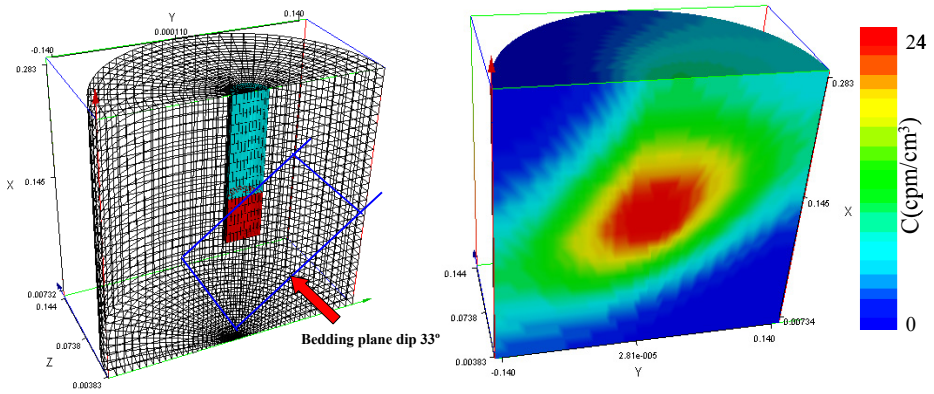

Figure 4*: Grid used in PORFLOW calculations (left). HTO results obtained with the best set of diffusion coefficient parallel and perpendicular to the bedding (right).*

At Mont Terri rock laboratory a large scale in situ experiment (DR) has been launched to investigate diffusion of non-sorbing to strongly sorbing nuclides. Combined laboratory and large scale in-situ migration studies could show that diffusion is the main transport process for radionuclides in Opalinus Clay [Tevissen et al., 2003]. Retention of radionuclides, on the other hand, has been predominantly investigated by batch sorption measurements. The objectives are threefold: (i) to obtain diffusion and retention data for moderately and strongly sorbing tracers, (ii) to improve diffusion data for rock anisotropy and (iii) to quantify effects of the borehole-disturbed zone for non-reactive tracers. The design has been validated by diffusion tests with non-sorbing and sorbing tracers [Palut et al., 2003; Van Loon et al., 2004; Wersin et al., 2008]. The injected tracers were tritium, I, Br, ^{22}Na, ^{85}Sr, Cs, ^{137}Cs, ^{133}Ba, ^{60}Co, ^{152}Eu, and ^{75}Se (planned). These tracers were added as a pulse to the fluid circulating in a packer system allowing the tracer to diffuse into the clay formation. Funmig allowed an extensive modelling exercise accompanying this experiment in which four distinct reactive transport models from four groups (*PSI, UDC, CSIC, GRS*) are being benchmarked [e.g., Gimmi, 2007; 2008; PID3.3.2].

Effective diffusion coefficients 'bedding perpendicular' were measured (*CEA*) for Cl^- and HTO on a set of Callovo-Oxfordian rock samples having carbonate contents covering the entire observed range in the formation. Rocks having extreme, and relatively rare, high carbonate contents were of particular interest since they will necessarily have very low fractions of the clay minerals governing RN diffusion (and sorption, cf. §4.2). The results for $D_e(Cl)$ show a 'threshold' effect, with $D_e(Cl)$ remaining in the normal range of values for the formation (5.10^{-12} $m^2.s^{-1}$) for carbonate fractions below ~35 wt%, then falling off progressively to roughly 40% of this value as carbonate increases to 70 wt%. This tendency is similar to that predicted by TDD modelling of the effect of increasing the fraction of non porous grains at the mesoscopic scale (§3.2).

Results of a large-scale, long-term (~10 year) in-situ diffusion test running in the HADES URL (Boom Clay, BE) with ^{14}C-labelled natural organic matter were analyzed, along with results from small-scale migration tests, in order to evaluate whether the latter could be used to predict the former, i.e. whether small-scale, short-term results for this retarded species could be up-scaled directly. The lab test results were interpreted with the classical diffusion-advection approach, yielding migration parameters which reasonably described the experimental data, without taking colloidal transport into account. The lab-derived parameters were able represent the in-situ experiment, with only a small modification of the diffusion coefficient. Inclusion of a colloid filtration term (attachment and detachment kinetics) in the modelling improved the simulation. A very good match with the experimental data was achieved when considering non-linear sorption (Freundlich isotherm) instead of linear sorption (Kd). It was concluded that more elaborate transport models are indeed able to better describe the migration of the colloidal NOM in the Boom Clay, but it remains a fitting exercise because there are no independent determinations of the attachment/detachment kinetics. Additional studies should allow improved estimation of the sorption term however.

One RTDC3 goal was to develop a comparative database of diffusion properties of different clayrock formations. The characteristics of $^{99}TcO_4^-$, HTO and $H^{14}CO_3^-$ in clayrock samples originating from two depths in the Boda Claystone formation were determined by *II-HAS***.** While the two depths show significant differences in mineralogy (e.g. absence or presence of analcime), the D_e values measured for the $^{99}TcO_4^-$ anion and HTO were generally coherent with results on other clayrocks, i.e. $D_e(TcO_4)$: $4.2 \cdot 10^{-12}$ $m^2 \cdot s^{-1}$ < $D_e(HTO)$: $1.4 \cdot 10^{-11}$ $m^2 \cdot s^{-1}$.

Diffusion at geological and Safety Case (SC) time-space scales

Performance assessment calculations in existing SC (cf. 1, 2, 3) show that non sorbing RN diffuse across the entire GBS thickness (roughly 50 meters thick) during typical PA timeframes (10^6 years). In all of these SC, single values for diffusion-determining parameters (D_e, D_a, ω) were used to represent RN diffusion throughout the entire GBS volume. The parameter values chosen for both base case (most probable) and sensitivity (pessimistic) calculations are demonstrably valid and robust, being based on statistical evaluation of measurements made on a representative population of cm-dm scale samples. One of the objectives of RTDC3 was to provide information and methods for supporting homogeneous representations of GBS diffusion properties. Three complementary approaches were taken along this line:

- A theoretical and statistical analysis of the effects of scaling on RN transport (*SCK•CEN*),
- An up-scaling methodology linking (i) diffusion parameter value variation as a function of rock mineralogy measured at the cm scale and (ii) rock mineralogy measured at the GBS scale, followed by comparative diffusion modelling with a homogeneous model (*Andra, CEA*),
- Natural tracer based studies (*UniBerne, GRS*).

A comprehensive evaluation of the potential effects of observed (or induced) spatial variability in the Boom clay formation properties on RN transport was carried out by *SCK•CEN*. The study shows that, from a theoretical standpoint, microscopic flow and transport processes can be up-scaled to the scale of the formation 'layers' so long as parameter values are associated with rock volumes equal to or exceeding that of a representative volume element (RVE) for the Boom clay (pluri-mm to cm). Consideration of two other types of information, statistical analysis of parameter values measured on cm scale samples from throughout the formation and in situ measurements integrating large rock volumes (hydraulic tests, diffusion experiments), allows a strong case to be made for using parameter values measured on small samples as a basis for determining a representative value and associated uncertainty applicable to the entire geological formation at the repository site.

A similar conclusion was reached regarding anion diffusion through the Callovo-Oxfordian formation using a method developed by *Andra* and *CEA*. The approach is based on a logical extension of the working hypothesis which guided studies at the mesoscopic (§3.2) and macroscopic (§3.3) scales, i.e. that non sorbing tracer diffusion should be determined largely by effects of rock mineral composition on porosity organization. It therefore constitutes the last step in up-scaling process understanding gained at small scales to the parameterization of model for non sorbing RN migration in the GBS for PA purposes. It consists of three main steps:

- Determination of the relationship between diffusion parameter values (D_e, ω) for Cl^- and carbonate mineral content in Callovo-Oxfordian rock samples (cf. §3.3). This relationship was used to define three rock classes having statistically different D_e values.
- Signal treatment and geo-statistical methods were used (i) to obtain vertical profiles of rock carbonate content with cm scale resolution from high resolution borehole log data and (ii) to assign formation intervals (10 cm thick) to one of the three $D_e(Cl)$ rock classes,
- Modelling of diffusion, using the above as a basis for meshing and with an anion source term located in the centre.

The calculated anion flux vs. time curve at the top of the formation was compared to that calculated for the same system but with a single D_e value used for the entire formation, i.e. the configuration used for PA calculations. The difference is insignificant.

In certain geological contexts information obtained by measuring and modelling spatial distributions of conservative (non sorbing) natural tracers can provide a powerful argument for supporting use of Fick's law representations of non sorbing RN transport at the GBS scale, based on parameter values measured at laboratory space-time scales. Such an approach requires measurement of natural tracer concentration profiles within a

geological formation (including boundary formations) followed by model interpretation to extract plausible Fick's law parameters[1]. *UniBerne* applied this approach to studying natural tracers (Cl, Br, He and water isotopes) in the Opalinus Clay and adjacent formations in the Mont Russelin anticline (Jura, CH). The Cl^- distribution shows a regular, well-defined profile, with the highest values being found in the centre of the Liassic clayrock anticline, close to the contact with Opalinus Clay. The data were modelled using a 2D geometry and the $D_p(Cl)$ value determined experimentally on Mont Terri samples. The results (Figure 5) show that the observed Cl tracer distributions are consistent with diffusion as the dominating transport process, assuming that the groundwater flow system in the overlying Dogger aquifer developed about 4 My ago, which is coherent with independent palaeo-hydrogeological evidence.

GRS modeled tracer profiles measured at the Mont Terri URL with the added objective of testing the benefits and disadvantages of using models of differing complexity to represent RN diffusion driven transport at geological (and GBS) space-time scales. The results show that, while both complex and simple models are able to represent the data satisfactorily, a higher degree in complexity does not improve the agreement between the simulations and the experimental data. The most probable reason for this is considered to be that the complexity of the model is too high and does not correspond with the level of detail and the quality of the input data.

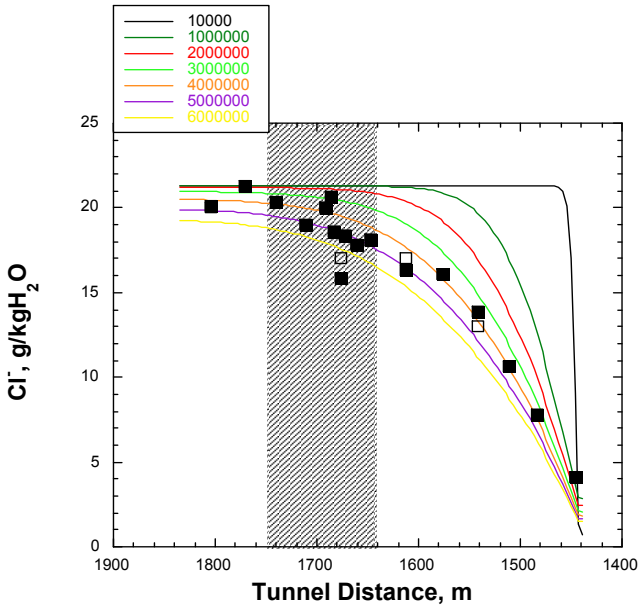

Figure 5: *Results of 2D diffusion modelling of chloride tracer concentration profiles using Dp(Cl) value determined on lab-scale sample. The curves indicate the time since imposition of boundary conditions by the overlying aquifer.*

[1] The OECD Nuclear Energy Agency 'CLAYTRAC Project: Natural Tracer Profiles Across Argillaceous Formations' (2008) treats this aspect in detail.

Understanding migration of sorbing RN in clayrocks

The principal method used for generating databases of RN sorption behaviour on clayrocks is by 'K_d' measurements in batch systems, i.e. using crushed clayrock material. K_d values obtained for many RN (e.g. actinides, ^{135}Cs) are sufficiently high such that, when used in PA modelling, these RN are entirely confined within the GBS over the simulation time frame. Three important questions of interest to future clayrock SC can be raised regarding this approach:

- Can the K_d dataset obtained for a given RN / dispersed clayrock system be interpreted in terms of a chemically plausible thermodynamic model, i.e. mass action laws for adsorbed RN species, surface site types and concentrations, other reactions…?
- Are the migration characteristics observed for a given RN in an intact clayrock coherent with the predicted behaviour based on batch sorption behaviour, i.e. either by direct use of Rd values or using the thermodynamic model?
- If not, can means be provided for selecting a K_d for PA use which compensates for the discrepancy, ideally in terms of justifiable (and robust) adaptations of parameter values in the thermodynamic model (i.e. mass action laws, activity correction model, extensive parameter values)?

Research carried out in Funmig focused mainly on enhancing understanding regarding the first and second questions, mostly for strongly sorbing RN or analogue elements, but also provided some insights into the latter aspect.

Fundamentals of RN sorption reactions on clays and clayrocks

The majority of the work on this subject was carried out within the framework of RTDC1 and the reader is invited to consult the corresponding final report for details. Nevertheless, the highlights of these actions are briefly mentioned hereafter for completeness.

Regarding surface speciation and redox reactions:

- The results of a study (*UJF-LGIT*) of the nature (hydration/hydrolysis state, inner/outer sphere complex) of Sm^{3+} species sorbed on synthetic montmorillonite samples using variety of analytical methods (neutron diffraction (ND), EXAFS, Quasi-elastic Neutron Scattering (QENS)) show somewhat contradictory results. ND measurements indicate that Sm^{3+} is bound to the clay surface and is probably partially hydrolyzed while EXAFS measurements indicate that Sm^{3+} is present as an outer-sphere complex with nine water molecules surrounding the cation. Quasielastic neutron scattering (QENS) experiments were performed with *Na-hectorite*, *Ni-hectorite* and *Sm-hectorite* samples in order to compare the diffusion mobility of water molecules in *Sm-hectorite* with that for other interlayer cations: *strongly hydrated* Ni^{2+} and relatively *weakly hydrated* Na^{+}. It was found that water mobility in Sm – hectorite sample is very close to the water mobility in the Ni-hectorite. This is only possible if Sm^{3+} ion is fully hydrated. A compromise with the neutron diffraction data can be found, assuming that not all adsorbed Sm interacts with water molecules, probably due to precipitation. It was discovered that water molecules hydrating Ni^{2+} and Sm^{3+} perform diffusion mobility measurable with a backscattering spectrometer. The diffusion coefficients of the exchangeable cations were found us-

ing slow exchange approximation to be D_{Ni} = (0.05 – 0.14) x 10^{-9} m^2/s and D_{Sm} = (0.04 – 0.18) x 10^{-9} m^2/s.

- The redox reactivity under anoxic conditions of Se(IV) with Fe(II) adsorbed on synthetic, structural Fe-free montmorillonite was studied by *UJF*, in collaboration with *BRGM*, *LPEC, LMPC/LMM*. The results show slow reduction of Se and formation of a nano-particulate Se(0) solid phase when selenite is added to a montmorillonite previously equilibrated with Fe^{2+} solution; this was not observed in Fe-free systems. These, and other, results clearly suggest that the Se and Fe redox reactions are not directly coupled, leading to the hypothesis that electrons produced in the absence of Se by oxidation of sorbed Fe(II) are stored, for example by formation of surface H_2 species, and are then available for the later Se(IV) reduction.

Regarding thermodynamic modelling of sorption:

- The results of batch sorption studies (*CIEMAT*) of Sr, Pu, selenite and europium sorption onto Na-smectite, Na-illite and mixed systems showed for selenite that (i) sorption was higher in smectite than in illite and, in both clays, was independent of ionic strength and decreased with pH, (ii) linear sorption isotherms over a broad concentration range ($1•10^{-10}$ to $1•10^{-4}$ M), and (iii) that data could be satisfactorily modelled (from pH 3 to 8) considering the formation of surface complexes at the edge sites of the clay and using a one site, non electrostatic model. Regarding Eu (III), results show that (i) ionic exchange is important at pH < 4, (ii) surface complexation becomes increasingly important as pH increases to 10, and (iii) that data could be represented satisfactorily using a model incorporating non-electrostatic, two site surface complexation and cation exchange.

- Measurements and modelling of Ni(II), Co(II) and U(VI) sorption on Opalinus Clay, and of Co(II) on illite were carried out by *PSI*, with the results for U(VI) being particularly illustrative. Here, predictive modelling of sorption was carried out using the 2 site protolysis, non electrostatic surface complexation and cation exchange sorption model used in previous studies to represent U(VI) sorption on purified Na-illite assuming that (i) illite is the main sorbing phase in the Opalinus Clay and (ii) only the UO_2^{2+} and the hydrolyzed species sorb. In the case of the clayrock, it was found that the U(VI) sorption isotherm could only be modelled if the neutral $Ca_2UO_2(CO_3)_3(aq)$ complex was included in the calculations and assumed to be non-sorbing.

- Sorption data for Cs, Sr, Am and Th on dispersed Boom Clay were gathered and interpreted (*SCK•CEN*) in terms of surface complexation models, and sorption experiments on compacted samples (clay disks) were performed for Cs and Sr to check the impact of compaction (decreased accessibility to sorption sites) on K_d, with no significant differences being observed. Cs sorption could be modelled using the same 3 site, cation-exchange model used by PSI for modelling sorption on Opalinus Clay using illite as model component. Similarly, Sr sorption could be modelled using a simple cation exchange model for argillaceous rocks based on illite as model clay. SCK•CEN also studied the influence of the natural organic matter (NOM) pre-

sent in the porewater on sorption of Eu(III) on illite in order to understand the Am(III) sorption onto Boom Clay. Tipping's Humic ion binding model VI was used to account for NOM interactions (succesfully introduced into Phreeqc code). Eu sorption behaviour on illite in presence of NOM could be interpreted with the 2SPNE SC/CE model in combination with the Humic Ion-binding model VI (Tipping). Interpretive modelling of Am and Th sorption onto Boom Clay is done using the Bradbury and Baeyens approach and are based on Am and Th sorption data on montmorillonite and illite as model components. As a first attempt to capture the interaction with NOM, a 1:1 RN-NOM surface complexation reaction was used. The above simple model currently is not able to describe the sorption isotherms and needs further refinement. In the future the Tipping model will be incorporated.

- *Armines* adapted the retention and porosity model developed for bentonite to COx clayrock by assuming additivity of the various mineralogical contributions, based principally on the content of interstratified illite/smectite (I/S) minerals and the illite to smectite ratio in the I/S minerals. The approach led to a reasonable quantitative representation of the CEC and surface complexation site densities as a function of mineralogical composition. Sorption isotherms calculated for Cs and Ni were in good agreement with measured K_d data.

Migration of (strongly) sorbing RN in intact clayrock

The most convincing (from a safety case stand point) approach for quantifying migration of highly sorbing RN in clayrock is direct measurement of D_a values (cf. Fick's second law, §1) in intact samples under conditions representative of the GBS. While this approach has been used in SC, it is much more frequent to estimate D_a using $D_a = \frac{D_e}{(\omega + \rho K_d)}$ based on (i) assumed D_e values for cationic RN and (ii) K_d datasets measured on crushed rock samples. The reason for this is evident from Fick's second law which tells us that the rate of propagation of a sorbing RN in a clayrock (i.e. the distance travelled by the migration front away from the source in a given period of time) will be inversely proportional to its K_d value. For example, for a RN having a K_d = 10 $m3.kg^{-1}$ (order of magnitude for actinides) and $D_e = 10^{-11}$ $m2.s^{-1}$ (order of magnitude for HTO), RN mass will have penetrated roughly 0.5 or 1.5 mm into a typical clayrock after respectively 1 or 10 years of contact. From a practical standpoint, this means that for a one year experimental time frame, one must be able to quantify RN mass distribution within a sub-mm thickness of rock in order to determine D_a. Despite such a challenge, RTDC3 considered that it was sufficiently important for safety case confidence building to take it on.

The work program was guided by two main objectives: (i) determining if K_d values measured in batch systems under varying conditions could be used to estimate RN sorption behaviour in the intact rock and (ii) determining if D_e values for strongly sorbing RN could be estimated based on values measured for non or weakly sorbing tracers. Studies were carried out on three different clayrocks (Opalinus Clay, Boom Clay, Callovo-Oxfordian clayrock) using elements representing the range of sorption behaviour for cationic RN: strongly-complexing (Am, Eu, Pu, U), moderately-sorbing (Cs Co, Cu), weakly-sorbing (e.g. Sr, Na). The main results concern:

- Development and application of new analytical methods for carrying out in-diffusion experiments and quantifying high K_d tracer migration in intact rock;
- Comparison of sorption equilibrium model parameter values determined in batch and compact rock systems;
- Comparison of D_e + sorption parameter value sets obtained by modelling data from in-diffusion experiments with predictions made using an assumed D_e value and batch sorption parameters.

Analytical method development

It was necessary to develop a variety of innovative analytical methods during Funmig in order to be able to quantify the migration of highly-sorbing tracers in intact clayrock samples. The 'hi-resolution abrasive peeling' method developed by *PSI* consists of diffusing tracer into a flat clayrock surface using a specially developed cell, for a given period of time (e.g. ~170 days for Eu(III)), and then abrasively removing roughly 10 μm thick layers of rock for total tracer concentration determination. With this method, tracer concentration profiles extending less than 200 μm into the rock could be determined with roughly 10 μm resolution. Along this same line, *CIEMAT* demonstrated that nuclear ion beam Rutherford Backscattering Spectroscopy (RBS) could be successfully used to quantify Eu(III) depth profiles extending to ~1.5 μm (~50 nm resolution) below a polished clayrock surface, after different in-diffusion times. *FZK-INE* developed a special cell for carrying out actinide in-diffusion experiments on clayrock samples maintained at in-situ confining pressures and an autoradiography technique for quantifying tracer distribution relative to the input surface. A different approach was taken by the *CEA* driven by the need to associate the spatial distribution of tracer mass after an in-diffusion experiment with the corresponding rock mineral-porosity organization for carrying out diffusion modelling by the TDD method (cf. §3.2). The developed method (cf. Figure 6) based on hi-resolution Laser Induced Breakdown Spectroscopy (LIBS), allows the simultaneous determination of tracer and rock mineral element distribution away from the tracer input surface with a ~3μm spatial resolution. *CEA* also developed column-based method for determining D_a parameters for sorbing RN diffusion into and out of ~ 2 mm thick clayrock 'plates', with the number of plates and flow rate being varied depending on RN the sorption and diffusion characteristics.

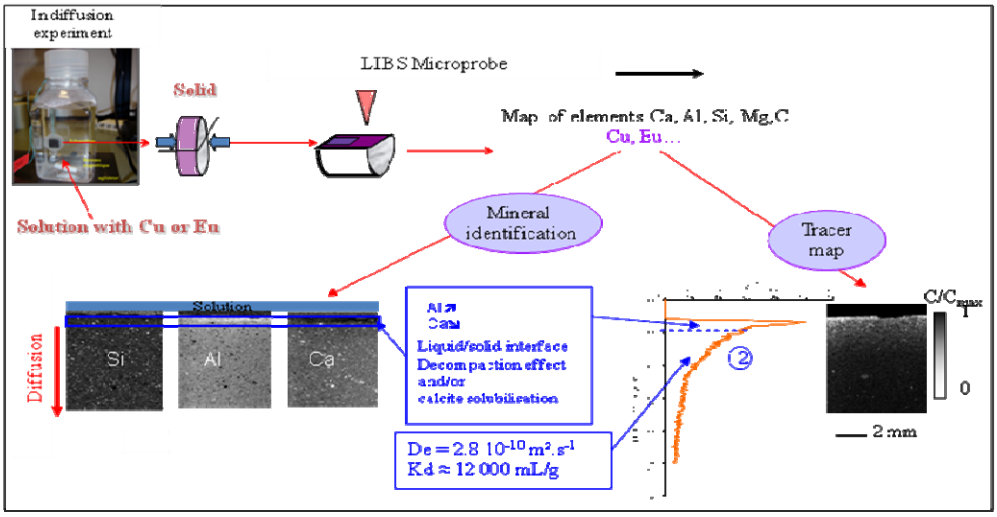

Figure 6: *Methods used for quantifying spatial distributions of both mineral and tracer concentration, here Cu, in intact clayrock samples (CEA).*

Results of comparison of RN sorption equilibrium in batch and intact rock systems

The question addressed here is quite simple – for a given mass of rock equilibrated with a given activity of a sorbing RN under otherwise identical conditions, does one measure the same total sorbed mass of RN if the rock is present as ground particles or as a compact solid? While this question can be answered fairly readily for weakly and moderately sorbing RN as will be shown below, it turns out to be quite difficult in the case of strongly sorbing RN. The key objective here is to reach an equilibrium state in systems containing compact rock samples, i.e. kinetics related to RN mass transport (diffusion) into the sample have reached insignificant levels. When this is the case, results can be interpreted using only a chemical equilibrium model, i.e. without diffusion. The results of measurements carried out by *PSI* (e.g. Figure 7) show that sorption equilibrium reached for Na^{+}, Sr^{2+} and Cs^{+} on compacted Opalinus clayrock are comparable (within a factor of 2) to corresponding states measured on crushed samples (Van Loon et al., 2005; Van Loon et al., 2008).

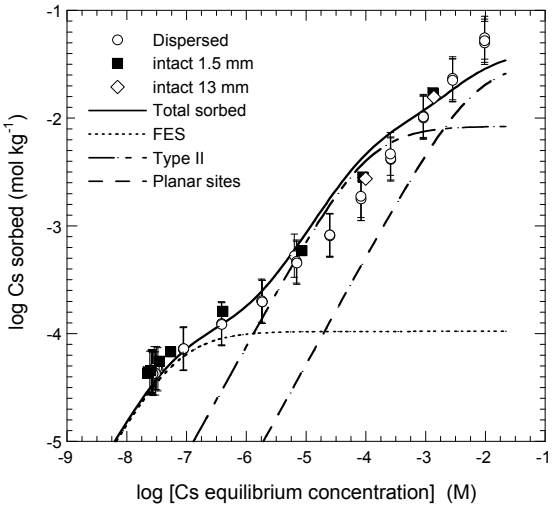

***Figure 7**: Cs sorption isotherm on OPA. The solid line is the calculated Cs isotherm using the generalised Cs sorption model and assuming an illite content of 21 wt. %. The contribution of Cs sorbed on the different illite sorption sites are shown by the various curves.*

Similar results were obtained by *SCK-CEN* for Sr and Cs on Boom Clay. The R_d values measured on compacted samples tend to be higher than for crushed rock which might be due to the longer equilibration times used for the compact material studies. Measurements of Co^{2+} sorption, while not completely attaining equilibrium within the nearly 700 day experimental time frame, indicate the same result. Taken together, these results tend to support the following conclusions:

- Crushed and whole rock samples have similar sorption site populations per unit mass (sorption site types and corresponding total concentrations),
- Similar mass action laws apply for sorption in intact and crushed materials,
- Sorption-induced retardation of RN mass transport (i.e. very low D_a value) results in very long time frames for reaching equilibrium for highly sorbing RN in compact rock systems. This limits the capacity to directly determine sorption equilibrium for actinides in compact rock.

RN migration experiments and model interpretation

A major part of the research carried out in RTDC3 was concentrated on measuring mass transfer of sorbing RN in compact clayrock-containing systems and interpreting the resulting datasets using numerical models coupling the effects of diffusion and sorption equilibrium. A wide variety of experimental techniques were used to study RN migration characteristics in rock volumes ranging from mm (cf. techniques mentioned above) to dm (laboratory and in-situ experiment) scales. Generally speaking, two types of information were sought (i) time-dependent evolution of RN tracer concentration in the source term and, in certain cases, in a 'sink' reservoir, and (ii) tracer mass distribution in the rock volume after a given time(s). Numerical modelling was then used to seek plausible sets of values for diffusion (e.g. D_a, D_e) and sorption (K_d, complexation model) parameters, and in certain cases the degree of spatial variability within the rock, leading to the best possible representation of the experimental dataset. The model re-

sults were then compared with those expected based on initial hypotheses concerning RN migration (e.g. K_d(intact rock) = K_d(batch), D_e(cations) = D_e(HTO), homogeneous porous medium), and conclusions drawn regarding the applicability or non applicability of the reference model for representing RN migration. The following sections briefly summarize the principal results of research carried out on three clayrocks: Opalinus Clay, Callovo-Oxfordian and Boom Clay.

Opalinus Clay

Migration in Opalinus clayrock of a wide range of weakly to strongly sorbing cations (Na^+, Sr^{2+}, Co^{2+}, Cs^+, U(VI), Eu(III), Pu(IV)) was studied using a number of differing experimental configurations. The results of Cs^+ in-diffusion and through-diffusion experiments carried out by *PSI* tend to show that RN migration behaviour is generally coherent with the expected sorption model but is significantly affected by relatively complex mass transport processes. One hypothesis is that the porosity is made up of well-connected and 'dead-end' pores, which would necessitate considering at least two D_a terms in the diffusion equation, with that for the 'dead end' pores representing both the kinetics of RN mass transport into this volume and RN retention on the sorption sites in contact with this porosity. In-diffusion studies of Co(II) and Eu(III), with profiles extending to less than 0.2 mm after roughly 200 days for the later (cf. Figure 8, left), also show evidence of mass transport complexity (dual path). The general conclusion is that mass transport of sorbing RN in clayrocks is still not well understood, especially given the difficulties associated with making measurements at such small spatial scales (modifications of surface layer properties….).

CIEMAT carried out in-diffusion studies using four techniques: diffusion from a solid source term in large-scale (dm) clayrock blocks (HTO and Sr), using a 'filter source sandwich' configuration (Sr, Co, Eu, U(VI), Cs) (cf. Figure 8, right), classical in-diffusion experiments (Na, Se, Sr, Cs, Co), and RBS detection (Eu). From the equation used to fit the experimental data of sorbing elements in classical in-diffusion experiments (Put and Henrion, 1992), K_d and D_a are estimated simultaneously. Generally speaking, the obtained K_d values were found to be significantly smaller (10% or smaller for Co and Cs) than those measured in batch experiments. On the other hand, the D_a range obtained for Cs (3 to 12.10^{-14} $m^2.s^{-1}$) is similar to the value obtained by *PSI* (~ 6.10^{-14} $m^2.s^{-1}$) and D_a values measured for Co and Eu are intermediate between the D_a values for fast and slow diffusion path values fit by *PSI*. This suggests that some of the differences between K_d and observed effects on D_a might be attributable to differences in the modelling approach used for taking sorption into account. For example, had the Kd values been fixed at those measured in batch experiments (cf. results in §4.2.2) and the fit made on the De value, the result would have given cation De values > De(HTO).

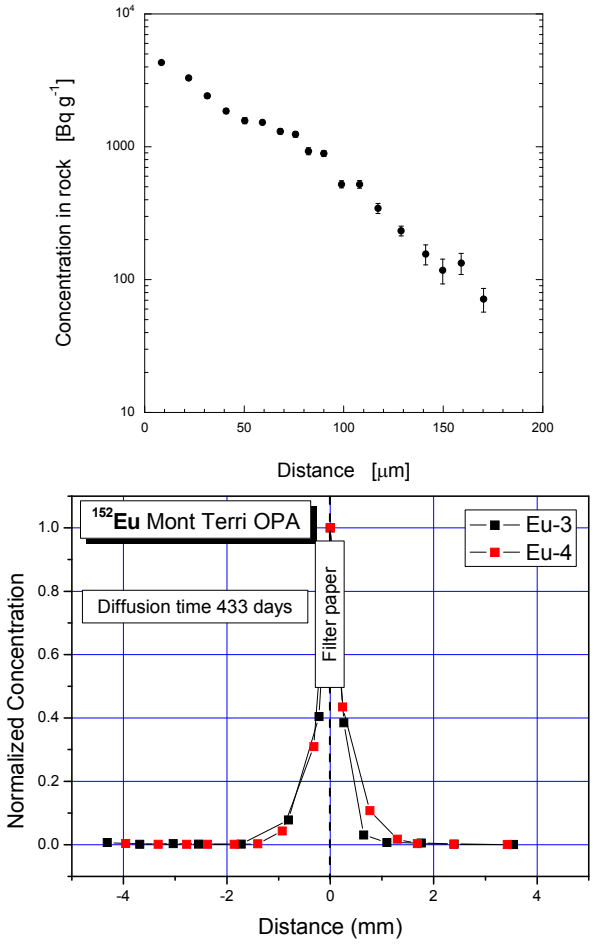

***Figure 8**: Activity vs. depth profiles measured after Eu in-diffusion into Opalinus clay samples (left) after 168 days using abrasive peeling method (PSI); (right) filter-sandwich experiment lasting 433 days, followed by slicing (CIEMAT).*

Migration of most of these tracers is also being studied by means of the DR in-situ experiment being carried out by Nagra/*PSI* at the Mont Terri URL, the first step of which was predictive modelling (*PSI*, *UDC, GRS*) of tracer mass loss from the source solution using a variety of numerical codes. While preliminary data on tracer loss from the injection interval tend to confirm the general behaviour expected based on measurements on rock samples, data modelling also shows that for strongly sorbing tracers, complexities in mass transfer (borehole mixing, diffusion in filters, etc.) strongly influence experimental data, making clear-cut estimations of values for diffusion-retention parameters in the undisturbed clayrock difficult. Some of these ambiguities will certainly be removed, at least for the more mobile tracers, when information on tracer distribution in the surrounding rock becomes available (post-Funmig) for providing further constraints on model interpretations.

Finally, Pu(V) diffusion into Opalinus clayrock samples kept under in-situ confining pressures was measured by *FZK-INE*, with results from both batch and in-diffusion experiments showing that Pu is reduced to the Pu(IV), probably by Fe(II) con-

tained in rock minerals (probably chlorite), and is retained (sorption or other process?) on preferential sites.

Callovo-Oxfordian

The Callovo-Oxfordian research program is, by design, quite similar to that described for the Opalinus clayrock since one of the objectives of RTDC3 was to generate comparable data sets for different clayrocks in order to identify common characteristics and eventual significant differences in RN migration properties. The principal difference between the two is in the working hypothesis, and consequent experimental approach, taken by a consortium of French partners (*CEA*, *ERM, Hydr'asa, Andra*) for quantifying and modelling migration of highly-sorbing RN in clayrock. The guiding assumption here was that, given the very small spatial scales covered by RN migration during the time frames of in-diffusion experiments owing to the preponderant effect of sorption, it would be important to be able to quantify how tracer mass present in the diffusion profile was distributed relative to rock mineral constituents and associated porosity. The approach taken (cf. Figures 1 & 7) involved carrying out, on a single, oriented cm-scale volume of clayrock:

- Characterization of the mineral-pore space organization and construction of the corresponding 2-3D numerical models, including analysis of grain organization (cf. §2.2), followed by TDD modelling of diffusion of non sorbing tracers (cf. §3.2);
- In-diffusing a highly-sorbing tracer (Eu, Cu) into the rock (gradient perpendicular to sedimentation plane) for a given period, then sectioning the rock perpendicular to bedding;
- Simultaneous mapping of tracer mass and mineral grain 2D spatial distributions, relative to the in-diffusion surface, using μLIBS and Electron Probe Micro Analyser (calculation of the average diffusion profile), followed by construction of numerical models of the in-diffusion zone;
- Inverse modelling of tracer diffusion (source term, spatial distribution) to determine D_a values for the porous mineral zones (clay matrix + disseminated pyrite), followed by comparison with batch K_d.

The results for Cu(II) (the most complete dataset available) are rich in information concerning both tracer migration phenomena and potential experimental artefacts which can make measurements on such small rock volumes difficult to interpret. Regarding the former, it was found that (i) Cu does not penetrate into, nor sorb significantly onto, the carbonate and quartz grains and associates preferentially with the pyrite minerals dispersed in the clay matrix, (ii) Cu diffusion profiles (clay and pyrite) developed over a distance of roughly 2 mm into the rock and (iii) evaluation of the entire dataset (reservoir + profile) yields values for D_e ($2.5.10^{-10}$ $m^2.s^{-1}$) and Rd (3500 mg/L) which are consistent both with results showing that D_e for cations in the COx are generally significantly higher than the value for HTO (~ $2.5.10^{-11}$ m^2s^{-1}) and measurements of K_d(Cu) which give values in the 3000 to 9000 range (note that Rd could be controlled by the redox reactivity of this tracer). On the other hand, detailed analysis also shows that the roughly 50 μm layer of rock in contact with the source solution is significantly perturbed, both in terms of its mineral-porosity composition/organization and its Cu(II) retention characteristics - the D_a in this zone is roughly two orders of magnitude less

than the rest of the profile. These observations have, by the way, quite a number of similarities with those for Co(II) in-diffusion in the Opalinus Clay.

CIEMAT carried out a program of 'filter sandwich', in-diffusion, and block-scale diffusion measurements similar to that described for the Opalinus clay rock, and obtained generally similar results, i.e. K_d extracted from fitted D_a values are significantly smaller than those observed in comparable batch (cf. §4.2.4).

Note finally that *FZK/INE* carried out similar measurements of Pu(V) migration in COx samples and obtained similar results as for Opalinus.

K_d values for Cs were determined (*CEA*) on the same set of 'variable carbonate content' COx samples studied in §3.2. As for D_e(Cl), the results exhibit a 'threshold' effect, with Kd remaining in the normal range of values for the formation for carbonate fractions below ~70 wt%, then falling off drastically to roughly 10 wt% of this value. For completeness it can be noted that, when this data is used to parameterize the distribution of Kd(Cs) values at the formation scale (cf. §3.4), the calculated Cs flux vs. time curve at the top of the formation is, as expected, identical to that calculated using a constant K_d for the entire formation.

Boom Clay

For Boom Clay, reliable and reproducible values for the D_a had already been obtained from different types of experiments (column migration type experiments, electromigration experiments), but they did not lead to trustworthy R values and thus no good comparison with sorption data was possible. A coupled transport simulation of a Cs diffusion profile implementing the 3 site, cation exchange model for Cs^+ sorption (cf. paragraph 4.1) was used to carry out a sensitivity analysis on the effect of increased pore diffusion coefficients (related to "surface diffusion" effects) and decreasing available sorption sites. Results show that good fits to the migration profile required either that (i) the total sorption site concentration needed to be decreased to a fraction (5%) of that used to model Cs sorption data obtained on dispersed and compact Boom Clay or (ii) the D_p value needed to be raised by an order of magnitude compared to the D_p value of HTO. Sorption experiments with Cs and Sr on compacted clay were performed and showed that compaction did not affect the accessibility of sorption sites seeming to support the second explanation. In-diffusion and through-diffusion were carried out and a good approximation of the R value was obtained by combining the data of the separate fits. Feeding these values for Cs and Sr into the relationship $R=1 + (\rho K_d/\eta)$ resulted in K_d values which matched the values from the sorption experiments. The following parameters for Cs and Sr migration and retention in Boom Clay are obtained: D_a(Cs)~$1.4.10^{-13}$ m²/s & ηR~12700 (logKd ~3.9), D_a(Sr) ~$7.8.10^{-12}$ m²/s & ηR~438 (log K_d~2.4). For Cs and Sr migration in Boom Clay, the relationship between R and K_d (under the approximation that at low concentrations sorption is a linear reversible process), seems valid. For transport modelling purposes, one can therefore introduce experimental measured sorption values or the mechanistic sorption model to simulate the transport without having to change sorption site densities. The common explanation for D_e values for cations exceeding that for HTO is that a supplementary diffusion 'pathway' is operant for sorbed cations, so-called "surface diffusion", the nature of which is still not understood.

Main messages for Clayrock Safety Cases

The overall results of RTDC3 can be summarized by returning to the three questions posed in the introduction:

- Do we have a sound theoretical basis for describing RN speciation in the porosity of highly-compacted clay materials and clayrocks, in particular the distribution of total RN mass between dissolved and sorbed species?

  A fairly positive response seems justified based on two main results. The first is the observation that similar equilibrium sorption states (K_d) are observed in dispersed and compacted materials for moderately sorbing cations (Sr^{2+}, Cs^{+}, Co^{2+}) for all clayrocks. This implies that the same sorption site populations are accessible under both conditions and that the corresponding mass action laws are valid. It was not possible to demonstrate this for highly sorbing RN (actinides…) because of the extremely long times needed to reach equilibrium conditions (associated with other problems), but there does not seem to be any clear reason why they should not have a similar behaviour. The work on pure clay systems provides a sound basis for partitioning the mass of both anionic and cationic RN between different porosity volumes (anionic exclusion, interlayer, EDL, bulk).

- Do we have a coherent conceptual model describing diffusion-driven transport of anionic and cationic RN in clayrocks?

  Here the answer is clearly mixed. For anions, yes. The results of the studies carried out at scales ranging from molecular/microscopic, to mesoscopic, to macroscopic, and geological formation scales offer a sound scientific basis for explaining and modelling migration of anionic RN. As for cations, the picture is not so clear, with all of the results tending to show that coupled diffusion-sorption migration is much more complex than expected, leading generally to greater mobility than that predicted by coupling Fick and batch K_d. Several hypotheses have been advanced for this, perhaps the most plausible being that cationic RN diffuse along more than one type of 'pathway' (or porosity) in a clayrock, each having a corresponding D_p value and sorption site population. In this case, mass transport kinetics could limit access to the sites in the lower D_p porosity. It should also not be forgotten that these studies are necessarily carried out on very small rock volumes, with the accompanying possibility that effects of mineral-porosity heterogeneity existing at this scale might also have an influence. It is not impossible that the reduced effect of sorption retardation observed at these mm scales becomes less important when migration over larger space (and time) scales are considered. In any case, more research is indicated in this area.

- Do we have credible strategies / methods for carrying out the up-scaling needed to obtain representative parameter values usable for performance assessment simulations of a clayrock geological barrier system, in particular taking into account the effects of spatial heterogeneity of rock physical-chemical properties.

Here the answer is an unqualified yes, backed up by the multiple lines of argument and demonstration provided by the theoretical, experimental, up-scaling and natural tracer studies presented above.

Acknowledgements

This project has been co-funded by the European Commission and performed as part of the sixth EURATOM Framework Programme for nuclear research and training activities (2002-2006) under contract FI6W-CT-2004-3.2.1.1-1 (FP6-516514).

References

Andra (2005), Dossier 2005 Argile

Nagra (2002), Project Opalinus Clay, Demonstration of disposal feasibility for spent fuel, vitrified high-level waste and long-lived intermediate-level waste, Safety Report, Technical report 02-05

NEA 'CLAYTRAC Project: Natural Tracer Profiles Across Argillaceous Formations' (2008)

ONDRAF/NIRAS (2001), Safety assessment and feasibility Interim Report 2 (Safir 2), Nirond 2001-05

Palut, J.-M.; Ph. Montarnal, A. Gautschi, E. Tevissen, E. Mouche. J. Contaminant Hydrology 61, 203 (2003).

Put, M., Henrion, P (1992) "Modelling of radionuclide migration and heat transport from an HLW-repository in Boom clay" EUR-14156

Tevissen, E., J.M. Soler, Mont Terri Project. DI Experiment. Synthesis Report. Mont Terri Technical Report TR 2001-05, swisstopo, Wabern, Switzerland, 2003.

Van Loon, L.R., Baeyens, B., Bradbury, M.H. (2005) Diffusion and retention of sodium and strontium in Opalinus Clay: comparison of sorption data from diffusion and batch sortpin measurements, and geochamical calculations. Applied Geochemistry 20, 2351-2363.

Van Loon, L.R.; P. Wersin, J.M. Soler, J. Eikenberg, Th. Gimmi, P. Hernán, S. Dewonck, S. Savoye, Radiochimica Acta 92, 757 (2004).

Wersin, P.; Soler, J. M., Van Loon, L., Eikenberg, J., Baeyens, B., Grolimund, D., Gimmi, T., Dewonck, S., Diffusion of HTO, Br-, I-, Cs+, Sr-85(2+) and Co-60(2+) in a clay formation: Results and modelling from an in situ experiment in Opalinus Clay, Applied Geochemistry, 23 (4), 678-691 (2008).

Publications and Communications

Peer reviewed publications

Alonso. U, T. Missana, M. García-Gutiérrez, A. Patelli, M. Siitari-Kauppi, V. Rigato (2009) "Diffusion coefficient measurements in consolidated clay by RBS micro-scale profiling" Applied Clay Science (in press).

Alonso. U.; Tiziana Missana, Miguel García-Gutiérrez, Alessandro Patelli, Marja Siitari-Kauppi, Valentino Rigato Diffusion coefficient measurements in consolidated clay by RBS micro – scale profiling. Applied Clay Science [accepted/

Charlet, L, A.C. Scheinost, C. Tournassat , J.M. Greneche, A. Gehin, A. Fernandez-Martınez, S. Coudert, D. Tisserand, J. Brendle (2007) Electron transfer at the mineral/water interface: Selenium reduction by ferrous iron sorbed on clay, Geochimica et Cosmochimica Acta 71 (2007) 5731–5749

Cormenzana. J.L., M. García-Gutiérrez, T. Missana, U. Alonso "Modelling large-scale laboratory HTO and strontium diffusion experiments in Mont Terri and Bure clay rocks". Physics and Chemistry of the Earth 33, 949-956 (2008).

García-Gutiérrez, M, J.L. Cormenzana, T. Missana, M. Mingarro, U. Alonso, J. Samper, Q. Yang, S. Yi. "Diffusion experiments in Callovo-Oxfordian clay from the Meuse/Haute-Marne URL, France: Experimental setup and data analyses". Physics and Chemistry of the Earth **33**, S125-S130 (2008).

Géhin.A., Grenèche.J.M., Tournassat.C., Brendlé.Miehé.J., Rancourt.D.G., Charlet.L. (2007) Reversible surface-sorption-induced electron-transfer oxidation of Fe(II) at reactive sites on a synthetic clay mineral., Geochimica et Cosmochimica acta, vol. 71, n°4, pp. 863-876

Gimmi, Th.; Modelling field diffusion experiments in clay rock: Influence of numerical representation of borehole and rock interface. Journal of Environmental Science for Sustainable Society, 2, 61-68 (2008).

Jakob, A., Pfingsten, W., Van Loon, L.R. (2008) Effects of sorption competition on caesium diffuson through compacted argillaceous rock – a case study. Accepted for Geochimica et Cosmochimica Acta.

Lázár, K., Máthé, Z., Földvári, M., Németh, T., Mell, P. (2008) Various stages of oxidation of chlorite as reflected in the Fe^{2+} and Fe^{3+} proportions in the Mössbauer spectra of minerals in Boda Claystone, Hyperfine Interactions, (submitted)

Leroy.P., Revil.A., Altmann.S., Tournassat.C. (2007) Modeling of the composition of the pore water in a clayrock geological formation (Callovo-Oxfordian, France)., Geochimica et Cosmochimica acta, Vol. 71, p. 1087-1097

Liu, X.; M. Fattahi, G. Montavon., B. Grambow. Selenide Retention onto pyrite under reducing conditions. Radiochim. Acta. 96 (2008) 473

Maes N., Salah S., Jacques D., Aertsens M. Van Gompel M., De Cannière P., Velitchkova N.(2008) Retention of Cs in Boom clay: Comparison of data from batch sorption tests and diffusion experiments on intact clay cores. Physics and Chemistry of the Earth 33, S149-S155.

Mell, P., Megyeri, J., Riess, L., Máthé, Z., Csicsák, J., Lázár, K., (2006) Sorption of Co, Cs, Sr and I onto argillaceous rock as studied by radiotracers, Journal of Radioanalytical and Nuclear Chemistry, 268 (2006) 405–410.

Mell, P., Megyeri, J., Riess, L., Máthé, Z., Hámos, G., Lázár, K., (2006) Diffusion of Sr, Cs, Co and I in argillaceous rock as studied by radiotracers, Journal of Radioanalytical and Nuclear Chemistry, 268, (2006) 411–417.

Montavon, G.; Azouazi, M.; Grasset, L.; Bailly, C.; Rabung, T.; Michel, R.; Grambow, B. Kerogen contribution to the transport of trivalent metal ions in the Callovo-Oxfordian formation. Article in preparation

Montavon, G.; Z. Guo, J. Lützenkirchen, E. Alhajji, M.A.M. Kedziorek, A.C.M. Bourg, B. Grambow. Interaction of selenite with MX-80 bentonite: Effect of minor phases, pH, selenite loading, solution composition and compaction, Colloids and Surfaces A: Physicochem. Eng. Aspects 332 (2009) 71–77

Samper. J. Q. Yang, S. Yi, M. García-Gutiérrez, T. Missana, M. Mingarro, U. Alonso, J.L. Cormenzana. "Numerical modelling of large-scale solid-source diffusion experiments in Callovo-Oxfordian clay. Physics and Chemistry of the Earth **33**, S208-S215 (2008).

Sobolev O, Charlet L. , Cuello G J, Gehin A. , Brendle J and Geoffroy N. (2008) Hydration and hydrolysis of samarium (III) in montmorillonite clay: a neutron diffraction study, J. Phys.: Condens. Matter 20 (10) 104207-104212.

Tournassat.C., Lerouge.C., Blanc.P., Brendlé.J., Greneche.J.M., Touzelet.S., Gaucher.E. (2008) Cation exchanged Fe(II) and Sr compared to other divalent cations (Ca, Mg) in Bure Callovian-Oxfordian formation, Implications for porewater composition modeling**.**, Applied Geochemistry *,* 23(4) 641-654.

Van Loon, L.R., Baeyens, B., Bradbury, M.H. (2008) The sorption behaviour of caesium on Opalinus Clay: a comparison between intact and crushed material. Submitted to Applied Geochemistry.

Van Loon, L.R., Müller, W. (2008) Diffusion and retention behaviour of trace amounts of ^{60}Co(II) and ^{134}Cs(I) in Opalinus Clay: first results from an in-diffusion experiment combined with a □-abrasive technique for profile analysis. To be submitted to Applied Geochemistry.

Communications & S&T Articles

Alonso, Ú., Missana, T., García-Gutiérrez, M., Patelli, A., Siitari-Kauppi, M., Leskinen, A., Rigato, V. (2007) Diffusion coefficients measurement in consolidated clays: a combination of micro-scale profiling and solid pore structure analyses. In: Clays in

natural and engineered barriers for radioactive waste confinement - Lille 2007 - 3rd International Meeting – Andra, 493-494

Appelo, C.A.J., Van Loon, L.R. (2008) Modeling of Cs-data from diffusion experiments in the laboratory and in-situ in DI-A experiments (phase 12) in Opalinus Clay. Part 1: Modeling laboratory data. Mont Terri Technical Report.

Charlet, L., Scheinost, AC., Grenèche, J.M., Tournassat, C., Géhin, A., Coudert, S., Brendlé.Miehé, J. (2006) Reactivity of ferrous iron in anoxic environments: electron transfers in Se(IV)-Fe(II)-mineral systems., in ACS National Meeting - 23rd - San Francisco - CA - 10-14/09/2006

Cormenzana, J.L., García-Gutiérrez, M., Missana, T., Alonso, Ú. (2007) Modelling large-scale laboratory diffusion experiments in Mont Terri and Bure clay rocks, Migration´ 07 – 11th International conference, 228 (Munich).

Diaz N, F. Goutelard, P.Turq (2007) A cross method of a nanoscale modelling and macroscopic data to estimate anion effective diffusion coefficient in argillite, Funmig Annual Meeting, Edinburgh.

Fernández, A.M., Altmann, S., Maes, N., Melón, A., Parneix J.C., Tournassat, C., Gaucher, E., De Craen, M. 2009. Characterization and comparison among different argillaceous formations. XIV International Clay Conference. Micro et Nano: Scientiae Mare Magnum. Italy, June 2009.

Fernández, A.M., Melón, A. 2009. Water states and types of water in different argillaceous formations. XIV International Clay Conference. Micro et Nano: Scientiae Mare Magnum. Italy, June 2009.

García-Gutiérrez, M., Cormenzana, J.L., Missana, T., Mingarro, M., Alonso, Ú., Samper, J., Yang, Q., Yi, S. (2007) Diffusion experiments in Callovo-Oxfordian clay from the Bure site, France. Experimental setup and data analyses. In: Clays in natural and engineered barriers for radioactive waste confinement - Lille 2007 - 3rd International Meeting – Andra, 493-494

García-Gutiérrez, M., Cormenzana, J.L., Missana, T., Mingarro, M., Alonso, Ú., Samper, J., Yang, Q., Yi, S. (2007) Large-scale diffusion experiments in Callovo-Oxfordian clay from the Bure site, France.

Goutelard F. S. Altmann, N. Diaz, Y. Charles, D. Hainos, Y. Larabi (2007) Impact of carbonate content of Callovo-Oxfordian rock on 36Cl, 137Cs and HTO migration properties, Funmig Annual Meeting, Edinburgh.

ISBN: 978-3-939355-02-1

Koroleva M, M. Mazurek, A. P . Alt-Epping, A. Gautschi, A.M. Fernández, H.N. Waber (2007) Identification and quantification of large-scale diffusion in a deep claystone formation (Opalinus Clay of Mont Russelin, Switzerland), 3rd International Meeting on Clays in Natural&Engineered Barriers for Radioactive Waste Confinement – ANDRA (Lille)

Lázár K, J. Megyeri, T, Szarvas, J-C. Parneix, Z. Máthé (2007), Diffusion of HTO, $^{99}TcO_4^-$ and $H^{14}CO_3^-$ in Boda Claystone samples: composition, porosity, and break-through measurements, Funmig Annual Meeting, Edinburgh.

Lázár K, J. Megyeri, Z. Máthé (2007) Diffusion of anionic species in borecore samples of Boda Claystone Formation, ibid. 2nd Annual FUNMIG Workshop Proceedings: - SKB Techical report TR-07-05, p409 – 414.

Lázár K, J. Megyeri, Z. Máthé, (2007) Influence of the mineral composition and the groundwater pH on the diffusion of $^{99}TcO_4^-$ and $H^{14}CO_3^-$ anions through borecore samples of Boda Claystone, 2nd Annual FUNMIG Workshop Proceedings: - SKB Techical report TR-07-05, p201 – 205.

Lerouge, C. M., P., Gaucher, E., Albrecht, A., and Tournassat, C., 2006. A geological, Mineralogical and Geochemical Gis for the Andra URL: A tool for the water-rock interactions modelling at a regional scale. *Bridging Clay*. (Oléron, France).

Lerouge, C., Gaucher, E., Beny, C., Tournassat, C., Blanc, P. (2006) Redox conditions in the callovian-oxfordian clayey formation., in FUNMIG - 2nd annual workshop - Stockholm - Suède - 21-23/11/2006

Liu, X.; D.J., Bruggeman C. , Salah S., Maes N. (2008) Influence of Boom Clay organic matter on the adsorption of Eu^{3+} by illite. 4th Annual FUNMIG Workshop Proceedings. Accepted

Liu, X.; M. Fattahi, G. Montavon, B. Grambow, Retention of selenide onto pyrite under redox potential conditions. Mobile Fission and Activation Products in Nuclear Waste Disposal, 16-19 January 2007, La Baule, France.

Maes N., Salah S., Jacques D., Aertsens M., Van Gompel M., De Cannière P., Velitchkova N. (2007) Retention of Cs in Boom Clay: comparison of data from batch sorption tests and diffusion experiments on intact clay cores, 3rd International Meeting on Clays in Natural&Engineered Barriers for Radioactive Waste Confinement – ANDRA (Lille)

Mazurier A, J.C. Parneix, J.C. Robinet (2007) X-ray microtomography applied to 3D clay rocks characterization, Journées annuelles de la SF2M - Société Française de Métallurgie et de Matériaux – Ecole des Mines de Saint-Etienne – 30 mai au 1er juin 2007 – Oral communication.

Mazurier A, J.C. Parneix, J.C. Robinet (2007) X-ray microtomography as an upscaling tool applied to 3D clay rock characterization. Funmig Annual Meeting, Edinburgh.

Miehé-Brendlé J A. C. Faust, L Vidal, C.Tournassat, J.-M.Grenèche, A.Gehin and L. Charlet, Synthesis, characterization and properties of iron-rich Na montmorillonite, Euroclay2007 (22-26 juillet 2007, Aveiro, Portugal)

Miehé-Brendlé J, A.C. Faust, L.Vidal, A. Géhin, L. Charlet, J-M. Grenèche, C. Tournassat, P.Blanc, E. Gaucher Synthesis, characterization and applications of montmorillonite containing Fe (III) in the octahedral sheet, Funmig Annual Meeting, Edinburgh.

Montavon, G.; Z. Guo, E. Alhajji, B. Grambow, Sorption of Se(IV) on compacted clay materials. Mobile Fission and Activation Products in Nuclear Waste Disposal, 16-19 January 2007, La Baule, France.

Robinet J.-C., Mazurier A., Sardini P., Prêt D., Boller E., Parneix J.-C. (2008) A new insight in mineral segmentation form tomographic images of clay rich sediments . 1st conference on 3D Imaging of Material And Systems, 8-12 septembre 2008.

Robinet JC, N. Diaz, P. Sardini, F. Goutelard, A. Bouchet, D. Menut, J-C Parneix, S. Sammartino,D. Prêt , M. Siitari-Kauppi, D. Coelho (2007) Multi-scale characterization of mineral and textural spatial heterogeneities in Callovo-Oxfordian argillite and its consequence on solute species diffusion modeling, poster 3rd International Meeting on Clays in Natural & Engineered Barriers for Radioactive Waste Confinement – ANDRA (Lille)

Robinet J-C, Pret D., Sardini P, Bouchet A, Parneix J-C (2007) Spatial organization of carbonates in Bure argilite from millimeter to micrometer scale, Funmig Annual Meeting, Edinburgh.

Robinet J-C, Pret D., Sardini P, Coelho D (2007) Solute diffusion in Bure argilite from millimeter to micrometer: the role of mineral and microstructural heterogeneities, Funmig Annual Meeting, Edinburgh.

Rübel A (2007) Modelling tracer profiles with approaches of different complexity, Funmig Annual Meeting, Edinburgh.

Rübel, A.; Becker, D.-A.; Fein, E. (2007): Radionuclide transport modelling to assess the safety of repositories in clays. GRS-228, Gesellschaft für Anlagen und Reaktorsicherheit (GRS) mbH, Braunschweig.

Samper J et al (2007) Model of large-scale solid source diffusion experiments in Callovo-Oxfordian clay, Funmig Annual Meeting, Edinburgh.

Samper J et al (2007) Numerical models for the design and interpretation of in situ diffusion and retention (DR) experiment in Opalinus Clay, Funmig Annual Meeting, Edinburgh.

Samper, J., Q. Yang, 2007, Scoping numerical calculation for the design of the in situ diffusion and retention (DR) experiment. In: 2nd Annual Workshop of the IP FUNMIG, SKB Technical Report TR-07-05, 337-343.

Samper, J., Q. Yang, M. García-Gutiérrez, T. Missana, M. Mingarro, Ú. Alonso, J.L. Cormenzana, 2007, Diffusion experiments in Callovo-Oxfordian Clay from the Bure site, France: 2 Model results, In: Clays in natural and engineered barriers for radioactive waste confinement - Lille 2007 - 3rd International Meeting – Andra, 493-494 (abstract).

Samper, J., Yang, Q., Yi, S., García-Gutiérrez, M., Missana, T., Mingarro, M., Alonso, Ú., Cormenzana, J.L. (2007) Model of large-scale solid source diffusion experiments in Callovo-Oxfordian clay. In: Clays in natural and engineered barriers for radioactive waste confinement - Lille 2007 - 3rd International Meeting – Andra, 493-494

Tournassat Ch, Yves Chapron, Philippe Leroy, Faïza Boulahya (2007a) Repartition and mobility of water and ions near clay surfaces. Part I. Molecular dynamics approach, Funmig Annual Meeting, Edinburgh.

Tournassat Ch, Yves Chapron, Philippe Leroy, Faïza Boulahya (2007b) Repartition and mobility of water and ions near clay surfaces. Part II. comparisons with macroscopic models and implications, Funmig Annual Meeting, Edinburgh.

Tournassat, C. (2008b) A predictive model for anion exclusion in compacted Na-montmorillonite. Funmig Annual Meeting, Karlsruhe.

Tournassat, C., Chapron, Y., Leroy, P., Bizi, M., Boulahya, F. (2008a) Comparison of molecular dynamics simulations with Triple Layer and modified Gouy-Chapman models in a dilute NaCl - montmorillonite system. Funmig Annual Meeting, Karlsruhe.

Tournassat, C., Greneche, J.M., Blanc, P., Brendlé, J., Charlet, L., Gaucher, E., Gehin, A., Lerouge, C. (2005) Mössbauer evidence for Fe(II) high redox reactivity in clay phases of Callovian-Oxfordian claystones. Methodological implications., in FUNMIG - 1st annual workshop - Saclay - France

Tournassat.C., Chapron.Y., Boulahya.F. (2007) Investigation of the clay water interface by the mean of molecular dynamics calculation. Comparison of two clay Force Fields., in Colloque du Groupe Français des Argiles - 5ème - Mulhouse - France - 18-19/04/2007

Tournassat.C., Lerouge.C., Brendlé.J., Greneche.J.M., Touzelet.S., Blanc.P., Gaucher.E. (2007) Cation exchanged Fe(II) and Sr as compared to other divalent cations (Ca, Mg) in the Callovian-Oxfordian formation. Implications for porewater composition modeling., in Clay in natural & engineered barriers for radioactive waste confinement - 3rd international meeting - Lille - France - 17-20/09/2007

Wersin, P., Th. Gimmi, J. M. Soler, S. Dewonck, S. Savoye, L. Van Loon, J. Eikenberg, B. Baeyens, Q. Yang, J. Samper, 2007, Diffusion and retention of radionuclides in Opalinus Clay : results from a long-term migration in-situ test, On the Chemistry and Migration Behaviour of Actinides and Fission Products in the Geosphere – Migration´ 07 – 11th International conference).

Annex

Comparison of the clayrock properties and porewater chemistry for Boom Clay, Callovo-Oxfordian, Opalinus Clay and Boda Claystone

The main mudrock characteristics and properties which have an important bearing on contaminant mobility were analysed in some core samples from four different argillaceous formation: Boom Clay, Callovo-Oxfordian, Opalinus Clay and Boda Claystone. The main characteristics are summarised in *Table 1* to *Table 6*.

Table 1. *General parameters*

Stratigraphic unit (name)	Site	Stratigraphic unit (age)	Age (Ma)	Clasification	Main Lithology	Burial Depth (m)	Thickness (m)	Origin	Max. Temp. (ºC)	Potential Disposal Depth (m)
Boom Clay	Mol (Belgium)	Rupelian (Logger Oligocene, Tertiary)	30-36	Plastic and Consolidated dark-grey clay rich in pyrite and organic matter	rhythmic alternation of silty clay and clayey silt with increasing silt content at the base and at the top	186-288 (186 max.)	102	Marine; deposited in a shallow ambient during several transgressions	16	>200
Callovo-Oxfordian	Meuse/ Haute-Marne (France)	From middle Callovian to lower Oxfordian (Jurassic)	152-158	Indurated dark-grey claystone	four units: mainly clayey at the bottom and turn to silt and calcareous at the top	420-555 (+400 max.)	130-145	Marine; sediments produced in a continuous manner and very calm conditions	40	--
Opalinus Clay	Mont Terri (Switzerland)	Lower and Middle part of Aalenian (Jurassic)	180	Indurated dark-grey silt/sandy claystone	overconsolidated clayshale with three facies: shaly, sandy and carbonate-rich sandy	230-320 (1350 max.)	160	Marine; sedimentation took place in degradative and oxic environment, with sulphate reduction during early diagenesis	85	400-800
Boda Claystone	Boda (Hungary)	Upper part of upper Rotliegend (Upper Permian)	250-260	Indurated brownish red and reddish brown claystone	overconsolidated, highly indurated albitic argillites	700-1600 (3500 max.)	700-1000	Lacustrine sediments deposited under oxidising and alkaline conditions	120	600-800

Table 2. *Physical properties*

Formation	Specific weight (g/cm^3)	Dry density (g/cm^3)	WATER CONTENT (%)	Physical porosity (%)	Degree of Saturation (%)	Water content at saturation (%)	Transport mechanism(*)	Diffusion effective coefficient, De (H_2O, m^2/s)(*)	Diffusion effective coefficient, De, (anion, m^2/s)(*)	Hydraulic Conductivity (m/s)(*)	Swelling Pressure (MPa)(*)	Uniaxial compressive strength (MPa)(*)
Boom Clay	2.695± 0.023	1.70 ± 0.06	21.3 ± 2.1	37 ± 2	98 ± 1	21.7± 1.9	Diffusion	$3.50\cdot10^{-19}$ (//) - $1.50\cdot10^{-10}$ (⊥)	Cl^-: $4.70\cdot10^{-11}$ (//) - $2.40\cdot10^{-11}$ (⊥)	$7.00\cdot10^{-12}$ (//) - $2.80\cdot10^{-10}$ (⊥)	0.9	2
Callovo-Oxfordian	2.717± 0.019	2.28 ± 0.07	7.27 ± 1.21	17 ± 4	97 ± 4	7.41 ± 1.01	Diffusion	$1.10\cdot10^{-21}$ (//) – $2.40\cdot10^{-11}$ (⊥)	I^-: $7.10\cdot10^{-12}$ (⊥)	$1.00\cdot10^{-15}$ - $1.00\cdot10^{-14}$	1.0 (//) - 1.0 (⊥)	25 (⊥)
Opalinus Clay	2.746 ±0.010	2.27 ± 0.03	6.9 ± 2.1	17 ± 5	91± 4	7.5 ± 0.4	Diffusion	$7.00\cdot10^{-11}$ (//) – $1.50\cdot10^{-11}$ (⊥)	Cl^-: $4.30\cdot10^{-11}$ (//) - $4.80\cdot10^{-12}$ (⊥)	$2.00\cdot10^{-13}$ (//) – $4.00\cdot10^{-14}$ (⊥)	0.5 (//) - 1.2 (⊥)	25.6 (⊥) - 10.5 (//)
Boda Claystone	2.716	2.57	2.1	5.4	100	2.1	Diffusion and Advection in brittle structures	--	--	$1.00\cdot10^{-12}$	--	115 (⊥)

(*) referente data from Boisson (2005)

Table 3. *Mineralogical composition*

Formation		Quartz (wt. %)	Plagioclases (wt. %)	K-Fd (wt.%)	Calcite (wt.%)	Siderite (wt. %)	Dolomite/ Ankerite (wt. %)	Pyrite (wt.%)	Hematite (wt. %)	TiO_2 (wt. %)	Analcime (wt. %)	Total Phyl-losilicates (wt. %)	Organic Matter (wt.%) (*)
Boom Clay		41 ± 4	1 ± 1	2 ± 1	1 ± 0	2	2 ± 1	2 ± 1	--	Traces	--	53 ± 4	2.4 ± 0.4
Callovo-Oxfordian	**R0 Upper horizons**	25 ± 8	1 ± 0	3 ± 2	23 ± 6	1	3 ± 1	1 ± 0	--	Traces	--	43 ± 10	0.8 ± 0.3
	R1 Lower horizons	26 ± 4	--	3 ± 3	33 ± 3	--	4 ± 1	1 ± 1	--	Traces	--	32 ± 6	1.4 ± 0.3
Opalinus Clay		23 ± 6	4 ± 4	6 ± 2	6 ± 2	8 ± 2	4 ± 1	2 ± 0	--	Traces	--	51 ± 4	1.5 ± 0.2
Boda Claystone		9	6	--	8	1	9	-	3	Traces	7	59	--

(*) All the data were obtained from XRD analysis except these obtained by thermogravimetric analysis

Table 4. *Mineralogical composition of the clay fraction*

Formation		Illite (wt. %)	I/S ML R=0 (wt. %)	I/S ML R=1 (wt. %)	Kaolinite (wt. %)	Chlorite (wt. %)	Clay content (wt. %)
Boom Clay		29 ± 3 (16 ± 3)	45 ± 6 (24 ± 3)	--	21 ± 2 (11 ± 1)	5 ± 2 (3 ± 1)	53 ± 4
Callovo-Oxfordian	**R0 Upper horizons**	23 (10)	63 (26)	--	12 (5)	3 (1)	44 ± 10
	R1 Lower horizons	50 (20)	--	7 (3)	37 (15)	7 (3)	32 ± 6
Opalinus Clay (Shaly/sandy facies)		46 ± 5 (23 ± 1)	--	13 ± 9 (6 ± 5)	38 ± 4 (19 ± 2)	4 ± 2 (2 ± 1)	51 ± 4
Boda Claystone		76 (45)	11 (6)	--	--	13 (8)	59

(*) In parentheses: percentage for the total phyllosilicates or clay content

Table 5. *Physico-chemical properties and geochemical porosity*

Formation	Total CEC (meq/100g)	Σcations (meq/100g)	Na^+ (meq/100g)	K^+ (meq/100g)	Mg^{2+} (meq/100g)	Ca^{2+} (meq/100g)	Sr^{2+} (meq/100g)	Ba^{2+} (meq/100g)	N_2-BET Surface Area (m^2/g)	Total Surface (m^2/g) at P/Po = 0.85	Cl (leach-ing) mol/kg rock	Cl porosity / Water loss porosity (geochemical porosity)
Boom Clay	25.28 ± 2.54	26.68 ± 2.03	8.18 ± 1.34	4.25 ± 0.21	6.44 ± 0.45	6.39 ± 0.30	0.08 ± 0.01	0.04 ± 0.01	41.7 ± 3.4	207 ± 17	1.43E-03	0.81
Callovo-Oxfordian	18.9 ± 6.2	18.9 ± 4.5	3.09 ± 1.1	2.68 ± 0.83	4.50 ± 1.38	8.22 ± 2.14	0.37 ± 0.13	0.006 ± 0.002	32.0 ± 7.7	165 ± 53	9.70E-05	0.54
Opalinus Clay	14.03 ± 0.99	14.87 ± 0.76	5.59 ± 0.58	2.21 ± 0.20	3.08 ± 0.52	3.08 ± 0.26	0.17 ± 0.01	0.002	34.2 ± 1.8	125 ± 16	7.38E-03	0.59
Boda Clay-stone	16.2 ± 0.3	15.9 ± 0.2	7.96 ± 0.00	3.04 ± 0.15	1.62 ± 0.00	3.14 ± 0.06	0.10 ± 0.00	0.032 ± 0.000	25.5 ± 0.2	93 ± 5	--	--

Table 6. *Chemical composition of the pore water*

Formation	Sample(*)	Water type	I (M)	Eh (mV, SHE)	pH	T (°C)	Cl (mg/L)	SO_4^{2-} (mg/L)	HCO_3^- (mg/L)	Br (mg/L)	Na (mg/L)	K (mg/L)	Ca (mg/L)	Mg (mg/L)	Fe (mg/L)	Sr (mg/L)	Si (mg/L)
Boom Clay	Reference	Na-HCO_3	0.02	-360 - -250	8.2	16	27	0.2	854	0.49	408	11	4	2.9	0.9	--	5.0
	Squeezed	Na-HCO_3	0.01	--	8.4		17.1	6.2	524	0.19	200	5.1	1.6	0.9	0.06	--	3.8
Callovo-Oxfordian	Reference	Na-Cl-SO_4	0.09	-200 ± 20	7.2	--	1455	1824	256	--	1288	34	304	142	--	15.7	10.2
	Squeezed	Na-Cl-SO_4	0.11	--	7.9	--	1425 ± 275	2450 ± 1207	215 ± 67	1.6 ± 1.2	1313 ± 272	22 ± 6	391 ± 283	141 ± 150	--	23 ± 13	--
Opalinus Clay	Reference (Shaly facies)	Na-Cl-SO_4	0.35	-227	7.3-7.96	13	10170	1320	152.5	35	5640	43.4	609	415	0.14	35	1.6
	Squeezed (Shaly/sandy facies)	Na-Cl-SO_4	0.24	--	7.7	--	5600	1900	131	17	4300	49	454	309	2.2	55	--
Boda Claystone	Reference	Na-HCO_3-SO_4	0.04	-342 - +50	6.97-9.23	48.5	25	750	850	--	700	7	20	17	0.75	2.8	15

(*) Reference pore waters were obtained from Boisson (2005), except for the Callovo-Oxfordian formation which was obtained from Vinsot et al. (2008)

RTD COMPONENT 4

Tiziana Missana
CIEMAT, Departamento de Medioambiente
Avenida Complutense, 22 – 28040 MADRID (SPAIN)
tiziana.missana@ciemat.es

Introduction

The overall aim of the component 4 of the FUNMIG project (RTDC 4) was the investigation, both at laboratory and *in-situ* scale, of specific processes influencing radionuclide migration in crystalline rock formations.

In the performance assessment (PA) of a deep geological repository (DGR) of radioactive waste in crystalline rocks, the main processes considered fundamental to describe radionuclide migration are: a) distribution of the groundwater flow; b) matrix diffusion and c) sorption. These processes were widely studied in the past and a large knowledge existed before starting FUNMIG.

Nevertheless, some aspects not completely understood were pointed out (i.e. effects of the heterogeneities, up-scaling...) and the work carried out in RTDC 4 was focused on them.

In RTDC 4, a great effort was made, to elucidate the role of bentonite colloids on radionuclide transport in crystalline rocks, because of their possible high relevance, although *colloids* are not directly included in PA. Part of this work has been carried out in collaboration with RTDC 2.

The studies carried out in this component benefit from supporting data from real sites (Forsmark and Laxemar) and *in-situ* data from the FEBEX gallery (NAGRA's Grimsel Test Site, GTS, Switzerland). At the GTS, an experiment simulating at real scale a high-level waste repository in granite was installed more than 11 years ago. This was a unique opportunity to study migration processes from the bentonite barrier to granite in a *realistic* environment.

The following organizations participated to the crystalline rock component, RTDC4: **AITEMIN** Spain; **AMPHOS21**, Spain; **CIEMAT**, Spain; **CSIC**, Spain; **FZK-INE**, Germany; **GEOPOINT**, Sweden; **HUT**, Finland; **IIF**, Germany, **JGUM**, Germany, **KTH**, Sweden; **NILPRP**, Rumania; **NRI-Rez**, Czech Rep; **UDC**, Spain; **UPC**, Spain; **UPV**, Spain; **HU**, Finland; **OVIUNI**, Spain; **VTT**, Finland. Furthermore 5 associated groups collaborated to the work of this component.

RTDC 4 was structured in 6 work packages (WP): **WP 4.1** "Characterisation of geochemical conditions in crystalline host rocks"; **WP 4.2** "Fluid flow system charac-

terisation"; **WP 4.3** "Generation, quantification, characterisation, stability and mobility of groundwater colloids"; **WP 4.4** "RN transport studies, including the effects of inorganic/organic colloids"; **WP 4.5** "Process identification and verification by real system analysis" and, finally, **WP 4.6** "Up-scaling of processes".

As the research work was organised around open *key-questions*, so that the structure was flexible and there was lot of inter-relation within WPs.

The work carried out during the forth year of the project was mainly focused to the analysis and interpretation of the data previously obtained and to summarize the main results obtained and their possible relevance to PA. This paper provides a short overview of the main conclusions reached in RTDC 4.

Main objectives of the performed studies.

The most important processes for PA of a DGR in crystalline rocks are: the distribution of the groundwater flow, matrix diffusion and sorption. These processes were considered relatively well-known before FUNMIG but the EC-project RETROCK [1] highlighted the existence of some aspects that needed more studies.

RETROCK pointed out also processes that, at moment, are not included in PA because they present high degree of uncertainties due to the lack of understanding or the lack of experimental data obtained in relevant conditions, but potentially of interest for PA (Colloids / Microbes / Gas mediated transport / Precipitation –dissolution / Off-diagonal Onsager processes/ Climate change).

The main aim of the work carried out within RTDC4 was to obtain (realistic) data, both from laboratory and in-situ for the validation of existing models, and to improve the knowledge on less known processes to facilitate their inclusion in PA models (e.g. colloid behavior).

To understand the role of the rock heterogeneities on distribution of the groundwater flow, matrix diffusion and sorption was an issue from a theoretical and experimental point of view.

Additional studies were related to the evaluation of models adequacy in describing transport in this complex environment and to the development of up-scaling methodologies.

Finally, in RTDC 4, the potential role of colloids on radionuclide migration was thoroughly analyzed. Recent studies showed that bentonite colloids can be generated from the engineered barriers [2] and that they could be particularly relevant for the migration of high sorbing elements as tri- or tetravalent actinides [3]. The complete description of radionuclide transport in the presence of colloids needs to understand colloidal behavior in crystalline groundwater (generation, stability, colloid-RN interactions and rock-colloid interactions). All these aspects were dealt with in different WPs of RTDC 4.

Advances within workpackage

Chemistry and in-situ studies

The importance of the study of the chemistry on radionuclide transport has to be underlined. It controls the aqueous speciation of radionuclides, their solubility and all the retention processes. Furthermore, it influences other mechanisms as colloids formation and stability. Therefore chemistry studies should be centered in answering this question: *What chemical reactions and sorption processes will occur in the rock and what are their effects on radionuclide mobility?*

The occurrence of chemical reactions and sorption processes occurring in the rocks is mainly site-specific and different scenarios and problems (i.e. climate) have to be analyzed. The main questions are: *Do in-situ studies and real system analyses, help to improve the knowledge of radionuclide migration? Do present geochemical models satisfactorily account for all the processes considered relevant? Are models satisfactorily calibrated in front of real systems? Do site-specific studies or in-situ studies help reducing uncertainties in PA?*

Real sites studies were shown to be a very important tool to improve the knowledge on radionuclide migration and to test the validity of the model used, also accounting for the site-specificity of the problems.

Site specific studies, as those carried out in the Swedish sites Forsmark and Laxemar by **GEOPOINT** and several **associated groups**, clearly represented a direct support for PA [4]. The evaluation of field geochemical data (Eh, pH, TOC, colloids, Mg-Ca, etc…) is needed to verify if they met safety criteria for site selection and to build confidence in the site.

On the other hand, these studies are fundamental to understand phenomena that cannot be obtained from laboratory studies. Advanced geochemical modeling used in these sites helps to generate understanding in terms of concepts, scenarios, spatial and temporal scales and on the models validation itself [4]. The understanding of the hydrogeochemical conditions of the past and present is the basis to predict future evolutions. Additionally, the complete characterization of a site allows gaining capability and confidence for the extrapolation of data when the information is scarce or not available.

A considerable progress data interpretation and understanding of relevant processes, in particular on groundwater origin and evolution, interactions of surface/deep ground-waters, redox front, microbes, gases and colloids was reached in the last years.

Important progresses were also obtained on modeling aspects by the integration of hydrochemistry with mineralogy, microbial data and reaching a closer integration with hydrogeology [5].

For what concerns the effects of climate, **HU** and **HUT** devoted their efforts to understand the effects of glacial melt water intrusion [6,7] on uranium migration in Palmottu.

Another problem raised in FUNMIG was to evaluate the possible effects of the bentonite barrier on the radionuclide transfer to the granite rock. The FEBEX real scale experiment (1996-2004), installed at the GTS decade ago, was considered an adequate site to obtain data under “realistic” repository conditions.

CIEMAT, **AITEMIN** and **CSIC** performed different types of investigations in the FEBEX tunnel. The main objectives of the studies were related to the understanding of mass transfer processes from the bentonite to granite: in particular, (a) the effects of the bentonite on the groundwater chemistry (important also for the validation of models) and (b) the presence and stability of bentonite colloids.

The migration of natural tracers as Na^+, Ca^{2+} or Cl^-, coming from the bentonite was analyzed as well as the migration of tracers as I^- and ReO_2^- that in FEBEX were placed at the bentonite surface [8].

These studies were supported by the previous identification of different interesting regions in the tunnel (faults, fractures, lamprophyre) [9]. Improved geophysical and hydro-geological studies (cm-dm scale) were also carried out. For the chemical analysis of the groundwater, 19 existent boreholes radial to the tunnel with 41 packed off sections were used, but during FUNMIG it was also considered necessary to drill 5 new boreholes for chemistry and geophysical studies.

The most important boreholes drilled within FUNMIG (FUN1 and FUN 2) were relatively near to the bentonite surface, with short packed off section to minimize dilution.

Small (but not negligible) increase in the chemistry of the groundwater sampled in the new boreholes with respect to the radial ones was observed. Based on the data obtained in these *in-situ* studies a mass-transfer conceptual model was developed [10,11]. **CIEMAT** analyzed and fit the Cl^- behaviour with a simple 1D diffusive model. These studies allowed determining in a real scale experiment the mean effective diffusion coefficient for Cl^- (D_e = 5.0E-11 m^2/s). These data were also modeled by **AMPHOS21** and **CSIC,** their results also suggested that mass transfer from bentonite to granite, in the conditions of the tunnel, is probably governed by diffusion. In any case, they highlighted that results may be sensitive to the groundwater pathway, and especially to the existence of fractures.

ONIUVI and **HU** measured the variation of porosity in depth in the different fractures and interesting information on the expected variation of diffusion coefficients within the granite from the surface exposed to the water flow to the matrix was obtained in zone of the tunnel with different characteristics.

Characterization of the fluid-flow paths and the up-scaling problem.

As mentioned before, one of the most important issues for PA of a DGR in crystalline rocks is the characterization of the fluid flow system, a key-point for evaluating which paths are available for both RN transport and retention.

In crystalline rocks, the main contribution to water and solute transport is advective, in the existing fracture network. The rest of the rock has much lower hydraulic conductivity and transport occur mainly by diffusion. The fracture network can be a very complex system and adequate simplifications are always needed for PA.

One key question is: *May the use of new and sophisticated techniques (with cm–dm resolution) for fracture characterisation reduce the uncertainties in PA ?*

In the FEBEX tunnel, that was already characterized before FUNMIG, a combination of different techniques used by **CSIC** (borehole televiewer, caliper, gamma, GPR and Cross-hole ultrasonic monitoring) allowed to obtain the images of three fracture zones, relatively sub-parallel to the FEBEX gallery, not detected before and that could play a role in the solute transport in the region [12].

On the basis of the hydraulic data, **UPC** calibrated the groundwater flow model of the FEBEX tunnel and observed that the pressure expected in the region analyzed in FUNMIG was lower than the expected, especially in those boreholes closer to the gallery. These results indicate the existence of a higher transmissivity zone and are in agreement with **CSIC** findings.

Obviously, a better system description leads to less uncertainty and can be a support for PA. This study was also important to validate the use of indirect visualization methods for the determination of fracture network in crystalline rocks.

As far as the techniques are improved, high level of detail for the main fluid paths can be obtained. Nevertheless, as in PA simplifications are needed, the problem of how dealt with heterogeneities in transport models arises.

The dependence of transport parameters with the scale needs to be treated from both a conceptual and modeling point of view and it is necessary to know if *adequate up-scaling methodologies for crystalline rocks exist and if they can be implemented in PA.*

Geo-statistical tools allow the description of the flow without the need of an exact knowledge of the flow-path and some of them are able to overcome problems related to classical advection-dispersion equation that cannot explain the dependence of the scale of transport parameters (up-scaling) and lead to underestimations of the late-time behavior of concentration breakthrough in highly heterogeneous media.

UPV and **UPC** analyzed the application up-scaling methodologies and evaluated their advantages/limitations in the context of PA [13,14].

The state of the art and comparison of different models (macro-dispersive, continuous-time random walk (CTRW), multirate mass transfer (MRMT) were analyzed for conservative transport. Furthermore, efficient algorithms to model MRMT, which seems to be the most promising to deal with both for conservative and reactive transport, were developed by **UPC**.

A methodology proposed in RTDC4, to up-scale transport is based upon the MRMT model. A new random walk particle tracking methodology to efficiently simulate MRMT solute transport was developed by **UPV** [15].

In contrast with the classical up scaling method, which is based on the standard macro-dispersive transport model, the proposed methodology is shown capable to properly reproduce the mean behavior of the main features associated with observed concentration breakthrough curves.

Modeling transport and chemistry

To link the modeling of fluid transport with chemistry would definitely be of interest for PA. Geochemical modeling has been shown to be a very important tool to understand and describe complex systems as mentioned in Section 3. The question that rises is: *Are we able to provide a "PA-usable model" for coupling transport and geochemistry in crystalline media?*

To model the interplay between transport and chemical reactions is non-trivial but possible. The main existing problem is related to the stiffness of reactive transport codes, difficult to implement in PA. **CSIC** developed a CHEmical PRocesses Object Oriented (CHEPROO) module: its modularity makes this code easy-to-link to other transport codes and possibly appropriate for PA.

A very difficult task from a modeling point of view is to combine flow and reactive transport taking into account the possible effects of the rock heterogeneities. On this challenging issue very important efforts were done by **UPC.**

In RTDC4, a methodology for the analytical solution for reaction rates for multispecies equilibrium and non-equilibrium reactive transport in heterogeneous media was developed [16,17], quantifying the impact of heterogeneity on reaction rates [18] as well as the effect of heterogeneities on mixing and spreading. New indicators for mixing were derived [19,20].

As a result of the studies a conservative transport research in a development stage exists, that will be coupled with the chemistry module CHEPROO.

Small scale heterogeneities, matrix diffusion and sorption.

The study of the small-scale structure of the rock is very important because small scale features may have an important influence on the overall transport behavior of water and solutes. Retention processes, for example, occurs at the micro-scale and the importance of matrix diffusion on radionuclide transport is largely affected by the rock microstructure.

HU, **OVIUNI**, **CIEMAT**, **IIF**, **JGUM** and **NILPRP** used different rock matrix characterization methods (PMMA method, X-ray computed tomography (XCT), confocal laser microscopy, PET, 3D dual-energy cone-beam tomography combined to X-ray fluorescence [21]) to study the effect of heterogeneities at the cm-μm scale. Their studies were used as a support of several radionuclide transport experiments.

Different methodologies were compared to highlight the applicability and limits of each technique [22,23]. The synergy of the use of different (no destructive) techniques on the same sample was highlighted in several experiments. The effects of physical and chemical rock heterogeneity on the main parameters needed for PA calculations (i.e. or porosity, diffusion coefficients or distribution coefficients) were also analyzed within different work packages.

In crystalline rocks, matrix diffusion is considered a very important retardation process, above all for not sorbing elements. The theoretical bases of matrix diffusion are well established and the mathematical treatment is similar in different PA. However, different problems were recognized. First of all, to obtain relevant experimental data is difficult because: a) artifacts might occur in small laboratory samples and b) diffusion lengths can be extremely short, above all for sorbing radionuclides thus rendering difficult the analysis of diffusion process.

The main question related to matrix diffusion experimental studies was: *Do new experimental approaches to overcome these experimental problems exist?*

By one hand, as mentioned in Section 3, it is of great interest to perform migration studies in real sites under conditions as realistic as possible. This is not always straightforward so that the use of large scale laboratory experiments might be useful to avoid large perturbations that can exist in the surface of small rock samples.

A large scale laboratory mock-up experiment (MUE) was constructed at **CIEMAT** to study tracer diffusion at the bentonite/granite interface. A large granite block (40 x 40 cm approx.) from GTS was used and characterized previous to the experiment by **OVIUNI.** A small cylindrical block of compacted FEBEX bentonite was placed in the centre of the granite block to mimic the granite/bentonite interface. A series of small boreholes were drilled monitoring tracer migration in the granite. Tracers were injected in a metallic filter placed in the bentonite. Numerical models of the experiment have been developed by **UDC** [24].The diffusive behavior of elements of different type (conservative as HTO and Cl^- and non-conservative as Cs) is being analyzed. HTO and Cl concentration remain almost constant during the first 150 days (99 - 98 %), the measured data are satisfactorily fit by the model. The slightly different behavior of HTO and Cl^- was explained by the existence of ionic exclusion.

Experiments in dynamic conditions, in fractured columns, showed that matrix diffusion plays an increasingly important role as the water flow rate decreased [25].

Another additional question was: *Do heterogeneities play a role in matrix diffusion process?*.

VTT analyzed spatial up-scaling of the retention by matrix diffusion [26]. Models as Time Domain Diffusion that explicitly take into account the heterogeneity of the rock matrix were developed. These models consider heterogeneous porosity patterns and relate residence time distribution to the pore-space geometry and diffusion in different rock zones is predicted to be different [27,28,29,30].

To validate these models, it was necessary to obtain diffusion coefficients and to correlate diffusion profiles with the physical (and mineralogical) properties of the rock in the same sample.

CIEMAT proposed a microscale approach to matrix diffusion combining diffusion studies and characterization matrix porosity at a mineral scale [31]. The Rutherford backscattering spectrometry (RBS) is a nuclear ion beam technique that allows measuring concentration profiles in a micrometric scale with a resolution that allows measurements within a single mineral. Additionally, as the diffusion profile is measured within micrometers, the diffusion times are reduced to a few days. This technique was particularly useful for heavy elements.

The RBS technique was also used by **NRI-Rez** to quantify Cs diffusion/sorption on single minerals in Czech granites [32] in combination with auto radiographic techniques.

The RBS technique allowed measuring diffusion coefficients at a micro-scale. The importance of the nature of the mineral grains and particularly grain porosity (more than mineralogy) was evidenced.

Sorption is another fundamental process for PA. In PA, sorption is treated following the "Kd approach". Kd values are usually derived from static "batch" experiments under site-specific conditions.

The limitations of the Kd-concept are widely recognized: Kd-approach does not take into account the chemistry of the pore solution and its variability. Besides, other relevant processes as precipitation, co-precipitation and solid solution formation may be hidden in Kd-values. To understand the effect of different retention processes a mechanistic approach is needed. This was widely treated in RTDC 1.

In RTDC 4, other problems related to Kd-values were evaluated. The first one was related to the experimental form used to obtain Kd values. As mentioned before, they are not usually obtained on intact rocks but on crushed material and crushing may significantly affect rock sorption properties. This way of determining Kd-values might be the cause of the large dispersion of Kd data values existing for crystalline rocks. By the other hand, the effects of the heterogeneities in sorption are neglected when Kd values are selected.

Thus, the main questions are: *May the determination of sorption / transport parameters in intact rocks help to reduce the uncertainties in the selection of Kd values? How does the heterogeneity affect retention?*

Different studies carried out in RTDC 4 showed that, in principle, experiments on intact granite provide more realistic values of Kd [33].

The use of intact rock samples allows the use of different techniques in the same samples whose results can be compared. Apart from sorption, other processes can be evaluated e.g. porosity distribution and diffusion, so that crossed-information can be obtained. Furthermore, the "scale dependence" can be experimentally evaluated. All these studies may represent an additional experimental support for the creation of transport parameters database.

To perform sorption studies on intact rocks, different "visualization" techniques are also available allowing the observation of the regions in which radionuclides interacts (e.g. modern autoradiography method [32] used by **NRI-Rez**). Moreover, this type of experiment allows accounting for heterogeneities.

CIEMAT carried out sorption experiments with small rock pieces using the particle induced X-ray emission technique (μPIXE). One of the main challenges of this study was to quantify radionuclide retention at a mineral level by the specific analyses of individual PIXE spectra in each scanned point within 2x2 mm^2 areas.

Small regions within single minerals can be selected and the Ka values in these regions calculated. This way, the variability of the surface distribution coefficient (K_a) is experimentally determined. Furthermore the studies showed that as the studied areas

increased in size the variability on Ka values decreased. This investigation tried to understand how the distribution coefficients could be up-scaled for consideration of the mineralogical heterogeneity found in any natural system.

The "colloid-problem"

As mentioned before, a large effort was made in RTDC 4 to analyze the possible role of bentonite colloids in RN transport. It is known that to be relevant in RN transport colloids have to fulfill a series of conditions which are mainly site-specific.

Previous studies at the GTS indicated that bentonite colloids are every stable in Grimsel water, therefore the site is adequate to perform in depth in-situ studies. In previous studies bentonite colloid migration in granite fractures was found to be unretarded and the recovery of bentonite colloids and highly sorbing tri- and tetravalent elements was very high.

The problem was that water flow conditions were not fully representative of those expected in a geological repository. Thus, it was considered necessary to perform more experimental studies at a laboratory scale, under constrained conditions as similar as possible to the real ones. **CIEMAT** and **FZK-INE** carried out the studies on inorganic colloids and bentonite colloids. **KTH** studied the kinetics of the complexation/sorption of cations to humic substances.

Many key questions were related to "the colloid problem". *The first one was: what are the main parameters affecting the generation of bentonite colloids from the compacted bentonite?*

To answer to the first question, different laboratory studies were carried out at stagnant (or low flow) conditions analyzing the effects of a) clay density, b) groundwater chemistry; c) clay type; d) surface exposed to hydration; e) pore size of extrusion layer. Results showed that a steady state in the generation process is reached after a time that can be related to the hydration of bentonite. The higher the clay density the higher the bentonite colloid concentration was, additionally, the bentonite colloid concentration depended also by the groundwater chemistry (salinity and pH). The chemistry controlled stability and size of generated colloids too.

Ca-homoionised clay did not form colloid in appreciable concentration, but the presence of Na in the exchange complex (20 %) completely changed the generation behavior (e.g. as-received FEBEX bentonite). Finally, the surface exposed to hydration (and the consequent existence extrusion paths) also affected colloid generation.

Bentonite colloids are stable over month in low mineralized and alkaline pH and their stability may increase in the presence of humic acids. Generation rate of colloids from bentonite were in the range of $6.5 \cdot 10^{-7}$ mg/cm^2·sec in Grimsel water. All this information can now be used to improve models of colloid generation.

The analysis of the colloid generation was also carried out at the FEBEX site. Water from the new drilled and old boreholes were analyzed with different techniques.

Clay colloids were detected in borehole FU1 (20-30 cm far from the bentonite) and they were compared to those obtained in the laboratory studies of bentonite colloid

generation in Grimsel water. The similarity in both microstructure and composition was shown. However, considering the quantity of Al (as indicator of the presence of bentonite), the concentration of colloids at 30 cm far from the bentonite and after 10 year is not higher than 1 ppm. This is an interesting result from a PA point of view.

Higher colloid concentrations were measured by PCS, showing that artifacts, possibly introduced during the excavation of the new boreholes, exist. The analysis of these artifacts for a better quantification of the "source term" is a very important issue at moment [34].

Additional studies are still being carried out to analyze the stability of bentonite colloids in the FEBEX tunnel and on the mineralogical characterization of fracture filling materials that can affect the natural colloid formation and rock-colloids interactions and consequent filtration processes. In particular, the presence of Ca-carbonate in fracture fillings can be relevant in the stability behavior of bentonite colloids in the FEBEX tunnel.

Filtration of colloid in the granitic medium is another complex aspect to be evaluated. The main questions are: *What are the main parameters affecting filtration of colloids in a crystalline rock? Is diffusion a retention mechanism for colloids? Can colloid diffusion coefficients be measured?*

Even in Grimsel water, where the chemical conditions favor high colloidal stability and in spite of the existence of "unfavorable" electrostatic conditions for colloid-rock attachment, filtration of bentonite colloid increased significantly when the hydrodynamic conditions approached the ones expected in a repository (low water flow rates) and when the roughness of the fracture surface increased. Thus, this is an indication that "plugging effects" cannot be ruled out in RN transport under certain conditions [35]. The flow is a very important parameter for the retention of colloids in a fracture.

The quantification of colloid retention under conditions unfavorable and favorable to electrostatic attachment was analyzed also by μPIXE [36] and fluorescence microscopy [37] in static experiments. Under favorable conditions, electrostatic attraction prevailed: strong adsorption of negatively charged colloids was in fact observed at pH values close or below the point of zero charge (pH_{PCZ}) of the mineral surface. The adsorption of polyvalent cations as Eu^{3+} at high concentration increased colloid attachment to minerals [37]. Under unfavorable conditions colloid attachment was still observed [37], for example in minerals like albite or orthoclase, and even in the alkaline regime [36]. In this case, colloid retention on granite was found to be strongly dependent on small scale chemical effects, roughness or non-uniform distribution of charge sites.

The effect of matrix diffusion on colloid (2-100 nm) retention was analyzed and colloid diffusion coefficients in granite could be experimentally measured for the first time by **CIEMAT**. Apparent diffusion coefficients of colloids in granite (approx. 10^{-18} m^2/s) were at least 3 orders of magnitude smaller than those for radionuclides measured in similar conditions [38]. These results revealed the small relevance of this process over others on colloid filtration.

Another question related to the role of colloids in radionuclide migration is the following: *Are we able to estimate the effect of bentonite colloid (at least conservatively) on the transport of critical radionuclides?*

A sensitivity study was carried out to calculate the effects of the presence of bentonite colloids on radionuclide release from the near-field [39] using data obtained in FUNMIG.

A colloid concentration of 100 ppm was used in the calculations (the maximum concentration observed in generation experiments) and higher sorption (10 or 100 times, case 1 and 2 respectively) on colloids than in compacted bentonite was assumed.

Calculations in these "conservative" conditions allowed calculating an increase factor in the peak rate for several radionuclides (e.g. ^{135}Cs (1.1, 2); ^{238}U(2, 9.2); ^{239}Pu (10, 93). The numbers in brackets correspond to case 1 and case 2 respectively). Calculations indicated that bentonite colloids have the potential to increase up to factor 100 the near field releases of strongly-sorbing radionuclides, such as curium, plutonium and thorium, compared with the base case. Calculations additionally showed that if radionuclide sorption on bentonite colloids is reversible, the release increase from the near field would lead to a similar increase in the doses that they produce. Doses due to these radionuclides are already very small due to their long travel times through the geosphere and total doses would be little affected.

On the contrary, if sorption on bentonite colloids is irreversible and bentonite colloids move un-retarded at groundwater velocity, these radionuclides would move through the geosphere without retardation and the doses can increase significantly. This clearly shows that the study of the irreversibility of RN-colloid attachment is an issue to be analyzed more in depth.

Column experiments were carried out to investigate the transport behavior of radionuclides of different type in the presence of bentonite colloids. Radionuclides as Pu and Eu showed high sorption onto the colloids. For these radionuclides only the breakthrough peak corresponding to the colloid-associated transport could be detected. Pu recovery was the expected considering quantity of bentonite colloid filtrated in the medium whereas Eu recovery was always lower than the expected.

The different behavior might be related to the different desorption behavior of tri and tetravalent elements from clay colloids [40]. The time-dependent desorption of Eu(III) from colloids studied by addition of humic acid as a competing ligand point to the establishment of equilibrium. A strong kinetic inhibition is however stated for Th(IV) desorption from bentonite colloids, where an equilibrium is not achieved even after several months.

For the lower sorbing Sr recovery the recovery was very similar with and without colloids but very different transport behavior was observed. Three different peaks were presents: the first one corresponding to the Sr adsorbed on colloids, a second one corresponding to the Sr as a solute and a third "unexpected" one, that can be due to the Sr sorption on the fracture surface "contaminated" by the retained colloids that produced further delay on Sr migration.

Filtration mechanisms and the irreversibility of radionuclide-colloid binding are amongst the most important aspects for describing their effect on radionuclide migra-

tion. Experiments under dynamic conditions seem to be essential to properly understand these processes.

Acknowledgments

I would greatly acknowledge all the persons, from the eighteen different organizations, that actively participated in the project and, in particular: AITEMIN: J. Suso, G. Carretero, J. Bueno; AMPHOS 21: D. Arcos, A. Delos; CIEMAT: U. Alonso, P. Gómez, M. García-Gutiérrez, B. Buil, A. Garralón, J. Peña, N. Albarran; CSIC: A. Pérez-Estaún, R. Carbonéll, C. Ayora, J. Carrera; FZK-INE: H. Geckeis, T. Schäfer, M. Bouby, A. Filby, H. Seher, W. Hauser; GEOPOINT and *associated groups*: M. Laaksoharju, J. Molinero; HUT: M. Markovaara-Koivisto, K. Keinsalo, J. Cedercreutz; IIF: M. Gründig, J. Kulenkampff; JGUM: M. Richter, F. Enzmann, M. Kersten; KTH: M. Jansson; NILRP: I. Tiseanu; NRI-Rez: V. Havlova, A. Laciok; UPC: M. Dentz, S. Bea, M. Saaltink, L. Martinez, M. Willmott, O. Silva; UPV: D. Fernandez, J. Gómez; UDC: J. Samper, Q. Jang; HU: M. Siitari-Kauppi, M. Leskinen, J. Suhksi; UNIOVI: M. Montoto, F. Mateo; VTT: A. Poteri.

References

[1] RETROCK (2005). Treatment of radionuclide transport in geosphere within safety assessment. Final Report EUR 21230 EN.

[2] T. Missana, U. Alonso, M.J. Turrero (2003). Generation and stability of bentonite colloids at the bentonite/granite interface of a deep geological radioactive waste repository, J. Cont. Hydr., 61(1-4), 17-31.

[3] H.Geckeis, T. Schäfer, W. Hauser, Th. Rabung, T. Missana, C. Degueldre, A Möri, J. Eikenberg, Th. Fierz, W.R. Alexander (2004). Results of the Colloid and Radionuclide Retention experiment (CRR) at the Grimsel Test Site (GTS), Switzerland.- Impact of reaction kinetics and speciation on radionuclide migration. Radiochimica Acta, 92(9-11), 1-10.

[4] M. Laaksoharju, J. Smellie, E.L. Tullborg, M. Gimeno, J.B. Gómez, L.F. Auqué, J. Molinero, I Gurban, L. Hallbeck, G. Buckau (2007): Hydrogeochemical methodology for constructing site descriptive models within the Swedish site investigation programme. Contibution to the WRI-12 conference in Kunming, China 2007.

[5] M. Laaksoharju, J. Smellie, E.L. Tullborg, M. Gimeno, J. Molinero, I. Gurban, L. Hallbeck (2008) Hydrogeochemical evaluation and modelling performed within the Site Investigation Programme, Appl. Geoch. 23 (7) 1761-1795.

[6] J. Suksi, K. Rasilainen, P. Pitkänen, (2006). Variations in 234U/238U activity ratios in groundwater – a key to flow system characterisation? Physics and Chemistry of the Earth 31, 556-571.

[7] M. Markovaara-Kovisto, K. Einsalo (2008) Response of uranium minerals to climatic changes- Example from Palmottu, Southern Finland. FUNMIG 4th Annual Workshop, Karlsruhe 24-27 November, 2008.

[8] M. Garcia-Gutierrez (2001). Tracers in the FEBEX proyect. CIEMAT/DIAE/54520/4/01

[9] Perez-Estaún, A., Carbonell, R., Martinez, L., Dentz, M., Suso, J., Carretero, G., Bueno, J., Buil, B., Garralon, A., Gomez, P., Arcos, D., Hernan, P., (2007), New boreholes to investigate the bentonite/crystalline rock interface in the FEBEX gallery (Grimsel). Rapport CEA-R-6122, 157-162.

[10] P. Gómez, B. Buil, A. Garralón, M.J. Turrero, L. Sánchez, and J.M. Durán, (2007). Geochemical gradients at the near-far field interface at the FEBEX experimental gallery (Grimsel Test Site). Water rock interaction WRI 12, T.D. Bullen and Y. Wang editors, Taylor & Francis Group, (ISBN 0415451361), Vol 2, pp. 583-587.

[11] B. Buil, P. Gómez,, J. Peña, A. Garralón, M.J. Turrero, L. Sánchez, J.M. Durán, (2008) Modelization of the mass transfer generated by bentonite into the granite at the FEBEX drift. Chemical Geology (submitted).

[12] R. Carbonell, A. Perez-Estaun, D. Marti (submitted) High resolution images of fractures within a Granitic Pluton, Near Surface Geophysics

[13] P. Salamon, D. Fernàndez-Garcia, J. J. Gómez-Hernández (2006), A review and numerical assessment of the random walk particle tracking method, J. Cont. Hydr. (ISSN 01697722), VOL. 86, 277-305, 2006.

[14] D. Fernàndez-Garcia, J. J. Gómez-Hernández (2007), Impact of upscaling on solute transport: Travel times, scale-dependence of dispersivity and propagation of uncertainty, Water Resources Research (ISSN 0043-1397), VOL. 43, W02423, doi:10.1029/2005WR004727, 2007.

[15] P. Salamon, D. Fernàndez-Garcia, J. J. Gómez-Hernández (2006), Modeling mass transfer processes using random walk particle tracking, Water Resources Research (ISSN 0043-1397), VOL. 42, W11417, doi:10.1029/2006WR004927, 2006.

[16] Sánchez-Vila, X., M. Dentz, L. Donado, Transport controlled reaction rates under local non-equilibrium conditions, Geophysical Research Letters, 34, L10404, 2007.

[17] De Simoni M., Sanchez-Vila X., Carrera J., and Saaltink M. (2007), A mixing ratios-based formulation for multicomponent reactive transport, Water Resour. Res. (43), W07419, doi:10.1029/2006WR005256.

[18] J. Luo, M. Dentz, J. Carrera, and P. Kitanidis, Effective reaction parameters for mixing controlled reactions in heterogeneous media, Water Resour. Res., 44, W02416, 2008.

[19] M. Dentz, J. Carrera (2007) Mixing and spreading in stratified flow. Phys. Fluid 19, 017107.

[20] M. Dentz, D. M. Tartakovsky, Four-point closure for transport in steady random flows, Phys. Rev. E, 77 066307, 2008.

[21] I. Tiseanu et al, Combined 3D tomography and X-ray fluorescence for crystalline host rock, presented at IP FUNMIG 2nd Annual Workshop, Stockholm, 21st-23rd November, 2006

[22] T. Lähdemäki, M. Kelokaski, M. Siitari-Kauppi, M. Voutilanen, M. Myllys, T. Timonen, F. Mateos, M. Montoto (2007). Characterising Low-permeable granitic rocks from micrometer to centimiter scale: X-ray microcomputed Tomography, Confocal laser scanning microscopy and 14C-PMMA method: Scientific basis for nuclear waste management XXX, Mat.Res.Soc.Symp. Proc. 985, 587-592.

[23] M. Kelokaski, M. Siitari-Kauppi, M. Montoto, F, Mateos, A. Martinez-Nistal, Fractographic evaluation of low permeable granitic rocks under CLSM and PMMA method from cm to mm scale. 1st. Annual Workshop Proceedings 6TH EC FP - FUNMIG IP Saclay (France) 28th Nov.- 1st. Dec. 2005

[24] J. Samper, Q. Jang, S. Yi, M. García-Gutiérrez, T. Missana, M. Mingarro (2009). Interpretation of a laboratory mock-up experiment of the bentonite/granite interface with a numerical model. 4th Annual Workshop proceedings Funmig, Karlsruhe, FZK Report (in press).

[25] J. Kulenkampff, M. Grundig, M. Richter, F. Enzmann, Evaluation of positron – emission tomography for visualisation of migration processes in geomaterials. Physics and Chemistry of the Earth, 33, 937-942.

[26] A. Poteri (2006) Spatial up-scaling of the retention by matrix diffusion, Posiva Work Report 2006-101.

[27] P. Sardini, F. Delay, H.K. Hellmuth, G. Porel and E. Oila (2003): interpretation of out diffusion experiments on crystalline rocks using random walk modelling. J. Cont. Hydr., 61:339-350.

[28] P. Sardini, J.C. Robinet, M. Sittari-Kauppi, F. Delay, K.H. Hellmut (2007), Direct simulation of heterogeneous diffusion and inversion procedure applied to an out diffusion experiment. Test case of Palmottu granite, J. Cont. Hydr., 93 21-37.

[29] P. Sardini., M. Siitari-Kauppi. D. Beaufort , K-H Hellmuth (2006) On the connected porosity of mineral aggregates in crystalline rocks, American Mineralogist 91, 1069-1080.

[30] J.C. Robinet, P. Sardini, F. Delay, K-H. Hellmuth The Effect of Rock Matrix Heterogeneities Near Fracture Walls on the Residence Time Distribution (RTD) of Solutes Transp. Porous Med (2008) 72:393–408

[31] M. Siitari-Kauppi, A. Leskinen, M. Kelokaski, L. Togneri, U. Alonso, T. Missana, M. Garcia-Gutérrez, A. Patelli (2007). Physical Matrix characterisation: studies of crystalline rocks and consolidated clays by PMMA Method and electron microscopy as a support of diffusion analyses. Informe Técnico CIEMAT 1127.

[32] V. Havlová et al. (2007): Multimethod approach to determination of sorption and retention within granitic rock. S+T publication, 3rd FUNMIG annual meeting, Nov. 26 – 29, Edinburgh, 2007 (being submitted)

[33] V. Havlova et al (2007): Migration and retention properties of the Czech granitic referenc sample PID 4.43 IP-FUNMIG.

[34] T. Missana, U. Alonso, N. Albarran, P. Gómez, B. Buil, Th. Schäfer, W. Hauser, H. Seher, A. Garralón. Bentonite colloid generation from a deep geological repository in granite: an in-situ study. Geochimica et Cosmochimica Acta, Vol 72 (12) Suppl S, A635 (2008). Goldschmidt 2008 Conference Vancouver July 2008.

[35] N. Albarran, T. Missana, Ú. Alonso, M. García-Gutiérrez, M. Mingarro, T. Lopez-Torrubia (2008). Transport of uranium in a granite fracture: effects of the presence of bentonite colloids. Scientific Bases for Nuclear Waste Management 33, Dic 2008 Boston, POSTER.

[36] U.Alonso, T. Missana, A. Patelli, D. Ceccato, N. Albarran, M. García-Gutiérrez, T. Lopez, V. Rigato (2008). Quantification of Au nanoparticle retention on a heterogeneous rock surface. Colloid and Surfaces A, Submitted

[37] A. Filby, M. Plaschke, H. Geckeis, Th. Fanghänel (2008) Interaction of latex colloids with mineral surfaces and Grimsel granodiorite. J. Cont. Hydrol, 102 (3-4), 273-284.

[38] U. Alonso, T. Missana, A, Patelli, V. Rigato, J. Ravagnan (2007). Colloid diffusion in crystalline rock: experimental methodology to measure diffusion coefficients and evaluate size dependence. Earth and Planetary Science Letters 259, 372-383.

[39] J. L. Cormenzana (2007) Effect of bentonite colloid on radionuclide releases from the near field. 3d Funmig Meeting, Edinburgh.

[40] M. Bouby, H. Geckeis (2007) On the dynamics of tetravalent actinide(th/pu)-humic acid interaction".11th Internat. Conf. on the Chemistry and Migration Behaviour of Actinides and Fission Products in the Geosphere (Migration 2007), München

RTD COMPONENT 5

U. Noseck
GRS mbH, Theodor-Heuss-Str., 4 D-38122 Braunschweig
Ulrich.Noseck@grs.de

Introduction

In RTDC5 geochemical processes at Ruprechtov site are studied as an analogue for potential processes in sedimentary layers in the overburden of host rocks for radioactive waste repositories

Key questions addressed are: Which processes control the mobility of uranium and other trace elements in the natural system? Which processes lead to the uranium immobilisation in the sedimentary layers? What is the role of colloids and, in particular, of organic matter? How stable are colloids in natural systems? Which properties and processes have impact on the generation of DOC in the natural system and how does DOC affect the mobility of uranium in the natural system?

Most of the experimental activities had been already finalised a year ago, e.g. the whole work on WP5.1 was finalised in 2007 and no more activities occurred in 2008. Therefore, within the last year most emphasis was put into the evaluation and integration of results in WP5.3 "real system analyses". In the following the progress in the work packages 5.2 and 5.3 is shown.

Advances in Work Package programs

WP5.2: Geochemical behaviour of radionuclides in the natural host rock

Some final investigations were performed by **UH**, **NRI** and **GRS** on immobile uranium forms, i.e. sequential extraction and isotope ratio analysis. As shown in Fig. 1 the results from sequential extraction experiments, performed in the years 2006, 2007 and 2008 showed a strong increase in the exchangeable fractions since 2006 accompanied by a decrease in the fraction of reduced/organic uranium (step 4). Since we have strong evidence that most of uranium in this step occur as U(IV) this indicates an oxidation of part of uranium (IV) to uranium (VI).

For the leachates from the extraction cycles in 2007 and 2008 $^{234}U/^{238}U$ activity ratios (ARs) were analysed. The results are shown in Fig. 2. There is a clear shift in the ratios in all fractions, most significantly in those from step 1, 2 and 4. The $^{234}U/^{238}U$-activity ratios in all leachates decreased in the 2008 analyses. At the same time the ura-

nium fraction increased mainly in step 1 and decreased mainly in step 4. Both observations together can be explained by oxidation of some U(IV) during storage after 2006, becoming more accessible and therefore leached already in step 1 instead of step 4. This process adds uranium with low $^{234}U/^{238}U$ activity ratio to the accessible fraction and lowers the AR of this fraction. This explains the lower $^{234}U/^{238}U$ ratio in step 1 (and 2) in the analysis from 2008.

Furthermore, the observation, that AR slightly decreases in the leachate from step 4 (and 5), indicates that the U(IV) fraction represents a mixture of different uranium forms with slight differences in their ARs. The U(IV) fraction, which became oxidised, exhibits a higher AR value. The results from intercomparison of U(IV)/U(VI) separation experiments in 2008 with those from 2006 are not yet available but will be documented in the final FUNMIG report. These results might support this hypothesis.

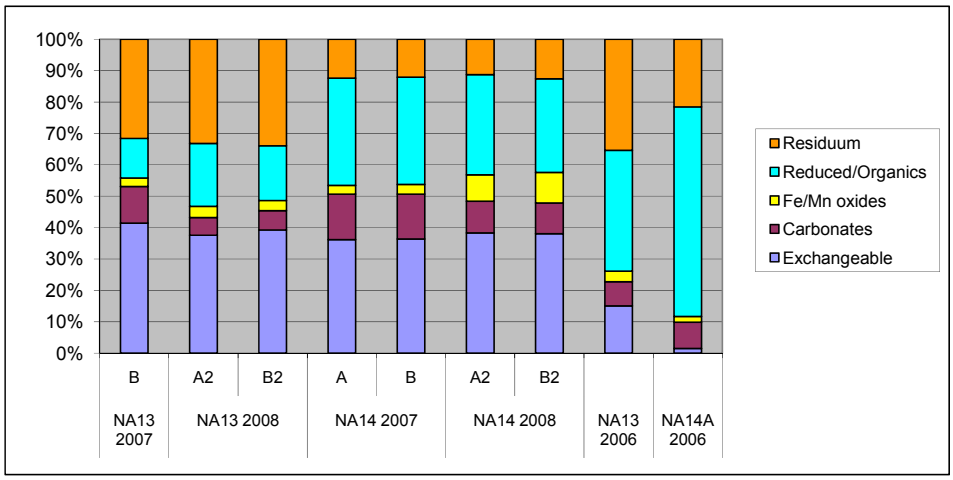

Figure 1: *Uranium fraction of uranium in the leachates from the different steps of the sequential extraction procedure. Data from SE cycles in 2006, 2007 and 2008.*

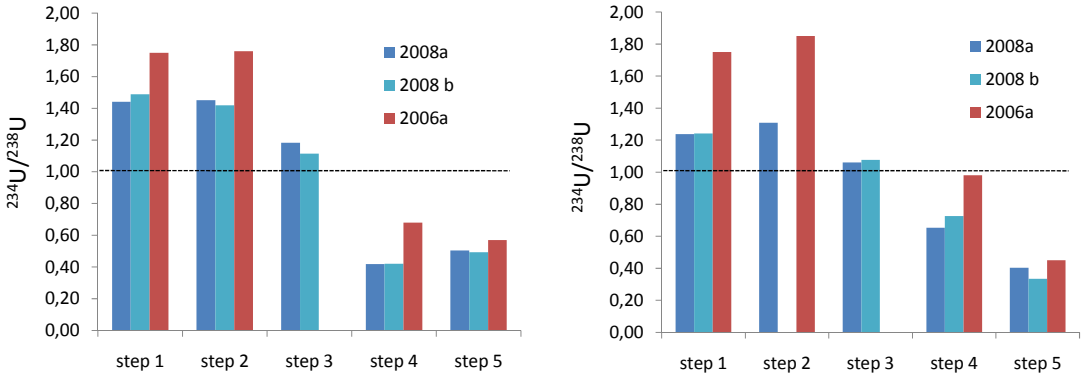

Figure 2: *$^{234}U/^{238}U$ activity ratios in the leachates from the different steps of the sequential extraction procedure (left NA13, right NA14). Data from SE cycles in 2006 and 2008.*

CTU as associated partner has finalised and published its contribution for RTDC5 (Vopalka et al. 2008). The isotopic exchange tests with ^{233}U were used to compare the results of exchangeable uranium determination with the results of the first steps of the sequential extraction experiments. The isotope exchange of uranium present in samples with ^{233}U proved that the first two steps of the sequential extraction procedure give a good information about the amount of U(VI) in rock samples that is attainable to transport by groundwater.

Great differences of qualities concerning U(VI) release/uptake was observed in the eight samples from the Ruprechtov site investigated. The differences that are related to both, the amount of exchangeable uranium in the samples studied and sorption/desorption behaviour of them arise from the differences of the chemical and mineralogical composition of the rock materials, from which the samples were prepared. The measured interaction isotherms showed a significant dependence of uranium uptake on the experimental phase ratio (V/m) values. The reason can be assigned to changes in liquid phase composition caused by dissolution of mineral phases.

WP5.3: Real System analyses

During the last year experimental results have been further evaluated, in particular by **GRS** and **NRI**. Two major topics were treated: the role and behaviour of organic matter and the geochemical behaviour of uranium in the system, including key processes that caused uranium enrichment at the site in the geological past.

Concerning the carbon behaviour isotope data have been further evaluated in cooperation with AGH in Poland, still with regard to the question on groundwater travel times and sources for DIC input into the clay/lignite horizon. Two different conceptual models have been addressed for further investigation of the carbon isotope composition evolution of the from the infiltration area to the clay/lignite horizon: (i) the open-system model assuming that the pore water in the unsaturated zone is in continuous contact with an infinite reservoir of soil CO_2 with constant parameters (partial pressure, carbon isotope composition) during the process of dissolution of mineral carbonate phase, (ii) the closed-system model where the infiltrating water first equilibrates with the soil CO_2 reservoir and then moves to the region where dissolution of mineral phase(s) takes place, without contact with the CO_2 reservoir.

The ^{14}C and ^{13}C contents measured in the sampled boreholes were plotted as a function of the DIC concentration (Fig. 3a and 3b). Superimposed on that are different trend lines predicted by the simple models mentioned above.

The trajectories marked in Fig. 3 by black lines (solid and dashed) indicate the initial evolution of the carbon isotope composition in DIC. First, soil CO_2 of prescribed characteristics (partial pressure 0.01 atm, $^{14}C/^{12}C$ ratio equal 100 pmc, $\delta^{13}C$ equal -24 ‰) dissolves gradually in the infiltrating water until saturation is reached. The saturation points are marked by stars. From those points on, the solution was allowed to evolve further under closed-system conditions (grey solid and dashed lines) by adding new carbon in the form of CO_2, devoid of ^{14}C. Two different $\delta^{13}C$ values of this additional carbon were considered: -27 ‰ and -16 ‰. The first value corresponds to CO_2 derived from decomposition of SOC, the second one representing a 1:1 mixture of biogenic CO_2 (-27 ‰) and endogenous CO_2 with $\delta^{13}C$ value of around -3 ‰.

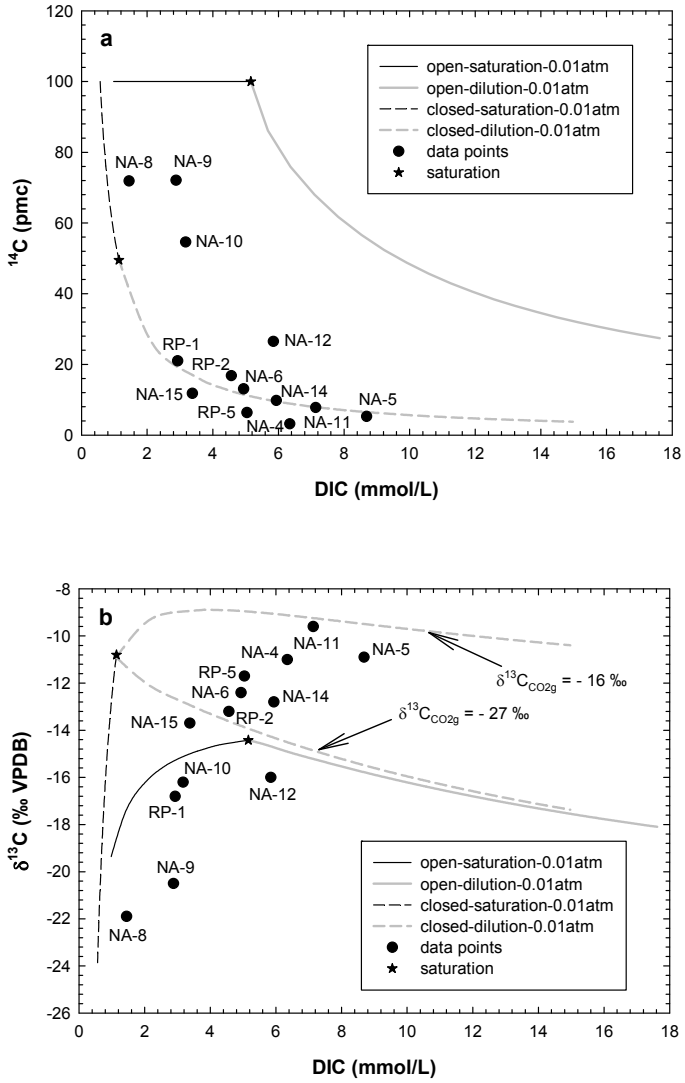

Figure 3: *Carbon isotope evolution of DIC under open- and closed-system conditions. Stars indicate saturation of the solution with respect to $CaCO_3$. Subsequent evolution of the DIC reservoir (grey lines), resulting from input of additional carbon, was calculated via consecutive equilibrium stages with a solid carbonate phase (Noseck et al., 2009)*

As seen in Fig. 3a, the ^{14}C data cluster around the closed-system trend lines with two-step addition of carbon to the solution. Few data points are located either slightly to the right-hand side (NA8, NA9, NA10, NA12) or slightly below (NA15, RP5, NA5, NA4) the trend line. The ^{13}C data (Fig. 3b) provide additional constraint on the process of adding additional carbon to the system. Again most of the data, in particular those from the clay lignite horizon can be described by the closed system model. The majority of data points are located between the trend lines representing two different $\delta^{13}C$ values of gaseous CO_2 entering the solution: -27 ‰ and -16 ‰. While $\delta^{13}C$ values observed in well RP2 reflects the dominating contribution of CO_2 from decomposition of organic matter, for borehole NA11 they suggest that both sources of CO_2 are represented in approximately equal proportions. The general result is that additional CO_2 input into the

system is evident and can explain the development of $\delta^{13}C$ and ^{14}C isotopes in DIC in the clay/lignite horizon. This is also confirmed by the results from inverse modelling. There is evidence that, some input of endogenous CO_2 occurs beside input by microbial degradation. All data and a detailed explanation can be found in (Noseck et al., 2009).

In summary, all isotope data give the evidence for CO_2 input into the clay lignite horizon by organic matter microbial degradation and to some extent addition from an additional source. In order to understand the rather low concentration of DOC in the clay lignite horizon the interrelation between sedimentary organic and dissolved organic matter (SOM and DOM) was investigated during FUNMIG. In 2008 main tasks have been the leaching experiments of SOM and the characterisation of organic matter fractions released by alkaline extraction, leaching experiments and natural DOM from Ruprechtov groundwater. All investigations have been finalised. The results confirm those from alkaline extraction, i.e. that only a very minor SOC fraction is accessible by degradation (2,8 % of SOM). This is illustrated by maximum concentrations of 40 mg/l C_{org} compared to concentrations of 650 mg/l C_{org} obtained from similar experiments with Boom clay. MALDI-TOF characterisation of organic substances obtained by alkaline extraction (humic acid HA 12/3) and by simple leaching showed that their structure is very similar to the structure of natural DOM in groundwater. This gives evidence that the extracted fractions, mainly humic acid HA 12/3, can be considered as representatives for the mobile organic matter at the site. A more detailed description of this work can be found in the S&T contribution in these proceedings (Havlova et al., 2008).

Considering all the results the role of organic matter can be summarised as follows. Its major impact appears in its influence on the redox conditions, which of course contributes to the long-term stability of uranium in this horizon. The role of SOC as sorbent for uranium is very low, which can be demonstrated by the fact that uranium is immobilised in the vicinity of SOC but not correlated with carbon. Similarly the impact of DOC as complexing agent for U(VI) in groundwater and therewith on the mobility of U(VI) is low, due to the low DOM concentrations, occurring in the clay/lignite horizon, and lower complexing affinity, determined for extracted natural humic acid HA 12/3. The low DOM concentration can be assigned to the low degradability of SOM (as discussed above) and to a quite strong ability of argillaceous sediments from the clay/lignite horizon to sorb organic substances, as was demonstrated for humic acid HA 12/3.

Concerning the behaviour of uranium in the Ruprechtov system a second cycle of U(IV)/U(VI) analyses in groundwater from the clay lignite horizon by the method from *Anderson* (1984) was performed. In this method U(IV) co-precipitates with NdF_3. In order not to disturb the system the analysis is performed under Ar atmosphere (Suksi et al., 2007). Due to some instrumental difficulties reliable values were only obtained for borehole NA6. The results confirm those from the first measurements. A fraction of 15-22 % of uranium occurred as U(IV). This can be regarded as a minimum value. The final geochemical calculations indicate that the redox potential in several wells in the clay/lignite horizon is controlled by the SO_4/HS^- couple. Under these conditions the majority of uranium is expected to occur in the reduced form U(IV). However, calculations with updated NEA TDB showed that the groundwater are located at the boundary of the stability ranges for U(IV) and U(VI) and that the high CO_2 partial pressure in the

system can stabilise part of uranium as U(VI), which can explain to some extent the observation that a large fraction of mobile uranium occur in the U(VI) redox state.

Nevertheless the uranium concentrations in all boreholes from the clay/lignite horizon are low, in a range between 0.4 and 2.1 ppb. Geochemical calculations showed that these low concentrations are controlled by amorphous uraninite and/or ningyoite, which are the relevant U-bearing mineral phases observed in the clay/lignite horizon. Since the conditions in the clay/lignite horizon are buffered by pyrite and organic matter and low permeable clay covers, it is expected that these conditions didn't significantly change in the recent past. This correlates well with the observations from the microscopic and macroscopic characterisation of immobile uranium, in particular with the activity ratios in the uranium decay chain, demonstrating a long-term stability of uranium(IV) in the clay/lignite horizon of more than one million years. A more detailed description on the uranium geochemistry can be found in an S&T contribution in these proceedings (Noseck et al. 2008).

References

Anderson RF, (1984): A method for determining the oxidation state of uranium in natural waters. Nucl. Inst. Meth. Phys Res. 223, 213-217.

Havlova V, Cervinka R, Havel J (2008): Interrelation of Mobile organic matter and sedimentary organic matter at the Ruprechtov site. 4th Annual Workshop Proceedings of the IP Project FUNMIG". Karlsruhe 24.-27. November 2008.

Noseck U, Suksi J, Havlova V, Cervinka, R. (2008): Uranium geochemistry at Ruprechtov site. 4th Annual Workshop Proceedings of the IP Project FUNMIG". Karlsruhe 24.-27. November 2008.

Noseck U, Rozanski K, Dulinski M, Havlova V, Sracek O, Brasser Th, Hercik M, Buckau G (2009): Carbon chemistry and groundwater dynamics at natural analogue site Ruprechtov, Czech Republic: insights from environmental isotopes. Accepted by Applied Geochemistry.

Suksi J, Salminen S (2007): Forsmark Site investigation. Study of U oxidation in groundwater with high U concentrations. SKB P-07-54, Stockholm.

Vopalka D, Havlova V, Andrlik M (2008) Characterization of U(VI) behaviour in the Ruprechtov site (CZ). Conference Proceedings 5th International Conference on Uranium Mining and Hydrogeology 2008, Freiberg, Germany.

RTD COMPONENT 6

B. Schwyn
Nagra, Hardstrasse 73, 5430 Wettingen, Switzerland
bernhard.schwyn@nagra.ch

Introduction

Within the Integrated Project FUNMIG RTD Component 6 plays the role of the coordinator for linking the scientific work with the application of its results in Performance Assessment. The linking itself is in the custody of RTDCs 1 – 5. An information exchange forum consisting of the Waste Management Organisations (WMOs) involved in FUNMIG on one hand and the Integration Monitoring Group (IMG), representing RTDCs 1 – 5 on the other hand acts as the above mentioned coordinator.

RTDC 6 is divided into three work packages (WPs):

– WP 6.1 deals with the boundary conditions to the near field including radionuclide fluxes and other influences caused by the near-field like corrosion products, colloids, oxidation fronts and gas.

– WP 6.2 is the core task of RDTC 6. Within this WP the scientific results of the project were collected and evaluated by the WMOs with respect to their use in a safety case.

– Within WP 6.3 sorption databases currently used by participating WMOs on one hand and sorption data acquired within FUNMIG on the other hand were compiled.

Advances in Work Package programs

WP 6.1: Boundary conditions

The topic of FUNMIG is the investigation of radionuclide migration through potential host rocks for a repository. Earlier in the project, boundary conditions to the near-field were documented for various European disposal concepts, namely for Spain, Switzerland, UK, France and Belgium as a prerequisite to have information on what radionuclides with which fluxes and in which concentrations may be released from the near-field of a repository into the surrounding rock (PID6.1.1). The results in the corresponding report (available in FUNMIG web since August 2006) identified the key radionuclides leaving the near field and confirmed the validity of the usual assumption that the radionuclides from the waste enter the far field groundwater in trace amounts only.

NF-PRO, a sister project within the sixth Framework Programme, was finished in 2007. It dealt with near-field processes in European disposal concepts. Results of NF-PRO concerning the interface of the near field with the geosphere are therefore relevant to FUNMIG and were considered for the final Boundary Conditions Report. In addition to radionuclide fluxes, the final report now includes a general discussion of the potential influences of the near-field on the geosphere. From the list of these potential influences the following topics are discussed in more detail:

The potential fluxes of iron corrosion products originating from the steel canisters was assessed and found to be very small, not exceeding 10^{-3} moles of iron per canister and year.

In context with the investigations carried out within RTDC 4 the potential influence of bentonite colloids on radionuclide transport in granitic rock was assessed. Only under the conservative assumption that colloids move unretarded and radionuclides sorb irreversibly to the colloids the increase of dose due to colloids is substantial for strongly sorbing radionuclides.

Based on experiments in the Belgian HADES underground research laboratory the potential influence of oxygen on the Boom Clay was assessed. There is strong evidence that oxidation effects will only take place in the excavation disturbed zone of the tunnels.

Gas production and transport in the near field of repositories for spent fuel and high level waste is discussed. The hydrogen gas mainly originating from canister corrosion is assumed to escape rapidly through fractures in crystalline rocks. The scenario analysis for dense clay rocks is more complicated. An important aspect is the fact that most of the gas is produced long before canister breaching and radionuclide release. In a two-phase flow region, formed by gas release from the near-field, diffusive radionuclide transport through the host rock may actually be reduced because water fills the pores only partially.

WP 6.2: Topics and processes dealt with in FUNMIG and their treatment in Peformance Assessment for a geologic repository

In its role to coordinate the linking of scientific results to their application in Performance Assessment, RTD Component 6 in co-work with IMG developed a tool to evaluate FUNMIG results with respect to their use in PA. (Nagra, 2006 and Nagra, 2007). The main features of this tool are summarised below:

The individual topics, processes and method developments within IP FUNMIG are listed and mapped to internationally accepted views for clay-rich and crystalline host rocks. FEPCAT (Mazurek et al. 2003) is a catalogue of Features, Events and Processes (FEPs) for argillaceous rocks. RETROCK (EU, 2005) was a European project on the treatment of radionuclide migration in fractured rocks within safety assessment. A list of processes identified by the participants as safety relevant was used as a quasi FEP catalogue. Outside FUNMIG the development of the ISIBEL FEP list for salt host rocks was completed during 2007. For the FEP mapping the structure of the project was adopted as depicted in Figure 1.

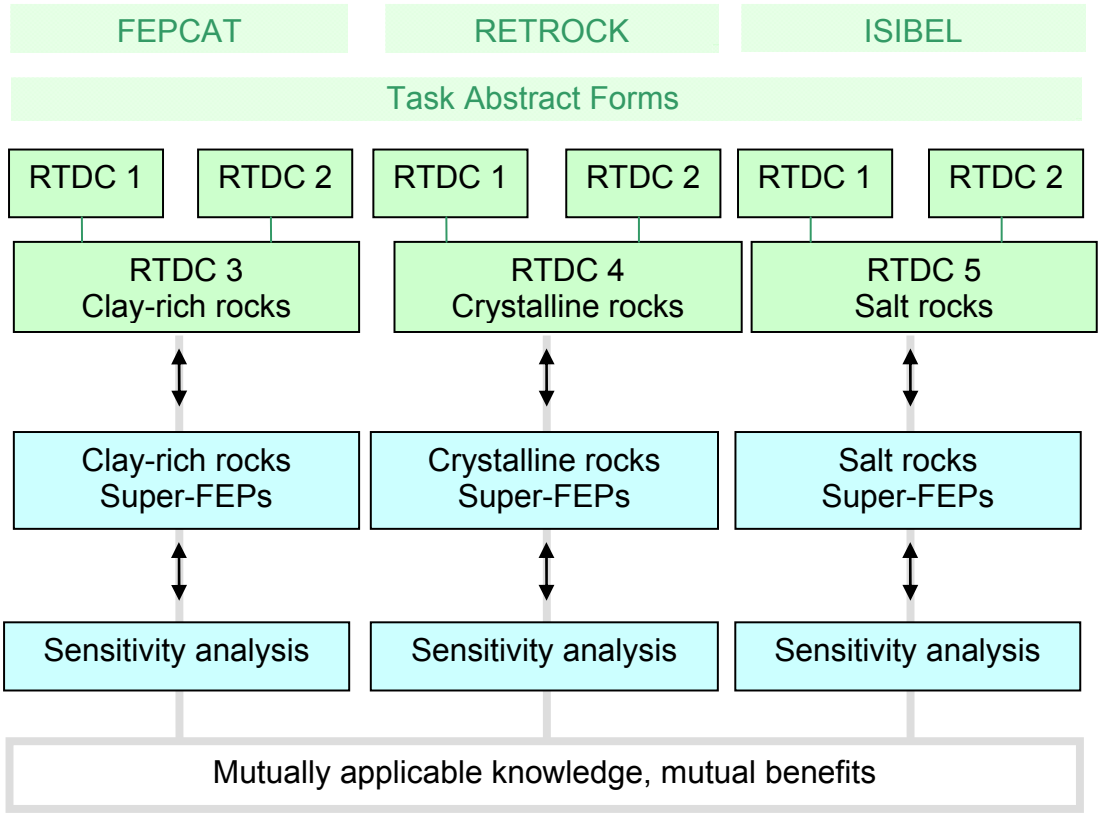

Figure 1: *Structure of task mapping and evaluation*

As input for the task evaluation the results of the IP FUNMIG were provided by the participants using a standardised Task Abstract Form (TAF). For each task the researchers provided the main results (abstract) together with motivation and aim, state of the art before FUNMIG, and achievements for the safety case from their point of view. If already available, references were given to track back the task for more details. The final report includes these concise descriptions of the tasks as a thorough catalogue of the investigations performed within IP FUNMIG.

Three Task Evaluation Tables (TETs) were prepared according to the three host rocks addressed, namely clay-rich rocks in RTDC 3, crystalline rocks in RTDC 4 and salt rocks in RTDC 5. The work of the two non host rock specific components RTDC 1 and RTDC 2 was included in each of the three host rock specific TETs.

Each line in the three TETs represents one FUNMIG task with a description provided by the involved researchers in the corresponding TAF.

For the final report (Nagra, 2009) the topics (TET columns) were revised by removing information related to the TET development and by lumping related information together. The final version each TET consists of 6 columns:

1. Task number
2. FUNMIG Tasks (title)
3. Investigated processes

- Task mapping to FEPs of the above mentioned catalogues

4. SA parameter
   - Affected parameters used in safety assessment (sorption coefficient, solubility, diffusion coefficient, ….)
5. Importance of improvements for SA parameter uncertainty improvement
6. Achieved improvements within FUNMIG subdivided into two columns
   a. Researcher's view
   b. WMO's view

Column 5 was filled in based on the WMO's general experience in safety analysis. In contrast to column 6b only the state of knowledge regarding the investigated process (before FUNMIG) was taken into account. High importance, therefore, indicates currently high uncertainties in SA, whereas low importance could indicate either an already high degree of knowledge or low sensitivity of a parameter or process in SA.

Entries in column 6a (researcher's view) were directly taken over from the Task Abstract Forms.

Entries in column 6b (WMO's view) were filled in based on an evaluation of the TAFs by each WMO and using their experience with the specific safety cases and taking into account the entries in the previously filled in columns. The criteria applied in filling in this column were the benefits for the WMO's future safety cases for the specific host rocks they consider (clay-rich, e.g. Boom Clay, Callovo Oxfordian, Opalinus Clay, crystalline and salt); i.e. improvements of the state of knowledge during FUNMIG and host rock specific conditions were considered and commented. The tasks were evaluated considering the improvement of knowledge and the improvement of data.

Using the filled in TETs the synthesis depicted in Figure 1 was carried out by lumping together the individual FEPs (to which FUNMIG tasks were mapped) to "Super-FEPs". Figure 2 shows that for the example of clay host rocks two partially overlapping "Super-FEPs" dominate the mapping of tasks, namely transport mechanisms and retardation. The corresponding parameters used in safety assessment are sorption coefficient, solubility, diffusion coefficient and accessible porosity. To simplify the discussions between different host rocks the procedure was used for crystalline host rocks too, with minor adaption to consider specific processes involved.

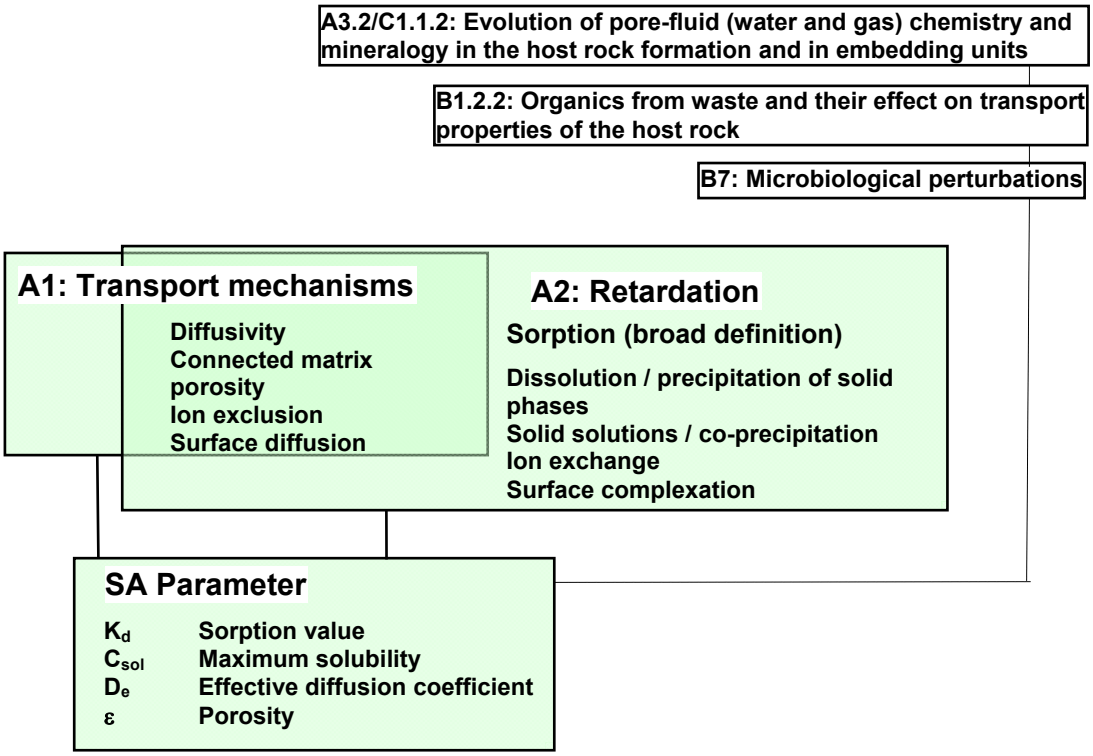

Figure 2: FEPs (taken from FEPCAT) to which the tasks were mapped, and concerned safety assessment parameters for the clay-rich host rock case

Concerning clay-rich host rocks all FEPs from FEPCAT which were addressed in FUNMIG are listed below; the ones in italic were judged by the WMOs as particularly important:

- *Diffusivity*
- *Connected matrix porosity*
- *Ion exclusion*
- Surface diffusion
- Colloid formation, transport and filtration
- *Lithology, mineralogy of rocks (REDOX!)*
- *Natural organics, complexation (Importance is restricted to Boom Clay)*
- *Porewater composition*
- Dissolution / precipitation of solid phases
- *Solid solutions / coprecipitation*
- *Ion exchange*
- *Surface complexation*
- *Thermodynamic and kinetic modelling data*

- *Evolution of pore-fluid (water and gas) chemistry and mineralogy in the host formation and in embedding units*
- *Organics from the waste and their effects on transport properties of the host rock (Importance is waste inventory specific and restricted to the UK)*
- Microbiological perturbation

The corresponding list for crystalline rocks mapped to RETROCK is given below:

- *Advection within fractures*
- *Diffusion within fractures*
- *Matrix diffusion (matrix porosity)*
- *Sorption on matrix pore surfaces and fracture walls (RN adsorption on granite and colloids)*
- Immobilisation
- *Colloid-related processes*
- Microbial processes

Since hermetical enclosure properties are attributed to the rock salt formation the overburden, work within FUNMIG is focussed on, is considered as supplemental barrier. Migration processes are therefore of lower relevance.

The synthesis by collecting the FEPs in Super-FEPs did not reveal groundbreaking findings. It rather confirmed the WMO's experience with FEPs related to the barrier function of the host rock for the radionuclides.

Also confirmed was the experience of some of the WMOs that the transferability of information between host rock types (cf. lower part of figure 1) is restricted to generic research topics. During the development of a disposal concept the needed information is turning successively more site specific. Indeed, the majority of the topics dealt with in FUNMIG was host rock oriented.

WP 6.3: Sorption databases

Sorption is considered to be the most important chemical retention process for radionuclides in the geosphere. In this regard, a special effort was undertaken to make the corresponding outcome of FUNMIG publicly available. In a first step sorption data, currently used by the participating waste management organisations in safety assessment, were compiled. In a second step the participants were asked to provide data measured and derived within FUNMIG. For this purpose a database structure in Access™ format was developed and made available to the FUNMIG partners. The database is designed to include the following details of sorption data:

- Origin (Team, Work Package, Bibliography, …)

- Sample description (Mineralogy, Sorbing element(s), Chemistry essentials, Preparative steps, Analytics)
- Experimental method (Equilibration and equilibrium check, Phase separation, Check for solid alterations)
- Experimental conditions (T, p, I, V/m, pH, Eh, concentrations, gas phase, time)
- K_d values (Ranges, uncertainties)
- Applied model (Isotherms, Ion Exchange, Surface Complexation, Surface Precipitation, Formation of Solid Solutions)
- Details for auxiliary data
- Fitting method and tool
- Parameter values (Ranges, uncertainties)

After reception of the sorption data from the participants the resulting database was made available on the FUNMIG intranet.

References

EU (2005): Treatment of radionuclide transport in geosphere within safety assessments (Retrock). Final Report. EUR 21230 EN. European Commission, Community Research, Brussels, 2005.

Mazurek, M., Pearson, F.J., Volkaert, G. & Bock, H. (2003): Features, events and processes evaluation catalogue for argillaceous media. OECD / NEA, Paris, 2003.

Nagra (2006): Fundamental Processes of radionuclide migration: Topics and processes dealt with in the IP FUNMIG and their treatment in the Safety Case of geologic repositories for radioactive waste. Nagra Arbeitsbericht 06-16. Nagra, Wettingen, 2006.

Nagra (2007): Fundamental Processes of radionuclide migration: Topics and processes dealt with in the IP FUNMIG and their treatment in the Safety Case of geologic repositories for radioactive waste, Update 2007. Nagra Arbeitsbericht 07-25. Nagra, Wettingen, 2006.

Nagra (2009): Topics and processes dealt with in the IP FUNMIG and their treatment in the Safety Case of geologic repositories for radioactive waste. Nagra Technical Report 09-01, Nagra, Wettingen, Switzerland, in preparation.

INDIVIDUAL SCIENTIFIC AND TECHNICAL CONTRIBUTIONS

List of contributions

A PREDICTIVE MODEL FOR ANION EXCLUSION IN COMPACTED NA-MONTMORILLONITE

Christophe Tournassat[1*]

[1] BRGM, French Geological Survey, Orléans, France

* Corresponding author: c.tournassat@brgm.fr

Abstract

Prediction of anion exclusion volume at montmorillonite surface as a function of ionic strength (see companion paper: comparison of molecular dynamic simulations with Triple Layer and modified Gouy-Chapman models in a dilute NaCl - montmorillonite system, this issue) was combined to a model linking the stacks of lamellae in montmorillonite quasi-crystals to a limiting value for diffuse layers overlap. After calibrating the model with literature data, we showed that this approach enables to reproduce fairly accurately anion accessible porosity and anion diffusion coefficients (effective or apparent) in a wide range of experimental conditions (montmorillonite dry density and NaCl concentrations) pointing out the effectiveness of a dual porosity approach for modelling anion diffusion in compacted Na-montmorillonite.

Introduction

In current concepts for radioactive wastes geological disposal, anions represent the potentially highest contribution to the performance assessment. Anions are typically weakly sorbed or even repelled from the negative clay surface constitutive of buffer (montmorillonite) or natural (e.g. Callovo-Oxfordian argilite) material in the multi-barrier systems. Clay anion exclusion is a well known process for a long time (see the pionnering work by Schofield, 1947). Its quantification and modelling in dilute clay suspension has been a matter of much research in the 50-60's (e.g. Bolt and Warkentin, 1958; Edwards et al., 1965; Edwards and Quirk, 1962). Reanalysis of these data led to the conclusion that the Modified Gouy-Chapman theory is able to predict fairly well the experimental data in NaCl ionic background when coupled to the consideration of montmorillonite quasi-crystal formation in the suspension (Sposito, 1992). Nevertheless, this agreement could be demonstrated only for quite low ionic strength below ~0.01 mol L^{-1} NaCl. In a companion paper (Comparison of molecular dynamic simulations with Triple Layer and modified Gouy-Chapman models in a dilute NaCl - montmorillonite system, this issue), we showed that corrections to the MGC theory are likely to be taken into account when dealing with concentration above 0.1 mol L^{-1}.

Despite the available knowledge on anion exclusion in dilute systems using MGC theory, there has been little effort to extend this type of approach to compacted

systems. The present study aims at proposing a simple prediction method for anion exclusion quantification in NaCl – montmorillonite from dilute suspension to compacted material.

List of abbreviations

d_{lim_ov}	limiting overlap distance between diffuse layers
p	mean number of clay TOT layer per stack
m_{clay}	mass of clay in the system
V_{clay}	TOT layer volume
ρ_{clay}	density of TOT layer
m_{w_int}	mass of interlayer water in the system
V_{w_int}	interlayer water volume
ρ_{w_int}	density of water in the interlayer
m_{w_pore}	mass of "micropore" water in the system
V_{w_pore}	"micropore" volume
ρ_{w_pores}	density of water in the micropores
V_{tot}	total volume
V_{w_bulk}	volume accessible to anions
V_{w_edl}	volume of water in the diffuse layer not accessible to anions
m_{imp}	mass of impurities
ρ_{imp}	density of impurities
S_{int}	surface area of montmorillonite
h_{int}	interlayer thickness.
d_{exc}	anionic exclusion distance at the external surfaces,:
d_{001}	XRD clay basal spacing and the crystallographic data for montmorillonite
h_{layer}	thickness of one clay layer
$r_{w/c}$	water clay mass ratio
S_{ab}	unit cell surface in the 001 direction corresponding to one unit cell formula
N_A	Avogadro number
M_{clay}	mass of one unit cell formula
x_1, x_2 and x_3	proportions of 1, 2 and 3 WL interlayers
x_{imp}	proportion of impurities in the bentonite
m_{bent}	mass of bentonite
D_e	effective diffusion coefficient of a given monovalent non-sorbing anion
D_0	diffusion coefficient in water
ε	anion accessible porosity
D_a	apparent diffusion coefficient

Anion exclusion in clayey media, conceptual and theoretical background

Conceptual representation of anion exclusion

In clay materials, water is distributed over different reservoir. As a consequence, it is necessary to define precisely these reservoirs and their links with the porosity term used in the diffusion and porosity equation. As a first approximation, the total volume

of the sample can be divided into three sub-volumes (Figure 1, left): the first one is the volume occupied by the TOT layers of the clay, the second one is the volume occupied by the water (and cations) in the interlayer space and the third one is the remaining volume between grains of stacked TOT layers of clay called here "micropore" water (this representation is analogous to this depicted in Bourg et al., 2006 or Grambow, 2006). This third volume can be itself divided into "bulk" water (i.e. not influenced by the external clay surfaces) and EDL (electrostatic diffuse layer) water. EDL water cannot be defined as a water volume having a fixed chemical composition: as a function of the distance to the clay surface, this composition changes with respect to anion exclusion and cation condensation. In order to simplify the system, we will consider in the following that EDL water refers to the equivalent volume of water where complete exclusion of anions occurs as defined by Equation 16 in the companion paper. The bulk water refers then to the water volume in the micropores minus this EDL water volume. As consequence, bulk water volume could be compared to experimental anion accessible porosity measurements in the same manner than done in companion paper with anion exclusion in montmorillonite suspensions.

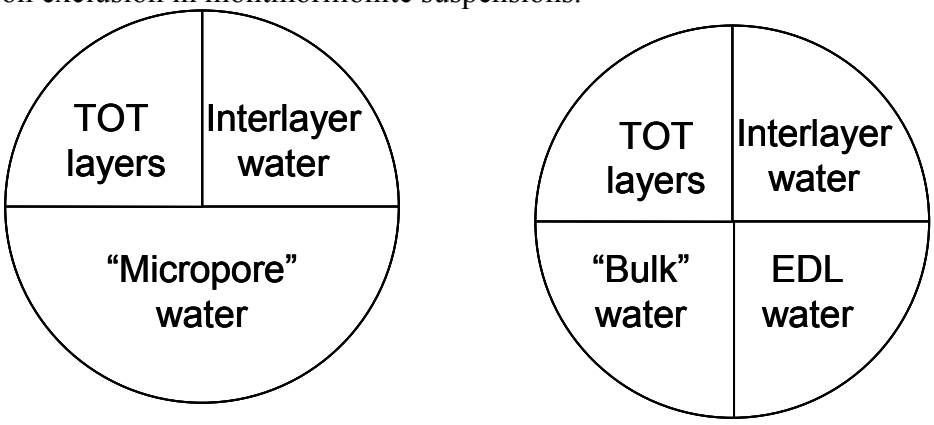

Figure 1. *Scheme of the volumes/mass repartitions in the successive modelling approaches presented in this paper*

From dilute to compacted system: working hypothesis

In dilute suspensions, Na-montmorillonite forms quasi-crystal made of stacked lamellae with ~1.4 lamellae in one quasi-crystal as demonstrated by various techniques (see companion paper, Schramm and Kwak, 1982; Shomer and Mingelgrin, 1978). While considering a compaction or a concentration of the system, distances between quasi-crystals will progressively decrease leading in turn to increasing diffuse layer overlaps. At this stage, two arrangements of the lamellae in the quasi-crystals can be foreseen: (i) a regular overlap of the diffuse layers or (ii) a stack of lamellae increasing the mean number of lamellae in a quasi-crystal decreasing the overall extent of the diffuse layer volume while increasing the interlayer volume (Figure 2).

In the present approach, we consider that the mean number of stacked lamellae (p) in a quasi-crystal is dependant on the compaction of the system and that the relationship between compaction of the system and lamellae staking is linked to a limiting overlap distance between diffuse layers (d_{lim_ov}). This concept is shown on Figure 2 In the following work, we hypothesize that the value d_{lim_ov} is a parameter only linked to the equivalent anionic exclusion distance and thus a function of ionic strength.

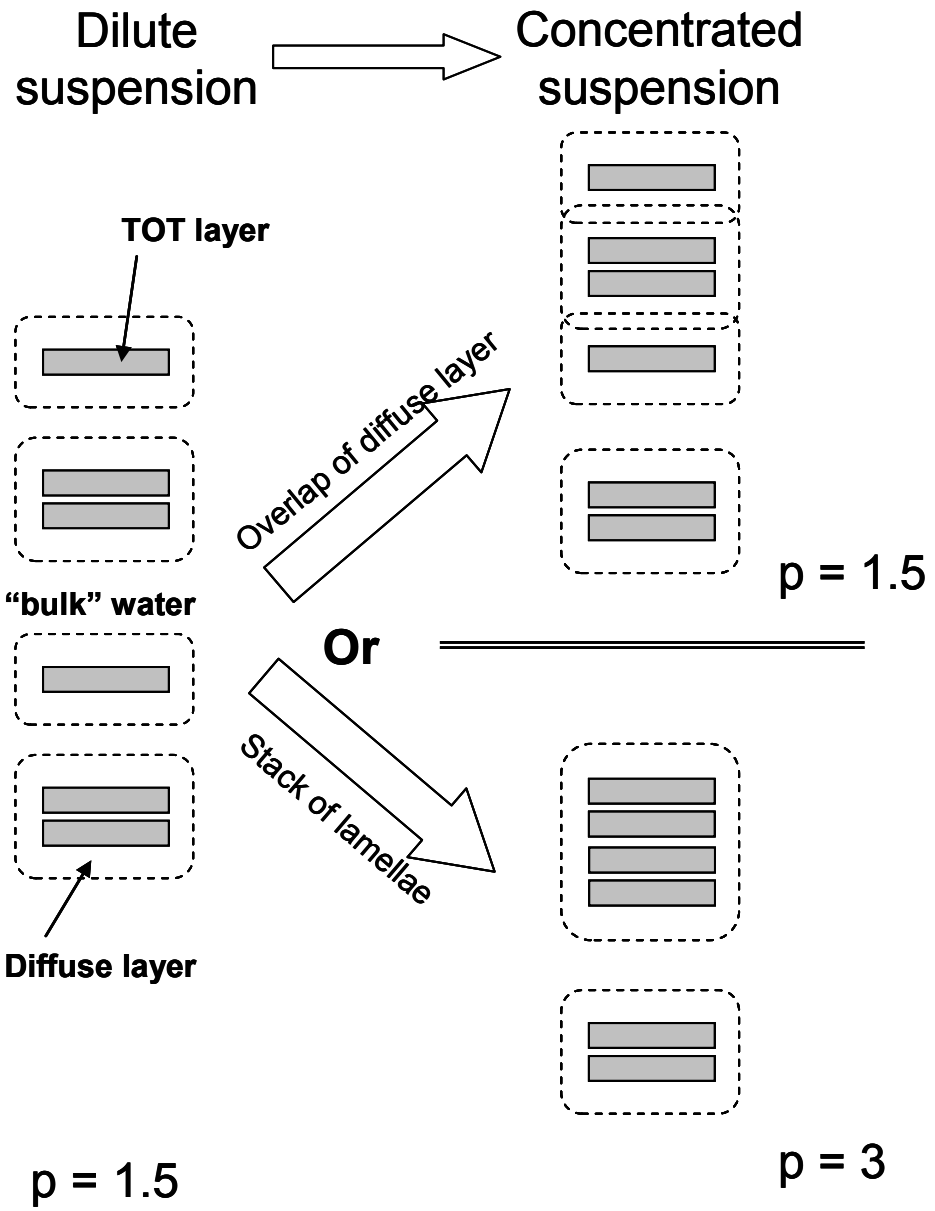

***Figure 2**. Conceptual scheme of the evolution of quasi-crystal size as a function of clay concentration in a suspension. p is the mean number of lamellae in a quasi-crystal.*

Quantification of anion exclusion

First we need to define some terms:

- Mass of clay in the system: m_{clay}
- TOT layer volume: V_{clay}
- Density of TOT layer: ρ_{clay}
- Mass of interlayer water in the system: m_{w_int}
- Interlayer water volume: V_{w_int}
- Density of water in the interlayer: ρ_{w_int}
- Mass of "micropore" water in the system: m_{w_pore}
- "Micropore" volume: V_{w_pore}

- Density of water in the micropores: ρ_{w_pores}

$$V_{w\_int} = \frac{m_{w\_int}}{\rho_{w\_int}}$$ Equation 1

$$V_{clay} = \frac{m_{clay}}{\rho_{clay}}$$ Equation 2

$$V_{w\_bulk} = \frac{m_{w\_bulk}}{\rho_{w\_bulk}}$$ Equation 3

$$V_{w\_edl} = \frac{m_{w\_edl}}{\rho_{w\_edl}}$$ Equation 4

$$V_{imp} = \frac{m_{imp}}{\rho_{imp}}$$ Equation 5

The density of water in the micropores (ρ_{w_pores}) at 25°C is considered at a value of 0.997 (water free of surface influence). The volume accessible to anions can be calculated as a function of the total volume (V_{tot}) according to:

$$V_{w\_bulk} = V_{tot} - \frac{m_{w\_int}}{\rho_{w\_int}} - \frac{m_{clay}}{\rho_{clay}} - \frac{m_{w\_edl}}{\rho_{w\_edl}} - \frac{m_{imp}}{\rho_{imp}}$$ Equation 6

For simplicity reasons, we considered that clay edge surfaces are negligible with regards to anion exclusion (Figure 3). This approximation is supported by the minor extent of edge surface area as compared to total surface in montmorillonite (0.5-2%, Tournassat et al., 2003; Yokoyama et al., 2005).

Interlayer water can be linked to the internal surface area of montmorillonite (S_{int}, see Figure 3) through the expression:

$$V_{w\_int} = \frac{S_{int} \times h_{int}}{2}$$ Equation 7

Where h_{int} is the interlayer thickness. Considering that all clay quasi-crystals contain a mean number p of stacked lamellae, it follows:

$$S_{ext} = \frac{S_{Tot}}{p}$$ Equation 8

$$S_{int} = S_{Tot} \times \left(1 - \frac{1}{p}\right)$$ Equation 9

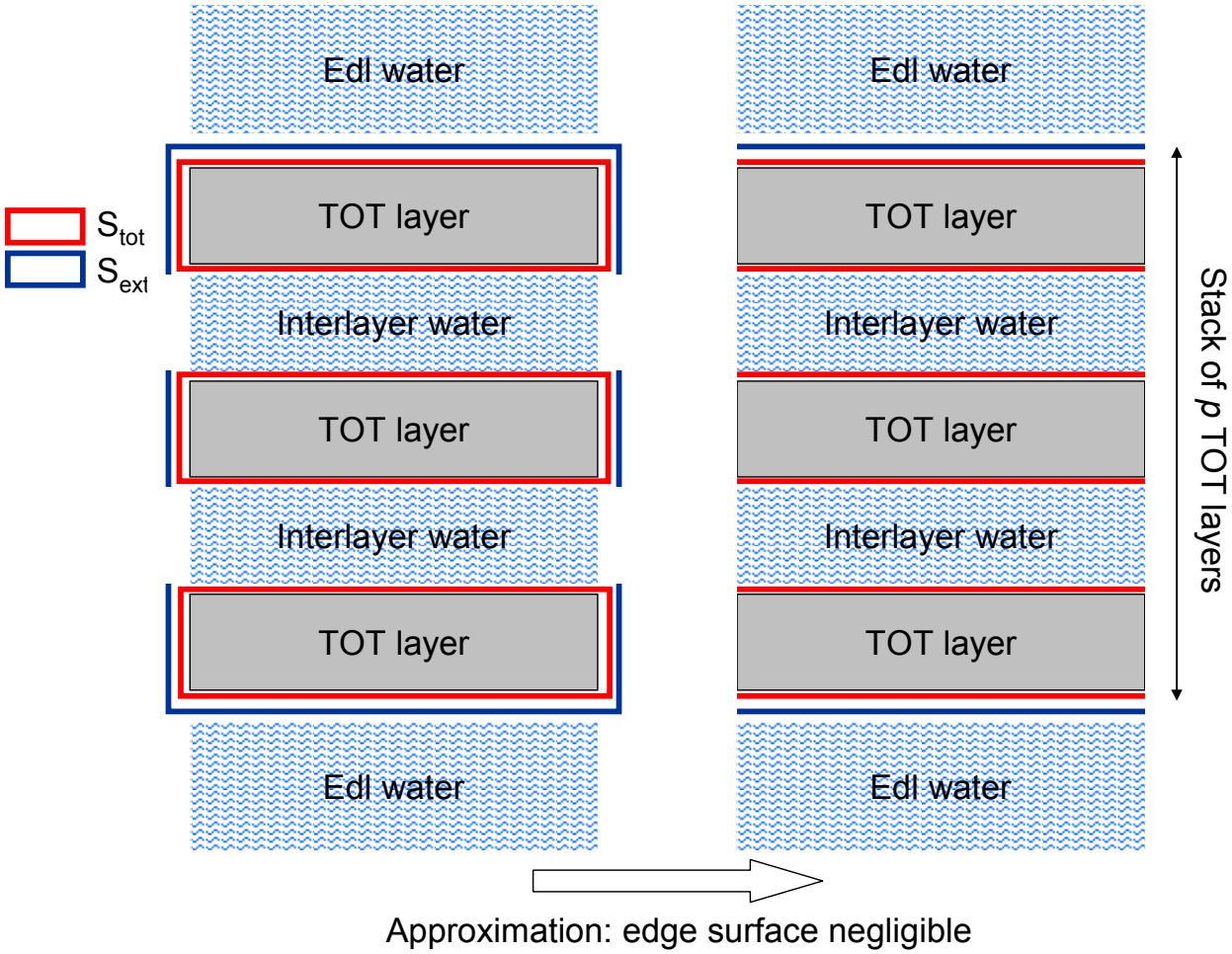

Figure 3. *Representation of the surfaces of montmorillonite and associated water.*

Knowing the anionic exclusion distance at the external surfaces, d_{exc}:

$$V_{w\_edl} = S_{ext} \times d_{exc}$$ Equation 10

The companion paper of the present study showed that d_{exc} can adequately be estimated through the application of the modified Gouy-Chapman theory (MGC) for NaCl concentration (C_0 in mol L^{-1}) lower than 0.01 mol L^{-1}, leading to an exclusion distance of ~1.9 κ^{-1} where κ is the Debye length:

$$\kappa^{-1} = \frac{3.037 \times 10^{-10}}{\sqrt{C_0}}$$ Equation 11

For concentration of 0.1 mol L^{-1}, this anion exclusion distance decreases at a value of ~1.2 κ^{-1}. From molecular dynamics data plotted in Marry et al., 2008, one can roughly estimate the exclusion distance at ~1 κ^{-1} for 1 mol L^{-1} concentration in near agreement with our value found at 0.1 mol L^{-1}.

In the following, we will apply the following rules:

- $d_{exc} = 1.9 \times \kappa^{-1}$ for $C_0 < 0.05$ mol L^{-1}
- $d_{exc} = (1.9 - (1.9 - 1.2)/ (0.1 - 0.05) \times C_0) \times \kappa^{-1}$ for $0.05 \leq C_0 \leq 0.1$ mol L^{-1}
- $d_{exc} = 1.2 \times \kappa^{-1}$ for $C_0 > 0.1$ mol L^{-1}

The parameter h_{int} can be obtained through the knowledge of the XRD d_{001} spacing and the crystallographic data for montmorillonite (Bourg, 2004)

$$h_{\text{int}} = d_{001} - h_{layer} \qquad \text{Equation 12}$$

For montmorillonite the distance between two most external oxygen atoms in the layer structure is ~6.54 Å. The thickness of the TOT layer is equal to this distance plus the radii of the oxygen atoms (1.3 Å) leading to a layer thickness of 9.1-9.2 Å, taken hereafter at 9.2 Å. Considering basal spacing (d_{001}) of 18.7 Å for a three layer hydrate and 15.4 Å for a two layer hydrate at 100% humidity (e.g. Kozaki et al., 2001; Sato et al., 1992) yields to $h^{3WL}_{int} = 9.5$ Å and $h^{2WL}_{int} = 6.2$ Å, i.e. respectively roughly 3 and 2 times the effective diameter of a water molecule (~3 Å). By analogy, we will consider in the following a value of $h^{1WL}_{int} = 3.1$ Å for the one layer hydrate interlayer at 100% humidity.

Knowing the mass of water in one interlayer, one can calculate interlayer water density (ρ_{int}). This can be achieved by considering Monte-Carlo and molecular dynamics data analysis from Tambach et al., 2004 and Chavez-Paez et al., 2001 (Figure 3 of Tambach et al., 2004). These authors give water clay mass ratio ($r_{w/c}$) as a function of d_{001} values: ~0.375 and 0.245 kg_{water}/kg_{clay} were obtained for 3 WL and 2 WL respectively. These calculations were performed in infinite periodical system so that:

$$r_{w/c} = \frac{h_{\text{int}} \times \rho_{\text{int}}}{h_{layer} \times \rho_{clay}} = \frac{h_{\text{int}} \times \rho_{\text{int}} \times S_{ab} \times N_A}{M_{clay}} \qquad \text{Equation 13}$$

Where S_{ab} is the unit cell surface in the 001 direction corresponding to one unit cell formula, N_A is the Avogadro number ($6.022\ 10^{23}$ mol^{-1}) and M_{clay} is the mass of one unit cell formula in kg/mol.

Table 1. *Structural parameters used in Equation 13*

	(Tambach et al., 2004)
$r_{w/c}$ at 18.7 Å (g_{water}/g_{clay})	0.375
$r_{w/c}$ at 15.4 Å (g_{water}/g_{clay})	0.245
s_{ab} (m^2/molecule)	48.3×10^{-20}
M_{clay} (kg/mol)	0.736

Using Equation 13 with parameters listed in Figure 1, one obtains interlayer water density equal to that of bulk water (difference less than 0.2%) for 3 WL and 2 WL. Considering the results obtained for external water (see companion paper), water density can be taken at the same value (ρ_w) in all of the water compartments and Equation 6 reduces to:

$$V_{w\_bulk} = V_{tot} - S_{tot} \times \left(\frac{h_{\text{int}}}{2} \times \left(1 - \frac{1}{p} \right) + \frac{d_{exc}}{p} \right) - \frac{m_{clay}}{\rho_{clay}} - \frac{m_{imp}}{\rho_{imp}}$$ Equation 14

The clay density depends on its structural formula, crystallographic cell parameters and considered h_{layer} value:

$$\rho_{clay} = \frac{M_{clay}}{S_{ab} \times N_A \times h_{clay}}$$ Equation 15

Bourg (Bourg, 2004) compiled S_{ab} values for natural montmorillonites and found a mean value of 46.4 ± 0.4 Å^2. Formula weights of montmorillonites depend principally on their iron content and on the charge compensating interlayer cations. There are little variations of their formula weight and Bourg concluded to a value of 746 ± 1 g mol^{-1}. Considering h_{int} = 9.2 Å yields ρ_{clay} = 2900 kg m^{-3}. The difference with the result obtained by Bourg is due to the consideration of a h_{int} value of 9.2 instead of 9.4 Å that in turn is due to our consideration of measured d_{001} spacing instead of values calculated from Monte Carlo simulations in Bourg study.

With these values one determines also the total specific surface area of basal and interlayer surface (*ssa*):

$$ssa = 2 \times \frac{S_{ab} \times N_A}{M_{clay}} = 749 \text{ m}^2 \text{ g}^{-1}$$ Equation 16

From Equation 14, it is then possible a priori to calculate the chloride accessible porosity in a montmorillonite medium equilibrated with NaCl solution. However some difficulties remain. It was possible to calculate h_{int} for 1, 2 or 3 WL but as a function of compaction, mixing between these different interlayer states occurs (Kozaki et al., 1998; Kozaki et al., 2001). The interlayer water term relative to h_{int} must then be related to the proportions x_1, x_2 and x_3 of 1, 2 and 3 WL interlayers (Bourg, 2004; Bourg et al., 2006):

$$V_{w\_\text{int}} = \frac{S_{\text{int}}}{2} \times \left(x_1 h_{\text{int}}^{1WL} + x_2 h_{\text{int}}^{2WL} + x_3 h_{\text{int}}^{3WL} \right)$$ Equation 17

As a consequence Equation 14 extends to:

$$V_{w\_bulk} = 1 - ssa \times m_{clay} \times \left(\frac{\left(x_1 h_{\text{int}}^{1WL} + x_2 h_{\text{int}}^{2WL} + x_3 h_{\text{int}}^{3WL} \right)}{2} \times \left(1 - \frac{1}{p} \right) + \frac{d_{exc}}{p} \right) - \frac{m_{clay}}{\rho_{clay}} - \frac{m_{imp}}{\rho_{imp}}$$ Equation 18

Methodology for model parameters estimation

Needed parameters

From Equation 18 needed parameters are:

- A relationship for the determination of x_1, x_2 and x_3 as a function of the compaction (i.e. the montmorillonite relative dry density)
- The mass and density of impurities in considered clay material
- A function for the determination of the value of p as a function of compaction

Determination of interlayer water content as a function of compaction

We rely here on a similar approach than that described in Bourg, 2004 and based on the work of Kozaki et al., 1998. Montmorillonite partial dry density ($\rho_{b,mont}$ in) is considered to be the key parameter in the determination of x_1, x_2 and x_3.

$$\rho_{b,mont} = \frac{m_{clay}}{V_{tot}}$$ Equation 19

From Kozaki et al. (1998, 2001), x_3 is equal to 1 up to $\rho_3 \sim 1300$ kg m^{-3} and x_2 is equal to 1 above $\rho_2 \sim 1600$ kg m^{-3}. Between these two values we considered a linear relationship:

$$x_3 = \frac{\rho_2 - \rho_{b,mont}}{\rho_2 - \rho_3} \text{ for } \rho_3 < \rho_{b,mont} < \rho_2$$ Equation 20

$$x_2 = 1 - x_3 \text{ for } \rho_3 < \rho_{b,mont} < \rho_2$$ Equation 21

Unfortunately, there is little data for the 2WL→1WL transition. Kozaki et al. did not detect this transition up to 1800 kg m^{-3} while Sanchez et al. (Sánchez et al.,) observed further partial replacement of 2WL by 1WL (see Table 2 of this reference with mean d_{001} value at 14.66 Å) at partial bentonite density of 1900 kg m^{-3} corresponding to a montmorillonite partial density of ~1750 kg m^{-3} (taking into account 9.9 % water content after air drying of the system, Van Loon et al., 2007 and impurity content less than 5% in mass, Sanchez, personnal communication).

Data on this transition are thus scarce and contradictory in the literature and we will thus focus firstly on data obtained at montmorillonite partial density lower than 1700 kg m^{-3}.

Determination of mass and density of impurities in clay materials

Experiments are often carried out not on pure montmorillonite systems but rather on bentonite, i.e. a clay material containing a high content of montmorillonite but also impurities (calcite, quartz, feldspars…). Mass of impurities can be obtained e.g. from mineralogical analysis (mainly XRD and chemical analysis) of the raw material and mean density can be calculated based on the density of each of the constituents. Based on the work of Madsen, 1998 and Komine, 2004, Bourg (2004) estimated the density of

impurities to 2.82 ± 0.58 kg dm^{-3}. Van Loon et al., 2007 report water uptake in diffusion cells as a function of bulk air dry density of bentonite and their data can therefore be used to constrain impurities volume and density in their system. Since the density of water in the different compartments has been proved to be nearly equal, the following equation applies:

$$V_{tot} = \frac{x_{imp} \times m_{bent}}{\rho_{imp}} + \frac{m_{bent} \times (1 - x_{imp})}{\rho_{clay}} + \frac{m_w}{\rho_w} \qquad \text{Equation 22}$$

where x_{imp} is the proportion of impurities in the bentonite (of mass m_{bent}).

Therefore:

$$V_{tot} - \frac{m_w}{\rho_w} - \frac{m_{bent}}{\rho_{clay}} - m_{imp} \times \left(\frac{1}{\rho_{imp}} - \frac{1}{\rho_{clay}} \right) = 0 \qquad \text{Equation 23}$$

This unique equation does not enable to fit m_{imp} and ρ_{imp} but it enables to constrain a reasonable range of values. After neglecting data with highest water uptake (leading to aberrant results), we varied ρ_{imp} and adjust m_{imp} accordingly by least square fitting of the data with regards to Equation 23. Results are shown on Figure 4. Considering information from XRD measurement (~30 % impurities, Van Loon et al., 2007), impurities density above 2.6 kg dm^{-3} is not acceptable and then one can not consider the density given by Bourg for MX80 impurities. We considered a mean density of 2.55 kg dm^{-3} for impurities (corresponding to 30% impurities), in near agreement with the density of the main impurity minerals, i.e. K-feldspar, albite and quartz.

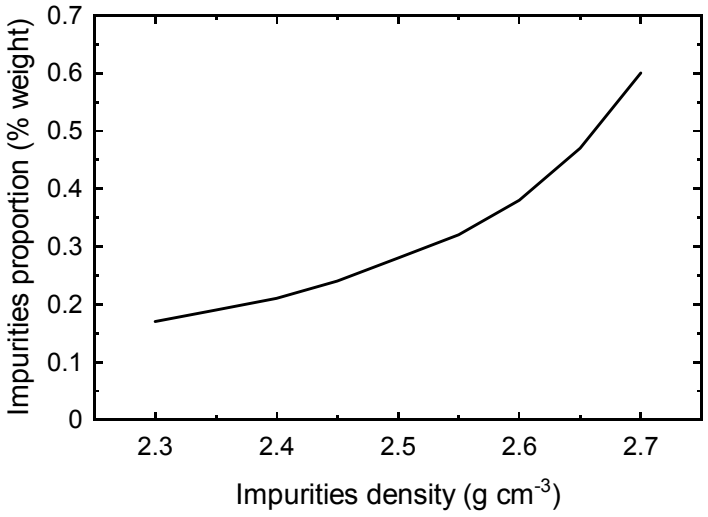

Figure 4. *Relationship between the considered impurities density and their proportion in the MX80 bentonite. Calculated with Equation 23 after the data from Van Loon et al., 2007.*

Determination of the lamella stacking parameter p as a function of compaction

The parameter *p* remains the only unknown in Equation 18. As a consequence it will be the only parameter fitted from anion exclusion volume measurements. By chance, most of these measurements available in the literature were obtained on a single material, i.e. MX80 bentonite (Molera et al., 2003; Muurinen et al., 2004; Muurinen et al., 2007; Muurinen et al., 1989; Van Loon et al., 2007). Although, variability of this commercial product mineralogical composition is unavoidable, we will consider that its mineral impurities content is the same in all of these studies.

As explained in the introductory part on conceptual model, we consider that the parameter *p* depends only on a limiting overlap distance of diffuse layers. If the overlap exceeds this distance d_{lim_ov}, the lamellae stack. This conceptual model is numerically translated with the following procedure:

Step 1: *p* value is fixed at 1.4 (known value for very diluted systems, see companion paper)

Step 2: the pore volume ($V_{w\_bulk} + V_{w\_edl}$) is calculated according to Equation 18 with $d_{exc} = 0$;

Step 3: a mean distance between two external surfaces of quasi-crystal (d_{pore}, analogous to a mean pore size) is calculated according to

$$d_{pore} = \frac{V_{w\_bulk} + V_{w\_edl}}{\frac{S_{ext} \times d_{exc}}{2}} = 2 \times p \times \frac{V_{w\_bulk} + V_{w\_edl}}{S_{Tot} \times d_{exc}} \qquad \text{Equation 24}$$

Step 4: d_{pore} is compared to d_{lim_ov}. If $d_{pore} < d_{lim\_ov}$ then *p* value is increased and the procedure restarts at step 2. If $d_{pore} > d_{lim\_ov}$ the procedure stops and *p* value is saved.

We considered an upper value for *p* equal to 100 corresponding to an external surface area of quasi-crystals of 7.5 m^2g^{-1}, i.e. commensurable with the edge surface area that remains fixed at 5-10 $m^2\ g^{-1}$ (Tournassat et al., 2003; Yokoyama et al., 2005). *p* values above this limit are then senseless in the considered approach that neglects these latter edge surfaces.

Results and discussion

Determination of the limiting distance for diffuse layer overlaps

The parameter d_{lim_ov} was fitted with the data from Molera et al., 2003; Muurinen et al., 1989; Van Loon et al., 2007. It was found that an unique d_{lim_ov} value equal to 2.65 times the exclusion distance d_{exc}, as determined by coupling MGC theory and molecular dynamics results, enables to reproduce fairly well the whole set of data. Thus, for the entire results presented below, the following relationship applies:

$$d_{\lim\_ov} = 2.65 \times d_{exc} \qquad \text{Equation 25}$$

Anion accessible porosities calculated accordingly are presented on Figure 5, Figure 6 and Figure 7

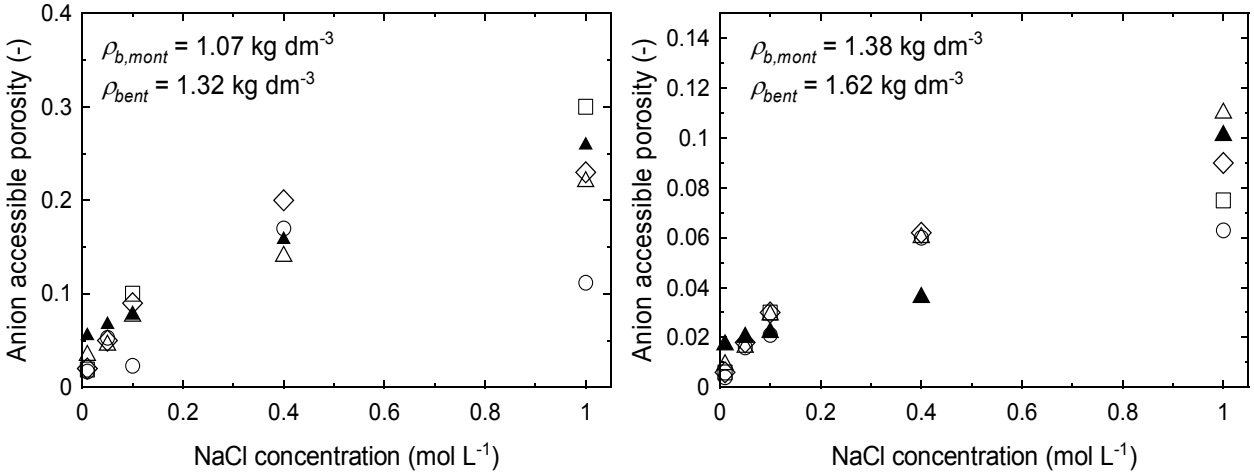

Figure 5. *Comparison of the modelled anion accessible porosity with data from Van Loon et al., 2007 as a function of NaCl concentration and dry montmorillonite partial density. Closed triangles: model. Open circles: data from through-diffusion; Open squares: data from out-diffusion; Open diamonds: data from ^{36}Cl mass balance; Open triangles: data from stable Cl mass balance.*

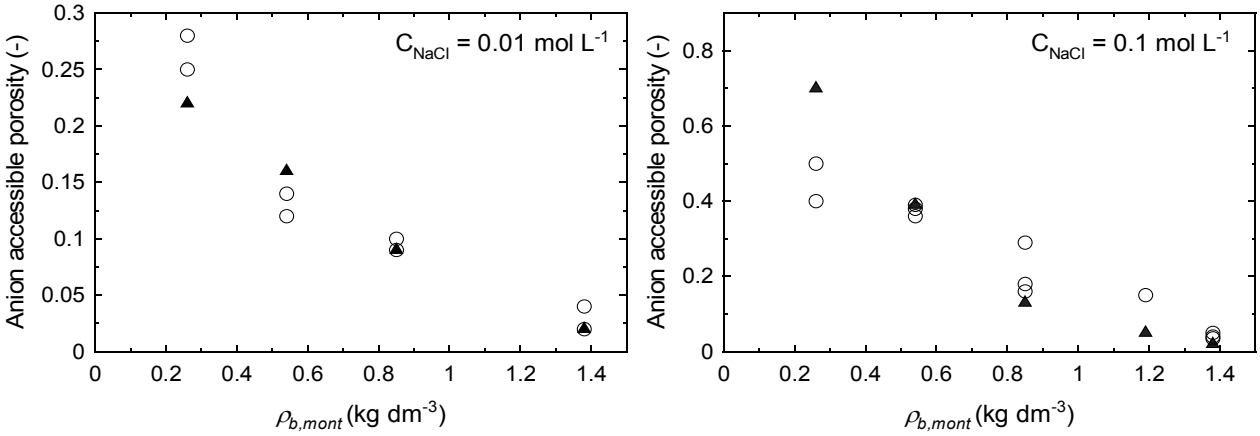

Figure 6. *Comparison of the modelled anion accessible porosity with data from Molera et al., 2003 as a function of NaCl concentration and dry montmorillonite partial density. Closed triangles: model. Open circles: experimental data.*

Predicting anion exclusion in a NaCl-montmorillonite system

Once d_{lim_ov} value was fitted, it was then possible to test the prediction capabilities of the model on data sets that were not used to calibrate the model. Data from Muurinen et al., 2004, with a wide range of experimental conditions enabled this test. The good agreement between experimental points and model prediction is shown on Figure 8 and validates the model at least for ionic strengths above 0.1 mol L^{-1}.

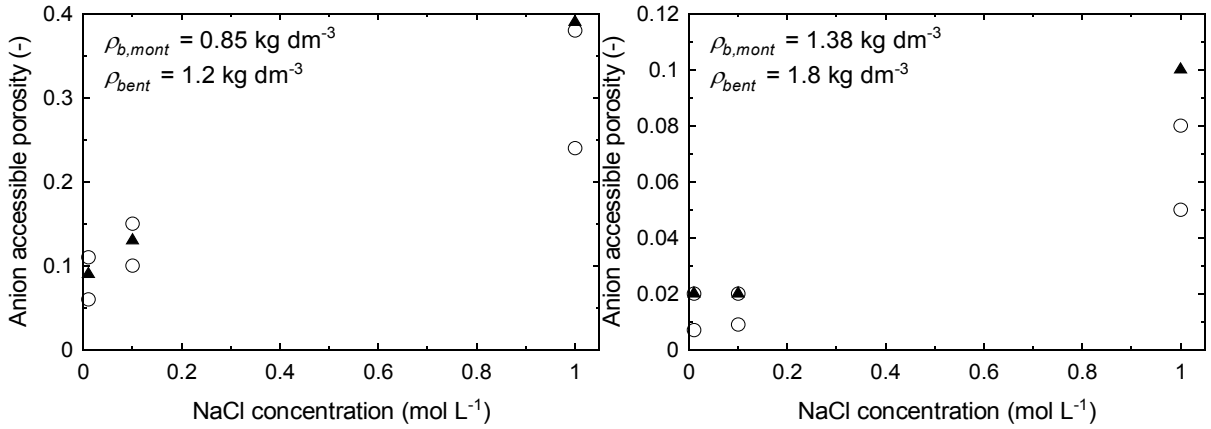

Figure 7. *Comparison of the modelled anion accessible porosity with data from Muurinen et al., 1989 as a function of NaCl concentration and dry montmorillonite partial density. Closed triangles: model. Open circles: experimental data.*

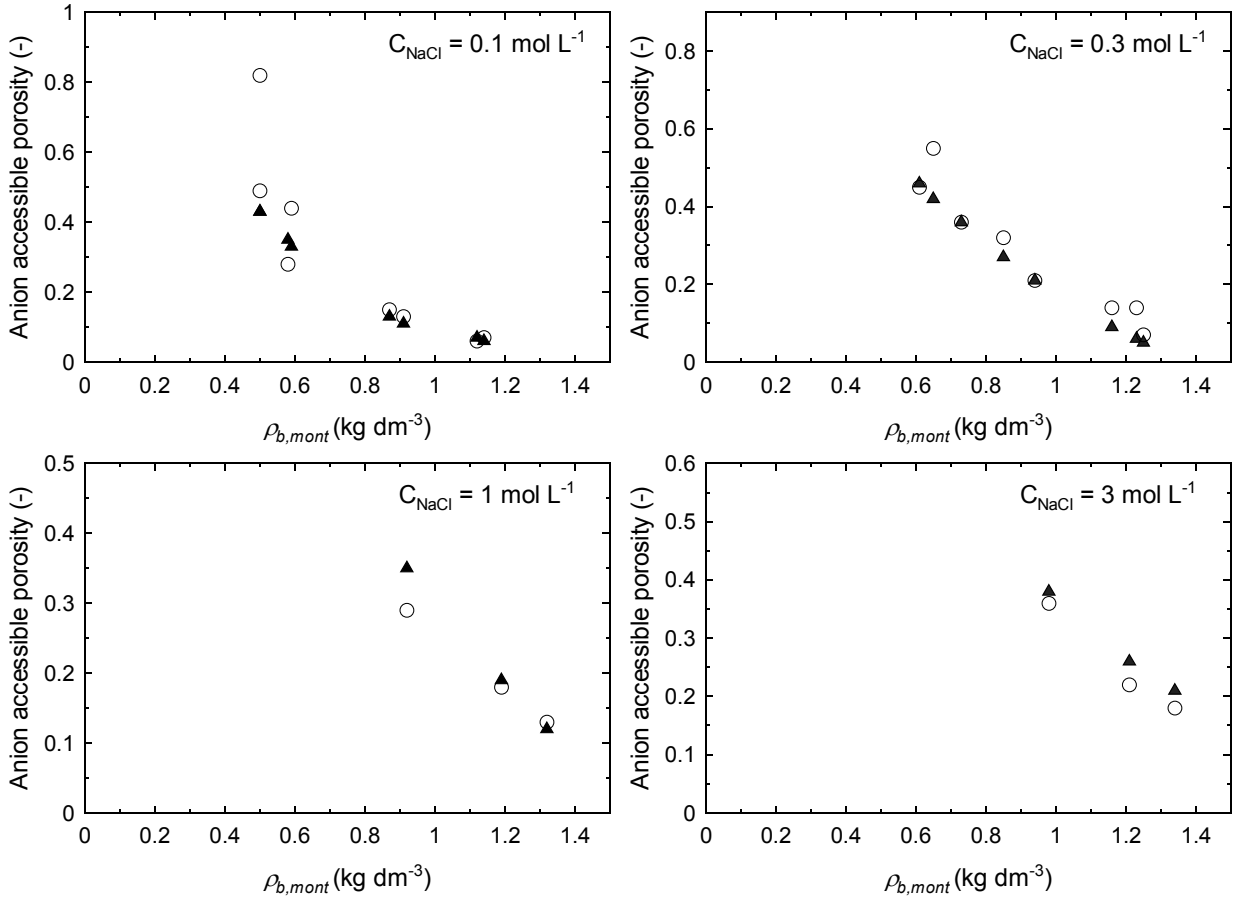

Figure 8. *Comparison of the modelled anion accessible porosity with data from Muurinen et al., 2004 as a function of NaCl concentration and dry montmorillonite partial density. Closed triangles: model. Open circles: experimental data.*

Extension of the model for montmorillonite dry densities higher than 1.7 kg dm^{-3}

We considered that the model with the same lamellae stacking parameters could also apply to density higher than 1700 kg m^{-3} by simply adding a relationship for the 2WL→1WL transition. Conditions similar to those given by Equation 20 and Equation 21 enabled to correctly fit the data from Van Loon et al., 2007 at montmorillonite dry density of 1730 kg m^{-3} (Figure 9).

Equation 26

$$x_2 = \frac{\rho_0 - \rho_{b,mont}}{\rho_0 - \rho_1} \text{ for } \rho_1 < \rho_{b,mont} < \rho_0$$

$$x_1 = 1 - x_2 \text{ for } \rho_1 < \rho_{b,mont} < \rho_0 \qquad \text{Equation 27}$$

With ρ_1 ~1700 kg m^{-3} and ρ_0 ~2000 kg m^{-3}. x_2 is equal to 1 up to ρ_1 ~1700 kg m^{-3}.

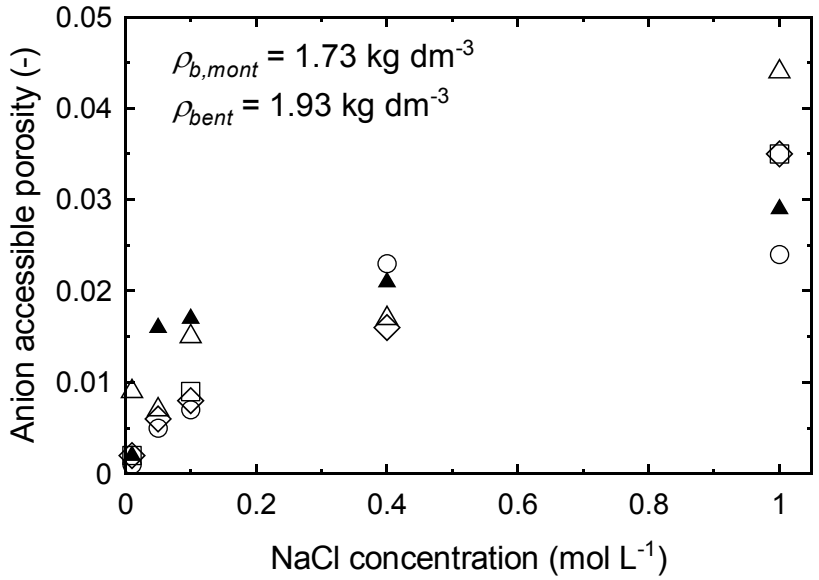

Figure 9. *Comparison of the predicted (closed triangles) and experimental porosity at high montmorillonite density ($\rho_{b,mont}$=1.73 kg dm^{-3}, data from Van Loon et al., 2007, Open circles: data from through-diffusion; Open squares: data from out-diffusion; Open diamonds: data from ^{36}Cl mass balance; Open triangles: data from stable Cl mass balance).*

Predicting anion diffusion coefficient in NaCl-montmorillonite systems

After Van Loon et al., 2007, an empirical relationships exists between the effective diffusion coefficient of a given monovalent non-sorbing anion (D_e), its diffusion coefficient in water (D_0 = 2.03 × 10^{-9} m^2 s^{-1} at 25°C, Li and Gregory, 1974) and its accessible porosity (ε):

$$D_e = D_0 \times \varepsilon^n \qquad \text{Equation 28}$$

These authors demonstrated that in case of Cl^- (or I^-) diffusion in a NaCl-montmorillonite system, the exponent *n* is nearly equal to 1.9. As a consequence, the present model should enable to predict effective diffusion coefficient in any NaCl-montmorillonite systems provided that the bentonite density and the NaCl concentration are given. This could be first tested with data already mentioned from Molera et al., 2003; Muurinen et al., 1989; Van Loon et al., 2007. As a function of diffusion experimental setup, either effective diffusion coefficient or apparent diffusion coefficient (D_a) are measured. Apparent diffusion coefficient is linked to effective diffusion coefficient with the relationship:

$$D_e = D_a \times \varepsilon \qquad \text{Equation 29}$$

Hence the present model can be also tested with regards to apparent diffusion coefficient through the relationship:

$$D_a = D_0 \times \varepsilon^{n-1} \qquad \text{Equation 30}$$

Figure 10 shows the good agreement between experimental measured data and predictions made with a *n* value of 2.

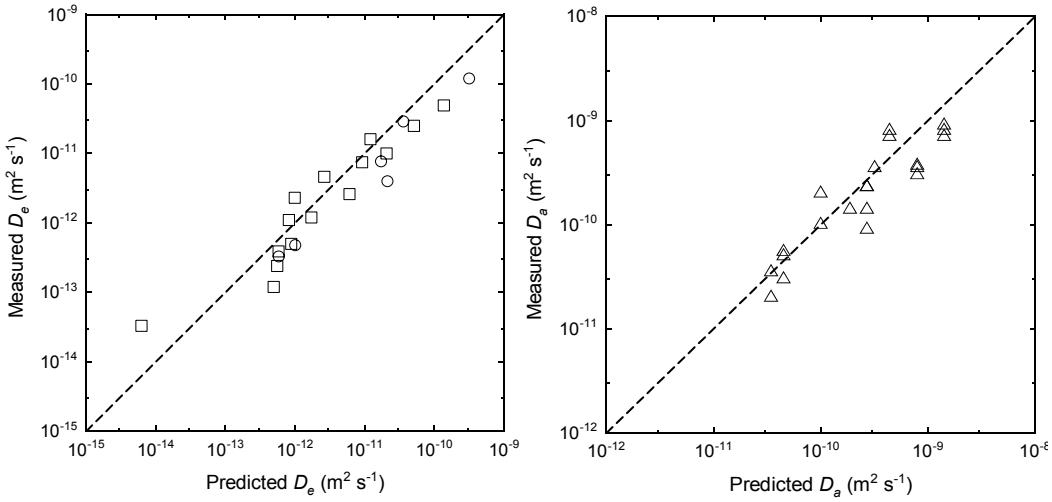

Figure 10. *Comparison of the predicted and experimental effective diffusive coefficients (left figure. Circles: data from Van Loon et al., 2007; squares: data from Muurinen et al., 1989) or apparent diffusion coefficient (right figure. Triangles: data from Molera et al., 2003). The dashed line represents the 1:1 relationship.*

Other data are also available for Cl^- diffusion but most of time experiment were performed at very low ionic strength. For instance Kozaki et al., 2001 and García-Gutiérrez et al., 2004 "equilibrated" their montmorillonite with distilled water until negative response to nitrate silver test before drying and compaction of their material. However, during the water resaturation period (up to 2.5 months, García-Gutiérrez et al., 2004), clay dissolves leading in turn to an unknown ionic strength in the system. The interpretation of their data must then be carried out by making hypothesis on the

ionic strength. Prediction of their data using ionic strength from 0.001 to 0.012 mol L^{-1} is shown on Figure 11. and Figure 12. There is little influence of the chosen ionic strength for montmorillonite dry density values below 1300 kg m^{-3}. Above this value, a marked effect is observed. An ionic strength of 0.012 mol L-1 enables to fit the whole set of data. Such ionic strength can be expected from bentonite constituent dissolution as already pointed out by Bourg, 2004.

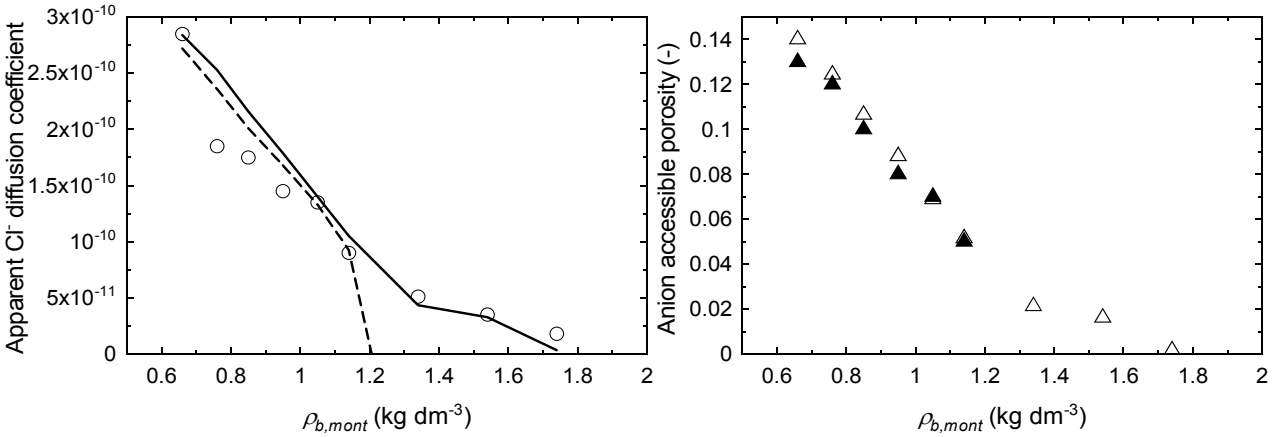

Figure 11. *Left figure: comparison of the predicted (plain line for ionic strength of 0.012 mol L^{-1} and dashed line for 0.001 mol L^{-1}) and experimental (open circles) apparent diffusion coefficient as a function of compaction in the experiments from Kozaki et al., 2001. Right figure: predicted porosity (open triangles for ionic strength of 0.012 mol L^{-1} and closed triangles for 0.001 mol L^{-1}).*

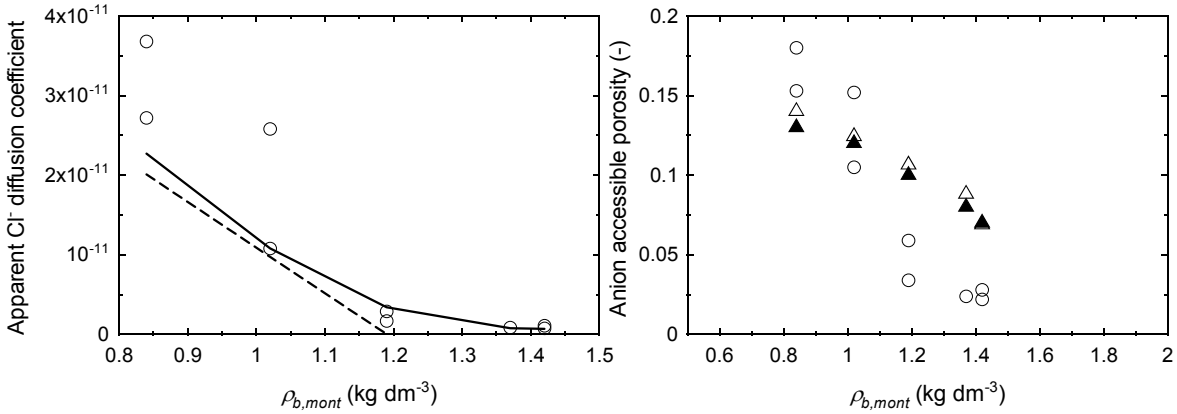

Figure 12. *Left figure: comparison of the predicted (plain line for ionic strength of 0.012 mol L^{-1} and dashed line for 0.001 mol L^{-1}) and experimental (open circles) effective diffusion coefficient as a function of compaction in the experiments from García-Gutiérrez et al., 2004. Right figure: predicted porosity (open triangles for ionic strength of 0.012 mol L^{-1} and closed triangles for 0.001 mol L^{-1}) and experimentally measured porosity (open circles, data from García-Gutiérrez et al., 2004).*

The model predicts negative anion accessible porosity values (an unphysical result) for montmorillonite dry density value above 1200 kg m^{-3} at low ionic strength (0.001 mol L^{-1}) showing the limit of the present model. However, the unavoidable partial dissolution of bentonite material certainly makes these conditions unlikely to

occur in natural and laboratory systems. This limit corresponds to the 3WL→2WL transition as identified by XRD pointing out that this transition is also certainly due to the excess of energy originating from the overlap of diffuse layers.

Implications for montmorillonite lamellae spatial arrangements in a compacted Na-montmorillonite

The real texture of a hydrated compacted clay sample will differ from the very simple representation given in the present paper. For instance, the number of stacked lamellae is certainly very different from the *p* parameter determined in the present study. Firstly this number of lamellae is unlikely unique but rather represented by a distribution between several sizes of (quasi)-crystals. Secondly, the model is based on a 1D binary representation of micropore separated in two reservoirs with or without anion. In the "real" system, one except zones enriched in anions and other depleted as expected from e.g. modified Gouy-Chapman theory or M.D. calculations (see companion paper) in a 3D framework. The parameter *p* in the present paper can then not been directly compared to montmorillonite textural observations but must be seen as an integration of both this geometrical/textural information and electrostatic mean effect.

Conclusion

We have shown that the decrease of anion accessible porosity as a function of bentonite compaction and decrease of ionic strength can be fairly accurately predicted with a relatively simple model that links the stacking of montmorillonite lamellae to the extent of diffuse layer overlap between two external surfaces of montmorillonite quasi-crystals.

This model coupled to an Archie law with factor value of 2 enables to reproduce a wide set of literature data on Cl^- (or I^-) apparent and effective diffusion coefficients as well as independently measured porosity values.

Despite its limitation, this model clearly point out the effectiveness of a dual porosity approach for modelling anion diffusion in compacted Na-montmorillonite.

Acknowledgment

This work has been supported by the ANDRA (French National Radioactive Waste Management Agency, under the supervision of Dr. S. Altmann), BRGM (French geological survey) and European Commission in the framework of the 6th PCRD Euratom IP FUNMIG.

References

Bolt, G.H. and Warkentin, B.P., 1958. The negative adsorption of anions by clay suspensions. Kolloid Zeitschrift, 156(1): 41-46.

Bourg, I.C., 2004. Tracer diffusion of water and inorganic ions in compacted saturated sodium bentonite, University of California, Berkeley, Berkeley, 384 pp.

Bourg, I.C., Sposito, G. and Bourg, A.C.M., 2006. Tracer diffusion in compacted, water-saturated bentonite. Clay. Clay. Miner., 54(3): 363-374.

Chavez-Paez, M., dePablo, L. and dePablo, J.J., 2001. Monte Carlo simulations of Ca-montmorillonite hydrates. The Journal of Chemical Physics, 114(24): 10948-10953.

Edwards, D.G., Posner, A.M. and Quirk, J.P., 1965. Repulsion of chloride ions by negatively charged clay surfaces. Part 2.-Monovalent cation montmorillonites. Transactions of the Faraday Society, 61: 2816-2819.

Edwards, D.G. and Quirk, J.P., 1962. Repulsion of chloride by montmorillonite. Journal of colloid science, 17(872-882).

García-Gutiérrez, M., Cormenzana, J.L., Missana, T. and Mingarro, M., 2004. Diffusion coefficients and accessible porosity for HTO and 36Cl in compacted FEBEX bentonite. Applied Clay Science, 26(1-4): 65-73.

Grambow, B., 2006. Report describing preliminary version (without osmotic equilibria) of the double-porosity model for simulating radionuclide transfer in compact clay materials, Armines. FP6-516514.

Komine, H., 2004. Simplified evaluation for swelling characteristics of bentonites. Eng. Geol., 71(3-4): 265-279.

Kozaki, T., Fujishima, A., Sato, S. and Ohashi, H., 1998. Self-diffusion of sodium ions in compacted montmorillonite. Nucl. Technol., 121: 63-69.

Kozaki, T., Inada, K., Sato, S. and Ohashi, H., 2001. Diffusion mechanism of chloride ions in sodium montmorillonite. J. Contam. Hydrol., 47(2-4): 159-170.

Li, Y.-H. and Gregory, S., 1974. Diffusion of ions in sea water and in deep-sea sediments. Geochim. Cosmochim. Acta, 38: 703-714.

Madsen, F.T., 1998. Clay mineralogical investigations related to nuclear waste disposal. Clay Miner., 33: 109-129.

Marry, V., Rotenberg, B. and Turq, P., 2008. Structure and dynamics of water at a clay surface from molecular dynamics simulation. Phys. Chem. Chem. Phys., 10: 4802-4813.

Molera, M., Eriksen, T. and Jansson, M., 2003. Anion diffusion pathways in bentonite clay compacted to different dry densities. Applied Clay Science, 23(1-4): 69-76.

Muurinen, A., Karnland, O. and Lehikoinen, J., 2004. Ion concentration caused by an external solution into the porewater of compacted bentonite. Phys. Chem. Earth., 29(1): 119-127.

Muurinen, A., Karnland, O. and Lehikoinen, J., 2007. Effect of homogenization on the microstructure and exclusion of chloride in compacted bentonite. Phys. Chem. Earth., 32(1-7): 485-490.

Muurinen, A., Penttilä-Hilthunen, P. and Uusheimo, K., 1989. Diffusion of chloride and uranium in comapcted sodium bentonite. In: W. Lutze and R.C. Ewing (Editors), Scientific basis for nuclear waste management XII, Mat. Res. Soc. Symp. Proc. Materials Research Society, Pittsburgh, PA, pp. 743-748.

Sánchez, F.G., Van Loon, L.R., Gimmi, T., Jakob, A., Glaus, M.A. and Diamond, L.W., Self-diffusion of water and its dependence on temperature and ionic strength in highly

compacted montmorillonite, illite and kaolinite. Appl. Geochem., In Press, Accepted Manuscript.

Sato, T., Watanabe, T. and Otsuka, R., 1992. Effects of layer charge, charge location, and energy change on expansion properties of dioctahedral smectites. Clay. Clay. Miner., 40: 103-113.

Schofield, R.K., 1947. Calculation of surface areas from measurements of negative adsorption. Nature, 160.

Schramm, L.L. and Kwak, J.C.T., 1982. Influence of exchangeable cation composition on the size and shape of montmorillonite particles in dilute suspension. Clay. Clay. Miner., 30(1): 40-48.

Shomer, I. and Mingelgrin, U., 1978. A direct procedure for determining the number of plates in tactoids of smectites: the Na/Ca-montmorillonite case. Clays & Clay Minerals, 26(2): 135-138.

Sposito, G., 1992. The diffuse-ion swarm near smectite particles suspended in 1:1 electrolyte solutions: modified Gouy-Chapman theory and quasicrystal formation. In: N. Güven and R.M. Pollastro (Editors), Clay-water interface and its rheological implications. Clay minerals society, pp. 127-156.

Tambach, T.J., Hensen, E.J.M. and Smit, B., 2004. Molecular simulations of swelling clay minerals. J. Phys. Chem. B, 108: 7586-7596.

Tournassat, C., Neaman, A., Villiéras, F., Bosbach, D. and Charlet, L., 2003. Nanomorphology of montmorillonite particles: Estimation of the clay edge sorption site density by low-pressure gas adsorption and AFM observations. Am. Mineral., 88(2): 1989-1995.

Van Loon, L.R., Glaus, M.A. and Müller, W., 2007. Anion exclusion effects in compacted bentonites: Towards a better understanding of anion diffusion. Appl. Geochem., 22(11): 2536-2552.

Yokoyama, S., Kuroda, M. and Sato, T., 2005. Atomic force microscopy study of montmorillonite dissolution under highly alkaline conditions. Clay. Clay. Miner., 53(2): 147-154.

COLLOID GENERATION BY EROSION OF COMPACTED BENTONITE UNDER DIFFERENT GEOCHEMICAL CONDITIONS

Seher H.[1,*], Albarran N.[2], Hauser W.[1], Götz R.[1],
Missana T.[2], Geckeis H.[1], Fanghänel T.[3,4], Schäfer T.[1]

[1] Forschungszentrum Karlsruhe GmbH, Institut für Nukleare Entsorgung, Postfach 36 40, D-76021 Karlsruhe, Germany
[2] CIEMAT, Dept. Medioambiente, Avenida Complutense, 22, 28040 Madrid, Spain
[3] European Commission, Joint Research Centre, Institute for Transuranium Elements, P.O. Box 2340, D-76125 Karlsruhe, Germany
[4] Ruprecht-Karls-Universität Heidelberg, Physikalisch-Chemisches Institut, Im Neuenheimer Feld 253, D-69120 Heidelberg, Germany

* Corresponding author: holger.seher@ine.fzk.de

Abstract

Bentonite colloid generation was investigated for mono- and divalent electrolytes (Na^+, Ca^{2+}) with various ionic strengths, pH and filter pore sizes (2 µm, 10 µm, 100 µm). Colloid concentration and average colloid diameter was measured with Laser-induced Breakdown Detection (LIBD). A pH and ionic strength dependent colloid generation was observed. For ionic strengths lower than the critical coagulation concentration (CCC) a colloid generation can be confirmed. The strong pH dependency of colloid stability in the sodium system previously investigated in coagulation experiments was confirmed in the colloid generation experiments presented in this study. A filter pore size dependent colloid generation mechanism could not be observed in the course of this study. In all experiments the colloid concentration reaches with time a plateau value. Exchange of the contact water leads to a rapid new-formation of colloids reaching again a plateau value. The reason for this observation (a) dynamic generation/aggregation equilibrium or (b) depletion of the colloid source is discussed in the manuscript.

Introduction

Colloids are known to be ubiquitous in natural ground waters and have been frequently discussed as potential carriers for radionuclides. Concepts for high-level nuclear waste disposal in crystalline rock foresee bentonite as appropriate backfill and buffer material both to inhibit ground water access to the waste canister and to retard radionuclide transport in form of colloidal phases (safety function “colloid filter”) away from the repository near field [1]. In previous studies we investigated the potential

colloid formation in the bentonite pore water granite ground water mixing zone [2], here we focused on the potential erosion of the compacted bentonite in contact with ground water. Bentonite colloid erosion is reported from the interface between the compacted bentonite buffer and granite [3; 4]. These results as well as laboratory bentonite erosion experiments [5] show a dependence of the colloid source term on ionic strength, pH, bentonite compaction and flow velocity.

The presented work discusses the effect of ionic strength in light of concentration ranges below and above the pH-dependent critical coagulation concentration (CCC) determined previously in batch-type coagulation studies and the bentonite confining filter plate pore size on the bentonite colloid formation. First results on the colloid generation at an already existing gel front are also presented and discussed.

Experimental

Material

For the experiments the smectite-rich Febex (full-scale engineered barrier experiment) bentonite from the deposit of Cabo de Gata, Almería (Spain) is used [6]. The exchangeable cation composition was determined prior to the experiment to be 99 ± 2.1 meq·$100^{-1}g^{-1}$. An overview of the used electrolytes, ionic strength and filter pore size in each experiment is given in Table 1.

Table 1: *Conditions for each experiment*

Nr.	Density [g·cm^{-3}]	Electrolyte	Ionic strength [mmol·L^{-1}]	Filter pore size [µm]	Filter material	pH start	pH end
E1	1.6	$NaHCO_3$	10	100		8.7	8.9
E2	1.6	$NaHCO_3$	5	100		9.5	9.6
E3	1.6	GTS GW*	0.964	100		7.7	7.2
E4	1.6	$CaCl_2$	1	100	stainless	6.1	7.7
E5	1.6	$CaCl_2$	5	100	steel	6.0	7.5
E6	1.6	NaCl	10	100		6.5	5.0
E7	2.0	GTS GW*	0.964	2		9.5	n.n.
E8	2.0	GTS GW*	0.964	10		9.5	9.5
E9	2.0	GTS GW*	0.964	10	peek	9.5	9.5

* GTS GW: Grimsel Test Site ground water

Experimental setup

A bentonite pellet is confined with a filter plate in all experiments. Two different experimental setups are used. The first setup (Figure 1a) consists of a stainless-steel cylinder in which the bentonite pellet is squeezed in between two filter plates of 100 µm pore size (CIEMAT setup), for more details see [5]. This reactor is submerged in 0.5 L electrolyte solution.

The FZK-INE setup (Figure 1b) consists of a two sided reactor. A bentonite pellet (19 mm diameter, 10 mm height) with a filter plate and a water tight spacer is

inserted into both sides. The reactor has two tubing connections on top and on the bottom of each side to pump the electrolyte solution in circulation through the reactor. One connector is located directly above the filter plate to mimic in later experiments flow induced shear stress on the bentonite surface (for the studies presented here this connection is sealed) and the second connection is designed 6 cm above the filter surface. The volume inside the reactor is 11.6 mL and the reservoir has a total volume of 1 L capacity. The flow velocity at the filter plate surface is $3.3 \cdot 10^{-6}$ m·sec^{-1}.The Reactor is constructed with stainless steel or PEEK material (see Table 1).

a b

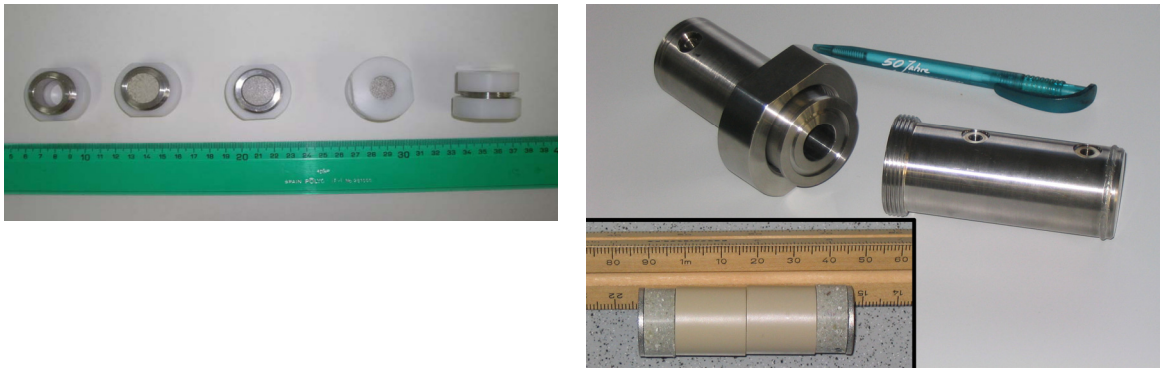

Figure 1: *(a) Reactor of the CIEMAT setup in different assembly stages. The bentonite pellet is squeezed into a stainless-steel cylinder by two filter plates. (b) Stainless steel reactor version of the FZK-INE experimental setup. Two bentonite pellets with the PEEK spacer and the filter plates are inserted.*

Analytical Methods

The colloid concentration and number-weighted average colloid diameter is determined with a Laser-induced Breakdown Detection (LIBD) system [7]. The sample solution is pumped through a silica flow-through cell. A dielectric breakdown is produced in the focus region of a pulsed laser beam (Nd: YAG-laser, Frequency: 15 Hz, Wavelength: 532 nm). The plasma generated by the breakdown event is monitored by a CCD-camera attached to an image-processing system. The system is calibrated with polystyrene reference particles.

A sample aliquot is taken, to detect the generated bentonite colloids via ICP-MS Al-signal. Additionally pH, Eh and Temperature are measured to monitor changes in the electrolyte solutions.

Results and discussion

The time dependent evolution of the colloid concentration and the number-weighted average colloid diameter determined by LIBD for the different experiments are presented in Figure 2. In order to compare the experimental results of the different setups used (experiment number E1 to E6 CIEMAT setup and E7 to E9 FZK-INE setup) all measured concentrations were recalculated to a volume of 1 L contact solution.

The data presented here are discussed on the basis of CCC, which is the concentration where the aggregation of colloids is solely diffusion controlled [8].

In the $NaHCO_3$-system with 5-10 mmol·L^{-1} ionic strength (experiments E1 to E2; Figure 2a) and a pH variation of 8.7-9.6 a comparable colloid concentration increase to a plateau value scattering between 7.1 ± 4.1 mg·L^{-1} and 2.6 ± 1.1 mg·L^{-1}, respectively, after approximately 17 days could be observed. Both experiments are with respect to the sodium concentration below the CCC (~ 0.3 mol; [9]) and only slow colloid coagulation is expected. The compacted bentonite in contact with Grimsel ground water (GTS GW) shows from the start of the experiments lower pH values (pH ~ 7.7) compared to the fresh GTS GW, which could be attributed to an influence of atmospheric CO_2. However, even under this circum- neutral pH the contact water solution ionic strength is below the CCC concentration of 20 mmol·L^{-1} found for monovalent ions. Therefore, the comparable colloid generation observed in the experiments E1 to E3 is in line with the knowledge from colloid stability investigations. The average number-weighted colloid size was in the 5 and 10 mmol·L^{-1} $NaHCO_3$ contact solution 158 ± 19 nm (5 mmol·L^{-1}, E1) and 159 ± 30 nm (10 mmol·L^{-1}, E2), respectively, whereas in the GTS GW a slightly higher average colloid diameter of 182 ± 27 nm (E3) could be detected.

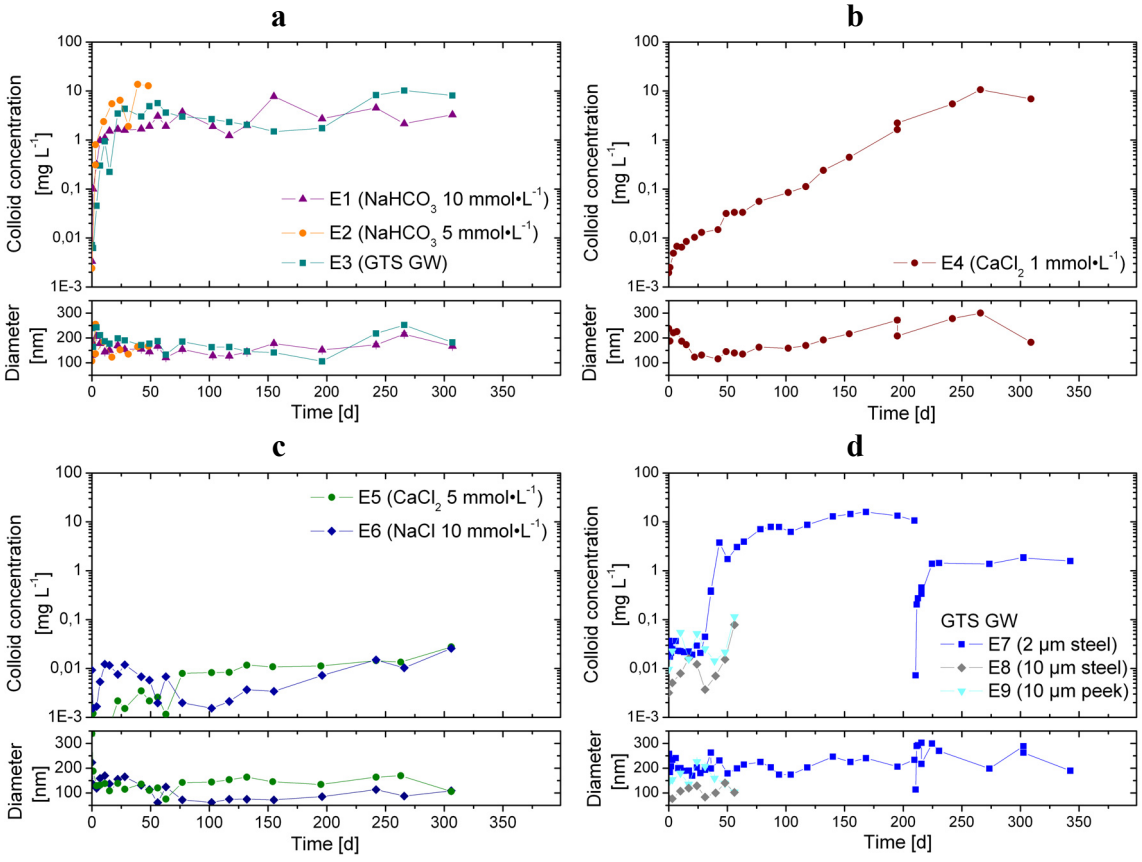

Figure 2: *LIBD colloid concentration and number-weighted average colloid diameter plotted against time. The electrolyte concentrations are given as ionic strength.*

The experiment in contact with a $CaCl_2$ solution of 1 mmol·L^{-1} ionic strength with pH variation ranging from 6.1 to 7.7 (experiment E4; Figure 2b) shows a delayed colloid release with a steady increase in colloid concentration over a period of approx. 250 days reaching uppermost concentration of 10.6 mg·L^{-1} and a plateau value of 5.3 ±

2.7 mg·L^{-1} in the latest measurements. Based on the pH independent CCC for $CaCl_2$ of 1 mmol·L^{-1} (I = 3 mmol·L^{-1} through $I = \frac{1}{2} \cdot c_j z_j^2$) reported in [1] and independently determined for Febex bentonite to be in the same range (data not shown) a mobilization of colloids is expected under these contact water conditions. Interestingly, the average colloid size within 155 days is around 189 ± 52 nm, but in the observation period after 200 days onwards this average colloid size increases to a value of 248 ± 50 nm. Here, the colloid concentration plateau value observed could be explained with a dynamic equilibrium of colloid generation and colloid agglomeration (as indicated by the increasing average colloid size) in the supernatant. Further investigations are in progress to elucidate this hypothesis. For a calcium concentration above the CCC (1.7 mmol·L^{-1} or I = 5 mmol·L^{-1}) no colloid generation can be observed (experiment E5; Figure 2c), which is fully in line with the colloid stability investigations and the determined CCC.
A further test with I = 10 mmol·L^{-1} NaCl was run at pH values ranging from 5.0 to 6.0. This comparison was needed as the CCC in the sodium system is strongly pH dependent [9] and the value of 10 mmol·L^{-1} was determined previously to be the CCC at pH 6. The results of these erosion experiments show clearly that within the observation period the colloid concentration found in solution remains almost constant around 7.3 ± 4.3 µg·L^{-1} with minimum values of 1.5 µg·L^{-1} and maximum values of 25.8 µg·L^{-1} in the latest measurement. The average colloid size was found to be the lowest observed in all experiments with 116 ± 42 nm.

An explanation for the observed lack in colloid generation under these slightly acidic pH conditions is the protonation of bentonite edge charges and therefore attraction to the permanently negative charged clay platelet faces (due to isomorphic substitution in the tetrahedral or octahedral layers) [10]. This colloid attraction responsible for the aggregation from solution also effectively hinders the release of colloids under these pH values, whereas under the same ionic strength at pH 8-9 due to the deprotonation of these edge groups edge charges a repulsive force is expected and also observed in the colloid generation experiments (see experiment E1; Fig. 2a).
The different colloid generation rates observed in this study can qualitatively be explained by the Schultz-Hardy-Rule [8], where lower concentration of divalent cations are needed for colloid coagulation compared to monovalent cations.

The experiments under variation of the filter pore size (experiment E7 and the newly started experiments E8 & E9; Figure 2d) in contact with GTS GW reach a plateau value after ~90 days with colloid concentration plateau values around 9.3 ± 3.4 mg·L^{-1}. This is very comparable to the concentrations of 7.1 ± 4.1 mg·L^{-1} and 2.6 ± 1.1 mg·L^{-1} observed for the experiments with 100µm pore size filter frits. The average colloid size in this experiment with 2µm average pore size filter is 210 ± 24 nm and very comparable to the average colloid size found for the 100µm filter frits of 182 ± 27 nm. A delay in the onset of colloid generation is observed for all three experiments which can be explained by the design of the set-up and the calculated traveling time in the reactor from the surface of the filter plate to the injection hole. The flow velocity at the injection hole of $2.8 \cdot 10^{-2}$ m·min^{-1} drops to $3.3 \cdot 10^{-6}$ m·min^{-1} at the filter plate as calculated by ADINA-F simulations. The higher delay in the onset of in experiments E8 and E9 is due to the lower initial flow velocity chosen. Overall, a pore size dependency on colloid generation or the colloid size mobilized could not be observed in our

experiments, but might be effective if the filter thickness (here 0.16 mm) is increased based on classical filtration theory [11].

To investigate a fully developed gel layer the water in experiment E7 was exchanged after 210 days. An instantaneous increase in colloid concentration can be observed and after 14 days a plateau value is again reached at concentrations of 1.5 ± 0.2 mg·L^{-1}. Furthermore, the mobilized average colloid size is considerably larger with 261 ± 43 nm after contact water exchange. The current interpretation of these observations is a potential depletion of the colloid source with time [12] and further investigations are in progress to gain detailed process understanding.

Summary and Conclusions

A pH and ionic strength dependent colloid generation from a compacted bentonite source was observed. For ionic strength lower than the CCC determined by colloid aggregation studies a colloid generation can be confirmed, whereas in experiments above the CCC bentonite erosion within the observation period of one year is negligible. The experiments furthermore showed that the strong pH dependency of colloid stability found in the sodium system has the same effect on the colloid generation. An effect of the filter pore size (2, 10 & 100µm) on the colloid generation could not be observed, but the effect of filter thickness has to be investigated in new experiments. Detailed post-mortem analysis of the reactors to characterize the bentonite-water contact zone and retrieve informations on the mineralogy, size distribution and exchangeable cation composition will not be finished within the project duration of IP FUNMIG.

References

1. SKB TR-06-09: Long-term safety for KBS-3 repository at Forsmark and Laxmar - a first evaluation, Technical Report TR-06-09 SKB October 2006.
2. Kunze, P., Seher, H., et al. (2008): The influence of colloid formation in a granite groundwater bentonite porewater mixing zone on radionuclide speciation. Journal of Contaminant Hydrology 102(3-4): 263-272.
3. Missana, T., Alonso, U., et al. (2003): Generation and stability of bentonite colloids at the bentonite/granite interface of a deep geological radioactive waste repository. Journal of Contaminant Hydrology 61(1-4): 17-31.
4. Baik, M.-H., Cho, W.-J., et al. (2007): Erosion of bentonite particles at the interface of a compacted bentonite and a fractured granite. Engineering Geology 91(2-4): 229-239.
5. Alonso, U., Missana, T., et al. (2007): Experimental approach to study the bentonite colloid generation source term in different geochemical conditions. 2nd Annual Workshop Proceedings of the Integrated Project "Fundamental Processes of Radionuclide Migration" - 6th EC FP IP FUNMIG. G. Buckau, B. Kienzler, L. Duro and V. Montoya. Stockholm, SKB. TR-07-05: 329-335.

6. Villar, M. V., Martín, P. L., et al. 05/98: FEBEX Bentonite: Origin, properties and fabrication of blocks, publicacion tecnica 05/98 ENRESA (empresa nacional de residuos radiactivos, s.a.)

7. Hauser, W., Geckeis, H., et al. (2002): A mobile laser-induced breakdown detection system and its application for the in situ-monitoring of colloid migration. Colloids and Surfaces A: Physicochemical and Engineering Aspects 203(1-3): 37-45.

8. van Olphen, H. (1977): Clay Colloid Chemistry - For Clay Technologists, Geologists and Soil Scientists, John Wiley & Sons.

9. Seher, H., Schäfer, T., et al. (2007): Febex bentonite colloid stability in ground water. 2nd Annual Workshop Proceedings of the Integrated Project "Fundamental Process of Radionuclide Migration" - 6 th EC FP IP FUNMIG. G. Buckau, B. Kienzler, L. Duro and V. Montoya. Stockholm, SKB. TR-07-05: 397-402.

10. Jasmund, K., Lagaly, G. (1993): Tonminerale und Tone: Struktur, Eigenschaften, Anwendungen und Einsatz in Industrie und Umwelt. Darmstadt, Steinkopff.

11. Yao, K.-M., Habibian, M. T., et al. (1971): Water and waste water filtration. Concepts and applications. Environmental Science & Technology 5(11): 1105-1112.

12. Kretzschmar, R., Borkovec, M., et al. (1999): Mobile subsurface colloids and their role in contaminant transport. Advances in Agronomy, Academic Press. Volume 66: 121-193.

COLLOID ATTACHMENT TO THE GRANITE SURFACE UNDER "UNFAVORABLE" CONDITIONS

Ursula Alonso[1*], Tiziana Missana[1], Miguel García-Gutiérrez[1], Alessandro Patelli[2], Daniele Ceccato[3], Nairoby Albarran[1], Trinidad Lopez-Torrubia[1], Valentino Rigato[3]

[1] CIEMAT, Madrid (E)
[2] CIVEN, Venezia-Marghera (I)
[3] INFN, Laboratori Nazionali di Legnaro, Legnaro-Padova (I)

*Corresponding author: ursula.alonso@ciemat.es

Abstract

An experimental methodology, based on the micro-Particle Induced X-Ray Emission (μPIXE) technique, was developed to quantify colloid surface distribution coefficients (K_a) in the granite surface at mineral scale. The retention of negatively charged Au nanoparticles of different size (2, 40 and 100 nm) was analyzed by static (batch) experiments. The experiments were performed at pH 9.5, where both the colloids and the granite minerals are negatively charged and therefore in conditions "unfavorable" to electrostatic attachment. Non-zero K_a values could be measured for colloid attachment on unfavorable areas, being the attachment mostly related to the existence of minerals with higher porosity or to physical defects of the granite surface. These results support the colloid retention observed under dynamic flow conditions in spite of the expected colloid /rock electrostatic repulsion. The colloid distribution coefficients can be used as input data for the description of colloid-mediated radionuclide transport in fractured media.

Introduction

Colloid transport in granite mainly takes place by advection in conductive fractures. Colloid transport is significantly different to that of a solute, because a fraction of colloids moved unretarded, compared to the water flow. But also, a colloid fraction is retained in the medium, being dependant on the experimental conditions. Colloid retention has been observed under flow conditions, even under the so-called unfavorable case, i.e. where both the whole rock surface and the colloids are negatively charged, so that repulsive forces must dominate (Missana et al., 2008; Schafer et al., 2004). Colloid deposition by gravity or colloid matrix diffusion alone could not either explain the observed retention (Alonso et al., 2007), so the colloid retention mechanisms in the unfavorable case are not yet fully understood.

Colloid deposition and retention on surfaces have been deeply studied, by different approaches, usually with pure materials with well-defined geometry (Chen et

al., 2007; Chen et al., 2001; Song and Elimelech, 1993; Song et al., 1994). Colloid / granite surface interactions were qualitatively analyzed in a former study (Alonso et al., 2004) but no quantitative study is yet available.

The aim of this study is to quantify the colloid retention on the heterogeneous granite surface at the mineral scale. Experiments are performed under static conditions under chemical conditions where repulsive colloid / rock electrostatic interactions are expected. Preferential retention minerals are analyzed by the nuclear ion beam technique μPIXE (micro-Particle Induced X-Ray Emission) (Johansson and Campbell, 1988). A novel analytical methodology to determine colloid distribution coefficients on the main minerals composing the granite is presented. The comparison to the favorable case is included elsewhere (Alonso et al., Submitted).

Materials and Methods

Commercial gold colloid suspensions of 2, 40 and 100 nm (BBInternational) were selected because they are negatively charged, stable at pH 9.5 and because they have similar electrostatic charge as the bentonite clay colloids that can be generated in a repository (Alonso et al., 2007). Main characteristics of the Au colloids are presented in Table 1.

Granite samples coming from the FEBEX experiment located at the Grimsel Test Site (Switzerland) (Huertas et al., 2000). Samples (cm^2) were cut in millimeter-sized slices and polished to minimize surface roughness. The mineral composition (in %) and structural formulas are presented in Table 2.

The granite average porosity is 0.75 %, quartz minerals and feldspars showed a porosity of 0.5 %, while dark minerals (generally micas and Fe-minerals) had higher porosity (> 1.4 %) (Leskinen et al., 2007).

Granite sheets were immersed in 7 ml of the 2, 40 and 100 nm Au colloids during 1 week at pH 9.5, where repulsive colloid-rock interactions are expected (Alonso et al., 2004). After immersion, granite samples were cleaned with ethyl alcohol to eliminate particles deposited on the surface.

Table 1. *Summary of the main characteristics of the "as received" gold colloids.*

Size (nm)	Particles/ml	Concentration (ppm)	Conductivity (μS/cm)	pH
2	$15 \cdot 10^{13}$	12.1 ± 0.2	8.0 ± 0.2	6.19
40	$9 \cdot 10^{10}$	58.2 ± 0.2	8.0 ± 0.2	6.16
100	$5.6 \cdot 10^{9}$	56.6 ± 0.2	9.0 ± 0.2	5.46

Table 2. *Structural formula and occurrence (in %) of the main granite minerals.*

Mineral	%	Formula	Mineral	%	Formula
Quartz	23 %	SiO_2	**Epidote**	5 %	$Ca_2Fe^{3+}Al_2Si_3O_{12}(OH)$
Plagioclase	23 %	$NaAlSi_3O_8$-$CaAlSi_2O_8$	**Sphene**	2 %	$CaTiSiO_4(OH,F)$
Feldspar	20 %	$KAlSi3O_8$	**Zircon**	trace	$ZrSiO_4$
Chlorite	3 %	$(Mg, Fe, Al)_{12}(Si, Al)_8O_{20}(OH)_{16}$	**Allanite**	1 %	$(Ca,Ce)_2(Fe^{2+},Fe^{3+})Al_2O(SiO_4)(Si_2O_7(OH)$
Biotite	14 %	$K(Mg,Fe)_3AlSi_3O_{10}(OH,F)_2$	**Apatite**	trace	$Ca_5(PO_4)_3(OH,F,Cl)$
Muscovite	8 %	$KAl_3Si_3O_{10}(OH,F)_2$	**Ilmenite**	1 %	$FeTiO_3$

Colloid retention experiments on granite: μPIXE measurements

Granite areas (2*2 mm^2) were analyzed by the nuclear ion beam technique micro-Particle Induced X- Ray Emission (μPIXE) (Johansson et al., 1995) at the Laboratori Nazionali di Legnaro (LNL-INFN, Italy). The μPIXE measurements were performed with 2 MeV protons, beam currents of 700 pA - 1 nA and, with a beam size of around 4 μm^2, giving a spatial resolution of 2 μm. Two filters (Mylar filter of 4 μm thickness and Mylar Funny filter of 50 μm with a hole in the centre that allows passing 11% of the total signal) where introduced to enhance the sensibility to heavy elements (as Au). The characteristic X-Ray emitted from the sample are recorded in each point of the studied area, and it is possible to obtain elemental distribution maps. The elements composing the different granite minerals and the Au distribution over the surface can be visualized. Moreover, by the analysis of the individual PIXE spectra obtained on the areas that we select, the quantification of the Au concentration is also possible.

PIXE analyses on specific minerals: Colloid surface distribution coefficients

Several areas were processed with the Mappix code (developed at the LNL, Italy) to obtain the individual PIXE spectra on the main identified minerals: quartz, plagioclase, feldspar, biotite, epidote, chlorite and ilmenite. PIXE spectra were analysed with the GUPIX code (Maxwell et al., 1995). The relative elemental concentrations for both the mineral composition and the Au concentration retained ($Au_{RETAINED}$) can be obtained From the X- Ray peak intensities. Details on the PIXE simulations can be found in (Alonso et al., Submitted). The value considered as $Au_{RETAINED}$ is the average Au concentration measured on the same mineral in at least three different areas. The error considered was the average standard deviation. The Au colloids distribution coefficients (K_a, in m), that represents the degree of colloid retention, can be calculated with the following equation:

$$k_a(m) = \left(\frac{Au_{RETAINED}/Sa}{(Au_{INI} - Au_{RETAINED})/V_{LIQ}} \right) \quad \text{(E.1)}$$

where Au_{INI} is the initial colloid concentration, S_A is the area of the analyzed mineral (in m^2) and V is the volume of colloid suspension (in m^3).

Results

Colloid retention experiments on granite: μPIXE measurements

As example, Figure 1 shows the elemental distribution maps obtained, on two different granite areas (2*2 mm^2) areas with Au colloids of 2 nm (Figure 1A and B), 40 nm (Figure 1C and D) and 100 nm (Figure 3E and F). Two different areas are shown for each colloid diameter, to point out the two main behaviors that were generally observed under the unfavorable case. Minerals identified like quartzes (Q), feldspars (F), epidotes (E), chlorites (C), allanites (A) and ilmenites (I) are indicated.

First of all, in all studied areas, Au colloid retention is observed on the granite surface despite the expected repulsion.

A clear relationship between Au presence and specific minerals was not observed, contrary to that observed under the favourable case, where attractive electrostatic interaction dominates (Alonso et al., Submitted).

Colloids were sometimes retained on Ca or Fe bearing minerals (Figures 1A, 1C and 1E). This relation can be explained local aggregation of colloids caused by the presence of bivalent ions like Ca. But also, Fe or Ca minerals have higher porosity (higher than 1.4 %) compared to 0.5 % or less showed by other minerals (Leskinen et al., 2007).

Sometimes, Au accumulation was observed in specific regions, not fully covering a mineral, suggesting that retention on those areas is not driven by the chemistry of the mineral surface, but must be caused by local physical and chemical inhomogeneities (roughness, defects, grain boundaries or small scale chemical heterogeneities). For example, Figure 1D shows that Au is retained in micro-fissures present in the quartz grain (clearly appreciated in the Si map). In addition, very high colloid retention is sometimes seen locally (Figure 1B and 1F), possibly caused by ripening effects: colloids are first retained on the surface additionally producing inhomogenities that increase the sedimentation rate of other particles (Camesano et al., 1999).

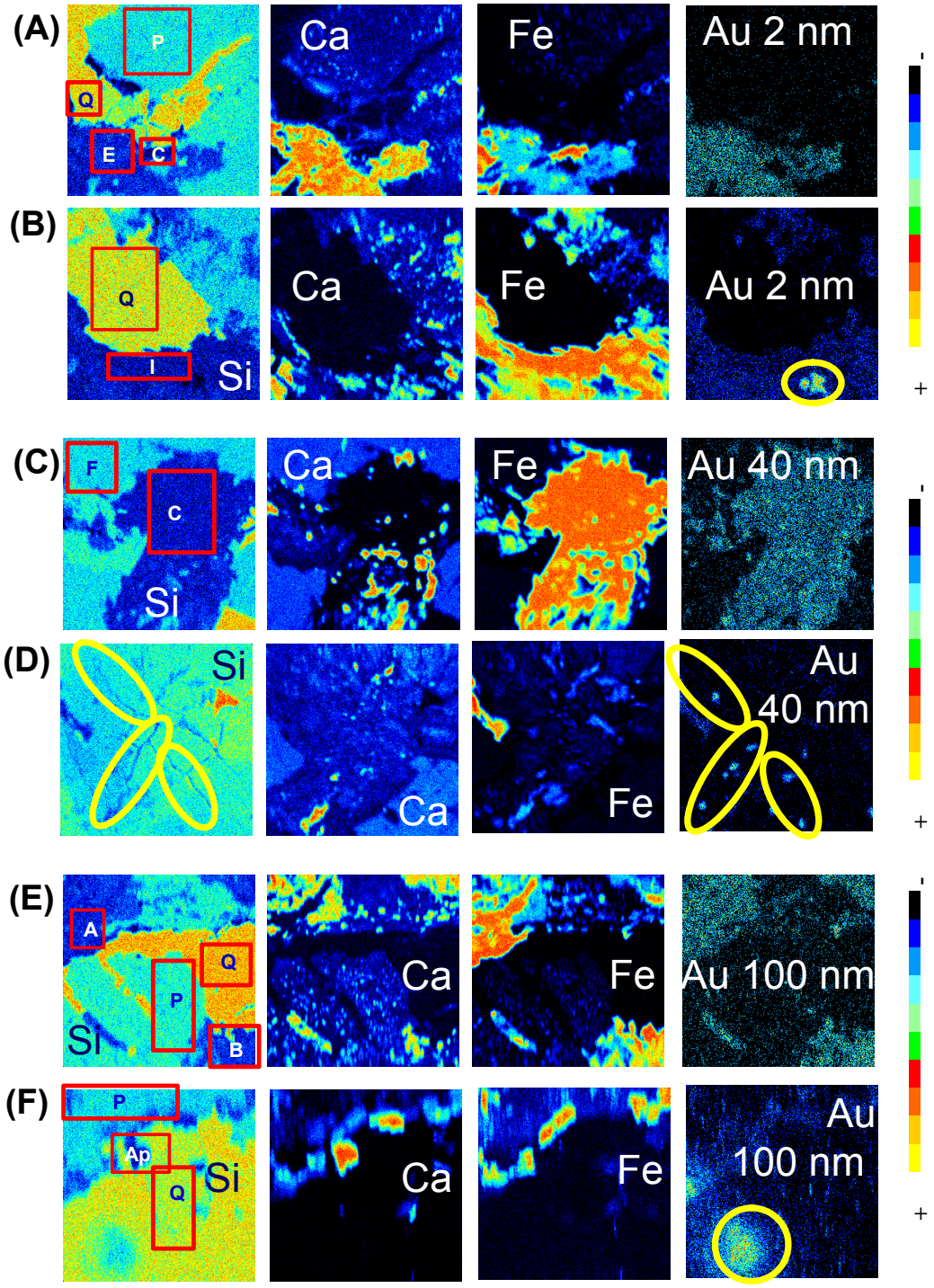

Figure 1. *Elemental distribution maps (Si, Ca, Fe, and Au) obtained by μPIXE on two 2*2 mm^2 granite areas with Au colloids of 2 nm (Areas A and B), 40 nm (Areas C and D) and 100 nm (Areas E and F). Red squares in the Si maps refer to the areas selected for quantitative analyses: (Q) quartz, (P) plagioclase, (E) epidote, (C) chlorite and (I) ilmenite. The ovals in the Si and Au maps show, areas not related to specific mineral where Au is retained (for example in quartz micro – fissures (D)).*

PIXE analyses on specific minerals: Colloid surface distribution coefficients

Table 3 presents the colloid surface distribution coefficients (K_a), obtained on the main minerals identified (marked squares marked in Si maps in Figure 1) and determined with E.1, for each colloid size.

The average distribution coefficients are rather scattered and not dependent on the mineral charge or on the colloid size. This suggests that retention in the unfavorable case is very dependent on the local physical and chemical heterogeneities. The K_a values measured can be as high as those observed in the favorable case (Alonso et al., Submitted). It is important to remark that areas with some dark mineral inside are usually studied, for better identification, so that the analysis is probably minimizing the effect of the areas of null retention. With the K_a values obtained on the individual minerals (Table 3) the average distribution coefficients on the granite surface can be calculated, accounting for the mineral occurrence within this granite (Table 2). The estimated average surface distribution coefficients for each diameter, under unfavorable conditions, are respectively: $K_{average}$ (2 nm) = $(1.1 \pm 0.2)\cdot10^{-3}$ m; $K_{average}$ (40 nm) = $(7.7 \pm 0.6)\cdot10^{-4}$ m; $K_{average}$ (100 nm) = $(7.6 \pm 0.7)\cdot10^{-4}$ m.

These no-null K_a values support the colloid retention observed under dynamic flow conditions in spite of the expected colloid /rock electrostatic repulsion (Missana et al., 2008; Schafer et al., 2004): This indicate that the different mechanisms that lead to colloid retention in fractured media have to be accounted for an appropriate description of colloid-mediated radionuclide transport in fractured media in a repository case. The colloid distribution coefficients obtained here can be used as input data for the description of colloid-mediated radionuclide transport in fractured media.

Table 3. *Distribution coefficients (K_a in m) measured on the main granite minerals for different size colloids 2 nm, 40 nm and 100 nm at pH 9.5.*

Mineral	K_a (2 nm)	K_a (40 nm)	K_a (100 nm)
Quartz	$(4.9 \pm 0.8)\cdot10^{-4}$	$(2.2 \pm 0.5)\cdot10^{-5}$	$(1.1 \pm 0.6)\cdot10^{-4}$
Plagioclase	$(1.9 \pm 0.3)\cdot10^{-3}$	$(2.7 \pm 0.7)\cdot10^{-5}$	$(2.6 \pm 0.2)\cdot10^{-4}$
k-Feldspar	$(8.2 \pm 0.6)\cdot10^{-4}$	$(2.1 \pm 0.5)\cdot10^{-5}$	$(9.0 \pm 0.2)\cdot10^{-4}$
Fe-biotite	$(1.1\pm 0.6)\cdot10^{-3}$	$(4.5 \pm 0.5)\cdot10^{-3}$	$(2.8 \pm 0.2)\cdot10^{-3}$
Fe- Epidote	$(5.9 \pm 0.5)\cdot10^{-3}$	$(3.9 \pm 0.4)\cdot10^{-4}$	$(1.6 \pm 0.2)\cdot10^{-4}$
Fe- Chlorite	$(3.9 \pm 0.2)\cdot10^{-3}$	$(5.1 \pm 0.5)\cdot10^{-4}$	$(1.6 \pm 0.2)\cdot10^{-3}$
Ilmenite	$(3.0 \pm 0.2)\cdot10^{-3}$	$(8.9 \pm 0.5)\cdot10^{-4}$	$(4.8 \pm 0.3)\cdot10^{-3}$

Summary and Conclusions

The methodology applied here, by the application of the μPIXE nuclear ion beam technique, allowed both visualizing and quantifying colloid retention on the granite surface under unfavorable cases, in terms of electrostatic interactions. Surface colloid retention distribution coefficients (K_a) were experimentally determined in a heterogeneous rock surface with Au nanoparticles. The methodology is sensitive enough to measure differences at mineral scale. Non-zero Ka values were measured, with no clear size dependence. In the unfavorable case, colloid retention is strongly dependent upon the nature of the local areas coming into contact. Small scale chemical

effects, roughness or non-uniform distribution of charge sites are playing a major role. In the favorable case these effects probably occur as well, but at less extent since fast filling of the favorable attractive areas, leads to a decrease in deposition rates on low coverage areas. No previous quantitative data of colloid retention on granite surface was available.

Acknowledgments

This work was supported by the EU within the FUNMIG project (Ref: FP6-516514), and the EURONS- EUROpean Nuclear Structure research Action (FP6-506065).

References

Alonso U, Missana T, Patelli A, Ceccato D, García-Gutiérrez M, Albarran N, Lopez-Torrubia T, Rigato V. (Submitted). Quantification of Au nanoparticles retention on a heterogeneous rock surface.: Colloids and Surfaces A: Physicochemical and Engineering Aspects.

Alonso U, Missana T, Patelli A, Ravagnan J, Rigato V. (2004) Experimental study of colloid interactions with rock surfaces. in Scientific Basis For Nuclear Waste Management XXVIII: MRS Symposium Procedures 824, 621-626. MRS, Warrandale, Pennsylvania, USA.

Alonso U, Missana T, Patelli A, Rigato V, Ravagnan J (2007) Colloid diffusion in crystalline rock: an experimental methodology to measure diffusion coefficients and evaluate colloid-size dependence.: Earth and Planetary Science Letters, v. 259, p. 372-383.

Camesano T.A, Unice K.M, Logan B.L, (1999) Blocking and ripening of colloids in porous media and their implications in bacterial transport.: Colloids and Surfaces A, v. 160, p. 291-308.

Chen G, Abichou T, Tawfiq K, Subranamian P.K, (2007) Impact of surface charge density on colloid deposition in unsaturated porous media: Colloids and Surfaces A: Physicochem. Eng. Aspects, v. 302, p. 342-348.

Chen J.Y, Ko C.-H, Bhattacharjee S. Elimelech M. (2001) Role of spatial distribution of porous medium surface charge heterogeneity in colloid transport: Colloids and Surfaces A: Physicochem. Eng. Aspects, v. 191, p. 3-15.

Huertas F, Fuentes-Santillana J.L, Jullien F, Rivas P, Linares J, Fariña P, Ghoreychi M, Jockwer N, Kickmaier W, Martínez M.A, Samper J, Alonso E, Elorza F.J, (2000) Full scale engineered barriers experiment for a deep geological repository for high-level radioactive waste in crystalline host rock., EC Final REPORT EUR 19147.

Johansson, S.A, Campbell J.L.E, Malmqvist K.G.E. (1995) Particle Induced X-Ray Emission Spectrometry (PIXE) Chemical Analysis, a series of monographs on analytical chemistry and its applications, v. 13, John Wiley& Sons, Ltd.

Johansson S.A.E., Campbell J.L.E. (1988) PIXE, a novel technique for elemental analysis, John Wiley& Sons, Ltd.

Kosakowsky G, (2004) Anomalous transport of colloids and solutes in a shear zone: Journal of Contaminant Hydrology, v. 72, p. 23-46.

Leskinen A., Penttinen L, Siitari-Kauppi M, Alonso U, García-Gutiérrez M, Missana T, Patelli A, (2007) Determination of granites' mineral specific porosities by PMMA method and FESEM/EDAX. In Scientific Basis for Nuclear Waste Management XXX, edited by D.S. Dunn, C. Poinssot, B. Beg. Mater. Res. Soc. Symp. Proc. 985, 0985-NN11-20,Warrendale, PA., USA.

Maxwell, J.A, Teesdale W, Campbell, J.L (1995) The GUPIX PIXE software package II: Nuclear Instruments and Methods in Physics Research B, v. 95, p. 407.

Missana T, Alonso U, García-Gutiérrez M, Mingarro M, (2008) Role of bentonite colloids on europium and plutonium migration in a granite fracture: Applied Geochemistry, v. 23, p. 1484-1497.

Schäfer T, Geckeis H, Bouby M, Fanghänel T, (2004) U, Th, Eu and colloid mobility in a granite fracture under near-natural flow conditions.: Radiochimica Acta, v. 92.

Song L, Elimelech M, (1993) Calculation of particle deposition rate under unfavourable particle - surface interactions: J. Chem. Soc. Faraday Trans, v. 89, p. 3443-3452.

Song L., Johnson P.R, Elimelech M, (1994) Kinetics of colloid deposition onto heterogeneously charged surfaces in porous media: Environmental Science and Technology, v. 28, p. 1164-1171.

COMPARISON OF MOLECULAR DYNAMICS SIMULATIONS WITH TRIPLE LAYER AND MODIFIED GOUY-CHAPMAN MODELS IN A DILUTE NaCl - MONTMORILLONITE SYSTEM.

Christophe Tournassat[1*], Yves Chapron[2], Philippe Leroy[1], Mohamed Bizi[1], Faïza Boulahya[1]

[1] BRGM, French Geological Survey, Orléans, France
[2] AIED, La Terrasse, France

* Corresponding author: c.tournassat@brgm.fr

Abstract

Molecular dynamics (M.D.) simulations of a montmorillonite water interface at the pore scale have been carrying out at low NaCl concentration in order to constrain cation, anion and water repartition and mobility as influenced by the mineral surface. M.D. results enabled to quantify anion exclusion and cation condensation at the surface. M.D. derived values could then be compared with macroscopic model results obtained from modified Gouy Chapman (MGC) theory. While Na concentration profile is well reproduced in the diffuse layer, anion exclusion seems to be overestimated by the MGC theory in our experimental conditions. We also showed that M.D. simulations in combination with zeta potential measurements can be used to constrained triple layer model (TLM) parameters by providing suitable values for the position of the β and d-planes. Capacitance values for clay basal surfaces are given accordingly.

Introduction

In the present study, we investigate the clay surfaces / water / solute interactions by means of molecular dynamics (M.D.) calculations in order to give an exact representation of the water, cations and anions concentration profiles in a solution influenced by a smectite surface at solute concentrations representative of the clayey media.

Up-scaling from M.D. simulations to macroscopic clay domains is then ensured by comparing the M.D. simulations results with well known macroscopic electrostatic modeling approach (MGC and TLM).

List of abbreviations

μ_e electrophoretic mobility
ζ zeta potentials

ε_0 permittivity of vacuum
ε dielectric constant, or permittivity of water
D relative permittivity of the media
η viscosity of water charge
σ surface charge
$\psi(x)$ electrostatic potential
F faraday constant
R gas constant
T temperature
N_A Avogadro number
a distance of closest approach of the considered ion to the surface
κ inverse of the Debye length
Z_i charge of ion i
c_{i0} concentration at "infinite" distance from the surface
a_i activity of ion i
ψ_β mean electric potential at the β-plane
Q_0 surface charge density of the 0 plane
Q_β surface charge density of the β plane
Q_d surface charge density in the diffuse layer
ψ_0 electrostatic potentials at the 0 plane
ψ_d electrostatic potentials at the d plane
C_1 constant capacitance of the inner part of the Stern layer
C_2 constant capacitance of the outer part of the Stern layer
ε_1 relative permittivity of the inner part of the Stern layer
ε_2 relative permittivity of the outer part of the Stern layer
D_s diffusion coefficients parallel to the surface
D_{0w} bulk water diffusion coefficients
$\varphi(x)$ cation condensation function at the interface
d_{ex} anion exclusion distance
V_{ex} anion exclusion volume
S_0 total specific surface area of single platelet of montmorillonite
S external part of the specific surface area
f fraction of single-layer platelets that form n-layer quasicrystals in a suspension
d_Q separation between single-layer platelets in a quasicrystal
n_{AV} average number of unit-layer platelet in the suspension
ε_z relative dielectric constants at zero field
ε_s relative dielectric constants at saturation ($\varepsilon_s = 6$)

Material and methods

Geometry of the M.D. system

A periodical 3D system was considered with two smectite layers inserted between two water boxes (Figure 1). The clay structure was built based on a mica structure (Pavese et al., 1997). Octahedral charge of the clay was ensured by random substitutions of Al^{3+} by Mg^{2+} using an exclusion rule so that two substitutions could not occur on two adjacent sites. The interlayer water structure was a two water layer

structure in agreement with XRD results on water saturated compacted Na-smectite at montmorillonite partial dry density in-between 1.6 and 1.8 kg/dm^3 (Kozaki et al., 1998). An interlayer water specific mass of ~0.24 kg_{water}/kg_{clay} (Chavez-Paez et al., 2001; Tambach et al., 2004) was considered together with a d-spacing of 15.7 Å in agreement with XRD measurements. The periodic conditions of the systems were: $a = b = 52.138$ Å with $\alpha = 120°$, $c = 169.5$ Å for a total of ~40 000 atoms of which ~ 11 500 water molecules (~34 500 atoms). The Mg for Al substitutions (32/200 for one layer and 36/200 for the other) result in a layer charge of ~ -0.9 $mol_c\ kg^{-1}$ (-0.722 protonic charge per nm^2) representative of a montmorillonite. Charge deficits were equilibrated by adding Na^+ surface cations. Half of the total charge is compensated by cations in the interlayer. The other half was randomly put at a distance of 3.2 ± 1 Å of the most external oxygen atoms of the structure. In the following the term "charge deficit of the clay structure" will refer to the charge deficit that is not compensated by interlayer cations. In addition, 10 Na^+ and 10 Cl^- ions were inserted in both upper and lower water boxes leading to a total concentration (and ionic strength) of ~0.10 mol L^{-1}, corresponding to a lowest concentration limit for statistical analysis of anion repartition profiles from molecular dynamics results (with regards to the computer capabilities devoted to the project) and (ii) to a ionic strength representative of natural conditions in clayey media (e.g. Vinsot et al., In Press).

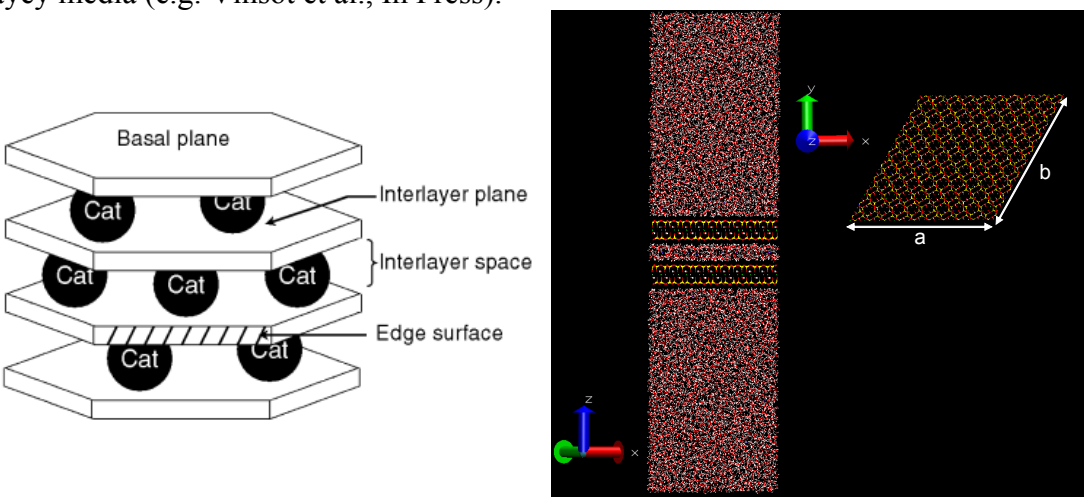

Figure 1. *Left, cartoon of stacked phyllosilicate layers. Cat = exchangeable cation. Right, geometry of the M.D. modeled system*

Clay and water force fields.

In the proposed simulations, CLAYFF force field (Cygan et al., 2004) describes external and internal clay mineral surface / water + ions interactions together with the modified SPC water model proposed by Cygan et al. for flexible water molecules. Additional simulations using SPCE force field charge parameters for water (Berendsen et al., 1987) were run in order to better scale the diffusion coefficients of solute species (models using SPC force field overestimate water self diffusion coefficient). Although CLAYFF enables the modeling of flexible clay network, we considered a rigid clay network for data post-processing simplicity reasons. The atoms in the clay structure (Si, Al, Mg, O and H atoms) were fixed but cations and water in the interlayer and on external surfaces were allowed to move.

Numerical methods.

Initial structure and coordinate files were prepared using XPLOR-NIH (Schwieters et al., 2006; Schwieters et al., 2003). NAMD (Kale et al., 1999) was used to perform molecular dynamics simulations in the NVT ensemble (constant number of particles, volume and temperature). All calculations were performed at 298 K and zero applied pressure. The coulombic interactions were calculated using the particle mesh Ewald sum. An equilibration period of 1 ns was applied to the systems before the first data were interpreted on a 5 ns period.

Post-processing of M.D. results.

Trajectories of atoms were sampled each 0.1 ps. Wordom (Seeber et al., 2007) was used to extract coordinate files as a function of time. Mean concentration profiles of H_2O (the oxygen atom position taken as the center of mass of the molecule), Na and Cl were calculated from coordinate files (with 0.5 Å and 0.01 Å resolutions) together with radial distribution function of water around Na and Cl as a function of clay surface distance. Diffusion coefficient parallel to the *ab* plane were calculated with the approach developed by Liu et al. for confined fluids and interface (Liu et al., 2004).

Zeta potential measurements on natural montmorillonite particles

Zeta potential measurements were performed on <2µm fraction of MX-80 bentonite. The whole extraction procedure is reported in Gailhanou et al., 2007. The same material was used. CEC of MX80 material has been determined by cation extraction using the cobalthexamine method (modified after Rémy and Orsini, 1976) and led to a value of 0.65 ± 0.04 mol_c/kg. Taking into account the impurities content (~23%, Gailhanou et al., 2007), the cation exchange capacity of the clay fraction is 0.84 $mol_c\ kg^{-1}$, corresponding to a surface charge of approximately -0.67 proton charge per nm^2.

Electrophoretic mobility (μ_e) measurements were performed on a ZetaSizer IV (Malvern Instrument Ltd) in optical configuration. Zeta potentials (ζ in V) were calculated using the Smoluchowski approximation:

$$\xi = \mu_e \cdot \frac{\eta}{\varepsilon}$$ Equation 1

where ε is the dielectric constant, or permittivity of water (in $C^2\ J^{-1}\ m^{-1}$) and ηis the viscosity of water (in Pa s);

Analyzed clay suspensions were prepared at a solid to water content of 0.1 $g.L^{-1}$ in Milli-Q water. Each suspension has been homogenised and dispersed by mechanical stirring and further ultrasonic treatment (2 minutes at 40 kHz). Ionic strength was then increased before measurements by adding analytical grade NaCl salts for a final concentration of 0.12 mol l^{-1}.

Na sorption and diffuse ion swarm modeling

MGC theory

The modified Gouy-Chapman theory enables a quantitative description of the anions and cations concentration profiles in the vicinity of an uniformly charged (with charge σ in protonic charge/m^2) and smooth surface and assuming that (i) the water is an uniform continuum characterized by its dielectric permittivity ($\varepsilon_0 \times D$ where ε_0 is the permittivity of vacuum, 8.85419×10^{-12} C V^{-1} m^{-1}, and D is the relative permittivity of the media) and (ii) that the potential of the mean force is proportional to $\psi(x)$, the mean electrostatic potential, at a distance x perpendicularly to the surface (Sposito, 2004).

In these conditions, Na^+ and Cl^- concentration profiles (c_i with i = Na^+ or Cl^-) in the system described on Figure 1 can be calculated according to the following equations system:

$$\frac{F\psi(x)}{RT} = 4 \times \operatorname{arctanh}\left[\tanh\left(\frac{F\psi(a)}{4RT} \right) \times \exp\left(-\kappa(x-a)\right) \right] \qquad \text{Equation 2}$$

$$c_i(x) = c_{i0} \times \exp\left(-Z_i \times \frac{F\psi(x)}{RT} \right) \qquad \text{Equation 3}$$

$$\kappa = \sqrt{\frac{2F^2 1000 c_{i0}}{\varepsilon_0 DRT}} \qquad \text{Equation 4}$$

$$\frac{F\psi(a)}{RT} = -2 \times \operatorname{arcsinh}\left(\frac{F^2|\sigma|}{2 \times \kappa\varepsilon_0 DRT \times N_A} \right) \qquad \text{Equation 5}$$

Where F is the faraday constant (96485 C mol^{-1}), R the gas constant (8.314 J mol^{-1} K^{-1}), T the temperature (K), N_A the Avogadro number ($6.022\ 10^{23}$ mol^{-1}), a the distance of closest approach of the considered ion to the surface (m), κ the inverse of the Debye length (m^{-1}), Z_i the charge of ion i (in our case +1/-1) and c_{i0} the concentration at "infinite" distance from the surface (in mol dm^{-3}).

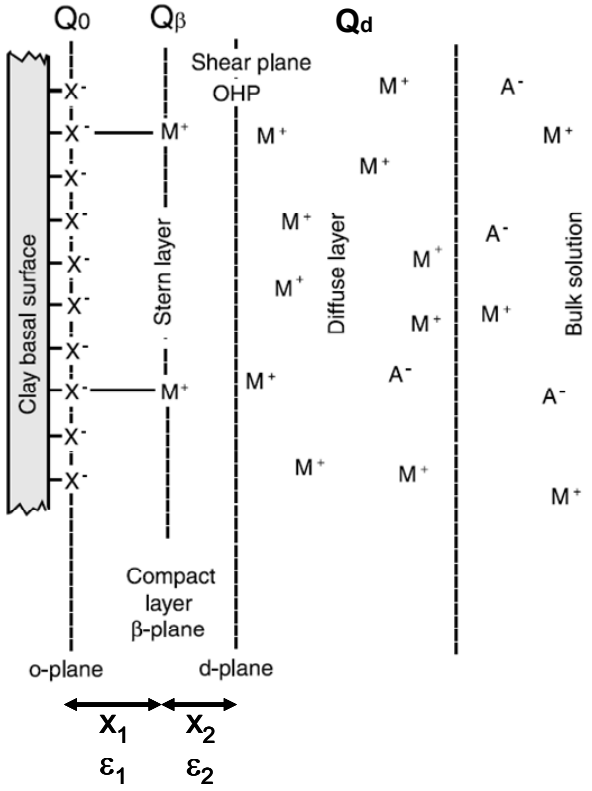

Figure 2. *Sketch of the electrical triple layer model at the clay basal surface in the case of a binary monovalent electrolyte, M represents the metal cations (e.g., Na^+) and A^- the anions (e.g., Cl^-). OHP represents the Outer Helmholtz Plane (d-plane), which coincides here with the shear plane along which the zeta potential is defined. The β-plane corresponds to the mean plane of the Stern layer while the 0-plane corresponds to the surface of the basal plane. x_1: distance from 0-plane to β-plane. In this space the dielectric permittivity ε_1 applies. x_2: distance from β-plane to d-plane. In this space the dielectric permittivity ε_2 applies. Modified after Leroy et al., 2007.*

TLM theory

The TLM used for describing the system shown on Figure 1 is very similar to that depicted in Leroy et al., 2007. As an approximation, the charged clay surface is supposed to be counterbalanced only by cations in the compact layer (β-plane, see Figure 2) and in the diffuse layer together with anion exclusion from the stern layer (complete exclusion) and the diffuse layer (anion concentration decrease as a function of the d-plane vicinity). No cation complexation in the 0 plane is considered. Cations compensating the deficit of charge in the Stern layer undergo the reaction:

$$X^{-}\cdots Na^{+} \underset{K_N}{\Leftrightarrow} X^{-} + Na^{+} \qquad \textit{Reaction 1}$$

where X^- represents a charged site at the clay surface and K_{Na} is the equilibrium constant (mol dm^{-3}) according to (Sposito, 2004):

$$K_{Na} = \frac{c_X a_{Na\,0}}{c_{X\,Na}} \exp\left(-\frac{F\psi_\beta}{RT}\right) = \left(\left|\frac{Q_0}{Q_\beta}\right| - 1\right) a_{Na\,0} \exp\left(-\frac{F\psi_\beta}{RT}\right) \quad \text{Equation 6}$$

Where a_i denotes activity (calculated using the Davies equation), ψ_β is the mean electric potential at the β-plane (V), and Q_0 and Q_β are the surface charge densities of the 0 and β planes respectively (C m^{-2}).

In these conditions, the following equations and parameters describe the system:

$$Q_0 = \frac{F\sigma}{N_A} \quad \text{Equation 7}$$

$$Q_d = -2\sqrt{2\varepsilon_0 DRTc_{i0}} \times \sinh\left(\frac{F\psi_d}{2RT}\right) \quad \text{Equation 8}$$

$$Q_\beta = -Q_0 - Q_d \quad \text{Equation 9}$$

$$\psi_\beta = \psi_d - \frac{Q_d}{C_2} \quad \text{Equation 10}$$

$$\psi_0 = \frac{Q_0}{C_1} + \psi_\beta \quad \text{Equation 11}$$

Where Q_d is the surface charge density in the diffuse layer (C m^{-2}), and ψ_0 and ψ_d are the electrostatic potentials at the 0 and d planes respectively (V). The parameters C_1 and C_2 represent the constant capacitances of the inner and outer part of the Stern layer (in F m^{-2}).

The diffuse layer composition can be calculated as a function of x, the distance from the d-plane, by setting $a = 0$ and by replacing $\psi(a)$ by ψ_d in equations 1 to 4.

Results and discussion

Molecular dynamics results

Figure 3 shows that there is very little influence of water force field (SPC or SPCE) on the M.D results for water density and Na^+ concentration profiles. For Cl^- profile, the scatter of the data (due to the low Cl^- concentration, 0.1 mol L^{-1} and consecutive bad statistic) seems to indicate that this difference could be due also to an insufficient time of simulation. For the following analysis, we decided to merge SPC and SPCE results in order to smooth this effect.

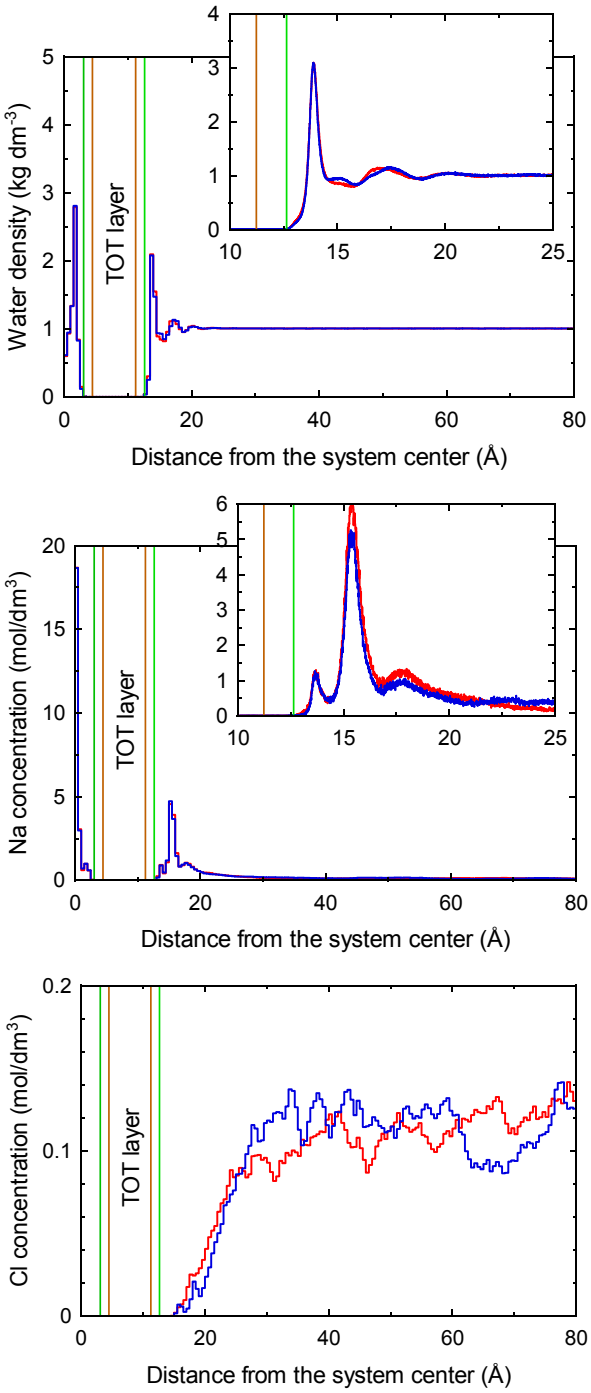

Figure 3 *Water (top), Na (middle) and Cl (bottom) concentration profiles as a function of the distance from the clay surface. Red line: results obtained with SPC water force field. Blue line: results obtained with SPCE water force field. Brown lines: coordinates of the more external oxygen atom of the structure. Green lines: coordinate of the more external oxygen atom + ionic radius of oxygen (taken at 1.4 Å). The center of the system corresponds to the middle of the interlayer showed on Figure 1. The resolution is 0.5 Å for large figures (mean of 5 ns trajectory) and 0.01 for inserts (mean of 1 ns trajectory).*

The water density profile was computed based on the position of the oxygen

atom of the water molecule. Water was found to be strongly structured in the first 5 Å from the clay surface, showing density oscillations up to a distance of 10 Å. The water maximum density depends on the spatial analysis resolution. At a 0.5 Å resolution, the first sorbed layer of water has a maximum density of about 2.0 kg dm^{-3}, a value below that observed in the interlayer space (~2.8 kg dm^{-3}). At finer resolution (0.01 Å), this difference in maximum density almost vanished with values of 3.1 and 3.4 kg dm^{-3} for first sorbed layer of water and interlayer water respectively. This water maximum density is comparable to the one calculated by M.D. on other clay mineral surfaces like muscovite or talc (Wang et al., 2006). The maximum density peak position is at ~2.65Å from the coordinate of most external oxygen atoms of the clay structure and corresponds therefore to the distance of one oxygen ion radius (r_O=1.4 Å) plus one radius of water molecule (r_{H2O}~1.25 Å). In the following the clay surface will refer to the coordinate of most external oxygen atoms plus the distance of one oxygen ion radius (with this "convention", the water density peak is located at ~1.25 Å from the clay surface). The mean water density in the structured water can be calculated with the density profile and is equal to the bulk water density when integrating the two first oscillations from the clay surface coordinate (density difference less than 2%).

The sodium concentration profile shows a "plane" of adsorbed sodium near of the surface and then the presence of a diffuse layer. The "plane" of sorbed Na is located at 2.8 Å from the surface with a start of the concentration peak at 1.8-1.9 Å in agreement with the distance of closest approach of Na^+ usually considered in MGC model (3.74/2 = 1.87 Å). In the sorption plane, Na is mostly present as outer-sphere complexes and keeps its 5-6 coordination waters as shown by radial distribution function of water around Na cations (Figure 4). A very minor part of Na (~6% of the surface charge) is engaged in sorption sites where Na hydration shell has lost up to 3 water molecules.

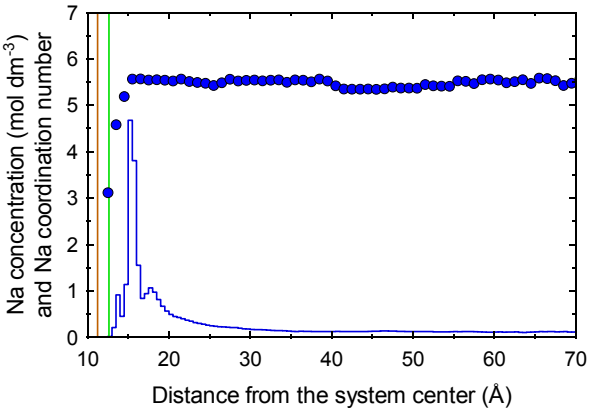

Figure 4. *Na concentration (blue line) and coordination profiles (blue circles, number of water molecules in first hydration shell taken at 3.2 Å from the Na atoms) as a function of distance from the centre of the system (mean of 5 ns SPC + 5 ns SPCE trajectories). Brown line: coordinates of the most external oxygen atom of the structure. Green line: coordinate of the more external oxygen atom + ionic radius of oxygen (taken at 1.4 Å). The center of the system corresponds to the middle of the interlayer showed on Figure 1. The resolution is 0.5 Å for Na concentration and 1 Å for the Na coordination.*

The result of the simulation shows a decreasing Cl concentration as Cl approaches the clay surface (Figure 3). Due to anion repulsion from the clay surface, the Cl concentration increased by 0.02 mol/L in the water far from the surface (~0.12 mol/L) as compared to the original "global" Cl concentration (0.1 mol/L). The closest distance of Cl approach is very near the clay surface and ends roughly when the "plane" of sorbed Na is met. Cl concentration becomes equal to Na concentration at about 25 Å from the clay surface (this length is slightly inferior to the size of the diffuse layer ≈ $2\kappa^{-1}$ ≈ 22 Å for c_{Na0} = 0.12 mol L^{-1}; see Equation 4).

Ions and water diffusion coefficients have been computed using the methods of Liu et al., 2004, applied to six distinct zones parallel to the clay surface: I: interlayer, II: Na inner-sphere and first peak of water density, III: main peak of sodium concentration, IV: second oscillation of water density and start of the diffuse layer, V: end of the diffuse layer and VI: bulk. These zones can be seen on Figure 5. Only diffusion coefficients parallel to the surface (D_s) have been computed. Calculated bulk water diffusion coefficients (D_{0w}) are 2.8 and 4.3 10^{-9} m^2 s^{-1} for SPCE and SPC force field respectively. While the SPC derived diffusion coefficient is in full agreement with the value reported in the literature (Berendsen et al., 1987), SPCE simulations led to larger value than usually reported (2.5 10^{-9} m^2 s^{-1}). Diffusion coefficients were scaled to the value obtained in the bulk water (D_{si}/D_{0i} where i = water, Na or Cl) for further comparisons. Once scaled, the changes in diffusion coefficient as a function of the clay surface distance remains similar whatever the force field (Table 2), showing a decrease of water and sodium mobility as they approach the surface in agreement with previously reported M.D. results (Marry et al., 2008). Note that Lockhart (Lockhart, 1980) considered in the Stern layer of a montmorillonite gel a minimum D_{sNa}/D_{0Na} value of 1/3 using the Stokes-Einstein relationship and considering the ration of fluid viscosities in the Stern and diffuse layers. The knowing of the diffusivities of the species in the "compact" layer is of paramount importance in the study of electrokinetic phenomena like electro-osmosis for example (Coelho et al., 1996), or the surface conductivity of the particles (Leroy and Revil, 2004).

Table 2. *Scaled diffusion coefficients as a function of (i) considered the force field and (ii) distance from the clay surface.*

	D_s/D_0 (10^{-9} m^2 s^{-1})					
	SPC			SPCE		
Zones	H_2O	Na^+	Cl^-	H_2O	Na^+	Cl^-
I	0.24	0.21		0.24	0.19	
II	0.34	0.05		0.36	0.16	
III	0.31	0.46		0.36	0.52	
IV	0.83	0.86	1.1	0.85	0.83	0.99
V	0.98	0.96	1.1	0.97	0.91	0.90
VI	1	1	1	1.00	1.00	1.00

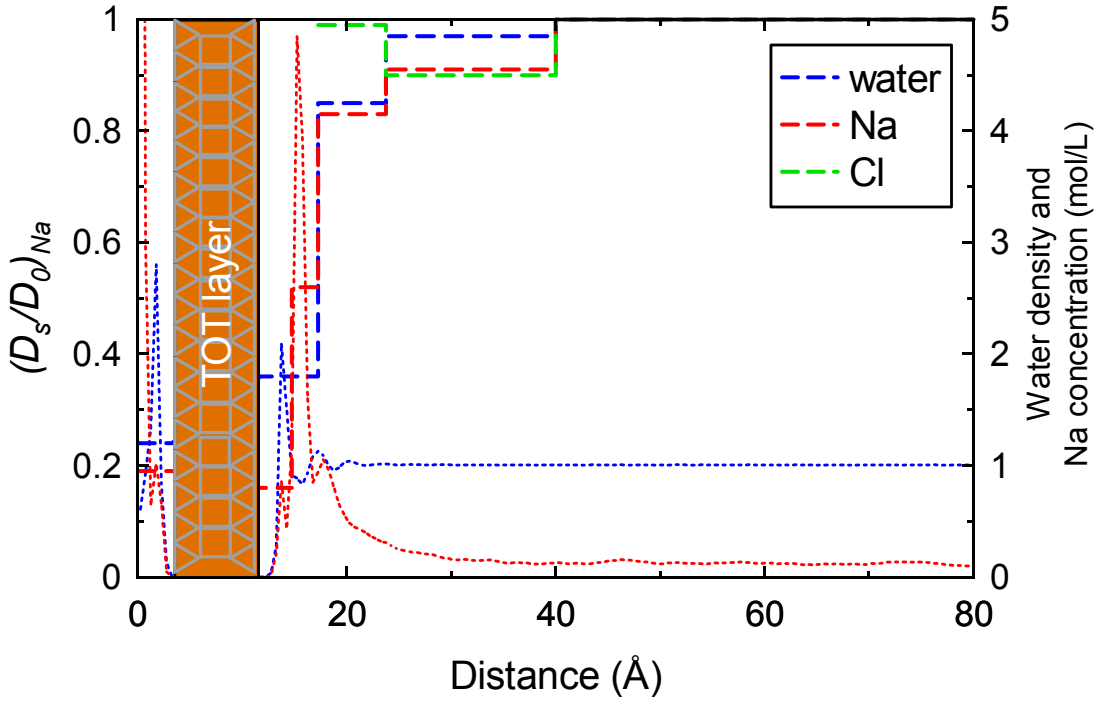

Figure 5. *Comparison of $D_s(x)/D_0$ of water, Na and Cl as a function of their distance from the surface of the clay (SPCE simulations). In dotted lines: water density and Na concentration.*

Comparison of M.D. results with MGC and TL models

For simplicity reasons, in the following the abscissa *x=0* (or clay surface) corresponds to the position at one oxygen ion radius from the clay most external oxygen atoms.

Anion exclusion and cation condensation

Figure 6 shows the Na and Cl concentration profile obtained from Equation 2 to Equation 5 and their comparisons with profiles obtained from M.D. calculations (mean of simulation performed with SPC and SPCE force fields). A 0.116 mol L^{-1} NaCl background concentration was chosen according to the mean concentration of Na and Cl on the last 20 Å of the M.D. profiles (0.116 and 0.116 mol L^{-1} respectively). The surface charge was taken equal to those exhibited by the clay surface in the M.D. simulation (-0.722 C m^{-2}). Distance of closest approach for Cl^- and Na^+ of 1.81 and 1.87 Å (Sposito, 2004) were considered.

There is an overall good agreement between the MGC model predictions and our M.D. results. Especially one notes the good agreement of sodium concentration profiles in the diffuse swarm for $x > 5$ Å. As expected, the MGC model is not able to reproduce exactly the position of the Na condensation zone. Cation condensation at the interface can be quantified by the following $\varphi(x)$ function (Sposito, 2004):

$$\varphi(x) = \frac{F}{|\sigma|}\int_{\frac{d_0}{2}}^{x}\left(c_{Na}(s) - c_0\right)ds$$ Equation 12

where $d_0/2$ is the distance of minimum approach of Na and $c_{Na}(s)$ represents the concentration of sodium near the surface.

This function can be calculated for both M.D. and MGC results. Figure 7 shows that cation condensation is shifted to higher x values and underestimated by the MGC model. However the extent of underestimation is low and the two curves could be almost superposed when considering that the small part of Na that undergoes a loss of water hydration becomes part of the surface charge term (then decreasing σ).

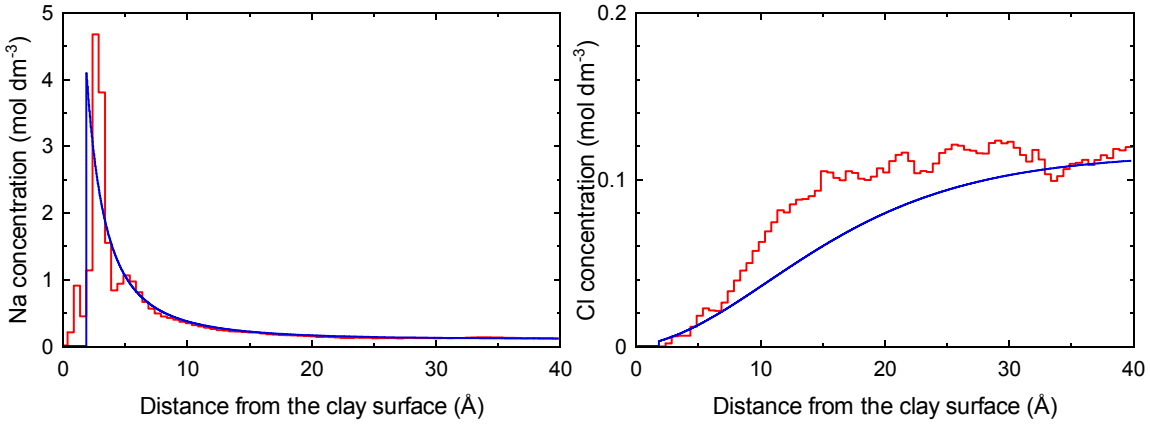

Figure 6. *Comparisons of Na and Cl concentration profiles obtained from Equation 2 to Equation 5(blue lines) with M.D. calculations (red lines). The green line corresponds to the coordinate of the most external oxygen atom of the structure + one oxygen ionic radius.*

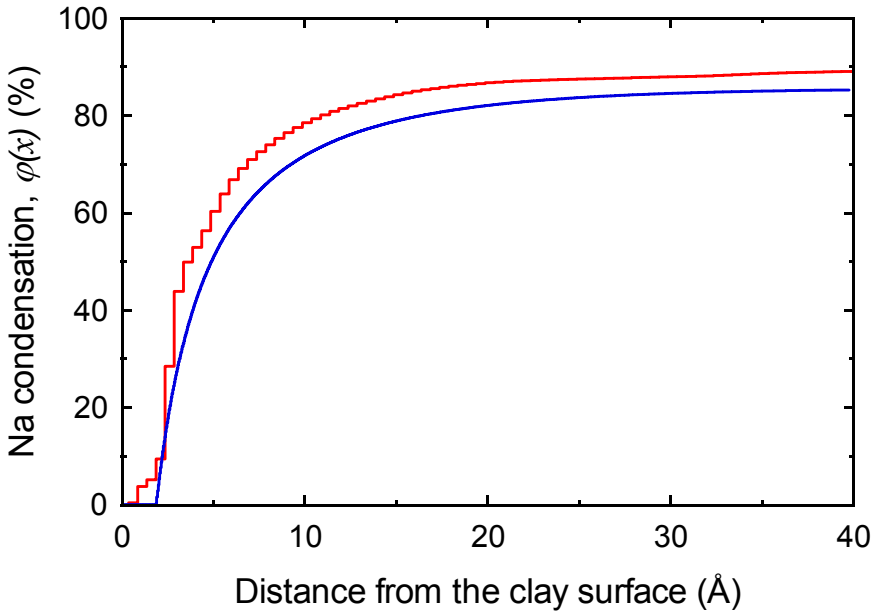

Figure 7 *Comparison of Na condensation functions obtained with M.D. calculations (red line) and MGC model (blue line).*

The MGC chloride concentration profile shows higher anion exclusion than the M.D. simulations. This difference can be appreciated more quantitatively by considering the anion exclusion distance given by the MGC model (Sposito, 1992):

$$d_{ex} = \lim_{x\to\infty} \int_{d_0/2}^{x} \left(1 - \frac{c_{Cl}(s)}{c_0}\right) ds + \frac{d_0}{2} = \frac{2}{\kappa}\left(1 - \exp\left[-\frac{F\left|\psi\left(\frac{d_0}{2}\right)\right|}{2RT}\right]\right) + \frac{d_0}{2} \qquad \text{Equation 13}$$

The integral expression can be evaluated also with the M.D. simulation results as a function of x:

$$d_{ex} = \lim_{x\to\infty}\left(D_{ex}^{DM}(x)\right) \qquad \text{Equation 14}$$

With

$$D_{ex}^{DM}(x) = \Delta x \times \sum_{i=0}^{x}\left(1 - \frac{c_{Cl}(i\times\Delta x)}{c_0}\right) \qquad \text{Equation 15}$$

where Δx is the resolution of the molecular dynamics trajectory analysis.

Because the determination of c_0 from molecular dynamics results is subject to non negligible uncertainty (due to statistical reasons), Figure 8 shows the $D_{ex}^{DM}(x)$ function as a function of x. The comparison of M.D. result with the value given by Equation 13 (16.5 Å ~ 1.9 κ^{-1}) shows MGC and M.D. predictions remain in fairly good agreement, M.D. calculations giving d_{ex} value at ~11 Å ~ 1.2 κ^{-1}.

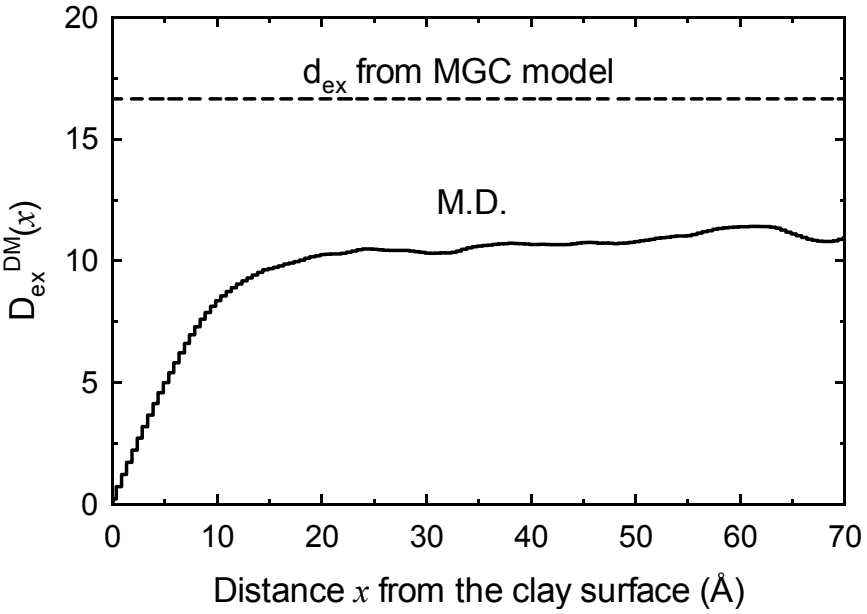

Figure 8. *Comparison of anion exclusion distance obtained from M.D. calculations analysis and MGC model.*

Several reasons (not exclusive each other) could explain the difference of anion exclusion distance estimated from our M.D. simulations and MGC model. The first one is an inaccuracy of the M.D. profile due to the low modelled Cl^- concentration

associated to an insufficient simulation time. For instance, Figure 6 shows persistent oscillations at distance from the clay surface greater than 20 Å. Second reason could be linked to the M.D. force field itself. However, this reason is unlikely because (i) Na behaviour is in agreement with MGC predictions and (ii) long range electrostatic interactions are the main contributor to Cl^- distribution. A third reason may be linked to the absence of ions-ions interactions in the MGC model, these interactions taking place in M.D. simulation with Cl attraction by the "plane" of Na cations. For instance, Carnie and Torrie (Carnie and Torrie, 1984) showed that MGC models become inaccurate for 1:1 electrolyte at concentration greater than 0.1 mol dm^{-3} based on Monte-Carlo calculations. Our simulations conditions would then stand at the limit of the MGC model applicability. Ideally, this could be tested by comparison with experimental exclusion volume at clay surfaces. Sposito (1992) showed that such experimental data (from Bolt and Warkentin, 1958; Edwards et al., 1965; Edwards and Quirk, 1962) can be accurately reproduced for NaCl concentrations less than 0.1 mol dm^{-3} using Equation 13 combined to an independent estimation of the external surface of a Na-montmorillonite:

$$V_{ex} = S \times d_{ex} + f \times S_0 \frac{d_Q}{2} \qquad \text{Equation 16}$$

S_0 is the total specific surface area of single platelet of montmorillonite i.e. ~760 m^2/g for a Na-montmorillonite, neglecting the edge surface (5-10 m^2/g, Tournassat et al., 2003; Yokoyama et al., 2005). S is the external part of the specific surface area (with formation of tactoids, part of the surface becomes interlayer surface). f is the fraction of single-layer platelets that form n-layer quasicrystals in a suspension ($0<f<1$). d_Q is the separation between single-layer platelets in a quasicrystal ($d_Q \sim 10$Å, Sposito, 1992).

The specific surface S is given by:

$$S = \frac{S_0}{n_{AV}} \qquad \text{Equation 17}$$

where n_{AV} is the average number of unit-layer platelet in the suspension. n_{AV} has been evaluated for Na-montmorillonite e.g. by light transmission and viscosity (n_{AV} = 1.4 ± 0.4 (2 s.d.), Schramm and Kwak, 1982a and references therein) or TEM measurements (n_{AV} = 1.4, Shomer and Mingelgrin, 1978). These values points out that most of the Na-montmorillonite platelet are dispersed or associated two by two. This is further confirmed by the standard deviation value of 0.5 for the average number of platelets as observed by TEM methods (Shomer and Mingelgrin, 1978). f can therefore be estimated with:

$$n_{AV} = f + (1 - f) \times 2 \qquad \text{Equation 18}$$

Equation 16 is almost insensitive to the clay surface charge: a change of charge from -0.125 C m^{-2} to -0.1 C m^{-2} results in volume exclusion differences less than 2%. For the following calculation, the surface charge considered in the present M.D. study will then be considered (-0.116 C m^{-2}). Even if it is clear to us that these data are not

sufficient to infirm or confirm the relevance of changing d_{ex} from 1.9 κ^{-1} to 1.2 κ^{-1} in conditions similar to those simulated in our M.D. calculations, one sees that M.D. results are in fairly good agreement with the experimental literature data shown on Figure 9

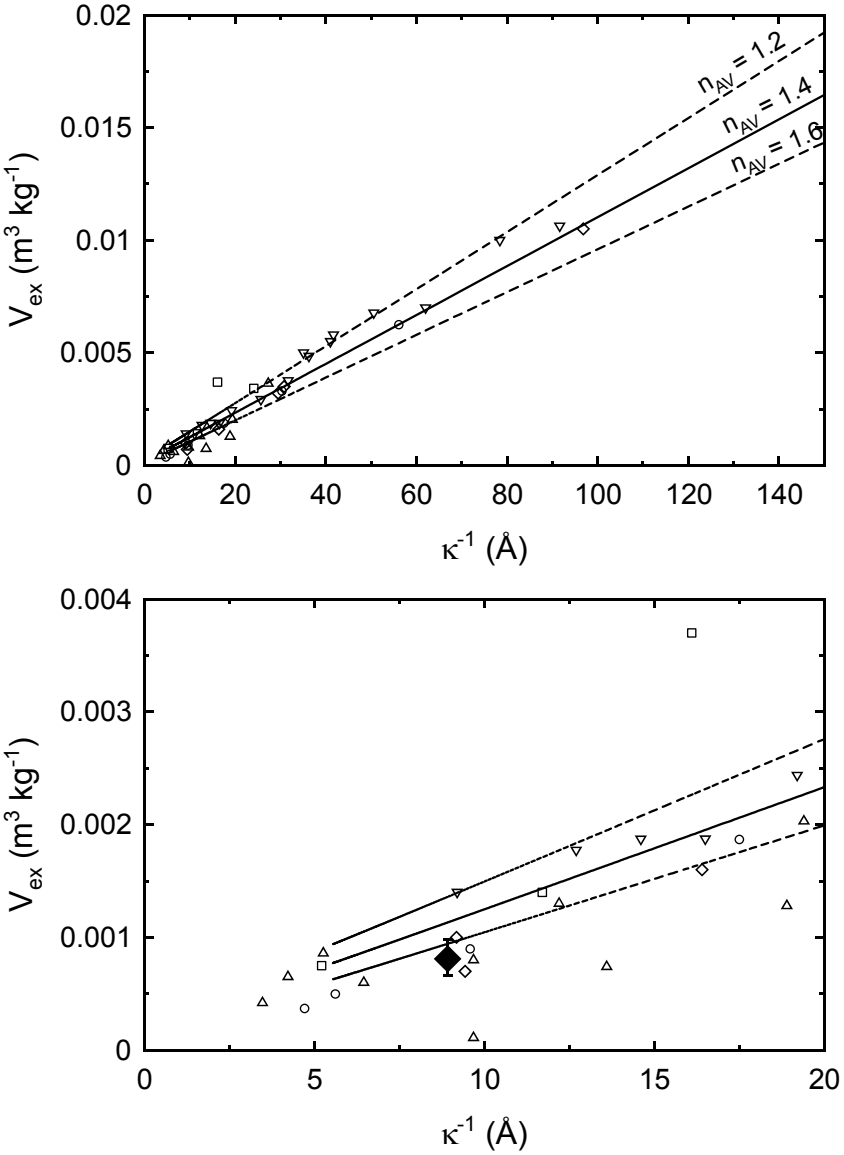

Figure 9. *Comparison of experimental chloride exclusion volume at Na-montmorillonite surface with Equation 16 (full and dashed lines with n_{AV} values varied from 1.2 to 1.6). Data are from Schramm and Kwak, 1982b (squares and up triangles: experiments at 2 and 4 g montmorillonite L^{-1} respectively), Edwards et al., 1965 (circles), Edwards and Quirk, 1962 (diamonds) and Bolt and Warkentin, 1958 (down triangles). Top: whole range of literature data. Bottom: zoom on the region representative of our M.D. simulation. The black diamond represents the exclusion volume calculated with d_{ex} = 1.2 κ^{-1} obtained from M.D. simulations. Its error band is representative of the n_{AV} variations from 1.2 to 1.6.*

TLM parameters derivation from M.D. concentration profiles

These parameters are the equilibrium constants associated with the surface complexation reactions, the surface site densities, and the capacitances of the inner and outer part of the Stern layer (Leroy and Revil, 2004; Leroy et al., 2007). They are of paramount importance for understanding the electrokinetic properties of charged porous media and especially clay-rich media.

For example, there are many unsolved questions regarding surface conductivity of particles in these media (Persello, 2002). Surface conductivity influences electrical conductivity and electrokinetic measurements (Coelho et al., 1996) and is frequency dependent (Leroy et al., 2008). This phenomenon is linked to the electrochemical properties of the mineral/water interface. When a charged surface is influenced by an external electrical field, it develops a surface electrical conductivity. This phenomenon is linked to the higher ionic concentrations in the vicinity of the surface described usually by the electrical double or triple layer model (Leroy and Revil, 2004). This surface conductivity is associated with ions motion along the surface. In the case of DC conductivity measurements, because of the very low mobility of the ions in the Stern layer, the Stern contribution to surface conductivity may be neglected (Leroy and Revil, 2004). Higher ionic concentrations in the mineral/water interface lead to higher surface conductivity, i.e., surface conductivity is very sensible to the ionic concentrations in the Stern and diffuse layers. On the other hand, the ionic concentrations depend on the parameters of the TLM.

In the case presented in this study, the values of the equilibrium constant K_{Na} associated with the sorption of sodium and of the capacitances C_1 and C_2 are needed to fit the experimental M.D. concentration profiles. The zeta potential is a key parameter to optimize the parameters of the TLM (Avena and De Pauli, 1998). However, the Henry's equation which links the zeta potential to the electrophoretic mobility gives an "apparent" zeta potential (underestimation of the "real" zeta potential, Alkafeef et al., 1999). In the case of highly charged minerals like clay minerals and at low salinity (typically $< 10^{-2}$ mol dm^{-3}), the electrophoretic mobility associated with the motion of colloidal suspensions under an applied electrical field is sensitive to the surface conductivity of the grains. The determination of the surface conductivity is needed to correct the electrophoretic measurements at low salinity. At high salinity (typically $> 10^{-1}$ mol dm^{-3}), the effect of the surface conductivity on the electrophoretic measurements can be neglected (Leroy and Revil, 2004). While, for clay minerals, electrical potential at the Outer Helmholtz Plane ψ_d can be associated to the zeta potential value, a parameter that can be calculated independently, the choices for capacitance values C_1 and C_2 must be considered as more empirical. In the present paragraph we discuss the potentiality of our simulation results to better constrain these parameters.

C_1 and C_2 values have been usually fixed at 1 and 0.2 F m^{-2} in TLM models for oxides (Kitamura et al., 1999) and clay minerals (Leroy and Revil, 2004; Leroy et al., 2007). This choice is nevertheless questionable (Hiemstra and Van Riemsdijk, 2006). The capacitance C_1 and C_2 can be related in the interface structure to the expression (see Appendix 1):

$$C_1 = \frac{\varepsilon_1 \times \varepsilon_0}{x_1}$$ Equation 19

$$C_2 = \frac{\varepsilon_2 \times \varepsilon_0}{x_2}$$ Equation 20

Where ε_1, ε_2, x_1 and x_2 are described on Figure 2. According toEquation 20, taking C_2 = 0.2 F m^{-2} leads to $x_2 \approx$ 20-35 Å (with ε_2 = 40 to 80) which is equivalent with too many water molecules to be physically realistic.

From Figure 3, the distance x_1 can be estimated at a value of 2.8 Å. The distance x_2 is difficult to estimate because the right part of the peak is wide and shows oscillations. The dielectric constants can not be estimated directly from our simulations. However, it is possible to constrain all of these values with the following procedure.

Neglecting adsorption on the 0-plane, the surface charge density of the d-plane (Q_d) is obtained through Equation 8 assuming ψ_d equal to the zeta potential of the montmorillonite-NaCl system. Q_β value can be then obtained through Equation 9. Zeta potentials measurements on montmorillonite are available in the literature at NaCl concentrations comparable to that simulated in the present work (~0.1 mol/L): for instance, Sondi et al. measured zeta potential of -30 mV at 0.1 mol/L NaCl with a montmorillonite from Croatia with a CEC of -1.24 mol$_c$ kg^{-1} equivalent to a surface charge of ~-1.1 proton charges per nm^2 (Sondi et al., 1996). The measurement carried out in the present study led to zeta potential of -38 mV at 0.12 mol/L for a montmorillonite with layer charge of -0.67 proton charge per nm^2. In the following, we will consider that zeta potential (and therefore ψ_d) has a value of -30 ± 10 mV for our system. Figure 10 shows the effect of this uncertainty on the Q_d and Q_β values.

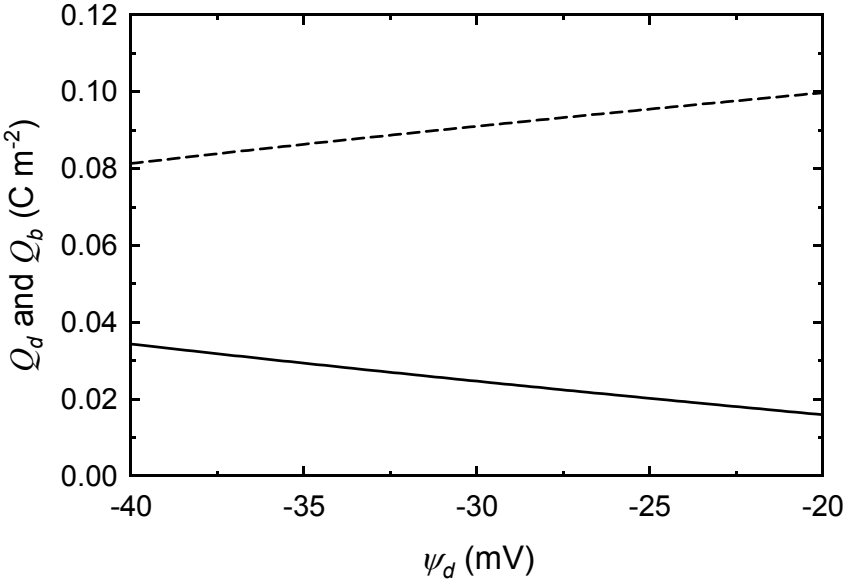

Figure 10. *Effect of ψ_d uncertainty on the Q_d (full line) and Q_β (dashed line) values.*

From Figure 10 it can be inferred that 70 to 86% of the charge is compensated by sodium cations in the Stern layers, 14 to 30% being compensated in the diffuse

swarm. These values can be reported on the corresponding M.D. profile (Figure 11), leading to an estimate of the x_1+x_2 value at 7.5 ± 1.8 Å. Given x_1=2.8 Å, x_2 value is 4.7 ± 1.8 Å, i.e. between one and more than twice the x_1 value.

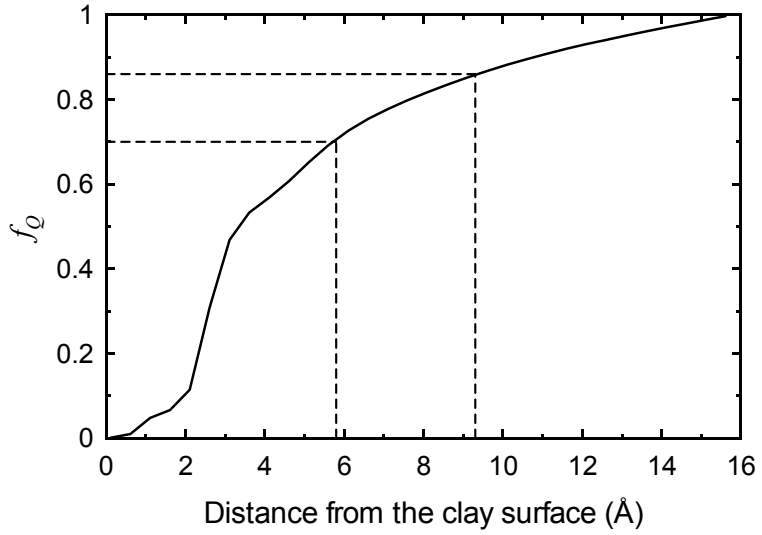

Figure 11. *Estimation of the x_1+x_2 value based on the comparison of cation compensation estimated from zeta potential measurements and M.D. profile. f_Q is the fraction of charge compensated in the Stern layers, neglecting the presence of anions. Horizontal and drop dashed lines corresponds to 70 and 86 % of compensated charges and give x_1+x_2 values of 5.8 and 9.3 Å.*

With x_1 and x_2 values, it becomes possible to estimate the capacitance values using Equation 19 and Equation 20 and an estimation of the dielectric constant ε_1 and ε_2. We made here two different working hypothesis:

- in the first hypothesis, we considered that $\varepsilon_1 = \varepsilon_2 = 40$ in agreement with new results obtained for oxides surfaces (Hiemstra and Van Riemsdijk, 2006);
- in the second hypthesis we considered that $\varepsilon_1 = \varepsilon_2$ and that the potential drop in surface potential ($\Delta\psi$) from the 0-plane to the d-plane is linked to the permittivity, assuming an homogeneous field in the Stern layers (Conway, 1981):

$$\Delta\psi = \psi_0 - \psi_d = \frac{Q_0}{C_1} - \frac{Q_d}{C_2} \qquad \text{Equation 21}$$

$$\varepsilon_r = \frac{\varepsilon_z - \varepsilon_s}{1 + b \times \left(-\frac{d\psi}{dx}\right)^2} + \varepsilon_s = \frac{\varepsilon_z - \varepsilon_s}{1 + b \times \left(-\frac{\Delta\psi}{x_1 + x_2}\right)^2} + \varepsilon_s \qquad \text{Equation 22}$$

ε_r is the relative permittivity coefficient of the Stern layers, ε_z and ε_s are the relative dielectric constants at zero field (ε_z = 78) and at saturation (ε_s = 6) respectively. $-\frac{d\psi}{dx}$ is the field strength in V m^{-1} and b is a constant (1.2 10^{-17} m^2 V^{-2}).

Table 3 summarize the sets of consistent parameters according to these two working hypothesis and as a function of the considered zeta potential value (-20, -30 or -40 mV).

Table 3. *Calculation of TLM parameters, x_1, x_2, ε_r, C_1, C_2 and K_{Na} for a Na-montmorillonite in NaCl 0.1 mol L^{-1} ionic background as a function of considered potential on the d-plane.*

ψ_d	x_1 (Å)	x_2 (Å)	ε_1	ε_2	C_1 (F m^{-2})	C_2 (F m^{-2})	K_{Na} (mol dm^{-3})
Hypothesis 1			$\varepsilon_1 = \varepsilon_2 = 40$				
-30 mV	2.8	4.7	40		1.26	0.75	0.32
-20 mV	2.8	6.5	40		1.26	0.54	0.11
-40 mV	2.8	3	40		1.26	1.22	0.62
Hypothesis 2			$\varepsilon_1 = \varepsilon_2 = \varepsilon_r$				
-30 mV	2.8	4.7	71		2.3	1.3	0.19
-20 mV	2.8	6.5	74		2.3	1.0	0.07
-40 mV	2.8	3	67		2.1	2.0	0.41

Based on the parameters given in Table 3 and on Equation 5, it is also possible to calculate K_{Na} (Equation 6, Table 3) and the diffuse swarm composition as a function of the distance to the clay surface (Figure 12). As a function of the chosen ψ_d value, the d-plane is located between the end of the second or the third oscillation of water density. Like for MGC model, anion exclusion is overestimated by the TL model as compared to M.D results. This effect is reduced when considering the lower value for ψ_d (-40 mV). In that case, the calculated anion exclusion distance value is 15.5 Å ~ 1.7 κ^{-1}. This choice lead also to the best representation of the sodium profile amongst those proposed and simplifies the parameterization of the TL model since $C_1 \sim C_2 \sim 1.25$ F m^{-2} with the first working hypothesis ($\varepsilon_1 = \varepsilon_2 = 40$) and $C_1 \sim C_2 \sim 2$ F m^{-2} with the second hypothesis ($\varepsilon_1 = \varepsilon_2 = \varepsilon_r$,Equation 22).

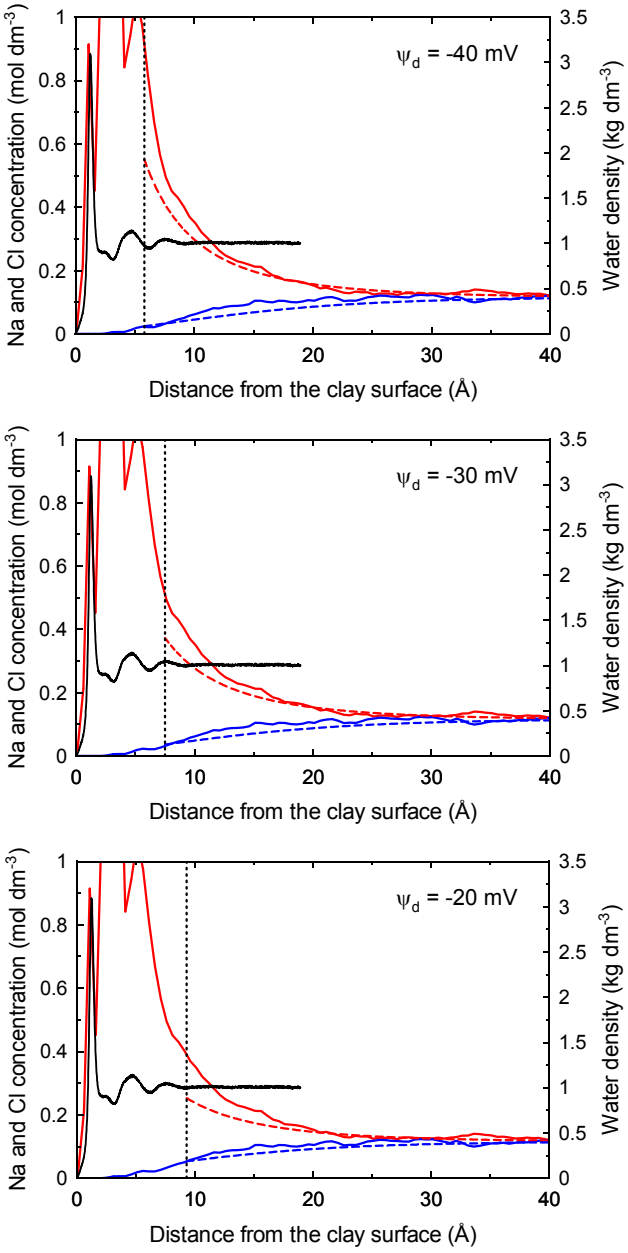

Figure 12. *Diffuse swarm composition from TLM with parameters given in Table 3 (hypothesis 2; Na: red dashed lines; Cl: blue dashed line) and comparison with M.D. results (Na: red full line; Cl: blue full line). Top: ψ_d = -0.04 V; middle: ψ_d = -0.03 V; bottom: ψ_d = -0.02 V. Vertical dotted lines represent the position of the d-plane. Full black line is the water density as a function of the distance from the clay surface.*

Representativity of MGC and TL models for external clay surfaces description

MGC model proved to be efficient to reproduce the M.D. concentration profiles in the diffuse layer although it probably overestimates anion exclusion at NaCl concentration greater than 0.1 mol dm^{-3}. As expected, the model fails in describing the structure of the cation condensation at the interface although there is a general

agreement in the quantification of this condensation. On the contrary, TL model enables to describe this condensation through the consideration of cations trapped in outer-sphere complex on the β-plane. The model could be even refined by considering the inner-sphere complex in the 0-plane (6% of the total charge from M.D. calculations). However, the model parameters could not be estimated independently of the M.D. simulations. In particular one notes the large difference in C_1 and C_2 parameters with usual considered values (e.g. see Leroy and Revil, 2004; Leroy et al., 2007). One conceptual problem arises when considering the fundamental hypothesis of a classic TL model. Cations trapped in outer-sphere complex should be considered as immobilized (Sposito, 1992; Sposito, 2004). Figure 5 shows the variations of the diffusion coefficient for H_2O, Na^+ and Cl^- parallel to the clay surface as a function of the distance from this surface. From these results, it is clear that Na ions in the β-plane (and also in the 0-plane) are not immobilized and can diffuse even if their mobility is reduced by one half at least. Their mobility perpendicular to the clay surface can be appreciated through the survival probability of one given Na ion in each compartment defined in section 4.1.5 and shown on Figure 5. Na cations in the "inner sphere" and β-plane compartments shows rapid decrease of their survival probability (Figure 13) representative of their exchange with adjacent compartments. As a consequence the diffuse layer model is more adapted to represent the water and ions organisation at a clay surface when taking into account ion mobility.

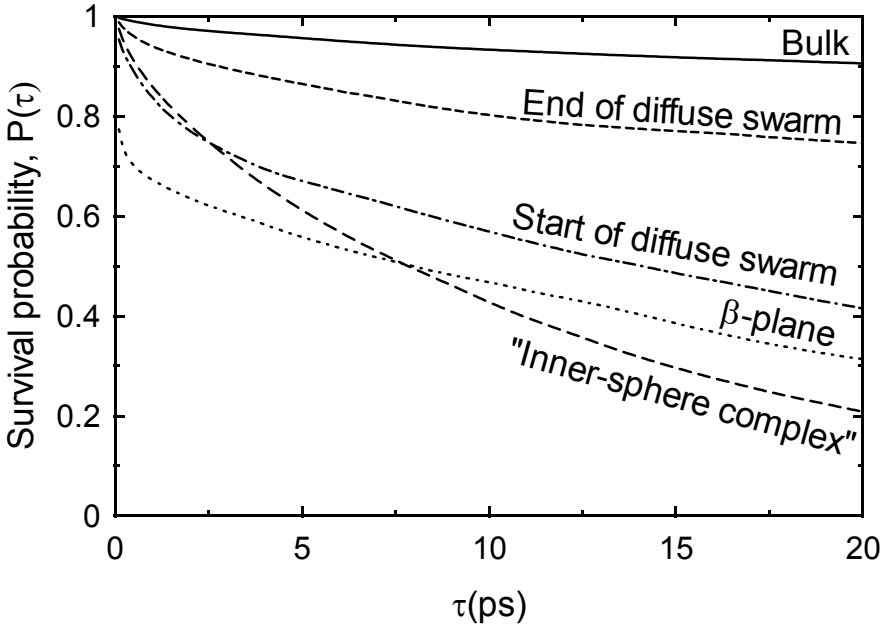

Figure 13. *Survival probability of Na cations in the different zones at clay surface (see section 4.1.5 andFigure 5). Calculation performed on a 1 ns trajectory with SPC force field.*

Conclusion

MGC and TL models capture the essential features of the observations gained from M.D. simulations made with a dilute NaCl Na-montmorillonite system: anion exclusion, cation condensation. MGC models reproduce correctly the Na concentration profile in the diffuse swarm after the Na adsorption "plane". However, we showed that

MGC models overestimate anion exclusion by a factor ~1.5 at ionic strength above 0.1 mol L^{-1}.

Our M.D. simulation enabled to calculate consistent capacitance parameters for a clay TLM model with potential applications on cation exchange reaction modelling.

Acknowledgment

This work has been supported by the ANDRA (French National Radioactive Waste Management Agency, under the supervision of Dr. S. Altmann), BRGM (French geological survey) and European Commission in the framework of the 6th PCRD Euratom IP FUNMIG.

Appendix 1

The fundamental electrostatic equation for the system is Poisson's equation

$$\nabla \cdot \mathbf{D} = \rho \qquad \text{Equation A1}$$

$$\nabla \cdot \left(-\varepsilon \nabla \psi \right) = \rho \qquad \text{Equation A2}$$

where **D** is the dielectric displacement (in C m^{-2}), ρ the volume density of charge (in C m^{-3}), ε the permittivity of the medium (in F m^{-1}), and ψ the electrostatic potential (in V). In the inner part of the Stern layer ($0 < x < x_1$), there is no electrical charge, and Equation A3 becomes

$$\frac{d}{dx}\left(-\varepsilon_1 \frac{d\psi}{dx} \right) = 0 \qquad \text{Equation A3}$$

Integration of Equation A3 gives

$$\psi_0 - \psi_\beta = \frac{Q_0 x_1}{\varepsilon_1} \qquad \text{Equation A4}$$

$$\psi_0 - \psi_\beta = \frac{Q_0}{C_1} \qquad \text{Equation A5}$$

Applying the same procedure to the region $x_1 < x < x_2$ (outer part of the Stern layer) gives

$$\psi_\beta - \psi_d = -\frac{Q_d}{\varepsilon_2}(x_2 - x_1) \qquad \text{Equation A5}$$

$$\psi_\beta - \psi_d = -\frac{Q_d}{C_2} \qquad \text{Equation A6}$$

The sub-layers treated here correspond to two molecular capacitors of capacitances C_1 and C_2 (in F m^{-2}).

References

Alkafeef, S. F., Gochin, R. J., and Smith, A. L., 1999. Measurement of the electrokinetic potential at reservoir rock surfaces avoiding the effect of surface conductivity. *Colloids and Surfaces A: Physicochemical and Engineering Aspects* **159**, 263-270.

Avena, M. J. and De Pauli, C., 1998. Proton adsorption and electrokinetics of an argentinean montmorillonite. *J. Colloid Interface Sci.* **202**, 195-204.

Berendsen, H. J. C., Grigera, J. R., and Straatsma, T. P., 1987. The missing term in effective pair potentials. *Journal of Physical Chemistry* **91**, 6269-6271.

Bolt, G. H. and Warkentin, B. P., 1958. The negative adsorption of anions by clay suspensions. *Kolloid Zeitschrift* **156**, 41-46.

Carnie, S. L. and Torrie, G. M., 1984. The statistical mechanics of the electrical double layer. *Adv. Chem. Phys.* **56**, 141-253.

Chavez-Paez, M., dePablo, L., and dePablo, J. J., 2001. Monte Carlo simulations of Ca-montmorillonite hydrates. *The Journal of Chemical Physics* **114**, 10948-10953.

Coelho, D., Shapiro, M., Thovert, J. F., and Adler, P. M., 1996. Electroosmotic Phenomena in Porous Media. *J. Colloid Interface Sci.* **181**, 169-190.

Conway, B. E., 1981. *Ionic hydration in chemistry and biophysics* Elsevier, Amsterdam.

Cygan, R. T., Liang, J.-J., and Kalinichev, A. G., 2004. Molecular models of hydroxide, oxyhydroxide, and clay phases and the development of a general force field. *J. Phys. Chem. B* **108**, 1255-1266.

Edwards, D. G., Posner, A. M., and Quirk, J. P., 1965. Repulsion of chloride ions by negatively charged clay surfaces. Part 2.-Monovalent cation montmorillonites. *Transactions of the Faraday Society* **61**, 2816-2819.

Edwards, D. G. and Quirk, J. P., 1962. Repulsion of chloride by montmorillonite. *Journal of colloid science* **17**.

Gailhanou, H., van Miltenburg, J. C., Rogez, J., Olives, J., Amouric, M., Gaucher, E. C., and Blanc, P., 2007. Thermodynamic properties of anhydrous smectite MX-80, illite IMt-2 and mixed-layer illite-smectite ISCz-1 as determined by calorimetric methods. Part I: Heat capacities, heat contents and entropies. *Geochim. Cosmochim. Acta* **71**, 5463-5473.

Hiemstra, T. and Van Riemsdijk, W. H., 2006. On the relationship between charge distribution, surface hydration, and the structure of the interface of metal hydroxides. *J. Colloid Interface Sci.* **301**, 1-18.

Kale, L., Skeel, R., Bhandarkar, M., Brunner, R., Gursoy, A., Krawetz, N., Phillips, J., Shinozaki, A., Varadarajan, K., and Schulten, K. J., 1999. NAMD2: greater scalability for parallel molecular dynamics. *J. Comput. Phys.* **151**, 238-312.

Kozaki, T., Fujishima, A., Sato, S., and Ohashi, H., 1998. Self-diffusion of sodium ions in compacted montmorillonite. *Nucl. Technol.* **121**, 63-69.

Leroy, P. and Revil, A., 2004. A triple-layer model of the surface electrochemical properties of clay minerals. *J. Colloid Interface Sci.* **270**, 371-380.

Leroy, P., Revil, A., Altmann, S., and Tournassat, C., 2007. Modeling the composition of the pore water in a clay-rock geological formation (Callovo-Oxfordian, France). *Geochim. Cosmochim. Acta* **71**, 1087-1097.

Leroy, P., Revil, A., Kemna, A., Cosenza, P., and Ghorbani, A., 2008. Complex conductivity of water-saturated packs of glass beads. *J. Colloid Interface Sci.* **321**, 103-117.

Liu, P., Harder, E., and Berne, B. J., 2004. On the calculation of diffusion coeffcients in confined fluids and interfaces with an application to the liquid-vapor interface of water. *J. Phys. Chem. B* **108**, 6595-6602.

Lockhart, N. C., 1980. Electrical properties and the surface characteristics and structure of clays. I. Swelling Clays. *J. Colloid Interface Sci.* **74**, 509-519.

Marry, V., Rotenberg, B., and Turq, P., 2008. Structure and dynamics of water at a clay surface from molecular dynamics simulation. *Phys. Chem. Chem. Phys.* **10**, 4802-4813.

Pavese, A., Ferraris, G., Prencipe, M., and Ibberson, R., 1997. Cation site ordering in phengite 3T from the Dora-Maira massif (western Alps): a variable-temperature neutron powder diffraction study. *Eur. J. Miner.* **9**, 1183-1190.

Persello, J., 2002. Interfacial Electrokinetics and Electrophoresis. In: Delgado, A. V. (Ed.), *Surface Science Series*. Dekker, New York.

Rémy, J. C. and Orsini, L., 1976. Utilisation du chlorure de cobaltihexamine pour la détermination simultanée de la capacité d'échange et des bases échangeables dans les sols. *Sciences du Sol* **4**, 269-275.

Schramm, L. L. and Kwak, J. C. T., 1982a. Influence of exchangeable cation composition on the size and shape of montmorillonite particles in dilute suspension. *Clay. Clay. Miner.* **30**, 40-48.

Schramm, L. L. and Kwak, J. C. T., 1982b. Interactions in clay suspensions: The distribution of ions in suspension and the influence of tactoid formation. *Colloid. Surface.* **3**, 43-60.

Schwieters, C. D., Kuszewski, J. J., and Clore, G. M., 2006. Using Xplor-NIH for NMR molecular structure determination. *Progress in NMR Spectroscopy* **48**, 47-62.

Schwieters, C. D., Kuszewski, J. J., Tjandra, N., and Clore, G. M., 2003. The Xplor-NIH NMR molecular structure determination package. *J. Magn. Reson.* **160**, 66-74.

Seeber, M., Cecchini, M., Rao, F., Settanni, G., and Caflisch, A., 2007. Wordom: a program for efficient analysis of molecular dynamics simulations *Bioinformatics* **23**, 2625-2627.

Shomer, I. and Mingelgrin, U., 1978. A direct procedure for determining the number of plates in tactoids of smectites: the Na/Ca-montmorillonite case. *Clays & Clay Minerals* **26**, 135-138.

Sondi, I., Biscan, J., and Pravdic, V., 1996. Electrokinetics of pure clay minerals revisited. *J. Colloid Interface Sci.* **178**, 514-522.

Sposito, G., 1992. The diffuse-ion swarm near smectite particles suspended in 1:1 electrolyte solutions: modified Gouy-Chapman theory and quasicrystal formation. In: Güven, N. and Pollastro, R. M. Eds.), *Clay-water interface and its rheological implications*. Clay minerals society.

Sposito, G., 2004. *The Surface Chemistry of Natural Particles*. Oxford University Press, New York.

Tambach, T. J., Hensen, E. J. M., and Smit, B., 2004. Molecular simulations of swelling clay minerals. *J. Phys. Chem. B* **108**, 7586-7596.

Tournassat, C., Neaman, A., Villiéras, F., Bosbach, D., and Charlet, L., 2003. Nanomorphology of montmorillonite particles: Estimation of the clay edge sorption site density by low-pressure gas adsorption and AFM observations. *Am. Mineral.* **88**, 1989-1995.

Vinsot, A., Mettler, S., and Wechner, S., In Press. In situ characterization of the Callovo-Oxfordian pore water composition. *Physics and chemistry of the earth*.

Wang, J., Kalinichev, A. G., and Kirkpatrick, R. J., 2006. Effects of substrate structure and composition on the structure, dynamics, and energetics of water at mineral surfaces: A molecular dynamics modeling study. *Geochim. Cosmochim. Acta* **70**, 562-582.

Yokoyama, S., Kuroda, M., and Sato, T., 2005. Atomic force microscopy study of montmorillonite dissolution under highly alkaline conditions. *Clay. Clay. Miner.* **53**, 147-154.

SPECTRAL AND TEMPORAL LUMINESCENT PROPERTIES OF Eu(III) IN AQUEOUS HUMIC SUBSTANCES SOLUTIONS AND SORPTIVE-FRACTIONATED HUMIC SAMPLES FROM DIFFERENT ORIGINS

Julien Brevet, Francis Claret, Pascal Reiller*

Commissariat à l'Energie Atomique (F)

*Corresponding author: pascal.reiller@cea.fr

Abstract

A study of the luminescence properties of the Eu(III) implied in HS complexes, or in fractionated HS at pH=5 was undertaken. Seven different extracts were contacted with Eu(III). It is shown that terrestrial extract on one hand, and aquatic extracts on the other hand, do seem to induce inner coherent luminescent properties of Eu(III) within each group. For the fractionated samples, clear modification of the Eu(III) environment are shown at the fractionation goes on.

Introduction

Both the complexation by natural organic matter (NOM) and the sorption of these complexes on minerals, play an important role in the transport properties of lanthanides (Ln) and actinides (An). Humic substances (HS), due to their colloidal properties induce a facilitated transport (Santschi *et al.*, 2002). Knowing the diversity of the HS, the relative homogeneity of their complexing behavior towards series of metals may seem surprising (Kim & Czerwinski, 1996; Kinniburgh *et al.*, 1999). Even if these models provide efficient descriptions of the phenomenon, the structure of Ln(III)-HS complexes is still an open question, as the structure of these natural ligands is still under debate.

The fractionation of humic substances on mineral surface has often precluded the interpretation of radionuclides' sorption results in ternary systems, *i.e.*, metal-humic-mineral. In most cases the additivity rule of the systems does not work. This phenomenon is thought to be the consequence of preferential sorption of certain classes of molecules from the humic mixture, most certainly aromatic molecules, leaving other classes in solution (Claret *et al.*, 2008). It has also recently been shown that the chemical neighbouring of Eu(III), probed by time-resolved laser induced luminescence, was different in pristine HS and with samples previously contacted with a mineral surface (Claret *et al.*, 2008). This change in the composition and maybe of structure of

the Eu(III) complexing sites can help in understanding the difficulties for interpreting the ternary systems.

The luminescence properties of Ln/An(III) is convenient to evaluate their chemical environment, and the influence of HS on the spectra received particular attention using time-resolved luminescence spectroscopy (TRLS) (Chung *et al.*, 2005; Marang *et al.*, 2008; Moulin *et al.*, 1999; Moulin *et al.*, 1992; Panak *et al.*, 1995). The luminescence enhancement is due to an energy transfer from a triplet energy level from the ligand to the Ln(III) ion. Up to now, the crystal ligand splitting of the solution spectra has not received attention for Eu(III)-HS complexes with the exception of the differences between carbonate and humic ligands (Moulin *et al.*, 1999) and $^7F_0 \rightarrow {}^5D_0$ excitation splitting (Shin & Choppin, 1999).

The aim of this study is first to evidence this crystal ligand splitting in solution using time-resolved luminescence spectra of several Eu(III)-HS complexes with a 1800 lines.mm^{-1} grating. Seven different humic extracts were used, in order to cover a wide span of origin. Second we will have a particular look on the structure of the Eu(III) luminescence spectra, in pristine HS and in sample which were subjected to sorption on α-alumina previously.

Materials and Methods

Preparation of solutions

Suwannee River FA (SRFA), and HA (SRHA), and Leonardite HA (LHA) were used as received from the International Humic Substances Society. Aldrich Humic Acid (PAHA) was purified treated following Kim *et al.* (1990). The Gorleben HA (Gohy-573) was provided by M. Wolf (GSF, Munich, Germany) (Wolf *et al.*, 2004). The Kleiner Kranishsee bog HA and KFA extracts (Johanngeorgenstadt, Saxony, Germany), were provided by K. Schmeide (Forschungszentrum Dresden, Germany) (Schmeide *et al.*, 1998). Europium(III) stock solution was obtained from the dissolution of Eu_2O_3 (Johnson Matthey, 99.99%) in $HClO_4$. The concentration ratio of 10^{-5} mol_{Eu}/200 mg_{HS} if sufficient to obtained a complete complexation of Eu(III) (Marang *et al.*, 2008). The ionic strength was fixed with $NaClO_4$ to 0.1 *m* and pH was adjusted using freshly prepared NaOH and $HClO_4$. The pH measurements were done using a modified ($NaClO_4$ 0.1 *m*, NaCl 10^{-2} *m*) combined-glass electrode (Radiometer Analytical XC111) that was calibrated with a 0.01 *m* $HClO_4$ solution, an equimolar 0.02 *m* NaH_2PO_4/Na_2HPO_4 solution and an equimolar 0.02 *m* $Na_2CO_3/NaHCO_3$ solution, all containing appropriate amounts of $NaClO_4$ to keep [Na^+] constant at 0.1 *m*.

Sorption Experiments

Suwannee River Fulvic Acid is used as received from the International Humic Substance Society (IHSS), and Gorlenben humic acid was obtained from Wolf *et al.* (2004). These humic extracts were chosen as representative of an aquatic extract (SRFA), and of a terrestrial extract obtained after oxidation of a sedimentary organic carbon. α-Al_2O_3 was obtained from Interchim and characterized by Alliot *et al.* (2005). Carbonates were removed from α-Al_2O_3 to avoid any carbonate induced surface property changes. The isoelectric point (pH_{IEP}) was determined by zeta potential

measurement to be at 9.5 (data not shown). The sorption studies were performed at pH = 6.1 ± 0.2. The ionic strength was fixed with $NaClO_4$ to 0.1 *m* and the pH was adjusted using freshly prepared NaOH and $HClO_4$.

Batch sorption experiments were conducted at room temperature using polycarbonate screwcap vials. The suspensions were shaken continuously for 24 hours and the pH was checked frequently until a constant pH value was reached (usually 2 to 4 hours). The solid phase was separated via a pre-centrifugation step performed in 30 ml Nalgene 3137-0030 centrifuge vials (50,000 g for 1 hour); the supernatant was then ultra-centrifuged in order to get rid of colloidal particles in 10 ml Beckman 355603 vials (246,960 g for 1 hour). FA and HA absorbance were measured at 254 nm using a Shimadzu UV-3150 spectrophotometer and the dissolved organic concentration (DOC) in solution was determined with a Shimadzu 5000 TOC analyzer. Sample were acidified and purged with argon in order to outgas inorganic carbon as CO_2.

The Eu(III) luminescence corresponds to the transitions of the $^5D_0$ excited state to the ground ^7F_j manifold (Bünzli, 1989). The excitation laser beam was generated by a 355 nm tripled output of a Continuum Nd-YAG laser, coupled to an optical parametric oscillator system (Panther II, Continuum, USA). The wavelength was tuned to 394.6 nm, providing about 1.6 mJ of energy in a 5 ns pulse with a repetition rate of 10 Hz. The time-resolved luminescence signal is collected at 90° and focused into a Actror spectrometer (slit 1 mm) equipped with 600/1200/1800 lines mm^{-1} gratings. The signal is collected during a gate width W=300 µs, at a gate delay D=10 µs after excitation. Every spectrum was accumulated 1000 times. Emission spectra were recorded between 550 and 650 nm using a CCD camera cooled at -15°C. Before measurement the pH was adjusted to 5 to limit hydrolysis and carbonate species of Eu(III).

Results and Discussion

$^5D_0 \rightarrow {}^7F_{0,1}$ emission spectra of pristine Eu-HS complexes

The different spectra are reported on Figure 1 for $^5D_0 \rightarrow {}^7F_{0,1}$. All the spectra were normalized to their respective maximum intensity. The strongly forbidden $^5D_0 \rightarrow {}^7F_0$ transition, typically barely seen for aqueous Eu^{3+}, is now as high in intensity as the $^5D_0 \rightarrow {}^7F_1$ in Eu(III)-HS complexes. The $\lambda(^7F_0)_{max} \approx 579$ nm and FWMH ≈ 1 nm are rather constants through the two series of samples in agreement with other determinations (Shin *et al.*, 1996; Shin & Choppin, 1999). One can also note that these FWMH values are higher that the ones obtained on 'simple' organic complexes (Frey & Horrocks, 1995; Horrocks & Sudnick, 1981). This is a further indication that HS provides a wide distribution of complexing sites, as in weathering gels and glasses (Ollier *et al.*, 2001). The deconvolution in two components (Shin *et al.*, 1996) is unlikely due to unfavourable signal to noise ratio at this number of accumulations. Further works are in progress to overpass this limitation.

The $\lambda(^7F_0)_{max}$ value for the Eu(III)-HS complexes are in agreement with the maximum emission of either a $EuCl^{2+}$ complex or Eu(III) in methanol (Albin *et al.*, 1984; Albin & Horrocks, 1985), indicating an average charge of -1 for the complexing

unit; the number of coordinated ligands, CN ≈ 2.0 from Choppin & Wang (1997). These values are in line with the complexation through a bidentate form of Eu(III) (Marang *et al.*, 2008).

The splitting due to the crystal field of the $^5D_0 \rightarrow {}^7F_1$ transition is only slightly different between aqueous Eu^{3+} and Eu(III)-HS complexes as one can note a narrowing of the transition, FWMH is 6.9 and 6.2 nm for Eu^{3+} and Eu(III)-SRFA, respectively. The $\lambda(^7F_1)_{max}$ do not seem to vary. This very slight variation agrees with the fact that this magnetic dipole transition is not prone to variation with symmetry. The other aquatic extracts do seem to have the same $\lambda(^7F_1)_{max}$. Concerning the GohyHA/LHA ('terrestrial') extracts plus PAHA, the situation is not clear as the low signal to noise ratio precludes a reliable analysis. The number of accumulation was kept as 1000 in order to avoid photochemical reaction (Monsallier *et al.*, 2001). Works are in progress to overpass this limitation.

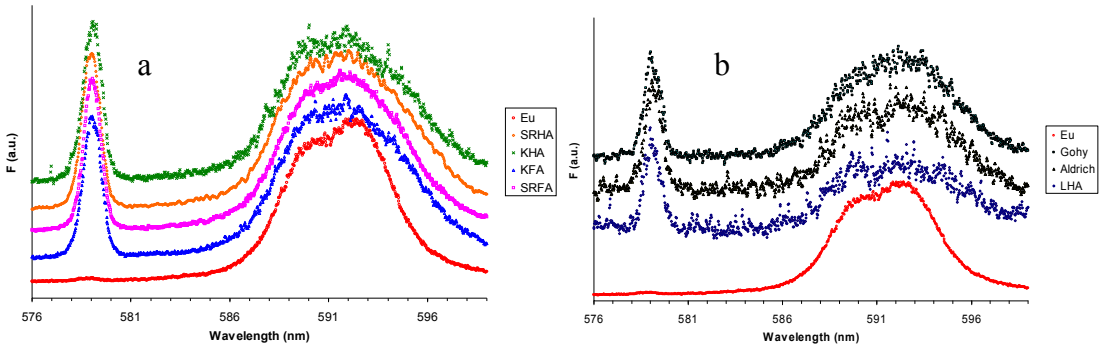

***Figure 1**: Eu(III) $^5D_0 \rightarrow {}^7F_0$ and $^5D_0 \rightarrow {}^7F_1$ transitions in 0.1 M $NaClO_4$ at pH=5, λ_{exc} = 394 nm, D=10 µs, W=300 µs, 1800 lines mm^{-1} grating of aqueous 10^{-5} mol/L Eu^{3+} (○), Eu (III) in SRFA (□), SRHA (◇),KHA (×), and KFA (△)(a),GohyHA (■), PAHA (▲), LHA (◆) (b).*

$^5D_0 \rightarrow {}^7F_2$ emission spectra

The analysis of $^5D_0 \rightarrow {}^7F_2$ in Figure 2 also leads to differences: a 1.3 nm blue shift from Eu^{3+} to Eu(III)-HS is observed. The splitting by the crystal ligand seem to be slightly different; for SRFA/SRHA/KFA/KHA (Figure 2a) the lowest wavelengths in $^5D_0 \rightarrow {}^7F_2$ seem to be more affected as a shoulder around 612.5 nm appears. The shoulder is enhanced in SRFA samples ($I_{612.5}/I_{614.5} \approx 0.1$); SRHA, KHA, and KFA are in an intermediate situation ($I_{612.5}/I_{614.5} \approx 1.3$), but when $\lambda \geq 613.6$ nm, all spectra are in perfect agreement. It is less important for GohyHA, LHA, and PAHA $I_{612.5}/I_{614.5} \approx 1.6$-1.7 (Figure 2b). This shoulder was also observed otherwise for Eu(III)-GohyHA complex {Marang, 2007 #1752}(Marang *et al.*, 2008), carbonate complexes (Vercouter, 2005), and Eu(III) in a humic-carbonate mix (Moulin *et al.*, 1999). The intensities when $\lambda \geq 615$ nm are also different between SRFA/SRHA/KFA/KAH and GohyHA/LHA/PAHA.

It can be hypothesized that the two groups of HS do provide slightly different symmetries for the complexation of Eu(III). For the SRFA/SRHA/KHA/KFA group, the decrease seems to have a lesser influence on the splitting. For Gohy/LHA/PAHA group, supposed to be 'terrestrial' samples, the symmetries seem to be directly comparable, and higher than aquatic samples as the shoulder around 612 nm is less important.

Interestingly, from the point of view of the Eu(III)-HS complex symmetry, the SRFA/SRHA samples originated from a black river, which can be submitted to modification by transport in the river flow and with the interaction with river sediments and dissolved minerals, are more different than the samples from the Kleiner Kranishsee Bog, which are supposed to be less submitted to transport-mediated modifications. The same remarks applies for GohyHA and LHA, which are originated from bacterial oxidation of a sedimentary carbon, or extracted from lignite, and thus less submitted to transport. These kind of changes in HS properties were also evidenced in column experiment using Aldrich HA (Johnson *et al.*, 2002), and in field studies (Aucour *et al.*, 2003). This could be also related with fractionation of HS during more 'static' batch retention experiments on surfaces (Claret *et al.*, 2008; Reiller *et al.*, 2006), where physical and chemical modifications of humic extracts were evidenced.

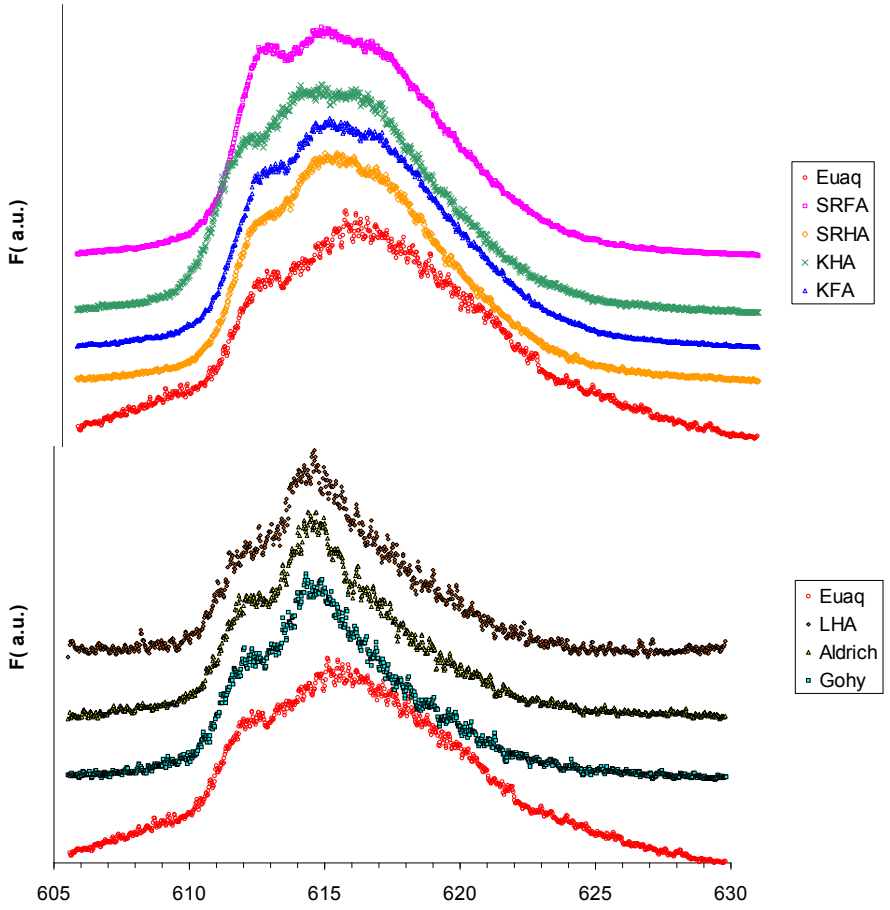

***Figure 2**: Eu(III) $^5D_0 \rightarrow {}^7F_2$ transitions in 0.1 M $NaClO_4$ at pH=5, λ_{exc} = 394 nm, D=10 µs, W=300 µs, , 1800 lines mm^{-1} grating of aqueous 10^{-5} mol/L Eu^{3+} (○), Eu (III) in SRFA (□), SRHA (◇), KHA (×), KFA (△) (a),GohyHA (■), PAHA (▲), LHA (◆).*

$^5D_0 \rightarrow {}^7F_2$ emission spectra of fractionated samples

The spectra of $^5D_0 \rightarrow {}^7F_2$ transition for Eu(III) at 5×10^{-3} mol_{Eu}/g_{HS}, complexed by pristine SRFA and in contact with four different supernatant obtained at R = 10, 15, 6.5, and 5 $mg_{HS}/g_{\alpha\text{-}Al_2O_3}$ complexes are reported in Figure 3. It has been shown by Claret *et al.* (2007; 2008) that these R values induce an extensive fractionation of SRFA, Particularly the $^5D_0 \rightarrow {}^7F_2/{}^5D_0 \rightarrow {}^7F_1$ ratio was decreasing indicating a decrease in both

the interaction intensity and the energy transfer between the triplet state of humics and excited states of Eu(III). In addition, these high definition spectra indicate that the Stark levels of this $^5D_0 \rightarrow {}^7F_2$ transition are also affected, which could mean that a change in the symmetry of Eu(III) in interaction with fractionated humics is occurring. This is a further proof that a profound modification of the humics is occurring during sorption.
This change in the spectra occurs around 612 nm, which was also identified has a critical spectral region for HS (Moulin *et al.*, 1999) and for other inorganic systems (Philippini, 2007; Vercouter, 2005).

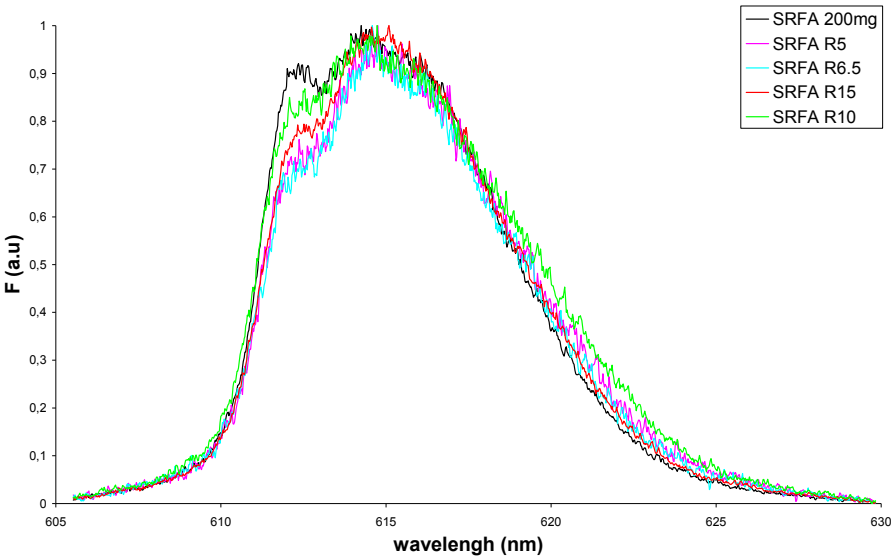

Figure 3: *$^5D_0 \rightarrow {}^7F_2$ luminescence spectra of europium(III) in SRFA (10^{-5} mol_{Eu}/L, 200 mg_{SRFA}/L, pH=5, I=0,1 M) and in four supernatants after sorption on α-alumina ($pH_{sorption}$=6, pH_{TRLS}=5); for every spectrum 5 × 10^{-3} mol_{Eu}/g_{HS}.*

The modifications in the chemical environment of Eu(III) in interaction with pristine humic extracts and with supernatants obtained after sorption on α-Al_2O_3 are a clear indication that a modification of the interaction intensity and of the complex symmetry is occurring in the bulk during sorption experiments. Hence, one can understand that, depending on the differences that are evidenced here, the additivity rule of the binary systems may, or may not, accurately represent the actual systems.

These modifications in composition or organisation of humic extracts in the bulk part of sorption experiments should also have consequences on the sorbed part. This subject is in development beyond the timeframe of this project.

Conclusion

In this work, it can be seen that even if humic extracts are diverse in essence, similarities can be found for the chemical environment of Eu(III)-HS complexes. The loss of symmetry compared to Eu^{3+} seem comparable for all the sample, nevertheless differences between two group of HS samples can be distinguished from the widths of the transition and from shoulders reflecting the ligand splitting. It seems that 'terrestrial' extracts, do provide a similar chemical environment for the complexation of Eu(III) in

term of crystal ligand splitting. Aquatic extracts do provide a different but also inner consistent chemical environment which can be slightly less symmetric compared to 'terrestrial' samples.
Clear modifications of the chemical environment of Eu(III) was evidenced in humic extracts which was subjected to sorption on α-Al_2O_3. These modifications revealed a change in the interaction intensity and in the symmetry around the Eu(III) ion. These changes could help to better understand the deviation from the additivity rule of binary systems for the study of ternary systems metal-humic-mineral.

Acknowledgment

This work was supported by the MRTRA project of the Risk Control Domain (CEA/DEN/DDIN)

References

Albin M., Cader B.M., Horrocks W.D. (1984): Lanthanide complexes of ionophores.2. spectroscopic characterization of Lanthanide(III) ion binding to lasalocid-A and A23187 in methanol, *Inorganic Chemistry*, **23**, 3045.

Albin M., Horrocks W.D. (1985): Europium(III) luminescence excitation spectroscopy - Quantitative correlation between the total charge on the ligands and the $^7F_0$->$^5D_0$ transition frequency in europium(III) complexes, *Inorganic Chemistry*, **24**, 895.

Alliot C., Bion L., Mercier F., Vitorge P., Toulhoat P. (2005): Effect of aqueous acetic, oxalic and carbonic acids on the adsorption of americium onto alpha-alumina, *Radiochimica Acta*, **93**, 435.

Aucour A.M., Tao F.A., Moreira-Turcq P., Seyler P., Sheppard S., Benedetti M.F. (2003): The Amazon River: behaviour of metals (Fe, Al, Mn) and dissolved organic matter in the initial mixing at the Rio Negro/Solimoes confluence, *Chemical Geology*, **197**, 271.

Bünzli J.C.G. (1989): Luminescent probes. In *Lanthanides probe in life, chemical and earth sciences - Theory and practice* (J. C. G. Bünzli & G. R. Choppin Eds.), p. Elsevier.

Choppin G.R., Wang Z.M. (1997): Correlation between ligand coordination number and the shift of the $^7F_0$-$^5D_0$ transition frequency in europium(III) complexes, *Inorganic Chemistry*, **36**, 249.

Chung K.H., Lee W., Cho Y., Choi G., Lee C. (2005): Comparison of synchronous and laser-induced fluorescence spectroscopy applied to the Eu(III)-fulvate complexation, *Talanta*, **65**, 389.

Claret F., Schäfer T., Reiller P. (2007): Sorption induced fractionation of fulvic acids. In *2nd Annual Workshop Proceeding of integrated project "Fundamental processes of Radionuclide Migration" - 6th EC FP IP FUNMIG, SKB Report TR-07-05* (G. Buckau, B. Kienzler, L. Duro, & V. Montoya Eds.), p. 253. http://www.skb.se/upload/publications/pdf/TR-07-05webb.pdf.

Claret F., Schäfer T., Brevet J., Reiller P.E. (2008): Fractionation of Suwannee River fulvic acid and Aldrich humic acids on α-Al_2O_3: spectroscopic evidences, *Environmental Science and Technology*, **42**, 8809.

Frey S.T., Horrocks W.D. (1995): On correlating the frequency of the $^7F_0$->$^5D_0$ transition in Eu^{3+} complexes with the sum of nephelauxetic parameters for all of the coordinating atoms, *Inorganica Chimica Acta*, **229**, 383.

Horrocks W.D., Sudnick D.R. (1981): Lanthanide ion luminescent probes of the structure of biologicalmacromolecules, *Accounts of Chemical Research*, **14**, 384.

Johnson W.P., Bao G.B., John W.W. (2002): Specific UV absorbance of Aldrich humic acid: changes during transport in aquifer sediment, *Environmental Science and Technology*, **36**, 608.

Kim J.I., Buckau G., Li G.H., Duschner H., Psarros N. (1990): Characterization of humic and fulvic acids from Gorleben groundwater, *Fresenius Journal of Analytical Chemistry*, **338**, 245.

Kim J.I., Czerwinski K.R. (1996): Complexation of metal ions with humic acid: metal ion charge neutralization model, *Radiochimica Acta*, **73**, 5.

Kinniburgh D.G., van Riemsdijk W.H., Koopal L.K., Borkovec M., Benedetti M.F., Avena M.J. (1999): Ion binding to natural organic matter: competition, heterogeneity, stoichiometry and thermodynamic consistency, *Colloids and Surfaces A*, **151**, 147.

Marang L., Reiller P.E., Eidner S., Kumke M.U., Benedetti M.F. (2008): Combining spectroscopic and potentiometric approaches to characterize competitive binding to humic substances, *Environmental Science and Technology*, **42**, 5094.

Monsallier J.M., Scherbaum F.J., Buckau G., Kim J.I., Kumke M.U., Specht C.H., Frimmel F.H. (2001): Influence of photochemical reactions on the complexation of humic acid with europium(III), *Journal of Photochemistry and Photobiology A: Chemistry*, **138**, 55.

Moulin C., Wei J., van Iseghem P., Laszak I., Plancque G., Moulin V. (1999): Europium complexes investigations in natural waters by time-resolved laser-induced fluorescence, *Analytica Chimica Acta*, **396**, 253.

Moulin V., Tits J., Moulin C., Decambox P., Mauchien P., de Ruty O. (1992): Complexation behaviour of humic substances towards actinides and lanthanides studied by time-resolved laser-induced spectrofluorimetry, *Radiochimica Acta*, **58/59**, 121.

Ollier N., Panczer G., Campagnon B., Boulon G., Jollivet P. (2001): Europium as a luminescent probe of an aluminoborosilicate nuclear glass and its weathering gels, *Journal of Luminescence*, **94**, 197.

Panak P., Klenze R., Kim J.I., Wimmer H. (1995): A study of intramolecular energy-transfer in Cm(III) complexes with aromatic ligands by time-resolved laser fluorescence spectroscopy, *Journal of Alloys and Compounds*, **225**, 261.

Philippini V. (2007): Mise en évidence d'un changement de la stoechiométrie du complexe carbonate limite au sein de la série des lanthanides(III). Thèse de l'université Paris-Sud XI, Paris-Sud XI.

Reiller P., Amekraz B., Moulin C. (2006): Sorption of Aldrich humic acid onto hematite: Insights into fractionation phenomena by electrospray ionization with quadrupole time-of-flight mass spectrometry, *Environmental Science and Technology*, **40**, 2235.

Santschi P.H., Roberts K.A., Guo L.D. (2002): Organic nature of colloidal actinides transported in surface water environments, *Environmental Science and Technology*, **36**, 3711.

Schmeide K., Zänker H., Heise K.H., Nitsche H. (1998): Isolation and purification of aquatic humic substances from the Bog "Kleiner Kranishsee". In *Effects of humic substances on the migration of radionuclides: Complexation and transport of actinides. First technical progress report, FZKA Report 6124* (G. Buckau Ed.), p. 161. Forschungszentrum Karlsruhe - Institut für Nukleare Entsorgung.

Shin H.S., Rhee S.W., Lee B.H., Moon C.H. (1996): Metal binding sites and partial structures of soil fulvic and humic acids compared: Aided by Eu(III) luminescence spectroscopy and DEPT/QUAT C-13 NMR pulse techniques, *Organic Geochemistry*, **24**, 523.

Shin H.S., Choppin G.R. (1999): A study of Eu(III)-humate complexation using Eu(III) luminescence spectroscopy, *Radiochimica Acta*, **86**, 167.

Vercouter T. (2005): Complexes aqueux de lanthanides (III) et actinides (III) avec les ions carbonates et sulfates. Etude thermodynamique par spectrofluorimétrie Laser résolue en temps et spectrométrie de masse à ionisation électrospray, Evry-Val d'Essonne.

Wolf M., Buckau G., Geyer S. (2004): Isolation and characterization of new batches of Gohy-573 humic and fulvic acids. In *Humic Substances in Performance Assessment of Nuclear Waste Disposal: Actinide and Iodine Migration in the Far-Field. Second Technical Progress Report, Report FZKA 6969, http://bibliothek.fzk.de/zb/berichte/FZKA6969.pdf* (G. Buckau Ed.), p. 111. Forschungszentrum Karlsruhe - Institut für Nukleare Entsorgung.

DIFFUSION OF COBALT, CESIUM AND EUROPIUM IN OPALINUS CLAY

Miguel García-Gutiérrez[1*], José Luis Cormenzana [2], Tiziana Missana[1], Manuel Mingarro[1], Úrsula Alonso[1]

[1] CIEMAT, Departamento de Medio Ambiente (Madrid, SPAIN)
[2] Empresarios Agrupados (Madrid, SPAIN)

* Corresponding author: miguel.garcia@ciemat.es

Abstract

This study addresses the diffusion of some representative sorbing elements, as cobalt, caesium and europium into the Opalinus Clay (OPA). The methodology used to determine diffusion coefficients is the "instantaneous planar source" method. In this setup, a paper filter impregnated with the tracer, is introduced between two clay samples, avoiding the contact between the tracer and the experimental vessels.
The apparent diffusion coefficients (D_a) perpendicular to the bedding plane, obtained with this method, fitting the experimental results with an analytical solutions, were $D_a(Co) = (2.4\text{-}3.5)\cdot10^{-14}$ m^2/s, $D_a(Cs) = (5.9\text{-}8.0)\cdot10^{-14}$ m^2/s, and $D_a(Eu) = (1.0\text{-}2.1)\cdot10^{-15}$ m^2/s respectively. With cobalt and caesium, classical in-diffusion experiments were also performed and similar D_a values were obtained but within a large dispersion.

To analyze the possible effects of the paper filter impregnated with the tracer on the determinations of D_a, with the analytical solution, one experiment was also analysed using a detailed model of the setup. The good agreement between the two modelling approaches, confirms the validity of this experimental setup and the analytical model fitting procedure.

Introduction

Clay formations are being considered as potential host rocks for radioactive waste disposal in many countries. In these materials, that present low hydraulic conductivity, diffusion is the main transport mechanism for radionuclides accidentally released from the canisters.

The Mont Terri Underground Research Laboratory (URL) is located in a service gallery of the Mont Terri motorway tunnel, near St. Ursanne in north-western Switzerland, and drilled in the Opalinus Clay (OPA). The OPA is currently under investigation to demonstrate the basic feasibility of disposing of spent fuel, vitrified high-level waste and long-lived intermediate-lived waste in Switzerland.

Diffusion is a process by which the mass is transported from one part of a system to another, by random molecular motion. The mathematical description of diffusion is based on the Fick's laws, which have to be modified for porous media, as clays, because several interactions between solid phases and solutes exist. The nature of the ions, of the porous medium, as well as the specific geochemical conditions, influence the diffusion process (Grathwohl, 1998).

Several studies about diffusion behaviour of neutral (HTO), anionic elements (Br^-, I^-, Cl^-), and weakly sorbing cationic elements (Na^+, Sr^{2+}) on clay formations exist (Descostes et al., (2008); Appelo and Wersin (2007)), but only few studies are available for medium sorbing elements such as Cs (Van Loon and Eikenberg, 2005) and no studies for Eu, a highly sorbing element.

Diffusion studies with sorbing elements are not straightforward to carry out, because it is necessary taking into account their sorption on the diffusion cells and/or stainless-steel filters used in the experimental set-ups. Strongly sorbing elements as europium can not be easily studied using classical through-diffusion or in-diffusion methods, because of their strong adsorption onto laboratory materials (vessels, cells, tubing…), so that their contact with these an experimental tools has to be minimized.

To avoid the contact of the tracer with the cell materials, the "instantaneous planar source" or "thin source" method was used in this study, in which a paper filter impregnated with the tracer is placed between two samples of clay. About 200 days were necessary to obtain a good concentration profile for diffusion of cobalt and caesium, and more than 400 days were needed for europium diffusion.

Materials and methods

The OPA samples were collected in the Mont Terri URL, at a depth between -200 and -300 m below the surface from the overdrilling of the DI-A2 in situ diffusion experiment (Wersin et al., 2008) in which several non-reactive and reactive tracers were injected in a packed-off borehole. The OPA was deposited about 180 million years ago as marine sediment consisting of fine mud particles. The consolidated material has a density of 2.3 – 2.4 g/cm^3. It has a thickness of ~ 100 m and contains between 40 and 80% clay minerals (illite, illite/smectite mixed-layer, chlorite, kaolinite), 10-40% quartz, 6-45% carbonates, 0-8% feldspars, 0-1.7% pyrite and 0.1-0.5% organic carbon (Mazurek, 1998).

When a filter paper tagged with a tracer is located between two samples of clay sandwiched in a cell, the tracer can diffuse into each sample. The apparent diffusion coefficient (D_a) can be obtained fitting the tracer concentration profile in the samples, at the end of the experiment.

Cylindrical samples of OPA clay of approximately 2 cm of diameter are drilled perpendicular to the bedding plane and introduced in stainless-steel rings. A Whatman nº 54 paper spiked with the tracer is placed between the two clay samples. The ring is closed with 2 end-pieces and two sintered filters and the diffusion cell is introduced in a closed vessel to avoid humidity loss. After the experimental time needed, the cell is disassembled, the clay is sliced and the tracer activity is measured in each slice to obtain the concentration profile within the consolidated clay.

The experiments were performed using ^{60}Co, ^{137}Cs and ^{152}Eu as tracers. In all the cases, the activity was measured directly in the solid samples by gamma counting (in the Cs case by the gamma emitter Ba in equilibrium) using a Packard Cobra II auto-gamma counter.

With Cs and Co, classical in-diffusion (ID) experiments were performed too. In these experiments the cell with the sample is immersed into a large volume of synthetic OPA pore water (Pearson, 1998). Afterwards water saturation of the sample the tracer is added to the reservoir and it can enter through one side of the clay sample. After a given time, the diffusion cell is disassembled, the sample cut into slices, and the activity in each slice measured to obtain a concentration profile in the clay. More details can be found in García-Gutiérrez at al., (2006).

The results of the experiments are modelled using the analytical solution for the instantaneous injection of a solute in a 1D semi-infinite medium. If the mass of tracer M is injected uniformly across the cross-section of area A, and the initial width of the tracer source is infinitesimally small, the apparent diffusion coefficient is evaluated from the following analytical solution (Crank, 1975):

$$C(x,t) = \frac{M}{2 \cdot A\sqrt{\pi \cdot D_a t}} \exp\left(-\frac{x^2}{4D_a t}\right) \quad (1)$$

where C is the tracer concentration in the clay, and x and t the diffusion length and time, respectively.

The analytical solution (1) does not considerer any potential effects related to the finite thickness and sorption properties of the paper filter. To analyze the effect of the filter a 1D model of the experimental setup and detailed calculations were done for a caesium experiment that confirmed the validity of using the analytical solution.

Experimental results and modelling

Four experiments with each tracer were performed. A first group of 6 experiments were performed with diffusion times of approximately 120, 180 and 200 days, for Cs, Co and Eu respectively. The diffusion time was enough for obtaining an evolved profile for Cs and Co but not for Eu. The second group of 6 experiments lasted 200 days for Cs and Co and 433 days for Eu. Good concentration profiles were obtained, even for Eu. All the experiments were fitted and D_a was determined in all the cases using equation (1).

An example of the concentration profiles is shown in Figure 1 (Co after 200 days (left) and for Eu after 433 days (right).

The apparent diffusion coefficients (D_a) obtained fitting the experimental results with the equation (1) are: $D_a(Cs) = (5.9 - 8.0)\cdot10^{-14}$ m^2/s, $D_a(Co) = (2.4 - 3.5)\cdot10^{-14}$ m^2/s, and $D_a(Eu) = (1.0 - 2.1)\cdot10^{-15}$ m^2/s. The deviation on the calculated D_a, is very small in all the cases.

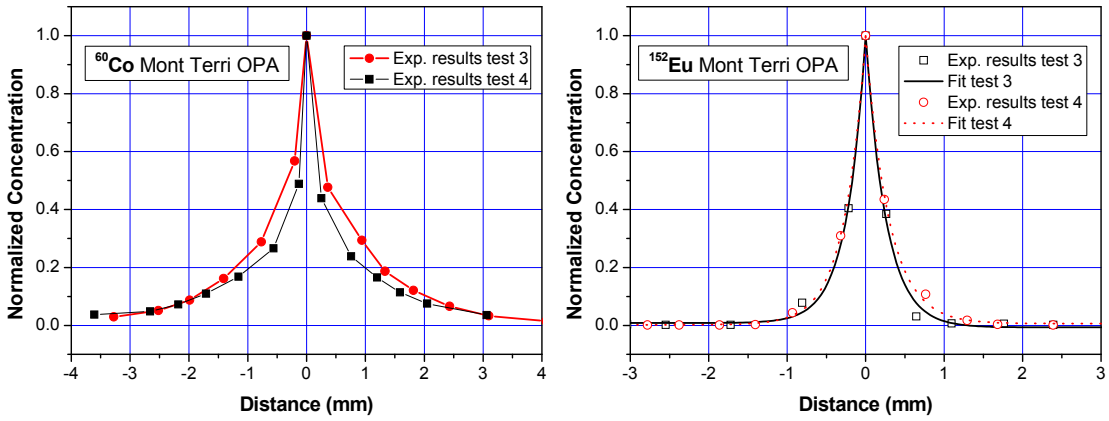

***Figure 1**: Experimental results of instantaneous planar source method. Left: Co concentration profiles after 200 days. Right: Eu concentration profiles and fits after 433 days of diffusion.*

ID experiments provided similar values but within a wider range: for caesium, $D_a(Cs) = (2.9 - 12)\cdot10^{-14}$ m^2/s and for cobalt, $D_a(Co) = (1.2 – 4.6)\cdot10^{-14}$ m^2/s.

Van Loon and Eikenberg (2005), using a high-resolution abrasive method for determining Cs diffusion profile, obtained a value for Cs diffusion of $D_a(Cs) = 5.6\cdot10^{-14}$ m^2/s (calculated from D_e and K_d values available in their work), which is in good agreement with the ranges of $D_a(Cs)$ presented here.

The "instantaneous planar source" method, followed by fit with the analytical solution, is therefore a simple and precise method to determine diffusion coefficients for sorbing elements.

In order to analyze completely the experiment accounting for the possible role of the paper filter in which the tracer is spiked, a detailed 1D model of the Cs experiment was done using GoldSim 9.60 computer code (GoldSim Technology Group, 2007). Wide probability distributions were assigned to all the transport parameters of the clay and the paper filter to take into account the uncertainty in the real values of these parameters. For clay the following ranges of values were used: porosity (0.08 to 0.20), porewater diffusion coefficient-D_p ($4\cdot10^{-11}$ to $5\cdot10^{-10}$ m^2/s), density of the solid (2400 to 3000 kg/m^3) and distribution coefficient-K_d (100 to 500 L/kg). For the paper filter the following ranges of values were used: porosity (0.3 to 0.7), porewater diffusion coefficient-D_p ($5\cdot10^{-10}$ to $2\cdot10^{-9}$ m^2/s), density of the solid (800 to 1600 kg/m^3) and distribution coefficient-K_d (200 to 1000 L/kg).

The probability distributions for the different parameters were sampled 2000 times, and for each set of values a complete diffusion calculation was done, and the activity in each slice was calculated. Of the 2000 calculations performed, only those in which the final concentration in the filter was similar to the measured value were retained. Around 500 individual calculations fulfilled this condition in the experiment with Cs presented here.

XY graphics were created representing the calculated activity in a given each slice (Y axis) vs. one of the 8 stochastic parameters (X axis), D_a(clay) and D_a(filter) in the approximately 500 calculations selected. Only for D_a(clay) a clear correlation was

observed, as shown in Figure 2 (left) for a clay slice near the filter. For the other 9 parameters correlation with the calculated activity is weak (as can be seen in Figure 2 (right) for K_d(clay) in the same slice. It can be seen in Figure 2 (left) that the activity in the slice depends nearly exclusively on D_a(clay). For a given value of D_a(clay) the range of values of the activity in the slice is very narrow, and includes the uncertainty in the transport parameters of the clay and the filter. In the other slices the same behaviour was observed.

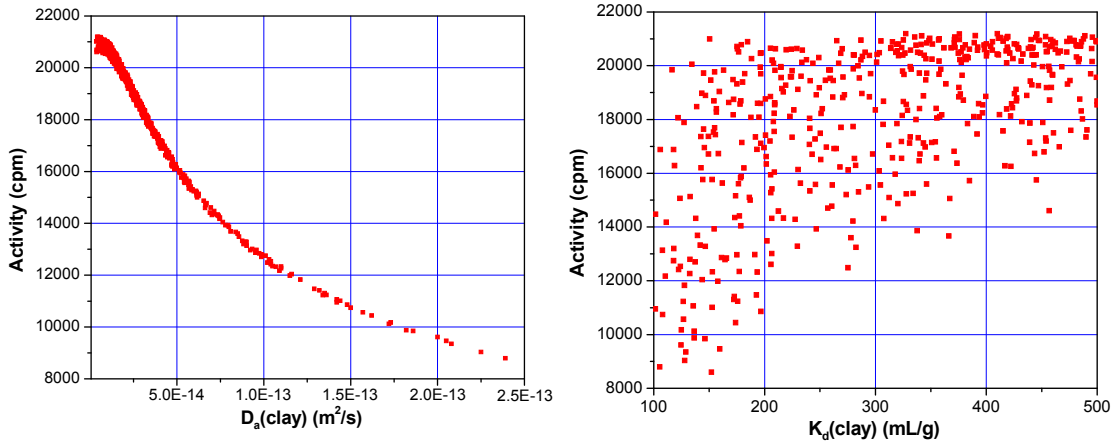

***Figure 2**: Calculated activity vs. D_a(clay) (left) or vs. K_d(clay) (right) in a slice near the filter in a Cs experiments using the detailed 1D model of the experiment.*

These results have been used to make a good estimation of D_a(clay). For each slice, a graphic of the calculated activity vs. D_a(clay) was done. From these graphs, and considering an uncertainty of ±5% in the activity measured, a range of D_a(clay) consistent with the activity measured in each slice was obtained. Figure 3 show the application for a slice, the band around the measured activity and the consistent range of D_a(clay) values. Combining the ranges of D_a(clay) values obtained for all the slices of the Cs experiment, a range of $D_a(Cs) = (6.0 - 9.1)\cdot10^{-14}$ m^2/s was calculated. The value obtained using the analytical solution in the same experiment was $D_a(Cs) = 8\cdot10^{-14}$ m^2/s, well centred in the range obtained with the detailed 1D model.

The good agreement between the values of D_a(Cs) obtained using the detailed 1D model and the simple analytical solution (that does not include the filter) confirm that: the effect of the paper filter is of small relevance, and it is appropriate to use the simple analytical solution (1) to model the “instantaneous planar source” experiments.

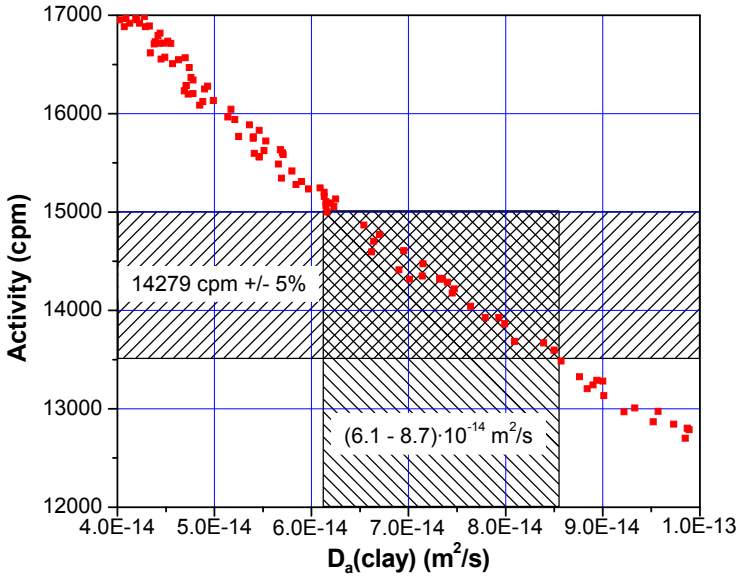

Figure 3. *Calculated activity vs. D_a(clay) in a slice of a Cs experiment. The ranges of experimental values (measured value ±5%) and the consistent D_a(clay) value are represented by bands.*

Summary and Conclusions

The "instantaneous planar source" was shown to be a simple and useful method to obtain apparent diffusion coefficients for sorbing elements (such as Cs and Co) and even for strongly sorbing elements, such as Eu in Opalinus Clay (OPA).

The experiments performed with the instantaneous source model can be modelled using the analytical solution for the instantaneous injection of solute in a 1D semi-infinite medium. The range of values for the apparent diffusion coefficients perpendicular to the bedding in OPA are: $D_a(Cs) = (5.9 – 8.0)\cdot10^{-14}$ m^2/s, $D_a(Co) = (2.4 – 3.5)\cdot10^{-14}$ m^2/s, and $D_a(Eu) = (1.0 – 2.1)\cdot10^{-15}$ m^2/s. The methods seems to be more precise than "conventional" in-diffusion tests where, for Cs and Co, D_a in the following ranges were obtained: $D_a(Cs) = (2.9 – 12)\cdot10^{-14}$ m^2/s and $D_a(Co) = (1.2 – 4.6)\cdot10^{-14}$ m^2/s.

D_a(Cs) values obtained in this work are in good agreement with the D_a value from Van Loon and Eikenberg (2005), $D_a(Cs) = 5.6\cdot10^{-14}$ m^2/s.

Acknowledgement

This work has been carried out in the frame of the ENRESA-CIEMAT association and partially funded by the EU within the FUNMIG (Fundamental Processes of radionuclide Migration) Project (Ref. FP6-516514).

References

Appelo, C.A.J., Wersin, P. (2007) "Multicomponent Diffusion Modeling in Clay Systems with Applications to the Diffusion of Tritium, Iodide, and Sodium in Opalinus Clay" Environ. Sci. Technol. 41, 5002-5007.

Crank, J. (1975) "The Mathematics of Diffusion", 2nd edition, Clarendon Press, Oxford.

Descostes, M., Blin, V., Bazer-Bachi, F., Meier, P., Grenut, B., Radwan, J., Schlegel, M.L., Buschaert, S., Coelho, D. Tevissen, E. (2008) "Diffusion of anionic species in Callovo-Oxfordian argillites and Oxfordian limestones (Meuse/Haute-Marne, France)" Applied Geochemistry 23, 655–677.

García-Gutiérrez, M., Cormenzana, J.L., Missana, T., Mingarro, M., Molinero, J. (2006) "Overview of laboratory methods employed for obtained diffusion coefficients in FEBEX compacted bentonite" J. of Iberian Geology 32 (1) 37-53.

GoldSim Technology Group, (2007). GoldSim User´s Guide. http://www.goldsim.com/

Grathwohl, P. (1998) "Diffusion in Natural Porous Media: Contaminant Transport, Sorption/Desorption and Disolution Kinetics" (Kluver Academic Publishers).

Mazurek, M. (1998) "Mineralogical composition of Opalinus Clay at Mont Terri. A laboratory intercomparation". Mont Terri Project Technical Note 98-41.

Pearson, F.J. (1998) "Opalinus Clay experimental water: A1 type, version 980318". Technical Report TM-44-98-07, Paul Scherrer Institut, Villigen, Switzerland.

Van Loon, L.R., Eikenberg, J. (2005) "A high-resolution abrasive method for determining diffusion profiles of sorbing radionuclides in dense argillaceous rocks" Applied Radiation and Isotopes, 63, 11-21.

Wersin, P., Soler, J.M., Van Loon, L., Eikenberg, J., Baeyens, B., Grolimund, D., Gimmi, T., Dewonck, S. (2008) "Diffusion of HTO, Br^-, I^-, Cs^+, $^{85}Sr^{2+}$ and $^{60}Co^{2+}$ in a clay formation: Results and modelling from an in situ experiment in Opalinus Clay" Applied Geochemistry 23, 678–691.

DIFFUSION OF ANIONIC SPECIES ($^{99}TcO_4^-$, $H^{14}CO_3^-$) AND HTO IN BODA CLAYSTONE BORECORE SAMPLES

Károly Lázár [1*], János Megyeri [1], Jean-Claude Parneix [2], Zoltán Máthé [3], Tibor Szarvas[1]

[1] Institute of Isotopes, Hung. Acad. Sci., Budapest, P.O.B 77, H-1525, HU
[2] ERM, rue Albin Haller, Espace 10, 86000 Poitiers, FR
[3] Mecsekérc Environmental, Esztergár L. 19. Pécs, H-7633, HU

* Corresponding author: lazar@iki.kfki.hu

Abstract

Diffusion rates of anionic species were determined on bore core samples originated from different depths of Boda Claystone formation (570 and 1000 m). Complementary characterisation of minerals was also performed. From break through measurements D_{eff} ~ 1 x 10^{-12} m^2 s^{-1} was obtained for $^{99}TcO_4^-$ and $H^{14}CO_3^-$, whereas the diffusion for HTO was faster, with D_{eff} ~ 1.4 x 10^{-11} m^2 s^{-1}.

Introduction

In the framework of the FUNMIG project various types of claystones (Callovo-Oxfordian, Opalinus, Boom) are extensively evaluated as for their properties playing role in the migration/retention processes of radionuclides from the aspect of the application as perspective media for storage of nuclear waste. A few measurements have also been performed on Boda Claystone samples.

The Boda Claystone exhibits particular features when comparing them to those of the previously mentioned clays. Namely, it is aged and consolidated, has low porosity, does not or only sporadically contains organic residues, etc. These properties are due to the particular paleoclimatic conditions of its genesis, when the sedimentation process had taken place in highy alkaline and oxidative waters at alternating drying up and semi-arid conditions. The formation was exposed to late and deep diagenetic alterations later, reaching temperatures c.a. 200 °C in the Lower Jurassic [Árkai et al.].

In the course of our studies samples exposed to different post diagenetic conditions resulting e.g. in different mineral composition were compared. They were collected from different dephts (570 and 1000 m). Principally, break through measurements were performed on bore core samples, and the primary information is the determination of the effective diffusion coefficients. In the present report we account on the later stage of studies and a summarizing comparing description is also given on the results of the measurements.

Characterization of the Boda Claystone samples used

Mineral composition

The mineral compositions of samples obtained from the different depths are characteristic and clearly show the different stages of the diagenesis.

Table1. *The main mineral constituents of Boda Claystone samples obtained from different depths (per cent)*

Component	570 m	~ 1000 m
Illite – muscovite	33	18
Analcime	23	-
Albite	12	59
Quartz	11	10
Calcite	9	2
Hematite	8	8
Chlorite	2	2
Smectite	2	2

High resolution XRD tomography

3D images of characteristic minerals were composed, e.g. showing the distribution of the fine grains of hematite (with the main diameter of a few microns). In the sample taken from 570 m depth more voluminous analcime particles were also displayed.

Porosimetry

Pore distribution determination was performed by autoradiography by high resolution imaging with ^{14}C-PMMA. The mean value of the porosity of the interconnected pores is centered around 2.5 % (± 0.5).

Mössbauer spectroscopy

Complementary Mössbauer measurements were also performed on the iron bearing components of the samples. The method is able to distinguish between the various oxidation states of iron (ferric and ferrous). The results are shown in Table 2 and Fig. 1.

Table 2. *Relative intensities of components in spectra of Figure 1.*

	570 m	1000 m
Hematite	64	59
Chlorite (Fe^{2+})	7	22
Fe^{3+} in other minerals	29	21

The diagenesis under oxidative conditions is clearly illustrated by the prevailing presence of hematite. The minor Fe^{2+} present in chlorite was probably formed in post diagenetic processes.

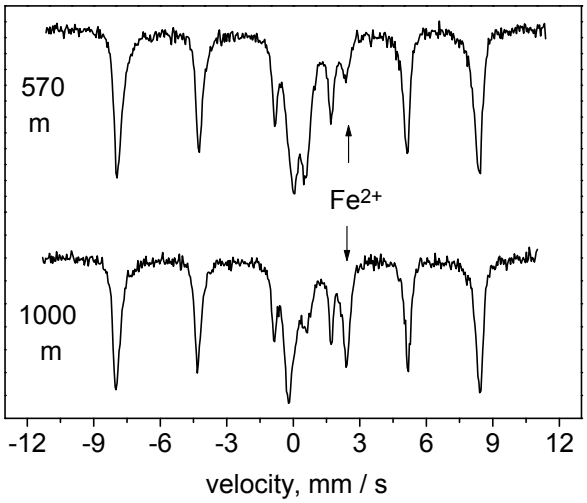

Figure 1. *Mössbauer spectra of the iron bearing components of Boda Claystone samples. The main component is hematite (sextet), the peak marked with Fe^{2+} belongs to chlorite.*

Break through measurements – determination of effective diffusion coefficients

Conventional break-through cells of cylindrical shape were used. The two outside compartments are separated with slices cut from the bore cores. These discs are located in the middle of cells. (The thickness of discs is c.a 8 mm, their diameters are 62 and 47 mm, for samples from 570 m and 1000 m, respectively). The compartments are filled with ground water, and one of them is spiked with radiotracer. The break through (the appearance and the increase of the concentration of the radiotracer in the opposite side) is measured in dependence of time. The effective diffusivity, D_{eff}, can be calculated from:

$$C(t) / C_0 = (A D_{eff}) t / (VL) - (\alpha A L) / 6V \quad , \qquad \text{(Eq. 1)}$$

where

C stands for the count rates, $C(t) / C_0$ is the relative activity change in the solution,
A: is the cross section of the sample disc,
D_{eff}: is the effective diffusivity coefficient,
V': is the volume of the solution in the cell,
L: is the thickness of the bore core disc,
t: is the time elapsed,
α: is the so-called rock capacity factor.

For the break-through experiments the ground water was spiked with $^{99}TcO_4^-$ (6.2 MBq, resulting in a concentration of 5 x 10^{-4} mol /L), $H^{14}CO_3^-$ (8 MBq, resulting in negligible change of the original concentration of HCO_3^- present in the ground water), and HTO (10 MBq). 20 microliter samples were taken regularly from the compartments, the activities of radioisotopes were measured by liquid scintillation detection in them. Break through measurements were performed at different conditions as shown in Table 3. Parallel measurements have been performed at each conditions, thus, 14 measuring cells were used altogether (Table 3).

Table 3. *List of measurements performed on the various samples*

Sample from	570 m	1000 m	1000 m
pH of water	8	8	12
$^{99}TcO_4^-$	X	X	X
$H^{14}CO_3^-$	X	X	X
HTO	X	n/a	n/a

Ground water

For the experiments synthetic ground water was used. The main ionic components are shown in Table 4.

Table 4. *Concentrations of the main components in the ground water (mili equiv/l*)

Cations		Anions	
Na^+	15.2	HCO_3^-	12.3
Ca^{2+}	0.3	SO_4^{2-}	2.5
Mg^{2+}	0.4	CO_3^{2-}	1.0
K^+	0.2	Cl^-	0.5

Break through of $^{99}TcO_4^-$

Through diffusion of $^{99}TcO_4^-$ follows the expected behaviour. Its break through commences at the early stage, indicating the lack of retarding interactions with the rock. Hence, the difference of the mineral composition of the two samples (570 and 1000 m depth) is not manifested. The rate of break through (the increase of activity) is linear in the $a/a_0 < 0.1$ region. From the initial slopes $D_{eff} \sim 1 \times 10^{-12}$ m^2 s^{-1} can be calculated (Fig. 2).

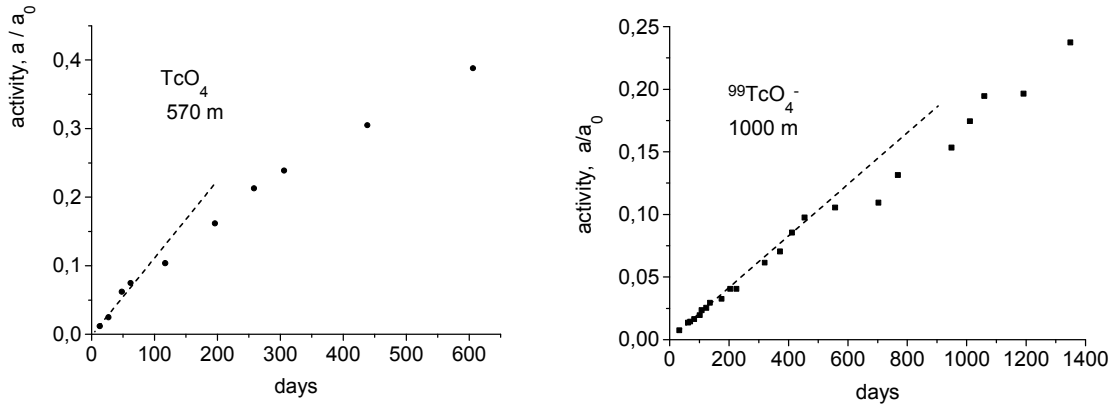

Figure 2. *Break through curves obtained for $^{99}TcO_4^-$ on samples from 570 (left) and 1000 m (right). pH of ground water is 8.*

Break through of $H^{14}CO_3^-$

$H^{14}CO_3^-$ exhibits similar rate for break through at pH = 8 than $^{99}TcO_4$, i.e. the same $D_{eff} \sim 1 \times 10^{-12}$ m^2 s^{-1} value can be estimated. The same value can be found at the measurements at pH = 12, with a noticeable difference. Namely, at pH = 12 the so

called rock capacity factor is significant. Two samples were measured with slightly different mineral compositions (Fig. 3).

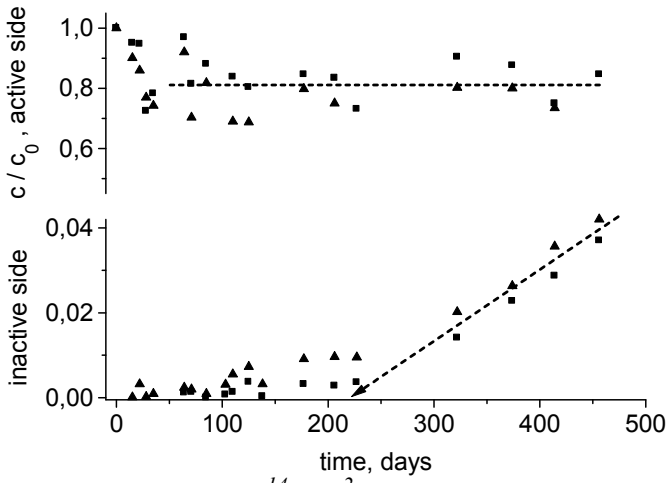

Figure 3. *The relative activities of $^{14}CO_3^{2-}$ in the active (top) and originally inactive (bottom) compartments at pH = 12. The delay in the commencement of the break through indicates the interaction between the solute and solid phases. (Two samples of different mineral compositions were measured distinguished by ▲ and ■ marks .)*

For the interpretation of the retarded start of break through formally Eq (1) may be applied. From the intercept with the X axis is the value of α (rock capacity factor) can also be calculated, the value is c.a. 1. For non-sorbing tracers the value of α is expected to be equal with the diffusion acessible porosity, ε, in a usual range $\varepsilon < 0.1$ [Van Loon, et al.]. The apparent value of α found in our measurements is an order of magnitude larger. For explanation it should be mentioned that the $OH^- + HCO_3^- <=> H_2O + CO_3^{2-}$ equilibrium is shifted to the right at pH = 12, i.e. the HCO_3^- present in large concentration in the ground water (Table 3) is converted to CO_3^{2-}. Under these conditions isotope exchange may proceed between the solid phase carbonates of the rock (e.g calcite, dolomite) and the carbonate anions in the solution. Thus, the large apparent value is probably a consequence of combination with isotope exchange processes as well.

Break through of HTO

The break through of HTO was measured in the sample originated from 570 m. From the initial slope fast diffusion can be calculated, namely $D_{eff} \sim 1.4 \times 10^{-11}$ m^2 s^{-1}. The break through curves exhibit a certain decline in the total activity of HTO. This can probably be attributed to the exchange of HTO with structural water and/or water of secondary pores (Fig. 4).

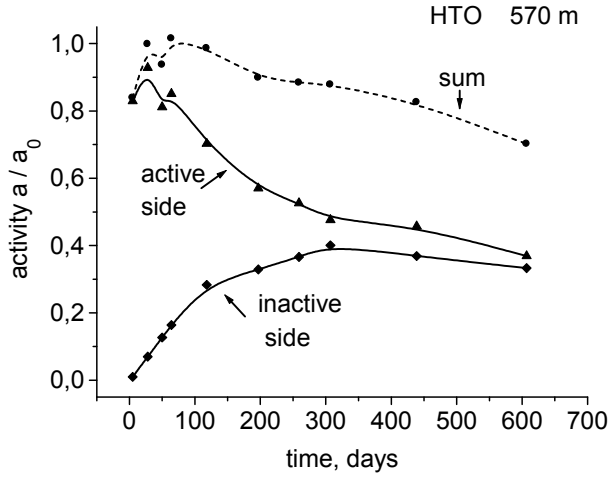

Figure 4. *Break through curve of HTO in sample from 570 m depth*.

Summary and Conclusions

D_{eff} ~ 1 x 10^{-12} m^2 s^{-1} were calculated for anionic non-interacting $^{99}TcO_4^-$ and $H^{14}CO_3^-$at pH = 8 on Boda Claystone samples. Similar D_{eff} was observed for $H^{14}CO_3^-$ at pH = 12, with significant interaction most probably with the carbonate minerals. The diffusion of HTO is considerably faster, $D_{eff, HTO}$ ~ 1.4 x 10^{-11} m^2 s^{-1} was observed.

These data are in good correspondence with those found for the $^{125}I^-$ in Boda Claystone [Mell et al.] and TcO_4^- and HTO in other clayrocks (Opalinus, and Callovo-Oxfordian) [Altmann et al.].

References

Altmann., S., Tournassat, Ch., Goutelard, F., Parneix, J.-C., Gimmi, T., Maes, N., Radionuclide migration in clay rich formations: Process understanding, integration and up-scaling for safety case use (RTDC3 & 1), EURADWASTE08, Oct. 20-23, Luxembourg.

Árkai, P., Balogh, K., Demény, A., Fórizs, I., Nagy, G., Máthé, Z., (2000) Composition, diagenetic and post-diagenetic alterations of a possible radioactive waste repository site: the Boda Albitic Claystone Formation, southern Hungary, *Acta Geologica Hungarica*, **43**, 351 - 360.

Mell, P., Megyeri, J., Riess, L., Máthé, Z., Hámos, G., Lázár, K. (2006) Diffusion of Sr, Cs, Co and I in argillaceous rock as studied by radiotracers, *Journal of Radioanalytical and Nuclear Chemistry* **268,** 411 – 417.

Van Loon, L.R., Soler, J.M., Bradbury, M.H., (2003) Diffusion of HTO, $^{36}Cl^-$, $^{125}I^-$ in Opalinus Clay samples from Mont Terri. Effect of confining pressure, *Journal of Contaminant Hydrology* **61,** 73 – 83.

EFFECT OF S(-II) DRIVEN CONVERSION OF IRON OXIDES TO FeS ON URANIUM MOBILITY

Vasso Alexandratos*, Thilo Behrends, Philippe Van Cappellen

Department of Earth Sciences – Geochemistry, Utrecht University (NL)

* Corresponding author: vasso@geo.uu.nl

Abstract

The mobility of uranium in natural environments is directly dependent on redox conditions. Adsorption onto iron oxides and formation of aqueous carbonate complexes are antagonistic processes affecting the mobility of U(VI). U(IV) is considered to be virtually immobile due to the low solubility of U(IV) minerals such as uraninite or pitchblende. This study investigates possible redox transformations of uranium under transient redox conditions. Specific focus lies on the fate of U as reductive dissolution of iron oxyhydroxides by S(-II) is initiated. In batch experiments sulfide was incrementally added to a lepidocrocite suspension containing adsorbed U(VI). The partitioning of uranium was monitored during the progressing transformation of lepidocrocite into FeS. Synchrotron-based X-ray absorption spectroscopy was used to resolve the oxidation state of uranium and to determine its coordination environment. Upon addition of sulfide intermediate release of U from the solid to the solution was observed. The mobilization of U was followed by immobilization in a later stage of the experiment but dissolved U concentration remained higher than before S(-II) addition within the time scale of the experiment. XAS reveals that the immobilization of U after S(-II) addition coincides with reduction of U(VI) to U(IV). However, the formation of uraninite, the expected product of U(VI) reduction under the experimental conditions, appears not to occur instantaneously upon U(VI) reduction but to proceed significantly slower than the reduction. Consequently, reduction of U(VI) and precipitation of U(IV) solids, due to a shift from oxic to sulfate reducing conditions is possible. However, kinetic effects might lead to an intermediate mobilization of U that should be considered for the risk assessment of nuclear waste repositories and the remediation of sites, contaminated with radionuclides

Introduction

Abiotic and microbial processes effecting uranium mobility in subsurface environments has been investigated in numerous studies due to their importance for the performance assessment of nuclear waste repositories and the remediation and risk assessment of sites contaminated with uranium. Some of these processes include uranium sorption on mineral surfaces and redox transformation of U(VI) to its reduced

form U(IV), leading to uranium precipitation and thus removal from an aquatic system (e.g. Morse and Choppin, 1991).

Subsurface environments are characterized by ongoing changes in redox conditions that influence not only the mobility of redox-sensitive uranium species but also induce changes in iron mineralogy with which uranium is closely associated. Iron oxides can significantly influence uranium transport by acting as a sorbent for uranyl. Macroscopic experiments and spectroscopic analyses have generally supported a strong adsorption of uranyl to iron oxides by forming inner sphere complexes at the mineral surfaces (e.g. Ho and Miller, 1986; Manceau et al., 1992; Waite et al., 1994; Giammar and Herring, 2001; O'Loughlin et al., 2003). Consequently, once uranium occurs in the environment as adsorbed onto iron oxides, changes in the redox regime, from oxic to anoxic and vice versa, will influence the mobilization of uranium.

When microbes use sulfate reduction as a main respiratory pathway, it results in the production of sulfide. The kinetics of reductive dissolution of iron oxides by S(-II) are well established (e.g. Poulton, 2003; Peiffer et al.,1992; Afornso & Stumm, 1992). In contrast, little is known not only about the kinetics of U reduction by S(-II) but the overall fate of uranium once its related substrate undergoes mineral transformation (e.g. Behrends & Van Cappellen, 2005; Liger et al., 1999). Field observations indicate that, contrary to thermodynamic considerations, stimulation of sulfate reduction in subsurface environments might lead to the mobilization of uranium instead of its immobilization by reduction (Anderson et al., 2003). In another case uranium as U(VI) does occur in anoxic bottom waters with high sulfide concentrations indicating that homogeneous reduction of U(VI) by S(-II) is kinetically hindered (Anderson et al., 1989). This implies that U(VI) adsorbed to iron oxides might be mobilized when the reductive dissolution of Fe(III) is faster than the reduction of U(VI) and Fe possibly outcompetes U as an oxidant for S(-II).

Here, we experimentally investigated the possibility of U mobilization upon reductive dissolution of iron oxides with adsorbed U(VI) by S(-II) and evaluate whether U(VI) can be reduced. Efforts began with an abiotic system where sulfide was incrementally added to a lepidocrocite suspension with preadsorbed U(VI). Our main purpose was to characterize the redox state and binding environment of uranium that is associated with lepidocrocite during the reaction with sulfide, and address the level of competition between uranium and iron reduction by sulfide and how could it play a further role in uranium transport within natural environments.

Methods and Materials

In a pH stat reactor U(VI) acetate was added to lepidocrocite suspension. After adsorption equilibrium was reached, variable amounts of S(-II) (in the form of sodium sulfide solution) were added and the partitioning of uranium, changes in iron redox state, and iron oxide mineralogy were monitored. Multiple sets of experiments were performed. Specifically, a first set of three suspensions with total uranium concentrations of 3, 6 and 12 uM was reacted with similar amounts of sulfide (8-10 mM), and a second set with identical uranium concentrations (6 uM) was reacted with varying amounts of sulfide (1, 5 and 8 mM). The pH during the reduction experiments was 8, the ionic strength was adjusted to 0.1M by adding NaCl solution. Sample

collection took place throughout the duration of the experiments. Concentrations of dissolved S(-II), U and Fe(II) were obtained with the use of ICP-MS and standard photometric methods after filtrating aliquots of the suspension. The solids were recovered by centrifugation and freeze dried for X-ray adsorption spectroscopy (XAS). For XAS, solid samples were prepared as pellets and were air tight sealed to avoid oxidation of reduced iron or uranium by oxygen during transportation. All experiments and sample manipulations were performed in a glove box under N(95%)-H(5%) mixed atmosphere. Collection of spectra took place at the FAME BM30M beamline, at the ESRF in Grenoble, France. XAFS spectra were recorded in the fluorescence mode at the U L_{III}-edge (~17.17 keV) in a cryostat at about 30K. For energy calibration, Y foil (K-edge = 17.038 keV) was used. Fitting of EXAFS spectra were done my using Artemis v. 0.8.11 (Ravel and Newville, 2005). The paths used in EXAFS fitting are listed in Table 1.

Table 1: *List of paths used in the EXAFS fitting. R_{ini} are the initial path lengths obtained from theoretical models. ΔR and σ^2 are parameters which were optimised in addition to the degeneracy of each pathway. The passive electron reduction factor S_0^2, was set to one and for each sample ΔE_0, an energy shift used to align the EXAFS spectra to the theory by shifting the E_0 used in the theory, was optimised. Not all paths were used for fitting the spectra of every sample.*

Path	R_{ini} [Å]	ΔR	σ^2
$U \rightarrow O_{ax}$	1.81	ΔR_1	σ^2_1
U→O2	2.37	ΔR_2	σ^2_2
U→O3	2.37	ΔR_3	σ^2_2
U→O4	2.37	ΔR_4	σ^2_2
$U \rightarrow O_{ax,1} \rightarrow U \rightarrow O_{ax,1}$	$2R(U \rightarrow O_{ax})$	$2\,\Delta R_1$	$4\sigma^2_1$
$U \rightarrow O_{ax,1} \rightarrow U \rightarrow O_{ax,2}$	$2R(U \rightarrow O_{ax})$	$2\,\Delta R_1$	$2\sigma^2_1$
$U \rightarrow O_{ax} \rightarrow O_{ax} \rightarrow U$	$2R(U \rightarrow O_{ax})$	$2\,\Delta R_1$	$2\sigma^2_1$
U→Fe	3.87	ΔR_5	σ^2_3
U→U	3.87	ΔR_6	σ^2_4

Results and Discussion

In all experiments mineral transformation from lepidocrocite to iron sulfide occurred by the very first sulfide injection in our system, an effect that was visible by the color change of the suspension. All added S(-II) was consumed within the first two hours after the initial sulfide injection, (Figure 1 shown as representative). The consumption of S(-II) was predominantly coupled to the production of Fe(II). A notable increase in Fe(II) concentrations in both solution and solid was observed.

Prior to sulfide addition to the system, the concentration of dissolved uranium (U(aq)) was below detection limits indicating the strong adsorption onto lepidocrocite. Each S(-II) addition induced an instantaneous increase in U(aq) concentration, reaching

levels up to about 5% of the total uranium concentration added to the system. U(aq) levels decreased after each S(-II) addition, however complete re-adsorption on the solid phase did not occur (Figure 1). Preliminary results suggested that the instantaneous mobilization and elevated concentrations of uranium in solution after sulfide addition might be due to 1) a loss of sorption sites during iron mineral transformation 2) competition between uranium and Fe(II) for reactive surface sites, 3) possible formation of uranium complexes with sulfides in solution (e.g. polysulfides). However, based on results from control experiments in which the iron oxide was replaced by silica gel we concluded that the initial mobilization of uranium was predominately caused by the loss of hydroxyl groups at the iron oxide surface due to adsorption of sulfide via a ligand exchange mechanism and lower tendency of U(VI) to form complexes with thiol than with hydroxyl groups.

The decrease in U(aq) concentration after one hour of reaction time may also suggest a possible re-immobilization caused by reduction of uranium and the precipitation of uraninite. Specifically, XAFS analysis on collected solids indicated successive transformation of U(VI) into U(IV) within hours; this is reflected in the decrease of the coordination number of axial oxygens. Figure 2 shows XANES spectra collected from samples of one of the experiments as a time-series. Formation of a U containing precipitate during the experiments is indicated by the appearance of U-U interactions in the EXAFS spectra (Figure 3a). The distance of the U-U scattering path (about 3.81 Å) is close but slightly shorter than the U-U distances in uraninite (3.87 Å) indicating the formation of a kind of UO_2.precipitate. The degeneracy of the path was for all samples below 2, which is significantly less than the U-U coordination number of 9 in uraninite. This suggests the formation of very small particles or only partial binding of U(IV) in the UO_2 precipitate. The formation of the precipitate seems not to occur instantaneously upon U(IV) formation but to be a slower process than U(VI) reduction. The contribution of U-U interactions as a feature was found more pronounced in experiments with highest FeS formation. This led us to the conclusion that FeS is the dominant reductant for U(VI) in these systems and interactions between U(VI) with FeS might be of significant importance for controlling the mobility in environments with ongoing microbial sulfate reduction. Evidence for sorption and reduction of U(VI) by the crystalline sulfides galena and pyrite has been given by Wersin et al. (1994), however very little is know about the interactions of U(VI) with amorphous FeS.

Summary and Conclusions

Feasibility of U(VI) reduction within the time scale of hours/day has been demonstrated. Despite the reduction of U(VI), dissolved U concentration in the system were higher than before S(-II) addition, in particular, shortly after S(-II) addition. This implies the possibility of U mobilization upon reduction of Fe-oxides with adsorbed U. Reasons for U mobilization might be the decrease of U(VI) adsorption upon exchange of OH^- with SH^- surface groups and the relatively slow formation of uraninite particles.

Table 2: *Optimised values for ΔE_0 and the degeneracy for the U-O_{ax} and U-U paths for the different samples. Missing numbers indicate that the paths was not used in the model.*

Reaction time [h]	ΔE_0 (eV)	N (U→O_{ax})	N (U→U)
0.	-2.9	2.0 ± 0.6	
2h	3.6	0.8 ± 0.3	
4h	1.4	0.5 ± 0.3	1.1 ± 1.2
24h	1.3	0.4 ± 0.3	1.7 ± 0.8
48h	0.5	0.4 ± 0.3	1.8 ± 1.0

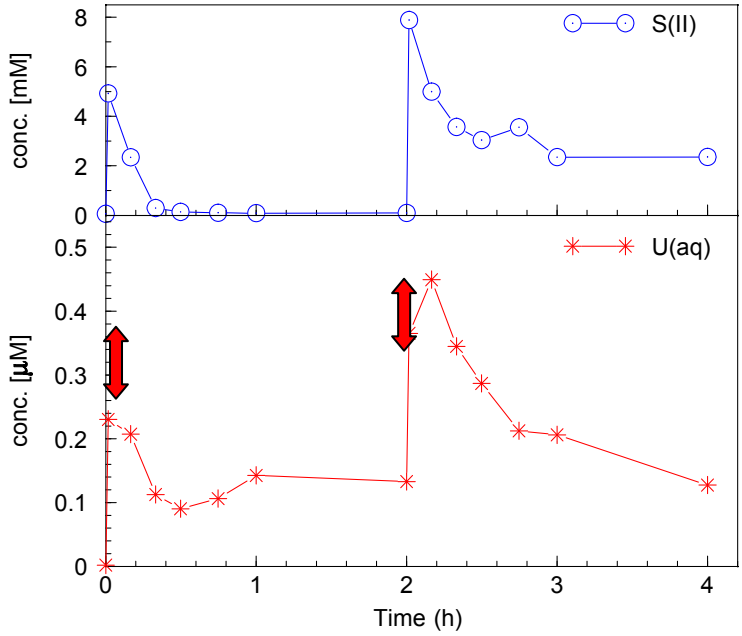

Figure 1: Top graph (blue) shows the kinetics of S(II) consumption after every addition, the first at 0 hours and the second at 2 hours. The graph below (red) shows the phase distribution of uranium in response to sulfide addition. Red arrows indicate the timings of S(II) addition. This figure shows representative profiles for sulfide and uranium analysis in solution from one of the six in total experiments.

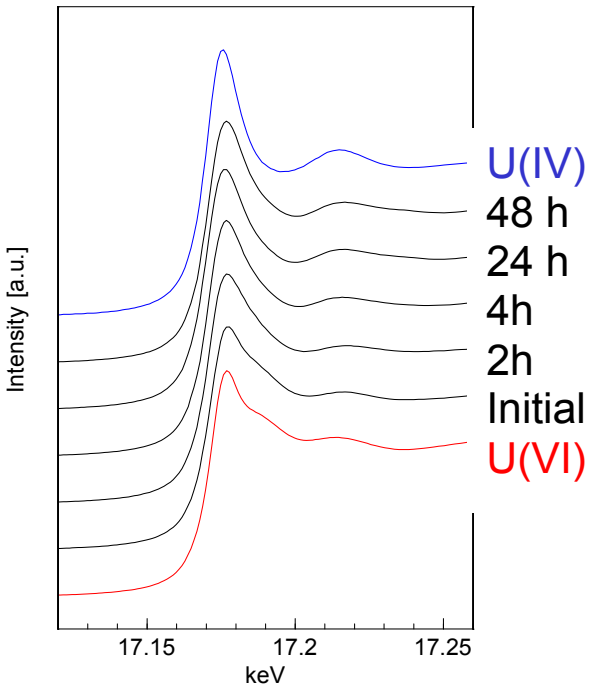

Figure 2: XANES spectra showing reduction of uranium as a function of time (hours). In this suspension 1 g/L of lepidocrocite was reacted with 12 uM U_{tot} and after equilibrium (24h) sulfide was added in the form of two injections (8 mM each). Highlighted with colors red and blue are the spectra used as standards for U(VI) and U(IV) respectively. Solid samples start at the initial state (Initial), where U(VI) is adsorbed by lepidocrocite. Samples after S(-II) additions were collected at 2, 4, 24 and 48 hour of reaction.

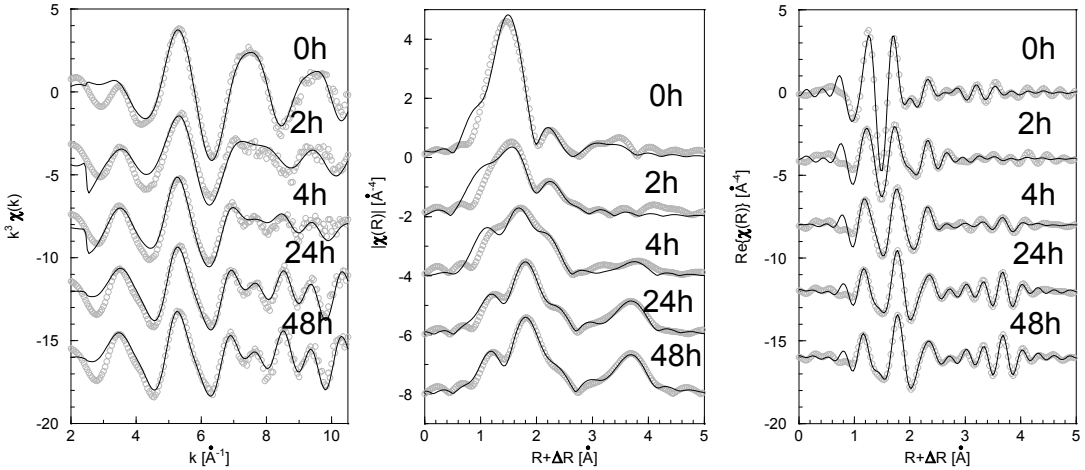

Figure 3: Results from EXAFS fitting presented for the k^3 weighted EXAFS spectra and the magnitude and real part of the Fourier transformed spectra from left to right. In this experiment 1 g/L of lepidocrocite was reacted with 12 uM U_{tot} and after equilibrium (24h) sulfide was added in the form of two injections (8 mM each). The sequence of spectra from top to bottom are from samples retrieved before S(-II) addition (0h) and after 2, 4, 24, and 48 h of reaction.

Acknowledgement

Authors are greateful to Dr A. Scheinost from the FZR for his assistance in the collection and analyses of XAS data as well as O. Proux and the staff from the FAME beamline at the ESRF for technical support. We also thank the ESRF for funding XAS experiments but also the EU for financial support (FUNMIG). **References**

Afonso M. dos Santos and Stumm Werner (1992), Reductive Dissolution of Iron(III) (Hydr)oxides by Hydrogen Sulfide, Langmuir, 8, 1671-1675.

Anderson RF, Fleisher MQ, LeHuray AP. 1989. Concentration, oxidation state and particulate flux of uranium in the Black Sea. Geochim. Cosmochim. Acta 53: 2215-2224.

Anderson R.T., Vrionis H. A., Ortis - Bernad I., Resch C. T., Long P.E., Dayvault R., Karp K., Marutzky S., Metzler D. R., Peakock A., White D. C., Lowe M., Lovely D. R., (2003) Stimulating in situ activity of *Geobacter* species to remove uranium from the groundwater of a uranium-contaminated aquifer. Appl. Environ. Microbiol. 69 (10), 5884-5891.

Behrends T. and Van Cappellen P. (2005), Competition between enzymatic and abiotic reduction of uranium(VI) under iron reducing conditions. Chemical Geology 220, pp. 315-327.

Giammar D.E and Herring J. G., (2001) Time scales for sorption-desorption and surface precipitation of uranyl on goethite. *Environ. Sci. Technol*. 35, 3332-3337.

Ho C. H. and Miller N. H. (1986) Adsorption of uranly species from bicarbonate solution onto hematite particles. *J. Colloid Interf. Sci.* 110, 165–171.

Liger E., Charlet L. and Van Cappellen P. (1999) Surface catalysis of uranium (VI) reduction by iron(II). Geochim. Cosmochim. Acta, 63, 2939-2955.

Morse J. W. and Choppin G. R. (1991) The chemistry of transuranic elements in natural waters. *Rev. Aquatic Sci. 4, l-22.*

Manceau A., Charlet L., Boisset M. C., Didier B., and Spadini L. (1992) Sorption and speciation of heavy metals on hydrous Fe and Mn oxides. From microscopic to macroscopic. *Applied Clay Sci.* 7, 201–230.

O'Loughlin , E.J., Kelly S.D., Cook R. E., Csencsits R., Kemner K.M., (2003) Reduction of uranium(VI) by mixed iron(II)/iron(III) hydroxide (green rust): Formation of UO2 nanoparticles. *Environ. Sci. Technol.* 37, 721-727.

Peiffer S., Afonso M., Wehrll B., Gachter R. (1992), Kinetics and Mechanism of the Reaction of H_2S with Lepidocrocite.,Environ. Sci. Technol., 26, 2408-2413.

Poulton, S.W. (2003) Sulfide oxidation and iron dissolution kinetics during the reaction of dissolved sulfide with ferrihydrite. Chemical Geology, 202, 79-94.

Ravel B. and Newville M. (2005) ATHENA, ARTEMIS, HEPHAESTUS: data analysis for x-ray absorption spectroscopy using IFEFFIT. *Journal of Synchrotron Radiation* **12**(4), 537-541.

Waite T. D., Davis J. A., Payne T. E., Waychunas G. A., and Xu N. (1994) Uranium(VI) adsorption to ferrihydrite: Application of a surface complexation model. *Geochim. Cosmochim. Acta* 58, 5465–5478.

Wersin P. Jr., Peresson P., Redden G., Leckie J. O., Harris D. W., (1994) Interaction between aqueous uranium (VI) and sulfide minerals: Spectroscopic evidence for sorption and reduction., *Geochim. Cosmochim. Acta* 58, 2829-2843.

EFFECTS OF EDTA ON SORPTION OF EU(III) AND NI(II) TO SOME MINERALS AT pH 6

Tara Lewis[1], Nick Evans[2*], Nick Bryan[3], Peter Warwick[2]

[1] Formally Department of Chemistry, Loughborough University, Loughborough, Leics, LE11 3TU (U.K.), now RWMD, NDA, Curie Avenue, Harwell, Oxon, OX11 0RH (U.K.)
[2] Dept. of Chemistry, University of Loughborough, Loughborough, LE11 3TU (U.K.)
[3] Centre for Radiochemistry Research, School of Chemistry, The University of Manchester, Oxford Road, Manchester, M13 9PL (U.K.)

*Corresponding author: n.d.m.evans@lboro.ac.uk

Abstract

Sorption behaviour of Eu(III) and Ni(II) onto montmorillonite, kaolinite and goethite in the presence of various concentrations of EDTA was studied. In general the presence of EDTA reduced the extent of Eu(III) and Ni(II) sorption onto the minerals, although the extent varied for each metal, with Eu sorption being more affected by increased EDTA concentrations. This may be explained by the differences the co-ordination chemistry of each metal to the EDTA and/or mineral surface.

Introduction

Anthropogenic organics such as EDTA can affect the sorption behaviour of metal ions [1]. The ligands may interact with specific sites on mineral surfaces, and so long as one or more ligand donor groups remain free, the ligand can facilitate metal ion sorption by acting as a bridge between the mineral surface site and the metal ion (i.e. type A ternary complex formation) thereby retarding their migration [2]. However, such ligands can also reduce metal sorption onto mineral surfaces and enhance metal mobility by forming stable water soluble complexes [3].

Several studies have been performed that have demonstrated the effect of EDTA on the solubility and sorption of heavy metals such as Ca, Mg, Ni, Co, Cu, Zn, Cd, and Fe in natural mineral/water systems [4][5][6]. The presence of EDTA has been shown to completely inhibit any sorption of metals such as Ni and Co to hydrous oxides under certain conditions [7]. Where ternary metal EDTA mineral complexes have been shown to exist it has been postulated that metal EDTA species adsorb at a 1:1 metal to EDTA ratio [8]. These studies have indicated that divalent metal-EDTA complexes can be highly sorbing onto goethite. To a lesser extent trivalent metal-EDTA complexes [9] and tetravalent-EDTA complexes [10][11][12][13] have also been studied, producing results that suggest these complexes are less sorbing due to the coordination of all the

carboxylic groups of the organic ligand with the metal ion, whereas in the case of a divalent metal complex one carboxylic group is free to coordinate with the mineral [14].

In this study the sorption of a trivalent and divalent metal ion (Eu^{3+} and (Ni^{2+}) on 2 clay minerals and goethite in the presence of varying concentrations of sodium EDTA was examined, to contrast the behaviour of 'simple' organics with the work preformed earlier on humic substances in identical conditions.

Experimental

Sorption of Eu(III) and Ni(II) in the presence of EDTA was studied by the batch sorption technique. Sigma Aldrich montmorillonite and kaolinite and Fluka alpha goethite (BET surface areas 267 $m^2\ g^{-1}$, 11 $m^2\ g^{-1}$, and 9.22 $m^2\ g^{-1}$, and total exchange capacities 22.6, 8.73, and 2.38 meq/100g, respectively) were used as supplied. Systems were prepared with 1 g of solid in triplicate as well as controls without solid. 20 cm^3 of EDTA at varying concentrations, in 0.1 mol dm^{-3} MES, at pH 6, were added. 0.1 cm^3 of active stock solution (^{152}Eu or ^{63}Ni) were weighed into each vial. The vials were then shaken on a 'Whirlimixer' for 30 s, followed by equilibration for 28 days at ambient temperature with constant shaking at 300 rpm. After filtration the activity of an aliquot was measured on a Packard Cobra 2 Auto Gamma Spectrophotometer (^{152}Eu), or a TRI-CARB 2750 TR/LL Liquid Scintillation Counter (^{63}Ni).

Results and Discussion

In studying the effect of EDTA on the sorption of Eu(III) and Ni(II), it is important to know which species dominate the speciation of each metal at the specific conditions prevailing in the system (pH = 6, I = 0.1 mol dm^{-3}). Calculations were performed using critically selected and estimated stability constants from the JCHESS Database [15] using the speciation programme JCHESS, for metal concentrations of 1 x 10^{-6} mol dm^{-3}. The J-plots are shown in Figures 1 and 2. These indicate that at pH 6 both Eu(III) and Ni(II) should remain mostly as their respective simple cations.

Data for the measured sorption of Eu^{3+} and Ni^{2+} to the clay minerals in the presence of varying amounts of EDTA are shown in Figures 3 and 4. These results show that in the presence of EDTA the fraction of Eu^{3+} sorbed is reduced across the entire EDTA concentration range. The same trend can be seen for nickel sorption to montmorillonite, kaolinite and goethite in the presence of EDTA.

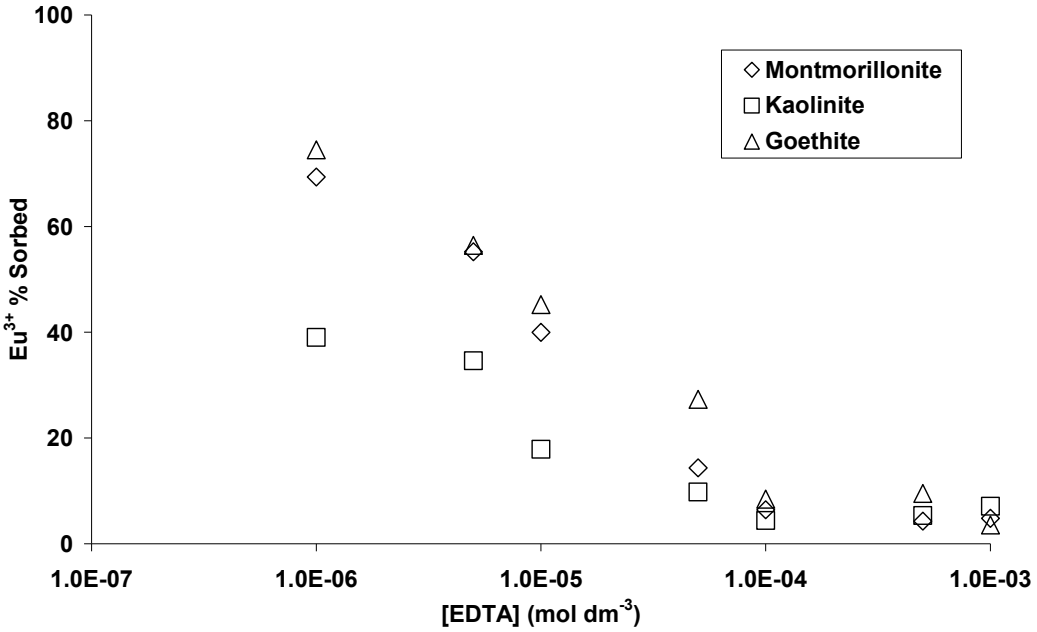

Figure 1: *Eu^{3+} sorption to minerals as a function of EDTA concentration at pH 6. Values for percentage sorption in the absence of EDTA being 98.1, 90.2 and 99% for montmorillonite, kaolinite and goethite respectively.*

For both metals the reduction of metal sorption due to the presence of EDTA is greatest for kaolinite and almost identical for montmorillonite and goethite. But the most striking observation in these data is the difference between the Eu^{3+} and Ni^{2+} sorption reductions. The EDTA reduces the fraction of Eu^{3+} sorbed at much lower EDTA concentrations, and to a much greater extent, compared to Ni^{2+}.

Figure 2: *Ni^{2+} sorption to minerals as a function of EDTA concentration at pH 6. Values for percentage sorption in the absence of EDTA being 68, 93.5 and 76.4% for montmorillonite, kaolinite and goethite respectively.*

Given the significant Eu^{3+} sorption reductions in the presence of EDTA, it is likely that the presence of surface ternary complexes is unlikely. The dominant complex species is probably the Eu^{3+} EDTA aqueous complex. There are limited data concerning trivalent EDTA mineral systems available in the literature [16]. Of the studies available, researchers have reported similar observations of dramatic metal sorption reduction to oxides and minerals in the presence of EDTA [17][[18]. Explanation of these data focussed on the competition between the ligand and oxide surface for competition of the metal ion. It would appear that trivalent metal EDTA complexes have been little studied [19], because all the carboxylic groups are coordinated to the metal ion and therefore no carboxylic groups are likely to be free to coordinate with the mineral [14][19]. In such a case it has been shown that if ternary complexes were to exist they would be due to the formation of weak outer sphere complexes [20]:

$$SOH + Eu^{3+} - EDTA^{-} + H^{+} = SOH_2^{+} \cdots^{-} EDTA - Eu^{3+}$$

From a review of the literature it is clear that at a metal/ligand ratio of 1 (which is applicable to the data presented here since the trace Eu^{3+} and Ni^{2+} concentrations are lower than the lowest EDTA concentration of 1 x 10^{-6} mol dm^{-3}), a single M-EDTA species predominates over a broad pH range [21], and that solution EDTA-metal complexes are reported to form by the formation of a carboxyl bond followed by ring closure through the formation of the amine bond [22].

Also notable from the literature is the greater interest in divalent metal EDTA mineral complexes. EDTA has been shown to enhance the sorption of some divalent metal ions onto oxide surfaces [23] explained by the formation of outer sphere ternary M^{2+} EDTA complexes. These observations agree with the data presented here for Ni^{2+}, where the EDTA has less impact on the Ni^{2+} sorption reduction, especially onto montmorillonite and goethite. For both montmorillonite and goethite more than 50% of the Ni^{2+} remains bound to the mineral in the presence of 5 x 10^{-4} mol dm^{-3} EDTA. This can be explained by the fact that for the case of a divalent metal-EDTA complex one carboxylic group is free to coordinate with the mineral. If this is the case the following surface reactions are possible [24]:

$$SOH + Ni^{2+} + EDTA^{4-} + H^{+} = S - EDTA - Ni^{-} + H_2O$$
$$SOH + Ni - EDTA^{2-} + H^{+} = S - EDTA - Ni^{-} + H_2O$$

However, similar results to those shown for Eu^{3+} have been observed for divalent metal ions such that the EDTA forms strong complexes with divalent transition metals and can stop sorption of divalent metal ions when EDTA solution concentrations are > 10^{-5} M [10]. This would agree with the results shown for the Ni^{2+}-kaolinite-EDTA ternary system. Another possible explanation for the higher sorption of Ni^{2+} to the minerals even in the presence of EDTA might also be due to the difference in stereochemistry of the metal sorption to the mineral surface. If Ni^{2+} sorbs by bidentate sorption, the EDTA has to dissociate two bonds compared with a monodentate bond that is expected for the Eu^{3+} mineral interaction.

Conclusions

The Eu^{3+} EDTA ternary system data suggest that the Eu-EDTA aqueous complex is dominant since Eu^{3+} sorption dramatically reduces in the presence of EDTA. In general it is accepted that Eu^{3+} usually has a total coordination number, CN_T of 9.0 in the formation of the 1:1 complex $Eu(EDTA)^-$; six from EDTA (four carboxylates, two nitrogens) binding and three from waters of hydration [25], making the formation of ternary complexes with the mineral surface unlikely.

The Ni^{2+} EDTA ternary data suggest that although EDTA has the ability to reduce Ni^{2+} sorption, the presence of ternary mineral complexes exist due to a non-coordinated carboxyl group of the EDTA available to coordinate with the mineral even when the EDTA is coordinated to a divalent metal ion. The data appears to support this theory particularly for montmorillonite and goethite. Bidentate sorption of Ni^{2+} to mineral surfaces as opposed to monodentate sorption of Eu^{3+} to mineral surfaces can also be considered as important to the different effect of EDTA on Eu^{3+} and Ni^{2+} sorption.

References

1. B. Kornilovich, G. Pshinko, L. Spasenova, and I. Kovalchuk. Influence of humic substances on the sorption interactions between lanthanide and actinide ions and clay minerals. Adsorption Science and Technology (2000), 18, pp 873.

2. R. Kummert, and W. Stumm. The surface complexation of organic acids on hydrous γ-Al_2O_3. Journal of Colloid and Interface Science (1983), 75, pp 373.

3. J. M. Zachara, C.C. Ainsworth, L. J. Felice, and C. T. Resch. Quinoline sorption to subsurface materials: role of pH and retention of the organic cation. Environmental Science and Technology (1986), 20, pp 620-627.

4. S. J. Gonsior, J. J. Sorci, M. J. Zoellner, and B. D. Landenberger. The Effect of ETA on Metal Solubilisation in River Sediment/Water Systems, Journal of Environmental Quality (1996), 26, pp 957.

5. J. L. Means, and D. A. Crerar. Migration of Radioactive Waste: Radionuclide Mobilization By Complexing Agents. Science (1978), Vol 200.

6. J. M. Zachara, S. C. Smith, and L. S. Kuzel. Adsorption and Dissociation of Co-EDTA complexes in iron-oxide containing subsurface sands, Geochimica and Cosmochimica Acta (1995), 59, 33, pp 4825.

7. J. Vuceta. Adsorption of Pb(II) and Cu(II) on α-Quartz from aqueous solution: Influence of pH, ionic strength, and complexing ligands. Ph.D Thesis, California Institute of Technology, Pasadena, California (1976).

8. D. C. Girvin, P. L. Gassmann, H. Bolton. Adsorption of aqueous cobalt ethylenediaminetetraacetate by δ-Al_2O_3. Soil Science (1993), 57, pp 47-57.

9. S. Holgersson. Studies on the effect of concrete on the chemistry in a repository for radioactive waste. Ph.D Thesis, Chalmers University of Technology (2000), Sweden.

10. G. R. Chopin, and D. Rai. Research program to determine redox properties and their effects on speciation and mobility of Pu in DOE wastes, EMSP 54893, (1998).

11. P. Cauchetier, and C. Guichard. Etude Electrochimique ey spectrophotometrique des complexes des ions du plutonium avec I'EDTA, J. Inorganic and Nuclear Chemistry, 37, 1771-1778, (1975).

12.I. Al Mahamid, K. A. Becraft, N. L. Hakem, R. C. Gatti, and H. Nitsche. Stability of Various Plutonium Valence States in the Presence of NTA and EDTA, Radiochimica Acta (1996), 74, 129.

13.N. L. Hakem, P. G. Allen, and E. R. Sylwester. Sorption and diffusion studies of Pu(IV) and Pu(IV)-EDTA onto and through Hanford Soil. Migration 1999, Tahoe, CA.

14. J. L. Campbell, and M. J. Eick. Effect of oxyanions on the EDTA-promoted dissolution of goethite. Clays and Clay Minerals (2002), 50, 3, pp 336-341.

15.Van der Lee, J.: A Users Guide to CHESS, Another Speciation and Surface Complexation Computer Code, École des Mines de Paris, Fontainebleau, France, (1998).

16.N. L. Hakem, P. G. Allen, and E. R. Sylwester. Sorption and Diffusion Studies of Pu(IV) and Pu(IV)-EDTA onto and through Hanford Soil. Migration 1999, Tahoe, CA.

17.J. Vuceta. Adsorption of Pb(II) and Cu(II) on α-Quartz from aqueous solution: Influence of pH, ionic strength, and complexing ligands. Ph.D Thesis, California Institute of Technology, Pasadena, California., (1976).

18.A. J. Weiss and P. Colombo. Evaluation of isotope migration-land burial, water chemistry at commercially operated low level radioactive waste disposal sites. Brookhaven National Laboratory Report, NUREG/CR-1325, (1980).

19.G. Fanger, K. Skagius, and M. Wiborgh. Project SAFE. Complexing Agents in SFR. January 2001. SKB Report R-01-04.

20.M. Ulrich. Dissertation ETH No. 9632, Zürich, 1991.

21.A. L. Bryce, W. A. Kornicker, and A. W. Elzerman. Nickel Adsorption to Hydrous Ferric Oxide in the Presence of EDTA: Effects of Component Addition Sequence. Environmental Science and Technology (1994), pp 28, 2353-2359.

22.D. W. Margerum, G. R. Cayley, D. C. Weatherburn, G. C. Pagenkopf. In Coordination Chemistry; A. Martell, E. Ed.; American Chemical Society: Washington, DC, 1978; Vol. 2, Chapter 1.

23. J. R. Bargar, P. Persson, and G. E. Brown, Jr. Outer-sphere adsorption of Pb(II)EDTA on Goethite. Geochimica et Cosmochimica Acta (1999), 63, pp 1957.

24. B. Nowack, J. Lützenkirchen, P. Behra, and L. Sigg. Modelling the adsorption of metal-EDTA complexes onto oxides. Environmental Science and Technology (1996), 30, pp 2397-2405.

25 J. N. Mathur, P. Thakur, C. J. Dodge, A. J. Francis, and G. R. Choppin, Coordination Modes in the Formation of the Ternary Am(III), Cm(III), and Eu(III) Complexes with EDTA and NTA: TRLFS, ^{13}C-NMR, EXAFS, and Thermodynamics of the Complexation, Inorganic Chemistry, (2006), 45, pp 8026–803

EUROPIUM ADSORPTION ONTO FEBEX SMECTITE

T. Missana*, U. Alonso, M. García-Gutiérrez, N. Albarran, T. López

CIEMAT, Departamento de Medioambiente (Madrid, ES)

* Corresponding author: tiziana.missana@ciemat.es

Abstract

The description of contaminant retention by a mechanistic approach is more precise and defendable than the usual K_d or sorption isotherm approach, particularly for safety assessment analysis of waste repositories. In this study, the adsorption of europium onto the FEBEX smectite, homoionised in Na, was analysed under a wide range of experimental conditions. The effects of the most important physico-chemical parameters such as pH (3-11), ionic strength ($1\cdot10^{-3}$ M to $2\cdot10^{-1}$ M in $NaClO_4$) and radionuclide concentration ($1\cdot10^{-10}$ to $1E^{-3}$ M) were independently studied.

Europium adsorption at low pH (<4) presented no dependence on pH and a significant dependence with the ionic strength, indicating the importance of ionic exchange processes. At higher pH, inner sphere surface complexation predominated.
Results were satisfactorily interpreted using a simple model which combines surface complexation and ionic exchange processes. The selectivity coefficients obtained from the experimental data were approximately constant in the range of ionic strengths from 0.2 to 0.05 M ($Log\,{}^{Eu}_{Na}K_{SEL} = 2.00 \pm 0.32$) but significantly decreased at lower ionic strengths. This could be the consequence of the effect of ions in solution, coming from clay dissolution, competing for the sorption sites. This effect was accounted for and also satisfactorily modelled.

Introduction

Compacted bentonite, mainly formed by the 2:1 clay smectite, is a suitable engineered barrier in HLRW repositories to delay radionuclide migration, since it presents high sorption capability for most cations.

The description of radionuclide retention by a mechanistic approach, based on a thermodynamic description of the radionuclide/solid system allows predicting sorption behaviour under a variety of conditions, and it is very important issue for the safety assessment of waste repositories.

To interpret and quantify the interactions occurring at the clay/water interface accounting for ionic exchange and surface complexation, the effects of the most important physico-chemical parameters such as pH, ionic strength and radionuclide concentration have to be studied independently. *Sorption edges* at constant ionic

strength and *sorption isotherms* at a constant pH are both needed to determine surface complexation constants and selectivity coefficients for a quasi-thermodynamic description of the system (BAEYENS and BRADBURY, 1997; BRADBURY and BAEYENS, 1997).

Bradbury and Baeyens studied and modelled with their 2SPNE SC/CE model (BRADBURY and BAEYENS, 1997) the europium adsorption on the Wyoming SWy-1 Na-montmorillonite using data (one sorption edge and two isotherms) obtained at only one ionic strength (0.1 M) (BRADBURY and BAEYENS, 2002). They applied a 2SPNE (non electrostatic) model which considers the existence of two different weak sites and one strong site for surface complexation.

In this study we used a two-site (one weak and one strong) non-electrostatic model that was capable of interpreting the sorption data in a very wide range of pH, ionic strength and element concentration. With this model, the whole set of experimental data could be accurately modelled.

Materials and Methods

Clay

The smectite used in these experiments comes from the Spanish deposit of Cortijo de Archidona (FEBEX bentonite). This clay contains mainly smectite (93±2%), with quartz (2±1%), plagioclase (3±1%), cristobalite (2±1%), potassium feldspar, calcite and trydimite as accessory minerals. Mineralogical studies showed that the smectite phase is actually made up of smectite-illite mixed layer with a 10-15 % of illite layers (CUADROS and LINARES, 1996). The cation exchange capacity (CEC) of the FEBEX clay is 102 ± 4 meq/100g, the BET surface area is 33 m^2g^{-1}. Further details on this clay can be found elsewhere (FERNANDEZ et al., 2004; HUERTAS et al., 2000). Previous to sorption experiments, the FEBEX clay was purified and homoionised in Na form. The concentration of the clay in the suspension to be used for sorption experiments was determined by gravimetry, after drying the solid and the electrolyte in the oven 2 days at 105 ºC. The solid to liquid ratio (S), used in these experiments was typically from 0.5 to 1 gL^{-1}.

Radionuclide

The radionuclide used in this study was $^{152}Eu(III)$ coming from a carrier-free solution of $^{152}EuCl_3$ diluted in HCl (solution at approx. pH=2).

Sorption Experiments

Sorption experiments were carried out in atmospheric conditions and at room temperature. Suspensions at different ionic strengths were used for the experiments (from $1 \cdot 10^{-3}$ M to 0.2 M in $NaClO_4$). Sorption edges were carried out by changing the pH from pH 3 to 11 with NaOH or HCl 0.1-1 M. Buffer solutions were used to maintain the pH stable over time for the samples with pH from 5.5 to 10. The pH was readjusted, if necessary, after the radionuclide addition.

The separation of clay from the supernatant was carried out by ultra-centrifuging (645000 g, 30 min) with a Beckman L90-Ultra ultracentrifuge. After the solid

separation, three aliquots of the supernatant from each tube were extracted for the analysis of the final activity that was measured by means of a NaI γ-counter (Packard Autogamma COBRA 2). The rest of the solution was used to check the final pH.

Mean distribution coefficients (K_d) were calculated from the three aliquots of the supernatant with this formula:

$$K_d = \frac{C_i - C_f}{C_f} \cdot \frac{V}{m} \qquad \text{E.1}$$

where C_i is the initial activity, C_f the final activity in the supernatant, m the mass of the solid and V the liquid volume.

The kinetics of the sorption process was first analysed to decide a proper experimental time for further experiments, which was fixed to 7 days.

Sorption isotherms were carried out at room temperature (22 ± 2 ºC) at a fixed pH and fixed background electrolyte concentrations and varying the radionuclide concentration. The highest concentrations (> $1 \cdot 10^{-6}$ M) were achieved by adding, in addition to the radiotracer, non radioactive Eu from $Eu(NO)_3$ salts of high purity. The separation, counting procedure and K_d determination were the same used for the sorption edges.

Modelling

Since in clays both ionic exchange and surface complexation may contribute in a different extent to the sorption of radionuclides, both contributions were taken into account. Sorption at the edge sites was accounted for considering the existence of both a strong S_SOH and a weak S_WOH site.

The acid-base properties of the weak sites, S_wOH, and their density were determined by potentiometric titrations (MISSANA et al., 2002), whereas the properties of strong sites (S_sOH) whose density is very small are usually determined by model fit. The density of S_SOH in the FEBEX Na-smectite was previously experimentally determined to be 0.061 μmol·m^{-2} (MISSANA and GARCIA-GUTIERREZ, 2007). A more detailed description of the modelling procedure can be found in ((MISSANA et al., 2008).

Results and Discussion

Figure 1 (left) shows the sorption edges (pH 3 to 11) obtained in Na-smectite at different ionic strengths (from I=$1 \cdot 10^{-3}$ M to 0.2 M in $NaClO_4$). K_d values, depending on pH and ionic strength, vary over more than three orders of magnitude. The experimental curves evidenced the existence of three different regions. In the first one, from pH 3 to pH 5, sorption is not dependent on pH but it is strongly dependent on the ionic strength. These characteristics seems indicating the predominance of ionic exchange mechanism for the Eu adsorption, in the acidic pH region. In the second region, from pH 6 to 7, at the lower ionic strengths a decrease in sorption is observed. In the third region, pH>7, sorption increases with pH and it is independent on the ionic strength.

Figure 1 (right) shows the sorption isotherms obtained at different ionic strengths. Isotherms data are expressed as the logarithm of the distribution coefficient ($Log(K_d)$) *vs.* the logarithm of the final Eu concentration in the liquid at the equilibrium ($Log(Eu_{fin})$). All the isotherms, independently on pH and ionic strength, present similar characteristics. Sorption is linear over a wide range of europium concentrations and decreases at the higher concentrations ($Log(Eu_{fin})>-6$) due to saturation of sorption sites.

A non negligible decrease of the calculated selectivity coefficients was observed when the ionic strength decreases: only in the region of ionic strength from 0.05 to 0.20 a mean value for the selectivity coefficient, with an error comparable to the experimental one, could be calculated ($Log\,{}^{Eu}_{Na}K_{SEL} = 2.00 \pm 0.32$). This dependence was accounted for and modelled considering that other (bivalent) ions present in solution, due to the partial dissolution of the clay, may compete for sorption. These effects would be more important at lower ionic strengths, when sorption by ionic exchange is favoured and the Na concentration decreases in respect to other potentially competing ions (MISSANA et al., 2008).

For the modelling of sorption of Eu by surface complexation the formation of the following species was considered:

$$SOH + Eu^{3+} \Leftrightarrow SOEu^{2+} + H^+$$
$$SOH + EuCO_3^+ \Leftrightarrow SOEuCO_3 + H^+$$
$$SOH + Eu(OH)_2^+ \Leftrightarrow SOEu(OH)_2 + H^+$$

Furthermore, for a perfect fit of all the experimental data the existence of two types of surface sites, *weak* and *strong*, was taken into account.

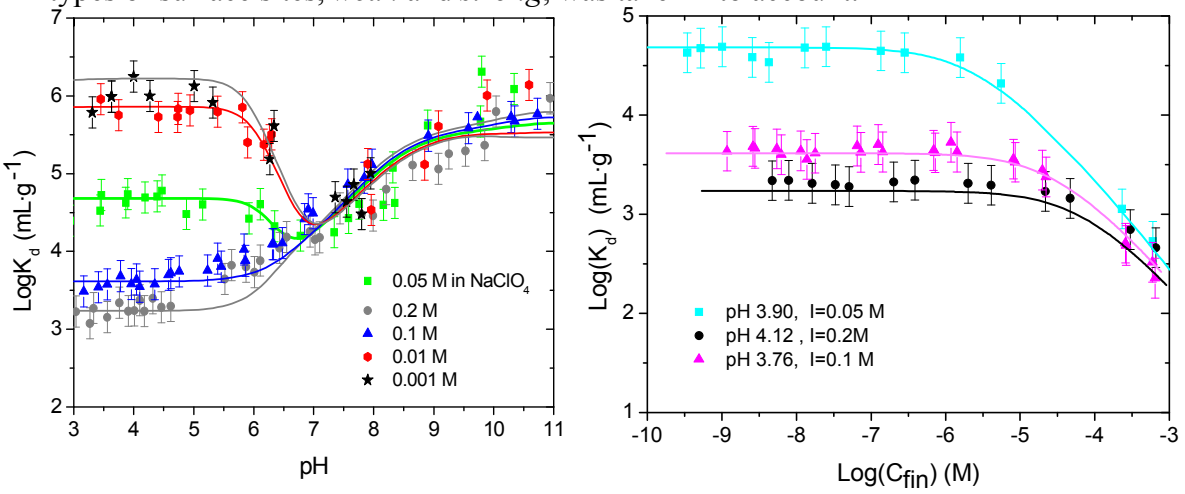

Figure 1: Left *Sorption edges at different ionic strength in $NaClO_4$. [Eu] = 9.9E-09 M..* ***Right****: Sorption isotherms. Continuous lines correspond to fit obtained with the final model (parameters in Table 1 for surface complexation;* $Log\,{}^{Eu}_{Na}K_{SEL} = 2.00$ *and* $Log\,{}^{M^{2+}}_{Na}K_{SEL} = 0.70$ *for cationic exchange).*

All the experimental data could be perfectly fit considering the formation of the three above mentioned complexes, both for weak and strong sites, in addition to the

ionic exchange contribution. The complexation constants obtained from the best match of the model with the experimental data are included in Table 1.

The model calculations are plotted as continuous lines in Figure 1 (right, edges and left, isotherms) superimposed to the experimental data. The model reproduced in a satisfactory way the whole set of experimental sorption edges (Figure 1) in the range of pH from 3 to 11 and over a wide range of ionic strengths (0.001 M to 0.2 M). Also all the isotherms were well reproduced indicating that sorption behaviour can be fit in a wide range of Eu concentration. More details can be found in Missana et al. (2008)

Table 1: *Parameters used for Eu surface complexation. Non electrostatic model.*

Species	Composition	LogK
S_wO^-	-1 H^+, 1 S_wOH	-8.4
$S_wOH_2^+$	-1 H^+, 1 S_wOH	5.3
S_sO^-	-1 H^+, 1 S_sOH	-9.9
$S_sOH_2^+$	-1 H^+, 1 S_sOH	4.8
S_wOEu^{2+}	-1 H^+, 1 S_wOH, 1 Eu^{3+}	-0.5
S_wOEuCO_3	-2 H^+, 1 S_wOH, 1 Eu^{3+}, 1HCO_3^-	-3.5
$S_wOEu(OH)_2$	-3H^+, 1 S_wOH, 1 Eu^{3+}, 2H_2O	-13.4
S_sOEu^{2+}	-1 H^+, 1 S_sOH, 1 Eu^{3+}	0.5
S_sOEuCO_3	-2 H^+, 1 S_sOH, 1 Eu^{3+}, 1HCO_3^-	-2.65
$S_sOEu(OH)_2$	-3H^+, 1 S_sOH, 1 Eu^{3+}, 2H_2O	-12.0

Conclusions

Europium adsorption onto the FEBEX smectite was studied under a wide range of pH, ionic strengths and europium concentrations. A model combining both surface complexation and ionic exchange was applied which succeeded in reproducing all the experimental data.

The mean selectivity coefficient determined for the Na-Eu exchange was ($Log\,{}^{Eu}_{Na}K_{SEL} = 2.00 \pm 0.32$) but the effect of competitive ions in solution, coming from partial dissolution of the clay, had to be accounted for to satisfactorily explain the anomalies in the ionic strength experimentally observed.

Eu speciation was affected by the presence of carbonate species. Sorption by surface complexation was explained by a non electrostatic model with the formation of the following complexes: $SOEu^{2+}$, $SOEuCO_3$ and $SOEu(OH)_2$ with weak and strong surface sites.

References

Baeyens B. and Bradbury M. H. (1997) A mechanistic description of Ni and Zn sorption on Na-montmorillonite .1. Titration and sorption measurements. *Journal of Contaminant Hydrology* **27**(3-4), 199-222.

Bradbury M. H. and Baeyens B. (1997) A mechanistic description of Ni and Zn sorption on Na-montmorillonite .2. Modelling. *Journal of Contaminant Hydrology* **27**(3-4), 223-248.

Bradbury M. H. and Baeyens B. (2002) Sorption of Eu on Na- and Ca--montmorillionites: Experimental investigations and modelling with cation exchange and surface complexation. *Geochimica et Cosmochimica Acta* **66**(13), 2325-2334.

Cuadros J. and Linares J. (1996) Experimental kinetic study of smectite-to-illite transformation. *Geochimica et Cosmochimica Acta* **60**(3), 439-453.

Fernandez A. M., Baeyens B., Bradbury M., and Rivas P. (2004) Analysis of the porewater chemical composition of a Spanish compacted bentonite used in an engineered barrier. *Physics and Chemistry of the Earth* **29**(1), 105-118.

Huertas F., Fuentes-Santillana J. L., Jullien F., Rivas P., Linares J., Fariña P., Ghoreychi M., Jockwer N., Kickmaier W., Martínez M. A., Samper J., Alonso E., and Elorza F. J. (2000) Full scale engineered barriers experiment for a deep geological repository for high-level radioactive waste in crystalline host rock. EC Final REPORT EUR 19147.

Missana T., Alonso U., García-Gutierrez M., Albarran N., and Lopez-Torrubia T. (2008) Experimental study and modeling of europium adsorption onto smectite clay colloids. CIEMAT/DMA/2G102/05/08, 28 pp. Madrid.

Missana T. and Garcia-Gutierrez M. (2007) Adsorption of bivalent ions (Ca(II), Sr(II) and Co(II)) onto FEBEX bentonite. *Physics and Chemistry of the Earth* **32**, 559-567.

Missana T., García-Gutierrez M., Fernández V., and P.Gil. (2002) Application of mechanistic models for the interpretation of radionuclides sorption in clays. Part 1". CIEMAT Technical Report CIEMAT/DIAE/54610/03., pp. 47..

EVIDENCE FOR SINGLE CM HUMATE COMPLEXES IN AQUEOUS SOLUTION IN THE PH_C-RANGE 3 TO 5.5

Markus Freyer[1], Clemens Walther[1], Thorsten Stumpf[1,2], Gunnar Buckau[1], Thomas Fanghänel[2,3]

[1]Forschungszentrum Karlsruhe, Institut für Nukleare Entsorgung, 76021 Karlsruhe, DE
[2]Physikalisch-Chemisches Institut, Ruprecht-Karls Universität, Im Neuenheimer Feld 253, 69120 Heidelberg, DE
[3]European Commission, Joint Research Center, Institute for Transuranium Elements, P.O. Box 2340, 76125 Karlsruhe, DE

*Corresponding auhor: markus.freyer@ine.fzk.de]

Abstract

Safety assessment of nuclear waste disposal includes determination of the possible impact of natural dissolved organic matter on the transport of actinide ions via groundwater into the biosphere. Thereby, much attention is paid to americium as it dominates the radiotoxicity of the nuclear waste after about 300 years and up to about 1.000 years (spent fuel) or 100.000 years (vitrified reprocessing waste). A trustworthy description of the influence benefits from a sound chemical process understanding of the americium humate complexation and transport processes. A problem in this respect is that studies by TRLFS lead to inconclusive results with respect to the nature of complex forms involved. In the present study the outcome of TRLFS measurements in H_2O and D_2O, and at room temperature and in liquid nitrogen are compared. It is shown that the Cm^{3+} ion interchanges between aquo ion (Cm^{3+}_{aq}) and humate complex (CmHA) on a time scale of milliseconds in a pH range between 3 and 5.5. Taking this interchange into account, the process can be described in the absence of ternary complexes by the 1:1 stoichiometry formation of one curium humate complex, or a sufficiently narrow distribution of complexes to be represented by one average complex.

Introduction

Reflecting the high radiotoxicity inventory of americium in HLW (Grenthe and Rydberg, 1986), the complexation of trivalent actinides with humic acid is of interest for the nuclear waste disposal Safety Case. With few exceptions, such complexation data in the absence of ternary complexes are interpreted as a single complex (or a single complex with a with a limited distribution width) with a 1:1 reaction stoichiometry. These complexes show very large variations in the reaction kinetics.

In addition to the radiotoxicity inventory relevant americium, also curium and different lanthanides have been used as chemical homologues (Czerwinski et al. 1996,

Monsallier et al. 2003). A particular advantage of using curium and lanthanides is that they provide chemical homologues with a variety of fluorescence properties, allowing sensitive studies especially with TRLFS (time resolved laser pulse induced fluorescence spectroscopy). By this method, information is obtained on absorption/excitation, emission and the time-function of fluorescence light emission (Lakowicz 1999). Accordingly, a great number of studies have been conducted by this method, using curium in the trace metal ion concentration range. Already in the absence of ternary complexes, however, the results of these studies are inconclusive. An unambiguous interpretation of the nature of complexes is not obtained. The particular problem may be summarized as follows: (i) Data in most cases do not allow resolution of more than one single complex (1:1 reaction stoichiometry), (ii) by TRLFS and EXAFS, this complex is shown to enclose at least two exchangeable kinetic modes that co-exist in similar amounts under equilibrium/steady-state conditions (Monsallier et al. 2003), (iii) the fluorescence emission show only one spectrum along with the fluorescence decay (Monsallier et al. 2003), (iv) the fluorescence decay functions show at least two distinguishable contributors, normally pointing to more than one co-existing species (Kim et al. 1991).

The present paper aims at identifying the reason(s) for the apparent contradictions in order to determine the number of complexes that are distinguishable by TRLFS. The key approach is to compare the fluorescence decay functions of curium humate complexes in H_2O and D_2O media. The different fluorescence lifetimes found are assessed against exchange processes taking place within the respective time frames. Based on this information, the different reported observations are brought together to a consistent description.

System properties

In order to study the emission of fluorescence light from the Cm(III) ion, the curium must be brought to an excited state via absorption of energy. This can be achieved by two different routes. Through irradiation of the sample, these different routes are (i) absorption of light by the Cm(III) ion (direct excitation), or (ii) absorption of light by a ligand followed by energy transfer to the complexed/bound curium ion (indirect excitation). Humic acid absorbs light basically over the entire visible range with the absorption coefficient smoothly decreasing with increasing wavelength. Contrary to this, Cm(III) has distinct absorption bands. As a result, indirect excitation will dominate when pumping the system with light having energies between the curium absorption bands. Pumping the system with light having energies corresponding to the Cm(III) absorption bands will lead to a mixture of indirect and direct excitation. The indirect excitation is competing with the fast ($k_{HAUV} \sim 10^8$ s^{-1}, Wimmer et al. 1992) fluorescence of the humic acid molecule itself and hence is by far not as effective as the absorption cross section of the HA (σ=6000$M^{-1}cm^{-1}$) might suggest. Comparison of the two different excitation routes gives information on the structure of the system studied. The peak positions of the absorption/excitation bands and the fluorescence emission bands also give information about the system and the ligand field around the complexed curium ion. Complexation of the Cm^{3+} ion causes the fluorescence emission to shift to longer wavelengths as a consequence of the ligand field (Edelstein et al. 2006). The stronger the complexing ligand is, the stronger the red-shift.

Finally, information is obtained from the fluorescence emission life-time. The Cm(III) ion has an intrinsic fluorescence lifetime. This life-time is lowered by the sum of different quench processes, especially energy transfer to hydration water and bound ligands. One of the most effective quenchers is the H_2O molecule. The energy of the electronic excitation of the Cm(III) ion corresponds to the fifth overtone of the H_2O stretching vibration (the basic stretching vibration having an energy of ν_{H2O}=3400 cm^{-1}). In D_2O, the frequency of the stretching vibration is only ν_{D2O}=2500 cm^{-1} requiring a higher order overtone excitation which is much less likely to occur. For this reason, as a good approximation, D_2O is considered a non-quenching ligand (though not absolutely correct, since the lifetime of the undisturbed Cm^{3+} ion exceeds τ=4 ms, whereas in D_2O the lifetime τ=1300 µs is observed). Changing the hydration between H_2O and D_2O thus provides the possibility to reasonably well quantify the sum of other quench routes. In addition, phenomena taking place at timescales comparable to the differences in heavy and light water quench processes can be distinguished by such comparison.

Humic acid complexation and fluorescence lifetime

The metal ion complexation with the humate ligand, on the example of Cm^{3+}, is written as (omitting the charges as they are not known):

$$Cm_{aq}^{3+} + HA \underset{k_B}{\overset{k_F}{\rightleftharpoons}} CmHA \qquad (1)$$

This expression is valid for one complex being formed, or a spectrum of complexes that can be represented by a sufficiently narrow distribution. The corresponding equilibrium constant is:

$$\beta' = \frac{[CmHA]}{[Cm_{aq}^{3+}][HA_{eff}]} = \frac{k_F}{k_B}\frac{1}{[HA_{eff}]} \qquad (2)$$

Where $[HA_{eff}]$ is the effective humate ligand concentration of the humic acid depending on pH, and k_F and k_B are the forward and backward reaction rates. If not only one complex is formed, but a sequence of complexes (or narrow distributions), equation (2) becomes extended by additional reaction rate couples with their humate ligand inventories. Different types of complexes will have different complexation environment and thus different fluorescence lifetimes. These can then be distinguished by different fluorescence lifetimes. The relation between the multitude of exponential decay functions, however, is not straight forward coupled to the number of complexes.

Mono-exponential decay is observed when only one complex is present. In this case the fluorescence spectra do not change with increasing delay after the laser pulse. In contrast, observation of bi-exponential decay strongly hints at the presence of two non-equivalent species and, since the shorter lived component decays faster, the fluorescence emission spectrum usually changes with increasing delay time. There are, however, exceptions, such as a system with two species undergoing continuous transformation into each other. In our case this would be exchange of the Cm(III) ion between the Cm^{3+} aquo ion and the Cm(III) humate complex. In such a case, the reaction rates k_F, k_B must be compared to the rates of fluorescence decay $k_{Fluo}(Cm^{3+})$ and k_{Fluo}(CmHA). For very slow reaction rates compared to the fluorescence decay rates (k_F, k_B << $k_{Fluo}(Cm^{3+})$ and k_{Fluo}(CmHA)), a bi-exponential decay is observed. For the opposite case (k_F, k_B >>

$k_{Fluo}(Cm^{3+})$ and $k_{Fluo}(CmHA)$) the interchange is too fast to be resolved by means of this fluorescence, resulting in a mono-exponential decay with one single apparent lifetime. The detailed mathematical treatment is discussed in (Freyer et al. submitted).

Results and Discussion

Previous measurements on the Cm humate complex revealed bi-exponential lifetime dependence of the fluorescence decay (Morgenstern et al. 2000). This may indicate the presence of two different species. The spectral shape of the fluorescence emission, however, does not change significantly for different delay time as it should if two species of different lifetimes were present. So far no satisfying explanation was offered for this apparent contradiction. In order to examine this behavior in detail, the Cm(III) humic acid system was studied in H_2O with pH_C 3.0 to pH_C 5.4. (Fig. 1, left) and in D_2O at pD_C 3.0 to pD_C 5.5 (Fig. 1, right).[1]

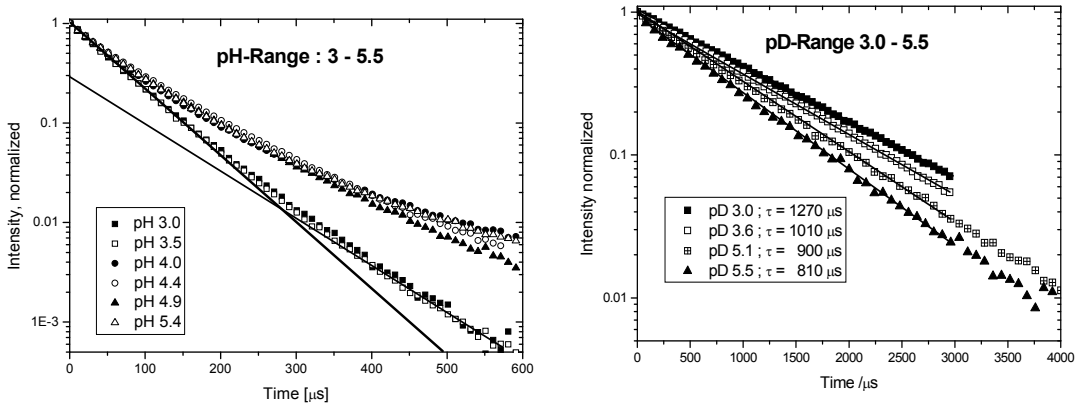

Figure. 1 *Fluorescence intensity as a function of delay time between laser pulse and detection for the system Cm^{3+} ($3x10^{-7}$M), HA (10mg/l) in H_2O (HCl, NaCl, I=0.1M) (left) and D_2O (right).*

The lifetimes are normalized with respect to intensity at t=0. The latter samples were prepared in an Ar glove box using deuterated chemicals of >99.9% purity, carefully avoiding contaminations by air oxygen or water. All resulting lifetimes obtained in D_2O show strictly mono-exponential behavior. At highest acidity (pD_c 3.0) the lifetime of τ~1200µs is close to the non-complexed Cm_{aq}^{3+} aquo ion coordinated by nine D_2O molecules (literature τ~1270µs, Lindqvist-Reis et al 2005). With increasing pD_c the lifetimes decrease, but the functionality remains strictly mono-exponential, in sharp contrast to the bi-exponential lifetimes measured at similar acidity in H_2O. After re-acidification to pD_c 2.0, a lifetime close to τ=1300µs was found for all D_2O samples, showing that the decrease of the lifetimes is not caused by contaminations of the samples with H_2O. This very much unexpected behavior can be explained in two ways (see also Fig. 2):

[1] pH_c is the H^+ concentration as measured by a combined glass electrode calibrated against HCl/NaCl standards

a) At each pD_c there is only one species present. This hypothesis requires that already the Cm^{3+} aquo is no longer present already at pD_c 3.0, since the observed lifetime falls short of τ~1270 µs characteristic for the non-complexed Cm^{3+} aquo ion. Furthermore, the quenching properties of CmHA complexes would have to change continuously with decreasing acidity, caused by for instance, configurationally induced changes of the humic molecule.

b) Both, the Cm^{3+}_{aq} aquo ion and the Cm-humate complex, are present simultaneously and transform into each other with a rate comparable to the fluorescence lifetime in D_2O. With increasing pD_c the equilibrium according to Eq. (1) shifts to the right in favor of the humate complex. Since the lifetime of the Cm humate complex is shorter than that of the free aquo ion in D_2O the mono-exponential lifetime decreases.

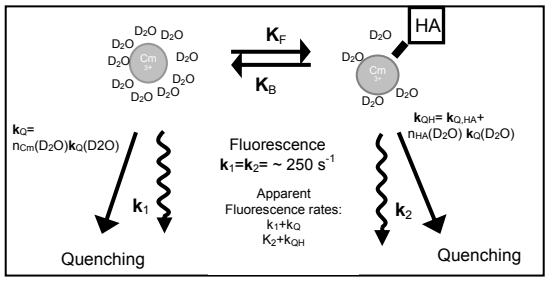

Figure.2: *Schematic description of the light emission and quench routes for aquo and humate complexes of Cm(III) in exchange with each other.*

In order to decide between alternatives **a** and **b** the following investigations were performed: The emission spectrum at pD_c 3.0 shows a single peak at 593.8 nm which is characteristic of the Cm^{3+} aquo ion. With increasing pD_c, a shoulder around 598 nm evolves and at pD_c 5.5 both contribution are of equal intensity. This suggests the presence of two components assumed by hypothesis **b**, and contradicts the assumption of a single species in **a**. In a further experiment, D_2O samples were shock frozen to 77 K (liquid nitrogen) and the optical emission compared to the one at room temperature. Freezing should prevent interchange and hence render possible the optical distinction of several different species. Fig. 3 shows the lifetimes for D_2O samples at room temperature and at 77 K. The monoexponential lifetime at room temperature changes to a biexponential curve at 77 K, with two components at τ_1=1090 µs and τ_2=474 µs, respectively.

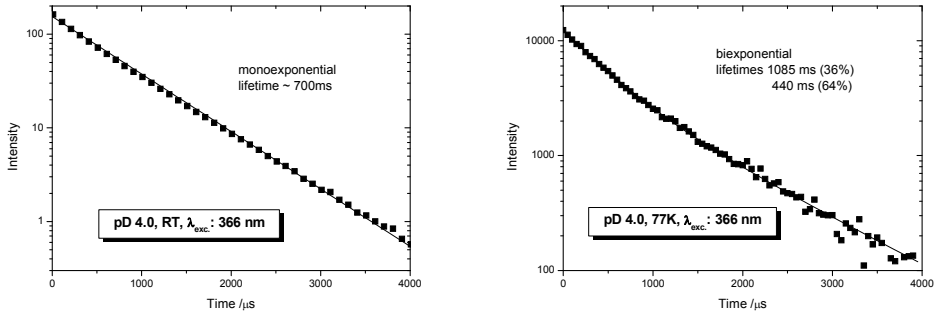

Figure. 3 *Fluorescence lifetimes at room temperature (left) and at 77K (right)*

The long lived component is very close to what one would expect from the undisturbed aquo ion in D_2O (1300 µs), the second compares well to the long lived component of the biexponential decay of the CmHA complex in D_2O. This is strong evidence for the presence of two species (hypothesis **b**).

Summary and Conclusions

In contrast to the interpretation of earlier studies of Cm^{3+} humate complexation (Kim et al. 1991, Morgenstern et al. 2000) most of them performed at higher pH and in H_2O, we find evidence for the formation of an interchange of the Cm ion between aquo ion and humat complex. This behavior is not completely surprising, for fast interchange was reported previously for systems of metal ions complexed by most inorganic ligands and some organic ligands such as glycolic acid (Stumpf et al 2002).The interchange rate is pH dependent and in the order of 1000 s^{-1}. The interchange reaction strongly influences the fluorescence lifetime in the weakly quenching solvent D_2O while a direct observation in H_2O is hindered by the short lifetimes. The present data was best described by assuming a reaction rate k_F = 450 s^{-1} for complex formation and a dissociation rate k_B according to Eq. (2). k_B decreases with pH due to the increase in effective ligand concentration of the humic acid and approaches zero for increasing pH indicating increasing stability of the complexes. When the interchange is prevented by shock freezing the samples, biexponential decay is observed and the ratio of long and short component changes for different excitation wavelengths, depending on whether aquo ion or complex has a higher absorption cross section.

The implication for the disposal Safety Case is related to trust in the capability of geochemical description of radionuclide transport relevant processes. The underlying reason for the apparent contradiction reported from earlier studies is resolved, and the complexation process is described by one complex exchanging with the non-complexed metal ion.

References

Czerwinski, K. R.; Kim, J. I.; Rhee, D. S.; Buckau, G. „Complexation of trivalent actinide ions (Am3+, Cm3+) with humic acid: The effect of ionic strength" (1996) *Radiochim. Acta*, *72*, 179.

Edelstein, N. M.; Klenze, R.; Fanghänel, T.; Hubert, S. "Optical properties of Cm(III) in crystals and solutions and their application to Cm(III) speciation" (2006) *Coord. Chem. Rev.*, *250*, 948-973

Freyer M., Walther C., Stumpf Th., Buckau G., Fanghänel Th. (submitted) "Formation of Cm Humate Complexes in aqueous solution at pHC 3 to 5.5: The role of fast interchange".

Frimmel, F. H.; Kumke, U. Fluorescence Decay of Humic Substances. A Comparative Study. In *Humic Substances - Structures, Properties and Uses*; Davies, G., Ghabbour, E. A., Eds (1998); Royal Soc. of Chemistry: Cambridge,; pp 113-122.

Grenthe, I.; Rydberg, J. (1986) Det radioaktiva avfallet. In *Kärnenergi I utveckling*; Ringström, B., Ed.; Bonniers Fakta Bokförlag

Kim, J. I.; Wimmer, H.; Klenze, R. (1991) „*Complexation of trivalent Actinide Ions (AM3+, CM3+) with Humic Acid - A Comparison of different experimental Methods". Radiochim. Acta*, *54*, 35-41.

Lakowicz, J. R. (1999) Principles of fluorescence spectroscopy; Kluwer: New York.

Lindqvist-Reis, P. Klenze, R. Schubert, G.Fanghanel, T " Hydration of Cm3+ in aqueous solution from 20 to 200 degrees C. A time-resolved laser fluorescence spectroscopy study ". Journal of Physical Chemistry B (2005). 109 (7): p. 3077-3083

Monsallier, J. M.; Artinger, R.; Denecke, M. A.; Scherbaum, F. J.; Buckau, G.; Kim, J. I. "Spectroscopic study (TRLFS and EXAFS) of the kinetics of An(III)/Ln(III) humate interaction (2003)" *Radiochim. Acta*, *91*, 567-574.

Morgenstern, M.; Klenze, R.; Kim, J. I. *"*The formation of mixed-hydroxo complexes of Cm(III) and Am(III) with humic acid in the neutral pH range" (2000) *Radiochim. Acta*, *88*, 7-16.

Stumpf, T.; Fanghänel, T.; Grenthe, I. "Complexation of trivalent actinide and lanthanide ions by glycolic acid: a TRLFS study" (2002) *J C S -Dalton Trans.* 3799-3804

FINITE ELEMENT MODELING OF FLOW AND TRANSPORT IN A SINGLE FRACTURE FROM THE ÄSPÖ HRL (SWEDEN)

Florian Huber[1*], Alexandra Pudewills[1], Frieder Enzmann[2], Thorsten Schäfer[1]

[1] Forschungszentrum Karlsruhe, Institut für Nukleare Entsorgung, Karlsruhe (GER)
[2] University of Mainz, Institute for Geosciences, D-55099 Mainz (GER)

* Corresponding author: Florian.Huber@ine.fzk.de

Abstract

In this contribution we present results of a numerical study concerning the fluid flow and tracer transport through a single fracture in a granite drill core. The goal of our work is to investigate the influence of fracture geometry and surface roughness/heterogeneity on the flow velocity distribution which in turn has a direct impact on solute transport. Possible chemical processes which can lead to a retardation of solutes have been excluded, to solely investigate the influence of geometrical features. Geometrical information of the single fracture was obtained by means of a μXCT with a spatial resolution of 80 μm. This spatial information served as direct input for finite element simulations in Semi-2D and 3D using commercial finite element code ADINA-F to calculate flow velocity distribution and tracer transport. Experimentally obtained HTO breakthrough curves (BTC) with core#8 show a significant tailing reflecting complex flow and transport processes. Calculated BTCs also exhibit a distinct tailing due to Taylor dispersion and trapping of the tracer in so called low velocity zones near the irregular fracture walls. The results clearly indicate the impact of spatial heterogeneities on the coupled flow and transport processes occurring in fractured rocks leading to a dispersion and retardation of solutes and therefore to distinct tailings in the BTCs.

Introduction

Fluid flow as well as mass transport through fractured rock plays an important role in both scientific and industrial issues ranging from e.g. petroleum engineering to the storage of nuclear waste in a deep geologic repository. Fractured rock behaves completely different compared to porous media concerning fluid flow, especially fractured rock systems with very low matrix permeability. In contrast to porous media, fluid flow through fractured rocks is bound to discrete roughly shaped planes, which act as main flow paths. As a consequence this issue has been extensively studied in the past by several authors [1-4]. Both experimental and theoretical approaches have been applied to shed light on the processes governing flow and transport in single fractures as

well as fracture networks. In most cases, fractures were treated with the parallel plate model or the streaming tube approach, where real natural fracture geometries are replaced by simplified and abstracted geometries. These simplifications have been made because of a more easily mathematical description resulting in a lesser computational effort. Besides, random fractures have been generated virtually by means of statistical and mathematical methods [5]. The governing equation describing fluid flow is the Navier-Stokes equation which represents a nonlinear system of partial differential equations, only to be solved numerically in 3D. Modern laboratory techniques, like e.g. computer tomography can serve as a non-destructive tool for characterisation of natural fractures in drill cores providing geometrical information which can be used directly in numerical codes to conduct flow and mass transport simulations on the measured scale. This more realistic approach has been applied in our study.

Core characterisation

The core used in this study comes from hard rock laboratory (HRL) in Äspö (Schweden) from the drill hole KOV 01 774.7-775.2. From a petrologic point of view, it would be classified as a diorite. For further geological, petrologic and geochemical details of the site, see [6]. Prior to characterisation, the core was sealed on the outside by sticking it in a custom made Plexiglas column. To gain information about geometry and orientation of the fracture and porosity and aperture distribution, it was scanned using a µXCT. For further details about the applied experimental techniques it is referred to [7]. The size of the core is 13.528 cm in length and 5.048 cm in diameter. With the aforementioned method and setup a resolution of 80 µm was achieved. The obtained CT data set was pre-processed using different computational tools for CT artefact reduction and segmentation of the fracture. By utilization of the complete CT dataset a connected porosity of 0.68% and an aperture distribution of the core could be derived. Figure 1 shows the fracture as rendered from the pre-processed data set. As expected for a real fracture, it possesses a complex 3D spatial geometry and fracture surface morphology. One side of the core shows a relatively sharp border, while the other side has a very irregular boundary. The last mentioned complex geometric feature is known/assumed to have a strong impact on the flow field and in consequence a strong influence for mass transport. Here occurrence of so called trapping zones is likely which can retard tracers and colloids when entering recirculation zones, e.g. through dispersion and/or diffusion [8].

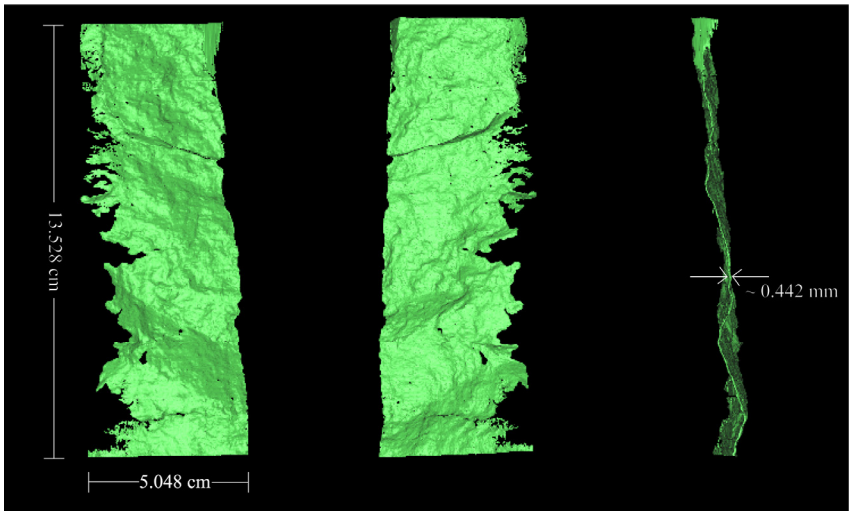

Figure 1: *Rendered 3D image of fracture in Core#8 on the basis of the μXCT data set which shows the complex overall geometry and surface morphology. Notice the very irregular boundary on one side of the fracture.*

Finite Element Model

We model the fluid flow and tracer transport through the fracture using the commercial finite element code ADINA-F [9, 10]. To study the effect of the fracture geometry two completely different models concerning the geometrical complexity have been generated. The first model in semi-2D dimension uses only mean values for the aperture, thus reducing most of the geometrical information of the CT data. The second model is a full 3D model using the complete CT data set, thus all of the geometrical information are considered. Mesh generation of the semi-2D was produced using the ADINA-F build-in mesh generator. The 3D volume mesh was generated out of the CT data set by means of the software 3-matic. Figure 2 shows both finite element meshes used in the study. All surfaces except the inlet at the bottom and the outlet at the top of the fracture are assigned no-slip (no-flow) boundary conditions.

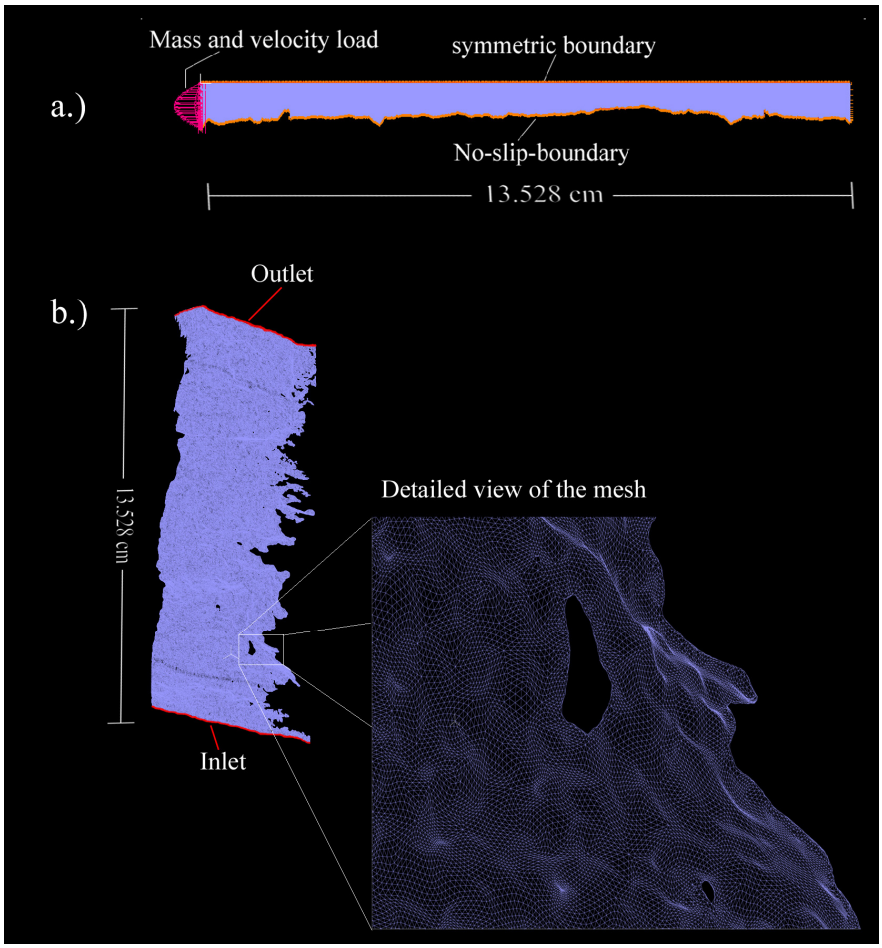

Figure 2: *a.) View of the semi-2D finite element mesh with the applied boundary and load conditions. Note that the aperture is shown as 30 times exaggerated for displaying reasons b.) 3D model with the inlet and outlet velocity boundary condition. The detailed view of a part of the 3D mesh shows an area inside the model where the fracture is closed.*

In the semi-2D mesh a symmetric boundary has been applied at one side of the fracture. At the inlet of both models parabolic velocity profiles have been applied as velocity boundary condition and the exact tracer input function from the experiment is used as mass load boundary condition. The possible existence of matrix porosity in the vicinity of the fracture boundary and especially on the very irregular side of the fracture are completely ignored, to exclusively study the influence of geometry information on the velocity flow field an thus on the mechanisms dominating mass transport. Due to the same reason, calculations are conducted without regarding any chemical processes like e.g. sorption or sorptive reduction. The flow is laminar and water as fluid is incompressible with a density of 998.1 kg/m^3 and a viscosity of 0.001 kg/ms. A diffusion coefficient of $2.5 \cdot 10^{-9}$ m/s^2 for HTO has been used. Both models are used to calculate a HTO breakthrough curve obtained by a migration experiment on core #8 with a flux of 0.1ml/min.

Mathematical description of fluid flow

The governing equation which describes complex fluid flow behaviour is the three-dimensional Navier-Stokes equation which is a non-linear system of partial differential equations satisfying the momentum, mass and energy conservation. For a

steady state laminar flow of a Newtonian fluid with constant density and viscosity the equation can be written in vector form as [11]

$$\rho(u \cdot \nabla)u = \mu\nabla^2 - \nabla p \quad (1)$$

$$\nabla \cdot u = 0 \quad (2)$$

where ρ = fluid density, μ = fluid viscosity, $u = (u_x, u_y, u_z)$ velocity vector and $p(x,y,z)$ = hydrodynamic pressure. Eq.(1) represents the momentum conservation and Eq.(2) the mass conservation. The inertial forces, viscous forces and pressure forces are described in Eq.(1) by the first, second and third term, respectively. Depending on the ratio of inertial to viscous forces, which is known as the Reynolds number, a simplification of the Navier-Stokes equation can be achieved. This is the case when inertial forces are small compared to viscous and pressure forces, so the Navier-Stokes equation reduces to the so called Stokes equation which can be expressed as

$$0 = \mu\nabla^2 u - \nabla p \quad (3)$$

The Stokes equation forms a system of linear partial equations and thus can be solved more easily. By applying no-slip (=no-flow) boundary conditions at the boundary walls one component in the velocity vector u (u_x, u_y, u_z) becomes zero which leads to a further simplification and thus lesser computational effort.

Results

Calculated velocity, pressure and mass distribution of the semi-2D model are shown in figure 3. As expected, a parabolic velocity profile has evolved and highest flow velocities correlate with zones of smaller aperture and vice versa. The pressure distribution shows a continuous gradient representing steady state flow conditions. A snapshot of tracer migration after 2250s reflects the parabolic velocity profile which leads to a dispersion. Figure 4 shows experimentally obtained breakthrough curves from migration experiments with core#8 in comparison with breakthrough curves calculated using the above described two finite element models. Regarding the semi-2D model, the peak correlates satisfactorily with the experimental peak position. A clear deviation in the tailing of the BTC is observed which can be explained by the averaging step of the geometrical information. The tailing is mainly produced by Taylor dispersion and to a lesser extends by molecular diffusion. It is obvious that the application of a mean aperture results in an averaging of the tailing in the calculated BTC.

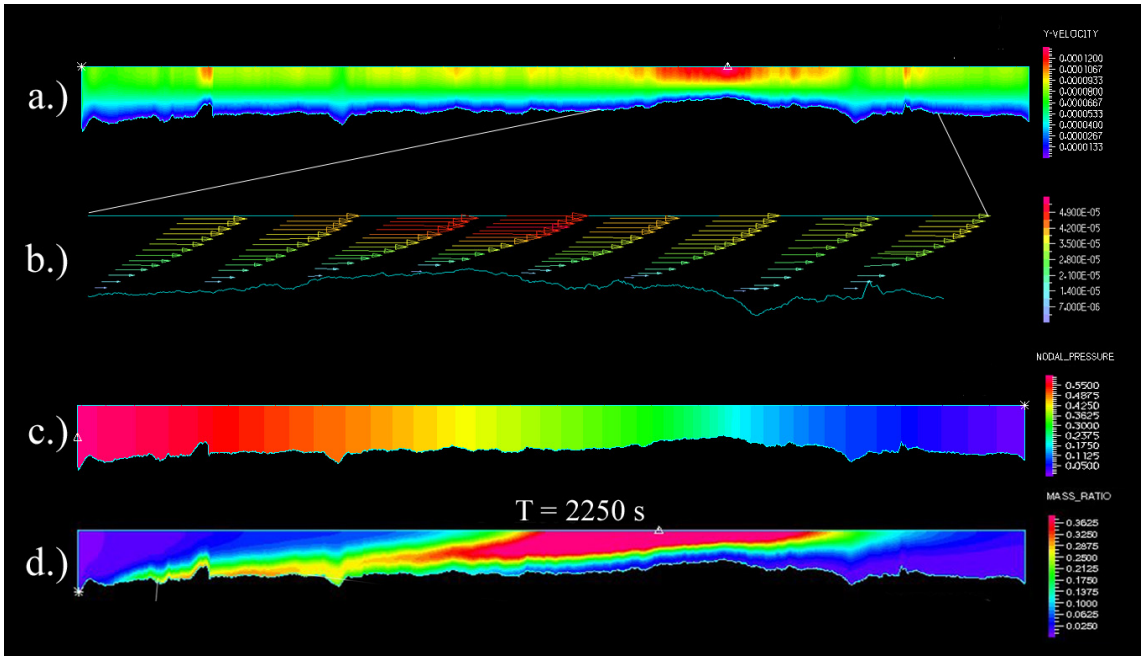

Figure 3: *Results of the semi-2D model. a.) velocity distribution in the fracture. b.) detailed view of a part of the model showing velocity vectors. c.) calculated pressure distribution. c.) snapshot of the migrating tracer at time 2250 sec.*

First calculations using the 3D model are conducted at the moment. First results show a peak position which is shifted to earlier times compared to the experimental BTC due to the fact that the same velocity has been used in the 3D simulations as in the semi-2D model. The velocity is some kind of a fitting parameter, because only the flux is known from the experiment which has to be recalculated by dividing it through the surface area of the inlet of the fracture. This surface is not exactly known because of the experimental setup and can only be roughly estimated. Nonetheless, the shape of the calculated peak is in relatively good accordance to the experimental HTO BTC. It has to be stated that no complete breakthrough curve has been simulated at the moment because of technical problems. From a visualization of the mass transport it can be derived that one can expect a distinct tailing in the BTC. Tracer distribution in the fracture shows a strong influence of the irregular side of the fracture where the tracer seems to be strongly retarded.

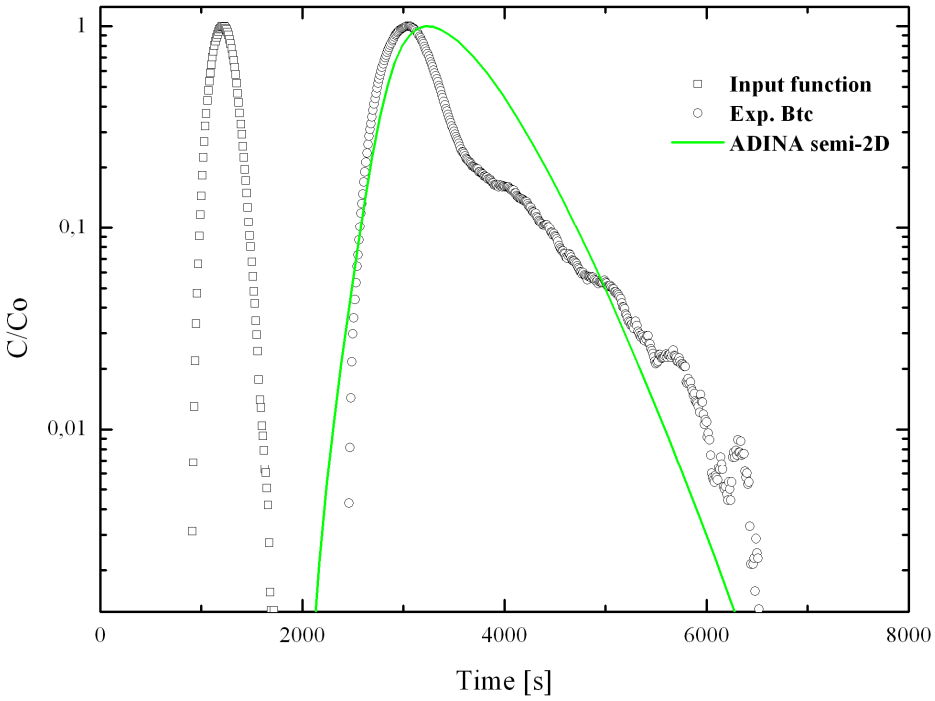

Figure 4: *Normalized experimental HTO (open symbols) and calculated (line) BTC as function of time.*

Summary and conclusions

Fluid and mass transport were simulated using the FEM approach on basis of datasets from a µXCT (resolution 80µm) of a single fracture in a diorite drill core. Goal of this study is to investigate the influence of real fracture geometry on the flow and transport behaviour. Two models have been presented. The semi-2D model only uses the averaged aperture of the fracture in contrast to the second model, a full 3D model using the full resolution of the CT dataset. Both models have been used to simulate a tracer migration experiment on the core#8. The semi-2D model results can reproduce the peak position quite satisfactorily but smoothes the tailing of the experimental BTC. These differences can be explained regarding the averaged fracture geometry information used in the model.

The current 3D model cannot reproduce the peak position, but matches the shape of the peak quite good. This deviation is due to the fact, that there is uncertainty at the moment about the real velocity at the inlet of the fracture which can only be roughly calculated out of the used flux in the migration experiment. It has to be stated that the shown results of the 3D model are of preliminary nature. Despite the greater computational and technical effort in creating a 3D model on a basis of CT data, our results could be a step towards a more fundamental understanding of the processes governing flow and mass transport in real single fractures.

References

[1] Moreno, L., et al., *Flow and Tracer Transport in a Single Fracture - a Stochastic-Model and Its Relation to Some Field Observations.* Water Resources Research, 1988. **24**(12): p. 2033-2048.

[2] Tsang, Y.W., et al., *Flow and Tracer Transport in Fractured Media - a Variable Aperture Channel Model and Its Properties.* Water Resources Research, 1988. **24**(12): p. 2049-2060.

[3] Meier, P.M., A. Medina, and J. Carrera, *Geostatistical inversion of cross-hole pumping tests for identifying preferential flow channels within a shear zone.* Ground Water, 2001. **39**(1): p. 10-17.

[4] Carrera, J., *An Overview of Uncertainties in Modeling Groundwater Solute Transport.* Journal of Contaminant Hydrology, 1993. **13**(1-4): p. 23-48.

[5] Tsang, C.F., C. Doughty, and M. Uchida, *Simple model representations of transport in a complex fracture and their effects on long-term predictions.* Water Resources Research, 2008. **44**(8).

[6] Laaksoharju, M., et al., *Hydrogeochemical conditions and evolution at the Aspo HRL, Sweden.* Applied Geochemistry, 1999. **14**(7): p. 835-859.

[7] Enzmann, F. and M. Kersten, *X-ray computed micro tomography (μ-XRT) results of a granitic drill core*, in *1st Annual workshop Proceedings of IP FUNMIG, report CEA R-6122*, P. Reiller, et al., Editors. 2006, Commissariat a l'energie atomique (CEA): Gif sur Yvette (France). p. 211-215.

[8] Boutt, D.F., et al., *Trapping zones: The effect of fracture roughness on the directional anisotropy of fluid flow and colloid transport in a single fracture.* Geophysical Research Letters, 2006. **33**(21).

[9] Bathe, K.J., H. Zhang, and S.H. Ji, *Finite element analysis of fluid flows fully coupled with structural interactions.* Computers & Structures, 1999. **72**(1-3): p. 1-16.

[10] Bathe, K.J., H. Zhang, and M.H. Wang, *Finite-Element Analysis of Incompressible and Compressible Fluid-Flows with Free Surfaces and Structural Interactions.* Computers & Structures, 1995. **56**(2-3): p. 193-213.

[11] Brush, D.J. and Thomson, N.R., *Fluid flow in synthetic rough-walled fractures: Navier-Stokes, Stokes and local cubic law simulations.* Water Resources Research, 2003. 39(4): p. 1085-1099.

RESPONSE OF URANIUM MINERALS TO CLIMATIC CHANGES - EXAMPLE FROM PALMOTTU, SOUTHERN FINLAND

Mira Markovaara-Koivisto[1*] and Klaus Einsalo[1]

[1] Helsinki University of Technology, PO Box 6200, 02015 TKK, Finland
* Corresponding author; Mira.Markovaara-Koivisto@tkk.fi

Keywords: uranium series disequilibrium, crystalline bedrock, Palmottu

Abstract

Nuclear waste will be deposited in Finland approximately at the depth of 300-400 meters in crystalline bedrock at Olkiluoto, western Finland. According to current understanding the depth of the permafrost during the next glaciations will never reach the repository level, and thus so not affect the repository. Possible glacial melt water may reach to the repository level and may pose a risk. The fate of naturally occurring uranium in crystalline bedrock, exposed with certainty to permafrost and melt water is studied and discussed here. This is done by identifying the natural uranium and thorium minerals in samples and measuring activity ratios of uranium and thorium isotopes from naturally uranium rich rock samples from Palmottu, Southern Finland. The samples were taken close to the surface, depth 0-31.56 m, where in addition to the groundwater seepage, permafrost and glacial melt water have undoubtedly affected.

Uranium and thorium were found to occur as primary minerals, uraninite and monazite, and as precipitates as secondary minerals, like uranophane, boltwoodite and thorite. The $^{230}Th/^{234}U$ and $^{234}U/^{238}U$ ratios showed leaching and accumulation of uranium caused by the on going precipitation/dissolution processes near rock surface, and in one case a very forceful leaching, explained by forceful impact of oxygenised glacial melt water or mineralogy being digested. The different uranium phases could not be dated from these samples due to the openness of the system, and the non-selectiveness of the leaching. Nevertheless uranophane crystals on the surfaces of water conductive fractures in parallel samples from the same drill cores have been dated by Read et al. (2008), and the ages coincide with the warm periods between glaciations. The activity ratios showed that uranium has migrated in the timeframes of the beginning of the last Weichsel glaciation until almost present day.

Introduction

Nuclear waste will be deposited in Finland approximately at the depth of 300-400 meters in crystalline bedrock at Olkiluoto. Possible glacial melt waters may intrude close to the repository level and pose a risk. In case the Engineering Barrier System (EBS) failed the nuclear waste could get into contact with the groundwater, and uranium could be released when affected by the fresh melt waters, oxidise into VI-state and migrate into the far field. The fate of shallow naturally occurring uranium in crystalline bedrock, exposed to oxidising conditions, is studied and discussed here. This is done by identifying the natural uranium and thorium minerals in samples and by measuring activity ratios of uranium and thorium isotopes from crushed, naturally uranium rich rock samples from Palmottu, Southern Finland. The samples were taken close to the surface, depth 0-31.56 m, where in addition to the groundwater seepage, permafrost and glacial melt water have undoubtedly affected. For comparison also parallel samples studied by Read et al. (2008) are presented and discussed here.

Samples

Sample R390 is a drill core, Ø = 42 mm (Figure 1A). One end of the sample is a natural fracture surface that shows some yellowish coating minerals. The sample is heterogeneous, containing large, pale pink feldspar grains (7 mm), a biotite concentration, scattered smaller greenish quartz grains, and in fractures a visible yellow filling. Some red Fe-hydroxides occur within the feldspar grains.

Figure 1. *Uranium rich samples from Palmottu, Southern Finland. A) R389, B) R390 and C) Boulder sample from left to right. Corresponding sample width is 3.2 cm, 4.1 cm and 3.5 cm.*

Sample R389 is one half of a drill core sample, Ø = 42 mm (Figure 1B). This sample is also heterogeneous and coarse-grained. Feldspar grains are moderately large, 2–10 mm. The space between grains are filled with small quartz grains and there are dark reddish Fe-hydroxide are present as infillings in the feldspar grains. Feldspar and quartz are unevenly distributed.

Boulder sample is mostly composed of greenish quartz, but containing some small, red and visibly altered feldspar grains (Figure 1C). Calcite occurs as fillings in fractures with apertures about 0.5 mm. Fe-hydroxide stains the grain boundaries of some minerals.

Methods

Mineralogical studies

Uranium and thorium mineralogy in the samples were studied with HITACHI S-4800 type scanning electron microscope (SEM) and Oxford instruments + INCA program for energy dispersive spectrometry (EDS) analyses and Cameca SX100-type wave dispersive spectrometry (WDS). The microprobe analyses were carried out with 15-20 keV acceleration voltage and 10-25 nA beam current. In back scattered electron (BSE) images the minerals are visualised according their chemical content, with different minerals appearing in varying shades of gray.

Uranium Series Disequilibrium (USD)

Activity ratios of uranium phases tell about the chemical conditions in which they were formed or have been influenced by. They can not tell about the phenomena inside the permafrost, because the rock was frozen and no reactions occurred. Underneath the permafrost the rock has been unfrozen, but the samples studied here, were close to the surface. Any reactions in these samples must have occurred before the permafrost propagated to the Palmottu area, after the glacier had turned into warm based glacier or during the interglacial periods.

Measuring activity ratios of different uranium and thorium isotopes can be used to study uranium minerals in fracture surfaces. If the groundwater system in which the uranium minerals have been situated is open, actual ages for the uranium minerals can not be calculated because some of the decaying uranium or the daughter nuclides may have been lost. In such case activity ratios can be used to tell what kind of chemical conditions prevailed at the time of mineral formation.

Samples for this study were taken from a naturally uranium rich granite of Palmottu. Two of the samples were drill cores from depth of 7.43 m and 31.45 m, and one sample was from a boulder buried in the till above the bedrock. The samples were crushed with a tungsten mill to have larger reactive surface areas for the following sequential leachings.

Samples were leached only with aqua regia, or sequentially first with artificial groundwater (Allard et al., 1991), then ammonium acetate and aqua regia. Artificial groundwater releases adsorbed and ion exchangeable phases and ammonium acetate releases adsorbed, specifically sorbed phases and phases associated with fracture calcite ($CaCO_3$). Aqua regia dissolves phases co-precipitated with hydrous Fe-oxides. It does not release phases incorporated in silicate residue (Chao, 1984; Pickering, 1986).

Crushed rock samples were allowed to react with artificial groundwater for 1 hour; the samples were centrifuged for 5 minutes and supernatants were pressed through 0.45 μm membrane filter. The same samples of crushed rock then were allowed to react with ammonium acetate for 1 hour, the samples were centrifuged for 5 minutes and supernatants were pressed through a 0.45 μm membrane filter. These solutions were then dried on a stove in decanters. The rock samples were then wet burned with concentrated HNO_3. The samples were rinsed into a decanter and aqua regia was added to them. The

rock samples were boiled for 30-40 minutes and dried. Then HCl was added and the supernatants were filtered into new decanters.

The supernatants were put through ion exchange resin and Th and U were separated. U^{6+} was reduced to U^{4+} by adding $TiCl_3$. The separated Th and U were slowly precipitated with CeF_3 in a refrigerator, then the solutions were filtered through a 0.45 µm membrane filter, and the α-activities on the filters were measured with an α-spectrometer.

Results

The samples were found to contains both uranium and thorium minerals. Primary minerals were uraninite (UO_2) and Ce-monazite [(Ce,La,Nd,Th)PO_4]. Secondary minerals were uranophane [$Ca(UO_2)_2SiO_3(OH)_2{\cdot}5(H_2O)$], possible boltwoodite [$HK(UO_2)(SiO_4){\cdot}1.5(H_2O)$] and thorite ($ThSiO_4$).

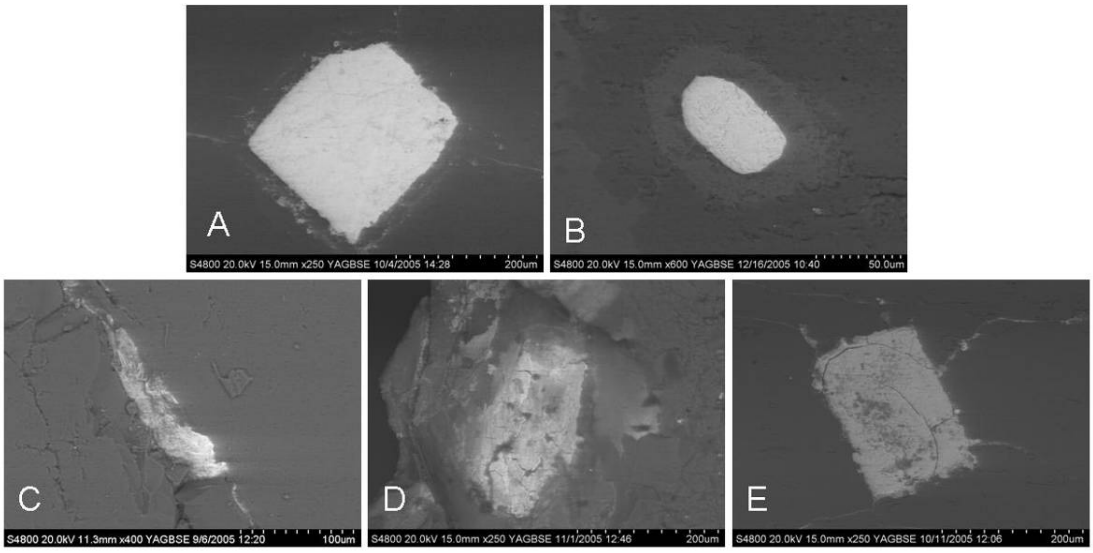

Figure 2 *BSE-images of uranium and thorium minerals in Palmottu samples. Primary minerals were A) uraninite and B) Ce-monazite. Secondary minerals were C) uranophane, possible D) boltwoodite and E) thorite.*

Uraninite is expected to dissolve partially in ammonium acetate (Bolle et al., 1988) and monazite stays in the residue. Uranophane, boltwoodite and thorite dissolve into the ammonium acetate.

Figure 3 shows the calculated $^{234}U/^{238}U$ and $^{230}Th/^{238}U$ activity ratios from this study and Read et al. (2008) in a Thiel's diagram. The isochrones can be used only for closed systems. In the upper part of the Palmottu hill this has most probably not been the case at least where the crushed rock samples are from.

Most of the activity ratios in the phases leached out from the crushed samples were depleted in ^{234}U. This indicates sudden release of uranium from primary uranium phase, uraninite. Only two phases, leached out with ammonium acetate, presented

$^{234}U/^{238}U$ >1. This ratio can be caused by digestion of the secondary phases. This is because groundwater has an excess ^{234}U, which is seen also in the secondary uranium minerals precipitated from it.

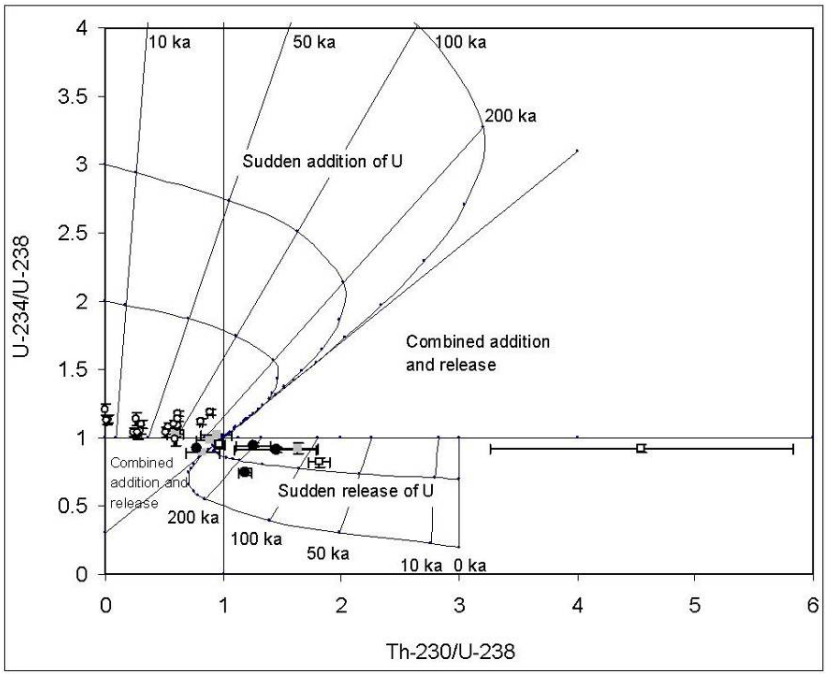

Figure 3. *A Thiel's diagram containing uranium and thorium isotope ratios of fractions released into aqua regia (white boxes) and into sequential leaching with ammonium acetate (grey) and aqua regia (black) Palmottu granite. For comparison also data from Read et al (2008, 2005) is presented (white circles).*

In this study most of the aqua regia digested phases were depleted in ^{234}U. This may be because of digestion of primary phases in which the more readily soluble ^{234}U has been released from the mineral grains.

Most of the measured phases digested with aqua regia had excess in ^{230}Th. Thorium content of the groundwater is low because it hydrolyses above pH 3, forms hydroxide species and adsorbs to surfaces (Ivanovich and Harmon, 1992), and thus uptake of thorium from solution into the precipitating uranium mineral is negligible (Read et al., 2008) and because uranium's daughter nuclide thorium does not move to aqueous solution, the excess indicates release of uranium. Aqua regia digests uraninite, which may have ^{230}Th excess due to release of uranium.

Uranium release has been remarkably intense for one phase leached with ammonium acetate (^{230}Th /^{238}U ~ 4.5±1.2). This and the other ^{230}Th enriched AR may be due to digestion of the thorite grains.

Discussion

Extremely high $^{230}Th/^{238}U$ ratios at the depth of 31.45 meters may be caused by digestion of thorite minerals or indicate forceful release of U from the secondary uranium minerals. The magnitude of this ratio would argue for a forceful release of uranium in the past, which influenced the more readily soluble phases, which was leached with ammonium acetate, more than the resistant phases, which was leached with aqua regia (Figure 3). This forceful dissolving factor could have been repeated impact of oxygenized glacial melt waters. Uranophane, the most common secondary uranium minerals at Palmottu, is known to be stable in oxygenised conditions (Read et al., 2008) and to exhibit a solubility minimum at pH 6-8 (Perez et al., 2000 in Read et al., 2008). But shallow groundwaters are often more acidic, and thus dissolve uranophane. Deep groundwaters are buffered, and thus preserve uranophane (Blyth et al., 2004 in Read et al., 2008).

In the study by Read et al. (2008) effort was put to separate the measures uranophane crystals from other minerals so that it is possible to get as accurate ages for the minerals as possible. In the present study, the rock was crushed and sequentially leached to separate the phases with different solubility. This does not assure dissolution of only one certain phase, but most of the phases, which are soluble in such conditions.

Table 1 shows $^{230}Th/^{238}U$ activity ratios found from Palmottu in earlier studies by Read et al. (2005, 2008) and calculated U-Th ages, and AR's in the new studies in this work. Einsalo et al. (2006) suggested that low AR ($^{230}Th/^{238}U$) deep in the bedrock indicate hydrological activity during recent glacial events. Low AR ($^{230}Th/^{238}U$) close to the surface, as with the samples studied here, indicate redox front phenomena and flow paths, where uranium has been able to precipitate. The same phenomenon was recognised by Read et al (2005). They found that surface samples have an extremely low $^{230}Th/^{238}U$ ratio indicating sudden addition of uranium and the recent formation of these minerals. Read et al. (2004, 2008) suggested that close to the surface the formation of secondary uranium minerals is an ongoing process, and that uranophane is most likely precipitate due to the high calcium content in the shallow groundwaters.

Table 1. *$^{230}Th/^{238}U$ activity ratios and U-Th ages for surface covering uranophane crystals (Read et al., 2005, 2008) and for minerals soluble in aqua regia, and in sequential leaching with ammonium acetate and aqua regia from Palmottu granite.*

Palmottu (Read at al., 2005)			Palmottu (Read et al., 2008)			Palmottu			
Depth (m)	$^{230}Th/^{238}U$	U-Th Age (yr)	Depth (m)	$^{230}Th/^{238}U$	U-Th Age (yr)	Depth (m)	$^{230}Th/^{238}U$	$^{230}Th/^{238}U$	
							Aqua regia	Sequential leaching	
								Ammonium acetate	Aqua regia
Surface	0.022±0.00006	2449	25.51a	0.62±0.02	90 992	Boulder	-	0.88±0.1	-
	0.01±0.00002	1208		0.53±0.01	73 814		-	0.60±0.07	1.45±0.36
	0.005±0.000004	545		0.30±0.008	36 485	7.43	0.97±0.04	0.83±0.14	1.25±0.14
	0.01±0.00002	1262		0.30±0.007	34 688		-	0.94±0.12	0.78±.014
	0.017±0.00004	1889		0.62±0.011	78 930	31.45	1.82±0.1	4.55±1.24	1.19±0.06
	0.011±0.00002	1170		0.26±0.006	27 762		-	1.64±0.16	-
	0.013±0.00003	1406	25.51b	0.60±0.01	86 701				
	0.005±0.000004	565		0.51±0.01	69 214				
	0.011±0.00002	1163		0.24±0.003	28 502				
	0.011±0000.2	1166		0.28±0.004	31 737				
7.03	0.81±0.01	135 262		0.61±0.011	78 036				
	0.62±0.008	83 639		0.31±0.007	343 200				
	0.58±0.01	81 351							
	0.88±0.02	139 132							

In this study, the boulder sample, taken also from the surface, had only minor depletion of $^{230}Th/^{238}U$. The surface samples in the earlier work by Read et al. had a low $^{230}Th/^{238}U$. These samples were taken from few centimetres inside the rock surface, and the samples in this study were taken from a boulder buried in the till. One possible explanation for this difference in the ARs of these samples is the different systems affecting them (Figure 4). The boulder sample is rich in both primary uraninite and secondary uranophane. But because of location of the boulder, uranium dissolved from the primary phases can be removed from the system in the boulder, but thorium stays in the boulder because it hydrated quickly and thus AR stays low. The samples taken from the bedrock surface may contain young secondary uranium migrated to the sampling site, and thus has very low thorium content.

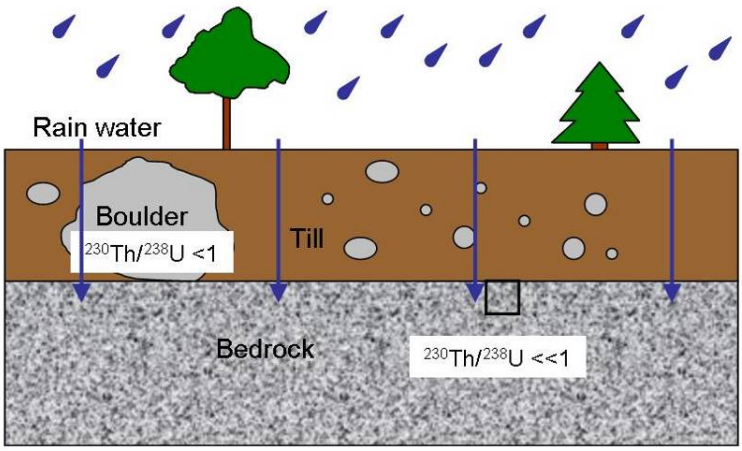

Figure 4. *A schematic image of the location of the boulder sample and the sample in Read et al. (2008) and different systems affecting their ARs.*

Conclusions

During permafrost uranium does not migrate in the shallow parts of the bedrock, because it needs liquid water to move. After the cold based glacier turns into warm based glacier or the glacier starts to melt and oxygenized melt water intrudes the bedrock, uranium phases start to dissolve into the groundwater, it migrates and forms relatively young secondary minerals. Read et al. (2008) showed that the formation of the secondary uranium minerals was halted during the last glacial maximum ca. 20 ka BP. On the other hand, the secondary uranium minerals displayed a cluster at the interglacials 27-37 ka BP, 70-100 ka BP and 0.5-3 ka BP. This clearly indicates that the formation of uranium minerals is an on-going process and they can be linked to climatic changes.

The samples studied in this work, presented ARs implying leaching and accumulation of uranium, which could be due to acidic rain water dissolving the secondary phases and subsequent precipitation of the uranium in the groundwater. In addition, ARs showed forceful leaching of uranium, which could have been caused by intrusion of oxygenized glacial melt water. Due to the openness of the system and non-selectiveness of the leaching method this study gave poorer results compared to studying secondary uranium mineral crystals separated from the other rock mass (Read et al., 2008).

References

Allard B., Karlsson F. and Neretnieks I., 1991. SKB Technical Report 91-50.

Chao T.T., 1984. Use of partial dissolution techniques in geochemical exploration. Journal of Geochemical Exploration, 20, pp. 101-135.

Bolle J.N., Martin H., Sondag F. and Fonseca E.C., 1988. Selective Chemical Extraction of Uranium from Mineral, Soil and Stream Sediment Samples at Horta da Vilariça, Northeastern Portugal. Uranium, 4, pp. 327-340.

Ivanovich M. and Harmon R.S. (Eds.), 1992. Uranium series disequilibrium: Applications to Earth, Marine and Environmental Sciences. 2nd ed. Clarendon Press, Oxford. 920 p.

Pickering W.F., 1986. Metal ion speciation – soil and sediments (A review). Ore Geology Reviews, 1, pp. 83-146.

Read D., Siitari-Kauppi M., Kelokaski M., Black S., Buckby T., Marcos N., Kaija J. and Hellmuth K-h., 2004. Natural Geochemical Fluxes in Finland as Indicators of Nuclear Repository Safety. Helsinki University of Technology, Geoenvironmental Technology, A Research Report 34, Espoo. 58 p.

Read D., Black S., Buckby T, Proust D., Marcos N. and Siitari-Kauppi M., 2005. Secondary Uranium Mineralization in Southern Fennoscandia. Helsinki University of Technology, Geoenvironmental Technology, A Research Report 2, Espoo. 37 p.

Read D., Black S., Buckby T., Hellmuth K-H., Marcos N. and Siitari-Kauppi M., 2008. Secondary Uranium Mineralization in Southern Finland and its Relationship to Recent Glacial Events. Global and Planetary Change, doi: 10.1016/j.gloplacha.2007.02.006.

HUMIC ACID FRACTIONATION STUDIED BY ASYMMETRIC FLOW FIELD FLOW FRACTIONATION

Aurélien Pitois[1], Liam G. Abrahamsen[1], Peter Ivanov[1], Nick D. Bryan[1,*] Nick Evans[2], Peter Warwick[2]

[1] Centre for Radiochemistry Research, School of Chemistry, University of Manchester (UK)
[2] Department of Chemistry, Loughborough University, Loughborough (UK)

* Corresponding author: nick.bryan@manchester.ac.uk

Abstract

A kinetic study of Aldrich humic acid sorption onto a quartz sand surface has revealed an initial rapid uptake of humic acid molecules followed by a much slower sorption. The humic acid molecular weight and chemical fractionation resulting from adsorption onto the simple quartz sand surface have been investigated for the two kinetic steps by coupled asymmetric flow-field flow fractionation-UV/visible absorption spectrophotometry. The molecular weight distribution of the residual humic acid in solution after adsorption deviated from the original molecular weight distribution, showing preferential adsorption of certain molecular weight components. This fractionation is different after the two kinetic steps. Humic acid molecules characterised by a molecular weight below 4800 Da and with a weight-average molecular weight (Mw) of 1450 Da were adsorbed after the fast kinetic step, whereas humic acid molecules in the molecular weight range 1400–9200 Da and of Mw 3700 Da were adsorbed during the slower uptake. Therefore, the adsorption of low molecular weight humic components takes place initially, and is then followed by the adsorption of higher molecular weight components. Chemical adsorptive fractionation, investigated by studying the 253 nm/203 nm absorbance ratio over time, shows that there is significant chemical/structural fractionation during the fast kinetic step. The trend for the sorption kinetics of europium onto the quartz sand surface in the presence of humic acid is similar to that of the humic acid itself.

Introduction

Previous work [e.g. 1] has shown that the formation of ternary complexes affects the partition of radionuclides between the solid and solution phase. Further, it has been shown that chemical/size fractionation accompanies the sorption of humic substances [e.g. 2]. Hence, it is important to study humic fractionation, because it could have a direct impact on the fate of radionuclides. This work has recently been published as a

full research paper [3], and a more detailed review of previous related studies is given there. The uptake of Aldrich humic acid onto this quartz sand sample has been reported previously [1]. Briefly, at an initial humic concentration of 100 ppm, there is an initial, rapid uptake of humic over the first few days, followed by a slower uptake of material over the following weeks. The object of this work is to study the reasons for this 'fast' and 'slow' behaviour.

Experimental

The sorption of pre-equilibrated (24 hr) humic acid and europium ions in the presence of humic acid onto a quartz sand surface have previously been studied (Conditions: 0.5 g/mL; [Eu]= 8×10^{-10} M; [HA]=20, 50, and 100 ppm; pH 6.0 ± 0.1; I= [$NaClO_4$] = 0.1) [1]. The fractionation of the same humic acid onto the same quartz sand surface was investigated after 3 and 45 days using coupled AFFF (Asymmetric Flowfield Flow Fractionation-UV/visible absorption spectrophotometry, AF 2000 Focus, Postnova Analytics, Landsberg, D) at an initial humic concentration of 100 ppm. The solution samples for the determination of Eu and HA binding and AFFF analysis were separated from the solid and prepared in the same way. AFFF analysis at different wavelengths was performed to investigate the chemical fractionation. The AFFF experimental conditions were: membrane 5 kDa regenerated cellulose; channel thickness 250 μm; injection volume 19.6 μL; detector flow rate 1 ml/min; cross-flow rate 4 ml/min; focus step injection flow and time 0.20 ml/min, 2 min; transition time 1 min; elution step time 15 min; carrier solution 0.005 M Tris solution, pH 9.1. Even though the molecular weight cut-off of the semi-permeable AFFF membrane is 5 kDa, humic molecules with molecular weights lower than 5 kDa are retained in the channel, since the negatively charged cellulose membrane repels the negatively charged polyelectrolytic humic molecules. The equipment was calibrated with polystyrene sulphonate standard colloids (1, 6, 10, and 30 kDa). More details are given in Pitois et al [3]. In this publication, the AFFF results are presented as mass data that have been obtained by comparison with the PSS standards. This is the standard method of presenting AFFF data in the literature. However, the technique actually separates samples by their size, rather than mass. PSS standards have a notional density of 1.055 cm^3/g, although this is the value determined for bulk samples and larger particles, and the effective density of the smaller standards used here may vary. Using this value, and assumimg that the humic species and PSS standards have the same (spherical) shape, a humic radius, R_{HA}, can be obtained using,

$$R_{HA} = 7.22\text{x}10^{-11} \text{ x } M_{PSS}$$

where M_{PSS} is the mass determined relative to the PSS standards. In theory, given the density of humic species in solution, it should be possible to produce a corrected humic mass, M_{CORR}, although the uncertainty in the solution partial specific volumes of dissolved humic species means that the multiplication factor is itself uncertain:

$$M_{CORR} = (1.75 \pm 0.75) \text{ x } M_{PSS}$$

As it is standard practice to report uncorrected masses from this technique, all of the mass data in the figures and quoted in the text are uncorrected, i.e., M_{PSS}.

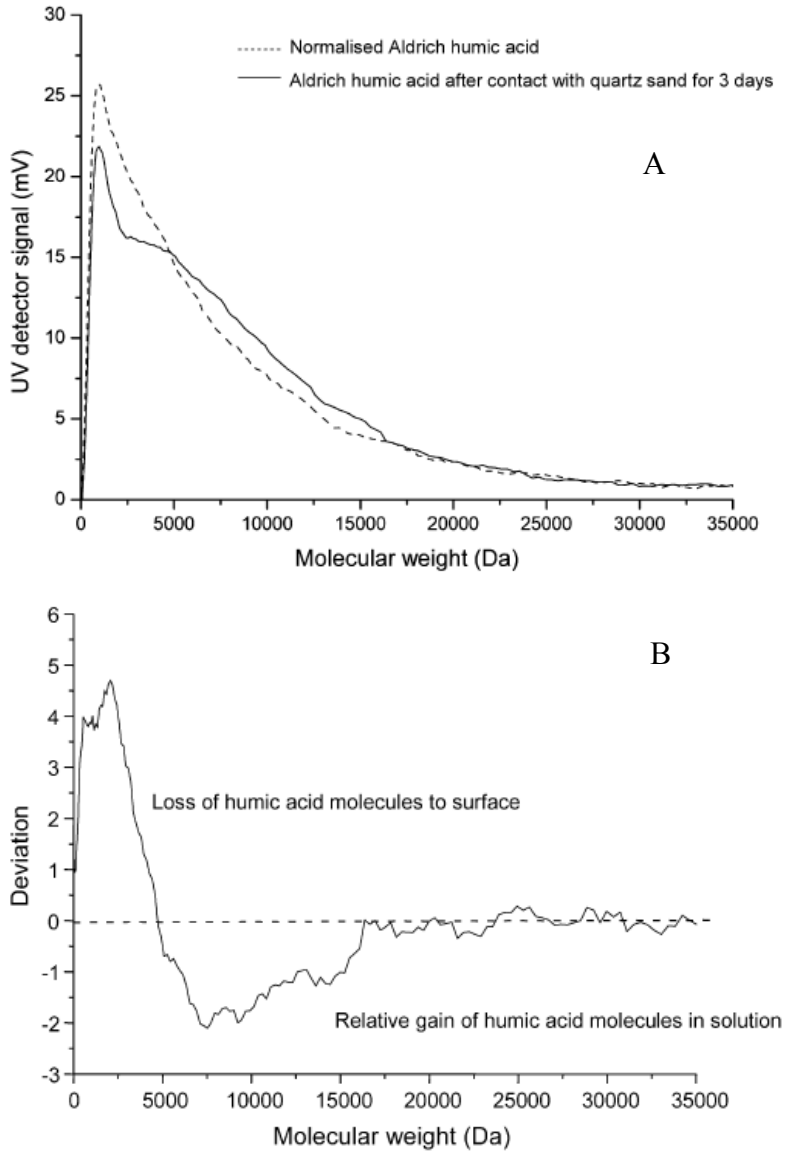

***Figure 1**: **(A)** **Normalised** molecular weight distribution of Aldrich humic acid before and after contact with quartz sand for 3 days; **(B)** **Relative** change in distribution. Note all masses are relative to the PSS standards*

Results and discussion

The normalised molecular weight distributions of Aldrich humic acid before and after contact with quartz sand for 3 days are presented in Fig. 1A. The distributions before and after contact are obviously different, indicating that there has been fractionation of the humic acid. The original Aldrich humic acid is characterised by a broad molecular weight distribution (up to 30,000–35,000 Da), a most probable molecular weight of 1000 Da (±150 Da) and a weight-average molecular weight *M*w of 3900 Da (±300 Da). These values fall within the range of values previously reported [3]. The residual humic acid remaining in solution after contact with the quartz sand surface for 3 days is characterised by a similar broad molecular weight distribution, a similar most probable molecular weight of 1000 Da (±150 Da), but a different weight-average

molecular weight *M*w of 4750 Da (±350 Da), a *M*w shift of 850 Da. This shift indicates a preferential sorption of lower molecular weight fractions. Of the original humic acid sample, 75% is composed of molecules having a molecular weight below 9500 Da (±500 Da); this value becomes 10,500 Da (±550 Da) for the humic acid remaining after sorption.

The preferential sorption of the low molecular weight humic acid fraction onto the quartz sand surface after 3 days has been investigated in more detail by determining the relative change in the distribution after 3 days (Fig. 1B). Humic acid molecules characterised by a molecular weight below 4800 Da (±350 Da) and a *M*w of 1450 Da (±200 Da) are preferentially adsorbed during the first step. Of the adsorbed humic acid, 75% is composed of molecules having a molecular weight below 2300 Da (±250 Da). The material preferentially sorbed onto the surface at this stage is approximately 16% of the total.

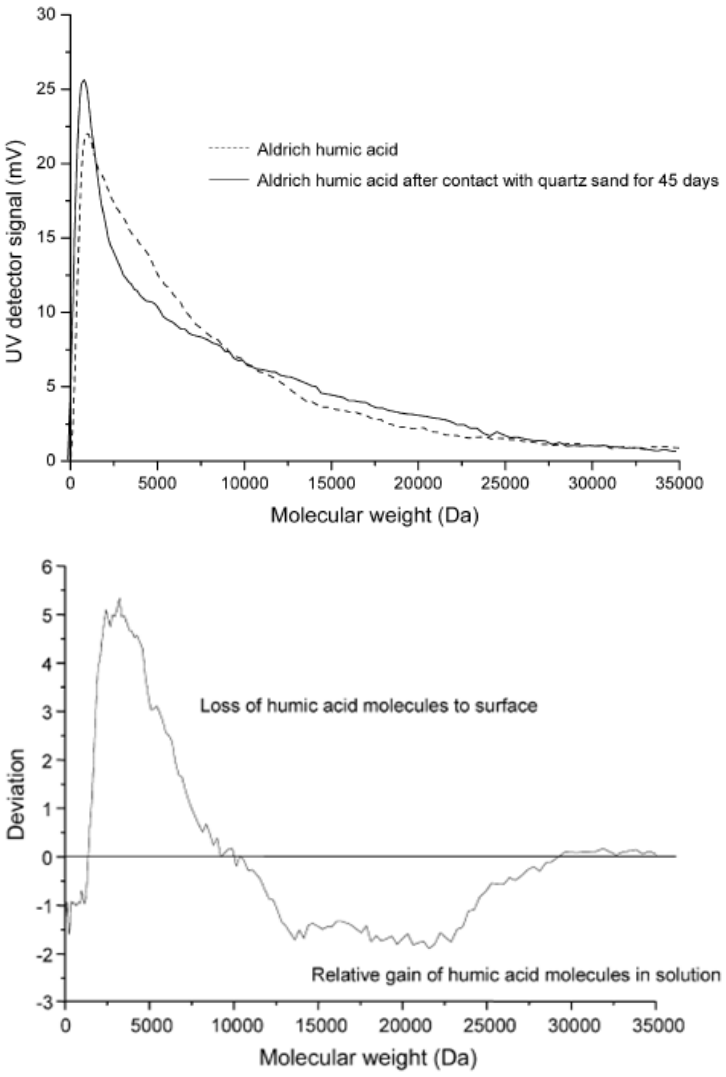

***Figure 2**: **(A)** **<u>Normalised</u>** distribution of Aldrich humic acid before and after contact with quartz sand for 45 days; **(B)** **<u>Relative</u>** change in distribution. Note all masses are relative to the PSS standards.*

A similar study and data interpretation have been performed for the humic acid after contact with the quartz sand surface for 45 days. The normalised molecular weight distributions before and after contact with quartz sand for 45 days and the relative change in distribution accompanying sorption after 45 days are presented in Fig. 2. The residual humic acid remaining in solution after contact with the quartz sand for 45 days is characterised by a broad molecular weight distribution and a most probable molecular weight of 1000 Da (±150 Da) similar to that of the initial sample, but a different *M*w of 3800 Da (±300 Da). This *M*w shift indicates a preferential sorption of higher molecular weights compared to those sorbed after only 3 days. Humic acid molecules in the molecular weight range 1400 Da (±200 Da)–9200 Da (±450 Da) and of *M*w 3700 Da (±250 Da) are preferentially adsorbed after 45 days. Of the adsorbed

humic acid 75% is composed of molecules having a molecular weight in the range 1400–4800 Da. The deviations from the original molecular weight distribution are significant. Fractionation is changing with time: the adsorption of lower molecular weight humic components takes place initially, followed by the adsorption of higher (but still not very large) molecular weight components. Raw molecular weight distributions of the original and the residual humic acid remaining in solution after contact with the quartz sand for 3 days and 45 days are shown in Fig. 3. No displacement of the low molecular weight fractions by the higher molecular weight fraction is observed over time. On thermodynamic grounds, an exchange between the small initially adsorbed molecules to chemically identical larger ones might be expected due to a related gain in translational entropy. Extremely slow kinetics or chemical structural differences between the species of different size may be why no displacement has been observed here and why the very large components do not appear to take part in sorption at all. Of course, there may have been dynamic exchange of low fractions for others of the same size. In the environment, very long equilibration times are possible, and so care must be taken before applying these results there. Further work on much longer timescales is required.

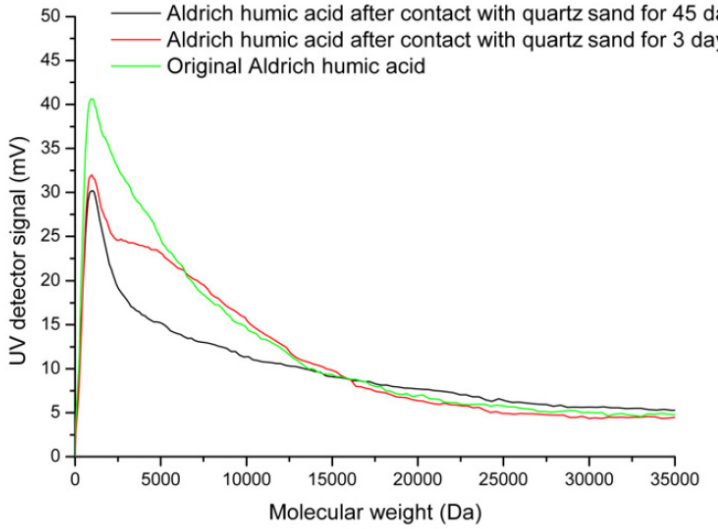

Figure 3: *Raw (**not normalised**) molecular weight distributions of the original humic acid and the residual humic acids remaining in solution after contact with the quartz sand for 3 days and 45 days. Note all masses are relative to the PSS standards.*

Chemical fractionation

Chemical fractionation has been investigated using the change in the 253/203 nm absorbance ratio over time. This ratio has been widely used as an indicator for humic acid chemical structural changes [4]. It has been suggested that this ratio is representative of the proportion of functional groups linked to aromatic structures in the humic acid molecules [5]. Data from IR, XANES and/or TRLFS would be required to confirm this is the case here. However, the change in ratio must indicate some structural differences. The variation in this ratio is presented in Fig. 4. There is a strong decrease of the 253/203 nm ratio during the first few days, suggesting that some humic components are preferentially adsorbed during the fast kinetic stage. It is significant that further sorption does take place between 3 and 45 days, but the 253/203 nm ratio

remains constant. This suggests that despite the preferential sorption over the first few days, there is no net preference over the next 42 days.

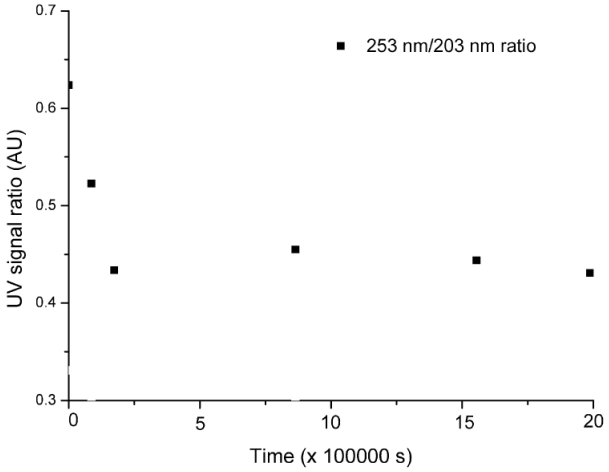

Figure 4: *Change of 253/203 nm absorbance ratio over time using the as indicator of chemical structure.*

The chemical fractionation of Aldrich humic acid after contact with quartz sand has also been investigated as a function of the molecular weight (by AFFF-UV). The results are presented in Fig. 5. The original Aldrich humic acid presents a high UV absorbance 253/203 nm ratio ($1.5 < x < 4.5$) for the low molecular weights (<1500 Da), an intermediate ratio ($0.7 < x < 1.5$) for the intermediate molecular weights (1500 Da < x < 13,000 Da), and a low ratio (<0.7) for the high molecular weights (>13,000 Da). The Aldrich humic acid after contact with quartz sand for 45 days presents the same general trend: the 253/203 nm ratio is higher for the low molecular weights and decreases with molecular weight, but this ratio is lower, compared to the original humic acid for the low and intermediate molecular weight fractions. This result is in good agreement with the size distribution and bulk 253/203 nm absorbance ratio data. The molecular weight distribution data suggested that very high molecular weight species were not affected by fractionation. These ratio data support that conclusion, since the plots in Fig. 5 converge at high masses. The results suggest that there is a chemical/structural difference between the different size fractions that have sorbed to the quartz sand surface.

Consequences for contaminant metal transport in the environment

The uptake of europium ions onto the quartz sand surface over time in the presence of different humic acid concentrations is shown in Fig. 6 as a function of initial humic acid concentration. The europium concentration is expressed as $\ln(C/C_0)$, where C is the europium concentration at time = t, and C_0 is the europium concentration prior to contact with quartz sand. In the absence of humic acid, europium is adsorbed very rapidly onto the quartz sand surface, and no significant kinetic behaviour is observed. In the presence of humic acid, europium sorption is clearly kinetically controlled. This is evidence for the formation of ternary complexes in the presence of humic acid, i.e., at least some part of the Eu^{3+} ions are binding to the humic that has sorbed on the surface [1]. The behaviour of europium is similar to that of the humic acid, i.e., an initial rapid fall in concentration, followed by a slower decrease for the

remainder of the experiment [1]. The behaviour of europium is dependent on that of the humic acid in these systems, but although the general kinetic behaviour is similar, a greater fraction of europium is removed in the initial, rapid stage than the fraction of humic acid in the humic acid–quartz sand binary system during the same period. This effect is probably due to some of the europium binding directly to the quartz sand, in addition to that bound via humic ternary complexes.

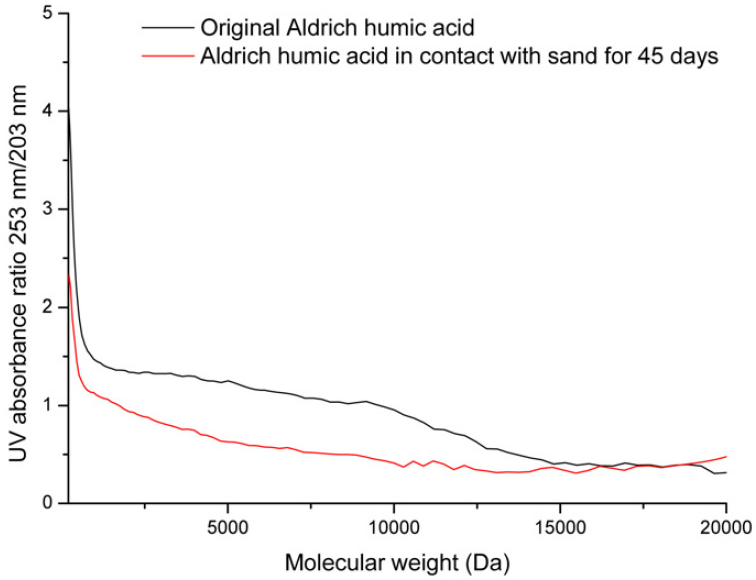

Figure 5: *Chemical adsorptive fractionation of Aldrich humic acid after contact with quartz sand for 45 days as a function of the molecular weight. Note all masses are relative to the PSS standards.*

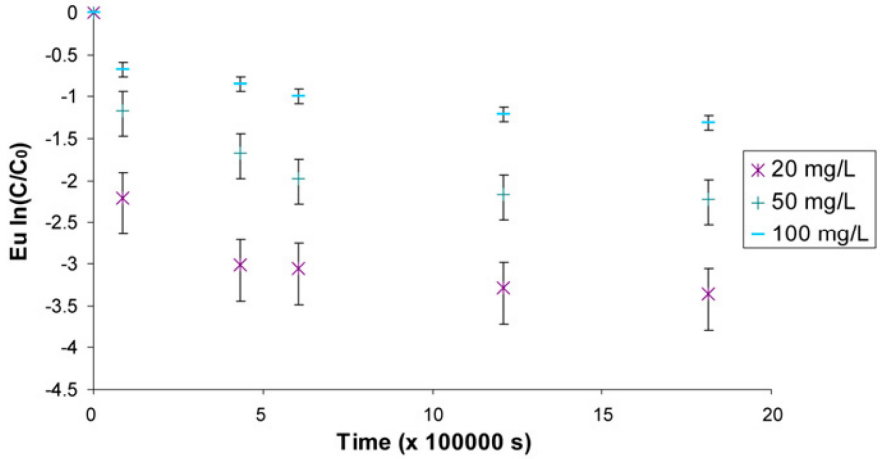

Figure 6: *Kinetics of europium sorption onto a quartz sand surface in the presence of various humic acid concentrations: 20, 50, and 100 ppm.*

Conclusions

Preferential adsorption of humic acid fractions onto mineral surfaces is significant, since it modifies the composition of the humic acid remaining in equilibrium in the aqueous phase. There is an initial, rapid uptake of humic acid molecules onto quartz sand followed by a much slower uptake. The molecular weight

distribution of residual humic acid in solution after adsorption deviates from the original distribution, showing preferential adsorption of certain molecular weight components. Weight average molecular weights (*M*w) originally, after the initial, rapid uptake (3 days), and after the slower uptake (45 days) were found to be 3900, 4750, and 3800 Da, respectively. Fractionation changes with time: humic acid molecules of molecular weight below 4800 Da and of *M*w 1450 Da were adsorbed after the fast kinetic step, whereas humic acid molecules in the molecular weight range 1400–9200 Da and of *M*w 3700 Da were adsorbed after the slower uptake. No displacement of low molecular weight fractions by higher molecular weight fractions has been observed over time, but we must be careful when interpreting these results. The data show no net displacement of small species. That does not mean that the same small species are sorbed after 3 and 45 days, i.e., these data are not evidence of pseudo-irreversible behaviour, and there may be continuous dynamic exchange that produces no net decrease in the amount sorbed.

In the ternary Eu^{3+}/HA/quartz sand system, the sorption behaviour of the Eu^{3+} is closely related to that of the humic acid, because of the slow sorption of Eu^{3+}/humic acid complexes. Previously, it has been shown that the slow sorption of humic–radionuclide complexes can have a significant impact on the transport of the radionuclide [6]. These results suggest that fractionation could be important in radionuclide transport. Currently bulk interaction constants are used to describe the interaction of humics and metal ions and their effects upon transport [6]. These results suggest that the chemical/structural nature of the individual humic species to which a radionuclide is bound could influence its fate, and that metal ions bound to smaller, more aromatic species are more likely to sorb, at least on a timescale of a few months. The results show that the rate of sorption depends upon the fraction. It has been shown that humic-radionuclide complexes with the same overall equilibrium affinity can show different transport behaviour if the rates of the sorption reactions are different [6]. Therefore, understanding humic fractionation is important if we are to predict the behaviour of radionuclides in the environment.

Acknowledgement

The authors are grateful to the European Union for funding.

References

[1] Bryan ND, Abrahamsen LG, Farrelly DH, Warwick P, Evans NDM and Knight L (2006)

A Provisional Humic Acid Ternary System Model, *Proceedings of the 1st FUNMIG Workshop*, Eds. Reiller P, Buckau G, Kienzler B, Duro L and Martell M, 220 – 224.

[2] Claret F, Schäfer T and Reiller P (2007) Sorption Induced Fractionation of Fulvic Acids, *Proceedings of the 2nd FUNMIG Workshop*, Eds. Buckau G, Kienzler B, Duro L and Montoya V, 247 – 253.

[3] Pitois A, Abrahamsen LG, Ivanov PI and Bryan ND (2008) Humic acid sorption onto a quartz sand surface: A kinetic study and insight into fractionation, *Journal of Colloid and Interface Science*, **325**, 93–100.

[4] Reiller P, Amekraz B and Moulin C (2006) *Environ. Sci. Technol*., **40**, 2235.

[5] Dijt JC, Stuart MAC and Fleer GJ (1994) *Macromolecules*, **27**, 3207.

[6] Bryan ND, Jones DLM, Keepax RE, Farrelly DH, Abrahamsen LG, Pitois A, Ivanov P, Warwick P, and Evans N (2007) The Role of Humic Non-Exchangeable Binding in the Promotion of Metal Ion Transport in the Environment, *Journal of Environmental Monitoring,* **9**, 2007, 329-347.

INFLUENCE OF SILICATE IONS ON Eu(III) AQUEOUS SPECIATION

Thomas Vercouter*, Florence Casanova, Amandine Calvo, Badia Amekraz†, Christophe Moulin††

CEA, DEN, Laboratory of Speciation of Radionuclides and Molecules,
F-91191 Gif-sur-Yvette, France.
† Current affiliations: AREVA NC BU-T, F-92084 La Défense, France.
†† Current affiliations: CEA, DIF, Service Radioanalyse, Chimie, Environnement,
F-91297 Arpajon, France.

* Corresponding author: thomas.vercouter@cea.fr

Abstract

Interactions of Eu(III) with silicate anions were investigated in undersaturated silica solutions from pH 2 to 7 by time-resolved laser-induced fluorescence spectroscopy (TRLFS) and electrospray ionisation mass spectrometry (ESI-MS). Although silicate is expected to be mostly monomeric under these conditions, the presence of silica oligomers was observed in some experimental conditions, which may significantly affect the speciation of trivalent metal ions in environmentally relevant conditions.

Introduction

Silicic acid $Si(OH)_4$ usually prevails in natural waters where pH < 9 and [Si] < 2 mM (solubility of amorphous silica). The silicate anion $SiO(OH)_3^-$ forms at higher pH. However, even at low pH, it can be a ligand for metal cations such as most of the RN, and especially the actinides uranium (Hrnecek and Irlweck, 1999; Jensen and Choppin, 1998; Moll et al., 1998; Pathak and Choppin, 2006; Porter and Weber, 1971; Satoh and Choppin, 1992), neptunium (Pathak and Choppin, 2007; Yusov et al., 2004), plutonium (Yusov and Fedoseev, 2003; Yusov et al., 2004), americium (Pathak and Choppin, 2006; Wadsak et al., 2000), and curium (Panak et al., 2005; Pathak and Choppin, 2006). The formation of 1:1 metal:ligand complexes has been evidenced in acidic solutions. For over-saturated Si solutions or at higher pH, silica polymerisation is favoured. The formation of oligomers has been evidenced for silica concentrations above 1 mM, which may lead to the formation of nanocolloidal particles (Icopini et al., 2005). The presence of polymeric silicate and/or colloidal particles may influence the speciation of metal cations. For instance, in alkaline solutions where soluble silicate oligomers are stabilized, complexation occurs with Eu(III) (Wang et al., 2005). In addition, for pH

closer to neutral pH, formation of colloidal particle incorporating Cm(III) was observed, even under conditions where predominance of the monosilicic acid was expected (Panak et al., 2005). Polymeric species are usually neglected in speciation modelling of RN in naturally relevant solutions. In order to account for them, it is required to better characterize the chemical forms of the ligands. The detection of oligomeric silicate compounds at low concentration is an analytical challenge, but electrospray ionization mass spectrometry (ESI-MS) has recently succeeded in detecting silicate oligomeric species formed in aqueous solutions containing structure-directing templates for the synthesis of zeolites or mesoporous structures (Bussian et al., 2000; Eggers et al., 2005; Pelster et al., 2007).

Eu(III) was used as a representative trivalent metal ion. The interactions with silicate species were studied by using time-resolved laser-induced fluorescence spectroscopy (TRLFS). ESI-MS was used to detect oligomeric silicates.

Experimental

Materials

Preparations and measurements were performed at (21±1)°C. The solutions were made with 0.1 M HCl (Titrex, Chem-Lab), 0.1 M HNO_3 (Fisher Scientific), carbonate-free 0.1 N NaOH (Prolabo, Titrinorm) and NaCl (Sigma-Aldrich, 99+%). A europium(III) stock solution was prepared by dissolution of $Eu(NO_3)_3{,}5H_2O$ (Aldrich, 99.9%) in a nitric acid solution. Silicic acid solutions were prepared by rapid hydrolysis of tetramethoxysilane (TMOS, Aldrich, 99+%) at pH 2-3 in HCl.

Titration experiments for TRLFS

Sample solutions were prepared from fresh silicic acid solutions (pH 2-3) with 0.1 M NaCl. Once europium was added to reach the desired concentration, the pH was adjusted with NaOH and measured using a combined Ag/AgCl electrode (XC161, Radiometer Analytical), calibrated with home-made buffers at 0.1 M NaCl. The concentration of monomeric silicate was determined by the classical β-silicomolybdate method.(Alexander, 1953) Ultracentrifugation was performed at 350,000 g on selected samples.

Time-Resolved Laser-induced Fluorescence Spectroscopy

The laser excitation source is an OPO laser system pumped by a Nd-YAG Laser (Continuum, USA), which delivers a 1 mJ laser beam at 393.8 nm. The repetition rate was 10 Hz and the pulse duration was about 5 ns. The detection set-up is detailed elsewhere (Vercouter et al., 2008). Detection was performed using a delay time of 10 µs and a gate width of 600 µs.

Electrospray Ionization Mass Spectrometry

Negative-ion mass spectra were recorded using the V-mode of a LCT Premier™ XE benchtop orthogonal acceleration time-of-flight mass spectrometer equipped with an electrospray ionization device (Waters, USA). The flow rate of the syringe pump was set at 5 µL/min. The capillary voltage was 2.5 kV. The sample cone voltage was set at

30 V. The cone temperature and desolvation temperature were set at 100°C and 150°C, respectively. Nitrogen gas flows of 50 and 450 L/hr were used for the nebullization and desolvation, respectively. Mass calibration from 100 to 1000 Da was performed using a standard NaI calibration solution. Spectra were acquired at 1 s/scan over a mass range of *m/z* 50-1200 and are the results of 50 scans accumulation.

Results and discussion

TRLFS Results

The fluorescence emissions of 1 µM Eu(III) solutions were measured as a function of the Si concentration (0.1-1 mM), pH (3-7), and ageing time. Within a few days after the preparation of the solutions, all the fluorescence spectra measured in the range 550-650 nm were composed of two bands centred at 592 and 616 nm, corresponding to the two main Eu(III) transitions $^5D_0 \rightarrow {}^7F_1$ and $^5D_0 \rightarrow {}^7F_2$, similar to the ones in the spectrum of the non-complexed Eu^{3+} aquo ion. After about ten days, and for pH > 4.5, the relative intensity of these two bands changed, and the bands became more asymmetrical (Figure 1). Particularly, the hypersensitive $^5D_0 \rightarrow {}^7F_2$ emission split into two bands at 613.5 and 618.0 nm. Moreover, a weak peak was observed at 579 nm corresponding to the $^5D_0 \rightarrow {}^7F_0$ transition. These spectroscopic modifications were particularly important at near-neutral pH, and at low Si content (0.1 mM), while they were less and less significant for increased [Si] up to 1 mM.

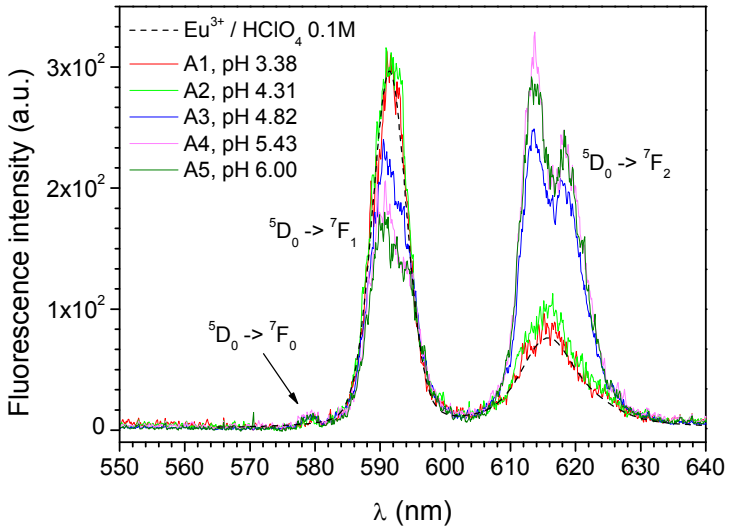

Figure 1: *TRLF spectra of 1µM Eu(III) solutions as a function of pH for 0.1 mM Si and after 18 days of equilibration.*

The evolution of the intensity ratio ($R_{2/1}$) of the $^5D_0 \rightarrow {}^7F_2$ and $^5D_0 \rightarrow {}^7F_1$ bands indicates changes of the Eu(III) speciation with time and pH (Figure 2). The higher this ratio is, the stronger the interactions between Eu^{3+} and compounds. It appears that no specific interactions can be detected within only a few days of equilibration, whereas Eu(III) species formed after 1 or 2 weeks.

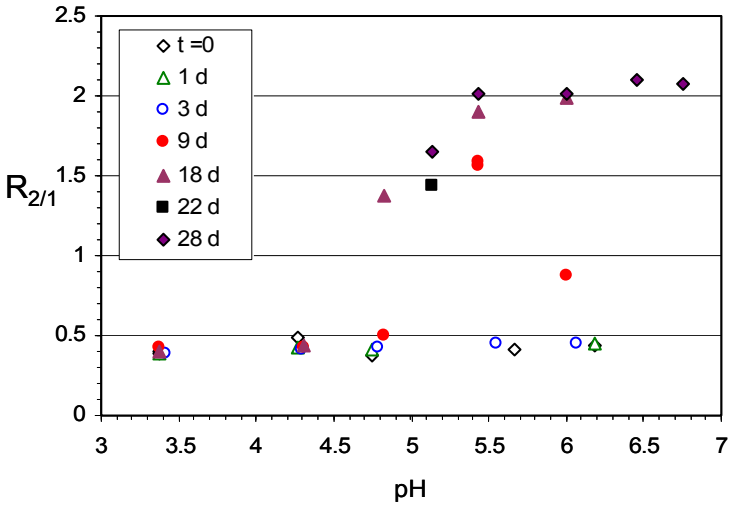

Figure 2: *Evolution of the intensity ratio ($R_{2/1}$) of the $^5D_0 \rightarrow {}^7F_2$ and $^5D_0 \rightarrow {}^7F_1$ Eu(III) bands for 0.1 mM Si solutions as a function of pH and time (in days).*

In undersaturated Si solutions, Eu^{3+} and $EuOSi(OH)_3^{2+}$ are expected to predominate according to the available thermodynamic data. The formation of the $EuOSi(OH)_3^{2+}$ complex has been evidenced in acidic conditions by various techniques, but should not have a fluorescence signature different to that of Eu^{3+} (Jensen and Choppin, 1996). This is in agreement with what was observed in the fresh sample solutions where a single spectrum was measured. The change of the fluorescence with time suggests the formation of other species that may have a relatively slow kinetic of formation. The formation of soluble complexes such as carbonate or hydroxide complexes can be reasonably excluded under our experimental conditions, and according to the fluorescence features. Moreover the formation of $Eu(OSi(OH)_3)_2^+$ is very unlikely because, if it exists, it would have required higher silicate concentration and higher pH to be observable. Then complexes with oligomeric silicates may explain these experimental results.

After the fluorescence measurements had reached a steady-state, the sample solutions were ultracentrifuged. The fluorescence of the supernatants exhibits different features, with lower $R_{2/1}$ values, and more symmetrical fluorescence bands (Figure 3). The overall intensities were lower than those measured prior to ultracentrifugation, which suggests that Eu(III) was partially removed from the solutions together with (colloidal) particles. The spectra of the supernatants were still different to those measured at low ageing times, suggesting the occurrence of complexation reactions with non-colloidal oligomeric silicate. Because the oligomerization rate is expected to be slow under such conditions, the concentrations of oligomeric silicate are likely increasing within the duration of the experiments. The reaction rate of silica oligomerization is dependent on pH, ionic strength, and the degree of oversaturation with respect to amorphous silica (Icopini et al., 2005). Under our conditions, the solutions were undersaturated, which means that no oligomeric silicate should have formed in opposition to our TRLFS results. However, it should be noted that colloidal silica particles were also observed under similar (undersaturated) conditions, and were concluded to interact with Cm^{3+} (Panak et al., 2005), which has a chemical behaviour analogous to that of Eu^{3+}.

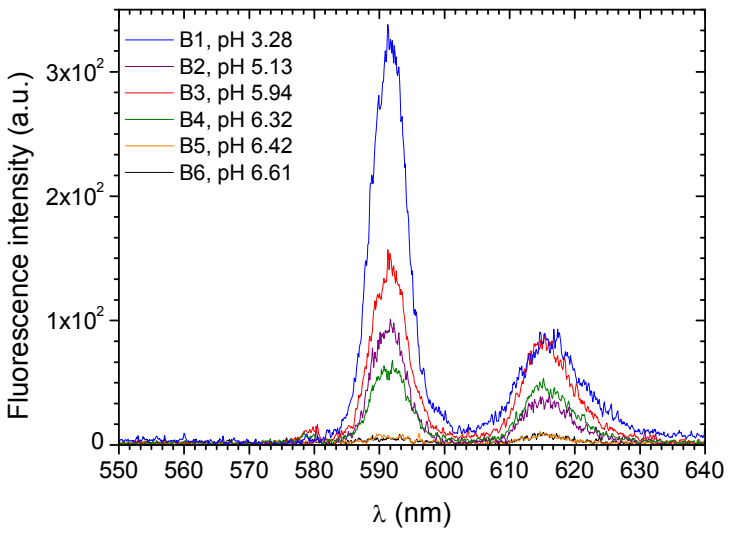

Figure 3: *TRLF spectra of supernatant solutions as a function of pH for 0.3 mM Si and after 47 days of equilibration.*

Consequently, experimental evidence of the presence of oligomeric silicate was required with a high-detection technique such as ESI-MS.

ESI-MS analysis

Millimolar silicate solutions were analysed by ESI-MS within two days after preparation. The pH was adjusted between 2 and 6.5 by HNO_3 addition. Single charge silicate species were detected in the gas phase according to their *m/z* values and isotopic fingerprints. Other peaks, also present in the spectra of blank solutions, were assigned to matrix compounds or impurities.

Oligomeric silicates were observed either as single molecules or as clusters with H_2O or HNO_3 (Figure 4). No methoxylated silicates were detected confirming complete hydrolysis of TMOS. Monomeric silicates $[SiO_3H]^-$, $[SiO_4H_3]^-$, $[SiO_4H_3,H_2O]^-$, and $[SiO_4H_4,NO_3]^-$, were detected at *m/z* 77, 95, 113, and 158, respectively. However, the main peaks correspond to nitrate clusters of dimeric, trimeric, tetrameric, pentameric silica, at *m/z* 236, 314, 374, and 452, respectively. $[SiO_3H]^-$ is formed in the gas phase by dehydroxylation of the monomer, leading to a Si=O double bond, as classically observed (Eggers et al., 2005; Knight and Kinrade, 2002; Pelster et al., 2006). Other condensed forms were possibly existing under our conditions, but they could not be unambiguously identified because different structures could be envisaged for a given *m/z* value. For instance, *m/z* 233 can be assigned to both cyclic trimeric silicate, and linear trimeric silicate with one water loss. The chemical formulae attributed to the peaks are consistent with other determinations in concentrated silica solutions (Bussian et al., 2000; Eggers et al., 2005; Pelster et al., 2006). Noticeably, some structures probably corresponding to dehydroxylated silicates were not observed in this work, suggesting that our ESI parameters were soft enough to limit dehydroxylation reactions during the ESI process.

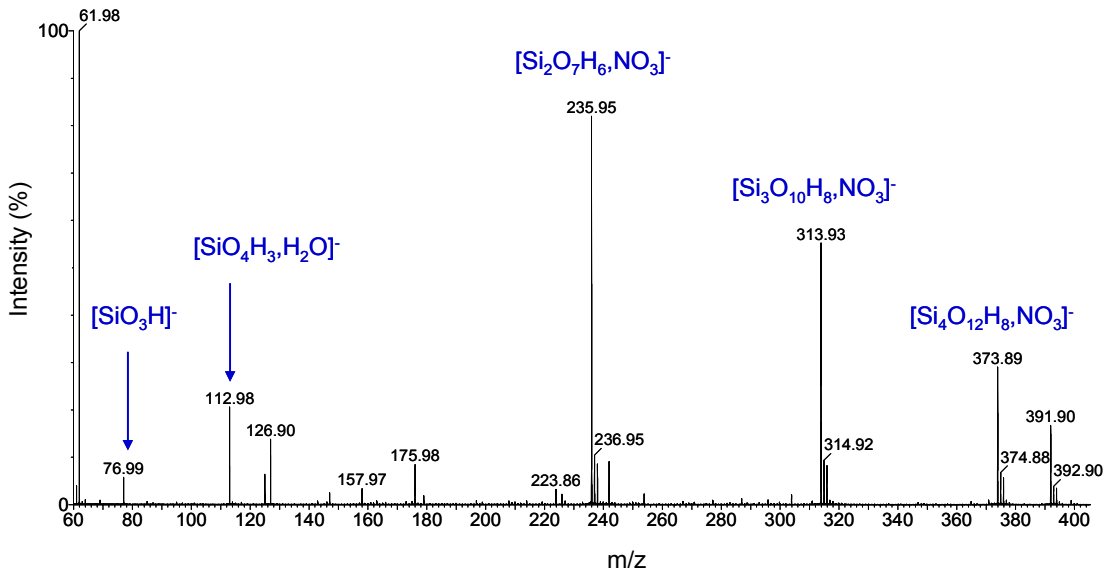

Figure 4: *ESI mass spectrum of a 1 mM silicate solution at pH 5.*

Since the intensities of the peaks were dependent on the ESI conditions, oligomerization induced by clustering of silicates during the ESI process cannot be excluded. We have analysed two series of solutions at the same pH and [Si], but prepared using two different Si mother solutions in which TMOS was hydrolyzed either in 1 mM HNO_3 or in deionized water. TMOS hydrolysis was total in the two cases (no methoxylated silicate were detected). The same peaks were found in both series despite different intensities. The hydrolysis conditions are supposed to affect the oligomerization processes in the aqueous solutions. Thus, the presence of small amounts of oligomeric silicates in the solutions is suspected although they were undersaturated with respect to amorphous silica.

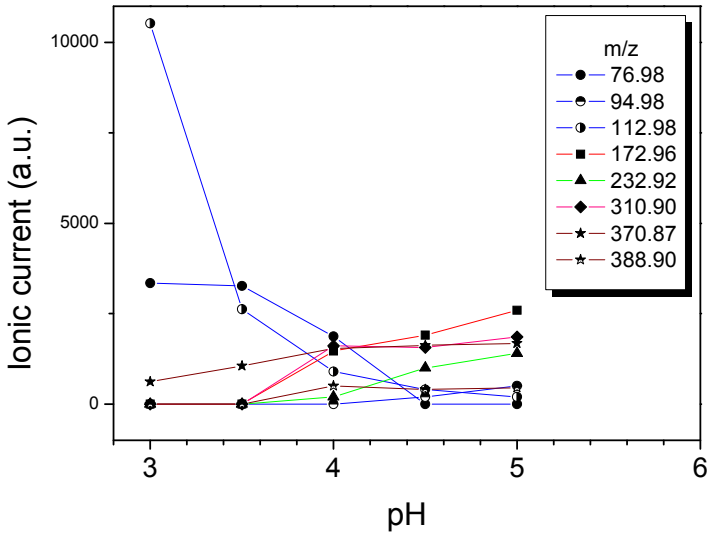

Figure 5: *pH dependence of the ionic currents of selected peaks in the ESI mass spectra of 1 mM silicate solutions.*

Except for the dehydroxylated form of the monomer $[SiO_3H]^-$, the intensities of the peaks of silicate molecules increased with pH (Figure 5). If the intensity change reflects different species distributions in the aqueous solutions, such a trend would be consistent with easier oligomerization when increasing pH. In the case of the nitrate clusters, which represent the most intense peaks, the intensities decrease with pH because the concentration of HNO_3 also decreases. Hence, the evolution of these peaks is concluded to be less informative.

Summary

At low Si concentrations, the Eu(III) fluorescence measured by TRLFS changed with time, suggesting slow formation of colloidal particles and molecular complexes in the solutions. Gas-phase oligomers were better detected by ESI-MS in solutions at near-neutral pH, as could be expected according to oligomerization reaction pathways. Thus, the ESI-MS technique succeeded to detect oligomeric silicates present in acidic solutions undersaturated with respect to silica.

Acknowledgement

This work was funded by DSOE/Basic Research and DDIN/DPRGD within the cooperative research and development CT4 program CEA-ANDRA-EDF, and the Integrated Project FUNMIG.

References

Alexander G. B. (1953) The reaction of low molecular weight silicic acids with molybdic acid. *Journal of the American Chemical Society* **75**, 5655-5657.

Bussian P., Sobott F., Brutschy B., Schrader W., and Schuth F. (2000) Speciation in solution: Silicate oligomers in aqueous solutions detected by mass spectrometry. *Angewandte Chemie-International Edition* **39**(21), 3901-+.

Eggers K., Eichner T., and Woenckhaus J. (2005) Mass spectrometric investigation of small silicate polyhedra in solution. *International Journal of Mass Spectrometry* **244**(1), 72-75.

Hrnecek E. and Irlweck K. (1999) Formation of uranium(VI) complexes with monomeric and polymeric species of silicic acid. *Radiochimica Acta* **87**(1-2), 29-35.

Icopini G. A., Brantley S. L., and Heaney P. J. (2005) Kinetics of silica oligomerization and nanocolloid formation as a function of pH and ionic strength at 25 degrees C. *Geochimica Et Cosmochimica Acta* **69**(2), 293-303.

Jensen M. P. and Choppin G. R. (1996) Complexation of europium(III) by aqueous orthosilicic acid. *Radiochimica Acta* **72**(3), 143-150.

Jensen M. P. and Choppin G. R. (1998) Complexation of uranyl(VI) by aqueous orthosilicic acid. *Radiochimica Acta* **82**, 83-88.

Knight C. T. G. and Kinrade S. D. (2002) Comment on "Identification of Precursor Species in the Formation of MFI Zeolite in the TPAOH-TEOS-H2O System". *J. Phys. Chem. B* **106**(12), 3329-3332.

Moll H., Geipel G., Brendler V., Bernhard G., and Nitsche H. (1998) Interaction of uranium(VI) with silicic acid in aqueous solutions studied by time-resolved laser-induced fluorescence spectroscopy (TRLFS). *Journal of Alloys and Compounds* **271**, 765-768.

Panak P. J., Kim M. A., Klenze R., Kim J. I., and Fanghänel T. (2005) Complexation of Cm(III) with aqueous silicic acid. *Radiochimica Acta* **93**(3), 133-139.

Pathak P. N. and Choppin G. R. (2006) Thermodynamic study of metal silicate complexation in perchlorate media. *Radiochimica Acta* **94**(2), 81-86.

Pathak P. N. and Choppin G. R. (2007) Silicate complexation of $NpO2^{+}$ ion in perchlorate media. *Journal of Radioanalytical and Nuclear Chemistry* **274**(1), 3-7.

Pelster S. A., Schrader W., and Schuth F. (2006) Monitoring temporal evolution of silicate species during hydrolysis and condensation of silicates using mass spectrometry. *Journal of the American Chemical Society* **128**(13), 4310-4317.

Pelster S. A., Schuth F., and Schrader W. (2007) Detailed Study on the Use of Electrospray Mass Spectrometry To Investigate Speciation in Concentrated Silicate Solutions. *Anal. Chem.* **79**(15), 6005-6012.

Porter R. A. and Weber J. W. J. (1971) The interaction of silicic acid with iron(III) and uranyl ions in dilute aqueous solution. *Journal of Inorganic and Nuclear Chemistry* **33**(8), 2443-2449.

Satoh I. and Choppin G. R. (1992) Interaction of Uranyl(Vi) with Silicic-Acid. *Radiochimica Acta* **56**(2), 85-87.

Vercouter T., Vitorge P., Amekraz B., and Moulin C. (2008) Stoichiometries and Thermodynamic Stabilities for Aqueous Sulfate Complexes of U(VI). *Inorganic Chemistry* **47**, 2180-2189.

Wadsak W., Hrnecek E., and Irlweck K. (2000) Formation of americium(III) complexes with aqueous silicic acid. *Radiochimica Acta* **88**(2), 61-64.

Wang Z., Felmy A. R., Xia Y. X., Qafoku O., Yantassee W., and Cho H. (2005) Complexation of Cm(III)/Eu(III) with silicates in basic solutions. *Radiochimica Acta* **93**(12), 741-748.

Yusov A. B. and Fedoseev A. M. (2003) Reaction of plutonium(VI) with orthosilicic acid $Si(OH)_4$. *Russian Journal of Coordination Chemistry* **29**(8), 582-590.

Yusov A. B., Fedosseev A. M., and Delegard C. H. (2004) Hydrolysis of Np(IV) and Pu(IV) and their complexation by aqueous $Si(OH)_4$. *Radiochimica Acta* **92**(12), 869-881.

INTERACTION OF BENTONITE COLLOIDS WITH EU AND TH IN PRESENCE OF HUMIC ACID: A FLOW FIELD-FLOW FRACTIONATION STUDY

Muriel Bouby*[1], Horst Geckeis[1], J. Lützenkirchen[1], Silvia Mihai[1,2],Thorsten Schäfer[1]

[1] Karlsruhe Institute of Technology, Forschungszentrum Kalrsruhe, Institut für Nukleare Entsorgung (INE), P.O. Box 3640, D-76021 Karlsruhe, Germany,
[2] Politehnica University, Faculty of Industrial Chemistry, Calea Grivitei 132, Bucharest 78122, Romania

* Corresponding author: bouby@ine.fzk.de

Abstract

This work examines the stability of bentonite colloids suspended in natural grimsel groundwater (pH 9.6) and the contact time effect on the sorption of Eu and Th onto bentonite colloids over three years, under anoxic conditions. In addition, humic acid (Gohy-573) is used as competing ligand to initiate desorption reactions after different contact times. The use of the Asymmetric Flow-Field Flow fractionation (AsFlFFF) coupled to UV-Vis spectrophotometry and ICP-MS detection provides quantitative data on the distribution of the elements to the different colloidal fractions present in suspensions (humic acid and bentonite colloids). The final pH in all solutions lies between 8.3 and 8.9. A clear agglomeration of bentonite colloids is observed with sizes varying initially from 15-300 nm up to more than 500 nm after 3 years, even at this high pH and low ionic strength groundwater. Th and Eu interact with bentonite colloids. In presence of humic acid, Eu desorption is slightly kinetically hindered in function of the contact time but tends to an equilibrium distribution of 10-90 % humic acid bound species. A similar result is obtained when the Eu, the bentonite colloids and the humic acid are mixed simultaneously. More interesting is the Th behavior. Even for the shortest contact time (1 day) between the Th and the bentonite colloids prior to humic acid addition, 30-50 % of the Th remains bentonite colloid –bound and 10-80 % is complexed with humic in the ternary system. Further studies will have to focus on the Th species responsible for the "irreversible" sorption process.

Introduction

The actinide mobility in the far-field of a repository site could be significantly influenced by colloidal species. It is therefore important to determine the stability, mobility and the interaction mechanism of actinides with colloids for long-term safety analysis. This is the aim of the Colloid and Radionuclide Retardation (CRR) project and it's continuation, namely the Colloid Formation and Migration project (CFM),

performed in fractured crystalline rock at the Nagra's Grimsel Test Site (GTS) in the central Swiss Alps [1-2]. The results obtained up to now for the CRR test shear zone conditions [1-3] indicate that colloids are present, mobile and stable under the given groundwater conditions, and more importantly radionuclide association with the colloids occurs. The question which remains concerns the reversibility or irreversibility of radionuclide-colloid association which has to be investigated in details. The present work presents: 1- A kinetic study over 3 years on the interaction of bentonite colloids with the elements Eu(III) and Th(IV) in the natural Grimsel Test Site groundwater, 2- A desorption study using humic acid as a ligand competing with the bentonite colloid surface.

Material and methods

Asymmetric Flow-Field Flow Fractionation(AsFlFFF) coupled to UV-Visible spectrophotometer and an ICP-Mass Spectrometer.

This sensitive colloid characterization method yields important information on the metal ion/colloid interaction mechanism. It has been previously used to characterize bentonite colloids [4] and their interaction with actinides or homologues [5]. Complete description of the equipment, size calibration and metal ion quantification method used in this work can be found in [6]. Only its main principle is recalled here: size fractionation of colloids is carried out in a thin ribbon-like channel according to their diffusion coefficient; smaller colloids are eluted prior to bigger ones.

Samples preparation

Bentonite colloid suspensions, elements and humic acid stock solutions.

The suspensions were prepared in natural groundwater from the GTS, sampled under inert gas conditions in 50 L Teflon coated stainless steel barrels from borehole BOMI 87.010 and transferred directly to the laboratory. The chemical composition of the Grimsel groundwater (GGW) is characterized by low ionic strength, low carbonate concentration and high pH [5,7].

The original bentonite FEBEX bentonite [8] comes from the Cortijo de Archidona deposit (Spain). Bentonite blocks were crushed, sieved (size fraction < 64 µm) and purified as indicated in [9]. The sieved powder (10 g) was equilibrated 4 days in 1 L LiCl (1M). The bentonite colloid suspension was then obtained by repeating four times cycles of suspending, centrifuging, decanting the supernatant and re-suspending the separated solid using an ultra sonic bath [1,10]. The final colloidal suspension has a colloid concentration of: (1230 ± 30) $mg.L^{-1}$ as deduced from the Al and Mg concentration measurements performed by ICP-MS.

A Th and Eu stock solution (named hereafter RN-cocktail) was prepared by using ICP-MS standard solutions at 1 $mg.ml^{-1}$ in HNO_3 5 % (Specpure, Alfa Aesar).
The humic acid (Gohy-HA-573) characteristics and stock solution preparation are described in [6].

Sample preparation: batch experiments

The solutions were prepared in a glove box. For the kinetic study, single-, two- and three-components suspensions have been prepared in parallel in GGW. They were

measured after different contact times (CT): freshly prepared, 2 weeks, 3 months, 5 months, 7 months, 10 months, 1 year, 3 years. The different sets of batch samples are described hereafter: **1-** "bentonite colloids alone": bentonite colloids (20 $mg.L^{-1}$) in GGW; **2-** "bentonite colloids-RN cocktail": bentonite colloids (20 $mg.L^{-1}$) + RN-cocktail in GGW (10 $\mu g.L^{-1}$ Th and Eu); **3-** "equilibrium system": GoHy-HA-573 (10 $mg.L^{-1}$) + Bentonite colloids (20 $mg.L^{-1}$) + RN-cocktail (10 $\mu g.L^{-1}$ Th and Eu) mixed simultaneously in GGW. The concentrations of Eu and Th in the batch samples are then, respectively, 6.6 10^{-8} M and 4.3 10^{-8} M. All the concentrations were checked by ICP-MS in the batch suspensions after preparation (mean of three replicates) and over 3 years. No adsorption on the walls of the 50 mL polyethylene tubes used as containers was observed.

For the reversibility study, an additional set of batch experiments was prepared: 4- 10 $mg.L^{-1}$ humic acid is added to the "bentonite colloid-RN cocktail" suspension, aged from 1 day up to 3 years. It is then transformed into a new "three-component suspension". The effect of the delayed addition of the humic acid is followed as a function of desorption time (DT) from 24 hours up to 1 year.

Results and discussion

The pH of all suspensions remained in the range [8.3-8.9] over 3 years. This is on average 1 pH unit lower than the GGW pH value and is due to the addition of a small amount of the RN-cocktail with low pH (~1.3). Sampling was performed in the glove box just before the analysis without shaking the tubes.

Bentonite colloid stability

Aluminium has been used as a tracer of the bentonite even if silicium is its main component (however, Si is difficult to measure by ICP-MS). The evolution of the Al-fractograms over time allows to state on the size and stability of the bentonite colloids. The Al-fractograms recorded over 3 years for the "bentonite colloid alone" suspension are presented on Figure 1. The corresponding Al recoveries are calculated (value in brackets in the inserted legend) and are assumed to represent the bentonite colloid recoveries. A marked evolution is visible in Figure 1A with a pronounced shift of the elution position of the Al-fractograms after 17 months but for constant and highly reproducible colloid recoveries (84 ± 3 %). This demonstrates a slow agglomeration process with a bentonite size distribution varying from 15-300 nm initially (with peak maxima at 40 nm and 150 nm) up to 50-500 nm after 18 months (peak maximum at 300 nm). Measurements performed after 3 years reveal a more pronounced agglomeration as seen on Figure 1B. At that time a small residual bentonite colloid fraction is observed at 300 nm while the major fraction has a size bigger than 500 nm. This leads to a change in the elution in the AsFlFFF, from the so-called "normal mode" where the smallest colloids are eluted first to the "hyperlayer mode" where the bigger colloids are eluted first. This could be confirmed by measuring the same suspension after a filtration at 450 nm. In this case, only a residual fraction at 300 nm was detected and the recovery decreased from 84 % down to only 3%. The effect is reproducible and was observed as well for all the other sets of samples containing bentonite colloids.

The agglomeration can be explained by the variation of the Li^+ to Ca^{2+} concentration ratio in the different suspensions. At the end of the colloid stock suspension preparation, Li^+ cations are placed in the clay interlayers (delamination process) and prevent the agglomeration of the small bentonite clay colloid platelets obtained, due to their hydration sphere, while the Ca^{2+} cations come from the GGW. The measured Li^+ to Ca^{2+} concentration ratio is still at 2.38 10^{-3} M to 2.03 10^{-4} M. When the bentonite colloid stock solution is diluted in GGW to prepare the batch samples, the ratio changes to 3.96 10^{-5} M to 2.03 10^{-4} M, i.e. Ca^{2+} is present in excess now. An ion exchange process might occur at the basal planes of the clay colloid platelets, leading to the slow agglomeration process evidenced by following the Al-fractogram evolution. Actually, the Ca hydration sphere might not be large enough to repel the clay platelets and might act as a bridge in between. Our hypothesis was confirmed by preparing a bentonite colloid stock suspension after equilibrating the initial FEBEX bentonite powder directly in GGW, without any initial cation-homoionization. A direct agglomeration of the clay colloids platelets due to the Ca concentration present in GGW was observed in the Al-fractograms (not shown here). The results clearly show that the agglomeration process is not finished after 17 months in GGW and it is impossible to say if a steady-state is reached after 3 years. This leads to a different conclusion compared to previous reports [3] probably because no study has been conducted over such a long period.

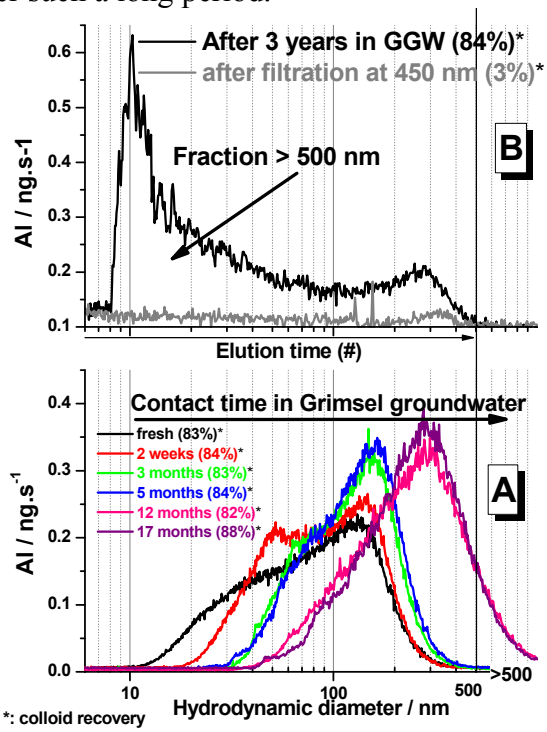

***Figure 1**: A: Al-fractograms evolution over 17 months.The colloid recoveries are indicated in bracket, based on the Al recovery. (#): There is here a change in the AsFlFFF elution mode, from the so-called "normal mode" where the smallest colloids are eluted first to the "hyperlayer mode" where the bigger colloids are eluted first. This is currently observed for colloids bigger than 500 nm. B: Al-fractograms obtained after 3 years, showing colloids bigger than 500 nm. The error on the peak position reproducibility is less than 5%.*

Kinetic studies

In addition to the Al-fractogram changes, the evolution of the Eu- and Th-fractograms has been followed over 3 years (Figure 2).

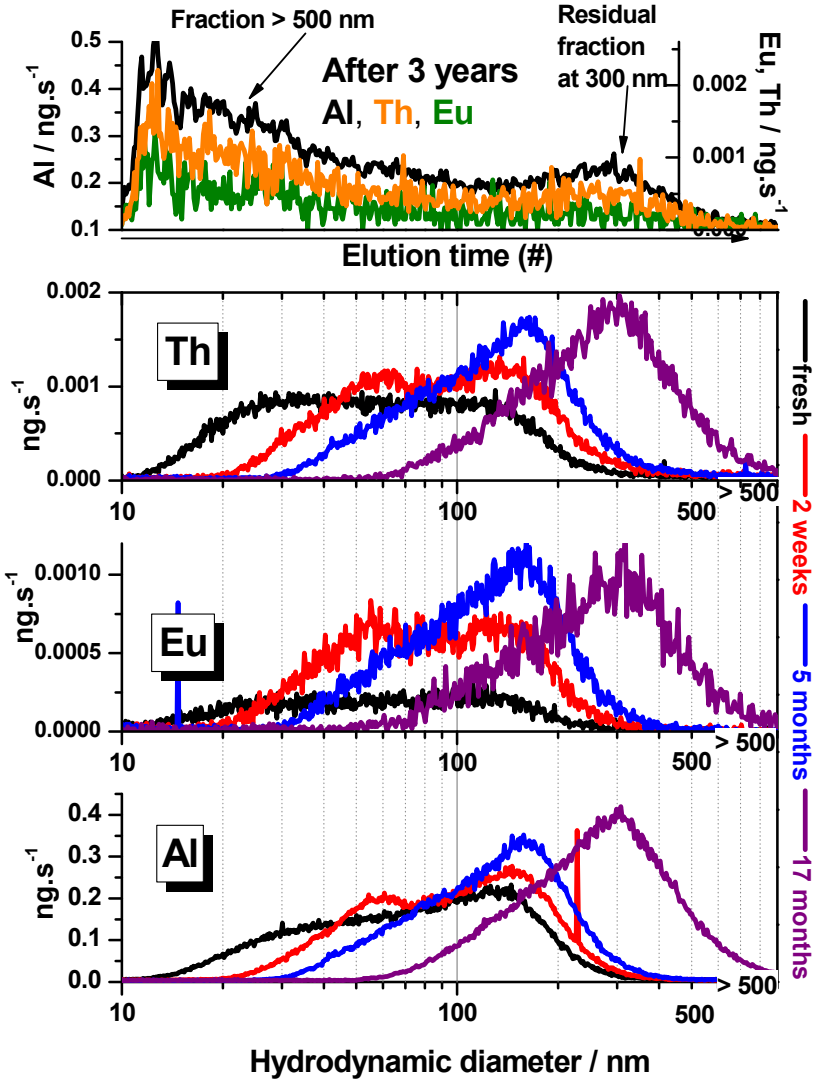

Figure 2: *Interaction of Eu and Th with bentonite colloids observed with their respective fractograms as a function of time. (#): For the solution measured after 3 years, one has to consider the change in the AsFlFFF elution mode, from the so-called "normal mode" where the smallest colloids are eluted first to the "hyperlayer mode" where the bigger colloids are eluted first.*

The agglomeration process is clearly reproducible with this other set of samples. The Eu- and Th-fractograms follow the Al-fractograms suggesting the Eu and Th attachment to the bentonite colloids. Actually, as seen from the shapes of the fractograms, metal ion attachment to smaller-sized bentonite colloids (when present or still visible) seems to be favored. This is attributed to a surface area effect, as smaller colloids have higher specific surface area and consequently a higher number of sites

available for sorption. According to previous CRR results [2], 80 % of Th and ~100 % of Eu are expected to be bound to bentonite colloids. Fractogram quantification allows determining the evolution of the percentage of each element bound to bentonite colloids considering that the element recovery obtained represents this percentage. Complementary results have been obtained by performing ultra filtration (polyethersulfone membrane with a 1000 kD pore size: ~17 nm according to [11]). (90 ± 5) % of Th are bentonite colloid bound over the first 17 months which is in agreement with the bentonite colloid recovery determined from the Al-fractograms. This value is corroborated by the additional ultra filtration data and agrees with previous results [2]. The results are different for Eu. The Eu bentonite colloid bound fraction determined in the first measurement (fresh solution) and the fraction found 2 weeks later, increases from 25 % to 60 %. This final value is much lower than expected (we expected around 100 % colloid bound Eu as measured previously and additionally by ultra filtration experiments). This can be explained by considering a competition between the bentonite colloids and the cellulose membrane for binding the Eu. The Eu is thought to partly desorb from the bentonite and then bind to the membrane, leading to this lower recovery value. This result gives a first indication on the "kinetic strength" of the complex formed between the bentonite and the different elements under study. Sorption strength appears to be higher for Th than for Eu. Finally the major conclusion is that the interaction between the bentonite colloids and Eu and Th is not subject to kinetic, at least over 17 months under these conditions. After 3 years, the percentage of bentonite colloid bound Th and Eu may slightly decrease down to 75 ± 5 % and 50 ± 5 %, respectively, while the Al recovery remains constant (84 ± 5%). The variations cannot be explained at the moment but may still lie within the analytical uncertainties.

Sorption reversibility

Humic acid was used as a competing ligand and added to the bentonite-RN cocktail suspension after a given contact time. The results are compared with those obtained after a simultaneous mixing of the three components (humic acid, bentonite colloids and RN-cocktail): considered as "equilibrium system". The different colloidal fractions (humic acid or bentonite) can be clearly differentiated by AsFlFFF. The evolution of the Eu and Th distributions between the bentonite colloids and the humic acid, as a function of the desorption time for different initial contact times prior to the humic acid addition, is shown quantitatively on the Figure 3.

Eu desorption is slightly kinetically hindered nevertheless, the final Eu repartition is similar to that obtained in the so-called "equilibrium system" (star symbols on Figure 3). Eu mainly binds to humic acid and Eu sorption to bentonite colloids is reversible at least over a contact period of 1 year. Th behavior after the addition of humic acid is different. First, the contact time prior to the addition of humic acid seems to have a stronger impact. Then, even though it is decreasing, the bentonite colloid bound Th fraction remains at ~ 30 % and does not attain the distribution found in the "equilibrium system" (15-17 %) even after 3 years desorption time. Th-fractions associated to humic acid vary from 50 % to 80 %, respectively. Th appears to be more strongly bound to the bentonite colloids than Eu. In conclusion, at the current state of this study, Th binding to bentonite colloids appears partly irreversible.

These results highlight the importance of the addition sequence in the case of Th.

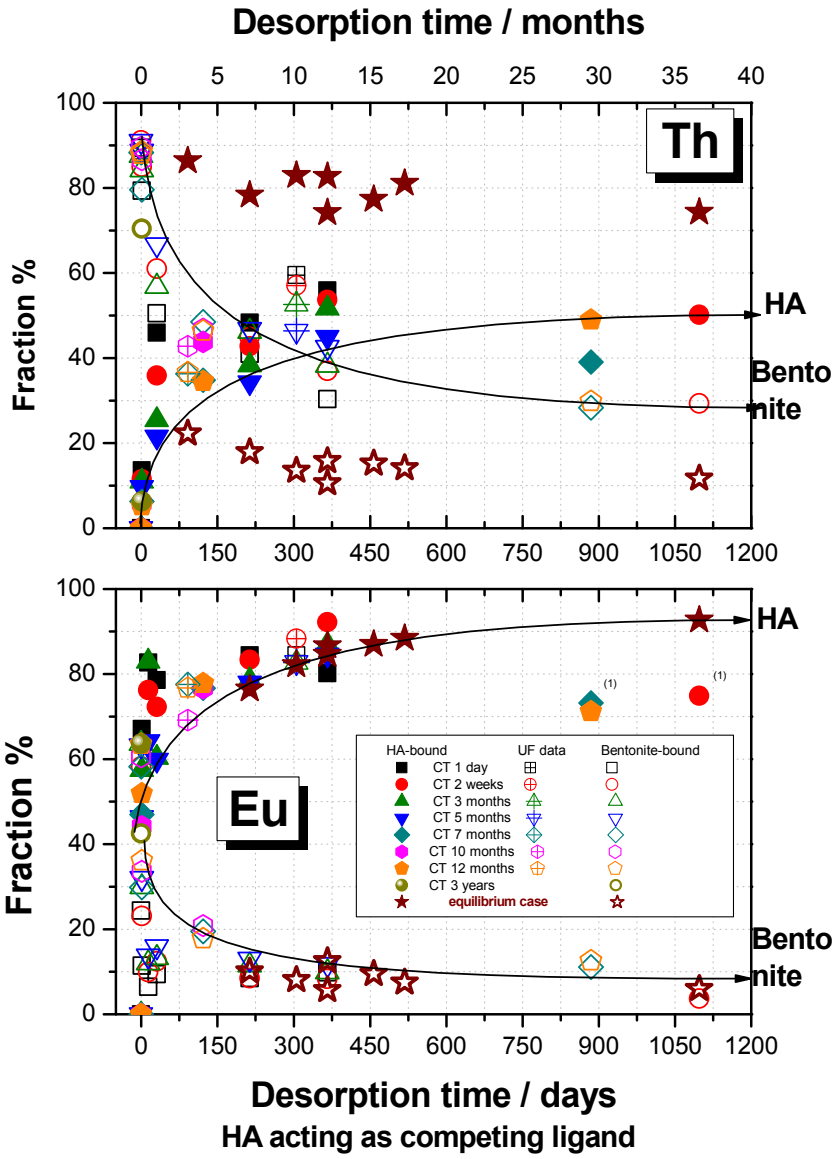

(1): membrane competition

Figure 3: *Effect of humic acid (HA) on the Eu and Th sorption on bentonite colloids. The Eu and Th desorption from bentonite colloids induced by HA addition is followed as a function of time (desorption time) for different initial contact time (CT) between the Eu or Th and bentonite colloids prior to the HA addition. See text for more details. The full symbols represent the fraction of Eu or Th desorbed and complexed by the HA while the open symbols represent the fraction of Eu or Th remaining bentonite colloid bound. The star symbols represent the element distributions between HA and bentonite colloids for the "equilibrium" system (see text).*

The effect of the addition sequence on the sorption/complexation results has been already demonstrated by numerous authors in different systems as discussed in detail in [12] where different reasons might be invoked to explain the Th results. 1- The initially adsorbed Th might be transformed to a less leachable surface precipitate

forming a Th hydroxide, a mixed layered double hydroxide (LDH) or a phyllosilicate phase within days where the forming solid may even stabilize upon ageing. 2- Th might experience a secondary diffusion processes into the clay. Further work is necessary to clarify the underlying process on a molecular scale.

Conclusions

* The bentonite colloids in the natural Grimsel ground water undergo a continuous agglomeration process over long time periods, at least up to 3 years. Their colloidal size distribution is determined by the water chemistry.
* For the interaction of bentonite colloids with Eu and Th no kinetics effects are observed, at least over 17 months.
* Further complementary studies have to be carried out to understand the kinetically hindered desorption ("irreversible" sorption?) of Th from the bentonite colloids by humic acid observed in this work, which is different to the findings for Eu.
* It was attempted (not shown here) to predict the radionuclide speciation at the clay surface and humic acid system by using the model of Bradbury and Bayens [13] combined with the Nica-Donnan model [14]. Preliminary results confirm the experimental tendencies. Work is in progress.

References

[1]: Mori, A., Alexander, W. R., Geckeis, H., Hauser, W., Schafer, T., Eikenberg, J., Fierz, T., Degueldre, C., Missana, T., Coll. Surf. A-Physicochem. Eng. Aspects 2003, 217 (1-3), p33

[2]: Geckeis, H., Schäfer, T., Hauser, W., Rabung, T., Missana, T., Degueldre, C., Mori, A., Eikenberg, J., Fierz, T., Alexander, W. R., Radiochim. Acta 2004, 92 (9-11), p765

[3]: Missana, T., Alonso, U., Turrero, M. J., J. Cont. Hydrol. 2003, 61, p17

[4]: Plaschke, M., Schafer, T., Bundschuh, T., Ngo Manh, T., Knopp, R., Geckeis, H., Kim, J.I., Anal. Chem 2001, 73(17), p4338

[5]: Schäfer, T.; Geckeis, H.; Bouby, M.; Fanghänel, T.; Radiochim. Acta 2004, 92(9-11), p731

[6]: Bouby, M., Geckeis, H., Geyer, F., accepted in Anal. Bioanal. Chem., 2008

[7]: Duro, L., Bruno, J., Rollin, C., Guimèra, J., Geckeis, H., Schüßler, W., Vejmelka, P., Shibata, M., Yoshida, Y., Ota, K., Yui, M., NAGRA Technical Report 99-218, 2000, Nagra, Wettingen, Switzerland

[8]: ENRESA Technical Publications 05/98, 1998, Madrid .

[9]: Möri, A., Geckeis, H., Fierz, T., Eikenberg, J., Degueldre, C., Hauser, W., Geyer, F. W., Schäfer, T., NAGRA Technical Report 03-01, 2004, Nagra, Wettingen, Switzerland

[10]: Bayens, B., Bradbury, M. H., PSI, Technical Report, Bericht n° 95/10,Willingen, 1995

[11]: www.millipore.com/techpublications/tech1/pf1172en00

[12]: Bouby, M., Geckeis, H., Lützenkirchen, J., Mihai, S., Schäfer, T., in preparation for EST.

[13]: Bradbury, M. H., Bayens, B., Geochim. Cosmochim. Acta 2005, 69 (4), p875.

[14]: Kinniburgh, D. G., van Riemsdijk, W. H., Koopal, L. K., Borkovec, M., Benedetti, M. F., Avena, M. J., Coll. Surf. A 1999, 151, p147

INTERACTION OF LATEX COLLOIDS WITH MINERAL SURFACES AND GRIMSEL GRANODIORITE

André Filby[1*], Markus Plaschke [1], Horst Geckeis[1], Thomas Fanghänel [2,3]

[1]Institute for Nuclear Waste Disposal, Forschungszentrum Karlsruhe, P.O. Box 3640, 76021 Karlsruhe (GER)
[2]European Commission, Joint Research Centre, Institute for Transuranium Elements, P.O. Box 2340, 76125 Karlsruhe (GER)
[3]Ruprecht-Karls-Universität Heidelberg, Physikalisch-Chemisches Institut, Im Neuenheimer Feld 253, 69120 Heidelberg (GER)

* Corresponding author: andre.filby@ine.fzk.de

Abstract

In the present study interaction of carboxylated fluorescent latex colloids, used as a model for bentonite colloids, with natural Grimsel granodiorite and some of its component minerals is studied by fluorescence microscopy and SEM/EDX. The experiments are carried out by varying the pH from 2-10. Strong adsorption is observed at pH values close to or below the points of zero charge (pH_{pzc}) of the mineral surfaces. The influence of Eu(III) on colloid adsorption is also investigated. Depending on mineral phase and pH, a significant increase of colloid adsorption is observed in the presence of Eu(III).

Introduction

Immobilization of long-lived radionuclides is the primary aim of nuclear waste disposal in deep geological formations. Storage in crystalline rock in combination with a multi-barrier system is considered as a feasible repository concept for high-level radioactive waste. The multi-barrier system consists of the waste matrix in metal canisters and the surrounding backfill material, e.g., compacted bentonite. Bentonite clay is an appropriate material due to its swelling properties and the ability to adsorb actinide ions from solution. Depending on the physico-chemical conditions the bentonite barrier may also generate colloids which can adsorb or incorporate radionuclides and transport them over considerable distances. On the other hand, colloids can be retained by interaction with mineral surfaces or by agglomeration. Both processes strongly depend on geochemical parameters, e.g., pH, ionic strength or colloid concentration.

From the present status of knowledge binding mechanisms of negatively charged colloids on natural mineral surfaces are not sufficiently understood. It can be expected

that electrostatic interaction will dominate colloid adsorption. However, it is not clear if additional binding mechanisms are present especially under unfavorable electrostatic conditions. The present study intends to answer this open question. Adsorption experiments of negatively charged fluorescent latex colloids on original granodiorite fracture filling material are performed. These colloids can be easily identified on the mineral surfaces by fluorescence microscopy and adsorbing mineral phases can be determined by SEM/EDX. Sorption of the same colloids on several single minerals (composing the granodiorite) is studied in order to support the experiments with the heterogeneous natural mineral. In this context the influence of different mineral properties such as permanent and variable charge on the sorption behavior is discussed. Furthermore, colloid sorption is also studied under unfavorable conditions (alkaline pH) and the influence of a polyvalent cation (Eu(III)) on colloid adsorption is addressed. The present paper is a summary of a full research paper (Filby et al., 2008).

Materials and Methods

Carboxylated polystyrene and bentonite colloids

Fluorescent carboxylate-modified polystyrene colloids with a diameter of 25 nm are purchased from Postnova Analytics (Landsberg/Lech, Germany). The nanospheres are rhodamine-labeled with an excitation wavelength of 552 nm and an emission wavelength of 580 nm. Sample solutions are prepared by diluting the colloid stock suspension with 10^{-2} M NaCl in Milli-Q water to a final colloid concentration of 0.05 g/l. Experiments in absence of Eu(III) are carried out at pH 2-10. The influence of Eu(III) aquo ions (CertiPUR Europium ICP Standard, Merck, Germany) was investigated only in the pH range of 2-6 since Eu(III) undergoes carbonate complexation and hydrolysis under alkaline conditions.

Sorption experiments with Grimsel granodiorite

The Grimsel granodiorite used for the sorption experiments is derived from fracture filling material taken from the Grimsel Test Site (GTS), Switzerland. The individual rock samples are equilibrated for three years in Grimsel groundwater (pH 9.6, ionic strength 10^{-3} M). A piece of Grimsel granodiorite with a dimension of 2×3 cm is withdrawn from the groundwater and rinsed thoroughly with MQ-water. Then the granodiorite is dipped into the colloid suspension. Colloids are allowed to adsorb from fluid to sample surface for 15 min. This sorption time is chosen because sorption experiments with longer sorption times up to 2 hours did not show an increase in colloid adsorption. The samples are then withdrawn from the suspension and thoroughly rinsed with MQ-water in order to remove any non-adsorbed latex colloids. After drying in an oven at 40°C, the rock samples are investigated by fluorescence microscopy (see section 2.4).

Sorption experiments with single minerals

All single minerals (muscovite, biotite, albite, orthoclase, apatite and quartz) are commercially available (Krantz Mineralien Kontor, Bonn, with exception of muscovite, which is purchased from Plano GmbH, Wetzlar, Germany). First, mineral surfaces are cleaned to remove any fluorescing impurities on the mineral surface. Minerals are immersed in and rinsed with chloroform, methanol and MQ-water. After this procedure the samples are placed in an oven at 40°C for approximately 3 hours. Sheet silicates like muscovite or biotite are freshly cleaved in order to obtain clean surfaces. Sorption experiments are carried out as described for the granodiorite (see section 2.2).

Measurement of fluorescence intensity and mineral composition

At least 50 fluorescence images of the surface are recorded for each sample. The obtained images have a size of 348×256 µm and the size of one pixel is 1 µm². The fluorescence intensity is quantified by reading out mean grey-scale values for a selected image area (WinSpec/32 software, Version 2.5.19.7, Roper Scientific) and is given as counts in an arbitrary scale [a.u.]. These values range from 0-255 (8-bit tiff-format), with 255 being the most intense signal. The fluorescence-optical images presented in this paper are processed in order to enhance image contrast.

SEM/EDX (CS44FE Field Emission SEM, Cam Scan, Cambridge, UK) is applied to identify the mineral phases. The samples are sputtered with a thin chromium layer and investigated with an acceleration voltage of 15 kV in order to minimize the penetration depth of the electron beam.

Surface coverage

The colloid surface coverage is determined by correlating fluorescence intensities of adsorbed colloids on muscovite (measured by fluorescence microscopy) with the number of colloids per area (determined by atomic force microscopy (AFM)). Colloid concentration is varied in a range of 0.5 to 2 g/l in order to find a sufficient number of colloids on a selected image area. Eu(III) is added with a concentration of 10^{-5} M in order to increase the colloid adsorption. Images are obtained by tapping-mode AFM (Dimension 3000, Digital Instruments, Santa Barbara, USA) on dried samples and the number of colloids per µm² is counted at several image areas with different fluorescence intensities. The area (A) occupied by a single spherical colloid can be calculated by $A = \pi r^2$, where r is the nominal colloid radius (12.5 nm). The surface coverage is obtained summing up values of A and relating this sum to the total image area. Surface coverage is given in percent. A fairly linear relation between surface coverage and the fluorescence intensity is found.

Results

In the present paper only the adsorption of carboxylated latex colloids on the sheet silicates **muscovite** and **biotite** is adressed. A more detailed study covering other single minerals of the Grimsel granodiorite system is found in Filby et al. (2008).

Fig. 1 shows fluorescence intensity/surface coverage vs. pH obtained from adsorption of carboxylated colloids and muscovite in presence/absence of Eu(III). Fig. 2 shows similar data obtained for biotite.

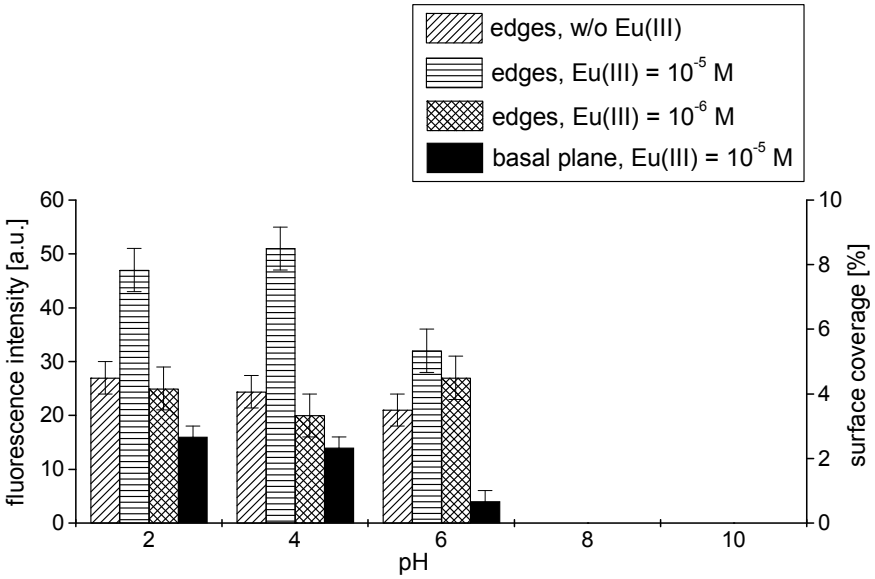

Figure 1: *Fluorescence intensity/surface coverage vs. pH for muscovite in the presence and absence of Eu(III) (see text).*

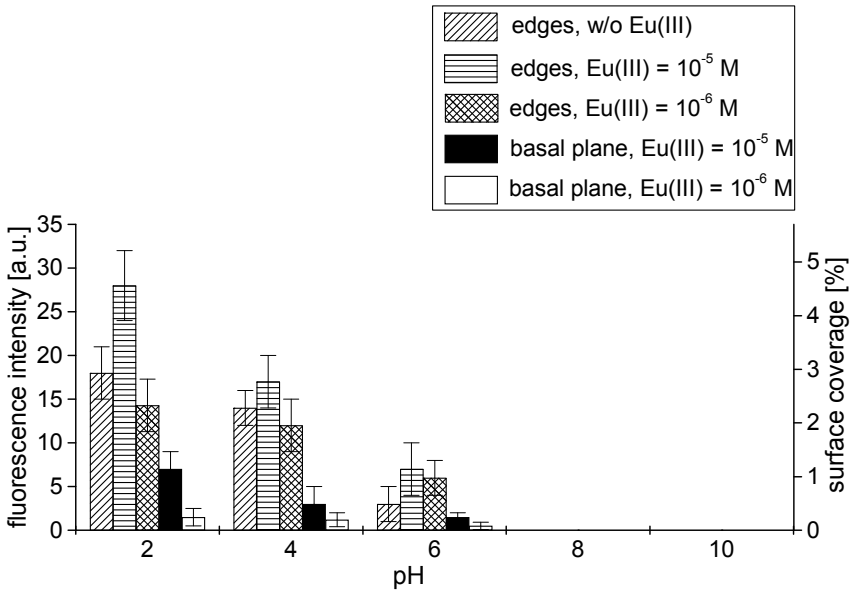

Figure 2: *Fluorescence intensity/surface coverage vs. pH of biotite in presence and absence of Eu(III) (see text).*

Colloid adsorption in the absence of Eu(III)

A significant fluorescence signal is detected on the mineral edges (diagonally lined bars in Figs. 1 and 2) under acidic conditions in absence of Eu(III) which decreases from pH 2 to 6. In contrast, under alkaline conditions, there is no fluorescence detected at the edges (pH 8-10, not shown). Under these conditions increasing

deprotonation of the aluminol-/silanol edge sites results in repulsive electrostatic forces. The pH_{pzc} values of muscovite and biotite surfaces are determined to 6.6 and 6.5, respectively (Sverjensky (1994). Therefore, both the muscovite and biotite surfaces are negatively charged at alkaline pH values and repulsion dominates. This corresponds to our finding that on the basal planes no colloid adsorption is detected in the alkaline pH regime and in absence of Eu(III) (not shown).

Colloid adsorption in the presence of Eu(III)

In the presence of Eu(III), a significant increase of fluorescence intensity is observed both on edges and planes. Black bars in Figs. 1 and 2 represent fluorescence intensities on basal planes in presence of 10^{-5} M Eu(III). In the case of biotite, there is also fluorescence detectable with a lower Eu(III) concentration (10^{-6} M) (white bars in Fig. 2). The sorption of the negatively charged colloids on permanent negatively charged basal planes can be explained by the formation of polyvalent cation bridges by Eu(III) as described in the literature (Greenland, 1971). The corresponding fluorescence intensities decrease from pH 2 to 6.

At the edges of both sheet silicates increased fluorescence intensities are found in the presence of 10^{-5} M Eu(III) from pH 2 to 6 (horizontally lined bars in Figs. 1 and 2). Colloids can obviously adsorb under these conditions on the edge aluminol- and silanol-groups although these groups are protonated at pH 2 (see Discussion and Conclusions).

At lower Eu(III) concentration (10^{-6} M) fluorescence intensities at the edges are for both minerals comparable to those obtained in absence of Eu(III) (cross-hatched bars in Figs. 1 and 2).

Summary for other single minerals/Grimsel granodiorite (from Filby et al., 2008)

On the feldspars **albite** and **orthoclase**, a significant influence of Eu(III) on colloid adsorption is observed, which, in the case of orthoclase, is dominated by the mineral edges. This is in agreement with a similar finding on the granodiorite. Strong adsorption is observed on the entire mineral surface of apatite, which is significantly increased in the presence of Eu(III). In accordance with this observation, **apatite** is identified as a strongly adsorbing mineral in the granodiorite. Sorption experiments with quartz also show measurable influence of Eu(III); weak sorption can even be found at pH 6, which is above the pH_{pzc} of quartz. To summarize, the sorption behaviour of colloids on single minerals and in the absence of Eu(III) is in reasonable agreement with simple electrostatic considerations. The strongest adsorption is always observed at pH values below the pH_{pzc}, where mineral surfaces are positively charged.

Regarding the Grimsel granodiorite system, colloid sorption mainly takes place on the minerals apatite, illite, titanite, biotite (pH 2-6) and K-feldspars (pH 2-4). Again, this is in agreement with the observations made with the single minerals. In the presence of Eu(III) increased colloid sorption both on single minerals and granodiorite is detected.

To conclude, our experiments show that colloid adsorption on mineral surfaces is mainly driven by electrostatic interactions. In contrast to the observations made by

Alonso et al. (2004) and Schäfer et al. (2004), colloid adsorption is not detected in the alkaline regime. It can not be excluded that weak adsorption takes place under these conditions which may not be detectable with our experimental setup.

References

Alonso, U., Missana, T., Patelli, A., Rigato, V., Ravagnan, J., (2004): μPIXE study on colloid heterogeneous retention due to colloid/rock electrostatic interactions. Laboratori Nazionali di Legnaro Annual Report 2004, 68-69.

Filby, A., Plaschke, M., Geckeis, H., Fanghänel, Th., (2008): Interaction of latex colloids with mineral surfaces and Grimsel granodiorite. Journal of Contaminant Hydrology 102, 273-284.

Greenland, D.J., (1971): Interaction between humic and fulvic acids and clays. Soil Science 111, 34-41.

Schäfer, T., Geckeis, H., Bouby, M, Fanghänel, T., (2004): U, Th, Eu and colloid mobility in a granite fracture under near-natural flow conditions. Radiochimica Acta 92, 731-737.

Sverjensky, D.A., (1994): Zero-point-of-charge prediction of crystal chemistry and salvation theory. Geochimica et Cosmochimica Acta 58, 3123-3129.

Takahashi, Y., Kimura, T., Kato, Y., Minaia, Y., Tomingaa, T., (1997): Hydration structure of Eu(III) on aqueous ion-exchange resins using laser-induced fluorescence spectroscopy. Chemical Communications 2, 223-224.

AQUEOUS UPTAKE OF URANIUM(VI) BY PYRITE UNDER BOOM CLAY CONDITIONS

Christophe Bruggeman*, Norbert Maes

SCK-CEN (BE)

* Corresponding author: Christophe.Bruggeman@sckcen.be

Abstract

The aqueous uptake of uranium(VI) on crushed natural pyrite was investigated under Boom Clay conditions, i.e., in a ~ 0.014 mol/L $NaHCO_3$ electrolyte with special emphasis on the role of dissolved organic matter (~ 70 ppm DOC). Macroscopic batch experiments with different initial concentrations of uranium(VI) (10^{-8} – 10^{-4} mol/L) were combined with XANES-EXAFS spectroscopy on the solid phase to elucidate the speciation of uranium in these systems, and to gain insight into the major reaction mechanisms playing between uranium and pyrite. It was found that the predominant valence state of uranium in solution is likely to be uranium(VI), while on the solid phase mixtures of uranium(IV) (amorphous UO_2 nanocolloids) and uranium(VI) (adsorbed onto Fe^{III} oxide sites) were observed. These observations indicate that in these conditions, the uranium solid-liquid distribution is governed by both reduction and adsorption processes.

Introduction

In Belgium the Boom Clay formation is studied as a reference host rock for geological disposal of high level radioactive waste. The safe disposal of nuclear waste in a geological host formation depends on the properties of the host formation to slow down (retention) the migration of the radionuclides once released. Redox reactions on mineral surfaces may significantly contribute to the immobilisation of actinides under Boom Clay conditions. Therefore, the role of redox controlling, Fe(II)-bearing minerals on the retention of U is studied, with a focus on the understanding of mineral surface reaction kinetics. The major redox-controlling phases in Boom Clay are considered to be pyrite, FeS_2 (1-5 w%), and siderite, $FeCO_3$ (0-1w%) (De Craen *et al*., 2004).

From literature, it is known that FeS_2 is able to (at least partially) reduce U(VI) to U(IV) (e.g. Wersin *et al*. (1994), Eglizaud *et al*. (2006)). However, most studies were performed in the acid-to-neutral pH range and in the absence of carbonate ligands, which are able to stabilize U(VI). Therefore, the question remains open whether FeS_2 is able to reduce U(VI) under Boom clay geochemical conditions (pH 8.3, ~14 $mmol \cdot l^{-1}$ $NaHCO_3$ electrolyte). Previous investigations on the interaction of U(VI) with FeS_2 under Boom Clay geochemical conditions (Delecaut, 2004), showed a quantitative

uptake of U(VI) by pyrite, which decreased with an increase in dissolved organic carbon (DOC). X-ray Absorption Near-Edge Spectroscopy (XANES) analysis of solid phase U on a single sample pointed to a partial reduction of U(VI) to U(IV). In combination with the observed remaining U solution concentration, these observations were interpreted in terms of the formation of a $UO_{2.33}$ precipitate, which imposed a solubility limit to the U solution concentration.

The aims of the present study are therefore to gain additional arguments and evidence for the reduction of U(VI) to U(IV) under Boom Clay geochemical conditions, and to further elucidate the nature of the precipitate formed. These aims will be achieved by performing batch uptake experiments of U(VI) by pyrite, in presence and absence of organic carbon. The electrolytes used mimic the groundwater of Boom Clay under *in situ* conditions. The U solid phase speciation will be analyzed with a combination of XANES and Extended X-ray Absorption Fine Structure (EXAFS) spectroscopy.

Experimental

Two series of pyrite-containing batch isotherm systems were prepared, respectively in synthetic Boom Clay water (SBCW, ~ 14 $mmol \cdot l^{-1}$ $NaHCO_3$, absence of dissolved organic carbon) and in real Boom Clay water (RBCW, EG/BS piezometer water from the HADES underground research facility, Mol, Belgium, ~ 70 $mg \cdot l^{-1}$ dissolved organic carbon), at pH 8.5(±0.3). The batch experiments were conducted under anaerobic conditions in a glove box with a controlled Ar – 5% H_2 – 0.4% CO_2 atmosphere (O_2 < 2 ppm). The FeS_2 that was used originated from a cubic single crystal which was ground and purified according to the procedure described in Decostes et al. (2001). In a subsequent step the FeS_2 was also preconditioned with the SBCW and RBCW electrolytes. U(VI) was added in a range of concentrations (from 10^{-8} to 10^{-4} $mol \cdot l^{-1}$), starting from a 10^{-1} $mol \cdot l^{-1}$ $UO_2(NO_3)_2.6H_2O$ solution, which was diluted in SBCW or RBCW, depending on the isotherm series. The final FeS_2 solution-to-solid ratio in the U-containing samples was about 5 $g \cdot l^{-1}$. The systems were allowed to equilibrate for 120 days.

The supernatant concentrations after centrifugation and 0.45 µm filtration, and after 300.000 and 30.000 Da ultrafiltration (Millipore centrifugal ultrafiltration units, PES membrane) were analyzed for pH, E_h, absorbance at 280 nm, U (ICP-MS), Fe (ICP-MS) and S (SO_4^{2-} and $S_2O_3^{2-}$, IEX).

Samples used for XANES and EXAFS analysis were prepared in an identical way as described above. The initial U(VI) concentration was 10^{-3} $mol \cdot l^{-1}$. A total of four samples was analysed, combining two different background electrolytes (SBCW and RBCW) and two different equilibration times (respectively 10 days and 120 days).
Samples used for XANES and EXAFS were prepared by separating the supernatant from the solid phase of the FeS_2-containing samples by centrifugation and decanting. The remaining pellets were washed with SBCW to dilute and remove any remaining U solution species. After the washing step, the pellets were dried under vacuum, a weighted amount was mixed with cellulose and transferred to 500 µl Eppendorf vials. Standard reference samples for XANES and EXAFS, either solutions or solids, were also prepared in such vials.

XANES and EXAFS measurements were carried out on either the Dubble beamline BM26A or the Rossendorf beamline (Robl) BM20 at the European Synchrotron Radiation Facility. A Si(111) double-crystal monochromator was used in channel-cut mode to collect uranium L_{III}-edge spectra. Measurements were performed in fluorescence mode using a 9-element monolithic Ge detector (Dubble) or a 13-element, high-throughput Ge-detector (Robl). The energy of the spectra was calibrated by simultaneous X-ray absorption spectra measurement of reference Y foil (first inflection point at 17038 eV). Each sample was measured at least three times, and the spectra were averaged and dead-time corrected using Sixpack v0.53 software running under the IFEFFIT program suite (Newville, 2001). XANES and EXAFS spectra were treated by the Athena and Artemis programs (Ravel and Newville, 2005) to subtract the background from the spectra, normalize the spectra, and extract EXAFS spectra. The program FEFF8 (Ankudinov *et al*., 1998; Rehr and Albers, 2000) was used to construct theoretical models on the basis of the crystallographic atomic positions of UO_2 (Wyckoff, 1960).

Results and discussion

Batch experiments

The U concentrations in the supernatants of the FeS_2-containing batch isotherm series after 120 days equilibration time are depicted in figure 1. Figure 1a (left) shows the series with SBCW (absence of organics) as background electrolyte, and figure 1b (right) shows the series with RBCW (~ 70 mg·l^{-1} dissolved organic carbon).

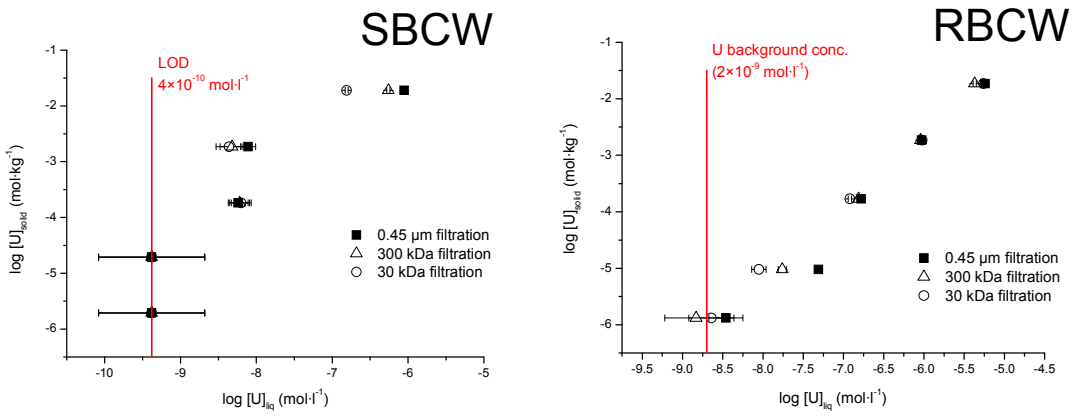

***Figure 1**: Logarithmic isotherm plots of the U solution concentration (mol·l^{-1}) versus the U solid phase concentration (mol·kg^{-1}) in batch systems containing ~ 5 g·l^{-1} FeS_2. Figure 1a (left) shows the series with SBCW as background electrolyte, figure 1b (right) with RBCW.*

As can be observed from figures 1a-b, the isotherms do not show a solubility-limited type mechanism dominating the FeS_2-containing samples. In the systems containing SBCW, two samples, with initial U(VI) concentrations of 10^{-8} and 10^{-7} mol·l^{-1}, have final U solution concentrations below the analytical detection limit (4×10^{-10} mol·l^{-1}). The two samples with initial U(VI) concentrations of 10^{-6} and 10^{-5} mol·l^{-1}, have final U solution concentrations of about $4\text{-}8\times10^{-9}$ mol·l^{-1}. Ultrafiltration does not

influence these concentrations, which was also observed by Delecaut (2004). The sample with highest initial U(VI) concentration (10^{-4} mol·l^{-1}) showed a much higher final U solution concentration (9×10^{-7} mol·l^{-1}), which decreased about one order of magnitude upon ultrafiltration at 30.000 Da.

In the samples containing RBCW, natural U present in the Boom clay piezometer water imposes a background concentration of 2×10^{-9} mol·l^{-1} (measured in a "blank" FeS_2 sample containing RBCW electrolyte). The sample containing the lowest initial U(VI) concentration of 10^{-8} mol·l^{-1}, shows final U concentrations around this value. All other samples display a Freundlich-like behavior with a linear relationship on log-log scale between the supernatant U concentration and the solid phase U concentration. The highest measured U solution concentration in the present set-up equals 5.8×10^{-6} mol·l^{-1}, which is one order of magnitude higher than measured by Delecaut (2004). This concentration is also markedly higher compared to the systems with SBCW as background electrolyte, and, in general, it can be stated that the presence of dissolved organic carbon decreases the uptake of U by FeS_2. Except for the lowest initial U(VI)-containing samples (10^{-8} and 10^{-7} mol·l^{-1}), no influence of ultrafiltration was observed, which is in contrast with the general finding made by Delecaut (2004).

Concerning the solution concentrations of Fe and S, no significant conclusions could be drawn. In the SBCW series, to which neither Fe nor S were added initially, Fe concentrations ranged between 4×10^{-7} and 2.8×10^{-6} mol·l^{-1}, while both SO_4^{2-} and $S_2O_3^{2-}$ were below detection limit (2.6×10^{-6} mol·l^{-1} and 8.9×10^{-6} mol·l^{-1} respectively). In the RBCW series, concentrations of both Fe and SO_4^{2-} were higher compared to SBCW, as a result from their presence in Boom Clay piezometer water (De Craen *et al*., 2004). Fe concentrations ranged between 1.4×10^{-5} and 2.6×10^{-5} mol·l^{-1}, while SO_4^{2-} concentrations between 3.8×10^{-6} and 9.6×10^{-6} mol·l^{-1} were obtained. Both ranges are within the scope of "undisturbed" piezometer water, and, thus, do not point to an oxidation of the FeS_2 phase. $S_2O_3^{2-}$ concentrations, not present in Boom Clay piezometer water and also a typical pyrite oxidation product, were below the limit of detection.

Geochemical modeling with Phreeqc v2 (Parkhurst and Appelo, 1999) using the latest NEA thermodynamic database for U (Guillaumont *et al*., 2003) demonstrates that under the conditions of the present experiments, uranium could be present in solution either as uranyl carbonate, $UO_2(CO_3)_3^{4-}$, or as hydrolyzed U(IV), $U(OH)_4$(aq). In the former case, complexation of U(VI) with DOC could occur, but as shown by Delecaut (2004), true complexation of U(VI) with Boom Clay humic substances is negligible under the conditions studied in the present experiments. This is highlighted in figures 2ab. Figure 2a displays the loss of DOC upon ultrafiltration of the supernatant solutions of the RBCW systems, while figure 2b shows the equal loss of U upon ultrafiltration. As is apparent from the samples containing the highest initial U(VI) concentration, the decrease in DOC does not result in an equal decrease of U. Only in the systems with lowest initial U(VI), a decrease in DOC results in a decrease of U, possibly due to the presence of U(IV) intrinsic or pseudo colloids, as was already observed by Delecaut (2004). Intrinsic U(IV) colloids might also be present in the sample with highest initial U(VI) concentration of the SBCW series, which would explain the loss of U from solution upon ultrafiltration.

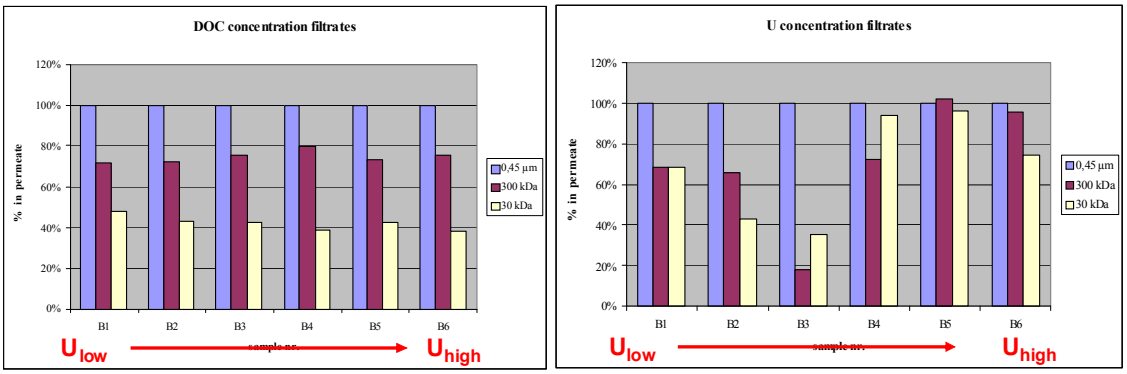

***Figure 2**: Influence of ultrafiltration at 300.000 and 30.000 MWCO on DOC (figure 2a – left) and U solution concentration (figure 2b – right), expressed in % as compared to 0.45 µm microfiltration (= 100 %). Samples are shown in order of increasing initial U(VI) concentration.*

Concluding, the present experiments do not show the imposition of a solubility limit, neither in the systems with SBCW electrolyte, or in the samples containing RBCW. The resulting isotherms show a Freundlich-like behavior. The dominant valence state in the supernatant solutions is likely to be U(VI), but in some samples the presence of U(IV) (as intrinsic or pseudo colloids) can not be ruled out. Therefore, it is likely, but not conclusively proven, that part of the U introduced to the systems is reduced from U(VI) to U(IV). In the presence of dissolved organic carbon, the final U solution concentration is steadily higher compared to the absence of DOC. However, true complexation of U(VI) by DOC is low. Therefore, the influence of dissolved organic carbon on the uptake of U by FeS_2 (as evidenced from the difference in isotherms between the SBCW and RBCW series) will probably result from its impact on the interaction of the FeS_2 mineral surface and associated functional groups with aqueous U(VI). The exact mechanism (blocking of sorption sites, changing of the surface charge, etc.) however remains unknown.

Because the present experimental setup does not allow concluding between a pure sorption of U(VI) or a sorption-reduction to U(IV), X-ray absorption spectroscopy is used to elucidate the resulting U solid phase speciation in systems similar as described above. This is discussed in the following section.

X-ray Absorption Spectroscopy

The normalised XANES spectra of the four U-FeS_2 systems, together with an aqueous U(VI) standard ($UO_2(CO_3)_3^{4-}$) are shown in figure 3. XANES, and more specifically the position of the absorption edge, provides information on the valence state of uranium. From figure 3 it can be observed that a shift of the absorption edge is occurring towards lower energy from the U(VI) standard to the U-FeS_2 samples. Moreover, also the shoulder in the XANES spectrum located directly after the absorption edge, which represents a multiple scattering feature resulting from the axial oxygen atoms of the uranyl unit, is disappearing in the U-FeS_2 samples. These two features indicate a shift of the valence state of U(VI) towards U(IV), in accordance with results from Delecaut (2004). However, also differences between the different U-FeS_2 samples can be noted: the strongest shift and strongest decrease of the shoulder are observed for the sample with SBCW electrolyte, equilibrated for 120 days. The weakest

shift and weakest decrease of the shoulder are observed for the samples with RBCW electrolyte (presence of DOC).

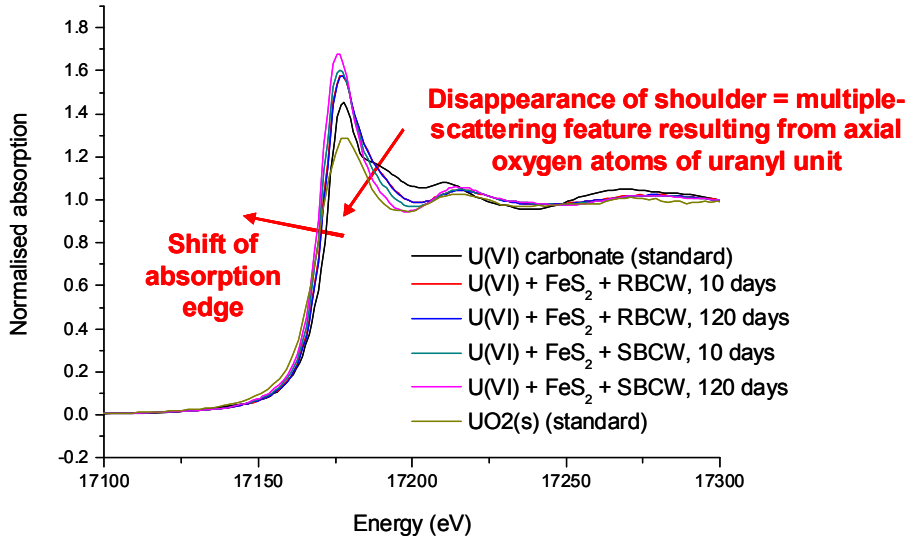

***Figure 3**: Comparison of normalized U L_{III}-XANES spectra for $UO_2(CO_3)_3^{4-}$ (reference) and U-FeS_2 samples*

Because of the differences noted for the different samples, it was tried to obtain more information on the number of potential U species in the 4 U-FeS_2 samples using principal component analysis with the Sixpack software. It was found that only 2 significant eigenvectors (principal components) were needed to accurately reconstruct the samples. In figure 4, the results of such reconstruction using these 2 principal components can be observed, for the two most "extreme" samples, i.e. in SBCW electrolyte and 120 days equilibration, and in RBCW electrolyte and 10 days equilibration. The fits of the spectra are > 99.5% accurate. A target transformation to relate the principle components to physical standards, showed that standards needed to reconstruct the experimental data were likely U(VI) adsorbed onto a Fe-oxide phase, and a UO_2(s) precipitate.

Information on the local environment of uranium atoms in the U-FeS_2 samples is provided by analysis of the EXAFS data. The Fourier transformed $X(k)*k^3$ EXAFS data are depicted in figure 5. The EXAFS data of all 4 samples can again be reconstructed using only two significant components extracted by Principal Component Analysis (data not shown). A hint of the two major species which make up the spectra can be extracted from qualitative analysis of the different shells in the Fourier spectra: the first shell is in fact comprised of two different features, one which represents the UO_2^{2+} unit, and one which represents the U-O path in uraninite. These two features become apparent when comparing the Fourier spectra of the different U-FeS_2 samples: completely in line with the observations made from the XANES spectra, it is noted that the spectra of SBCW-containing samples are more composed of U(IV) (with a higher contribution of U(IV) at longer equilibration time), while the spectra of RBCW-containing samples are more composed of U(VI) (no significant difference between the

two equilibration times). The shells at larger distance, which are again indicative of scattering paths of the uraninite structure, confirm these observations.

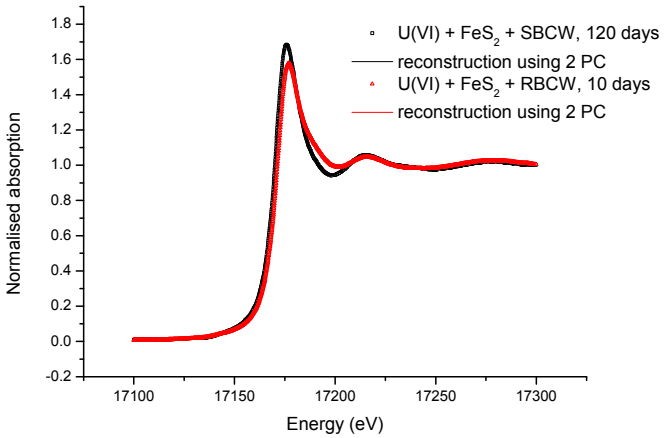

***Figure 4**: Examples of U L_{III}-XANES spectra of two U-FeS_2 samples compared with the reproduced data using two significant abstract components extracted by Principal Component Analysis (Note: lines from reconstruction overlap completely with experimental data points)*

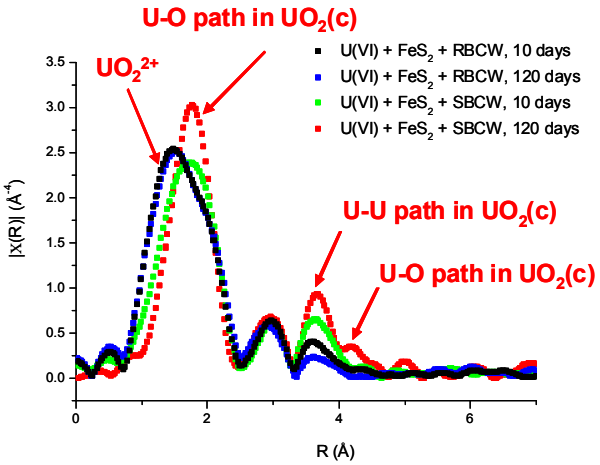

***Figure 5**: Fourier-transformed X(k)*k³ data for the different U-FeS_2 systems.*

Summary and Conclusions

As a conclusion, it can be stated that in the U-FeS_2 systems, at least partial reduction of U(VI) to U(IV) occurs, forming a uraninite-like structure and possibly UO_2 nanocolloids, similar to the observations made by O'Loughlin *et al*. (2003) for the reduction of U(VI) by green rust. In fact, in all samples, both U(VI) (probably adsorbed onto Fe-containing functional groups) and U(IV) structures were detected. The amount of U(IV) was the highest in systems with SBCW (absence of DOC) background electrolyte, and increased with increasing equilibration time. These observations clearly

point to a kinetically-driven reduction process, which seems to be somewhat inhibited by the presence of DOC.

Acknowledgement

This work is undertaken in close co-operation with, and with the financial support of NIRAS/ONDRAF and EC in the frame of the 6FP FUNMIG project. The critical follow-up by and fruitful discussions with Mrs. A. Dierckx, Mr. S.Brassines, Mr. R. Gens and Mr. M. Van Geet (NIRAS/ONDRAF) are very much appreciated.
NOW/FWO Vlaanderen and the European Synchrotron Radiation Facility provided facilities and financial support for performing measurements at DUBBLE and ROBL respectively. We thank S.Nikitenko and A.Scheinost for their help during XAFS measurements, and A.Scheinost for his kind help in U spectra interpretation.

References

- Ankudinov A.L., Ravel B., Rehr J.J., Conradson S.D. (1998) Real-space multiple-scattering calculation and interpretation of x-ray abosrption near-edge structure, *Physical Review B*, **58**, 7565-7576
- De Craen M., Wang L., Van Geet M., Moors H. (2004) Geochemistry of the Boom clay pore water at the Mol site, SCK•CEN-BLG-990, SCK•CEN, Mol (Belgium)
- Delécaut G. (2004): The geochemical behaviour of uranium in the Boom clay. PhD Thesis Louvain-La-Neuve & SCK•CEN.
- Descostes M., Mercier F., Beaucaire C., Zuddas P., Trocellier P. (2001): Nature and distribution of chemical species on oxidized pyrite surface: complementarity of XPS and nuclear microprobe analysis, *Nuclear Instruments and Methods in Physics Research B*, **181**, 603-609
- Eglizaud N., Miserque F., Simoni E., Schlegel M., Descostes M. (2006) Uranium(VI) interaction with pyrite (FeS_2): chemical and spectroscopic studies, *Radiochimica Acta*, **94**, 651-656
- Newville M. (2001) *IFEFFIT* : interactive XAFS analysis and *FEFF* fitting, *Journal of Synchrotron Radiation*, **8**, 322-324
- O'Loughlin E.J., Kelly S.D., Cook R.E., Csencsits R., Kemner K.M. (2003) Reduction of uranium(VI) by mixed iron(II)/iron(III) hydroxide (green rust): formation of UO_2 nanoparticles, *Environmental Science & Technology*, **37**, 721-727
- Parkhurst D.L., Appelo C.A.J. (1999): User's guide to Phreeqc (version 2) – A computer program for speciation, batch-reaction, one-dimensional transport, and inverse geochemical calculations. Water-resources investigations report 99-4259, US Dept of the Interior, USGS, Denver, Colorado (USA)
- Ravel B., Newville M. (2005) *ATHENA*, *ARTEMIS*, *HEPHAESTUS*: data analysis for X-ray absorption spectroscopy using *IFEFFIT*, *Journal of Synchrotron Radiation*, **12**, 537-541

- Rehr J.J., Albers, R.C. (2000) Theoretical approaches to X-ray absorption fine structure, *Reviews of Modern Physics*, **72**, 621-654
- Wersin P., Hochella M., Persson P., Redden G., Leckie J., Harris D. (1994) Interaction between uranium(VI) and sulfide minerals: spectroscopic evidence for sorption and reduction. *Geochimica et Cosmochimica Acta*, **58**, 2829-2843
- Wyckoff R.W.G. (1960) Crystal Structures, Interscience Publishers, New York (USA)

INTERACTION OF URANYL WITH QUARTZ – INFLUENCE OF DISSOLVED SILICA

J. Lützenkirchen*, F. Huber

Karlsruhe Institute of Technology, Forschungszentrum Karlsruhe, Institut für Nukleare Entsorgung (INE), P.O. Box 3640, D-76021 Karlsruhe, Germany

* Corresponding author: johannes@ine.fzk.de

Abstract

In this contribution we present previously unavailable experimental data for the uranyl-quartz system in the absence of carbonate. Furthermore, we have measured the amount of dissolved silica. The absence of carbonate allows us to constrain the surface complexation model for the pure quartz-uranyl model while previously all parameters had to be fitted to data from carbonate containing systems. Measured dissolved silica concentrations were found to be in non-equilibrium with any solid phase but between quartz and amorphous silica. A comprehensive analysis of the effect of the silica is presented, where silica is considered to compete in solution only (i.e. no ternary surface complexes including silica are considered). The model including measured total aqueous silica concentrations yields the best fit to the data. Models using the same surface complexes but with either no silica in solution at all or silica concentrations in solution in equilibrium with quartz yield slightly worse fits to the experimental uptake data. The parameters of the three models do not differ significantly, though.

Introduction

Radionuclide migration from a potential repository into the biosphere via the water path is the standard assumption for safety assessment. Radionuclides interact depending on their properties with solid particles, either immobile as matrix components of barrier, host rock, aquifer or soil or mobile as “quasi-solute” colloids. One major challenge for quantification of these interactions is to describe the distribution of the radionuclides among the different states (i.e. as solute, as bound to mobile carriers or adsorbed to immobile matrix components). The general framework to describe these interactions is available through aqueous solution (Grenthe et al., 1997) and surface complexation models (Lützenkirchen, 2006) in terms of equilibrium models. In general a sound parameterization of the various parts of such models depends (i) on the availability of thermodynamic data for the particular composition of water and particulate components and (ii) spectroscopic back-up of the thermodynamic models. Concerning the first point the quality of thermodynamic data set applied to a given problem usually will depend on the availability and the quality of concomitant

experimental data (with respect to the respective compositions, i.e. are all components and their respective amounts known, and the actual speciation, i.e. are all relevant species in the natural multi-component system known). As for the second point much progress has been made in the last two decades in particular since a broad agreement has emerged that the reliability of the models is increased when they include the available microscopic mechanisms. Again the challenge is to involve multi-component systems such as those in natural environments in systematic studies and to obtain a sound model.

The typical build-up of a model for a well-defined laboratory system starts from defining the aqueous speciation scheme. This is either obtained from available, preferably self-consistent, peer-reviewed thermodynamic data such as within NEA (e.g. Guillaumont et al., 2003) or IUPAC (e.g. Powell et al., 2005) or determined experimentally for the respective experimental conditions such as by Gunneriussion and Sjöberg (1993). These data are then fixed for all subsequent model calculations. For the surface complexation modeling the acid-base model for the surface is required. This part of the surface complexation model is equivalent to the hydrolysis of cations or protolysis of anions in solution. Again once determined it is fixed for all subsequent model calculations. The final surface complexation study involves the adsorption of a solute (e.g. a radionuclide) to the surface of interest. In the present study we are interested in the uranyl-quartz system. Uranyl aqueous speciation is defined based on the NEA-TDB data (Guillaumont et al., 2003). We work in 0.01 M sodium nitrate media and therefore we consider as components in solution uranyl, nitrate, sodium and silica. Dissolved silica makes the system a priori a ternary aqueous system. Usually the effect of dissolved silica is not considered. In the titration of quartz or amorphous silica, there is a significant effect on proton or hydroxide balances at pH values beyond 8. However, the formation of the uranyl – silicato complex is relevant in the pH range from 4 to 8. This aspect is discussed in detail in this contribution.

Material and methods

Several samples of MIN-U-SIL (quartz) were obtained from U.S. Silica Company. They were heated to 600 °C, acid washed and then washed extensively with Milli-Q-water. No attempt to remove the fines from the samples was made. The specific surface areas of the final samples used for the experiments were measured and are summarized in table 1.

pH measurements were done using a combination electrode and a pH meter calibrated against at least 5 commercial buffers. Uranyl and silica were measured by ICP-MS.

A uranyl stock solution was prepared from an ICP-MS standard. The concentration of the stock solution was then verified by ICP-MS.

Batch experiments were carried out in two ways. 1. In a first series of experiments a batch containing an known amount MIN-U-SIL in 0.01 M sodium nitrate medium was prepared at low pH (around 3) and the desired amount of uranyl stock solution was added. From the stirred suspension known aliquots were transferred to test tubes. 2. In the second set of experiments the MIN-U-SIL suspension was prepared as described above and known amounts were transferred to the test tubes. Then aliquots

from the uranyl stock solution were pippetted into the test tubes. All sets of experiments were done by streaming Argon (previously sent through washing bottles of sodium hydroxide and 0.01 M sodium nitrate solutions) over the suspension. Prior to filling samples into test-tubes the test-tubes, were flushed with Argon. For both cases, pH adjustment was done by adding carbonate free sodium hydroxide to the test-tubes. The amount added was based on previous experiments in the absence of uranyl to cover a given pH range. Again Argon was flushed over the samples during the manipulations.

The test-tubes were equilibrated for at least 5 days. The final pH was measured either in the suspension or in the supernatant. Solid liquid separation was done by centrifugation. Only clear supernatants were analysed for U and Si.

Table 1: *Summary of specific surface areas of the MIN-U-SIL samples used for the adsorption experiments and uranyl to surface area ratio in the experiments.*

MIN-U-SIL	5	10	15	30	40
Specific surface area in m^2/g	6.5	3.6	2.4	2.1	1.8
Total amount of uranyl per surface area in $nmol/m^2$	0.64	0.52	0.69	0.68	0.32

Results and discussion

The specific surface areas of the quartz samples are higher than previously reported values (Kohler et al., 1996). This is probably due to the fines present in the samples (Lützenkirchen and Huber, 2007). The amount of uranyl per surface area in the various systems is low and comparable.

Figure 1 shows the adsorption data collected for the 5 samples of MIN-U-SIL. The behavior for these conditions is independent on the size of the particles.

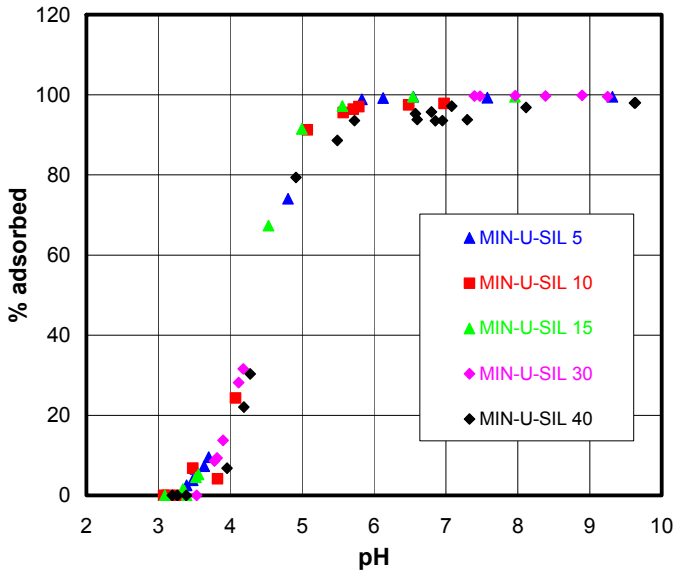

Figure 1: *Experimental data from the batch-experiments for the uranyl-quartz (MIN-U-SIL) systems for conditions as given in Table 1.*

Compared to the presence of carbonate, which causes the amount of uranyl adsorbed to decrease at higher pH, the adsorption of uranyl in our experiments remained

at nearly 100 % at pH > 6. This would indicate that the precautions taken to exclude carbon dioxide were successful.

Figure 2 shows the measured silica concentrations in the same systems. It is obvious that the data are not in equilibrium with quartz, which should yield a horizontal line at about 0.1 millimolar concentrations up to pH 8. The measured values are between amorphous silica and quartz. This might be explained by previous suggestions that at the surface of quartz in contact with water a gel-like layer forms which is more similar to a hydrous form. Using the recommended thermodynamic data from the NEA-TDB for silica, we calculated the percentage contribution of the H_4SiO_4 species to the total dissolved silica (figure 3). Figure 4 shows the results. Clearly, for 4.5 < pH < 7.5 uranyl would form significant amounts of complexes with dissolved silica if it was not adsorbed. Furthermore, the onset of aqueous complexation coincides with the onset of adsorption corroborating previous analogies between aqueous and surface complexation behavior. From Figure 2 it is clear that it would be impossible to include the actual effect of silica on the aqueous speciation of uranyl based on an equilibrium approach. Two extreme cases (which would be possibly considered if experimentally determined dissolved silica was not available) could involve no silica at all (because of slow dissolution of the quartz) or equilibrium concentrations with respect to quartz (because of long equilibration times).

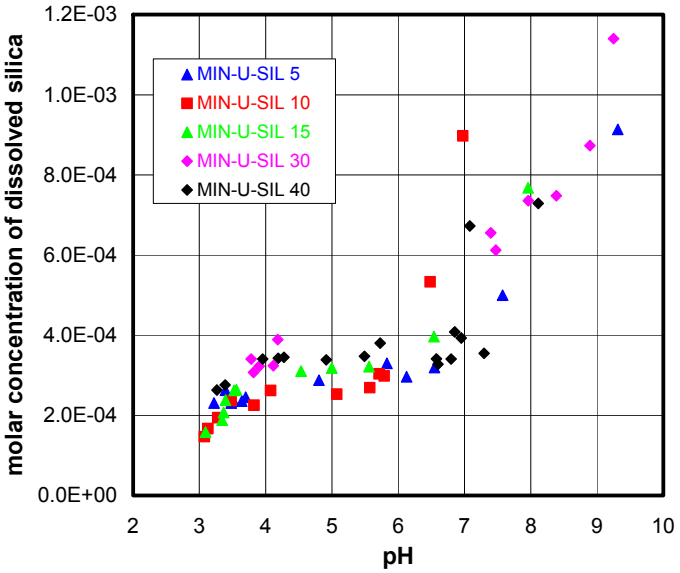

Figure 2: *Experimental data for the analytically determined aqueous silica concentrations from the batch-experiments for the uranyl-quartz (MIN-U-SIL) system.*

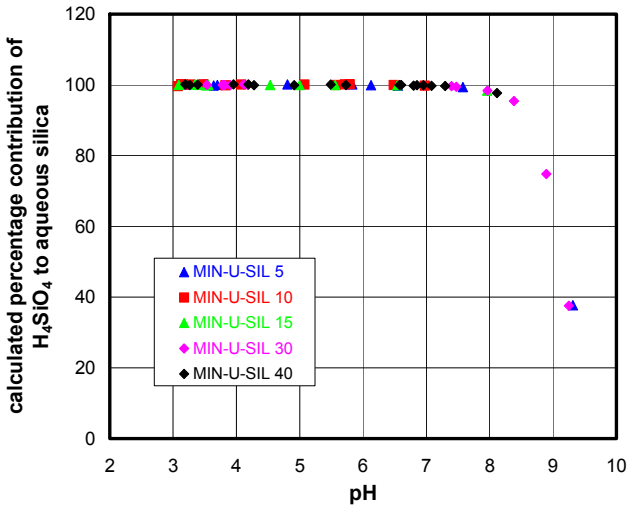

Figure 3: *Percentage contribution of the species H_4SiO_4 to total measured aqueous silica.*

Consequently, three different models were applied to the data in figure 1 which differed with respect to the treatment of silica. The benchmark model includes the measured silica concentrations. The results of the best fit model are shown in figure 5 in terms of K_d (in terms of uranyl adsorbed in moles per surface area per uranyl in solution in molar concentration). The full symbols are experimental data and the open symbols are the model calculations. Since the total dissolved silica cannot be obtained by calculations, the calculations need to be done point by point. Overall the fit to the data by the model is satisfactory. We notice that the discrepancies at the higher pH (i.e. at or near 100 % adsorption) are simply due to the errors in measurement (here by ICP-MS, i.e. low uranyl concentrations include high uncertainty).

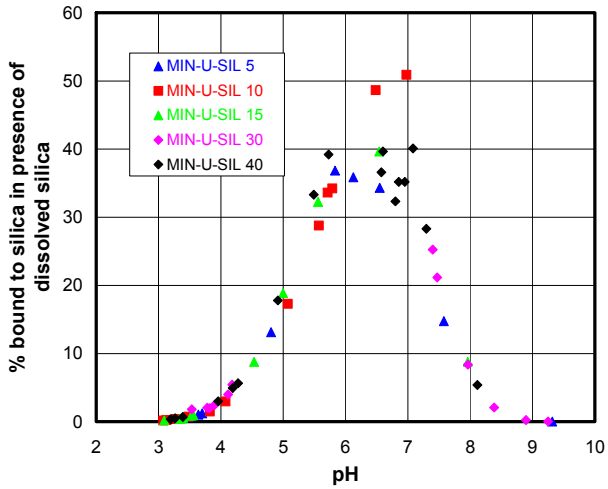

Figure 4: *Percentage of total uranyl bound to dissolved silica in the respective system. This plot was calculated using the experimentally measured silica concentrations and involving the silica species (overall 9 species including H_4SiO_4) from pp. 152/153 and uranyl species (overall 11 species including UO_2^{2+}) from pp. 64/65 and the species ($UO_2SiO(OH)_3^+$) from p. 73 of Guillaumont et al. (2003).*

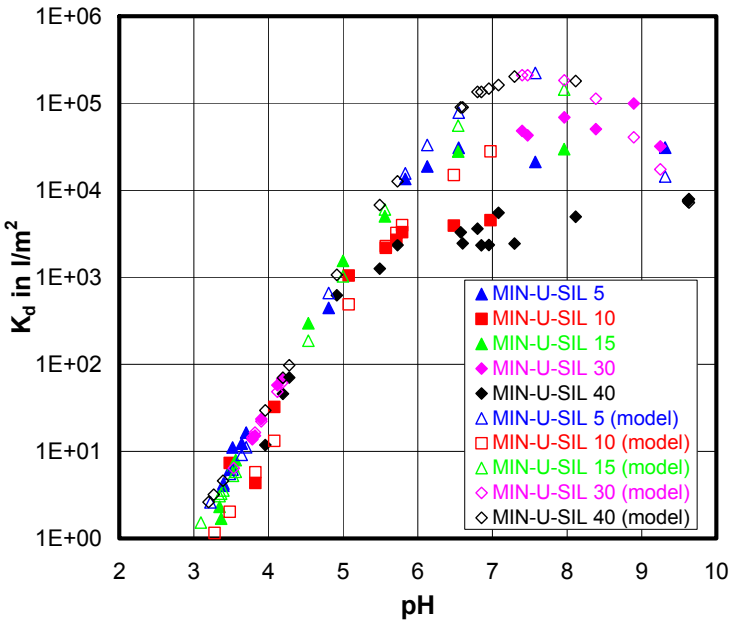

Figure 5: *Model performance for uranyl uptake on quartz in terms of K_d as a function of pH. Model using total measured silica. Full symbols are experimental data, open symbols the corresponding results obtained by the model.*

Table 2 compares the three different model options in terms of goodness of fit. The model involving the complete analytical results is used as a benchmark and also yields the best fit. However, the differences to the two other models are insignificant. Whether accurate experimental data are used or not can therefore not be inferred from model performance. The parameters resulting from the modeling exercises are not varying significantly between model options. This is explained by the competition between hydrolysis and silica complexation in solution (i.e. in case silica is not present in solution, the hydrolysis of uranyl in solution is strong).

Table 2: *Comparison of model results with respect to the treatment of dissolved silica (normalization of the goodness of fit parameter for the option where the experimentally obtained values of dissolved silica were used).*

Model option	Result in terms of goodness of fit
Experimental values of dissolved Si	1.000 (benchmark)
no dissolved Si	1.011
equilibrium amount of dissolved Si	1.012

Conclusions

The experimental results for dissolved silica obtained within our study on uranyl adsorption to quartz suggest that it is important to analytically determine the concentration of aqueous silica, since it is not related to any equilibrium concentration (with quartz or amorphous silica). Only this way it is assured that accurate speciation calculations can be performed with respect to total silica in solution. Model calculations suggest that uranyl adsorption to quartz competes with uranyl complexation by silica in solution.

The measured aqueous silica concentrations do not correspond to equilibrium data but are higher than quartz equilibrium concentrations. This means that an equilibrium model is unable to reproduce such data.
The surface complexation modeling shows that for the uranyl-quartz system the resulting surface complexation model is not significantly affected by the silica effect in solution both in terms of goodness of fit and the resulting model parameters.

References

I. Grenthe, I. Puigdomenech, B. Allard, 1997: Modelling in Aquatic Chemistry, OECD Nuclear Energy Agency, OECD Publishing.

J. Lützenkirchen, 2006: Surface complexation modelling, Academic Press.

R. Guillaumont, T. Fanghänel, J. Fuger, I. Grenthe, V. Neck, D.A. Palmer, M.H. Rand, 2003: Update on the Chemical Thermodynamics of Uranium, Neptunium, Plutonium, Americium and Technetium, Elsevier.

K. J. Powell, P. L. Brown, R. H. Byrne, T. Gajda, G. Hefter, S. Sjöverg, H. Wanner, 2005: Chemical Speciation of environmentally significant heavy metals with inorganic ligands, Part1: The Hg^{2+}-Cl^-, OH^-, CO_3^{2-}, SO_4^{2-}, and PO_4^{3-} aqueous systems, Pure Appl. Chem. 77: 4, 739–800.

L. Gunneriusson, S. Sjöberg 1993: Surface complexation in the H+-goethite-Hg(II)-chloride system, J. Colloid Interf. Sci. 156: 1, 121-128.

M. Kohler, G.P. Curtis, D.B. Kent, J.A. Davis, 1996. Experimental investigation and modelling of uranium(VI) transport under variable chemical conditions, Water Res. Res., 32: 1, 3539-3551.

J. Lützenkirchen, F. Huber, 2007: Heterogeneities in adsorption from aqueous solution - An example of the effect of surface coverage, Ads. Sci. Techn. 25: 7, 503-516.

F. Huber, J. Lützenkirchen, 2008: Submitted to Aquatic Geochemistry.

Ln(III) CO-PRECIPITATION WITH HECTORITE: SPECTROSCOPIC INSIGHTS

Nicolas Finck[1,2*], Michel L. Schlegel [3], Thorsten Stumpf[1], Clemens Walther[1], Kathy Dardenne[1], and Dirk Bosbach [1,2]

[1] Institut für Nukleare Entsorgung (INE) Forschungszentrum Karlsruhe, P.O. Box 3640, D-76021 Karlsruhe, Germany.
[2] Helmholtz Virtual Institute "Advanced Solid-Aqueous RadioGeochemistry", Germany.
[3] CEA, DEN/DPC/SCP/LRSI, F-91191 Gif-sur-Yvette, France.

* Corresponding author: Nicolas.Finck@ine.fzk.de

Abstract

Eu(III) was co-precipitated with the clay mineral hectorite following a multi-step synthesis procedure. Different species associated with the synthetic hectorite and the synthesis protocol were characterized by Time-Resolved Laser Fluorescence Spectroscopy (TRLFS) and Extended X-ray Absorption Fine Structure (EXAFS) spectroscopy. TRLFS data indicated that the lanthanide may be incorporated in the octahedral layer of the brucite precursor and of the clay mineral. EXAFS data strongly suggested the presence of Eu(III) in a clay-like environment, and ruled out the formation of an Eu(III)-containing amorphous silica phase.

Introduction

Understanding the interactions of clay minerals and radionuclides (RNs) is essential to predict the reliability of nuclear waste disposal in geological repositories. Eventually, the waste matrix gets into contact with groundwater and various secondary phases can form upon alteration/dissolution of high-level nuclear waste (HLW) glass and represent a significant retention potential for RNs. Hectorite ($Na_{0.4}[Mg_{2.6}Li_{0.4}Si_4O_{10}(OH)_2]$), a trioctahedral smectite, is one of the secondary phases identified within the alteration layer of corroded HLW glass (Zwicky et al., 1989). This clay mineral may retain RNs by incorporation into the bulk structure via co-precipitation. Trapped in structural sites, RN would be effectively "blocked" from further migration in the geosphere, in particular if a thermodynamically stable solid solution forms.

Several concepts of HLW repository suggest that reducing conditions may prevail, so the actinides Am, Cm, and some fractions of Pu may occur in their trivalent redox state. Because the ionic radii of the trivalent actinide (or 5*f* element) Cm (^{VI}Cm(III) 0.97 Å; Shannon, 1976) and of its nonradioactive chemical homologue

(Chapman and Smellie, 1986), the trivalent lanthanide (or 4*f* element) Eu (^{VI}Eu(III) 0.95 Å; Shannon, 1976), are within the values expected to accommodate sixfold coordination by oxygens, the incorporation of *f* elements may occur by substitution of ions in the octahedral lattice sites. Recent TRLFS investigations on Eu(III) co-precipitation with hectorite (Pieper et al., 2006) suggested a trivalent lanthanide incorporation into a solid phase. A TRLFS study on Cm(III) co-precipitation with hectorite suggested an octahedral substitution mechanism (Brandt et al., 2007).

Based on this background, Eu(III) was used as molecular probe to further investigate the uptake of trivalent *f* elements by co-precipitation with clay minerals. The Eu(III) molecular environment was monitored at successive stages of the hectorite multi-step synthesis protocol developed by Carrado et al. (1997a,b, 2000). Site selective TRLFS measurements were combined with EXAFS experiments to characterize different Eu(III) species during distinct reaction steps.

Experimental

Samples preparation and characterization

Hectorite was co-precipitated in the presence of Eu(III) following a multi-step synthesis procedure (Carrado et al., 1997a,b, 2000). Briefly, an Eu(III)-containing $Mg(OH)_2$ sol was refluxed in the presence of a silica sol, LiF and an organic cation for eight days. Separately, an Eu(III)-containing $Mg(OH)_2$ precursor ((Mg/Eu) hydroxide) and an Eu(III)-sorbed silica gel (Eu/silica) were prepared as reference compounds.

Prior to TRLFS and EXAFS investigations, the Eu(III)-doped hectorite and the (Mg/Eu) hydroxide were characterized by X-Ray Diffraction (XRD) and Attenuated Total Reflectance – Fourier-Transform Infrared (ATR-FTIR) spectroscopy. No influence of the co-precipitated lanthanide could be observed on the XRD pattern. ATR-FTIR (Bruker®, IFS 55) spectra (data not shown) clearly identified the synthetic clay mineral as hectorite (Madejovà and Komadel, 2001; Carrado et al., 1997a). The IR spectrum for (Mg/Eu) hydroxide was mainly characterized by a band around 3700 cm^{-1} corresponding to the hydroxyl stretching frequency (Brindley and Kao, 1984).

TRLFS measurements

TRLFS measurements (T < 20 K) were performed with an excimer pumped dye laser system operating at a frequency of 20 Hz. Direct excitation of the Eu(III) *D*-level was carried out using the dye Coumarin 153. The Eu(III) fluorescence emission was detected by an optical multichannel system. The fluorescence decay times were determined by varying the delay time between laser pulse and camera gating. Further details may be found elsewhere (Finck et al., 2008).

EXAFS measurements

Cancellations effects between backscatterers surrounding the absorbing atom and located in the octahedral (~3.05-3.10 Å) and tetrahedral (~3.20-3.25 Å) sheets were mitigated by performing Polarized EXAFS (P-EXAFS) experiments (Manceau et al., 1988). This was achieved by varying the angle α between the electric field vector **E** of the incident X-ray beam and the clay mineral plane. Europium(III) L_{III}-edge EXAFS spectra were recorded at the XAS beamline (ANKA, 2007) at the ANKA synchrotron

light source at Karlsruhe (Germany). The Eu(III)-doped hectorite was prepared as self-supporting film and was mounted on a goniometer to record EXAFS spectra at α = 10°, 35°, and 60°. Powder EXAFS data were collected for (Mg/Eu) hydroxide and Eu/silica. All data were collected in fluorescence-yield detection mode using a 5-element Ge solid state detector (Canberra). Analysis of the EXAFS data was realized following standard procedures by using Athena and Artemis interfaces to the Ifeffit software (Ravel and Newville, 2005a,b). The spectra were apodized with a Kaiser-Bessel window and Fourier-transformed. Theoretical fit was performed in R-space using single scattering phase and amplitude functions calculated with feff8 (Ankudinov et al., 1998).

Results and discussion

TRLFS investigations

An intense peak, centred at 579.5 nm, with a full-width at half maximum (FWHM) of 2.5 nm, and a smaller peak at 581.2 nm (FWHM ~0.4 nm) were observed in the excitation spectrum of the $^7F_0 \rightarrow {}^5D_0$ transition recorded for the (Mg/Eu) hydroxide precursor (Mg:Eu = ~9700:1; Figure 1 left). Emission spectra were recorded and the emission decay times of the Eu(III) species were determined for several excitation wavelengths: 578.0, 578.5, 579.6 and 581.2 nm (Finck et al., 2008). Three $^5D_0 \rightarrow {}^7F_J$ (J = 0, 1, 2) transitions are displayed in the emission spectra (Figure 1 right). The modification of the spectrum shape with the excitation wavelength demonstrates the existence of different species. Decay time values of 350 ± 30 µs and 1700 ± 100 µs were used to successfully fit the time-dependent emission intensity decays. The long-lived species (minor component; 1700 ± 100 µs) corresponds to Eu(III) having lost its entire primary hydration sphere (Horrocks and Sudnick, 1979). The shorter decay time (350 ± 30 µs) may correspond to Eu(III) bound to 2.5 ± 0.5 H_2O in the inner coordination sphere, or alternatively to 5 ± 1 hydroxyl groups, as the fluorescence quenching by OH^- is half as efficient as by H_2O (Supkowski and Horrocks, 2002). In brucite ($Mg(OH)_2$), the Mg atom is in the centre of an octahedron of hydroxyls. The presence of 5 ± 1 OH groups in the Eu(III) first coordination sphere is therefore consistent with an approximate replacement of Mg^{2+} by Eu^{3+} in the brucite octahedral sheet.

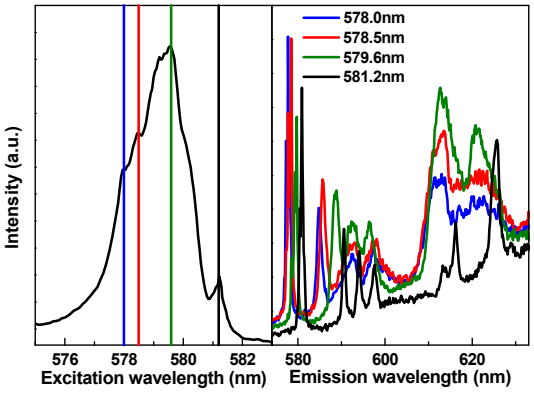

***Figure 1**: Excitation (left) and emission (right) spectra for the (Mg/Eu) hydroxide precursor (Mg:Eu = ~ 9700:1).*

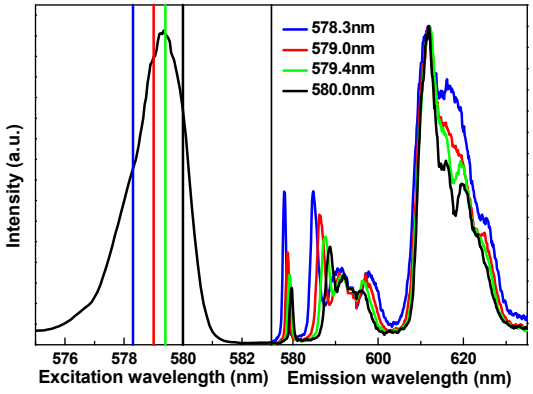

***Figure 2:** Excitation (left) and emission (right) spectra for the Eu(III)-doped hectorite (Mg:Eu = ~ 9700:1).*

Figure 2 (left) shows that the excitation spectrum of the $^7F_0 \rightarrow {}^5D_0$ transition recorded for the Eu(III)-containing hectorite (Mg:Eu = ~9700:1) displays a single intense peak (FWHM 2 nm) centred at 579.4 nm. Considering the peak FWHM obtained for the (Mg/Eu) hydroxide (2.5 nm; Figure 1 left), different species may be convoluted in this signal. Emission spectra were recorded and the emission decay times of the Eu(III) species were determined for several excitation wavelengths: 578.3, 579.0, 579.4 and 580.0 nm (Finck et al., 2008). Three $^5D_0 \rightarrow {}^7F_J$ (J = 0, 1, 2) transitions are observed in the emission spectra (Figure 2 right). The spectrum shape modification with the excitation wavelength indicates the presence of a suite of coordination environments. The fit to time-dependent emission intensity yielded two decay time values of 580 ± 50 µs and 1890 ± 100 µs. Again, the long-lived species (minor component; 1890 ± 100 µs) corresponds to Eu(III) having lost its entire primary hydration sphere (Horrocks and Sudnick, 1979). The second decay time value (580 ± 50 µs) is consistent with a species having 1.0 ± 0.5 H_2O or 2 ± 1 hydroxyl groups (Supkowski and Horrocks, 2002) in the inner coordination sphere. These 2 ± 1 OH^- quenchers present in the first Eu(III) coordination sphere are in accordance with the two OH groups binding each octahedral cation in the clay octahedral layer.

EXAFS investigations

Further structural information was obtained by collecting EXAFS data. The second Fourier Transforms (FTs) peak for the Eu(III) co-precipitated hectorite (Mg:Eu = 130:1) prepared as self-supporting film (α = 35°) is located at higher distance than for the Eu/silica and the (Mg/Eu) hydroxide samples (dotted lines in Figure 3). This suggests that the Eu(III) crystallochemical environment in the clay mineral is distinct from those in Eu/silica and in (Mg/Eu) hydroxide

Current spectral simulation for the Eu/silica sample indicates the presence of ~6.5 oxygens at 2.41 Å in the Eu first coordination shell. Three Si shells located at 3.16, 3.88 and 4.29 Å, and containing ~1.0, ~1.5 and ~1.0 atom, respectively, provide a satisfactory fit to next-nearest EXAFS contributions. The short Eu – Si distance of 3.16 Å suggests Eu binding to the edges of Si tetrahedra.

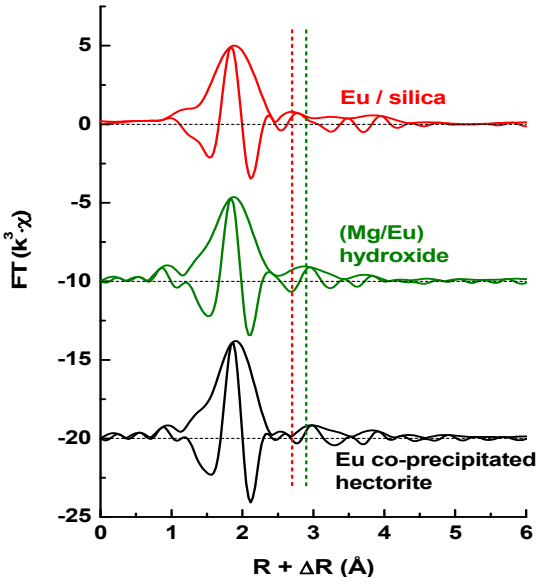

Figure 3: *Fourier transform (FT) magnitude and imaginary part for Eu(III)-containing samples.*

The modelling of the data for the (Mg/Eu) hydroxide indicates the presence of ~6.5 oxygens at 2.39 Å and ~1.5 Mg at 3.39 Å. A distorted, 6-fold oxygen coordinated octahedral lattice site is strongly suggested, with Eu(III) located off the median plane according to geometrical consideration. The low number of detected backscatterer may be due to local structural disorder. The fit was improved by including a C shell (~1 atom) at 2.99 Å, suggesting the formation of carbonate species.

The modelling of FT peak at R + ΔR

~2 Å for the Eu(III) co-precipitated hectorite yielded ~7 oxygens at 2.42 Å. The next-nearest FT was well modelled with ~3.0 Mg (3.22 Å) and ~1.5 Si (3.37 Å), supporting a clay-related environment for Eu(III). The low number of detected neighbours indicates a locally distorted structure. Again, the fit was improved by including ~1.5 C atom at 3.14 Å, suggesting the formation of carbonate species. The modelling of the P-EXAFS spectra (collected at 10°, 35° and 60°, and extrapolated at 90°) revealed only a small angular effect on the coordination numbers (Finck et al., 2007). The number of neighbour Mg increased slightly from ~3.2 to ~3.8, whereas the number of Si backscatterer was almost unaffected (~1.5 atom). This result strongly indicates a distorted clay-related environment.

Summary and Conclusions

Hectorite was co-precipitated in the presence of Eu(III) as chemical non-radioactive homologue for trivalent actinides. TRLFS data combined with EXAFS results indicate that the probed lanthanide is located in a strained clay-like octahedral environment. The extent of incorporation may be limited, as suggested by the presence of carbonate species. This carbonate species may hypothetically correspond to the dehydrated species detected by TRLFS ((Mg/Eu) hydroxide and hectorite).

This study implements the molecular-level understanding of the *f* element binding mechanism to clay mineral in aqueous systems. The neoformation of clay minerals by reaction of water with minerals opens the possibility of RN structural incorporation by co-precipitation in alteration phases. The thermodynamic stability of this secondary phase needs to be verified.

Acknowledgements

N.F. gratefully acknowledges financial support by the Network of Excellence Actinet. Many thanks to S. Büchner, M. Schmidt and S. Heck for their help. We thank ANKA for the provision of beamtime and S. Mangold for assistance at the XAS beamline. This work was co-financed by the Helmholtz association by supporting the young investigators group “Aufklärung geochemischer Reaktionsmechanismen an der Wasser/Mineralphasen Grenzfläche”.

References

ANKA, 2007. Instrumentation Book, Institute for Synchrotron Radiation, Forschungszentrum Karlsruhe, Germany.

Ankudinov A.L., Ravel B., Rehr J.J., and Conradson S.D., 1998. Real-space multiplescattering calculation and interpretation of X-ray absorption near-edge structure. Phys. Rev. B 58, 7565-7576.

Brandt H., Bosbach D., Panak P., and Fanghänel T., 2007. Structural incorporation of Cm(III) in trioctahedral smectite hectorite: A time-resolved laser fluorescence spectroscopy (TRLFS) study. Geochim. Cosmochim. Acta 71 (1), 145-154.

Brindley G.W., and Kao C.C., 1984. Structural and IR relations among brucite-like divalent metal hydroxides. Phys. Chem. Miner. 10 (4), 187-191.

Carrado K.A., Thiyagarajan P., and Song K., 1997a. A study of organo-clay crystallization. Clay Miner. 32, 29-40.

Carrado K.A., Zajac G.W., Song K., and Brenner J.R., 1997b. Crystal growth of organohectorite clay as revealed by atomic force microscopy. Langmuir 13, 2895-2902.

Carrado K.A., Xu L., Gregory D.M., Song K., Seifert S., and Botto R.E., 2000. Crystallization of a layered silicate clay as monitored by small-angle X-ray scattering and NMR. Chem. Mater. 12, 3052-3059.

Chapman N.A., and Smellie J.A.T., 1986. Introduction and summary of the workshop: natural analogues to the conditions around a final repository for high-level radioactive waste. Chem. Geol. 55, 167-173.

Finck N., Schlegel M.L., and Bosbach D., 2007. Eu(III)/Lu(III) coprecipitation with trioctahedral smectite hectorite, ANKA Annual Report 2007, 153-155.

Finck N., Stumpf T., Walther C., and Bosbach D., 2008. TRLFS characterization of Eu(III)-doped synthetic organo-hectorite. J. Contam. Hydrol. 102, 253-262.

Horrocks W.DeW. Jr., and Sudnick D.R., 1979. Lanthanides ion probes of structure in biology. Laser induced luminescence decay constants provide a direct measure of the number of metal-coordinated water molecules. J. Am. Chem. Soc. 101 (2), 334-340.

Madejovà J., and Komadel P., 2001. Baseline studies of the Clay Minerals Society source clays: infrared methods. Clays Clay Miner. 49 (5), 410-432.

Manceau A., Bonnin D., Kaiser P., and Fretigny C., 1988. Polarized EXAFS of biotite and chlorite. Phys. Chem. Miner. 16, 180-185.

Pieper H., Bosbach D., Panak P.J., Rabung T., and Fanghänel T., 2006. Eu(III) coprecipitation with the trioctahedral clay mineral, hectorite. Clays Clay Miner. 54 (1), 47-55.

Ravel B., and Newville M., 2005a. ATHENA, ARTEMIS, HEPHAESTUS: Data analysis for X-ray absorption spectroscopy using IFEFFIT. J. Synchrotron Rad. 12, 537-5341. Ravel B., and Newville M., 2005b. ATHENA and ARTEMIS: Interactive graphical data analysis using IFEFFIT. Phys. Scripta T115, 1007-1010.

Shannon R.D., 1976. Revised effective ionic radii and systematic studies of interatomic distances in halides and chalcogenides. Acta Cryst. A 32, 751-767.

Supkowski R.M., and Horrocks W.DeW. Jr., 2002. On the determination of water molecules, *q*, coordinated to europium(III) ions in solution from luminescence decay lifetimes. Inorg. Chim. Acta 340, 44-48.

Zwicky H.U., Grambow B., Magrabi C., Aerne E.T., Bradley R., Barnes B., Graber T., Mohos M., and Werme L.O., 1989. Corrosion behaviour of British Magnox waste glass in pure water. Mater. Res. Soc. Symp. Proc. 127, 129-136.

Np(V) REDOX INTERACTION BY ANTHRAQUINONE USED AS A MODEL REDOX COMPOUND FOR HUMIC SUBSTANCES

N.S. Shcherbina [1,2], N.L. Banik[1], C.M. Marquardt[1,*], S.N. Kalmykov[2]

[1] Institut für Nukleare Entsorgung, Forschungszentrum Karlsruhe, Postfach 3640, D-76021 Karlsruhe, Germany, (D),
[2] Department of Chemistry, Lomonosov Moscow State University, 119992, Moscow, Russia, (RUS)

* Corresponding author: marquardt@ine.fzk.de

Abstract

The Np(V) reduction by 9,10-anthrahydroquinone-2,6-disulfonate (AH_2DS) was studied. Various amounts of AH_2DS were formed by redox titration of anthraquinone (AQDS) with sodium dithionite at pH 7 and 11, resulting in rather low redox potentials between –0.1 and –0.57 V. Strong dependence of Np(V) reduction kinetics from redox potential was demonstrated: no reduction at +0.4 V, slow and incomplete reduction in the system with Eh –0.17 V at concentration ratio of AH_2DS to Np(V) of 0.55 and complete reduction within 6 days at Eh in the range from –0.18 to –0.21 V at AH_2DS to Np(V) concentration ratios of 1.3 and 2.88. However, the results indicate a time-limiting step in the reaction mechanism between Np(V) and AH_2DS.

Introduction

Humic substances (HS) significantly affect redox sensitive actinides (e.g. U, Np and Pu) speciation, and therefore migration in aquifer systems [1]. Osterberg and Shirshova [2] reported the value for the HS apparent redox potential of +0.528 V at zero pH that decreases to +0.234 V at pH 7. Thus, the reduction of Np(V) is from thermodynamical aspects difficult, although Np(V) reduction was observed in experiments in presence of HS [1]. It is assumed that hydroquinone/quinone moieties are important electron-donating/accepting groups and can be responsible for the redox properties of HS [3]. Previous experiments showed that an increase of hydroquinone moieties in humic derivatives magnifies the reducing capacity of HS [4]. The main findings were consistent with quinone moieties as the dominant electron acceptors. It was demonstrated that the reduction rate of Np(V) by HS with enhanced quinonoid moiety decreases with increasing pH [4]. But this is in contrast with results from [5] for the reduction of Pu(V) by a humic rich groundwater. The reason for such discrepancy is unclear so far and hence, more detailed investigation is needed to elucidate the reaction of Np with quinones as electron-accepting groups in HS. In order to exclude the impact of cation complexation on the value of formal electrode potential of Np(V)/Np(IV)

couple, we have studied the Np(V) reduction by model low molecular weight reductant 9,10-anthrahydroquinone-2,6-disulfonate (AH_2DS), that simulates the reducing entities of humic substances. It was previously showed that electrochemical properties of this model AH_2DS is very similar to that of natural organic matter [3]. Thermodynamic estimations showed that reduction of Np(V) in the presence of AH_2DS is more profitable, than by hydroquinone because of the lower standard electrode potential [6]. The use of AH_2DS is advantageous because both reduced form (AH_2DS) and the oxidized form (AQDS) can be monitored by UV-Vis spectroscopy: their absorption bands lies far away from those for $Np(V)O_2^+$. Therefore collecting of overall spectrum allows getting information about species of interest. At the same time redox potential of the AH_2DS/AQDS system could be reliably measured because of its reversibility and fast redox kinetics.

Experimental

Reagents and solutions

Analytical grade reagents were used to prepare all solutions. Stock solutions of Np(V), 9,10-anthraquinone-2,6-disulfonate (Aldrich) and sodium dithionite (Merck, Darmstadt) were prepared in Milli-Q water in a glove box filled with argon (Ar, <10 ppm of O_2). A stock solution of Np-237 with concentration of $4.7 \cdot 10^{-4}$ M in 0.1 M $HClO_4$ was used in the experiments. 0.1 M NaCl was used in all experiments as background electrolyte.

AQDS reduction

To prepare redox buffer solutions with various Eh values, the AQDS (oxidised form $2 \cdot 10^{-3}$ M) was reduced to AH_2DS using various amounts of sodium dithionite (for details see Table 1). The redox potentials of the AH_2DS/AQDS solutions were measured within 15-20 minutes using a Metrohm single chain Pt-Ag/AgCl electrode normalized versus SHE. Speciation of AQDS-AH_2DS system was checked by spectrophotometry in the wavelength interval from 250 nm to 500 nm. Concentrations of AQDS was monitored by the absorption band at 328 nm with a molar extinction coefficient of 5245 $M^{-1} \cdot cm^{-1}$at pH 9-11 which is rather close to those reported in [7] (4600 $M^{-1} \cdot cm^{-1}$), [8] (5800 $M^{-1} \cdot cm^{-1}$) and [9] (5200 $M^{-1} \cdot cm^{-1}$). Quantification of reduced species AH_2DS was performed by measuring the absorption at 386 nm and using extinction coefficient of 6700 $M^{-1} \cdot cm^{-1}$ from [9].

Np(V) reduction by AH_2DS/AQDS

Aliquots of the Np(V) stock solution were mixed with anthraquinone solution with various AH_2DS/AQDS ratios corresponding to various Eh values. The total concentrations of anthraquinone and Np(V) in the solution were $2 \cdot 10^{-4}$ M, and $5 \cdot 10^{-5}$ M, respectively. The redox potential of the solutions was measured after certain reaction times (0, 2, 7, and 13 d). Changes of the Np speciation were monitored by NIR spectrophotometry using Cary-5E (Varian). Concentration of Np(V) was measured by tracing of peak intensity at 981 nm using molar extinction coefficient of 395 $M^{-1} \cdot cm^{-1}$ [10].

Results and Discussion

Potentiometric titration of AQDS

The data for reduction of AQDS by potentiometric titration with sodium dithionite are summarised in Table 1. Titration of AQDS was performed at high pH values because $Na_2S_2O_4$ is rather unstable in neutral and acidic pH range, but at pH 9-11 it can be stored for a relatively long period [11,12]. The values of redox potential of AH_2DS/AQDS systems at pH 11 did not change over more than two weeks denoting that the system is stable. Afterwards, solutions of AH_2DS/AQDS with pH 11 were diluted by the factor of 10 in $1 \cdot 10^{-3}$ M PIPES buffer to obtain the solutions with pH 7. At this pH no changes in redox potential over time under the Ar atmosphere was established. As already mentioned, the redox potential of the solution decreases with increasing of AH_2DS/AQDS ratio (Tab. 1) that correlates with the decrease in the absorption at 328 nm for the AQDS (Fig. 1).

***Table 1**: Potentiometric titration data for AH_2DS/AQDS system*

$C_{0AQDS} \cdot 10^{-4}$, M	$C_{0Na2S2O4}, \cdot 10^{-4}$, M	pH_0	Eh_0, mV (vs. SHE)	$C(AH_2DS)$, M
2.00	0.00	7.0	401	0
1.95	0.49	7.0	-73	$5.30 \cdot 10^{-6}$
1.92	0.80	7.0	-132	$1.19 \cdot 10^{-5}$
1.92	0.80	7.27	-166	$2.73 \cdot 10^{-5}$
1.89	1.10	7.0	-139	$1.45 \cdot 10^{-5}$
1.86	1.40	7.0	-151	$2.07 \cdot 10^{-5}$
1.82	1.82	7.0	-162	$2.74 \cdot 10^{-5}$
1.82	1.82	7.25	-182	$6.29 \cdot 10^{-5}$
1.76	2.35	7.0	-172	$4.08 \cdot 10^{-5}$
1.74	2,61	7.26	-211	$1.44 \cdot 10^{-4}$
1.71	2.86	6.9	-188	$8.09 \cdot 10^{-5}$
1.60	4.00	7.0	-383	$1.76 \cdot 10^{-4}$
1.50	5.00	7.0	-403	$2.00 \cdot 10^{-4}$*
1.50	5.00	7.26	-428	$2.00 \cdot 10^{-4}$*

*Non-consumed dithionite is present in solution. The absorption spectra of dithionite (250-360 nm) superposes the spectra of AQDS/AH_2DS, that makes calculation of AQDS and AH_2DS equilibrium concentration difficult.

After addition of $Na_2S_2O_4$, absorption bands at 386, 403, and 446 nm appear in the spectra (Fig. 1), which were attributed to absorption of different forms of reduced AH_2DS. Intensity of these peaks changes with pH, indicating either different stability or protonation – deprotonation of involved species. Kelsall and Thompson [7] reported that reduction of AQDS could form several species including radicals. Stability of these species is strongly affected by pH (it can be stabilized at pH > 9) and oxygen content. According to [7, 9] one could conclude that the absorption maxima in Fig. 1 are

attributed to absorption of the following species: AQDS (328 nm) with molar extinction coefficients of $5.2 \cdot 10^3$ $L \cdot mol^{-1} \cdot cm^{-1}$ and the reduced species AH_2DS (386 nm) with molar extinction coefficients of $6.7 \cdot 10^3$ $L \cdot mol^{-1} \cdot cm^{-1}$ (taken from [9]). Actually, both species have fully deprotonated sulphonic acid groups and possess a charge of –2, which is omitted in the following. These molar extinction coefficients were used to calculate the concentration of each form. In Table 1 the redox potentials and the content of reduced species formed under given conditions are summarized.

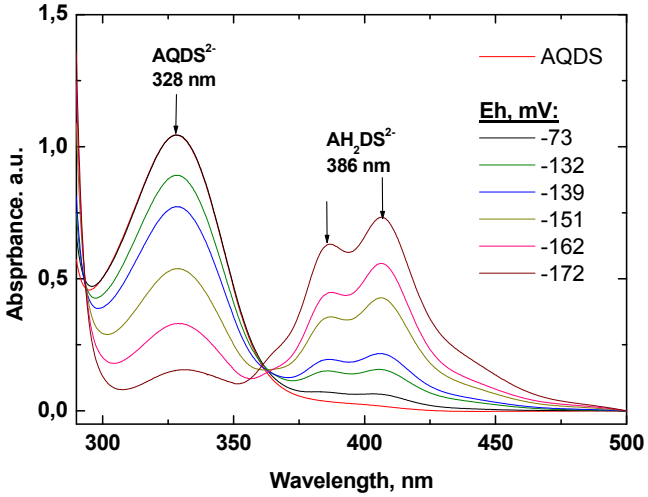

Figure. 1: *Spectra of AQDS being titrated by $Na_2S_2O_4$ in $1 \cdot 10^{-3}$ M PIPES buffer (pH ≈ 7) in 0.1 M NaCl.*

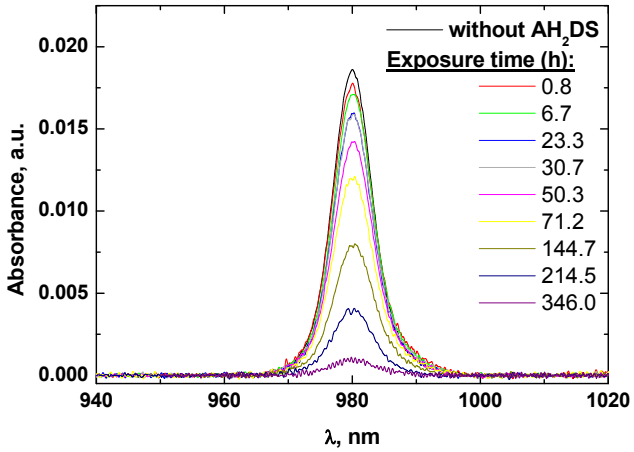

Figure 2 *Reduction kinetics of Np(V) measured by NIR absorption spectrometry; Eh -182 mV, $C(Np)_{tot} = 5 \cdot 10^{-5}$ M, $[AQDS]_{tot} = 2 \cdot 10^{-4}$ M, pH = 7.25.*

Np(V) reduction by AH_2DS/AQDS

The Np(V) reduction was studied in four solutions with different AH_2DS content, in AQDS solution (oxidized form only) and $Na_2S_2O_4$ solution. As it is presented in Fig. 2, the neptunium spectra consist of one narrow peak at 980 nm, which corresponds to the aquo ion NpO_2^+. The spectra do not show any other bands of Np(V), indicating either absence or extremely low Np(V) complexation with anthrahydroquinone or dithionite. With increasing reaction time the absorption decreases as a result of Np(V) reduction to Np(IV). At pH 7.25 the tetravalent Np

occurs mainly as amorphous NpO_2, colloidal NpO_2, or both, which settled down on the bottom of the cuvettes.

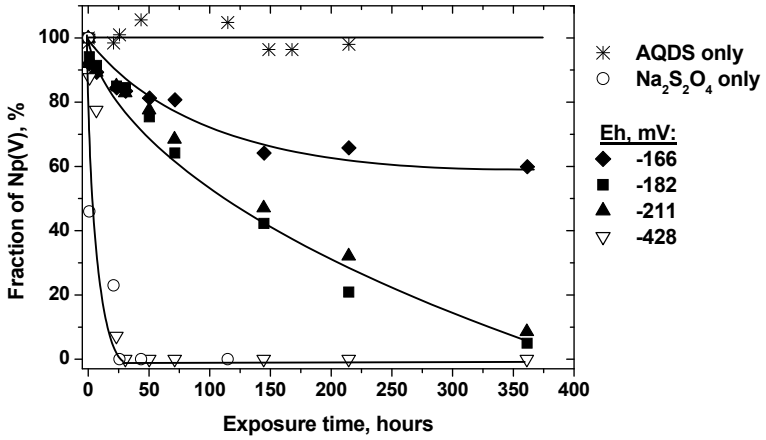

Figure 3: *Np(V) Reduction in AH_2DS/AQDS system at different values of redox potential in 0.1 M NaCl solution; $C_{tot}(Np) = 5 \cdot 10^{-5}$ M, $C_{tot}(AQDS) = 2 \cdot 10^{-4}$ M, pH 7.25.*

The rates of Np(V) reduction at constant C(Np(V)) depends on the concentration of AH_2DS, which is reflected by the Eh value in solution (Fig. 3). Anthraquinone AQDS does not reduce Np(V) during whole exposure time because the redox potential Eh = 400 mV of the solution is too high for Np(V) reduction. In the solution with Eh = -166 mV the Np(V) is only partially reduced until the major amount of $C(AH_2DS) = 2.73 \cdot 10^{-5}$ M, that is 55% of $C(Np)_{tot}$, is consumed. The system reaches a quasi-equilibrium when about 40% of $C(Np)_{tot}$ is reduced. In the systems with Eh = -182 mV and Eh = -211 mV Np(V) is reduced quantitatively within ~15 days. In these solutions the $C(AH_2DS)$ exceeds the C(Np(V)) by a factor of 1.3 and 2.9, respectively. However, the reduction rates keep constant, although the Eh value continues to decrease. This is a hint at a rate limited reaction of Np(V) with AH_2DS. Both rate curves can be plotted by $ln(C_o/C_t)$ vs. t (not shown) representing a pseudo-first order reaction with respect to Np(V). In the solution with unconsumed $Na_2S_2O_4$ (Eh = -428 mV), the highest reduction rate is observed that is similar to the rate for reduction by pure dithionite without AH_2DS. Here, the reduction reaction is controlled by dithionite and however, the reaction mechanism changes and is not anymore rate limited. Additionally, a linear fit is not possible for these data.

Summary and Conclusions

Spectroscopic studies and redox titration of 9,10-anthraquinone-2,6-disulfonate with $Na_2S_2O_4$ demonstrates that different species are present at pH 7 and 11 in AH_2DS/AQDS system. This work showed clearly, that in the absence of complexing agents anthrahydroquinones (AH_2DS) reduces Np(V) to Np(IV) at negative redox potentials. The larger $C(AH_2DS)$ is the faster is the rate of Np(V) reduction, until a rate-limiting step is reached. In future activities thermodynamic calculations should show whether the reduction obeys equilibrium thermodynamics, and whether radical species play a role.

Acknowledgement

This work was supported by FUNMIG and a DAAD fellowship.

References

[1] Artinger, R., Marquardt, C.M., Kim, J.I., Seibert, A., Trautmann, N., Kratz, J.V. (2000): Humic Colloid-Borne Np Migration: Influence of the Oxidation State. Radiochim. Acta, **88**, 609-612

[2] Osterberg, R., Shirshova, L. (1997): Oscillating, nonequilibrium properties of Humic Acids. Geochim. Cosmochim. Acta, **61**, 4599-4604

[3] Nurmi, T.J., Tratnyek, P.G. (2002) Electrochemical Properties of Natural Organic Matter (NOM), Fractions of NOM, and Model Biogeochemical Electron Shuttles. Envir. Sci. Technol., **36 (4)**, 617-624

[4] Shcherbina, N.S., Perminova, I.V., Kalmykov, S.N., Kovalenko, A.N., Haire, R.G., Novikov, A.P. (2007): Redox and Complexation interaction of Np(V) with Quinonoid-Enriched Humic Derivatives. Envir. Sci. Technol., **41 (20)**, 7010-7015

[5] Marquardt, C.M., Seibert, A., Artinger, R., Denecke, M.A., Kuczewski, B., Schild, D., Fanghaenel, Th. (2004): The Redox Behaviour of Plutonium in Humic Rich Groundwater. Radiochim. Acta, **92**, 617-623

[6] Burgos, W.D., Yilin Fang, Royer, R.A., Yeh, G.T., Stone, J.J., Jeon, B.H., Dempsey, B.A. (2003): Reduction-based Modelling of Quinone-Mediated Bacterial Iron(III) Reduction. Geochim. Cosmochim. Acta., **67**, N. 15, 2735-2748

[7] Kelsall, G.H., Thompson, I. (1993): Redox Chemistry of H_2S Oxidation by the British Gas Stretford Process. Part III: Electrochemical Behaviour of Anthraquinone 2,7 Disulfonate in Alkaline Electrolytes. Journal of Applied Electrochemistry, **23**, 296-307

[8] Gamage, R.S.K.A., McQuillan, A. J., Peake, B.M.. (1991): Ultraviolet-Visible and Electron Paramagnetic Resonance Spectroelectrochemical Studies of the Reduction Products of some Anthraquinone Sulphonates in Aqueous Solutions. J. Chem. Soc. Faraday Trans., **87(22)**, 3653-3660

[9] Liu, C., Zachara, J.M., Foster-Mills, N.S., Strickland, F. (2007): Kinetics of Reductive Dissolution of Hematite by Bioreduced Antraquinone-2,6-disulfonate. Envir. Sci. Technol., **41**, 7730-7735

[10] Marquardt, C.M., Kim, J.I. (1998): Complexation of Np(V) with Humic Acid: Intercomparison Results from Different Laboratories. Radiochim. Acta. **80**, 129-137

[11] Kovacs, K.M., Rabai, G. (2002): Mechanisms of the Oscillatory Decomposition of the Dithionite ion in a Flow Reactor. Chem. Comm., 790-791

[12] Kelsall, G.H., Thompson, I. (1993): Redox Chemistry of H_2S Oxidation by the British Gas Stretford Process. Part I: Thermodynamics of sulphur-water systems at 298K. **23**, 279-286

INTERPRETATION OF A LABORATORY MOCK-UP EXPERIMENT OF THE BENTONITE/GRANITE INTERFACE WITH A NUMERICAL MODEL

Javier Samper[1], Qinchung. Yang[1], Shuping Yi[1], Miguel García-Gutiérrez[2], Tiziana Missana[2], and Manuel Mingarro[2]

1. Escuela Técnica Superior de Ingenieros de Caminos, Canales y Puertos. Universidad de A Coruña, Campus de Elviña, 15192, Spain
2. CIEMAT, Departamento de Medio Ambiente, Av. Complutense 22, 28040 Madrid, Spain

*Corresponding author: jsamper@udc.es

Abstract

Performance assessment of a deep geological repository requires understanding diffusion and determining diffusion parameters under real conditions because diffusion is a key transport mechanism in hosting geological formation. FEBEX (Full-scale Engineered Barrier EXperiment) is a demonstration and research project dealing with the bentonite engineered barrier designed for sealing and containment of the high-level radioactive waste repository. To support field investigations of FEBEX *in situ* test, a large–scale laboratory mock-up experiment (MUE) is being performed at CIEMAT facilities to study tracer migration at the bentonite/granite interface. Numerical models of MUE are presented here for HTO, $^{36}Cl^-$ and $^{137}Cs^+$. Experiments are modeled with 2-D axi-symmetric finite element grids and are solved with CORE^{2D} V4. Model results indicate that numerical solutions with reference parameters reproduce measured data for HTO and $^{36}Cl^-$ but show large discrepancies for $^{137}Cs^+$. Relevant diffusion and retention parameters are identified by sensitivity analysis for tracer concentrations in borehole, bentonite and granite, respectively. Interpretation of $^{137}Cs^+$ data measured in the tracer chamber is perfomed by taking into account the uncertainties in initial activity C_0 and initial time t_0. Optimum values of C_0 and t_0 are obtained. The best fit is obtained with $D_{e\text{-filter}}$ equal to $2.03 \cdot 10^{-10}$ m^2/s and $K_{d\text{-bentonite}}$ equal to 5 $m^3 \cdot Kg^{-1}$.

Key words: mock-up experiment, bentonite/granite interface, diffusion, numerical model, sensitivity analysis, tritium, $^{36}Cl^-$, cesium.

Introduction

A large–scale laboratory mock-up experiment is carried out by CIEMAT to provide laboratory support for the field investigations at the FEBEX *in situ* test gallery.

This experiment aims at studying the mass transfer from the bentonite to granite and identifying the relevant transport parameters for critical radionuclides. Scoping calculations for the design of the experiment were reported by Samper *et al.* (2006a) and Samper *et al.* (2007). The main objective of this contribution is to present the available data for the laboratory mock-up experiment and the numerical model of the experiment. This model provides quantitative information on mass transfer mechanisms and parameters at the bentonite/granite interface of a repository in granite.

Mock-up laboratory experiment

Cylindrical rock blocks were obtained from the FEBEX gallery (Figure 1) near the location of heater 1 which was dismantled in 2002. Two of such blocks (RB0-1 and RB15-1) are from granite region whereas the third one (RB27-2) was taken from the lamprophyre area. The mock-up experiment is performed on block RB0-1 (see Figure 1) which has a diameter of 38.8 cm and is from 30 to 40 cm high.

Tracer migration at the bentonite/granite interface is mimicked by placing a small cylindrical plug of compacted FEBEX bentonite at the centre of the granite block. After installing the sampling system, the whole block is immersed in a bath with groundwater to maintain water hydration. A series of small boreholes were drilled for water sampling and monitoring tracer migration.

Tracers were injected in a column filter placed in the centre of the bentonite cylinder. The tracer injection zone will be denoted here as the tracer section. Tracers include: HTO (conservative), $^{36}Cl^-$ (conservative, but suffering from anion exclusion) and $^{137}Cs^+$ (sorbing).

Sixteen monitoring boreholes of 16 mm of diameter were drilled along block radii at different angles and elevations. This set of boreholes allows for a 3D monitoring of tracer migration. The scheme of the test with the location of monitoring boreholes drilled in the granite block is shown in Figure 2.

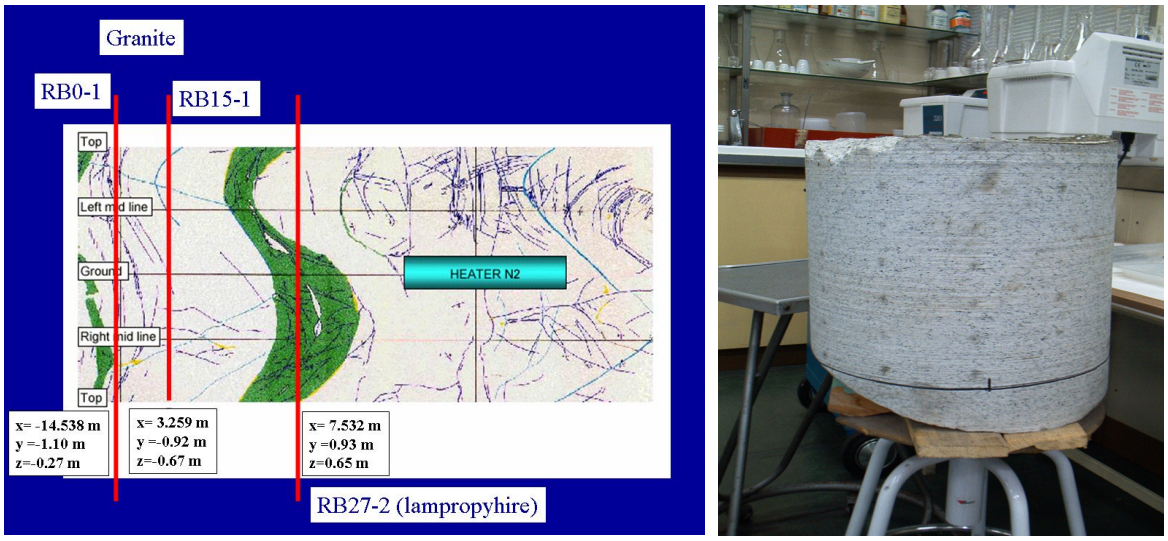

Figure 1. *FEBEX gallery with location of rock samples (left) and block RB0-1 used for the mock-up experiment (right).*

Numerical model

Mock-up experiment has been simulated with CORE2D V4 (Samper *et al.,* 2003) a 2-D finite element multicomponent reactive transport code which accounts for a wide range of chemical reactions that has been widely used to model laboratory and in situ experiments including the CERBERUS Experiment in Boom clay (Zhang *et al.*, 2008), interpret the Redox Zone Experiment in a fracture zone of the Äspö site (Molinero and Samper, 2006), model inverse reactive transport (Dai and Samper, 2006), evaluate the long-term geochemical evolution of radioactive waste repositories in clay (Yang *et al.,* 2008) and granite (Yang *et al.,* 2007) and model the transport of corrosion products and their geochemical interactions with bentonite (Samper *et al.*, 2008).

Given the symmetry with respect to sample axis, numerical calculations of MUE are performed with a 2-D axi-symmetric anisotropic model which considers four material zones: 1) Tracer section where tracers are injected, 2) Filter, 3) Bentonite and 4) Granite (Figure 3). Experiments have been modelled using an approach similar to that used for modelling diffusion experiments in Opalinus clay (Samper *et al.,* 2006b).

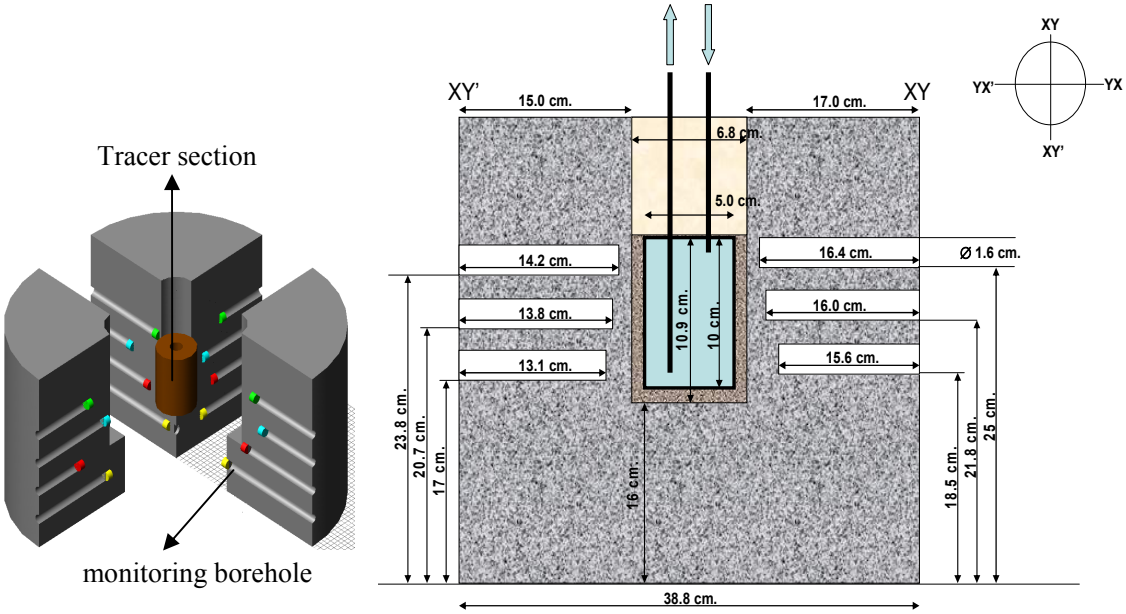

Figure 2. *Scheme of the mock-p experiment (left) with indication of the geometry and monitoring boreholes (right).*

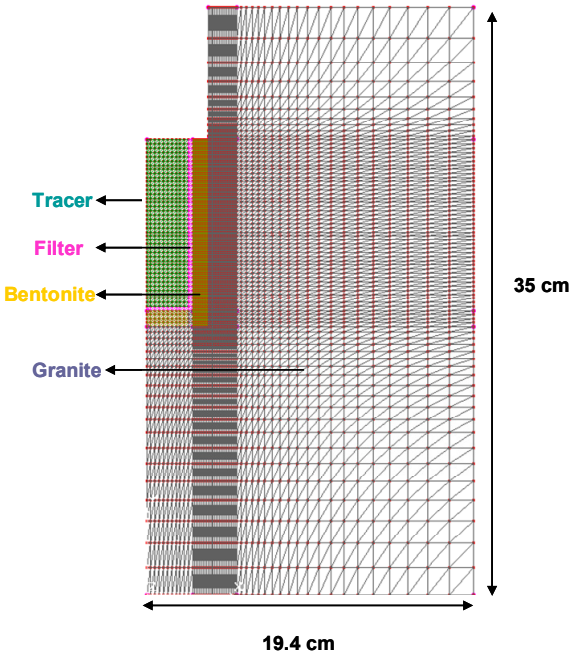

Figure 3. *2D finite element grid used for the numerical model of the mock-p experiment.*

Bentonite parameters adopted for scoping calculations were derived from previous CIEMAT experiments on FEBEX bentonite (García-Gutiérrez *et al.,* 2005) while those of granite were taken from CIEMAT experiments on granite columns (García-Gutiérrez, 2000). They are listed in Table 1. Initial tracer activities are equal to zero everywhere except in the borehole where activities per unit volume of water were prescribed according to known total tracer activities. The borehole containing the tracer does not represent a constant-concentration boundary condition, but a fixed initial-mass boundary condition. A no-flow condition is used in all model boundaries because tracers cannot leave the granite block.

Table 1. *Reference transport parameters of HTO, $^{36}Cl^-$ and $^{137}Cs^+$ for bentonite (B), granite (G) and filter (F) used for scoping calculations (porosity of filter from García-Gutiérrez, personal communication. D_e of filter is computed from those in bentonite with Archie´s law and an exponent of 1.33).*

	Porosity			K_d (m^3/kg)		D_e (m^2/s)		
Tracer	B	G	F	B	G	B	G	F
HTO	0.57	0.01	0.5	0.00	0.00	$5.8\cdot10^{-11}$	$1.5\cdot10^{-13}$	$4.87\cdot10^{-11}$
$^{36}Cl^-$	0.05	0.005	0.5	0.00	0.00	$9.3\cdot10^{-13}$	$2.3\cdot10^{-14}$	$7.81\cdot10^{-13}$
$^{137}Cs^+$	0.57	0.01	0.5	1	0.225	$8.03\cdot10^{-10}$	$6.0\cdot10^{-13}$	$6.76\cdot10^{-10}$

Note: B=Bentonite, G=Granite, F=Filter

Testing the numerical model with available data

Tracer data at present are available only at the tracer section. Tracers have not yet been detected at any of the 16 boreholes. Measured tracer concentrations at the tracer section are shown in Figure 4. Measured HTO data show a lot of scatter. $^{36}Cl^-$

data remains constant and does not show major changes. It can be seen that HTO and Cl data remain almost constant during the first 150 days of the test. Chloride is an anion suffering anion exclusion and its concentration after 1 year is 98.79% of its initial value while neutral HTO decreased to 97.82 %. $^{137}Cs^{+}$ did disappear after 80 days because this tracer undergoes sorption.

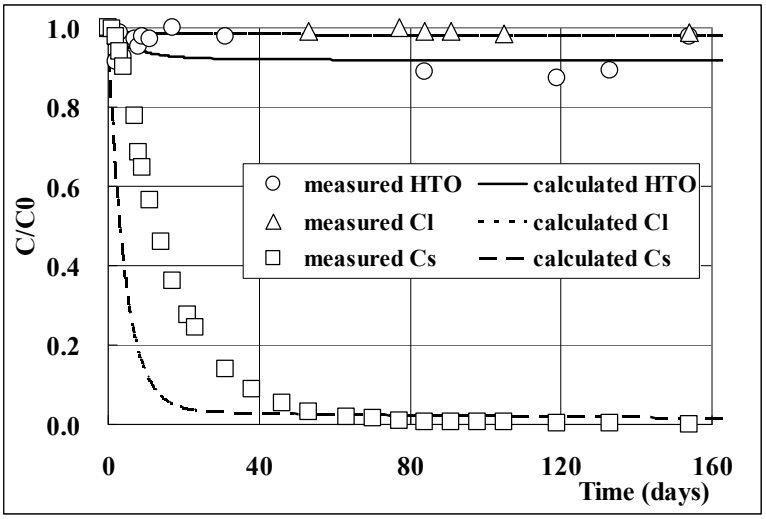

Figure 4. *Time evolution of normalized tracer concentrations in tracer section, measured (symbols) and computed (lines).*

Sensitivity runs were performed by changing one-at-a-time the relevant parameters for $^{137}Cs^{+}$. Computed concentrations of $^{137}Cs^{+}$ in the tracer section are clearly sensitive to the effective diffusion coefficient of the filter (Figure 5) and slightly sensitive to the distribution coefficient of bentonite (Figure 6). They, however, lack sensitivity to the distribution coefficient and effective diffusion coefficient of granite (figures not shown here).

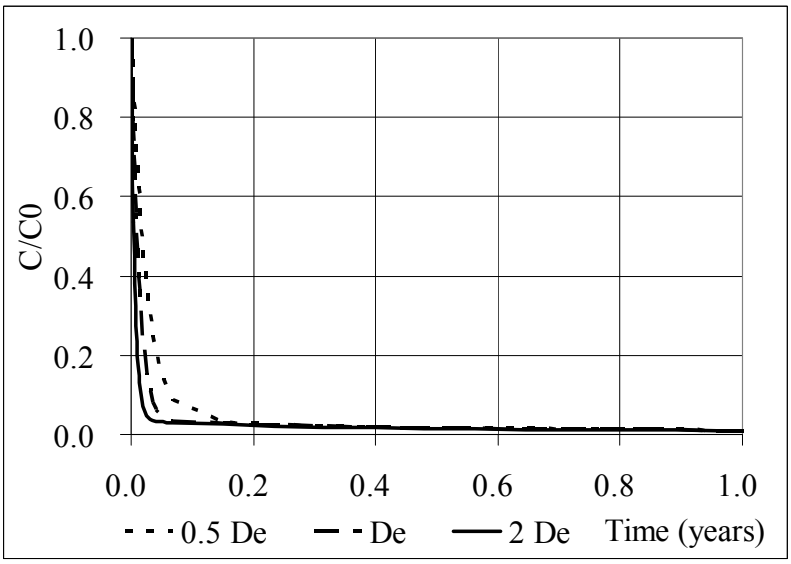

Figure 5. *Sensitivity of $^{137}Cs^{+}$ concentration in the tracer section to changes in effective diffusion coefficient of filter.*

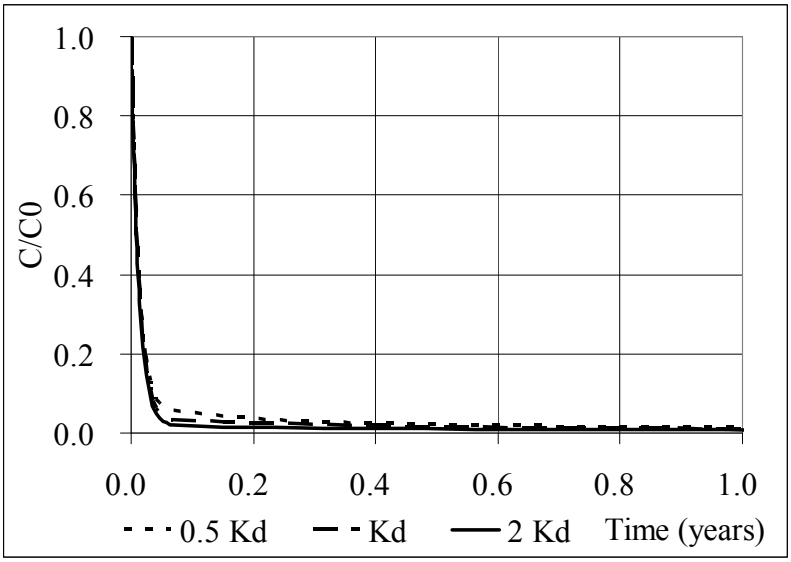

Figure 6. *Sensitivity of $^{137}Cs^{+}$ concentration in the tracer section to changes in distribution coefficient of bentonite.*

Based on the results of sensitivity analyses, measured $^{137}Cs^{+}$ data in the tracer section were fitted by adjusting the effective diffusion of the filter, $D_{e\text{-filter}}$, and the K_d of the bentonite, $K_{d\text{-bentonite}}$ and by taking into account of the uncertainties in the values of initial tracer activity, C_0, and the value of t_0, the time at which tracer injection started. Model results indicate that the optimum C_0 is equal to 19000 cpm/mL while the measured $^{137}Cs^{+}$ raw data is 18752.05 cpm/mL. The optimum value of t_0 is equal to the initial given time minus 2 days. This difference is interpreted as the lag time between tracer injection and the effective mixing of the tracer in the circulation system. A perfect fit is obtained for $^{137}Cs^{+}$ data with $D_{e\text{-filter}}$ of $2.03 \cdot 10^{-10}$ m^2/s (0.3 times its reference value) and $K_{d\text{-bentonite}}$ of 5 $m^3 \cdot Kg^{-1}$ (5 times larger than its reference value). Figure 7 illustrates the comparison between model results and measured data. Also shown for comparison purposes is the reference solution. It should be noticed that $^{137}Cs^{+}$ data in injection system provide information only about filter and bentonite parameters but not on granite parameters.

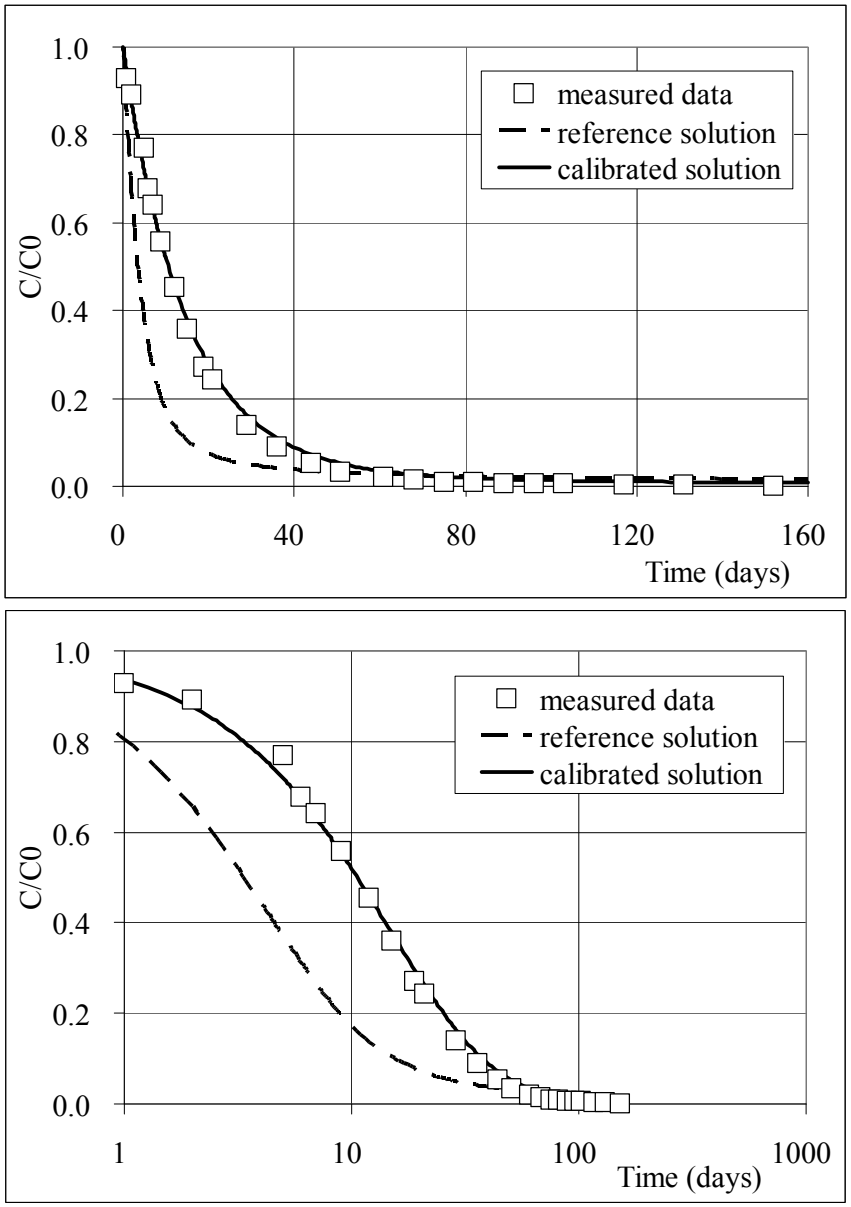

Figure 7. *Comparison of measured (symbols) and computed (lines) $^{137}Cs^{+}$ normalized concentrations with reference and calibrated parameters.*

Conclusions

A 2-D axi-symmetric model has been used to analyze tracer diffusion across the bentonite/granite interface. Numerical solutions of HTO and $^{36}Cl^{-}$ reproduce the measured data with reference parameters. Results of sensitivity analysis show that normalized $^{137}Cs^{+}$ concentrations in the tracer section are very sensitive to the effective diffusion of the filter and slightly sensitive to the distribution coefficient of the bentonite, but lack sensitivity to the parameters of granite, indicating the uncertainties in granite parameters do not affect the estimation of filter and bentonite parameters.

There are some uncertainties in filter properties which affect significantly the dilution of $^{137}Cs^{+}$ in the tracer section. Interpretation of $^{137}Cs^{+}$ data in the tracer section shows that this tracer is controlled mostly by the effective diffusion of filter and the distribution coefficient of bentonite. The best fit is obtained with $D_{e\text{-filter}} = 2.03 \cdot 10^{-10}$ m^2/s and $K_{d\text{-bentonite}} = 5\ m^3 \cdot Kg^{-1}$. $^{137}Cs^{+}$ data in the injection system provide information only about filter and bentonite parameters but not on granite.

Acknowledgements

This work has been funded by ENRESA and EU within FUNMIG (FUNdamental Processes of radionuclide MIGration) Project (Ref. FP6-516514). Partial funding for UDC contribution has been obtained also from Spanish Ministry of Science and Technology (CICYT Project CGL2006-09080) and University of La Coruña through a research scholarship awarded to Q. Yang. We thank also the reviewer of this contribution for comments and recommendations which have improved the paper.

References

Dai Z., Samper, J., 2006. Inverse modeling of water flow and multicomponent reactive transport in coastal aquifer systems. J. of Hydrol. Vol. 327, Issues 3-4, 447-461.

García-Gutiérrez, M., 2000. Base de Datos de Sorción, Difusión y Solubilidad para la Evaluación del Comportamiento. Informes Técnicos Ciemat, 96pp.

García-Gutiérrez, M., J.L. Cormenzana, T. Missana, M. Mingarro, J. Molinero, 2005. Overview of laboratory methods employed for obtaining diffusion coefficients in FEBEX compacted bentonite. Journal of Iberian Geology 32 (1): 37-53.

Molinero, J., Samper, J., 2006. Modeling of reactive solute transport in fracture zones of granitic bedrocks. J. Cont. Hydrol., 82, 293–318.

Samper, J., Yang, C., and Montenegro, L., 2003. Users Manual of CORE^{2D} version 4: A COde for groundwater flow and REactive solute transport. Universidad de A Coruña, A Coruña, Spain.

Samper, J., C. Lu, & L. Montenegro, 2008d, Coupled hydrogeochemical calculations of the interactions of corrosion products and bentonite, Physics and Chemistry of the Earth, Vol. 33. Supplement 1, S306-S316. doi:10.1016/j.pce.2008.10.009

Samper, J., Q. Yang, C. Yang, M. García-Gutiérrez, P.L. Martín and T. Missana, 2006a, Decision on the optimisation, design and installation of mock-up experiment, Milestone 4.4.1 of FUNMIG Integrated Project, University of La Coruña, June 2006, 37 pp.

Samper, J., Yang, C., Naves, A., Yllera, A., Hernández, A., Molinero, J., Soler, J.M., Hernán, P., Mayor, J.C. & Astudillo, J. 2006b A fully 3-D anisotropic numerical model of the DI-B *in situ* diffusion experiment in the Opalinus Clay formation. Physics and Chemistry of the Earth 31, 531-540.

Samper, J., Q. Yang , M. García-Gutiérrez, T. Missana, and M. Mingarro, 2007. Scoping calculations for the design of a laboratory mock-up experiment of

bentonite/granite interface. 3rd Annual Workshop Proceedings 6TH EC FP - FUNMIG IP, Edinburgh 26th – 29th November 2007, 8 pp.

Zhang G, J. Samper & L. Montenegro, 2008, Coupled thermo-hydro-bio-geochemical reactive transport model of the CERBERUS heating and radiation experiment in Boom clay, Appl Geochem, Vol 23/4: 932-949.

Yang C, J Samper, J Molinero and M Bonilla, 2007, Modelling geochemical and microbial consumption of dissolved oxygen after backfilling a high level radioactive waste repository, J Cont Hydrol, 93 130–148.

Yang, C., J. Samper, & L. Montenegro, 2008, A coupled non-isothermal reactive transport model for long-term geochemical evolution of a HLW repository in clay, Environmental Geology, 53:1627–1638. DOI 10.1007/s00254-007-0770-2.

SORPTION OF Cm(III) AND Gd(III) ONTO GIBBSITE, α-$Al(OH)_3$

Nina Huittinen[1*], Thomas Rabung[2], Johannes Lützenkirchen[2], Scott Mitchell[3], Barry Bickmore[4], Jukka Lehto[1], Horst Geckeis[2]

[1] Laboratory of Radiochemistry, University of Helsinki (FIN)
[2] Institut für Nukleare Entsorgung, Forschungszentrum Karlsruhe (GER)
[3] Anadarko Petroleum Corporation (USA)
[4] Department of Geological Sciences, Brigham Young University (USA)

* Corresponding author: nina.huittinen@helsinki.fi

Abstract

The sorption of Gd(III) and Cm(III) onto gibbsite, α-$Al(OH)_3$ is studied by batch experiments and time-resolved laser fluorescence spectroscopy (TRLFS). Experiments are conducted under argon atmosphere to exclude atmospheric CO_2 that may influence the surface and solution speciation in the studied system. Batch experiments are done in two different electrolytes 0.1 M $NaClO_4$ and 0.1 M/0.01 NaCl at a constant mineral concentration of 2.2 g/l. The metal ion concentration is varied between $6.4*10^{-9}$ M and $6.4*10^{-5}$ M. For Gd(III) concentrations up to $6.4*10^{-7}$ M the pH dependent sorption is congruent while a shift of the pH-edge to higher pH values for the two higher Gd(III) concentrations is observed. Spectroscopic investigations are performed with Cm(III) and gibbsite concentrations of $2*10^{-7}$ M and 0.5 g/l respectively. From the emission spectra two different inner-sphere surface complexes can be identified together with a third species appearing in the pH range 6-11. This species is assigned to a coprecipitated or incorporated Cm(III) species forming as a result of applied experimental procedure. Emission bands of the Cm(III) gibbsite surface complexes appear at comparable wavelengths as reported for Cm(III) species bound to aluminum oxides, e.g. sapphire single crystals and γ-Al_2O_3.

Introduction

The final disposal of spent nuclear fuel is considered in deep geological clay- and bedrock formations. Should groundwater penetrate the repository after sealing, a possible release of radionuclides into the geosphere may take place. The migration of these radionuclides is influenced by solid-solute interactions between the metal ions and surrounding mineral surfaces. For a nuclear safety assessment it is thus important to understand the chemistry behind radionuclide reactions at the groundwater-mineral interface, including characterization of the surface species and determination of involved mechanisms.

To date a great number of studies involving metal ion sorption on different aluminum oxides/hydroxides have been conducted [1-5]. Pure aluminum oxides/hydroxides are rare in nature, but these minerals contain reactive aluminol groups present on the surfaces of aluminosilicates that are found in vast quantities in natural systems. Furthermore, these aluminum oxides/hydroxides display similar mineralogical structures as iron oxides/hydroxides do and can thus be used as models for these iron containing minerals which cannot be investigated by TRLFS as follows from their fluorescent quenching properties. The aim of this work is to study trivalent metal ion sorption onto a pure aluminum hydroxide, gibbsite that should display stable thermodynamic properties in aqueous environments. Results from previous work by Rabung et al. [6, 7] and Stumpf et al. [8], where the sorption of trivalent actinides onto α- and γ-alumina has been investigated, are compared with the findings of the present study.

Experimental study

Gibbsite synthesis and characterization

For the gibbsite synthesis a 0.33 M aluminum chloride solution was titrated with 1 M NaOH until a pH value of 4.5, at which amorphous aluminum hydroxide was precipitated. The precipitation was carried out in a glove box under argon atmosphere (O_2< 1 ppm) to eliminate possible contamination of atmospheric CO_2. The aluminum hydroxide precipitate was dialyzed against deionized water (MilliQ) at a temperature of 70°C. Water exchange was done every day for the four first weeks, and 2-3 times per week for a total time span of 4 months. The pH and solid content of the final product were 4.2 and 41.9 ± 1 g/l respectively. Gibbsite particles are shaped as hexagonal platelets, with a large basal plane accounting for the majority of the surface area, and short edge planes, figure 1. The diameter and height of these particles were determined with Atomic Force Microscopy, AFM and an N_2-BET analysis was done to evaluate the specific surface area of the mineral. The mineralogical purity and surface composition was examined with XRD and X-ray photoelectron spectroscopy, XPS respectively.

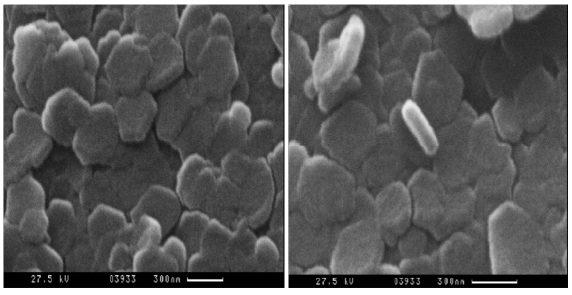

Figure 1: *SEM images of the synthetic gibbsite.*

To determine the isoelectric point, IEP of the mineral, i.e. the pH value at which the net surface charge equals zero, ζ-potential measurements were performed in 0.1/0.01 M $NaClO_4$ and MilliQ water. The gibbsite suspension was diluted in the three different media to a final concentration of 1 g/l. pH adjustments were done from 4.95 to approximately 12 with NaOH.

Batch sorption studies of Gd(III) onto gibbsite

Batch experiments were conducted in a glove box under argon atmosphere (O_2 < 1ppm) to exclude atmospheric CO_2 that influences the solution speciation of trivalent actinides through the formation of carbonate species that may adsorb onto gibbsite. Gd(III) sorption onto gibbsite was investigated as a function of pH in different electrolytes and ionic strengths; 0.1 M $NaClO_4$ and 0.1 M/0.01 M NaCl. The gibbsite concentration was fixed to 2.2 g/l in each batch, while the Gd^{3+} concentration was varied between $6.4*10^{-9}$ M and $6.4*10^{-5}$ M. pH adjustments were done in small steps by addition of CO_2-free NaOH. The sample solutions were shaken periodically for 3-7 days to reach sorption equilibrium. After the equilibration time the samples were centrifuged at 18 000 rpm and the aluminum and gadolinium contents were analyzed from the supernatant with ICP-MS.

Spectroscopic investigation of Cm(III) sorption onto gibbsite

Samples for TRLFS measurements were prepared under the same conditions as the batch experiments. Two series of three parallel samples were prepared in 0.1 M $NaClO_4$ with gibbsite and curium concentrations of 0.5 g/l and $2*10^{-7}$ M respectively. For one sample series the gibbsite suspension was diluted directly in the electrolyte, "gibbsite suspension". The other series was prepared by using solid gibbsite, (freeze dried gibbsite), re-suspended in the electrolyte, "freeze dried gibbsite I". For comparison experiments were performed with another freeze dried gibbsite (referred to as "freeze dried gibbsite II") previously characterized by Mitchell [9]. Solutions were shaken periodically for 2-3 days to reach sorption equilibrium. For details on the laser setup see e.g. reference 7.

Results

Gibbsite synthesis and characterization

XRD and XPS results indicated a clean, well crystallized synthetic product with minor amounts of chloride on the mineral surface, originating from the use of $AlCl_3$ in the synthesis. The gibbsite particle diameter and height assessed from 25 particles in the AFM survey were 250 ± 60 nm and 16.8 ± 10.4 nm respectively. The specific surface area of the platelets was determined to be 49.5 m^2/g. The pH value 11.1 was obtained for the IEP of gibbsite.

Batch sorption studies of Gd(III) onto gibbsite

Figure 2 presents the $\log K_d$ vs. pH diagram for Gd concentrations ranging from $6.4*10^{-9}$ M to $6.4*10^{-5}$ M in 0.1 M $NaClO_4$. For the lower Gd concentrations uptake starts above pH 5.5 and is complete at around pH 7.5. At metal ion concentrations of $6.4*10^{-6}$ and $6.4*10^{-5}$ M a shift of the pH curve to higher pH values occurs and complete sorption is attained at pH 8.5 instead of 7.5. In the ideal sorption range (linear isotherm) the position of the pH-edge at a given solid concentration is independent of the metal ion concentration as observed in the present study for Gd concentrations up to $6.4*10^{-7}$ M. At higher metal ion concentrations deviations from ideal sorption behaviour cause a shift of the pH edge to higher pH values (relative amount of metal ion uptake no longer unaffected by the total metal ion concentration). Non-ideal behaviour may result

for example from saturation effects or surface binding site heterogeneity [10]. At the highest Gd concentration used in the present study, a saturation of 35 % of the singly coordinated surface hydroxyl sites on the gibbsite edge planes was calculated, using an average value of 8.5 nm^{-2} for the surface site density, and assuming sorption taking place as mono-dentate surface complex formation only at crystal edges. Surface sites would be completely saturated by sorbed metal ions if we suppose tridentate binding of trivalent Gd.

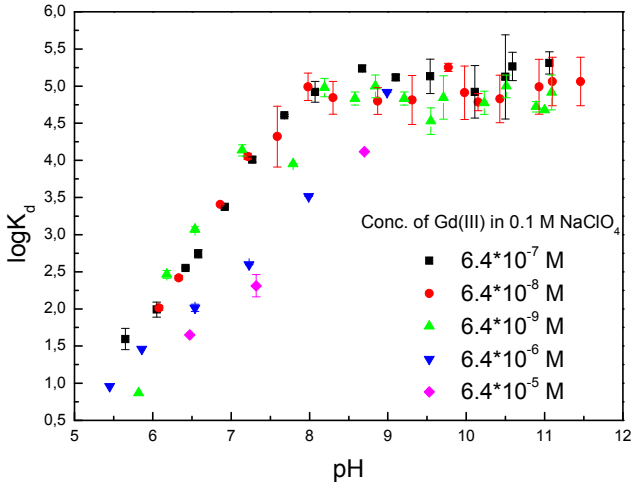

Figure 2: Gd sorption to gibbsite plotted as $logK_d$ vs pH; Gd-concentrations: $6.4*10^{-9}$ M - $6.4*10^{-5}$ M in 0.1 M $NaClO_4$, 2.2 g/l gibbsite.

Spectroscopic investigation of Cm(III) sorption onto gibbsite

Figure 3a-b presents the curium emission spectra of the two gibbsite sample series, "gibbsite suspension" and "freeze-dried gibbsite I", normalized to the highest peak positions.

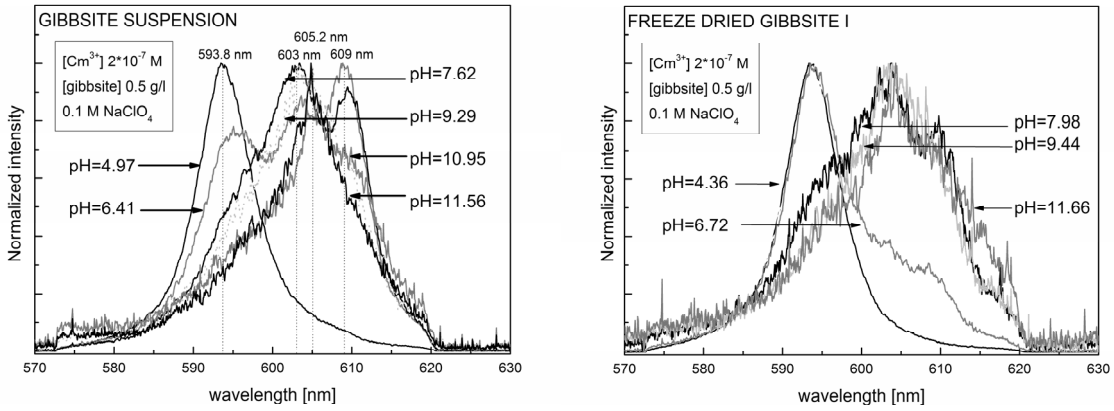

Figure 3: *a) Left - Curium emission spectra of the sample series "gibbsite suspension" b) Right - Curium emission spectra of the sample series "freeze-dried gibbsite I".*

As observed in the previous investigations of curium sorption onto various aluminum oxides by Stumpf et al. [8] and Rabung et al. [6,7] both series of curium emission spectra in the present study show only one emission peak attributed to the unsorbed curium aquo ion with a maximum at 593.8 nm for pH values below 5. The decrease of the curium aqua ion peak as the pH is raised and sorption onto the mineral surface takes place is being accompanied by a red shift of the emission bands to longer wavelengths and the development of new peak maxima at about 603.0 nm and 605.2 nm can be observed. A surprising difference in emission spectra obtained in this study, when compared to previous investigations, is the appearance of a resolved peak at about 609 nm. This peak develops in the pH range from 6 to 11. The contribution of this species increases up to pH 9, decreases when pH is further raised to 11 and disappears at higher pH. The strong red-shift in spectra up to 609 nm and the non-expected pH dependent appearance of this band are distinct indications for the appearance of a Cm-species different from a surface complex. TRLFS suggests the existence of a strong ligand field effect pointing to the occurrence of a coprecipitation or incorporation mechanism. Our experiments were conducted by successively increasing the pH in the gibbsite suspension after Cm addition starting from pH ~ 4. By continuously increasing the pH we move from high to low gibbsite solubility domains. As a result, aluminum hydroxide precipitates from oversaturated solutions, either covering already adsorbed curium or forming a $Al/Cm(OH)_3$ coprecipitate. When Al solubility increases at alkaline pH, newly formed $Al(OH)_3$ redissolves and only surface complexed Cm can be detected. The possibility of curium incorporation was studied using a gibbsite sample provided by Mitchell [9] "freeze dried gibbsite II" that had not shown a distinct peak at 609 nm in previous experiments. The sample was allowed to age in suspension with a Cm(III) concentration of $2*10^{-7}$ M for 15 days at pH 6.8. After this period of time, the sample was measured again. No peak at 609 nm could be observed in the emission spectrum. Al ions at a concentration of 10^{-4} M were added to the suspension to exceed the solubility limit of aluminum hydroxide, and the emission spectrum was recorded 0-4 days after Al addition. One day after the addition, a peak close to 609 nm developed and even increased with time up to 4 days, figure 4. This finding supports the hypothesis of Cm interaction with Al related to oversaturation of gibbsite and thus potential incorporation at the aluminum hydroxide surface and explains the unexpected spectral evolution with pH.

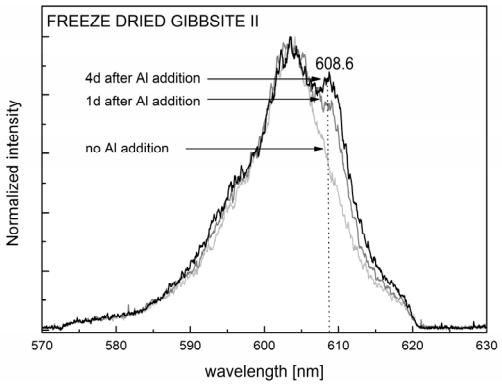

Figure 4: *Curium emission spectra of the "freeze-dried gibbsite II" sample after addition of 10^{-4} M aluminum.*

Summary and Conclusions

The results of the present study reveal two modes of Cm interaction with gibbsite: Inner-sphere surface complexation and incorporation into the solid matrix. TRLFS parameters obtained for the inner-sphere surface complexes are comparable to what has been obtained for Cm sorbed to various sapphire surface planes ((012), (110), (018), and (104)) [6]. The identification of an incorporated Cm species as a consequence of pH variations in our experiment might be considered as an experimental artifact in a first instance. It is, however, a clear proof, that mineral surfaces cannot be considered as 'inert' with regard to chemical variations as done in many studies. In forthcoming experiments we will prepare a gibbsite batch stored at around pH=7, i.e. at the solubility minimum of gibbsite. Sorption measurements will then be performed starting from the gibbsite solubility minimum by varying the pH to the acidic range and to the alkaline range. By this procedure, precipitation of $Al(OH)_3$ solid should be avoided and thus also Cm incorporation.

Acknowledgement

We thank A. Bauer, D. Schild, M. Plaschke for XRD, XPS and AFM measurements, respectively, and F.W. Geyer, C. Walschburger and A. Kaufmann for ICP-MS analysis. We are grateful for financial support for N. Huittinen from the European Commission via the *European Region Action Scheme for the Mobility of University Students* - Erasmus. The present work was done in the context of two programs financed by the European Commission; ACTINET and FUNMIG (FP6-516514), and a grant to B.R. Bickmore by the U.S. National Science Foundation (grant EAR-0525340).

References

[1] O. Tochiyama, H. Yamazaki, N. Li, J. Nucl. Sci. Technol. 33 (1996) 846-851.

[2] Sh. Yu, X. Li, A. Ren, D. Shao, Ch. Chen, X. Wang, J. Radioanal. Nucl. Chem. 268 (2006) 387-392.

[3] H.X. Zhang, Z. Dong, Z.Y. Tao, Colloids Surf., A 278 (2006) 46-52.

[4] D. Xu, Q.L. Ning, X. Zhou, C.L. Chen, X.L. Tan, A.D. Wu, X. Wang, J. Radioanal. Nucl. Chem. 266 (2005) 419-424.

[5] N. Baumann, V. Brendler, T. Arnold, G. Geipel, G. Bernhard, J. Colloid Interface Sci. 290 (2005) 318–324.

[6] Th. Rabung, D. Schild, H. Geckeis, R. Klenze, Th. Fanghanel, J. Phys. Chem. B 108 (2004) 17160-17165.

[7] Th. Rabung, H. Geckeis, X.K. Wang, J. Rothe, M.A. Denecke, R. Klenze, Th. Fanghänel, Radiochim. Acta. 94 (2006) 609-618.

[8] T. Stumpf, Th. Rabung, R. Klenze, H. Geckeis, J.I. Kim, J. Colloid Interface Sci. 238 (2001).

[9] S.C. Mitchell, Brigham Young University (2005).

[10] P.W. Schindler, W. Stumm: Aquatic Surface Chemistry, Wiley-Interscience, New York, 1987, 83–107.

SORPTION ON BIOTITE

Markus Olin[1*#], Esa Puukko[2], Eini Puhakka[1], Martti Hakanen[2], Antero Lindberg[3], Jarmo Lehikoinen[1$]

[1]VTT Technical Research Centre of Finland (FI)
[2]University of Helsinki (FI)
[3]Geological Survey of Finland (FI)
Present address: [#]Science consulting cheq&diff (FI), [$]B+Tech Oy (FI)

* Corresponding author: markus.olin@cheqdiff.fi

Abstract

Gneissic rock types are common in the coastal regions of the Baltic Sea and in the area of the planned deep repository at Olkiluoto. Based on experimental data and molecular modelling of mineral surfaces, the chemical reactions governing the sorption of Ni(II) and Eu(III) were interpreted using well-established thermodynamic sorption models. Two biotites were selected for the experiments and were characterised: they differ according to their origin, they were not pure biotite, but included other mineral phases, too, and they included other exchangeable cations than potassium alone. The titration experiments were performed on both biotites. The sorption experiments with nickel and europium on the biotites were successfully carried out, as was their modelling. The adsorption modelling was supported by molecular-level calculations to obtain an insight into biotite surface at the molecular level. It was possible to compare differences between potassium and nickel on minerals surfaces.

Introduction

The reference option for the Finnish nuclear waste management is geological disposal for all types of nuclear waste. The safety of geological disposal is based on a multi-barrier system: copper canisters where spent fuel is enclosed; compacted bentonite clay in disposal holes surrounding and protecting the canister; and bedrock (minerals, water-conducting fractures and groundwater). A wealth of phenomena and processes has to be understood when considering the safety of the multi-barrier system in the spent-fuel repository. One of them, sorption of radionuclides on mineral surfaces will retard their migration significantly, and for performance assessment, it is important to quantify both the sorption and its uncertainties. The objective of the work was to interpret from experimental data the chemical reactions governing the adsorption of radionuclides as well as their adsorption kinetics and reversibility. For more details, look for Olin *et al.* (2008).

Methods

Selection

The main rock types in the area of the planned repository are mica gneiss, granodiorite and pegmatite granite that is often coarse grained and poor in micaceous minerals (Anttila *et al.,* 1999; Pitkänen *et al.,* 2003). Earlier studies on the sorption of cesium and plutonium have shown that in fresh rocks, they sorb preferentially on dark minerals, especially on biotite (Pinnioja *et al.*, 1986; Koskinen *et al.*, 1988; Huitti *et al.*, 1998). Thin sections of apparently homogenous granodiorite and mica gneiss (selected from the drill-core archives of the Geological Survey of Finland, GSF) were taken for optical mineralogical analysis. Autoradiography of the thin rock sections was performed to study the sorption of radionuclides Ni-63 and Eu-152, and additionally also Cs-134 and Am-241, on different minerals, following the method of Lindberg *et al*. (1983).

Characterisation

The separation of biotite from granodiorite and mica gneiss was performed by a process including several steps with High Intensity Magnetic Separation (HIMS) and heavy liquid media separation. Of the two biotite fractions produced, the one from granodiorite is designated as OLB-A, and the one from mica gneiss as OLB-B. In addition, GSF had a sample of pegmatitic biotite from a biotite deposit at Luumäki in south-eastern Finland, designated as LMB. The elemental compositions of the biotite samples were determined after total dissolution by the ICP-AES and ICP-MS methods. The surface areas were determined by the BET/N_2 method. Some samples were analysed also by XRD and XRF to find out the mineral phases. The surface-acidity constants of biotite were determined by acid-base titrations in $NaClO_4$ solutions and the cation-exchange capacities (CEC) using the ammonium-acetate method.

Sorption experiments

The sorption of nickel and europium on biotite samples was determined in 0.05 M and 0.5 M $NaClO_4$ solutions, which were buffered at pH 3 to 9.5. The experiments were performed in a glove box under argon atmosphere in order to prevent the effect of carbon dioxide. The ground water simulants, Allard MR (granite water) and OLSR (saline water) contained no added carbonate. The sorption experiments were performed in various combinations of biotite and rock samples and solutions (Table 1).

Table 1: *Experiments performed.*

Sample	Type	Radionuclide	Solution
OLB-A	Biotite separated from granodiorite	Eu-152, Ni-63	0.05 M and 0.5 M $NaClO_4$, Allard MR, OLSR
OLB-B	Biotite separated from mica gneiss	Eu-152, Ni-63	0.05 M and 0.5 M $NaClO_4$, Allard MR, OLSR
LMB	Natural biotite from Luumäki, Finland	Eu-152, Ni-63	0.05 M and 0.5 M $NaClO_4$, Allard MR, OLSR
OL-A	Granodiorite rock sample	Eu-152, Ni-63	0.05 M and 0.5 M $NaClO_4$, Allard MR, OLSR
OL-B	Mica gneiss rock sample	Eu-152, Ni-63	0.05 M and 0.5 M $NaClO_4$, Allard MR, OLSR

Surface reaction modelling

The titration results were fitted by applying either the diffuse-layer or the constant-capacitance surface-charging model (FITEQL v. 4.0 software). The 1-p*K* approach for the surface hydrolysis is given by

(1) $\equiv SOH^{(½)+} = \equiv SO^{(½)-} + H^+$ K_a

where $\equiv SOH^{(½)+}$ and $\equiv SO^{(½)-}$ denote a protonated and deprotonated surface functional group, respectively, and K_a is the acidity constant. Nickel sorption on biotite was modelled with a cation-exchange reaction,

(2) $2NaX + Ni^{2+} = NiX_2 + 2Na^+$ K_{NiX_2}

and a surface-complexation reaction,

(3) $\equiv SOH^{(½)+} + Ni^{2+} = \equiv SONi^{(1½)+} + H^+$ K_{SONi}

Europium sorption on biotite was modelled with

(4) $\equiv SOH^{(½)+} + Eu^{3+} = \equiv SOEu^{(2½)+} + H^+$ K_{SOEu}

and

(5) $3NaX + Eu^{3+} = EuX_3 + 3Na^+$ K_{EuX_3}

Molecular-level modelling

Molecular modelling was applied in order to find out differences in the molecular-level structures of minerals observed in granodiorite and mica gneiss. The starting point for the modelling studies was the crystallographic structure of eight minerals: biotite, chlorite, cordierite, epidote, K-feldspar, muscovite, plagioclase and sillimanite (Accelrys, 2001; Accelrys, 2005). Of these, biotite was selected for detailed model calculations, where crystal and surface structures of biotite and its relative minerals were studied with the density-functional method CASTEP implemented into Materials Studio versions 3.2 (Accelrys, 2005), 4.0 (Accelrys, 2006) and 4.2 (Accelrys, 2007).

Results

Selection

The rock thin sections were photographed under normal- and crossed-polarized light. In the scale of the thin sections (1.5×2.5 cm^2), there is mineralogical heterogeneity, as indicated for mica gneiss in Figure 1. Three typical samples of thin sections of both rock types were used in the analysis of the mineral composition (Table 2). The compositions are in agreement with earlier analyses of these rock types from the same area (Hakanen and Hölttä, 1992; Kulmala *et al.,* 1996). The sorption of the radionuclides Ni-63, Cs-134, Eu-152 and Am-241 is presented in Table 3. For all tracers, sorption takes place mainly on dark minerals (Figure 1), pointing out the importance of biotite on the sorption on crystalline rock.

Characterisation of biotite

The specific surface area of the separated biotite samples was analysed with the BET/N_2 method at the laboratory of Tampere Technical University. Table 4 presents the

surface area of the biotite samples. Table 5 presents the total CEC of the biotite samples and the percentage of each exchangeable cation of the CEC. The main exchangeable cations were Ca^{2+} and K^{+} in the separated biotite samples (Table 5). A total dissolution of biotite samples was performed and the elemental composition of biotite samples was determined by ICP-AES and ICP-MS, and complemented by XRF-analysis of the biotites The elemental ratios of the separated biotite samples show that these biotite samples are similar in composition of the major elements, although the ratios differ from the ideal elemental composition of biotite (Table 6).

Figure 1: *The photograph (left) and Am-241 autoradiography (right) images of the thin rock sections (mica gneiss) B6.*

Table 2: *Main mineral composition mean values (vol%) and standard deviation of granodiorite (A) and mica gneiss (B) thin rock sections.*

Mineral	Mean (A)	Std. (A)	Mean (B)	Std. (B)
Quartz	24.8	0.9	30.9	3.1
Plagioclase	40.7	1.9	21.5	6.2
K-feldspar	14.5	3.0	9.4	1.4
Biotite	15.3	3.6	28.8	7.5
Muscovite/ sericite	2.2	1.2	3.3	1.9

Table 3: *The percentage of radionuclides sorbed on thin sections of granodiorite and mica gneiss in 0.05 M NaCl at pH 6.*

Solid	Ni-63	Cs-134	Eu-152	Am-241	Biotite content
Granodiorite	5.9	41.0	95.5	90.6	15.3
Mica gneiss	19.9	77.7	95.4	98.8	28.8

Table4 : *The specific surface area of the biotite and crushed rock samples.*

Sample	Specific surface area (m^2/g)
OLB-A (biotite from granodiorite)	1.0
OLB-B (biotite from mica gneiss)	1.3
LM (crushed biotite from Luumäki)	4.7
OL-A (granodiorite)	0.2
OL-B (mica gneiss)	0.9

Table 5: *Total cation-exchange capacity (TOT CEC) of the biotite samples and the contribution of individual elements to TOT CEC (values from 1-day experiments).*

Biotite	Na (% CEC)	K (% CEC)	Mg (% CEC)	Ca (% CEC)	TOT CEC (meq/100g)
OLB-A	0	18	29	53	1.3
OLB-B	0.003	29	29	42	1.6
LMB	0	77	20	3	1.7

Table 6: *Elemental composition: mean values (w%), ratio of Luumäki to average of Olkiluoto (L/AB), and (1/3)*(max-min) or variance between samples (% of mean value).*

Element	OLB_A	OLB_B	LMB	L/AB	var_A	var_B	var_L
Fe	17.6	14.6	20.4	1.27	3.4	4.2	5.5
Si	17.1	18.1	17.5	0.99	2.3	1.0	2.2
Al	9.10	10.63	9.92	1.01	1.3	0.5	2.2
K	5.39	5.48	5.44	1.00	4.8	14.2	15.0
Mg	3.74	4.01	0.84	0.22	0.3	4.8	5.6
Ti	1.67	1.36	1.13	0.74	3.8	1.8	5.4
Ca	0.752	0.137	0.068	0.15	54.5	9.1	4.9
Na	0.472	0.345	0.118	0.29	21.5	20.8	25.7
F	0.442	0.347	1.136	2.88	34.8	0.0	0.0

Sorption experiments

The ionic strength seemed to have no effect on the sorption of nickel. The main difference between the biotite samples was found at pH values, where the distribution coefficient (R_d) values started to increase: with the separated biotite samples, the pH was 6–6.5, whereas with the Luumäki biotite, the pH was around 7. Europium results showed clear differences at low pH values (<5) between the two ionic strengths; R_d values at 0.05 M were more than one order of magnitude higher than at 0.5 M. At high pH, the europium R_d values were high at both ionic strengths.

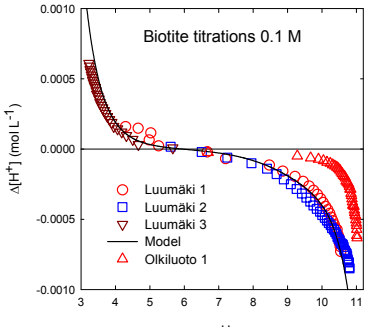

Figure 2: *Symbols: Experimental titration results, surface charge of biotites in 0.1 M $NaClO_4$ as a function of pH., for the Luumäki and Olkiluoto biotite samples. Line: Model fit to the Luumäki biotite data.*

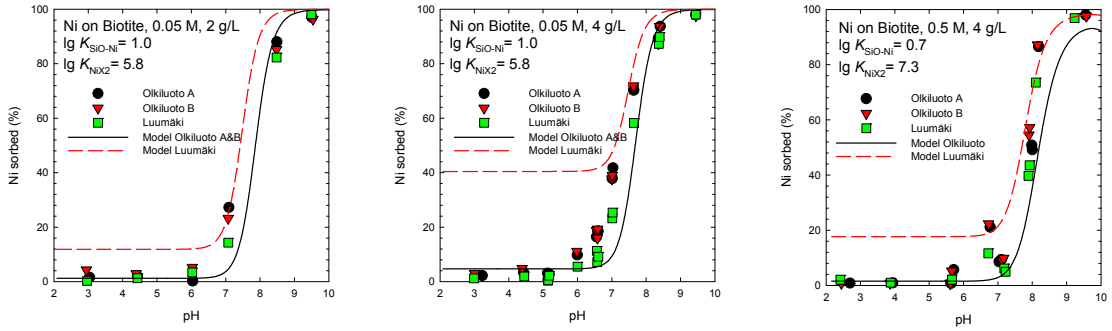

Figure 3*: Ni on biotite: % sorbed, symbols: experimental, lines: model fits. Total concentration of Ni was about $5 \cdot 10^{-7}$ M.*

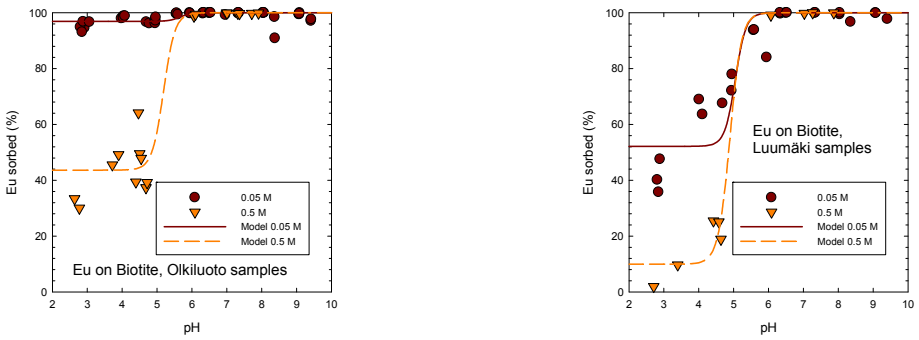

Figure 4: *Eu on biotite: % sorbed; symbols: experimental, lines: model fits. Total concentration of Eu was about $2 \cdot 10^{-7}$ M, which is below any known oversaturation.*

Table 7: *Cation-exchange (Gaines-Thomas) selectivity (lg K) for europium on biotite.*

Ionic strength	Olkiluoto	Luumäki
0.05 M	9.7	9.9
0.5 M	14.1	11.9

Surface reaction modelling

The model interpretation of the titration of the Luumäki biotite was done by assuming one hydrolysable surface site. The model fits on the acidic side gave a much lower surface site concentration than those on the basic side. Nevertheless, the basic-side fitting (surface site density 64 µmol/g and log $K_a = 5.75$) yielded satisfactory results at all pH values (see Figure 3).

The logarithm of the Gaines-Thomas cation-exchange selectivity for nickel and the binding constant for surface complexation were optimised to be 5.8 and 1.0, respectively, for the 0.05 M ionic strength, and 7.3 and 0.7, respectively for the 0.5 M solution (Figure 3). Both the experimental and optimised model results for europium are shown in Figure 4. The model lines were calculated by applying the same lg K_{SOEU} (= 6.55) for the surface-complexation reaction, but the cation-exchange selectivity is sample- and ionic-strength specific (see Table 7). Application of cation-exchange is based both on the known cation-exchange capacity of biotite and much better optimised models with cation-exchange.

Any single set of parameters of nickel or europium reactions was not possible to optimise for the used ionic strengths: biotite surface model may need some additional or more complicated reactions.

Molecular-level modelling

The structure of biotite consists of a sheet-like structure, where the sheets are connected to each other by potassium cation layers. The calculated lattice parameters of the energetically stable biotite structure are a = 528.4 pm, b = 916.2 pm, c = 2 077.3 pm and c/a = 3.931 (Figure 5a). Construction of surface models to molecular modelling studies revealed that the smallest meaningful models are very atomic-rich causing very long calculation times with the CASTEP. Therefore, two end-members of biotite (annite and phlogopite) were included in the modelling. In annite, all Mg^{2+} ions are substituted by Fe^{2+} ions, and, in phlogopite, Fe^{2+} is substituted by Mg^{2+} (Accelrys, 2001). The optimized lattice parameters of annite are a = 513.1 pm, b = 893.3 pm, c = 1 037.3 pm,

and c/a = 2.022 (Figure 5b), and those of phlogopite are a = 520.2 pm, b = 905,1 pm, c = 1 036.4 pm, and c/a = 1.992 (Figure 5c).

After the model structures for biotite were constructed, the effect of the cation-exchange of K^+, Cs^+ and Ni^{2+} on the mineral structures was calculated. The topmost K^+ was replaced directly with Cs^+ or Ni^{2+}. Optimized surface structures for annite are shown in Figure 6, which shows clearly how differently the studied ions position themselves, if they are allowed to move in the energetically most favourable position. All of the studied cations change their location on the surface compared to their location in the bulk structure. Cesium transfers from the potassium-filled cavity more than potassium itself, while nickel is on the surface far away from the cavity.

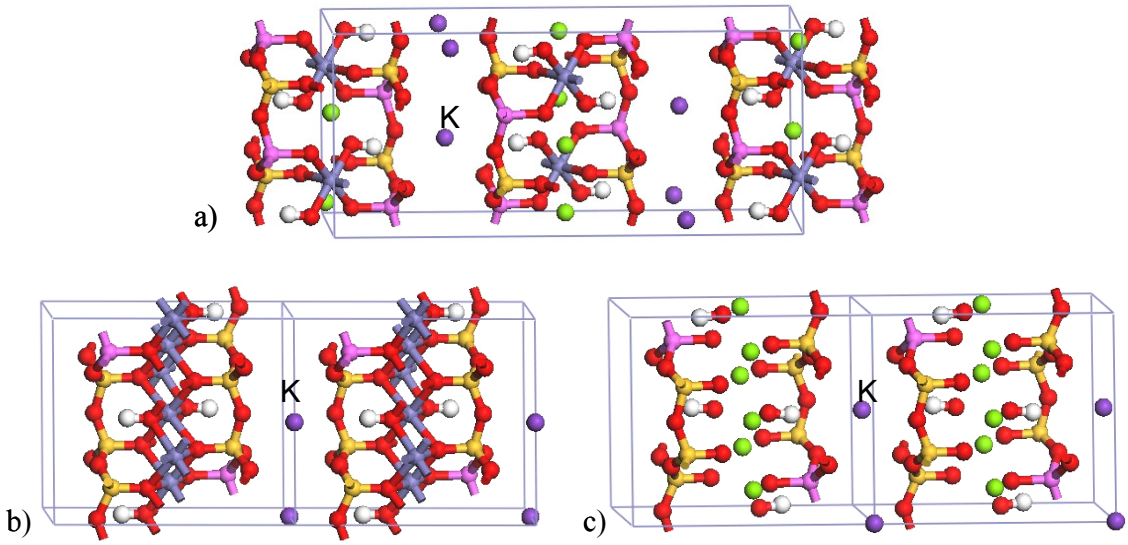

Figure 5: *The optimized unit cells: a) biotite $K_4[Mg_8,Fe(III)_4]Al_8Si_8O_{40}(OH)_8$, b) annite $K_2Fe(II)_6Al_2Si_6O_{20}(OH)_4$ and c) phlogopite $K_2Mg_6Al_2Si_6O_{20}(OH)_4$. Green spheres: magnesium. Blue spheres: iron. Yellow spheres: silicon. Aniline red spheres: aluminum. Red spheres: oxygen. White spheres: hydrogen.*

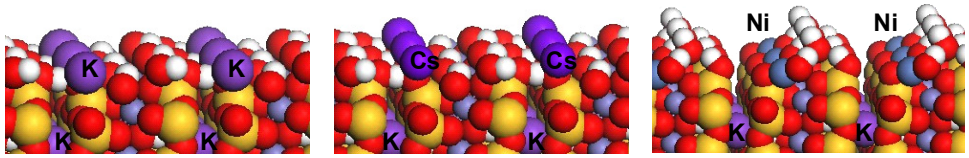

Figure 6*: Annite (110)-surface. The topmost cation was varied: K^+ left, Cs^+ middle and Ni^{2+} right. Yellow spheres: silicon. Red spheres: oxygen. White spheres: hydrogen. Small blue spheres: iron.*

Summary and conclusions

The experimental programme to study biotite and its surface reactions was realised as planned. It was observed that Olkiluoto and Luumäki biotites have differences in chemical composition and probably in structure, too. This is understandable due their different formation environments. Therefore, as expected, in model optimisation, no single set of parameters suitable for both types was found. Even

with the same sample type, the variation of ionic strength caused differences in sorption (in the low-pH range) for both Ni and Eu that were not possible to explain by a single cation-exchange reaction. Therefore, it is recommended to use site specific materials in sorption studies aimed at the determination of radionuclide retardation parameters. Molecular modelling was performed to yield supporting information for the selection of surface reactions. Interesting differences between the studied cations (K, Cs and Ni) were observed. Based on the results, molecular level modelling seems as a very promising methodology to gain deeper insight into the selection of appropriate surface reactions to explain a multitude of mechanisms affecting radionuclide retardation. Need for molecular level studies comes forward from needs to receive more specific structural information about minerals, especially their surface and layered structures, for cation-exchange studies. Traditionally, it demands very extensive work to define e.g cation-exchange positions on mineral surfaces and diffusion paths during cation-exchange process. When mineral types and structures are known and specified by experimentally, molecular modelling can use this data, and no other experimental parameters are needed. This feature of molecular modelling is its benefit and weakness: it is possible to study pure minerals without any defects. On the other hand, possible defects of minerals can be taken into account in studies without any surroundings effects. When structural and electrostatic properties of minerals are known based on the experimental and modelling work, it is easier to choose surface site models and reactions for surface reaction modelling and to receive more accurate results in radionuclide retardation in crystalline rock.

References

Accelrys. 2001. Cerius^2, Release 4.6. San Diego: Acclerys Software Inc.

Accelrys. 2005. MS Modeling, Release 3.2. San Diego: Accelrys Software Inc.

Accelrys. 2006. MS Modeling, Release 4.0. San Diego: Accelrys Software Inc.

Accelrys. 2007. MS Modeling, Release 4.2. San Diego: Accelrys Software Inc.

Anttila P., Ahokas H., Front K., Hinkkanen H., Johansson E., Paulamäki S., Riekkola R., Saari J., Saksa P., Snellman M., Wikström L. & Öhberg A. 1999. Final disposal of spent fuel in Finnish bedrock - Olkiluoto site report. Report Posiva 99-10, Helsinki.

Hakanen M. & Hölttä P. 1992. Review of sorption and diffusion parameters for TVO-92. Report YJT-92-14, Helsinki.

Huitti T., Hakanen M. & Lindberg A. 1998. Sorption of Cesium on Olkiluoto mica-gneiss, granodiorite and granite. Report Posiva 98-11, Helsinki.

Koskinen A. Hakanen M. & Lindberg A. 1988. Sorption experiments at oxic and anoxic conditions. Report YJT-88-05, Helsinki.

Kulmala S., Hakanen M. & Lindberg A. 1996. Sorption of protactinium on rocks in ground waters from Posiva investigation sites. Report Posiva 96-18, Helsinki.

Lindberg A., Pinnioja S. & Nikula A. 1983. Sorption of radionuclides in rock, mineralogic factors and autoradiography. Report YJT-83-02, Helsinki.

Olin M., Puukko E., Puhakka E., Hakanen M. & Lindberg A. & Lehikoinen, J. 2008. Final results of sorption on biotite. Research Report VTT-R-08147-08, Espoo.

Pinnioja S., Hietanen R. & Alaluusua M. 1986. Review of the sorption data of the main radionuclides in low and intermediate level nuclear wastes for Finnish bedrock (in Finnish). Report YJT-86-02, Helsinki.

Pitkänen P., Partanen S. & Luukkonen A. 2003. Hydrogeological interpretation of baseline groundwater conditions at the Olkiluoto site. Report Posiva 2003-07, Olkiluoto.

STUDY OF THE SOLUTE TRANSFER BETWEEN NEAR FIELD AND FAR FIELD IN THE FEBEX GALLERY

Buil, B.*, Gómez, P., Peña, J., Garralón, A., Turrero, M.J., Sánchez, L., Durán, J.M.

CIEMAT, Unidad de Barreras de Ingeniería y Geológica. Dpto. de Medioambiente (Spain)

*corresponding author: belen.buil@ciemat.es

Abstract

The study carried out in the FEBEX drift located at the Grimsel Test Site (Switzerland) aims to provide the basis to understand the major geochemical conditions prevailing in crystalline rock and at the bentonite/crystalline rock interface. The FEBEX experiment, based on the Spanish concept for a high level waste repository, offers the possibility to study the mass transfer at the near field-far field interface. Two boreholes were drilled parallel to the FEBEX gallery near the contact granite/bentonite interface (20 and 60cm) with the objective of providing insights on the mass transfer from the bentonite to the granite. Periodic sampling campaigns and the analysis of the major ions and the tracers (placed onto the bentonite) in groundwater reveal two facts: (a) the existence of a mass transfer from the bentonite, that is able to explain the ionic content of Cl and Na found in the sampled granitic groundwater; (b) the concentration of the natural tracers coming from the bentonite porewater increase with time in the granitic groundwater.

Assuming the mass transfer from the bentonite to the granite, a transport modeling has been performed, in order to simulate increase of Cl and Na concentration in granitic groundwaters. It has been considered a diffusive transport transverse to the drift direction, from the bentonite-granite contact to the section FU1-4 (20 cm). Modeled results corroborate the importance of diffusive transport from bentonite to granite. An effective diffusion coefficient of $D_e = 5 \cdot 10^{-11}$ m^2/s has been calculated.

Introduction

The FEBEX experiment, based on the Spanish concept for a high level waste repository, offers the possibility of studying the mass transfer at the near field-far field interface. The study carried out in the FEBEX drift located at the Grimsel Test Site (Switzerland) aims to provide the basis to understand the major geochemical conditions prevailing in the crystalline rock and at the bentonite/crystalline rock interface (Missana et al., 2007).

The study of the hydrogeochemical processes related to the migration of solutes in crystalline rocks has been carried out in nineteen radial boreholes (all of them

equipped with packers isolating a total of 41 packed-off sections) and two parallel boreholes (FU-1, FU-2; also called Funmig boreholes) located in the test site of the FEBEX drift (Gómez et al., 2007) (Fig 1). These last boreholes are parallel to the axis of the FEBEX drift, relatively close to the bentonite interface (20 cm and 60 cm, respectively), and intersect several structural regions of interest to the objective of this work (Carbonell et al., 2007). The sampling sections in the boreholes are as small as possible in order to make sure that the water samples are from the selected fractures.

Periodic sampling campaigns from 2006 to 2008 were carried out in radial and parallel boreholes with the objective of provide insights about the mass transfer from the bentonite to the granite.

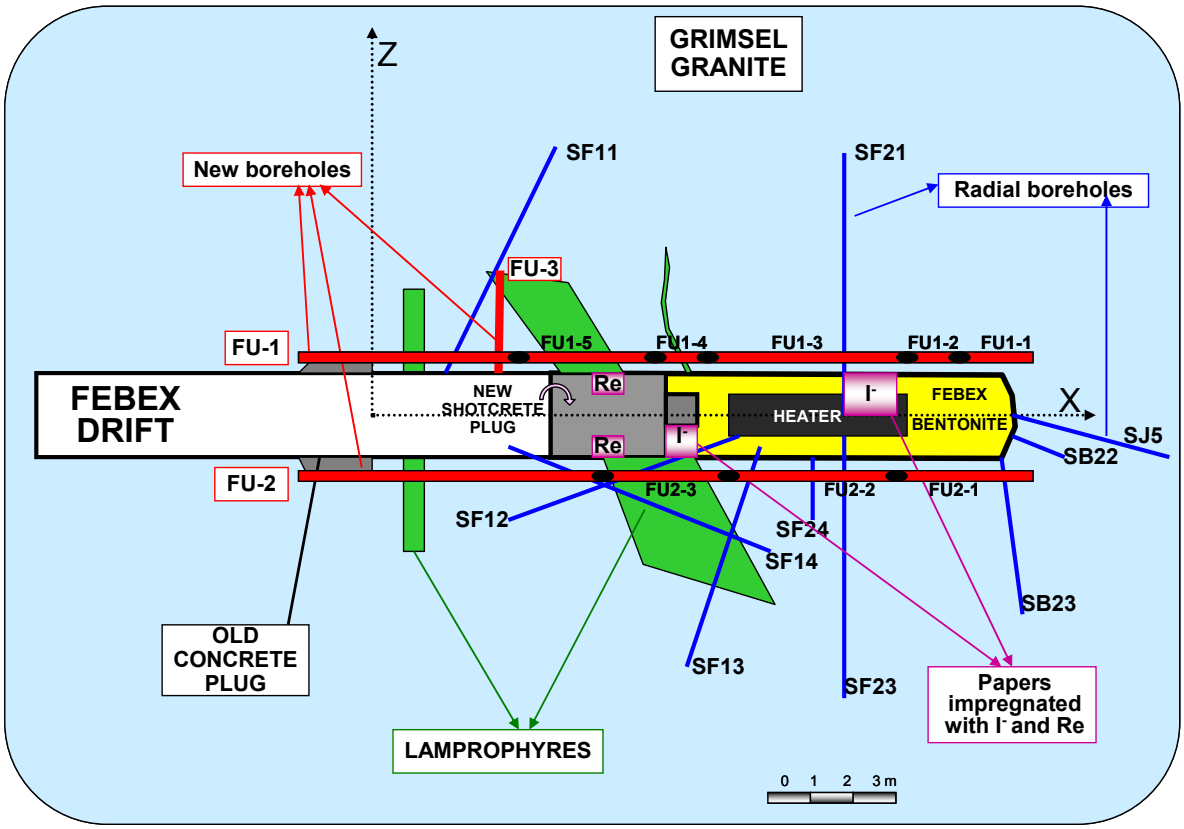

Figure 1. *Basis layout of the FEBEX experiment. Schematic of the borehole FU-1 and FU-2 instrumentation and location of the artificial tracers.*

Results

The waters from the radial boreholes can be classified as near neutral to alkaline (pH ranges from 6.9 to 9.8) with low electric conductivity values ranging from 76 to 236 μS/cm, which is their most important characteristic.

Attending to their major ions, the waters can be classified in three groups: 1.- HCO_3-Na-Ca–type, 2.- HCO_3-Na-type and 3.- HCO_3-Ca-type, although, the relative concentration of Ca and Na ions in the waters shows small variations. The principal control factor of the chemical composition of these waters is its interaction with the host rock, as it reflects its saturation indexes (around zero) regarding to the main granitic

minerals (Gómez et al., 2007). Significant temporary variations in waters have not been observed. Chlorine and sodium are considered as natural tracers of the mass solute transfer between the bentonite porewater and the granite groundwater. The porewater of the FEBEX bentonite is a Na-Cl type water with a high content of magnesium and calcium, high electrical conductivity and neutral pH (ENRESA, 2000). Due to the low concentration in the sampled water from the boreholes of these tracer elements, no conclusive evidences on the existence of transport processes from bentonite barrier to the granitic host rock can be drawn (Buil et al., 2006).

Groundwater sampled from borehole FU-1 (20 cm from the bentonite surface) have pH ranging from 6.3 to 8.2 and their electrical conductivity is the highest of all the groundwaters sampled inside the drift (385µS/cm). They are Ca-HCO3 type waters except groundwater coming from interval 4 (FU1-4) that has evolved from Ca-HCO3 in 2006 and 2007 to Na-Cl type waters in 2008.

The groundwater sampled in the three packed-off sections of borehole FU-2 are dilute (155-231 µS/cm), Ca-HCO3 or Ca-Na-HCO_3 type waters and slightly neutral (pH ranges from 6.2 to 7.6).

The results of the chemical analysis in the waters from Funmig boreholes highlight the existence of a mass transfer process from the bentonite into the granite. This assertion is based on the results of the chemical analyses of some natural tracers coming from the bentonite porewater, e.g. Cl, Na, and Ca, which are in very low concentration in the groundwater from the radial boreholes, but are two orders of magnitude higher in some packed-off sections of the Funmig boreholes. Some of the evidences regarding the analysis of these natural tracers are presented next:

a) There is a high concentration of natural tracers in the water of the Funmig boreholes as compared to the waters collected in the radial boreholes (Fig 2). A significant percentage of the exchangeable complex of the bentonite, mainly Ca, K, Mg, Na and Sr, is likely mobilized by the waters. It is worth to emphasize that the high concentration of ions could be measured in these boreholes due to their proximity to the bentonite barrier (20 cm and 60 cm), as well as by the smaller length of the packed-off sections (around 1 m) as compared to those in the radial boreholes (around 7 m).

b) There is a high concentration of Na, Ca and Cl concentration in the FU1-4 section as compared to the rest of sections of Funmig boreholes (Fig 3). It could be related to the presence of a small lamprophyre dyke that could facilitate the solute mass transfer between the bentonite and the granite. The small size of this packed-off section (0.87 m) and therefore the one with the smallest volumetric capacity (2 litres), could mean a low impact of a dilution process.

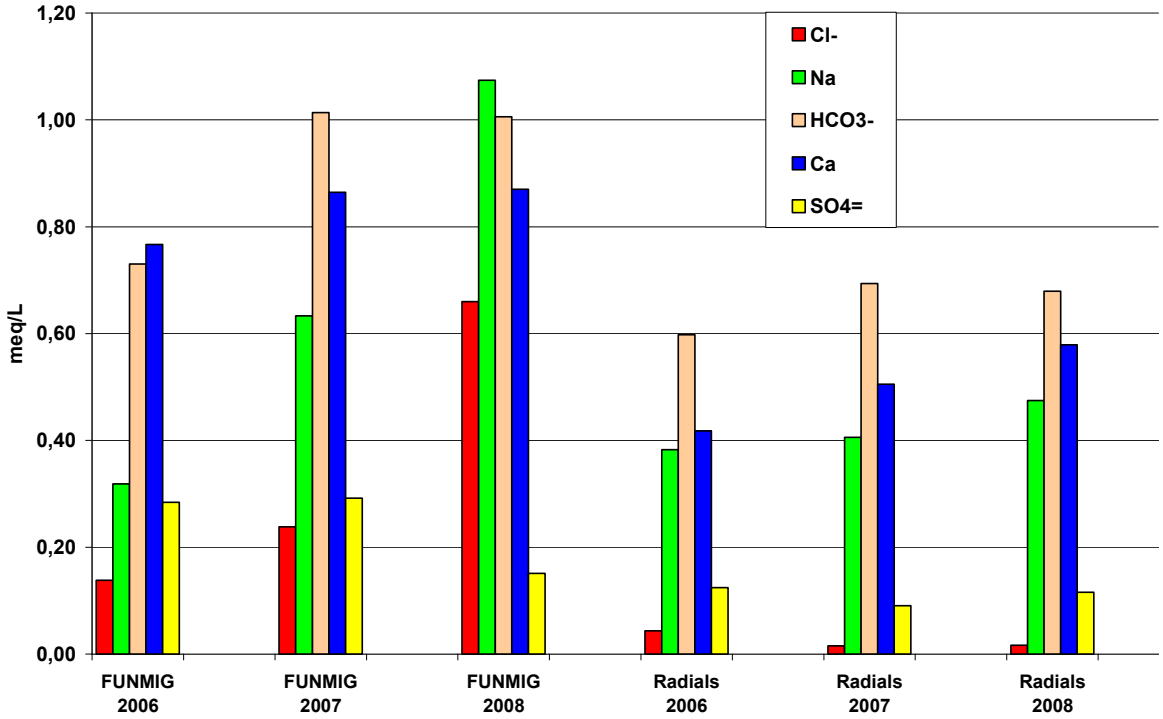

Figure 2: *Mean concentration of Cl^-, Na^+, HCO_3^-, Ca^{2+} and SO_4^{2-} in groundwater coming from Funmig boreholes is higher than in radial boreholes.*

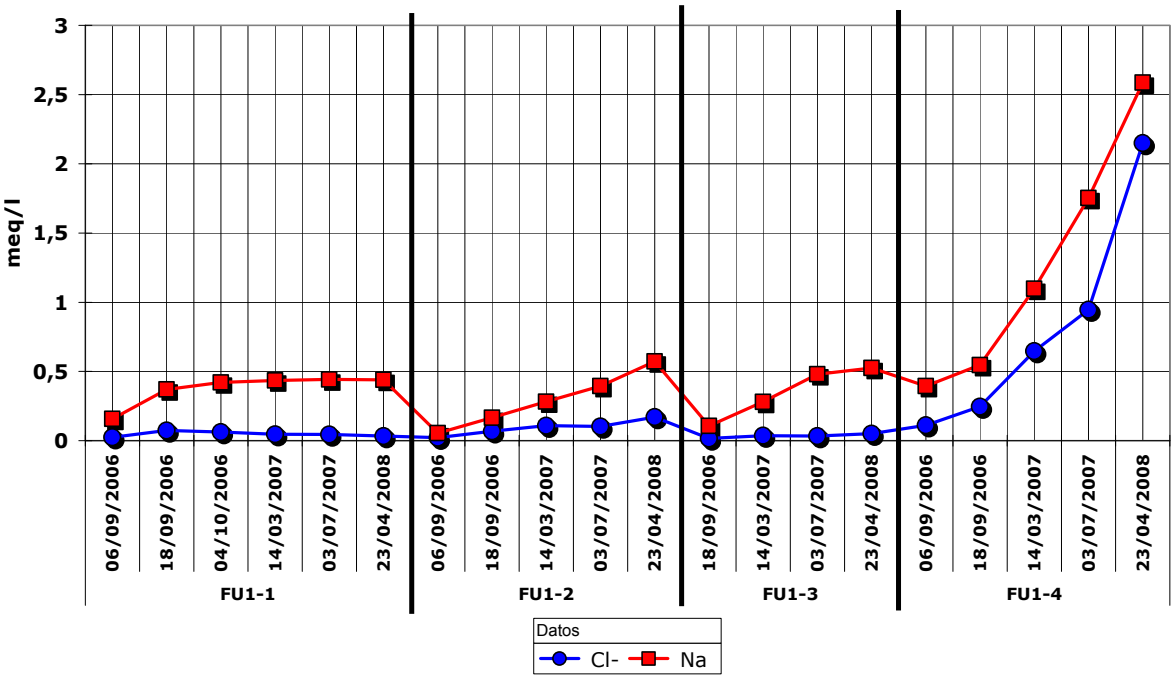

Figure 3: *Na and Cl concentration vs time in the packed-off sections of the FU-1 borehole*

c) There is an appreciable increase of Na and Cl concentration in time in the waters sampled from the borehole FU-1, especially in the interval FU1-4. On the other hand, the Na/Cl ratio in water from the interval FU1-4 is similar to the Na/Cl ratio in the

bentonite porewater. For this reason, Cl and Na are considered as the main natural tracers indicating the mass transfer process between the bentonite porewater and the granite.

d) There is small concentration of iodine and rhenium (tracers placed at the external surface of some bentonite blocks during their installation in 1996) in the water from the closest boreholes to the bentonite surface (FU2-3 and FU1-4).

Assuming the mass transfer from the bentonite to the granite, a 1D transport modeling was performed, in order to simulate the chemical composition of the water from the drilled boreholes. The code used for calculations is PHREEQC, using llnl.dat as thermodynamic database (Parkhust and Appelo, 1999). The simulation was carried out in a perpendicular direction to the gallery axis, starting at the bentonite-granite contact and ending at the section FU1-4 (20 cm). A constant concentration condition (Dirichlet condition) has been assigned to the node representing the bentonite-granite contact whereas a no-flow condition (Neuman condition) has been associated to the node representing the section FU1-4 (Peña et al., 2008).

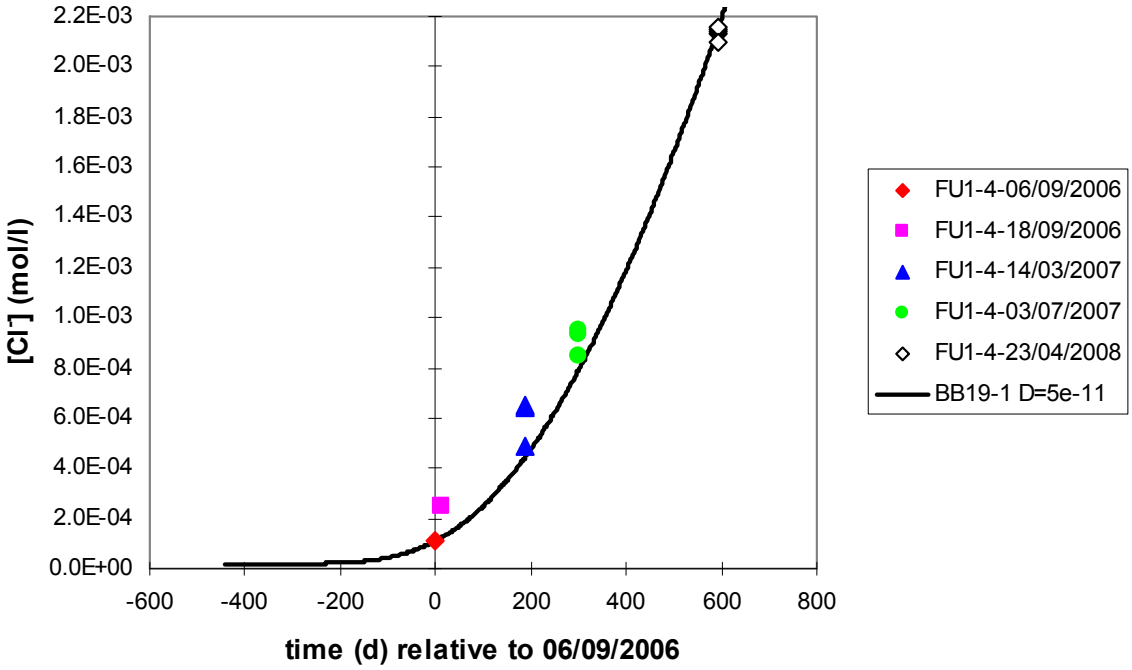

Figure 4: *Results of transport modelling considering the bentonite porewater and the water from the FU1-4 interval provide a De≈ 5,0E-11 for the diffusive transport of chloride. A good match between the result of the simulation (black line) and the analytical data (symbols) can be observed.*

The gradient of the natural tracer concentration between the bentonite and the granite led to consider a diffusive transport for modelling purposes. Two types of water were considered: boundary water corresponding to the bentonite porewater nearest to the granite-bentonite interface; and initial granitic water from the section FU1-3. This choice is based on the proximity of this section to the simulated section (FU1-4) and on its hydraulic characteristics (T, K, S, S_w and L).

The effective diffusion coefficient was calibrated using the measured chloride concentrations in the interval FU1-4 from 2006 to 2008.

The Cl and Na concentration determined in the granite groundwater at 20 cm from the bentonite interface (FU1-4), can be explained by a diffusion transport with a De≈ 5,0E-11 (Fig 4). Therefore, the results corroborate the importance of diffusive transport from the bentonite to the granite (Buil et al., submitted).

Summary and Conclusions

A mass transfer process from the bentonite to the granite must be considered. It is based on the following evidences:

- Slightly contents of natural tracers coming from the bentonite porewater (Na, Cl, Ca), are present in some packed-off sections of boreholes FU-1 located at 20cm from the bentonite surface.
- Increase of the Cl and Na concentration in time in FU1-4 and FU2-1 sections.
- Presence of iodine, and probably rhenium in the section FU1-4, which is the nearest to the bentonite surface.

Diffusive transport modeling was used to describe the mass transfer process, showing that an effective diffusion coefficient in granite of De≈ 5.0E-11 m^2/s can explain the diffusive transport of chlorides and sodium from the bentonite to granite

The importance of these results are related to the performance assessment due to the analogy between ^{36}Cl (one of the dominant radionuclides in the average annual doses in the reference scenario) and the Cl ion. Probably the safety case should take into account the probable transport of conservative solutes from the bentonite into the granite.

Acknowledgement

This work is being performed within the framework of the “FUNMIG” research project (FP6-516514) funded by EU and ENRESA

References

Buil, B., Gómez, P., Garralón, A., Peña, J., Turrero, M.J., Missana, T., Alonso, U., Sánchez, L., Durán, J.M. (2007). Geochemical gradients generated by the bentonite into the granite in a in situ experiment. 3nd Annual Workshop Proceedings of the Integrated Project “Fundamental Processes of Radionuclide Migration” 6th EC FP IP FUNMIG. Edinburg

Buil, B., Gómez, P., Peña, J., Garralón, A., Turrero, M.J., Sánchez, L., Durán, J.M Modelization of the mass transfer generated by the bentonite into the granite at the FEBEX drift, Chemical Geology submitted.

Carbonell, R. Pérez-Estaún, A. Missana, T. Suso, J. Carretero, G. Bueno, J. Martínez, L. Buil, B. Garralón, A. Gómez, P, Hernán, P.(2007). Geology and Geophysics of new

boreholes at Febex site. 2nd Annual Workshop Proceedings of the Integrated Project "Fundamental Processes of Radionuclide Migration" 6th EC FP IP FUNMIG. SKB Technical Report TR-07-05 pp.307-314.

ENRESA, 2000. FEBEX Project. Full-scale engineered barriers experiment for a deep geological repository for high level radioactive waste in crystalline host rock. Final Report, Publicación Técnica ENRESA 1/2000, Madrid.

Gómez, P., Buil, B., Garralón, A., Turrero, M.J., Sánchez, L. and Durán, J.M. (2007) Geochemical gradients at the near-far field interface at the FEBEX gallery (Grimsel). Water rock interaction WRI 12, T.D. Bullen and Y. Wang editors, Taylor & Francis Group, Vol 2, pp.583-587.

Missana, T. Pérez-Estaún, A. Carbonell, R. Suso, J. Carretero, G. Bueno, J. Martínez, L. Buil, B. Garralón, A. Gómez, P, Hernán, P. (2007). Overview of the activities carried out at the FEBEX site. 2nd Annual Workshop Proceedings of the Integrated Project "Fundamental Processes of Radionuclide Migration" 6th EC FP IP FUNMIG. SKB Technical Report TR-07-05 pp.417-423.

Parkhust, D.L. and Appelo, C.A.J., 1999. User's guide to PHREEQC (Version 2)- A computer program for speciation, reaction-path, 1D-Transport and inverse geochemical calculations. Report 99-4259, U.S. Geological Survey. Water Resources Investigations.
Peña, J., Buil, B., Gómez, P., Garralón, A., Turrero, M.J., Missana, T., Alonso, U., Sánchez, L., Durán, J.M. (2008). Modelling of the hydrochemical influence of the bentonite barrier in a geological repository. The FEBEX Experiment. Geochimica et Cosmochimica Acta 72(12) 735-735

TRIVALENT METAL ION INTERACTION WITH ALUMINIUM OXIDES/HYDROXIDES

Tomas Kupcik [1*], Nina Huittinuen [2], Thomas Rabung [1], Johannes Lützenkirchen [1]; Horst Geckeis[1]; Thomas Fanghänel [3,4]

[1] Forschungszentrum Karlsruhe, Institut für Nukleare Entsorgung, P.O. Box 3640, 76021 Karlsruhe, Germany
[2] University of Helsinki, Laboratory of Radiochemistry, P.O. Box 55, 00014 Helsinki, Finland
[3] Universität Heidelberg, Physikalisch-Chemisches Institut, Im Neunheimer Feld 253, 69120 Heidelberg, Germany
[4] European Comission, Joint Research Centre, Institute for Transuranium Elements, P.O. Box 2340, 76125 Karlsruhe, Germany

* Corresponding author: kupcik@ine.fzk.de

Abstract

Sorption of trivalent Cm(III) and Eu(III) onto gibbsite, bayerite and α–Al_2O_3 powder is investigated by batch experiments and time-resolved laser fluorescence spectroscopy (TRLFS). The pH dependent sorption is followed at constant ionic strength of 0.1 M $NaClO_4$ under argon atmosphere in a pH range between 4 and 11. Eu(III) sorption onto α–Al_2O_3 powder starts at pH > 4, indicating inner sphere surface complexation. From the TRLFS emission spectra for Cm(III) sorption onto α–Al_2O_3 powder and bayerite, the presence of two or more different Cm(III) surface species can be derived. The pH dependent dissolution and precipitation of gibbsite significantly affects the speciation of sorbed Cm(III). Equilibration of a gibbsite suspension in the solubility minimum and increasing or decreasing the pH inhibits the formation of an "incorporated" Cm(III) species and leads to two Cm(III) surface sorbed species with emission peak maxima at 604 nm and 605 nm. Additionally, as the density of surface sites at the edges of bayerite is higher compared to gibbsite, and since bayerite has a lower IEP than gibbsite, the adsorption edge is shifted to lower pH values as compared to gibbsite.

Introduction

For the long-term performance assessment of a nuclear waste repository in deep geological formations, knowledge on the aquatic and geochemical reactions of actinide ions in the near- and far-field of this repository are desired. Besides attachment to mobile colloidal phases, retardation processes such as sorption and incorporation reactions at the water/mineral interface influence the mobility of the released

radionuclides. Therefore, mechanistic insight into radionuclide interactions with mineral surfaces is of major importance. For a fundamental understanding of sorption/incorporation processes and a reliable thermodynamic description by surface complexation models, surface species have to be identified, characterized and quantified.

To gain deeper insight into geochemical processes at mineral surfaces, speciation studies with Cm(III) and Eu(III) have been performed. Time-resolved laser fluorescence spectroscopy (TRLFS) is a versatile tool to elucidate the sorption mechanisms on surfaces, allowing studies in the submicromolar concentration range (analytical detection limit for Cm(III) $5 \cdot 10^{-12}$ mol·L^{-1}).

For speciation of Cm(III), the intensive absorption band at 396.6 nm is used for excitation, the emission spectra are recorded in the range of 570 – 630 nm. The position of the emission band depends on the ligand field splitting, allowing the distinction of different species.

In the context of nuclear waste disposal, aluminium oxides/-hydroxides are of minor importance, but they are considered as isomorphous model phases for trivalent iron oxides/hydroxides and other Al-containing minerals present in nature. Among these, clays are of great importance for metal ion retardation. In contrast to iron oxides/hydroxides aluminium oxides/hydroxides show no absorption in the visible light region, thus allowing TRLFS experiments.

Previous TRLFS experiments on Cm(III) sorption onto α–Al_2O_3 single crystals and γ–Al_2O_3 colloids show, that sorption onto the (001) α–Al_2O_3 surface differs with regard to peak position (601.3 nm) and fluorescence lifetime (τ = 107 μs) compared to the other four crystal planes (λ = 603.6 nm and τ = 158 – 192 μs)[1]. In case of γ–Al_2O_3, three different Cm(III) surface species at different pH are identified by their emission spectra with peak maxima at 600.6 nm, 602.5 nm and 605.7 nm but no variation of emission decay was detected (constant lifetimes of 110 μs)[2].

As pure Al-oxide surfaces are not thermodynamically stable in water and undergo (surface) phase transformations into the hydroxides [3,4] , speciation investigations with Eu(III) and Cm(III) are being extended to the pure Al-hydroxides gibbsite and bayerite, both synthesised at INE.

Eu(III)/Cm(III) sorption onto α–Al_2O_3 powder

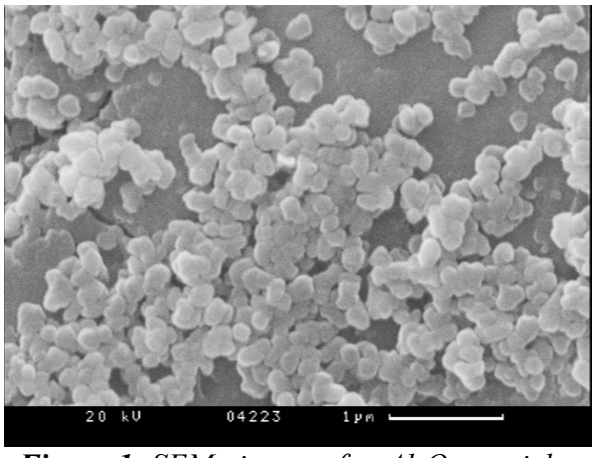

Figure 1: *SEM picture of α–Al_2O_3 particles*

α–Al_2O_3 powder was supplied by Taimicron (TM-DAR). SEM pictures show a homogeneous microstucture with spherical particles but undefined crystal planes with an average particle size of 200 nm (Figure 1).

The value for the isoelectric point (IEP), measured by micro electrophoresis is 9.8 in $NaClO_4$ and 10.2 in NaCl (Figure 2). These values are in good agreement with previous IEP measurements in different electrolytes [5]

Eu(III) sorption onto α–Al_2O_3 powder starts at pH > 4 at low Eu(III) concentrations and slightly above pH 5 at higher metal ion concentrations (Figure 3). At these pH values, the surface is positively charged, indicating the formation of an inner sphere surface complex. A shift in the pH edges with increasing Eu(III) concentration is observed, which may be due to surface saturation effects and different surface binding sites. In case of gibbsite, the pH shift was also observed, but at significantly higher metal ion concentrations.

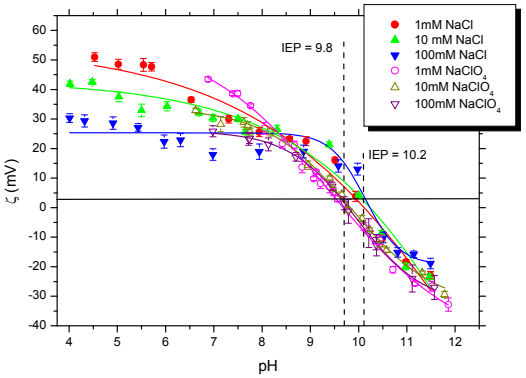

Figure 2: *ζ potential of 1g·L^{-1} α–Al_2O_3 in NaCl and $NaClO_4$; lines are to guide the eye*

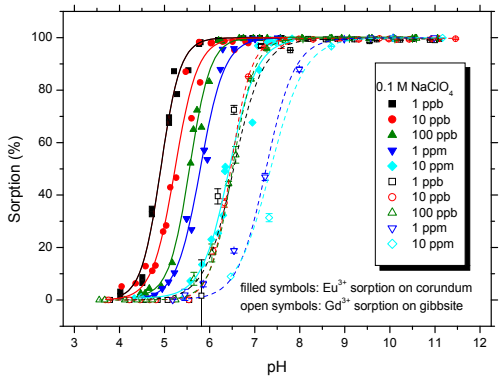

Figure 3: *pH edges for sorption studies onto α–Al_2O_3 powder with Eu(III) (filled symbols) and onto gibbsite with Gd(III) (open symbols [6] ; lines are to guide the eye*

Normalized emission spectra characterising Cm(III) sorption onto α–Al_2O_3 powder at various pH are shown in Figure 4a. Sorption starts at pH > 4 with the appearance of a shoulder in the emission spectrum at 600 nm. The observed redshift is caused by a change in the ligand field of the Cm(III) first coordination sphere and indicates an initial surface sorbed Cm(III) species.

Increasing the pH from 4.0 to 7.0 is accompanied by a further redshift of the spectra, leading to a Cm(III) emission band at 602 nm. At pH 7.0, no Cm^{3+} aquo ion is present and the little variation in the spectra from pH 7.0 to 10.0 is due to a constant species distribution in this range. Increasing the pH to 11.0, a Cm(III) emission band at 604 nm appears (Figure 4b). As no peak deconvolution has been performed so far, the exact speciation of sorbed Cm(III) cannot be given. But from the peak shifts, the presence of two or more Cm(III) sorption species can be interpreted.

As the α–Al_2O_3 surface is not thermodynamically stable in the presence of water and undergoes surface conversion into gibbsite/bayerite, metal ion sorption could take place both at the pure unaltered oxide surface and at the generated hydroxide (gibbsite/bayerite) surface.

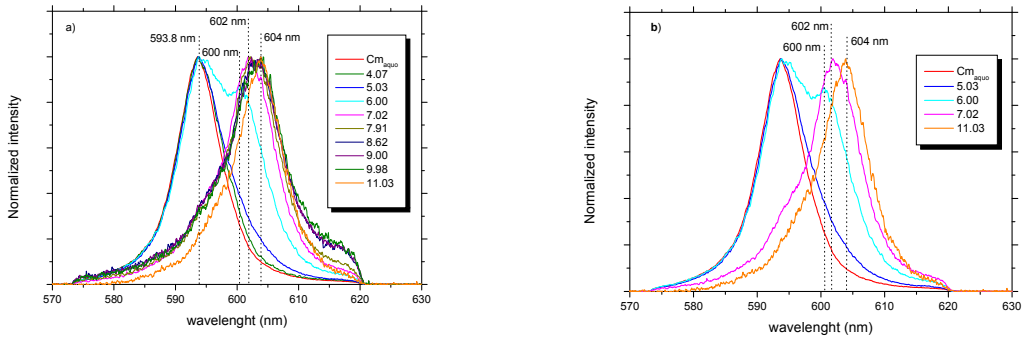

Figure 4: *TRLFS spectra of $2 \cdot 10^{-7}$ mol·L^{-1} Cm(III) in 0.5 g·L^{-1} aqueous α–Al_2O_3 powder suspension (0.1 M $NaClO_4$) at various pH* ***(a)*** *and at selected pH values* ***(b)****; spectra are scaled to same peak height*

Cm(III) sorption onto gibbsite and bayerite

Synthesis and Cm(III) sorption onto bayerite

Bayerite microrods were synthesised by titration of an aluminate solution with HCl to pH 9 at elevated temperatures [7]. The purity, morphology and surface area of the product were characterized by XRD, SEM and BET, respectively. XRD spectra indicate the synthesis of pure bayerite, while SEM pictures show 1-5 µm long rod shaped crystals together with small particles with mixed morphologies (Figure 5). The BET surface area was determined to 14 m^2·g^{-1}.

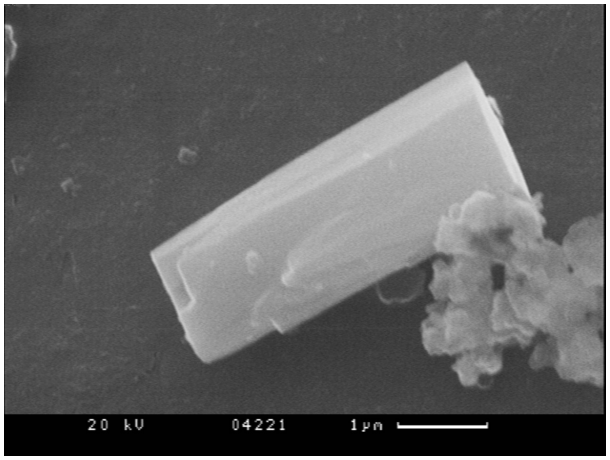

Figure 5: *SEM picture of bayerite (β-$Al(OH)_3$)*

The TRLFS emission spectra for Cm(III) sorption onto bayerite at various pH are shown in Figure 6. Sorption starts at pH > 4, similar to α–Al_2O_3 powder. A gradual redshift of the Cm(III) fluorescence emission band with increasing pH is observed, caused by a change in the ligand field of the Cm(III) first coordination sphere and indicating different Cm(III) surface sorbed species. A detailed peak deconvolution is in progess.

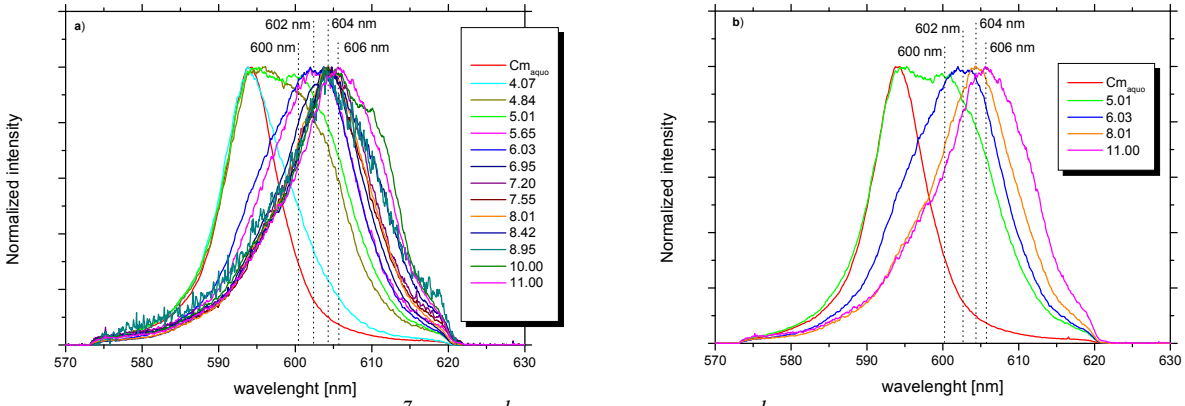

Figure 6: *TRLFS spectra of $2 \cdot 10^{-7}$ mol·L^{-1} Cm(III) in 0.5 g·L^{-1} aqueous bayerite suspension (0.1 M $NaClO_4$) at various pH* ***(a)*** *and at selected pH values* ***(b)****; spectra are scaled to same peak height*

Cm(III) sorption onto gibbsite

In earlier sorption studies on gibbsite, using an equilibrated gibbsite stock suspension at pH 4.3, four different Cm(III) species were identified: the free Cm^{3+} aquo ion (593.8 nm), two surface species (603.0 and 605.2 nm) and a surface species with a strong red shifted peak (609 nm)[6]. The fact, that the new Cm(III) species (609 nm) appears in the pH region from 5.5 to 10 and disappears at high pH, indicates a surface precipitation process and the incorporation of Cm(III) into the Al-hydoxide structure as a result of dissolution and re-precipitation due to oversaturation of Al(III) in the pH range 5 to 9. A new approach involves a gibbsite suspension, which is adjusted to the minimum of the solubility (pH = 6.2) and equilibrated for four months before starting the Cm(III) sorption studies.

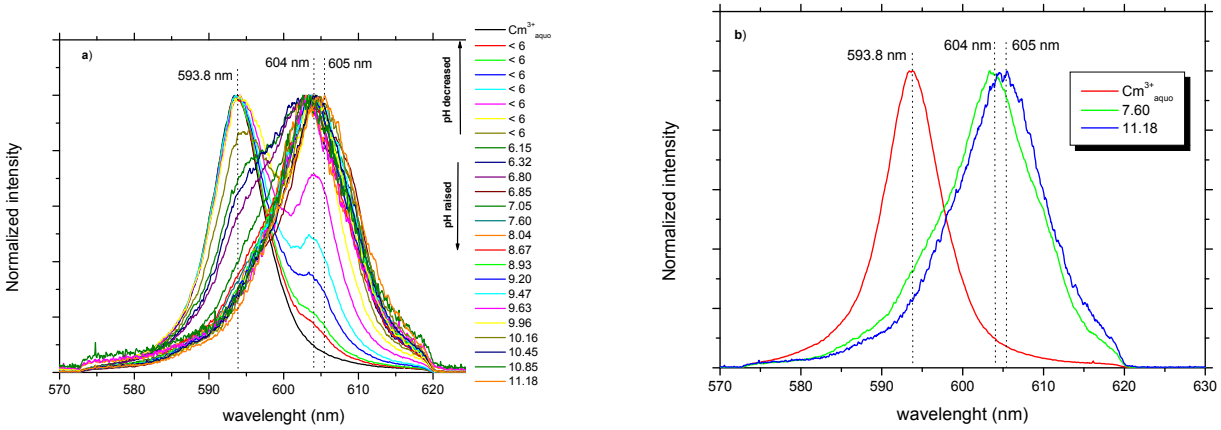

Figure 7: *TRLFS spectra of $2 \cdot 10^{-7}$ mol·L^{-1} Cm(III) in 0.5 g·L^{-1} aqueous gibbsite suspension after equillibration at pH 6.2 (0.1 M $NaClO_4$) at various pH* ***(a)*** *and at selected pH values* ***(b)****; spectra are scaled to same peak height*

The pH is increased and decreased, respectively, starting from pH = 6.2, in two sets of experiments. After equilibration of the gibbsite suspension at pH 6.2 and a subsequent increase or decrease in the pH, the formation of the 609 nm species is not observed, confirming the assumption of an „incorporated“ Cm(III) species (Figure 7a). A redshift of the emission band with increasing pH is observed. The intensity of the emission band of the Cm^{3+} aquo ion (593.8 nm) decreases and a shoulder appears at 604

nm, indicating the formation of a surface species (Cm(III) surface complex 1). At pH 7.6, no Cm^{3+} aquo ion is present any more and little variation in the spectra from pH 7.6 to 10.5 indicates a relatively constant species distribution in this range. A further increase of the pH leads to a further red shift of the emission band and points to a second surface species (Cm(III) surface complex 2; 605 nm; Figure 7b).

Summary and conclusions

Eu(III) sorption onto α–Al_2O_3 powder starts at pH > 4 by inner sphere surface complexation. Due to surface saturation effects and different surface binding sites, a shift in the pH edges with increasing Eu(III) concentration is observed. TRLFS emission spectra for Cm(III) sorption onto α–Al_2O_3 powder and bayerite microrods, which were synthesised by titration of an aluminate solution to pH 9 at elevated temperatures, show the presence of at least two different Cm(III) surface species. pH dependent dissolution and precipitation of gibbsite affects significantly the speciation of sorbed Cm(III). Equilibration of the gibbsite suspension in the solubility minimum and increasing or decreasing the pH prevents the formation of the "incorporated" Cm(III) species and leads to the formation of two surface sorbed Cm(III) species.

Acknowledgement

The present work was done in the context of FUNMIG, financed by the European Commission. The authors thank Annika Kaufmann for conduction the ICP-MS investigations, Tanja Kisely for performing the BET measurements and Eva Soballa for the SEM observations. Financial support from EnBW, Karlsruhe, Germany, and the Helmholtz association of National Research Centres, Bonn, Germany, is gratefully acknowledged.

References

[1]Rabung Th, Schild D, Geckeis H, Klenze R, Fanghänel, Th (2004): Cm(III) sorption onto Sapphire (α-Al_2O_3) Single Crystals, J. Phys. Chem. B, 108, 17160.

[2]Rabung Th, Geckeis H, Wang X K, Rothe J, Denecke M A, Klenze R, Fanghänel Th (2006): Cm(III) Sorption onto γ-Al_2O_3, Radiochim. Acta, 94, 609.

[3] Lee D H, Sr. Condrate R A (1995): An FTIR spectral investigation of the structural species found on alumina surfaces, Mater. Lett., 23, 241.

[4]Lefèvre G, Duc M, Lepeut P, Caplain R, Fédoroff M (2002): Hydration of γ-Alumina in Water and Its Effects on Surface Reactivity, Langmuir, 18, 7530.

[5] Johnson S B, Scales P J, Healy T W (1999): The Binding of Monovalent Electrolyte ions on α-Alumina, Langmuir, 15, 2836.

[6] Huittinen N: Sorption of Gd(III) and Cm(III) onto gibbsite, Submitted to J. Colloid Interface Sci.

[7]Lefèvre G, Fédoroff M (2002): Synthesis of Bayerite (β-$Al(OH)_3$) microrods by neutralization of aluminate ions at constant pH, Mater. Lett., 56, 978.

COMPLEXATION CONSTANTS UPDATE: CARBONATE AND SULPHATE COMPLEXES OF ACTINIDES AND LANTHANIDES

Thomas Vercouter*, Pierre Vitorge, Badia Amekraz†, Christophe Moulin††

CEA, DEN, Laboratory of Speciation of Radionuclides and Molecules,
F-91191 Gif-sur-Yvette, France.
† Current affiliations: AREVA NC BU-T, F-92084 La Défense, France.
†† Current affiliations: CEA, DIF, Service Radioanalyse, Chimie, Environnement,
F-91297 Arpajon, France.

* Corresponding author: thomas.vercouter@cea.fr

Abstract

This paper summarizes thermodynamic data that have been determined at CEA for complexation reactions of the actinides Am(III), Cm(III), and U(VI), and the lanthanides La(III), and Eu(III) by the inorganic anions carbonate and sulphate. Solubility of Am(III) in carbonate solutions also provided values of the solubility products of Am(III) solid phases. Measurements have been performed between 10 and 70°C, which have enabled to determine enthalpies and entropies of reactions.

Introduction

The determination of the stability of the carbonate and sulphate complexes of actinide and lanthanide ions has been the object of a large number of experimental investigations. The trivalent f-block cations have been much studied because reducing conditions should be prevailing in underground waters that may be in contact with the high-level radioactive waste. Depending on the physico-chemical conditions, speciation calculations show that uranium may be found in the form of U(VI) in underground waters, and having reliable chemical data for its speciation is also of fundamental significance to assess whether or not this more mobile form of uranium could be present. However, discrepancies between thermodynamic data exist as emphasized in the NEA/OECD database (GUILLAUMONT et al., 2003; SILVA et al., 1995). Moreover, very few data about the temperature effect on the complex or solid phase formations are available.

The present work summarizes experimental results on the interactions of Ln(III) and An(III) with carbonate and sulphate anions, determined by solubility measurements and Time-Resolved Laser-induced Fluorescence Spectroscopy (TRLFS), and on the UO_2^{2+} complexes with sulphate by TRLFS. The temperature dependence of equilibrium

constants has also been determined and thermodynamic parameters such as enthalpy, entropy and heat capacity of reactions are reported.

Carbonate complexes and solids

Am(III) in carbonated solutions studied by solubility measurements

As hard Lewis acids, Am(III), Cm(III), and Eu(III) are often considered chemical analogues. However, as stated in the NEA/OECD reviewing works (GUILLAUMONT et al., 2003; SILVA et al., 1995), discrepancies between the stability constants proposed for Am(III) and Cm(III) carbonate complexes are pointed out; furthermore the stoichiometry of the complex formed in concentrated carbonate solutions (limiting complex) would be $Am(CO_3)_3^{3-}$ and $Cm(CO_3)_4^{5-}$, and both stoichiometries have been proposed for Eu(III). These differences suggest either real chemical differences or erroneous conclusions from the analysis of experimental data. It should be noted that the formation of the carbonate complexes in concentrated solutions is highly dependent on ion activities and that complexation model and short-range ion interaction models (Specific Ion interaction Theory (SIT), Pitzer model, etc) are closely correlated. Consequently, the data treatment is model-dependent, and the derived thermodynamic data might be accompanied with increased uncertainties.
We have investigated the speciation of the three f-block metal ions, Am(III), Cm(III), and Eu(III), in carbonated solutions by using slope analysis of solubility measurements, and TRLFS. The detailed results are reported elsewhere (VERCOUTER, 2004). Only the main outcomes are given here.

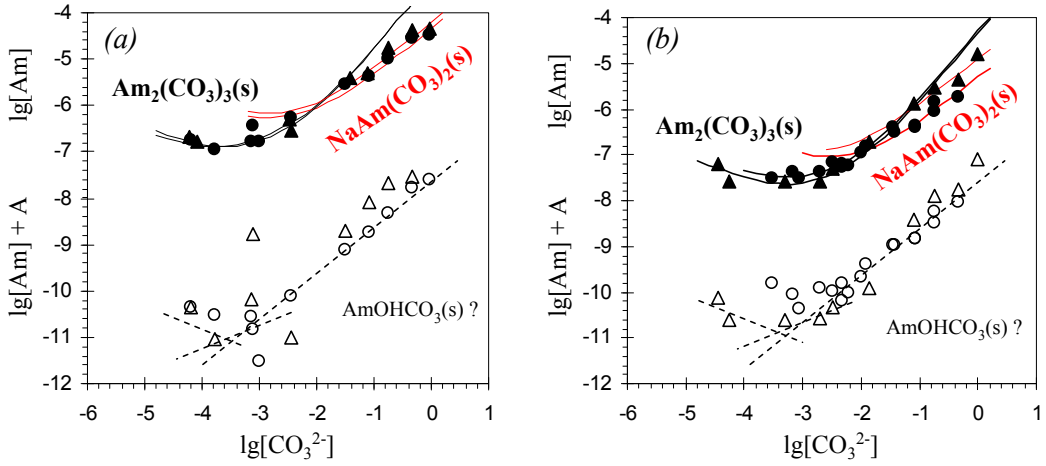

Figure 1: *Solubility of Am(III), [Am], in bicarbonate and carbonate solutions with 4M NaCl measured (●) in phase 1 (cooling) and (▲) in phase 2 (heating) for (a) T = 30°C and (b) T = 70°C. The slope analysis suggests that (—) $Am_2(CO_3)_3(s)$ and (—) $NaAm(CO_3)_2(s)$ control the solubility. In the case $AmOHCO_3(s)$ would control the solubility, lg[Am] + A is represented (open symbols), where $A = -0.5 \lg P_{CO2} + 0.5 \lg(K_w^2 K_{p2})$, $\lg K_w = -14.17$ (K_w is the ionic product of water) and $\lg K_{p2} = 17.70$ (K_{p2} is the equilibrium constant for $CO_3^{2-} + 2\ H^+ \rightleftharpoons CO_2(g) + H_2O$); if this interpretation is correct, lg[Am] + A should vary continuously with $\lg[CO_3^{2-}]$ and exhibit half-integer slopes (---), which is not evidenced graphically.*

Table 1: *Summary of equilibrium constants determined at (22±2)°C for Am(III) (solubility measurements), Eu(III) and Cm(III) (TRLFS).*

Equilibrium reaction	I medium	M	0.1M $NaClO_4$	3M $NaClO_4$	0.1M NaCl	4M NaCl
$M^{3+} + CO_3^{2-} \rightleftharpoons MCO_3^+$	β_1	Am	6.5±0.2	5.6_0±0.3	6.1±0.4	
		Eu				
$MCO_3^+ + CO_3^{2-} \rightleftharpoons M(CO_3)_2^-$	K_2	Am	4.7±0.2	3.4_5±0.3	3.7±0.4	3.8±0.1
		Eu				
$M(CO_3)_2^- + CO_3^{2-} \rightleftharpoons M(CO_3)_3^{3-}$	K_3	Am		2.4_8±0.3 2.0±0.1	1.6±0.4	2.0±0.1
		Cm	1.4±0.3			
		Eu				
$M^{3+} + 2\ CO_3^{2-} \rightleftharpoons M(CO_3)_2^-$	β_2	Am	11.2±0.2	9.0_5±0.3	9.8±0.4	
		Eu				
$M^{3+} + 3\ CO_3^{2-} \rightleftharpoons M(CO_3)_3^{3-}$	β_3	Am	12.6±0.3	11.5_3±0.3	11.4±0.4	
		Eu				
$0.5\ M_2(CO_3)_3(s) \rightleftharpoons M^{3+} + 1.5\ CO_3^{2-}$	$K_{s1.5}$	Am	-15.0±0.2	-15.1_0±0.2	-15.5±0.4	
$NaM(CO_3)_2(s) \rightleftharpoons M^{3+} + 2\ CO_3^{2-} + Na^+$	K_{s2}	Am	-17.5±0.5			
		Eu				
$M_2(CO_3)_3(s) + H_2O \rightleftharpoons 2\ MOHCO_3(s) + CO_2(g)$	${}^*K_{ps1.5\text{-}1}$	Am	-2.0±0.3			
$M_2(CO_3)_3(s) + CO_3^{2-} + 2\ Na^+ \rightleftharpoons 2\ NaM(CO_3)_2(s)$	$K_{s1.5\text{-}2}$	Am		1.2±0.3	3.4±0.4	0.6±0.3

We have proposed other interpretations of solubility measurements of Am(III) in carbonated solutions at $NaClO_4$ 3M (ROBOUCH, 1987), and 0.1M and 4M NaCl (GIFFAUT, 1994), previously performed in the laboratory (VERCOUTER, 2004). After correcting the raw data from batch experiments for the possible modification of the $CO_2(g)$ partial pressure in equilibrium with the solutions, different interpretations were tested, based on the nature of the solubility-controlling solid phase and its possible change during the experiments, in order to explain the solubility measurements performed at ambient temperature (22±2°C) in different ionic media, and between 20 and 70°C in 4M NaCl. The nature of the solubility-controlling phase can only be determined from the shape of the solubility curves described by the data points. In the experiments as a function of the temperature, the temperature of the batch solutions was varied step by step from 70°C down to 20°C (phase 1), and then up to 70°C again (phase 2). As an example, data at 30 and 70°C were selected because measurements were made during the two phases of the temperature change (Figure 1). The data points from the two phases more or less overlap, which confirm that equilibrium was achieved,

and that the solid phases had not significantly been altered by the temperature cycle, except maybe for measurements at $[CO_3^{2-}]$>0.1M at 70°C comparing the results from the phase 1 and 2. After testing different interpretations, it is concluded that $Am_2(CO_3)_3(s)$ and $NaAm(CO_3)_2(s)$ are the most probable solubility-controlling phases according to the low scattering of the data around the corresponding theoretical solubility curves (see the close symbols in Figure 1). On the contrary, a control of the solubility by $AmOHCO_3(s)$, which was considered in the original publication (GIFFAUT, 1994), is more unlikely according to the scattering of the data points around what would be the theoretical curve (see the open symbols in Figure 1). From this interpretation, a set of thermodynamic parameters have been derived for both complexation and dissolution reactions, and are reported in the tables 1 and 2. The $AmCO_3^+$, $Am(CO_3)_2^-$, and $Am(CO_3)_3^{3-}$ stoichiometries have been confirmed as in the original works, but the complexation constants and the relative stabilities of the solid compounds $Am_2(CO_3)_3(s)$, $AmOHCO_3(s)$ and $NaAm(CO_3)_2(s)$ were significantly altered.

Table 2: *Thermodynamic data at 25°C for Am(III) (NaCl 4M), and Cm(III) ($NaClO_4$ 3M)*

Equilibrium reaction	lg K	$\Delta_r G$ kJ·mol^{-1}	$\Delta_r H$ kJ·mol^{-1}	$\Delta_r C_p$ J·mol^{-1}·K^{-1}	$\Delta_r S$ J·mol^{-1}·K^{-1}
$0.5\ Am_2(CO_3)_3(s) \rightleftharpoons AmCO_3^+ + 0.5\ CO_3^{2-}$	-20.6±0.1	51.1±0.6	-63.1±8.4	1850±390	-383±34
$0.5\ Am_2(CO_3)_3(s) + 0.5\ CO_3^{2-} \rightleftharpoons Am(CO_3)_2^-$	-5.3±0.1	30.1±0.6	-42.9±3.2		-245±22
$0.5\ Am_2(CO_3)_3(s) + 1.5\ CO_3^{2-} \rightleftharpoons Am(CO_3)_3^{3-}$	-3.2±0.1	18.3±0.6	-45.6±3.5		-214±22
$NaAm(CO_3)_2(s) + CO_3^{2-} \rightleftharpoons Na^+ + Am(CO_3)_3^{3-}$	-3.6±0.1	20.5±0.6	-41.5±7.3		-208±31
$AmCO_3^+ + CO_3^{2-} \rightleftharpoons Am(CO_3)_2^-$	3.8±0.1	-21.5±0.6	-5.7±12.1	-1340±560	53±45
$Am(CO_3)_2^- + CO_3^{2-} \rightleftharpoons Am(CO_3)_3^{3-}$	2.0±0.1	-11.4±0.6	10±10		72±39
$Cm(CO_3)_2^- + CO_3^{2-} \rightleftharpoons Cm(CO_3)_3^{3-}$	2.0±0.1	-11.5±0.6	12.2±4.4		79±24

Eu(III) and Cm(III) in carbonated solutions studied by TRLFS

The complexation reactions of Eu(III) with the carbonate ligands have been studied by using TRLFS on buffered solutions at either controlled $CO_2(g)$ partial pressure or with dissolved sodium bicarbonate and/or carbonate salts. The ionic strength was maintained by the addition of $NaClO_4$. Thank to the high detection limit of our TRLFS set-up, very low Eu(III) concentrations (down to 20 nM) were used in order to avoid precipitation. Sensitivity analysis of the TRLFS data was consistent with the formation of carbonate complexes as major species, but did not enable us to unambiguously determine whether the stoichiometry of the limiting complex was $Eu(CO_3)_3^{3-}$ or $Eu(CO_3)_4^{5-}$ (VERCOUTER, 2004). With the help of solubility measurements of $NaEu(CO_3)_2(s)$, we have concluded that $Eu(CO_3)_3^{3-}$ forms in concentrated Na_2CO_3 solutions (VERCOUTER et al., 2005a). Thus equilibrium constants were finally deduced from the TRLFS data (Table 1). In similar Na_2CO_3 solutions as for the study of Eu(III) complexes, the temperature influence on the formation constant K_3 for the limiting carbonate complex of Cm(III) was determined for the first time by TRLFS (VERCOUTER et al., 2005b). The enthalpy and entropy of the reaction have been

derived from the Van't Hoff plot. The temperature-dependence of lg K_3 compared very well between Cm(III) and Am(III) (Table 2). This result supports the analogy between the two cations even in concentrated carbonate solutions, on the contrary to what is proposed by (GUILLAUMONT et al., 2003).

Data comparison using the SIT formula

The SIT formula allowed us, with the estimation of ion interaction parameters, to calculate the activity coefficients of the complexes and to extrapolate the equilibrium constants to reference conditions, in consistency with the approach selected in the NEA/OECD databases (Table 3). The constants of a given equilibrium reaction that have been determined for the different cations Am(III), Cm(III), and Eu(III) have values with overlapping uncertainties. The only significant difference between Am(III) and Eu(III) is for lg $K_2°$. Accurate determination of lg $K_2°$ is only possible under a narrow range of carbonate concentration, and it cannot be excluded that the uncertainties of ±0.3 are rather optimistic, especially for the data from the solubility measurements; indeed, two lg $K_2°$ values, 4.7 and 3.7, were determined at I=0.1M. Although the ionic medium was different (NaCl vs $NaClO_4$), one can expect that it has not a remarkable effect on the values. So, the lg $K_2°$ values from solubility experiments are to be used with caution, while the data from TRLFS on Eu(III) is probably more accurate.

Table 3: lg $K°$ for reactions with carbonate after extrapolation to I = 0.

Equilibrium reaction	M	Am	Cm	Eu
$M^{3+} + CO_3^{2-} \rightleftharpoons MCO_3^+$	β_1	7.7±0.3		7.8±0.2
$MCO_3^+ + CO_3^{2-} \rightleftharpoons M(CO_3)_2^-$	K_2	4.3±0.3		5.1±0.3
$M(CO_3)_2^- + CO_3^{2-} \rightleftharpoons M(CO_3)_3^{3-}$	K_3	1.3±0.3	0.9±0.1	1.0±0.3
$M^{3+} + 2\ CO_3^{2-} \rightleftharpoons M(CO_3)_2^-$	β_2	12.0±0.3		12.9±0.2
$M^{3+} + 3\ CO_3^{2-} \rightleftharpoons M(CO_3)_3^{3-}$	β_3	13.3±0.3		13.0±0.3
$0.5\ M_2(CO_3)_3(s) \rightleftharpoons M^{3+} + 1.5\ CO_3^{2-}$	$K_{s1.5}$	-17.5±0.4		
$NaM(CO_3)_2(s) \rightleftharpoons M^{3+} + 2\ CO_3^{2-} + Na^+$	K_{s2}	-21.5±0.5		-20.9±0.5
$M_2(CO_3)_3(s) + H_2O \rightleftharpoons 2\ MOHCO_3(s) + CO_2(g)$	${}^*K_{ps1.5\text{-}1}$	-2.0±0.3		
$M_2(CO_3)_3(s) + CO_3^{2-} + 2\ Na^+ \rightleftharpoons 2\ NaM(CO_3)_2(s)$	$K_{s1.5\text{-}2}$	4.0±0.4		

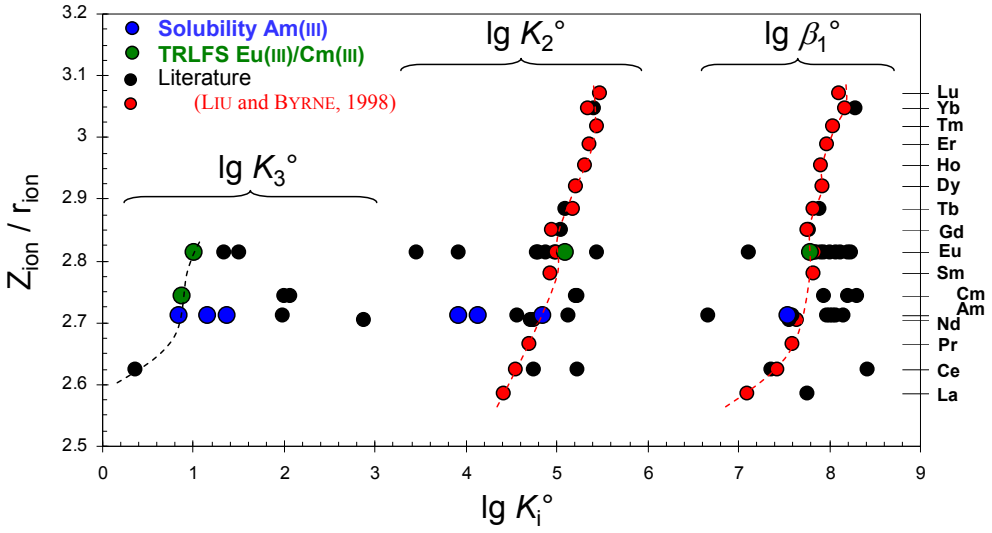

***Figure 2**: Comparison of the values of lg K_i° (i = 1-3) (K_1 = □$_1$) as functions of the charge-over-ionic radius ratio Z_{ion} / r_{ion} for An^{3+} and Ln^{3+} ions.*

The available data from the literature exhibit significant discrepancies that considerably limit their use for relevant speciation calculations (Figure 2). However, according to (LIU and BYRNE, 1998), the lg K° values increase as the ratio of the charge over the ionic radius of the metal ion increases. The equilibrium constants that we have determined from solubility and spectroscopic methods are consistent with this trend, except a larger deviation for some of the K_2° (and β_2°) values derived from the solubility data, for which the uncertainty should probably be increased due to the small predominance domain of the di-carbonate complex. The stepwise formation constants for the carbonate complexes of Am(III), Cm(III), and Eu(III) are very comparable, which supports the validity of the analogy.

Sulphate complexation

Sulphate complexes of Eu(III) studied by TRLFS

The $EuSO_4^+$ and $Eu(SO_4)_2^-$ complexes were identified at variable ionic strength by TRLFS. The concentrations of each Eu(III) species were measured from the fluorescence spectra, and the corresponding equilibrium constants were derived and extrapolated to zero ionic strength with the use of the SIT formula. It should be noted that sulphate has a moderate complexing power toward Ln(III), and therefore the amount of sulphate that is required to study the complexation is such that it can be of the same order of magnitude as the amount of the background electrolyte ($NaClO_4$); hence, the SIT formula was developed to account for the contribution of sulphate in the activity coefficients of the Eu(III) species. The lg K° values (Table 4) are in good agreement with a large number of data obtained by classical techniques for Eu, Am and Cm, which supports the good analogy between these cations and the relevance of the SIT parameters that were used in the data treatment. The results however significantly differ with the ones from another TRLFS study on Cm(III), selected in the updated NEA/OECD database (GUILLAUMONT et al., 2003). This work is detailed in (VERCOUTER et al., 2005c).

Sulphate complexes of U(VI) studied by TRLFS

TRLFS experiments were performed to investigate the complex formation of U(VI) with sulphate. The stoichiometries of the sulphate complexes, particularly $UO_2(SO_4)_3^{4-}$, were confirmed. The dependence of the formation constants on the temperature was also investigated by measuring fluorescence spectra between 10 and 80°C at controlled ionic strength. Quantitative determination of the species concentrations from the spectra was not straightforward because of possible fluorescence quenching effects that depend on concentrations, and because fluorescence may provide information on the chemistry of both the ground state and the excited state of U(VI) species (SZABO et al., 2006). Using peak deconvolution applied to fluorescence spectra that were measured in sulphate solutions with 0.1M $NaClO_4$, we managed to obtain quantitative data that are reported in the table 4. This work is detailed in (VERCOUTER et al., 2008). The thermodynamic data were compared to the NEA/OECD selected ones (GUILLAUMONT et al., 2003): for lg $\beta_1°$ and lg $K_2°$, the values $3.2_ç$ and 1.0_4, respectively, agree fairly well with 3.15±0.02 and 0.99±0.07 recommended by the NEA/OECD; $\Delta_r H_2°$ is also in good agreement with 15.6±1.3 kJ·mol^{-1} whereas $\Delta_r H_1°$ is about ten kJ·mol^{-1} higher than the value 19.5±1.6 kJ·mol^{-1}.

Table 4: Thermodynamic data at 25°C for Eu(III), and U(VI).

Equilibrium reaction		lg $K°$	$\Delta_r G°$ kJ·mol^{-1}	$\Delta_r H°$ kJ·mol^{-1}	$\Delta_r S°$ J·mol^{-1}·K^{-1}
$Eu^{3+} + SO_4^{2-} \rightleftharpoons EuSO_4^+$	β_1	3.7_8±0.1	-21.6±0.6		
$EuSO_4^+ + SO_4^{2-} \rightleftharpoons Eu(SO_4)_2^-$	K_2	1.5±0.2	-8.6±1.2		
$UO_2^{2+} + SO_4^{2-} \rightleftharpoons UO_2SO_4(aq)$	β_1	$3.2_ç$±0.1	-18.7±0.6	29.1±4.0	145±13
$UO_2SO_4(aq) + SO_4^{2-} \rightleftharpoons UO_2(SO_4)_2^{2-}$	K_2	1.0_4±0.1	-5.9±0.6	16.6±4.5	77±15

Conclusion

Complexation reactions of Am(III), Cm(III), Eu(III), and U(VI) with carbonate and sulphate anions have been studied by solubility measurements and TRLFS. In the case of interactions with carbonate, the stoichiometries of the aqueous mono-, di-, and tricarbonate complexes of M(III) were confirmed. Values of the constants of equilibrium reactions have been determined in various ionic media and at different temperatures. The proposed set of values show that the three trivalent cations can be treated as analogues even in concentrated solutions, on the contrary to what was recommended by the NEA/OECD thermochemical database for Am(III) and Cm(III). From the solubility measurements, constants of equilibrium reactions involving Am(III) solid phases were obtained, which enables to assess their relative stability. Interactions of Eu(III) and U(VI) with sulphate were investigated, and complex formation constants were determined. Whereas a good agreement with many literature data was observed, some data were found to be significantly different with data selected by the NEA/OECD. Enthalpy and entropy of reactions were determined, and can be used to assess the temperature effect on complex and solid phase stabilities, for which little information was available.

Acknowledgement

This work was funded by DSOE/Basic Research and DDIN/DPRGD within the cooperative research and development CT4 program CEA-ANDRA-EDF, and the Integrated Project FUNMIG.

References

Giffaut E. (1994) Influence des ions chlorures sur la chimie des actinides, Paris-sud.

Guillaumont R., Fanghänel T., Fuger J., Grenthe I., Neck V., Palmer D. A., and Rand M. H. (2003) *Update on the Chemical Thermodynamics of Uranium, Neptunium, Plutonium, Americium and Technetium*. Elsevier B.V.

Liu X. W. and Byrne R. H. (1998) Comprehensive investigation of yttrium and rare earth element complexation by carbonate ions using ICP mass spectrometry. *Journal of Solution Chemistry* **27**(9), 803-815.

Robouch P. B. (1987) Contribution à la prévision du comportement de l'américium, du plutonium et du neptunium dans la géosphère ; données géochimiques, Louis Pasteur.

Silva R. J., Bidoglio G., Rand M. H., Robouch P. B., Wanner H., and Puigdomenech I. (1995) *Chemical Thermodynamics of Americium*. Elsevier B.V.

Szabo Z., Toraishi T., Vallet V., and Grenthe I. (2006) Solution coordination chemistry of actinides: Thermodynamics, structure and reaction mechanisms. *Coordination Chemistry Reviews* **250**(7-8), 784-815.

Vercouter T. (2004) Complexes aqueux de lanthanides(III) et actinides(III) avec les ions carbonate et sulfate. Etude thermodynamique par spectrofluorimétrie laser résolue en temps et spectrométrie de masse à ionisation électrospray, Université Evry Val d'Essonne.

Vercouter T., Vitorge P., Trigoulet N., Giffaut E., and Moulin C. (2005a) $Eu(CO_3)_3^{3-}$ and the limiting carbonate complexes of other M^{3+} f-elements in aqueous solutions: a solubility and TRLFS study. *New Journal of Chemistry* **29**(4), 544-553.

Vercouter T., Vitorge P., Amekraz B., Giffaut E., Hubert S., and Moulin C. (2005b) Stabilities of the Aqueous Complexes $Cm(CO_3)_3^{3-}$ and $Am(CO_3)_3^{3-}$ in the Temperature Range 10-70 °C. *Inorganic Chemistry* **44**(16), 5833-5843.

Vercouter T., Amekraz B., Moulin C., Giffaut E., and Vitorge P. (2005c) Sulfate Complexation of Trivalent Lanthanides Probed by Nanoelectrospray Mass Spectrometry and Time-Resolved Laser-Induced Luminescence. *Inorganic Chemistry* **44**(21), 7570-7581.

Vercouter T., Vitorge P., Amekraz B., and Moulin C. (2008) Stoichiometries and Thermodynamic Stabilities for Aqueous Sulfate Complexes of U(VI). *Inorganic Chemistry* **47**, 2180-2189.

SILICATE COMPLEXATION OF TRIVALENT LANTHANIDES AND ACTINIDES

Thomas Vercouter*, Badia Amekraz†, Christophe Moulin††

CEA, DEN, Laboratory of Speciation of Radionuclides and Molecules,
F-91191 Gif-sur-Yvette, France.
† Current affiliations: AREVA NC BU-T, F-92084 La Défense, France.
†† Current affiliations: CEA, DIF, Service Radioanalyse, Chimie, Environnement,
F-91297 Arpajon, France.

* Corresponding author: thomas.vercouter@cea.fr

Abstract

This paper summarizes the thermodynamic data available for the formation of silicate complexes of trivalent lanthanide and actinide ions. The objective was to identify the need for further investigations of the interaction between these metal ions and silicate in aqueous solutions.

Introduction

The state of the knowledge about silicate complexation of trivalent f-block ions, actinides An(III) and lanthanides Ln(III), was examined. This survey is based on a CEA technical report released in 1999 (PERETROUKHINE, 1999), and the more recent literature, specially the updated NEA/OECD database (GUILLAUMONT et al., 2003) and publications. The aim is to figure out whether the available data are sufficient for predictive purposes of the speciation of An(III) in the presence of Si species, that is:

- the number of independent determinations of complex formation constants and the reliability of the values of the stability of silicate aqueous complexes;
- the physico-chemical conditions that were investigated (temperature, pH, [Si], …) and the occurrence of Si polymerisation;
- the characterisation of possible complexes with polynuclear silicate anions.

Silicate speciation

Monosilicic acid (or orthosilicic acid), $Si(OH)_4(aq)$, and polysilic acid may exist in aqueous solutions. The first *pKa* of the monosilicic acid (or orthosilicic acid),

$Si(OH)_4(aq)$, ranges between 9.46 and 9.86 at zero ionic strength (PANAK et al., 2005), and corresponds to the following equilibrium

$$Si(OH)_4(aq) \leftrightarrow SiO(OH)_3^- + H^+$$

The value 9.81 ± 0.02 is recommended by (GUILLAUMONT et al., 2003).
The second *pKa* is estimated around 11.5 for the reaction

$$SiO(OH)_3^- \leftrightarrow SiO(OH)_2^{2-} + H^+$$

It is claimed that the monosilicic acid dominates at pH < 9 when the Si concentration is below the solubility of the amorphous silica SiO_2 (2 mM). For higher pH, formation of polysilicates occurs, which increases the solubility of SiO_2. The rate of polymerisation is dependent on the chemical and physico-chemical conditions (ILER, 1979).

The concentration of the monosilicic acid is often determined by the colorimetric β-silicomolybdate method, which is based on the reactivity of hetero polymolybdate with silicate, and the strong absorbance of the resulting complex (ALEXANDER, 1953; BION, 1999). When the absorbance is measured 1 or 2h after addition of molybdate, only the complex formed with monosilicic acid is supposedly responsible of the absorbance, whereas the reaction with polysilicic acid is slower. Consequently, it is known as a method for titration of $Si(OH)_4(aq)$ even when polysilicic acid is present. After longer time of contact with the molybdate, reactions occur with polysilicic acids, when present. However, it has been argued that, even at short reaction time, this technique rather provides the total concentration of the soluble monomeric, dimeric and trimeric silicic acids when such oligomers are also present in solution (ILER, 1979).

As a consequence, small oligomeric silicic acids might be hardly detected. However, they could be potential ligands of metal cations since they have similar hydroxyl moieties as those of the monosilicic acid. Moreover, there might be bias in the determinations of complexation constants between monosilicic acid and metal cations if oligomeric silicic acids were also present, but not detected under the experimental conditions.

Interaction with M^{3+}

The monosilicate anion, $SiO(OH)_3^-$, has been observed to complex Eu^{3+}, Am^{3+}, and Cm^{3+} (JENSEN, 1994; JENSEN and CHOPPIN, 1996; PANAK et al., 2005; PATHAK and CHOPPIN, 2006; STEINLE et al., 1997; THAKUR et al., 2007; WADSAK et al., 2000; WANG et al., 2005), with a 1:1 stoichiometry according to the following equilibria

$$M^{3+} + Si(OH)_4(aq) \leftrightarrow MSiO(OH)_3^{2+} + H^+ \qquad K_1$$
$$M^{3+} + SiO(OH)_3^- \leftrightarrow MSiO(OH)_3^{2+} \qquad \beta_1$$

The formation of $M(SiO(OH)_3)_2^+$ (β_2) has also been considered, as well as the interaction with polymeric or colloidal forms of silica, which is discussed below.

Europium(III)

Eu(III) complexation by monosilicicate was studied by Choppin and coworkers, and the data reported in (JENSEN, 1994; JENSEN and CHOPPIN, 1996) were also discussed in a previous survey (PERETROUKHINE, 1999). The lg β_1 values were obtained at I = 0.1M by solvent extraction and time-resolved laser-induced fluorescence spectroscopy (TRLFS) and are in very good agreement (Table **4**). The investigations were conducted at pH < 9, and [Si] was chosen as to prevent from the formation of polysilicate according to the authors. Eu(III) seems to form the $Eu(SiO(OH)_3)_2^+$ complex at pH > 8 according to the authors, which appears to be disagreed by similar experiments on the analogous Cm(III), which rather suggest the formation of colloidal Cm(III) silicate species at such pH (PANAK et al., 2005). Values of lg β_1 were measured by solvent extraction at I = 0.2M as a function of the temperature (5-45°C) by (PATHAK and CHOPPIN, 2006), and enthalpy and entropy of the reaction were determined: $\Delta_r H_1$ = 14.5±1.0 kJ·mol^{-1} and $\Delta_r S_1$ = 197.7±3.2 J·mol^{-1}·K^{-1} at I=0.2M ($NaClO_4$). Similar experiments were carried out at 25°C and different ionic strengths under conditions where polysilicic acid was present (THAKUR et al., 2007).

***Table** 4 Conditional formation constants for $Eu^{3+} + SiO(OH)_3^- \leftrightarrow EuSiO(OH)_3^{2+}$ (β_1) and $Eu^{3+} + 2SiO(OH)_3^- \leftrightarrow Eu(SiO(OH)_3)_2^+$ (β_2) at 25°C.*

Method	Medium	pH	[Si] (mM)	lg β_1	(lg β_2)	Ref.
Solv. extr.	0.1M NaCl	3.5-4.6	0-9	7.16±0.34		(JENSEN and CHOPPIN, 1996)
Solv. extr.	0.1M $NaClO_4$	5-9	<2.3	7.25±0.13	(11.7±0.4)	(JENSEN and CHOPPIN, 1996)
TRLFS	0.1M $NaClO_4$	5.8-6.4	0.3-2	7.36±0.15		(JENSEN and CHOPPIN, 1996)
Solv. extr.	0.2M $NaClO_4$	3.2	0.7-8	7.79±0.01		(PATHAK and CHOPPIN, 2006)
Solv. extr.	0.20M $NaClO_4$	3.5	2-200	7.81±0.11		(THAKUR et al., 2007)
Solv. extr.	0.50M $NaClO_4$	3.5	2-200	7.62±0.08		(THAKUR et al., 2007)
Solv. extr.	0.75M $NaClO_4$	3.5	2-200	7.43±0.12		(THAKUR et al., 2007)
Solv. extr.	1.00M $NaClO_4$	3.5	2-200	7.38±0.13		(THAKUR et al., 2007)
Review	0.1M $NaClO_4$			7.26±0.21	(11.7±0.4)	(PERETROUKHINE, 1999)

The lg β_1 values were converted to lg K_1 values to account for the different *pKa* values used originally, and extrapolation to I = 0 was performed for a better comparison using the Specific Ion interaction Theory (SIT) from (GUILLAUMONT et al., 2003) (Table 5). The lg K_1° values are distributed into two groups of values around -1.9 (JENSEN and CHOPPIN, 1996) or -1.2 (PATHAK and CHOPPIN, 2006; THAKUR et al., 2007). All these data were proposed by the group of Choppin. However, the discrepancies were not discussed. A possible biais on some values might originate from the presence of polysilicic acid since the Si concentrations were higher than the solubility of amorphous silica in some of the experimental conditions.

Solubility measurements of $Eu(OH)_3$(s) in alkaline silicate solutions in pH range 7.5-12.5 are consistent with complex formation of Eu(III) (WANG et al., 2005). Accordingly, the authors interpreted additional TRLFS experiments on Cm(III) solutions at pH 12 with the formation of complexes that involve polysilicates, which are stable at such high pH, because the increase of the fluorescence intensity of Cm(III) followed approximately the calculated concentrations of these anions.

Table 5 *Formation constants at 25°C converted for Eu^{3+} + $Si(OH)_4(aq)$ ↔ $EuSiO(OH)_3^{2+}$ + H^+ (K_1) from Table 4. We have extrapolated lg K_1 to I = 0 (lg K_1°) with the SIT parameter $\Delta\varepsilon$ = 0.04±0.05 kg mol^{-1} (GUILLAUMONT et al., 2003).*

Method	Medium	*pKa*	lg K_1	lg K_1°	Ref.
Solv. extr.	0.1M NaCl	9.59	–2.43±0.34	–1.99±0.35	(JENSEN and CHOPPIN, 1996)
Solv. extr.	0.1M $NaClO_4$	9.59	–2.34±0.13	–1.90±0.14	(JENSEN and CHOPPIN, 1996)
TRLFS	0.1M $NaClO_4$	9.59	–2.23±0.15	–1.79±0.16	(JENSEN and CHOPPIN, 1996)
Solv. extr.	0.2M $NaClO_4$	9.54	–1.76±0.01	–1.20±0.03	(PATHAK and CHOPPIN, 2006)
Solv. extr.	0.20M $NaClO_4$	9.55	–1.74±0.11	–1.18±0.11	(THAKUR et al., 2007)
Solv. extr.	0.50M $NaClO_4$	9.50	–1.88±0.08	–1.16±0.08	(THAKUR et al., 2007)
Solv. extr.	0.75M $NaClO_4$	9.49	–2.06±0.12	–1.26±0.12	(THAKUR et al., 2007)
Solv. extr.	1.00M $NaClO_4$	9.48	–2.10±0.13	–1.24±0.12	(THAKUR et al., 2007)
Review	0.1M $NaClO_4$	9.59	–2.33±0.39	–1.89±0.41	(PERETROUKHINE, 1999)

Americium/curium(III)

Data have been reviewed in 2003 by the NEA/OECD (GUILLAUMONT et al., 2003), and two studies (STEINLE et al., 1997; WADSAK et al., 2000) were found to give relevant results for the monosilicate aqueous complex $CmSiO(OH)_3^{2+}$ and $AmSiO(OH)_3^{2+}$ (Table 6). The formation constants for both cations are in good agreement, and the mean value –1.68 ± 0.18 was selected for lg K_1° at 25°C. A brief description of the work by (STEINLE et al., 1997) is given in (GUILLAUMONT et al., 2003): a 0.36 mM solution of monosilicic acid has been prepared by rapid acidification of sodium silicate, and the investigations were conducted at pH < 5.5. One can expect that this procedure prevented polymerisation of silicate unless metastable oligomeric species have formed. So polymerisation cannot be excluded. In (WADSAK et al., 2000), fractions of polymeric silicate were observed in the solutions ([Si] = 30 mM), but the determination of lg K_1 was considered to be still relevant. However, pH was lower than 3.8, which appears to be low to clearly observe the formation of $AmSiO(OH)_3^{2+}$.

Since this review, new data have been reported in the literature for the interaction between silicates and Am(III) or Cm(III). The interaction of Cm(III) with aqueous mono- and polysilicates has been studied by TRLFS in wider chemical conditions than previous ones (PANAK et al., 2005). The first complexation constant has been derived from the fluorescence spectra (Table 6). The formation of colloidal species of Cm^{3+} was thoroughly studied using ultracentrifugation. The main conclusions of this work are that different colloidal species formed in addition to $CmSiO(OH)_3^{2+}$, whereas no $Cm(SiO(OH)_3)_2^+$ bisorthosilicate complex was observed. Increasing [Si] and pH favoured the formation of badly defined species for which fluorescence characteristics were close, but variable. These were considered as "transitional" species, probably oligomeric, polymeric or colloidal. At [Si] = 13 mM, a Cm-silicate colloidal species was suggested from the fluorescence spectra, where Cm^{3+} would be imbedded into the bulk structure of silica colloids.

Values of lg β_1 were measured for Cm(III) at I = 0.2M as a function of temperature, and the enthalpy and entropy of the reaction were determined: $\Delta_r H_1$ = 15.8±2.0 kJ·mol^{-1} and $\Delta_r S_1$ = 203.0±6.4 J·mol^{-1}·K^{-1} at I=0.2M ($NaClO_4$), in good agreement with the values for Eu(III) (PATHAK and CHOPPIN, 2006). Complexation of Am(III) and Cm(III) was investigated at 25°C as a function of ionic strength (THAKUR et al., 2007), similarly to the Eu(III) experiments discussed above. The corresponding lg K_1° values at 25°C are reported in Table 6.

Like for the comparison of lg $K_1°$ values for Eu(III), discrepancies are observed. The results from (THAKUR et al., 2007) predict a higher stability of the silicate complexes compared to the other studies. Again, an effect of the presence of polysilicic acid cannot be ruled out whereas it was claimed by (THAKUR et al., 2007) that it could be ignored at pH around 3.5.

Table 6 *Formation constants at 25°C for $M^{3+} + Si(OH)_4(aq) \leftrightarrow MSiO(OH)_3^{2+} + H^+$ (K_1) with M=Am and Cm. We have extrapolated lg K_1 to I = 0 (lg $K_1°$) with the SIT parameter $\Delta\varepsilon = 0.04\pm0.05$ kg mol^{-1} (GUILLAUMONT et al., 2003).*

An	Method	Medium	pH	[Si] (mM)	lg K_1	lg $K_1°$	Ref.
Am	Solv. extr.	0.2M $NaClO_4$	3.0-3.8	30	–2.16±0.04	–1.61±0.08	(WADSAK et al., 2000)
Am	Solv. extr.	0.20M $NaClO_4$	3.5	2-200	–1.53±0.10	–0.97±0.10	(THAKUR et al., 2007)
Am	Solv. extr.	0.50M $NaClO_4$	3.5	2-200	–1.64±0.09	–0.92±0.09	(THAKUR et al., 2007)
Am	Solv. extr.	0.75M $NaClO_4$	3.5	2-200	–1.79±0.11	–0.93±0.11	(THAKUR et al., 2007)
Am	Solv. extr.	1.00M $NaClO_4$	3.5	2-200	–1.81±0.12	–0.95±0.12	(THAKUR et al., 2007)
Cm	TRLFS	0.1M $NaClO_4$	5.0-5.5	0.36	–2.2±0.1	–1.76±0.10	(STEINLE et al., 1997)
Cm	TRLFS	0.03M NaCl	1.5-9.0	0.27-0.96	–2.34±0.10	–2.07±0.10	(PANAK et al., 2005)
Cm	Solv.Extr.	0.2M $NaClO_4$	3.2	2-17	–1.71±0.02	–1.24±0.04	(PATHAK and CHOPPIN, 2006)
Cm	Solv. extr.	0.20M $NaClO_4$	3.5	2-200	–1.77±0.08	–1.21±0.08	(THAKUR et al., 2007)
Cm	Solv. extr.	0.50M $NaClO_4$	3.5	2-200	–1.91±0.10	–1.19±0.10	(THAKUR et al., 2007)
Cm	Solv. extr.	0.75M $NaClO_4$	3.5	2-200	–2.07±0.09	–1.26±0.09	(THAKUR et al., 2007)
Cm	Solv. extr.	1.00M $NaClO_4$	3.5	2-200	–2.11±0.13	–1.25±0.13	(THAKUR et al., 2007)
Am/Cm	Review	$I \rightarrow 0$				–1.68±0.18	(GUILLAUMONT et al., 2003)

Comparison of formation constants

The values of lg K_1 measured for Eu(III), Am(III), and Cm(III) were plotted as a function of ionic strength to evaluate the discrepancies (Figure 1). It can be observed that the values for Am(III) and Cm(III) recommended by (GUILLAUMONT et al., 2003) only agree with a few experimental values. The values for Cm(III) from (PANAK et al., 2005) is significantly lower than the predicted one, whereas the values from (THAKUR et al., 2007) for Am(III) and Cm(III) are significantly higher.

The variation of lg K_1 with the ionic strength data from (THAKUR et al., 2007) are however consistent with the trend predicted by the SIT parameters recommended by (GUILLAUMONT et al., 2003). For every cation extrapolated lg $K_1°$ values from the lg K_1 values at the different ionic strengths with the SIT formula give virtually the same value, which supports the reliability of the $\Delta\varepsilon$ coefficient used. It can also be observed that the data for Eu(III) and Cm(III) from (THAKUR et al., 2007) are very similar, which would support the chemical analogy between these two elements; however the values for Am(III) are slightly higher, which could indicate either a slightly different chemical behaviour compared to Eu(III) and Cm(III), or a systematic error on the Am(III) results.

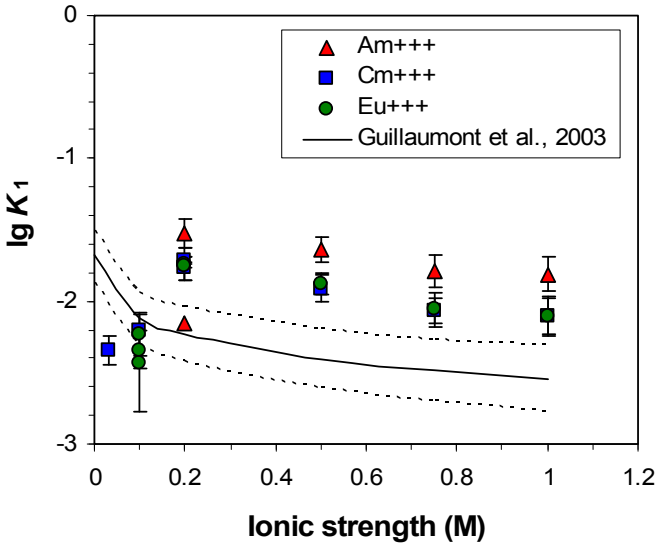

Figure 1: *Values of the formation constants of the monosilicate complexes of Am(III), Cm(III), and Eu(III) as a function of the experimental ionic strengths (see Table 5 and Table 6). The theoretical curve from (GUILLAUMONT et al., 2003) is represented with the corresponding uncertainties (dashed line).*

Conclusions

From this survey of the literature data the following remarks can be formulated:

- Concerning the number of data determinations, complexation constants were measured by two techniques: solvent extraction and TRLFS. The formation of the monosilicic complexes of Am(III), Cm(III) and Eu(III) seems to be well evidenced despite differences in the values of the formation constants of less than one order of magnitude. These differences might result from an effect of partial polymerization of silicates. Indeed, formation of polysilicic acid may have occurred in some of the experimental conditions investigated, which could have biased the interpretation of the data. For instance, a $M(SiO(OH)_3)_2^+$ bisorthosilicate complex has been proposed by (JENSEN and CHOPPIN, 1996) in a solvent extraction study for M = Eu at pH > 6; however, the TRLFS study by (PANAK et al., 2005) did not confirm the formation of the analogous complex for M = Cm, but rather supported the formation of colloidal species at pH > 5. Despite discrepancies in the lg $K°$ values, the analogy between at least Eu(III) and Cm(III) seems to be relevant, since the values measured for these two cations in a same study (PATHAK and CHOPPIN, 2006; THAKUR et al., 2007) are similar. New determinations of the formation constants of $MSiO(OH)_3^{2+}$, with a particular attention to prevent from polymerization, would be welcome. The effect of the ionic strength on the lg K_1 values was studied and appears to be correctly accounted for with the SIT formula. The temperature effect was also studied and a single set of $\Delta_r H_1$ and $\Delta_r S_1$ values is available. Moreover, the formation of $M(SiO(OH)_3)_2^+$, if it can occur, has not been proven yet.

- Measurements were mostly carried out in acidic conditions where complexation is more easily observable. The Si concentration was either above the solubility of the amorphous silica (2 mM) or below it, and is a key parameter. It is clear that polymerization occurs for [Si] > 2 mM even in acidic solutions. However, silicate species other than monosilicic acid can also be created at lower concentrations: colloidal species of Cm^{3+} were observed for [Si] = 0.27 mM at pH 6.5 and removed by ultracentrifugation (PANAK et al., 2005). Thus, it appears that even at low [Si], polymerisation of silicate or formation of colloidal particles may occur, which would change the metal speciation as well.

- The distribution of Cm(III) between the aqueous complex $CmSiO(OH)_3^{2+}$ and colloids was determined by TRLFS and ultracentrifugation from pH 3 to 9 (PANAK et al., 2005). It cannot be excluded that trivalent metal ions can interact with silicate polymers under such conditions, as it is the case for Eu(III) at high pH according to (WANG et al., 2005). The nature of such species (stoichiometry) and the corresponding thermodynamic formation constants might be of fundamental importance in the speciation of trivalent f-block cations in groundwaters. The formation of colloidal or oligomeric species in dilute conditions may modify the speciation of trivalent metal cations (unless dissociation of oligomers can be promoted in natural conditions (DIETZEL, 2000)).

Acknowledgement

This work was funded by DSOE/Basic Research and DDIN/DPRGD within the cooperative research and development CT4 program CEA-ANDRA-EDF, and the Integrated Project FUNMIG.

References

Alexander G. B. (1953) The reaction of low molecular weight silicic acids with molybdic acid. *Journal of the American Chemical Society* **75**, 5655-5657.

Bion L. (1999) Synthèse et caractérisation de solutions aqueuses d'acide orthosilicique H_4SiO_4 en vue de l'étude de la complexation de lanthanides et d'actinides. CEA report, N.T. SESD 99-55, pp. 128-136.

Dietzel M. (2000) Dissolution of silicates and the stability of polysilicic acid. *Geochimica Et Cosmochimica Acta* **64**(19), 3275-3281.

Guillaumont R., Fanghänel T., Fuger J., Grenthe I., Neck V., Palmer D. A., and Rand M. H. (2003) *Update on the Chemical Thermodynamics of Uranium, Neptunium, Plutonium, Americium and Technetium*. Elsevier B.V.

Iler R. K. (1979) *The Chemistry of Silica*. John Wiley and Sons.

Jensen M. P. (1994) Complexation studies of europium(III) and uranium(VI) complexation by aqueous orthosilicic acid, Florida State University.

Jensen M. P. and Choppin G. R. (1996) Complexation of europium(III) by aqueous orthosilicic acid. *Radiochimica Acta* **72**(3), 143-150.

Panak P. J., Kim M. A., Klenze R., Kim J. I., and Fanghänel T. (2005) Complexation of Cm(III) with aqueous silicic acid. *Radiochimica Acta* **93**(3), 133-139.

Pathak P. N. and Choppin G. R. (2006) Thermodynamic study of metal silicate complexation in perchlorate media. *Radiochimica Acta* **94**(2), 81-86.

Peretroukhine V. (1999) The effect of soluble silicon – oxygen compounds on the behaviour and migration of actinides in natural waters and liquid radioactive wastes: Survey of published data. CEA report, N.T. SESD 99-55, pp. 105-127.

Steinle E., Fanghänel T., and Klenze R. (1997) Complexing of Cm(III) with monosilicic acid. FZK report, FZKA-6036, pp. 143-152.

Thakur P., Singh D. K., and Choppin G. R. (2007) Polymerization study of o-Si(OH)(4) and complexation with Am(III), Eu(III) and Cm(III). *Inorganica Chimica Acta* **360**(12), 3705-3711.

Wadsak W., Hrnecek E., and Irlweck K. (2000) Formation of americium(III) complexes with aqueous silicic acid. *Radiochimica Acta* **88**(2), 61-64.

Wang Z., Felmy A. R., Xia Y. X., Qafoku O., Yantassee W., and Cho H. (2005) Complexation of Cm(III)/Eu(III) with silicates in basic solutions. *Radiochimica Acta* **93**(12), 741-748.

ROCK MATRIX CHARACTERISATION FROM MICRO TO CENTIMETRIC SCALES OF SELECTED ROCK CORES FROM BOREHOLES FUN-05-001 (GRIMSEL TEST SITE - SWITZERLAND)

Félix Mateos[1*], Modesto Montoto[1], Marja Siitari-Kauppi[2], Jussi Ikonen[2]

[1] Group of Petrophysics. Department of Geology. University of Oviedo (ESP) Félix Mateos Redondo. Facultad de Geología.
c/ Jesús Arias de Velasco s/n. 33005. Oviedo (España).
[2] Laboratory of Radiochemistry. University of Helsinki (FIN)

* Corresponding author: fjmateos@geol.uniovi.es.

Abstract

The physical properties of the granite matrix pores are at the heart of a proper understanding and representation of radionuclide migration. The main objective of this paper is to demonstrate the advantages that confocal laser scanning microscopy (CLSM) and ^{14}C methylmethacrylate autoradiography method (^{14}C-PMMA) offer to visualize the rock structures adjacent to water pathways and water bearing fissures from micrometric to decimetre scales in the FUNMIG framework. Linking these two rock matrix characterisation methods, the open conductive porosity can be determined from cubic centimetre sized rock samples. The gap between macroscopic and microscopic methods of investigation is filled and this methodology provides quantitative information about nanometre-range porosity from decimeter scale volumes. Three samples presented here are from the rock cores from borehole FUN-05-001, Febex site at Grimsel Test Site – Switzerland. The most hydraulically active zones have been selected for the rock matrix characterization studies at the μm – cm scale. To contribute with the two mentioned techniques, CLSM and ^{14}C-PMMA, to a better imaging and mapping of the water path-ways at the μm-cm scale in low permeable crystalline (fissured) rocks is the aim of this work.

Introduction

Over extended periods, long-lived radionuclides (RN) or activation products within geologic disposal sites may be released from the fuel and migrate to the geo/biosphere. In the bedrock, contaminants will be transported along fractures by advection and retarded by sorption on mineral surfaces and by molecular diffusion into stagnant pore water in the matrix along a connected system of pores and micro-fissures. Within the framework of the internationally accepted “geological solution” for the final disposal of high level radioactive wastes, the water movements and their path-ways, at any scale, through the rock-mass disposal site is one of the key questions to be

understood and predicted. At the rock-matrix scale, that water circulation is basically conditioned by the capacity of water for flowing through the connected pores and fissures; that is, through the open conductive porosity. The key aspects required for the characterization and understanding of the hydrogeological behaviour of the rock-matrix have been summarized in Montoto [1,2,3], as well as the application of different microscopical techniques for evaluating the rock-forming components and mapping the water path-ways versus rock texture and mineralogy.

The imaging, mapping and further quantification of the open effective porosity in low permeable granitic rocks, have been classically performed under fluorescence microscopy, autoradiography and scanning electron microscopy (secondary electrons detector and/or back-scattered electrons detector). From the 90' new techniques and procedures: confocal laser scanning microscopy (CLSM), ^{14}C-polymethylmethacrylate (^{14}C-PMMA) impregnation technique [4,5] and microfocus X-ray computer tomography µCT [6] have been developed for those objectives; more specifically, for a 3D imaging of the water path-ways that at the rock matrix scale, affect the candidate crystalline rocks for the final disposal of HLW.

Methodology

Sampling

Samples of selected rock cores from boreholes FUN-05-001 (Grimsel Test Site - Switzerland). The most hydraulically active zones have been selected for the micro-fractographic studies at the µm – cm scale. A macroscopical detail of rock cores from Febex tunnel at Grimsel Test Site, are presented in Fig. 1.

Figure 1: *A) FUN05-001: 14,63-14,81 m and FUN05-001: 14,74-15,13 m (August fracture); B) FUN05-001: 17,43-17,53 m and FUN05-001: 17,53-17,86 m (September fault zone) and C) FUN05-001: 8,22-8,64 m (June fracture).*

Microfractographic characterization

CLSM offers the ability to collect serial optical sections (or virtual sections) from thick specimens by the elimination of image out-of-focus information; that is, the big advantage of confocal microscopy is the possibility to collect light exclusively from a single plane of the interior of the rock thin section. A pinhole sitting conjugated to the focal plane (i.e. confocal) keeps light from the detector that is reflected/emitted from others than the focal plane; the laser scanning microscope scans the sample sequentially point by point and line by line and assembles the pixel information to one image; that way optical slices of the specimen are imaged with high contrast and high resolution in x, y and z. By moving the focus plane single images (optical slices) can be put together to build up a three dimensional stack that can be digitally processed afterwards (Fig. 2).

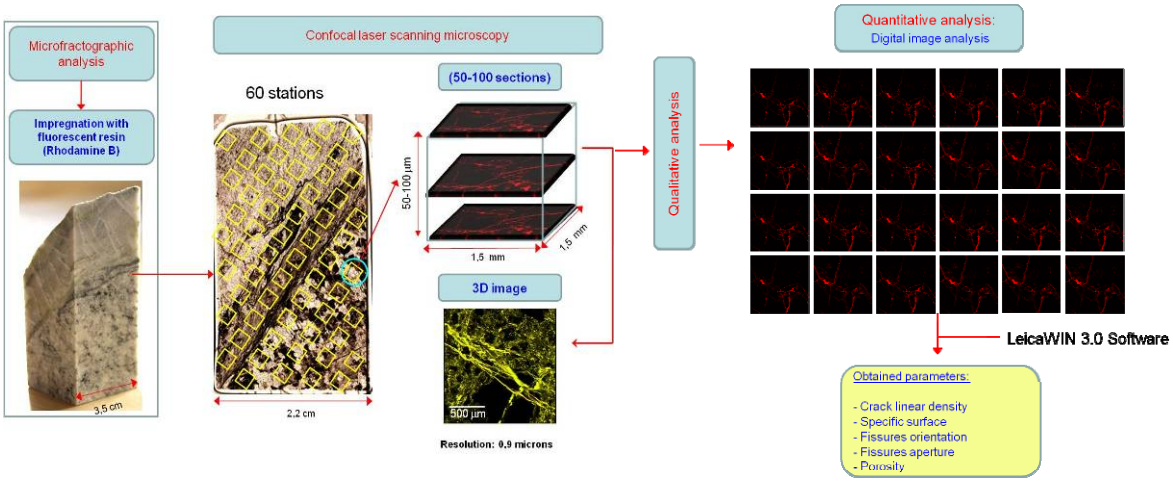

Figure 2. *Illustration about qualitative and quantitative analysis by confocal laser scanning microscopy technique.*

The PMMA method

The PMMA method involves impregnation of centimeter-scale rock cores with ^{14}C labelled methylmethacrylate (^{14}C-MMA) in vacuum. A fourth part of the rock cores FUN05-001: 8,22-8,64 m, June, FUN05-001: 14,74-15,13 m; August fracture and FUN05-001: 17,53-17,86 m; September fault zone were dried in vacuum (T=100 ºC) for 12 days. After drying the samples were impregnated in vacuum for 10 days with a tracer activity of 518 kBq/mL (labeled monomer from the Russian Scientific Centre for Applied Chemistry, St. Petersburg, Russia).

The impregnated samples were polymerized by a ^{60}Co-source so that ^{14}C polymethyl-methacrylate was fixed into the pore space of the rock. The total irradiation dose was 50 kGy. There after the samples were sawn for autoradiography. First the sawn surfaces were to exposed on the conventional x-ray films (Kodak Biomax MR, Kodak-Pathé, Paris, France) for 5 to 14 days. Qualitative and quantitative interpretation of results was based on digital image analysis of these films. The autoradiographs were digitized with a table-top scanner (CanoScan 9900F, Canon, optical resolution 2400 dpi) [6]. The digitized autoradiographs were analysed by Matlab 7.0 using the Image

Processing Toolbox (The MathWorks, 3 Apple Hill drive Natick MA 01760-2098, USA). Program Mankeli (Version 2, 2005) measures film intensities from 8-bit images and converts them to optical densities which are converted with the help of calibration sources to activities. The activities are converted to porosities after beta correction. The amount of tracer in the sample, and the volumetric porosity, can be thus derived from the blackening of the film caused by the radiation emitted from the plane surface of the rock section. If the pore sizes are well below the resolution of the autoradiography, the major fraction of the beta radiation emitted is attenuated by silicate. The tracer can thus be considered to be diluted by silicate. For the ^{14}C-PMMA method to be used, the bulk density must be known, there must be only two phases (i.e. mineral and PMMA), and the pores and minerals must be homogeneously distributed below the lateral resolution limit of the autoradiography.
Figure 3 presents the schematic illustration of the ^{14}C PMMA method.

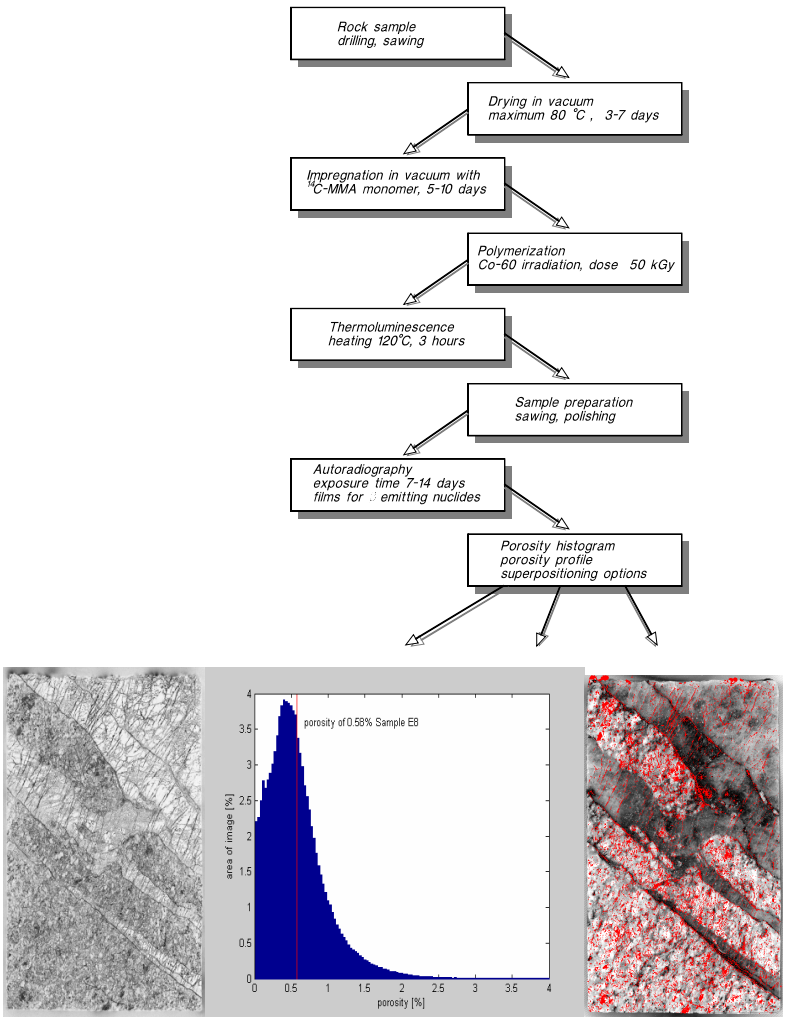

Figure 3: *Procedure of the PMMA method which consist of experimental part and digital image analysis tools.*

Results

Microfractographic characterization

In this chapter are summarized some of the results focusing on the porosity profiles that show the changes in mm-µm scales within the matrix next to the flowing water pathways in the bedrock.
For example, in August fracture (FUN05-001: 14,74-15,13 m), open CLSM porosity was 3,09 % in the altered vein and 2.51% in the matrix. The obtained profiles show a very important decrease in the porosity value (Fig. 4), in the contact between granite and vein, in relation to an impermeable band (B). Plenty of microfissures crossed the vein perpendicular to the conducting fracture surface.

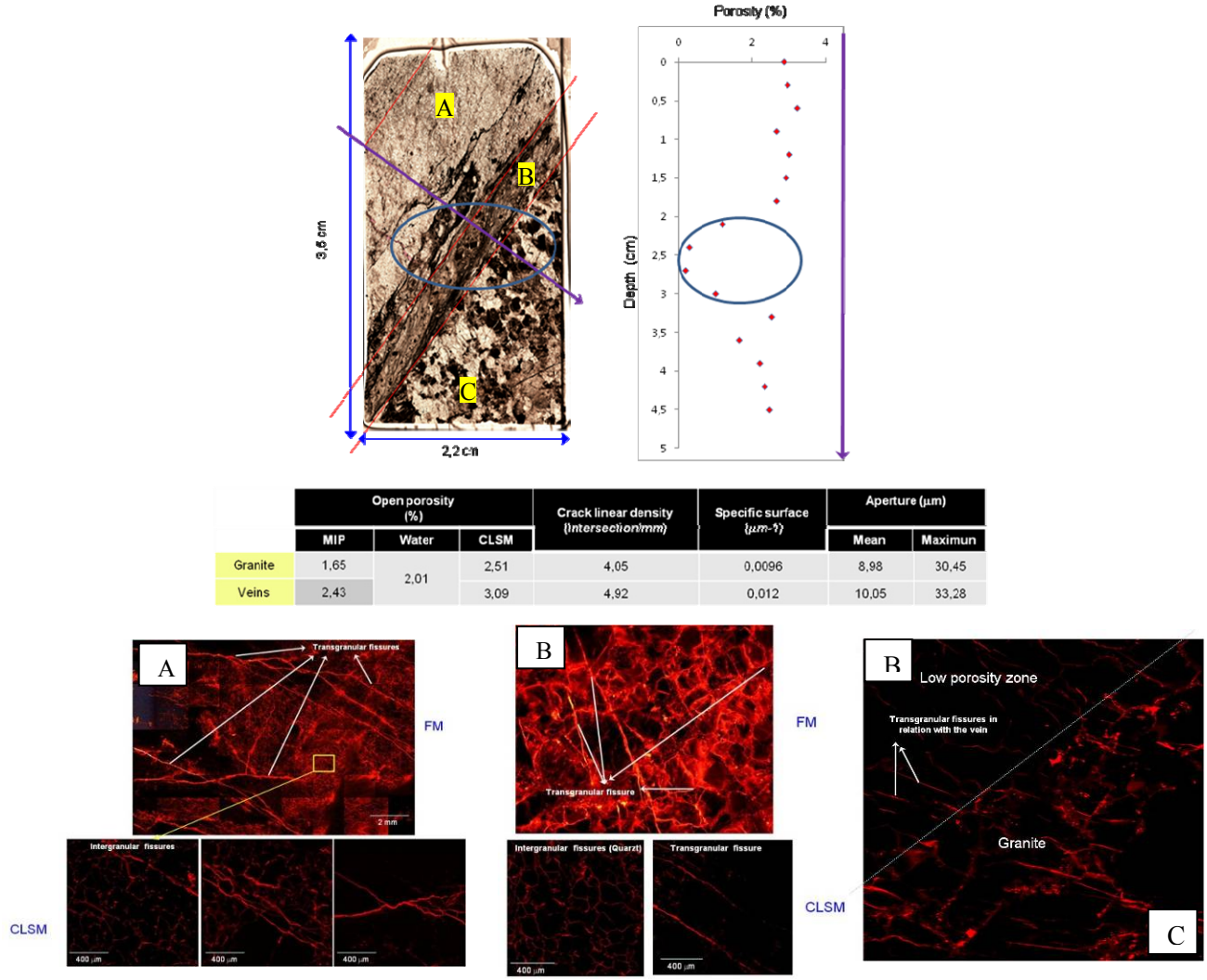

	Open porosity (%)			Crack linear density (Intersection/mm)	Specific surface (µm-1)	Aperture (µm)	
	MIP	Water	CLSM			Mean	Maximun
Granite	1,65	2,01	2,51	4,05	0,0096	8,98	30,45
Veins	2,43		3,09	4,92	0,012	10,05	33,28

Figure 4: *On the top, open porosity profile obtained along August fracture rock core by mean of CLSM and image digital analysis (DIA). On the bottom, some CLSM images in relation to zones of different open porosities observed under CLSM. The results of open porosity (august fracture)measured by different techniques are summarized in the table.*

The PMMA method

In this chapter are summarized the PMMA results focusing on the porosity profiles that show the changes in cm scales within the matrix next to the flowing water pathways in the bedrock.

For example, in August fracture (FUN05-001: 14,74-15,13 m), the total PMMA porosity varied between 1% and 1.5% in the altered vein. However the PMMA porosity in the rock matrix was about 2%. Plenty of micro fractures transect the vein perpendicular to the fracture surface indicating straightforward transport pathways for particles.

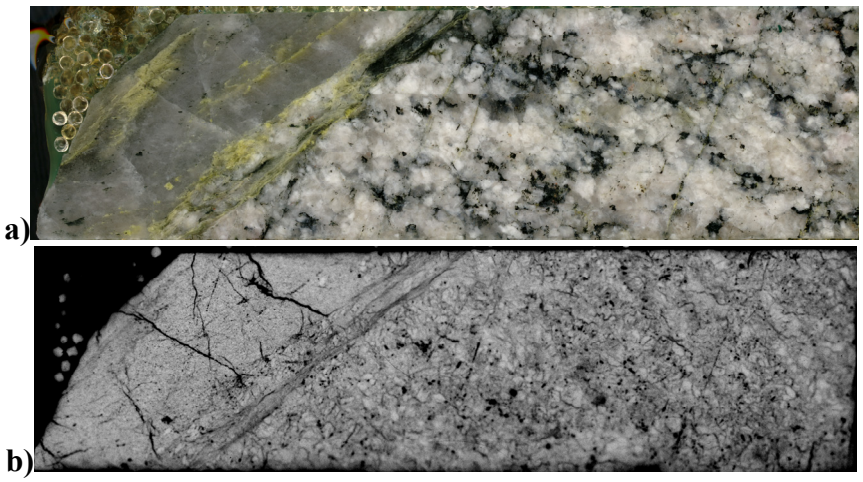

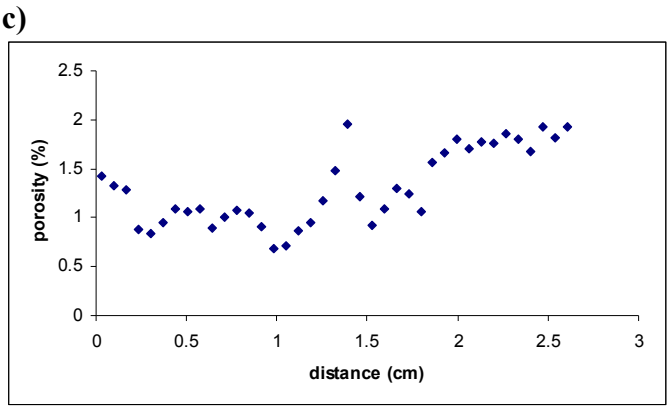

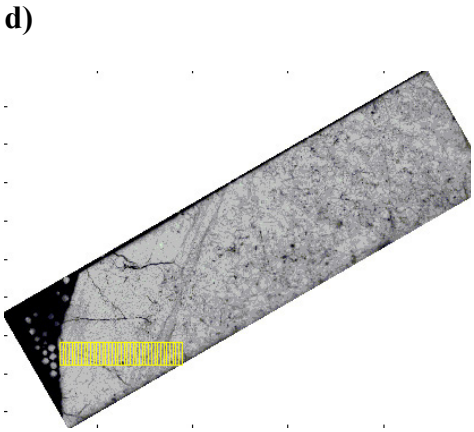

Figure 5: *a) the photo image of sawn August fracture and b) the corresponding PMMA autoradiograph. The darker the shade on the autoradiograph, higher the porosity measured. Sample width is 9 cm. On the bottom, a) porosity profile of sample and d) yellow area measured in the porosity profile.*

Conclusions

Table I presents the porosities measured by the different techniques. The total porosity values measured by ^{14}CPMMA method are slightly lower than with the CLSM and other methods (water or MIP).

However a significant increased porosity zone was not found by these techniques in the sample FUN05-001: 17,43-17,53 (September fault zone). In sample FUN05-001: 8,22-8,64 (June fracture) numerous micro fractures starting from the fracture surface and extending to a depth of 5 mm from the water flowing fracture surface were found. Thus the porous zone was about 5 mm wide. The "porous zones" are taken account of when evaluating RN migration from the conductive water flow paths into the matrix giving "diffusion depth" values of geosphere model parameters.

The two centimetre thick vein showed lower porosity than the virgin rock matrix in sample FUN05-001: 14,74 -15,13 (August fracture) by the PMMA method. However the micro fractures that transects the vein act as pathways for migration from the fracture surface into the rock matrix. The fine grained minerals of the 2 cm thick vein are quartz, calcite, phyllosilicates and pyrite. At mm-µm scale, under CLSM, it is possible to observe a thin band (1 cm), in the vein-granite contact, where the value of the porosity is very low (see porosity profile of figure 4).

The micro fractures which make the porosity pattern of the matrix adjacent to the water conducting fracture very complex act as the migration pathways for RN´s from the flowing water. However these micro fractures are difficult to take into account within PA model calculations due to the complexity and heterogeneity. New modelling tools [7] to cover these features in transport modelling exist. These tools could be used to evaluate the spatial RN diffusion in the rock matrices based on the exact structure data determined by the methods presented here.

Table I: *The open porosity values measured by different techniques are presented. In PMMA method error of 10% is evaluated.*

Sample/Depth		MIP porosity (%)	WATER porosity (%)	CLMS porosity (%)	PMMA porosity (%)±10%
FUN05-001 8,22-8,64 m (June fracture)		1,62	1,81	1,56	1,6
FUN05-001 14,74-15,13 m (August fracture)	Granite	2,01	2,01	2,51	2
	Vein	2,96		3,09	1-1.5
FUN05-001 17,43-17,53 m (September fault zone)		3,06	2,96	2,71	2,3

One of the main advantages of complementing the two techniques here is the wide range of scales they cover; the results of ^{14}C PMMA at the cm-dm scale are outstanding and the same with CLSM at the µm-cm; therefore, as the examples here included related to HLW studies prove, by complementing these two techniques a wider range of scale, dm-µm, can be covered; this represents a clear advantage for fractographic analysis at the intact rock, or rock matrix, structural scale.

References

1. Montoto, M., Martínez-Nistal, A., Rodriguez-Rey, A., Fernández-Merayo, N., Soriano, P. (1995): Microfractography of granitic rocks under Confocal Laser Scanning Microscopy. Journal of Microscopy 177 (2), 138.

2. Montoto, M (2004): Petrophysics at teh rock matrix scale: hydraulic properties and petrographic interpretation. ENRESA (Madrid, Spain), Technical Reports 03-11.297p. ISSN: 1134-380X.

3. Montoto, M. and Mateos, F. (2006): Characterization of water pathways in low permeable rocks at the rock matrix scale: Methodological review. Journal of Iberian Geology 32 (2) 197-213.

4. Hellmuth, K-H., Siitari-Kauppi, M., Lindberg, A. (1993): Study of porosity and migration path-ways in crystalline rock by impregnation with 14C-polymethylmethacrylate. Journal of Contaminant Hydrology 13, 403 (1993).

5. Hellmuth. K-H., Klobes, P., Meyer, K., Röhl-Kuhn, B., Siitari-Kauppi, M., Hartikainen, K., Hartikainen, J., Timonen, J. (1995): Matrix retardation studies: size and structure of the accessable pore space in fresh and altered crystalline rock, Z. geol. Wiss. 23 (5/6), 691 (1995).

6. Lähdemäki, T., Kelokaski, M., Siitari-Kauppi, M., Voutilainen, M., Myllys, M., Turpeinen, T., Timonen, J., Mateos, F. and Montoto, M. (2007): Characterizing Low-Permeable Granitic Rock from Micrometer to Centimeter Scale: X-ray Microcomputed Tomography, Confocal Laser Scanning Microscopy and the 14C-PMMA Method. In: D.S. Dunn, C. Poinssot, B. Begg (eds.), Scientific Basis for Nuclear Waste Management XXX, Mater. Res. Soc. Symp. Proc. 985 (2007) 587-592

7. Sardini P. Robinet J-C. Siitari-Kauppi M. Delay F. Hellmuth K-H (2007) Direct simulation of heterogeneous diffusion and inversion procedure applied to an out-diffusion experiment. Test case of Palmottu granite, Journal of Contaminant Hydrology 93, 21-37

URANIUM GEOCHEMISTRY AT RUPRECHTOV SITE

Ulrich Noseck [1*], Juhani Suksi [2], Vaclava Havlova [3], Radek Cervinka [3]

[1] Gesellschaft für Anlagen- und Reaktorsicherheit (GRS) mbH (D)
[2] University of Helsinki (FI)
[3] Nuclear Research Institute Řež plc (CZ)

* Corresponding author: Ulrich.noseck@grs.de

Abstract

Groundwater data from Ruprechtov site have been evaluated with special emphasis on uranium behaviour in the uranium-rich clay/lignite horizon. In this horizon in-situ Eh-values in the range of -160 to -280 mV seem to be determined by the SO_4^{2-}/HS^- couple. Under these conditions U(IV) is expected to be the preferential redox state in solution. However, first measurements in borehole NA6 showed only an U(IV) fraction of about 20 %. Thermodynamic calculations revealed that the high CO_2 partial pressure in the clay/lignite horizon can stabilise hexavalent uranium, which can explain the occurrence of U(VI). The calculations indicated that the low uranium concentrations in the range between 0.2 and 2.1µg/l are controlled by amorphous UO_2. This also confirms the findings from previous work that the U(IV) phases are long-term stable under the reducing conditions in the clay/lignite horizon.

Introduction

During the investigations at Ruprechtov site key processes leading to immobilisation of uranium in the so-called clay/lignite horizon were identified (e.g. Noseck et al. 2008a). It could be shown that the major amount of uranium was deposited in form of U(IV) minerals and that these immobile U(IV) phases have been stable for more than 1 Million years. Uranium series disequilibria showed no evidence for uranium removal from the system. In order to understand the long-term stability of uranium in the clay/lignite horizon the geochemical conditions at Ruprechtov site are evaluated and discussed with major emphasis on the mobility of uranium.

Methods

The methods applied for sampling and the analytical methods for detection of major and trace elements are described in (Noseck et al. 2008b). Eh and pH-values have been measured in-situ by a multi parameter probe with a Pt-electrode for Eh measurement. Analyses of U(IV)/U(VI) fractions in groundwater have been performed

by co-precipitation with NdF_3 using the method from (Anderson 1984) following the scheme of (Suksi et al. 2007).

Thermodynamic calculations have been performed with Geochemists Workbench (GWB; Bethke, 2006) and with the updated NEA TDB database (Guillaumont et al. 2003, Yoshida 2004). All input data for the calculations are taken from (Noseck et al. 2008b, table 1) and from additional data listed in this paper.

Results and discussion

A detailed compilation and description of the Ruprechtov groundwater data can be found in (Noseck et al. 2008b). The geochemical conditions at the site are characterised by low mineralised waters with ionic strengths in the range of 0.003 mol/l to 0.02 mol/l. Nearly all waters in the clay/lignite horizon are of Ca-HCO_3-type with total DIC concentrations up to 450 mg/l. The pH-values vary in a range of 6.2 to 8, the Eh-values from 435 mV to -280 mV. More oxidising conditions with lower pH-values are found in the near-surface granite waters of the infiltration area.

In the clay/lignite horizon the conditions are reducing supported by the mineral phases pyrite and siderite occurring with content up to 2 % in sediment samples from this horizon. Eh-values have been measured on-site and in-situ. The first method is more susceptible to disturbances by the contact with atmosphere, which is probably responsible for higher Eh values observed in on-site measurements. In-situ probe measurements of Eh-values in the clay/lignite horizon always showed an Eh decrease during the analyses. In order to find the stable values long-term measurements for three boreholes (NA6, NA12 and NA13) have been performed. This measurement showed a stabilisation of the Eh-value after few days. We decided to trust these values most and used them for the following interpretation. Selected data for boreholes considered here are compiled in Tab. 1.

Tab. 1: *Specific groundwater data for selected boreholes*

Well No.	Area	Horizon [m]	Eh [mV]	U [µg/l]	Fe^{2+} [mg/l]	S^{2-} [mg/l]	$\delta^{34}S$ [‰]	SO_4^{2-} [mg/l]
NA4	Clay / lignite	34.5 – 36.5	n.a.	0.15	1.8	0.1	24.63	19.8
NA6		33.4 - 37.4	-280	0.8	0.7	0.11	23.5	49.5
NA12		36.5 - 39.3	-160	0.2	2	n.a.	20.11	22.9
NA13		42.2 - 48	-252	2.1	0.7	0.065	n.a.	22.9
NA8	granite	8.5 - 24	48	1.58	n.a.	n.a.	-8.5	59.1
NA10		19.5 - 27.5	240	8.6	n.a.	n.a.	0.2	40.8
RP1		5 - 18	149	11.1	n.a.	n.a	3.48	19.8

n.a. = not analysed

Figure 1 shows uranium concentrations of all groundwater wells at Ruprechtov. The boreholes from the infiltration area in granite, NA8, NA10 and RP1 are depicted on the right of the diagram. These values are in a range of 1.8 to 12 µg/l. The uranium concentrations in the clay/lignite horizon are below 2.1 µg/l and with two exceptions below 1µg/l. As expected the values in the more reducing clay/lignite horizon are lower than those in the more oxidising granitic waters.

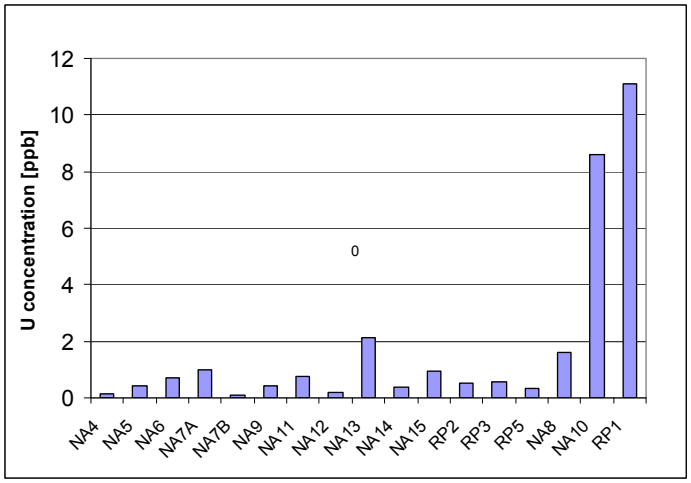

Figure 1: *Uranium concentrations in Ruprechtov wells*

The uranium mobility is strongly impacted by its speciation, in particular by the local redox conditions and the availability of complexing agents like carbonates (e.g. Langmuir 1978). Therefore, firstly, the redox conditions in the clay/lignite horizon are discussed. Redox conditions in natural systems could be controlled by different and heterogeneous redox couples. The clay/lignite layers are quite heterogenous typically containing quartz and clay minerals (smectite, illite, kaolinite) as major components, organic matter and to lower extent minerals as anatase, pyrite and siderite (Noseck and Brasser 2006). Due to the occurrence of significant amounts of dissolved sulphide and sulphide minerals the redox pairs SO_4^{2-}/HS^-, and the heterogeneous redox pairs SO_4^{2-} /pyrite have been included. Many natural systems are dominated by redox pairs of iron. Therefore we also calculated the couple $Fe^{2+}/Fe(OH)_3$ considering a relatively fresh amorphous precipitate according to data from (Langmuir 1997). There is no indication of goethite or haematite occurring in the clay/lignite horizon. The results are shown in Figure 2. The measured Eh- values from the three boreholes are compared with values calculated from these redox pairs.

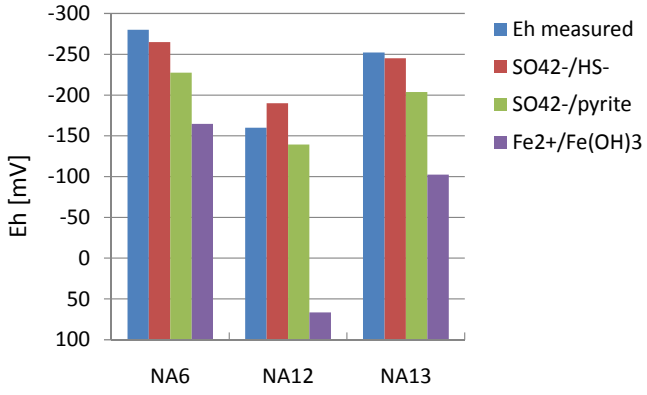

Figure 2: *Measured Eh-values compared to potential redox pairs*

A reasonably well agreement is found between the redox potential measured by the Pt-electrode and the SO_4^{2-}/HS^- couple, whereas the redox pair $Fe^{2+}/Fe(OH)_3$ shows

low agreement in particular for borehole NA12. As discussed in (Noseck et al. 2008b) there is strong evidence that microbial sulphate reduction and oxidation of organic matter occurs in the clay lignite horizon. In particular the $\delta^{34}S$ values in the boreholes from the clay/lignite horizon are strongly increased with respect to the values in the infiltration waters (see table 1). The observed sulphide values in the clay/lignite waters are significant but not too high, lying in a range of 0.05 and 0.12 mg/l. Microbial catalysis efficiently accelerates the sulphate reduction and operational redox potentials resulting from this kinetic process may closely approximate equilibrium values (e.g. Stumm et al. 1996). This might explain the agreement of measured and calculated values for the SO_4^{2-}/HS^- couple.

The uranium speciation calculations have been performed with GWB and the updated NEA TDB database. A major difference to the NEA TDB version from 1992 is the value for the uranium(IV)-hydroxo complex in solution:

$$U(OH)_4 + 4H^+ = U^{4+} + 4H_2O \quad (1)$$

The lower stability of this complex (log K = 10.05 for reaction (1)) compared to the value from 1992 database (log K = 4.54) is leading to lower redox potentials calculated for the U(IV)/U(VI) transition in the neutral pH range. The Eh/pH diagram for typical conditions at Ruprechtov site is shown in Figure 3. The data for granite groundwater from the infiltration area are dominated by uranyl-carbonato complexes, whereas the groundwaters from the clay/lignite horizon are at the boundary of the stability fields for the tetravalent aqueous $U(OH)_4$ complex and the hexavalent complexes $UO_2(CO_3)_3^{4-}$ and $UO_2(CO_3)_2^{2-}$.

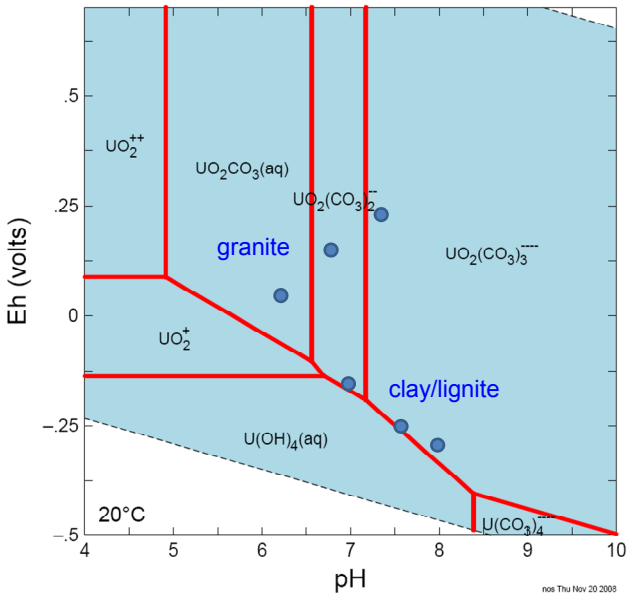

Figure 3: *pH/Eh-diagram for Ruprechtov groundwaters. U concentration 10^{-3} mg/l, CO_2 activity = 10^{-3}.*

Results from speciation calculations for the conditions found in NA6 and a pH range between 6 and 8 are shown in Figure 4. The increasing role of carbonate complexes with increasing alkalinity is clearly illustrated. Due to the high CO_2 partial pressure (from microbial SOC degradation and probably CO_2 exhalation; cf. Noseck et

al. 2008b) in this system even for quite reducing conditions part of the dissolved uranium can be stabilised as U(VI) by carbonato complexes. The calculated fraction of U(IV) in groundwater NA6 at pH8 assuming equilibrium is shown on the right in Figure 4.

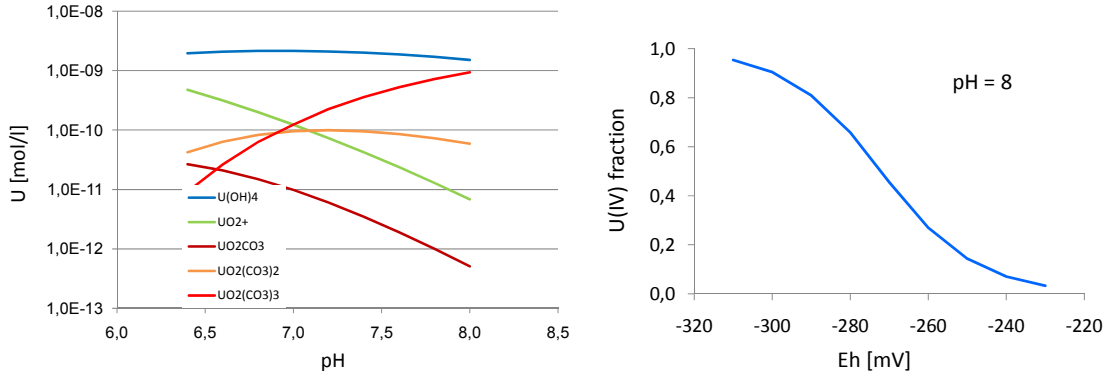

Figure 4: *Left: Uranium speciation in solution for NA6 groundwater in dependence of pH (Total U concentration $6 \cdot 10^{-4}$ mg/l, total DIC concentration as HCO_3 =290 mg/l)) Right: fraction of U(IV) in dependence of Eh-value at pH 8, for conditions of NA6 groundwater.*

For all three clay/lignite groundwaters the expected U(IV) fractions in solution have been calculated. To verify the oxidation state of uranium in groundwater a method for separation of U(IV) and U(VI) in solution was applied (see section methods). So far, only data for NA6 are available. In the first campaign total U concentration of 5.5 µg/l with U-fractions of 15.2 % and 22.2 % and from the second campaign a total U concentration of 0.91 and a U(IV) fraction of 16.6 % was found. According to the thermodynamic calculations a uranium(IV) fraction of about >60 % is expected. The results from the calculations for the different groundwaters and the measured values are listed in Tab. 2.

Tab. 2: *Calculated and measured U(IV) fractions in groundwaters from clay/lignite horizon*

Borehole	U(IV) fraction in groundwater [%]	
	calculation	analysis
NA6	66	15 - 22
NA12	35	n.a.
NA13	55	n.a.

n.a = not analysed

U(IV)/U(VI) analyses have also been performed in groundwaters from Forsmark site. These waters are slightly less reducing with Eh-values between -140 and -200 mV and pH-values between 7 and 8.5 (Laaksoharju et al. 2006). Here groundwater is dominated by U(VI) with U(IV) fractions of <5 %.

An appropriate method to understand which uranium phases control the uranium solubility in the natural system is the calculation of saturation indices. In many reducing groundwater systems uraninites or pitchblendes of stoichiometry UO_{2+x} are found to be

the phases controlling the dissolved uranium concentration. In the uranium enriched sediments at Ruprechtov site two secondary uranium(IV) phases have been observed, UO_2 and ningyoite ($CaU(PO_4)_2 \cdot 1\text{-}2H_2O$). Since no stoichiometric determination of the UO_2 phase was performed, saturation indices of different U(IV) mineral phases are taken into account. Thermodynamic data for ningyoite are not available in the NEA TDB and have been taken from recommendations in (Langmuir 1997).

The calculation results are shown in Figure 5. The groundwaters from the clay/lignite horizon are strongly oversaturated with respect to the crystalline uraninite and coffinite indicated by saturation indices (SI) in the range between 5 and 7. The mixed valence uranium oxides $UO_{2.25}$ and $UO_{2.33}$ are also oversaturated (SI between 2.5 and 4). The mixed valence oxide $UO_{2,66}$ is always undersaturated with SI values below -0.8. No saturation of U(VI) minerals was found. Assuming an uncertainty range of ±0.6 (shadowed area in Figure 4) for the saturation index resulting from uncertainties in the thermodynamic data, the results indicate that the uranium concentration is controlled by amorphous UO_2. SI values for ningyoite are also near saturation in groundwater NA6 and NA13 but not for NA12. So, there is generally good agreement with observed mineralisations in the clay/lignite horizon. Metastable amorphous UO_2 has been shown also in other studies to be likely the uranium controlling mineral phase, e.g. (Iwatsuki et al. 2004). These results also indicate that no U-release is expected under the geochemical conditions in the clay/lignite horizon, in agreement with very low $^{234}U/^{238}U$ activity ratios observed in the uranium(IV) mineral phases as indicators for their long-term stability (Noseck et al. 2008a).

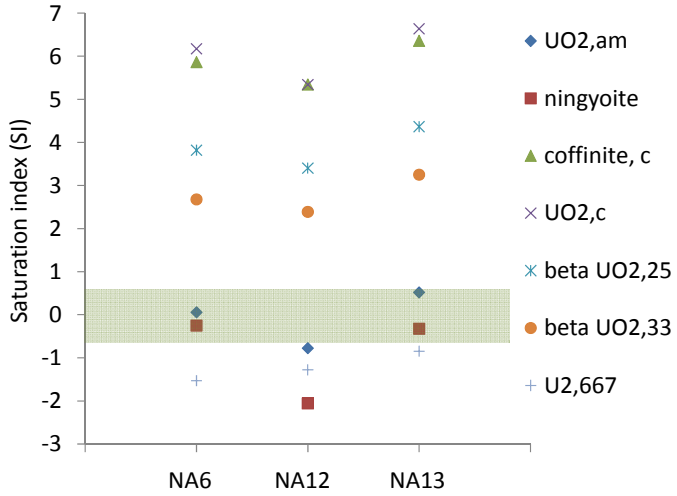

Figure 5: *Saturation indices of various U(IV) minerals calculated for groundwaters NA6, NA12 and NA13.*

Conclusions

The thermodynamic evaluation of the aqueous speciation and solubility behaviour of uranium in the reducing clay/lignite horizon indicate that the uranium concentrations are controlled by amorphous UO_2 or ningyoite. Saturation indices of crystalline uraninite and coffinite as well as mixed oxides are greatly exceeded. The

results clearly explain the high stability of immobile uranium phases in the clay/lignite horizon, which was shown by uranium decay series disequilibria and described in previous papers.

All results from thermodynamic calculations indicate that U(IV) is the predominant redox state in the clay/lignite layers at Ruprechtov site. However, due to the high CO_2 partial pressure in the system carbonato complexes can stabilise hexavalent uranium in solution, which might explain that redox state analyses performed in borehole NA6 showed only 20 % U(IV). Nevertheless, there is also a need to optimise the U(IV)/U(VI) determination method in order to completely avoid contamination by atmosphere. This optimisation as well as improvement of Eh determination by use of additional electrodes is planned to be performed within a future national project eventually in association with the new European project RECOSY.

Acknowledgement

This work has been financed by the German Federal Ministry of Economics (BMWi) under contract no's 02 E 9551 and 02 E 9995, by RAWRA (CZ) and Czech Ministry of Trade and Industry (Pokrok 1H-PK25) and by the European Commission within the integrated project FUNMIG (EURATOM, FP6, Contract No. 516514).

References

Anderson RF, (1984): A method for determining the oxidation state of uranium in natural waters. Nucl. Inst. Meth. Phys Res. 223, 213-217.

Bethke CM (2006): The Geochemist's Workbench Release 6.0, Hydrogeology Program, University of Illinois.

Guillaumont R, Fanghänel Th, Fuger J, Grenthe I, Neck V, Palmer DA, Rand MH, OECD (2003): NEA-TDB, Chemical Thermodynamics, Vol. 5. Update on the chemical thermodynamics of uranium, neptunium, plutonium, americium and technetium. Elsevier.

Iwatsuki T, Arthur R, Ota K, Metcalfe R (2004): Solubility constraints on uranium concentrations in groundwaters of the Tono uranium deposit, Japan. Radiochim. Acta 92, 789 – 796.

Langmuir D (1978): Uranium solution-mineral equilibria at low temperatures with application to sedimentary ore deposits. Geochim. Cosmochim. Acta 42, 547-569.

Langmuir, D (1997): Aqueous environmental geochemistry. Prentice Hall, Upper Saddle River, New York, p. 600.

Laaksoharju M, Smellie J, Tullborg E-L, Gimeno M, Gómez J, Gurban I, Hallbeck L, Auqué L, Buckau G, Gascoyne M., Raposo J (2006): Hydrogeochemical evaluation of the Forsmark site, modelling stage 2.1. SKB-R06-96, Stockholm.

Noseck U, Brasser Th, Suksi J, Havlova V, Hercik M, Denecke MA, Förster HJ (2008): Identification of Uranium enrichment Scenarios by Multi-Method Characterization of Immobile Uranium phases. Phys. Chem. Earth, 33, 969-977.

Noseck U, Rozanski K, Dulinski M, Havlova V, Sracek O, Brasser Th, Hercik M, Buckau G (2008b): Characterisation of hydrogeology and carbon chemistry by use of natural isotopes – Ruprechtov site, Czech Republic. Accepted by Appl. Geochem.

Stumm W, Morgan JJ (1995): Aquatic Chemistry. 3rd ed. John Wiley & Sons, New York.

Suksi J, Salminen S (2007): Forsmark Site investigation. Study of U oxidation in groundwater with high U concentrations. SKB P-07-54, Stockholm.

Yoshida Y, Shibata M (2004): Establishment of Data Base Files of Thermodynamic Data developed by OECD/NEA Part II - Thermodynamic data of Tc, U, Np, Pu and Am with auxiliary species, JNC Technical Report, JNC TN8400 2004-025.

INTERRELATION OF MOBILE ORGANIC MATTER AND SEDIMENTARY ORGANIC MATTER AT THE RUPRECHTOV SITE

Václava Havlová[1], Radek Červinka[1*], Josef Havel [2]

[1] Nuclear Research Institute Rez plc, Waste Disposal Department, Husinec- Rez, 250 68, Czech Republic
[2] Department of Analytical Chemistry, Faculty of Science, Masaryk University, Kotlářská 2, 611 37 Brno, Czech Republic

* Corresponding author: crv@ujv.cz

Abstract

The study was focused on mobile organic matter quantification from the Ruprechtov natural analogue site (CZ) and its characterisation. Only a small fraction of sedimentary organic matter can be released into the solution: 2.8 %. The release rate is dependent on the organic matter composition and the degree of coalification. The mobile organic matter can be represented by extracted natural humic acid. The correspondence was clarified by MALDI-TOF MS spectra which showed high degree of similarity with those of organic substances from natural mobile organic matter in Ruprechtov groundwater and with those leached from the sediment in contact with solution. MALDI-TOF spectra also proved that the mobile organic matter consists of small independent molecules with molecular weight up to 1000 Da.

Introduction

The study was focused on mobile organic substances and their characterisation from the Ruprechtov natural analogue site (CZ). Mobile organic matter (MOM), as defined in Maes et al., 2004, is the fraction of total natural organic matter (NOM) that can be released into the system (groundwater) from sedimentary organic matter and is available for complexation/sorption interactions with other ions (radionuclides are of particular interest in this context). However, the determination of MOM availability is complicated. The problem can be formulated into several questions:

1. How can we define the MOM fraction of sedimentary organic matter (SOM) in the Ruprechtov sedimentary samples?
2. Is the fraction, which is released during simple leaching experiments from SOM into the leaching solution representative for the natural MOM fraction?
3. Moreover, can the extracted humic acid (HA), being widely recognised as a strong complexing agent and used for complexation experiments with radionuclides, also be considered as MOM representative?

4. How do these artificially released organic substances correspond with mobile natural organic substances in Ruprechtov groundwater?

The attempt to answer the questions is presented in the following article.

The site characterisation

The geology of the Ruprechtov site was described in detail in several contributions (e.g. Havlova et al., 2007; Noseck et al., 2008 a, b). The main accumulation of SOM is situated within Tertiary argillitized tuffs and tuffits in the so-called clay/lignite horizon. The SOM forms partly massive coal seams, partly is being dispersed in the clayey sediments. The highest SOM content was determined up to 40 wt. %. However, the groundwater content of dissolved organic matter (DOM) was found to be low (below 5 mg/l $C_{org.}$).

Methods

An outline of the SOM investigation and characterization from Ruprechtov site can be found in Cervinka et al., 2007. The key approach taken in the study presented was to extract natural organic substances from SOM, using two different methods (batch leaching experiment and alkaline extraction, used for humic acid (HA) extraction), to characterize them using the modern analytical method MALDI-TOF MS, and to compare the results with natural dissolved organic matter from Ruprechtov groundwater.

Batch leaching experiment

The batch leaching experiments were aimed to demonstrate the rate of MOM release and SOM degradability in contact with groundwater. Four sediment samples (NA-13, NA-12/4, NA-12 and NA-14) with different SOM content were selected for the experiment (see Tab. 1).

Table 1: *Sample from the Ruprechtov site, selection for batch leaching experiment*

Sample	Depth (m)	SOM content (wt. % of C_{org})
NA-12	36.44 – 36.90	4.07
NA-12/4	38.9	2.33
NA-13	46.4	0.97
NA-14A	51.73	7.85

The experiments were performed in the pH range from 6 to 8 using a simple batch technique. 1 g of each sediment sample (ground and homogenized) was contacted with 40 ml of solution at different pH (6, 6.5, 7, 8). Due to the high content of pyrite in the sediment samples (namely NA-14) the original Ruprechtov groundwater could not be used because it is not possible to keep the pH constant during the experiments. Instead, a 0.1M phosphate buffer (Na_2HPO_4 + NaH_2PO_4) was used as solvent. The vials were agitated for 12 days, then centrifuged and decanted. Organic carbon content (C_{org}) in the leachate was analysed using an automatic analyser Schimadzu TOC-5000A

(Czech Institute of Chemical Technology, Prague). All the experiments were performed under oxidising conditions.
The released MOM fraction was determined as a ratio of released C_{org} per 1 g of sample (mg/g) vers. content of C_{org}. in sediment (mg/g).

Natural humic acid extraction
The natural humic substance HA-12/3 from Ruprechtov sample (borehole NA-12, 36.44 – 36.90 m, C_{org} = 4.07 wt. %) was extracted using the alkaline extraction procedure referred by IHSS after Swift, 1996, (see Fig. 1, Cervinka et al., 2007).

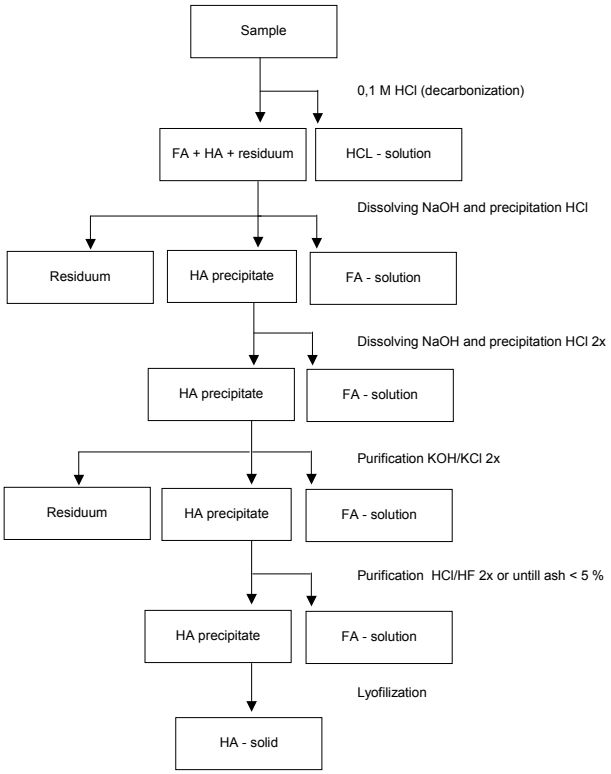

Figure 1: *Alkaline separation scheme according to IHSS (after Swift, 1996)*

The extracted natural humic acid (HA-12/3; 3 g) was characterized using element analysis, ash and moisture content, UV-Vis spectroscopy, FTIR spectroscopy, acidobasic titrations and MALDI-TOF MS (Cervinka et al., 2007).

MALDI-TOF MS
The modern analytical method MALDI-TOF MS (Matrix Assisted Laser Desorption/Ionisation Time of Flight Mass Spectrometry; Masaryk University, Brno; e.g. Remmler et al., 1995) was used for characterization of the organic substances.
Mass spectra were measured using the AXIMA-CFR mass spectrometer from Shimadzu (Kratos Analytical, Manchester, UK). The spectra were measured in the laser desorption ionization (LDI) mode without using any matrix. All samples used were dissolved in NaOH solution. 1 μl of solution was dropped to a sample plate, dried in an air stream at room temperature and inserted into the vacuum chamber of the instrument. After

reaching a vacuum of $1 \cdot 10^{-5}$ Pa the mass spectra were measured. The resulting spectra were always accumulated from at least 1000 shots.

Following that, the three organic substances from the Ruprechtov site were characterised and compared:

- leachate from the batch leaching experiment (sample NA-12/4 leachate; 38.9 m)
- extracted natural humic acid HA-12/3 (extracted from borehole NA-12; 36.44-36.90 m, Cervinka et al., 2007)
- groundwater sample from borehole NA-12 (sampled in 36.5-39.3 m filter horizon)

Results

The average of the released fraction from sedimentary samples using the batch leaching technique was 2.8 % of SOM (expressed as C_{org}). The released fraction was inversely proportional to the total content of SOM in the sample: the more SOM present in the sample, the less OM fraction is released. The trend is illustrated in Fig. 2. A decrease of the releasable fraction can be obviously connected with a higher humification stage of OM-rich samples, reported elsewhere e.g. Pettersson et al. (1994), Gonzales et al. (1994). The content of organic matter increased in the sequences NA-13 (carbonaceous clay) < NA-12/4 < NA-12 < NA-14A (coal).
The maximum released C_{org} concentration for Ruprechtov samples did not exceed 40 mg/l, which is rather low. MOM fractions of Boom clay leached out by synthetic groundwater reached C_{org} concentrations up to 650 mg/l (Maes et al., 2004).

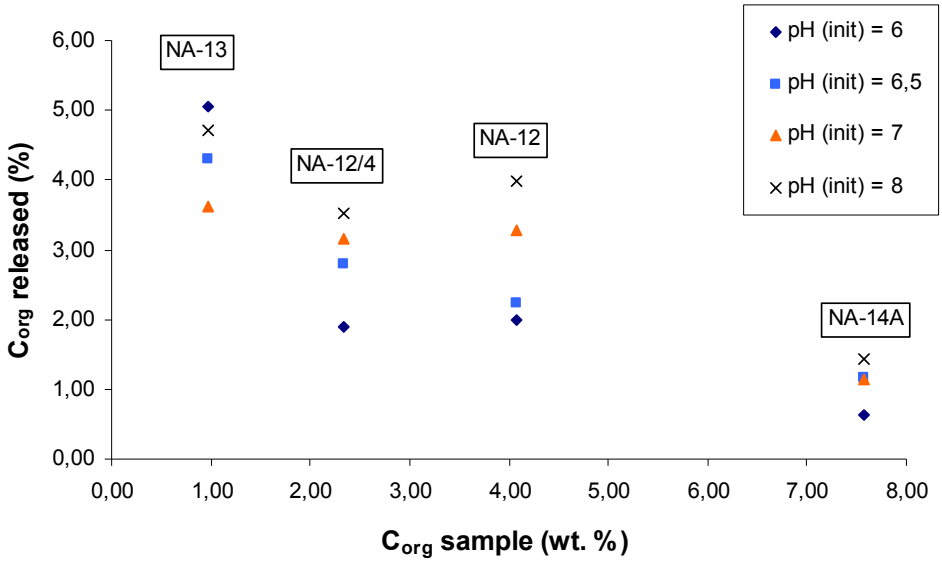

Figure 2: *OM fraction released into the solution (C_{org} released (%) vers C_{org} sample (wt. %) and pH-value.*

The MALDI-TOF MS measurement of extracted HA-12/3 showed that the spectra are dominated by lower molecular weight peaks, confirming the presence of low molecular compounds with a number of peaks about 400 – 600 Da (mass/charge in

chart) and about 800 Da. High molecular weight compounds were presented in less extent. The spectra is presented in Fig. 3, green colour.
The results support a recent change in natural humic acid consideration: humic acids are presumed to consist of small independent molecules with low molecular weight below 1000 Da (Simpson et al., 2002). The shift was made mainly due to new analytical methods involved in HA characterization, e.g. MALDI-TOF MS, ESI-MS, TOF-SIMS and Overhauser-NMR.

Finally, MALDI-TOF MS spectra were measured for the NA-12/4 leachate and groundwater MOM (NA-12 borehole). The results are also presented in Fig. 3.
A noticeable fingerprint can be found: The peaks in the range about 25 – 145, 250, 353 – 381, 413, 492 – 500 and 590 – 600 Da (mass/charge in the chart) can be identified for all three samples. Those are composed of molecules with similar molecular weight, predominantly low. Analytical uncertainties, caused by the content of other dissolved substances in solution and different laser intensities, caused slight differences and shifts in the spectra. However the congruence of the main peaks is evident.

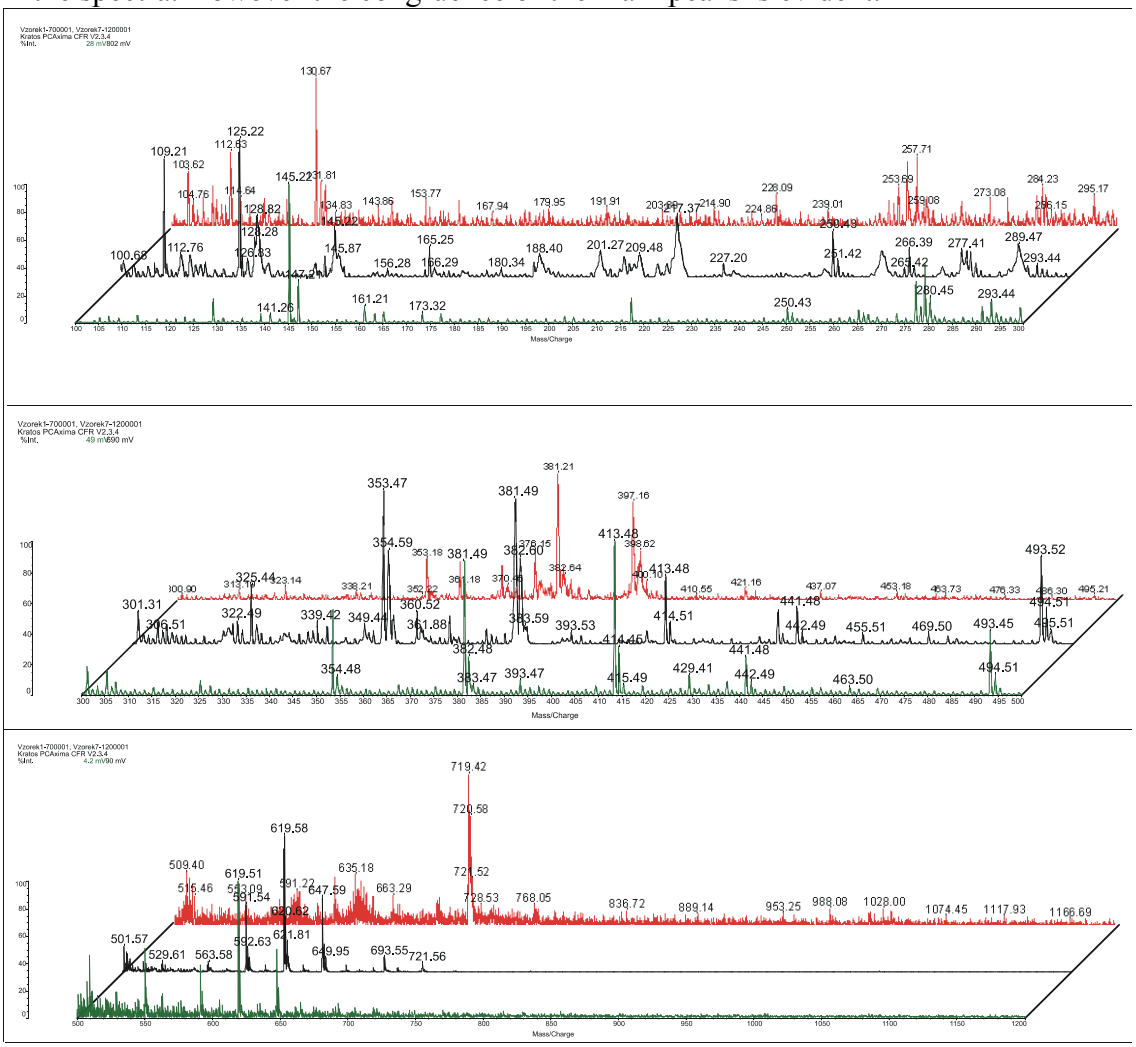

Figure 3: *Comparison of MALDI-TOF spectra: green – extracted HA-12/3 (NA-12 [36.44-36.9 m]), black – NA-12/4 leachate [38.9 m], red – NA-12 groundwater [36.5-39.3 m filter horizon], (mass/charge here = Da).*

Therefore, the organic compounds released either by artificial dissolution of SOM (batch leaching, alkaline extraction) or originating from natural groundwater from the Ruprechtov site exhibit similar molecular weight composition. Moreover, considering good agreement with natural groundwater DOM, the extracted and purified natural humic acid HA-12/3 can be considered as representative of the MOM fraction at the Ruprechtov site and can be used for further experiments simulating MOM interaction with radionuclides (Cervinka et al., 2008). A data set with basic characteristic data is available (Cervinka et al., 2007).

Conclusions

The availability of mobile organic matter at the Ruprechtov site is mainly dependent on the sedimentary organic matter composition and degree of coalification. Only a small fraction of mobile organic matter from Ruprechtov sediment samples, i.e an avg. 2.8 wt % of SOM, can be released into the solution. This probably explains the low DOM concentration (< 5mg/l) in Ruprechtov groundwater.
The extracted natural humic acid HA-12/3 from SOM is characterised by low molecular weight molecules (below 1000 Da). This compound can be considered as a mobile organic matter representative for Ruprechtov site. MALDI-TOF MS spectra showed a high similarity with those organic substances released using batch leaching experiments and with those originated from natural groundwater MOM. The MALDI-TOF MS spectra identified a fingerprint, i.e. spectra segments, that are to some extent identical for all of organic compounds released.

Acknowledgement

This work has been financed by the German Federal Ministry of Economics (BMWi) under contract no's 02 E 9551 and 02 E 9995, by RAWRA (CZ) and Czech Ministry of Trade and Industry (Pokrok 1H-PK25) and by the European Commission within the integrated project FUNMIG (EURATOM, FP6, Contract No. 516514).

References

Hauser W., Geckeis H., Götz R., Noseck U., Laciok A. (2006): Colloid Detection in Natural Ground Water from Ruprechtov by Laser-Induced Breakdown Detection. 2nd Annual Meeting of EC Integrated Project FUNMIG, SKB Report TR 07-05.

Cervinka R. (2008): Report on Uranium complexation by isolated humic substances from the Ruprechtov site. PID 2.2.20, EC Integrated Project FUNMIG.

Cervinka, R., Havlova, V.; Noseck, U.; Brasser, Th., Stamberg, K. (2007): Characterisation of organic matter and natural humic substances extracted from real clay environment. 3rd annual meeting of IP FUNMIG, 25-29.11.2007, Edinborough, Great Britain.

Gonzalez-Vila F. J, del Rio F. C, Almendros G. Martin G. (1994): Structural relationship between humic fractions from peat and lignites from the Miocene Granada basin. Fuel, Vol.73, No. 2.

Havlova V., Brasser Th., Cervinka R., Noseck U., Laciok A., Hercik M., Denecke M., Suksi J., Dulinski M., Rozanski K. (2007): Ruprechtov Site (CZ): Geological Evolution, Uranium Forms, Role of Organic Matter and Suitability as a Natural Analogue for RN Transport and Retention in Lignitic Clay. Proc. of REPOSAFE Conference, Braunschweig, Nov. 5-9, 2007, submitted.

IHSS, International Humic Substances Society, http://www.ihss.gatech.edu/.

Lenhart, J. J. Cabaniss, S. E. MacCarthy, P. Honeyman, B. D. (2000): Uranium(VI) complexation with citric, humic and fulvic acids. Radiochim. Acta, 88, 345-354.

Maes N. (2004): Migration Case Study: Transport of radionuclides in a reducing clay environment. Final Report. Nuclear Science and Technology. EUR 21025 EN. European Commission.

Noseck U., Brasser Th., Suksi J., Havlova V., Hercik M., Denecke M.A., Förster H.J., (2008a): Identification of uranium enrichment scenarios by multi-method characterisation of immobile uranium phases. J.Phys.Chem.Earth, doi:10.1016/j.pce.2008.05.018.

Noseck U., Rozanski K., Dulinski M., Havlova V., Sracek O., Brassera Th., Hercik M., Buckau G., (2008b): Characterisation of hydrogeology and carbon chemistry by use of natural isotopes – Ruprechtov site, Czech Republic. Submitted to Applied Geochem.

Pettersson C., Ephraim J., Allard, B. (1994): On the composition and properties of humic substances isolated from deep groundwater and surface waters. Organic Geochemistry, 21, 5, 443-451.

Remmler, M., A. Georgi and F.-D. Kopinke (1995): Evaluation of matrix assisted laser desorption time of flight (TOF) mass spectrometry as a method to determine the molecular mass distribution of humic acids. Eur. Mass. Spectrom., 1, 403–407.

Simpson A. J., Kingery W. L., Hayes M. H., Spraul M., Humpfer E., Dvortsak P., Kerssebaum R., Godejohann M., Hofmann M. (2002): Molecular structures and associations of humic substances in the terrestrial environment. Naturwissenschaften 89, 2, 84-88.

Swift, R.S. (1996): Organic matter characterization. , in Sparks D.L., Methods of Soil Analysis, část 3. Chemical Methods. Soil Science Society of America Book Series Number 5. American Society of Agronomy, Madison, WI., pp.1018.

INFLUENCE OF BOOM CLAY ORGANIC MATTER ON THE ADSORPTION OF Eu^{3+} BY ILLITE

De-Jun Liu[1,2], Christophe Bruggeman[1], Sonia Salah[1], Norbert Maes[1,*]

[1] SCK-CEN (Belgium)
[2] CIAE (China)

* Corresponding author: nmaes@sckcen.be

Abstract

Batch sorption isotherm experiments were designed to evaluate the influence of organic material on the sorption of Eu^{3+} (1×10^{-8} – 5×10^{-7} M) on Silver Hill illite under conditions representative for the Boom Clay. Eu sorption isotherms were measured in SBCW (synthetic Boom Clay Water) background electrolyte (pH 8.3) in the presence of 40 ppm dissolved organic matter with different molecular weight distributions. Reversibility and establishment of chemical equilibrium were checked by varying the order of mixing of the three different components (Eu, organic matter, and illite). Phase separation was carried out by a consecutive procedure of centrifugation (2 hrs at 21 000g) and ultrafiltration (30KD) to distinguish immobile (larger colloids) from mobile (small colloids and dissolved species) Eu fractions.

The Eu distribution in all ternary systems, measured both after centrifugation and after ultrafiltration, followed a linear sorption relation. The presence of dissolved organic matter in solution after centrifugation decreased the Eu distribution coefficients by an order of magnitude because of complexation reactions between Eu and organic matter. After ultrafiltration, the amount of dissolved organic matter and Eu concentration decreased relative to the size distributions of the different organic matter batches which resulted in increased distribution coefficients. This observation leads to the conclusion that the decreased sorption onto illite due to the formation of Eu-NOM colloids, may be translated into an increased retention of Eu under *in situ* conditions because of the immobility of the large-size NOM molecules.

Eu sorption onto illite could be described using the 2 SPNE SC/CE surface complexation model. Eu complexation constants to natural organic matter were fitted from solubility experiments above $EuOHCO_3$ using Humic-Ion Binding model VI. Application of the additivity rule for the ternary systems clearly indicated that the two separate models were able to explain the measured solid-liquid distributions, both after centrifugation and after ultrafiltration.

Introduction

In Belgium the argillaceous Boom Clay formation is considered as a reference for methodological studies on the deep geological disposal of high level radioactive waste because of its many favourable physical and geochemical characteristics. In Boom Clay pore water (~ 10^{-2} mol/l $NaHCO_3$), the most important reactions for lanthanide and actinide ions influencing their speciation and mobility, are hydrolysis and complexation with naturally occurring ligands such as inorganic carbonate and dissolved organic matter (~ 100 ppm DOC). Given the colloidal migration behaviour of negatively-charged dissolved organic matter, an adequate understanding of radionuclide-NOM (Natural Organic Matter) interactions in presence of competing adsorbing solid phases such as clay minerals, is mandatory for confidence building with respect to the knowledge of radionuclide migration behaviour under *in situ* conditions, and for providing data to be used in performance assessment calculations.

In the present study, the influence of mobile and immobile NOM on the adsorption of Eu^{3+} by illite will be investigated and compared to the adsorption in absence of NOM. Europium is studied as a chemical analogue for trivalent actinides, who are known to possess high affinity for NOM functional groups. Illite is the most important constituting clay mineral in Boom Clay and is considered to be the main adsorption sink of Eu^{3+} under *in situ* conditions. In recent years many studies on the adsorption of Eu^{3+} on illite and montmorillonite have been performed to elucidate the sorption mechanism and associated parameters[4-8]. Especially, Bradbury M. H. and Baeyens B. have successfully developed and applied a relatively simple quasi-mechanistic 2 site protolysis non electrostatic surface complexation and cation exchange model (2SPNE SC/CE model) to describe the sorption of Eu^{3+} on montmorillonite and illite under a variety of conditions with respect to pH, ionic strength and Eu^{3+} concentration [5-8]. In the present study, this model will be used to describe Eu^{3+} adsorption on illite in the presence of HA.

With respect to the interaction of Eu^{3+} with NOM, a recent study by Liu *et al.*[9] showed that the increase of aqueous Eu concentration with increasing dissolved organic carbon concentration above $EuOHCO_3$ precipitate in Synthetic Boom Clay Water (SBCW) background electrolyte could be described by Humic-Ion Binding Model VI[10]. The data from these solubility experiments, together with the fitted interaction (complexation) constants will be used in the present experiment to account for Eu-NOM interactions. Different NOM types will be investigated, exhibiting different size distributions. Distinction between mobile and immobile NOM will be made based on ultrafiltration at 30000 MWCO of the supernatant solutions after centrifugation.

Experimental

A glovebox with a controlled Ar-0.4%CO_2 atmosphere was used in the experiments to simulate the anaerobic atmosphere and representative CO_2 partial pressure for *in situ* Boom Clay conditions. Two different types of Boom Clay Water were used in the sorption experiments: Real Boom Clay Water (RBCW) and Synthetic Boom Clay Water (SBCW). RBCW was sampled from a piezometer (codename EG/BS) installed in the HADES underground laboratory in Mol at the depth of -250 m below the surface. SBCW was prepared to obtain the same composition as RBCW apart from the presence of dissolved organic matter[11].

Illite (< 63 µm, dried sieving) was conditioned by dialyzing with SBCW prior to use. A stock suspension of illite was prepared by mixing SBCW and conditioned illite. Boom Clay NOM with size distribution different from NOM present in piezometer water (RBCW) was obtained by mixing Boom Clay solid phase with RBCW or SBCW at different solid-to-liquid ratio (S/L) in a shaker for about one month in a glovebox. This procedure is known to liberate large NOM molecules, which do not feature in the sampled piezometer water. The mixture was centrifuged at a 21000g for 2 hours and the supernatant solution was used as NOM pool.
The concentration of NOM was obtained by measuring the UV absorbance at 280 nm (Perkin-Elmer Lambda 40P). The UV absorbance was linked to a DOC value making use of a linear relationship obtained from calibration curves of NOM solutions that were measured by UV and OC determinations (IL 550 TOC-TN Analysis Systems, Hach Company, Germany). The concentration of ^{152}Eu was measured using a gamma counter (5000 Series Gamma Counting Systems, Packard Instrument Company, USA).

Description of sorption measurements

Batch sorption experiments were designed to produce sorption data sets as a function of Eu^{3+} concentration at otherwise constant conditions (sorption isotherms). Eu stock solutions were prepared and consisted of SBCW and stable Eu at different concentrations ($5.9x10^{-7}$~$1.8x10^{-8}$ mol/l), each spiked with an identical trace amount of ^{152}Eu. The initial ^{152}Eu activity of Eu stock solutions was ~330 Bq/ml, which was used to calculate sorption ratios

Eu sorption isotherms on illite in absence of NOM (so-called “binary systems”) were measured by mixing 1 ml aliquots of conditioned illite suspension (25.6 g/l) with 15 ml of the different Eu stock solutions. The pH value of the obtained suspension was adjusted to about 8.2 with 1 mol/l HCl or 1 mol/l NaOH. The closed tubes were then shaken end-over-end for two weeks. Phase separation was carried out by centrifugation (21000g for 2hrs) and ultra-filtration (30KD) to distinguish immobile colloids from mobile colloids and dissolved species. Prior to use, filters of 30kD were conditioned with a 1 ml sample aliquot. The pH of the supernatant solution after centrifugation was determined.

Eu sorption isotherms on illite in presence of NOM (so-called “ternary systems”) were measured using two different procedures, mainly with the goal of investigating the order of mixing (*i.e.*, system reversibility) of the different components in the ternary systems on the overall adsorption. In a first series of experiments, Eu was first contacted with NOM-containing solution and this mixture was then added to illite. 9 ml aliquots of the different Eu stock solutions were mixed with 6 ml aliquots of the different NOM solutions (all having a TOC of about 100 ppm) for at least one day. 1 ml illite suspension (25.6 g/l) was then added to the mixed solutions, and the pH value was adjusted to about 8.2. In a second set of experiments Eu was added to suspensions consisting of illite pre-equilibrated with the different NOM solutions. 1 ml illite suspensions (25.6 g/l) were mixed with 6 ml aliquots of the different NOM solutions (TOC of about 100 ppm) and these suspensions were allowed to equilibrate for two weeks. 9 ml aliquots of the different Eu stock solutions were subsequently added to the illite-NOM suspensions and the pH value was adjusted to about 8.2. After two weeks, the resulting suspensions were analyzed for [Eu], TOC (UV), pH, and aqueous composition.

For the purpose of comparison, the sorption of the different NOM pools on illite was also investigated in parallel. NOM sorption isotherms on illite were measured by mixing 1 ml aliquots of conditioned illite suspension (76.6 g/l) with 15 ml of the different NOM stock solutions with different TOC concentration (10-80 ppm). pH value of solution was adjusted to about 8.2 if necessary and these suspensions were allowed to equilibrate for two weeks. Similarly, phase separation was carried out by centrifugation (21000g for 2hrs) and ultra-filtration (30KD).

Results and discussion

NOM is a key factor controlling the aqueous and solid phase speciation of trivalent actinides under Boom Clay geochemical conditions. Up to now, most focus was laid on NOM acting as an agent which increases the aqueous concentration and solubility, and therefore the mobility of long-lived RN, through complexation reactions. However, > 99% of NOM in Boom Clay is considered as immobile and the impact of NOM on the mobility of RN cannot be properly assessed without a sufficient understanding of the complexing properties of the different organic matter pools. Therefore, the adsorption of Eu^{3+} in ternary systems consisting of NOM and illite has been measured, with a specific focus on the size distribution (and therefore the mobilization potential) of NOM.

Sorption of Eu on illite (Binary system) and modelling

The binary sorption kinetics of Eu on illite in SBCW (absence of NOM) were rapid, reaching equilibrium in less than 2 days. The sorption tests were stopped after 14 days. After phase separation, the equilibrium concentration (c_{eq}) of Eu in the solutions was measured and the equilibrium sorption capacity (n_{eq}) of Eu was calculated to obtain sorption isotherms and sorption distribution ratio, as shown in figure 1. The Eu distribution was independent of the phase separation procedure, indicating that the formation of inorganic colloids containing Eu is negligible. The sorption isotherms and sorption distribution ratio of Eu on illite in SBCW could be modelled quite well by the 2 SPNE SC/CE model and associated parameters[8], introduced into Phreeqc v2.13, using the NAGRA/PSI[12] database for aqueous Eu speciation (figure 1).

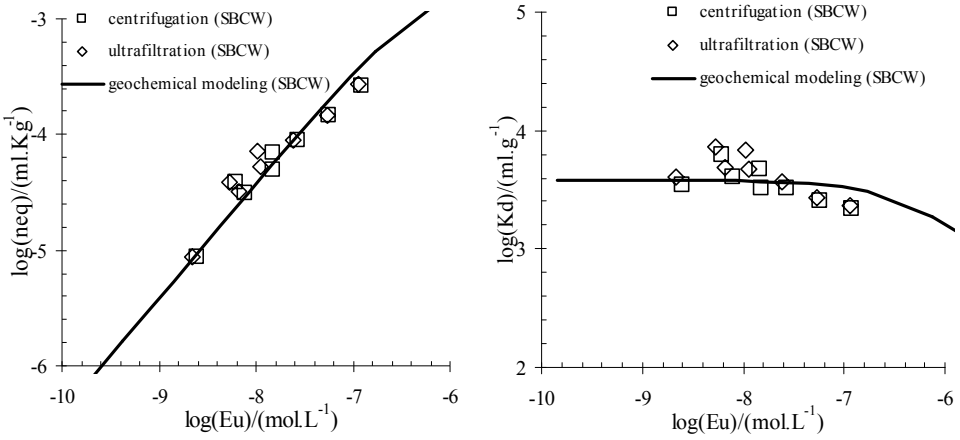

Figure 1: *Experimental and modelling results of Eu sorption on illite after phase separation in SBCW media (Without natural organic matter)*

Size distribution of NOM batches

Boom Clay NOM was liberated by mixing Boom Clay with RBCW (S/L = 1:10) or SBCW (S/L = 1:5.5) for one month. The obtained supernatant solutions were used as NOM pools. The size distribution of NOM liberated from Boom Clay is different from that present in sampled piezometer porewater (RBCW), as seen from figure 2. Suspending Boom Clay in water liberates a lot of larger, otherwise immobile NOM molecules, which gives an indication on the size-cut off for mobile colloids in Boom Clay. Based on the difference between the size distribution of RBCW and the distributions of the suspensions we can state that molecules >300 000 MWCO can be considered as immobile in Boom Clay.

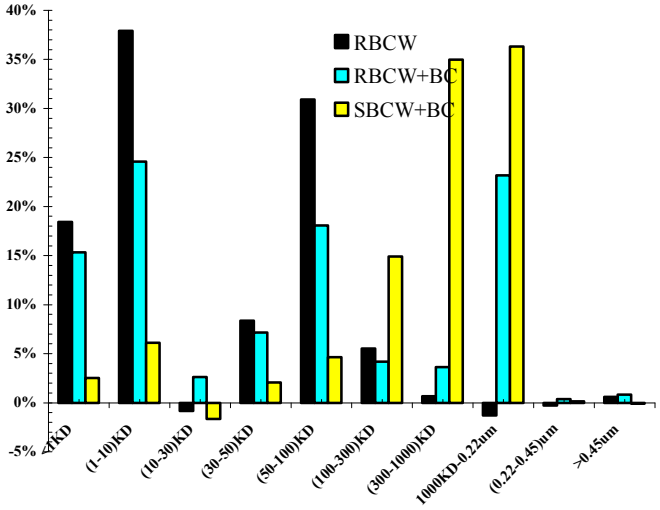

Figure 2: *The NOM size distribution of the different clay waters used in the experiments*

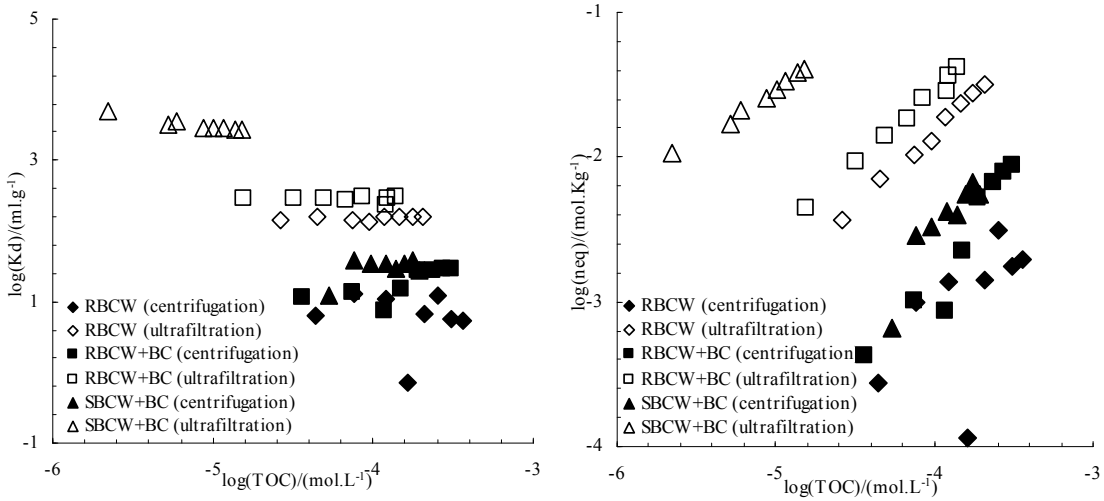

Figure 3: *Experimental results of NOM sorption on illite after phase separation*

Sorption of NOM on illite

To fully understand the adsorption behaviour of elements that strongly interact with NOM, it is also important to study the NOM sorption [13]. The sorption kinetics of NOM on illite were rapid, reaching equilibrium in less than 1 day. Subsequent sorption experiments were shaken for at least 14 days. It was observed (figure 3) that after centrifugation the sorption of NOM on illite was very weak but depends on the size distribution (LogKd~0.8-1.5). The different high sorption distribution ratio for NOM after ultrafiltration also indicated the role of size distribution of the different NOM, not sorption of NOM on illite (see figure 2).

Sorption of Eu on illite/NOM (Ternary system)

In the ternary systems, reversibility and the establishment of chemical equilibrium were checked by varying the order of mixing (and pre-equilibrating) of the three different components (Eu, organic matter, and illite). The experimental results indicated that all the sorption kinetics of ternary systems were rapid, reaching equilibrium in less than 2 days. The sorption tests were stopped after 14 days. For all the ternary sorption experiments, the equilibrium concentration (c_{eq}) of Eu in the solutions was measured and the equilibrium sorption capacity (n_{eq}) of Eu in different systems was calculated. The experimental results, together with the modelling results are given in Figure 4

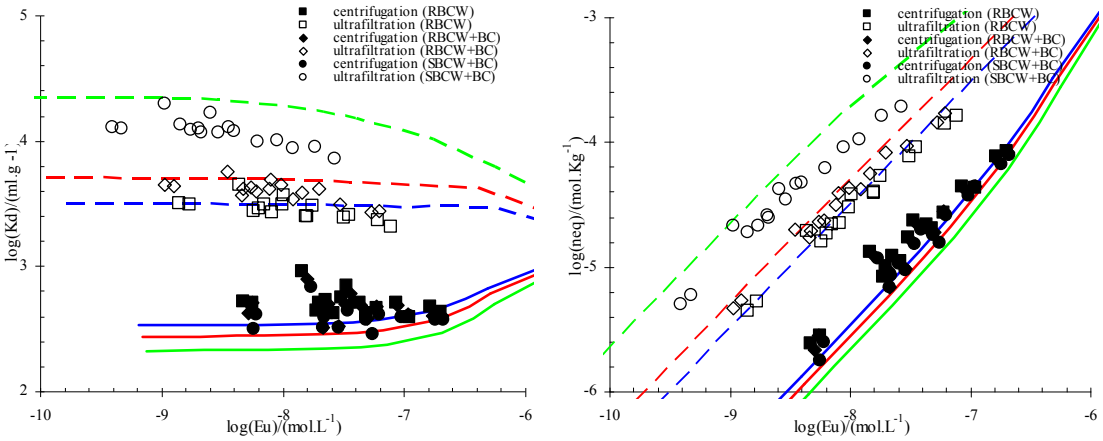

Figure 4: *Influence of natural organic matter on the Eu sorption on illite, experimental data and modelled curves.*

As variation in the order of mixing did not have a significant impact on the sorption (, it can be concluded that chemical equilibrium was established and sufficient reversibility was attained in all the ternary sorption systems.

As can be seen from figure 4, the K_d value of the ultrafiltered systems was about one order of magnitude higher compared to the centrifuged systems. This exemplifies the role of large NOM colloids acting as a sorption sink under *in situ* Boom Clay conditions (the Eu concentration associated with these larger NOM colloids are regarded as part of the solid phase). The differences noted between the different data sets, again highlight the impact of the size distribution of the used NOM pools.

Modelling of ternary system

In a previous study[9] on Eu solubility in RBCW, the interaction between NOM and Eu^{3+} could be modelled using Tipping's Humic Ion-binding model VI, introduced into Phreeqc v2.13. The constants used in the model for two size fractions of NOM were: Log $K_{MA}^{0.45\ \mu m}$ = 4.00, PEC (proton exchange capacity) = 4.00 meq/g; Log K_{MA}^{30KDa} = 2.30, PEC = 2.00 meq/g.

This model was now used for the more complicated system consisting of illite, NOM, and carbonate.

Modelling the experimental data using a simple additivity rule over-predicted the Eu^{3+} solution concentration in centrifuged ternary systems and seriously under-predicted the Eu^{3+} solution concentration in filtered ternary systems. Therefore the interaction parameters were adapted using the following guidelines[14]:

1) due to the presence of negatively charged NOM, the surface of illite can become more negative and adsorption of Eu increases, which will increase the log K of Eu-illite;

2) due to the presence of illite particles, NOM molecules can become more positively charged and complexation of Eu decreases, which will decrease the log K of Eu-NOM. It is assumed that larger NOM molecules are more affected than smaller NOM molecules due to electrostatics.

The following parameters were adapted, according to the above considerations, to fit the data: increase Eu-illite log K values with 0.5, change of Log K_{MA}^{30KDa} = 2.05, and Log $K_{MA}^{0.45\ \mu m\ (centrifugation)}$ = 2.10. The proton exchange capacity for RBCW used in the model was consistent with that of Eu(III) solubility in RBCW[9] and was not adapted. The surface complexation reactions and the corresponding Eu-illite logK values are given in table 1. The parameters used in the Tipping model to describe the Eu-NOM interaction are given in table 2.

Table 1: *The surface complexation reactions and corresponding logK values used for the modelling of the Eu sorption on illite in the presence and absence of NOM*

surface complexation reactions	$logK_{Eu\text{-}illite}$	
	sorption experiments without NOM (SBCW)	sorption experiments with NOM
$Ill\_sOH + Eu^{+3} = Ill\_sOEu^{+2} + H^+$	3.1	3.6
$Ill\_sOH + Eu^{+3} + H_2O = Ill\_sOEuOH^+ + 2H^+$	-4.2	-3.7
$Ill\_sOH + Eu^{+3} + 2H_2O = Ill\_sOEu(OH)_2 + 3H^+$	-12.5	-12.0
$Ill\_wOH + Eu^{+3} = Ill\_wOEu^{+2} + H^+$	0.3	0.8
$Ill\_wOH + Eu^{+3} + H_2O = Ill\_wOEuOH^+ + 2H^+$	-6.2	-5.7

Table 2: *The log K_{MA} of Eu-NOM and PEC of RBCW used in the Tipping model for the present sorption experiments and former solubility experiments [9]*

	sorption experiments		solubility experiments	
	Centrifugation	ultra-filtration of 30 KDa	0.45 µm	ultra-filtration of 30 KDa
$logK_{MA}$	2.10	2.05	4.00	2.30
PEC (meq/g)	4.00	2.00	4.00	2.00

Summary and Conclusions

In absence of humic substances, the measured sorption isotherm could be well reproduced using the 2 SPNE SC/CE surface complexation model and associated parameters[8]. With respect to the influence of humic substances on the Eu distribution, the sorption of dissolved organic matter on illite was very weak but dependent on the size distribution.
In the ternary systems, the order of mixing Eu-NOM to illite or Eu to NOM-illite, did not have a significant effect on the Eu sorption, indicating reversibility of the system, and chemical equilibrium. The presence of dissolved organic matter in solution decreased the Eu distribution coefficients by an order of magnitude because of complexation reactions between Eu and organic matter. However, the overall retention may be increased because of the immobility of high molecular-weight NOM molecules under *in situ* conditions.
The sorption behaviour of Eu on illite in media containing NOM (ternary sorption system) could also be interpreted with the 2SPNE SC/CE model in combination with a humic ion-binding model VI (Tipping), which was used previously to describe $Eu(OH)_3$ solubility experiments in NOM containing Boom Clay water.

Acknowledgement

Mr. D. J. Liu acknowledges the financial support of the Belgian Government via FOD wetenschapsbeleid as a visiting scientist. This work is undertaken in close co-operation with, and with the financial support of NIRAS-ONDRAF and EC in the frame of the 6FP FUNMIG project. The critical follow-up by and fruitful discussions with Mrs. A. Dierckx, Mr. R. Gens (N/O) are very much appreciated

References

[1] Maes A, De Brabandere J, Cremers A. (1998) A modified Schubert method for the measurement of the stability of europium humic acid complexes in alkaline conditions. Radiochim. Acta 44/45, 51.
[2] Dierckx A, Maes A, Vancluysen J. (1994) Mixed complex complex formation of Eu3+ with humic acid and complexing ligand, Radiochim. Acta 66/67, 149.
[3] Maes A, De Brabandere J, Cremers A. (1991) Complexation of Eu^{3+} and Am^{3+} with humic substances. Radiochim. Acta 52/53, 41.
[4] Wang L, Maes A, De Cannière P. (1998) Sorption of europium on illite (Silver Hill Montana). Radiochim. Acta 82, 233-237.
[5] Bradbury M. H. and Baeyens B. (2002) Sorption of Eu on Ca-montmorillonite: experimental investigations and modelling with cation exchange and surface complexation. Geochim. Cosmochim. Acta 66(13), 2325-2334.
[6] Bradbury M. H. and Baeyens B. (2005) Modelling the sorption of Mn(II), Co(II), Ni(II), Zn(II), Cd(II), Eu(III), Am(III), Sn(IV), Th(IV), Np(V) and U(VI) on montmorillonite: Linear free energy relationships and estimates of surface binding constants for some elected heavy metals and actinides. Geochim. Cosmochim. Acta 69(4), 875-892.

[7] Rabung TH., Pierret M. C., Bauer A. (2005) Sorption of Eu(III)/Cm(III) on Ca-montmorillonite and Na-illite. Part 1: Batch sorption and time-resolved laser fluorescence spectroscopy experiments. Geochim. Cosmochim. Acta 69(23), 5393-5402.
[8] Bradbury M. H., Baeyens B., Geckeis H. (2005) Sorption of Eu(III)/Cm(III) on Ca-montmorillonite and Na-illite. Part 2: Surface complexation modelling. Geochim. Cosmochim. Acta 69(23), 5403-5412.
[9] D. J. Liu, C. Bruggeman, N. Maes (2008) The influence of natural organic material on the speciation and solubility of Eu in Boom Clay porewater. Radiochim. Acta 96, 711-720.
[10] E. Tipping (1998) Humic ion-binding model VI: An improved description of the interactions of the protons and metal ions with humic substances. Aquatic Geochemistry 4, 3-48.
[11] De Craen M., Wang L., Van Geet M., Moors H. (2004) Geochemistry of Boom Clay pore Water, SCK-CEN-BLG-990, Mol, Belgium, pp. 108.
[12] W. Hummel, U. Berner, E. Curti (2002) Chemical Thermodynamic Data Base 01/01. Nagra / PSI Technical Report. July 2002.
[13] Bryan, N. D., Barlow, J., Warwick, P., Stephens S. (2005) The simultaneous modelling of metal ion and humic substance transport in column experiments. Journal of Environmental Monitoring 7, 196-202.
[14] Vermeer A.W.P., McCulloch J.K., van Riemsdijk W.H., Koopal L. (1999) Metal ion adsorption to complexes of humic acid and metal oxides: deviations from the additivity rule. Environ. Sci. Technol. 33, 3892-3897.

UPDATE ON REAL SITE PROCESS ANALYSIS IN CRYSTALLINE ROCK

Marcus Laaksoharju[1*], John Smellie[2], Eva-Lena Tullborg[3], Jorge Molinero[4], Maria Gimeno[5], Gunnar Buckau[6]

[1] Geopoint AB (SE)
[2] Conterra AB (SE)
[3] Terralogica AB (SE)
[4] Amphos (ES)
[5] University of Zaragoza (ES)
[6] FZK-INE (DE)

* Corresponding author; marcus@geopoint.se

Abstract

Processes determining the groundwater system in crystalline rock based on actual site analysis of data from Forsmark are presented and discussed. The discussion is based on site investigations in crystalline bedrock within the Swedish programme leading to the construction and operation of a high level nuclear waste repository. Presented is a detailed description and understanding of issues related to groundwater origin and evolution, interactions of surface/deep groundwater systems, bedrock buffer capacity, uranium behaviour, microbes, gases and colloids.

The results and modelling methods used within the SKB hydrochemical and hydrogeological programmes can be used in site performance assessment (PA) and safety assessment (SA). The obtained data and process understanding can be used: 1) for input parameter values in calculating long-term repository safety, and 2) to understand the present undisturbed hydrogeochemical conditions and how these conditions will change in the future. Parameter values for safety analysis include pH, Eh, S^{2-}, SO_4, HCO_3, HPO_4 and TDS together with colloids, fulvic and humic acids, other organics, bacteria and nitrogen.

Introduction

The Swedish Nuclear Fuel and Waste Management Company (SKB) is undertaking site characterisation at two different locations, the Forsmark and Laxemar areas, with the objective of siting a geological repository for spent nuclear fuel. In this paper examples from the Forsmark site modelling are given. The investigations were conducted in a series of regular campaigns each culminating in a 'data freeze', i.e. date beyond which no further data were incorporated in the database for interpretation and modelling. After each data freeze, the site data were analysed and site descriptive

modelling was carried out with the purpose to develop a Site Descriptive Model (SDM) of the site. A Site Descriptive Model is a synthesis of geology, rock mechanics, thermal properties, hydrogeology, hydrogeochemistry and a surface system description.

The scope of the modelling steps, 1.2 and 2.1 (SKB R-05-18; SKB R-05-17; SKB R-05-17; SKB R-06-38; SKB R-06-69; Laaksoharju et al., 2007a,b; Laaksoharju et al., 2008a) were limited, whereas the final step based on data freezes 2.2 and 2.3, resulted in a final hydrogeochemical site description (Laaksoharju et al, 2008b).

Objectives

The overall objectives of the hydrogeochemical site description for Forsmark are to first establish a detailed understanding of the hydrogeochemical conditions at the site, and to use this understanding to develop models that address the needs identified by the safety assessment groups during the site investigation phase. Issues of concern to safety assessement are radionuclide transport and technical barrier behaviour, both of which are dependent on the chemistry of groundwater and porewater and their evolution with time (Laaksoharju et al, 2008b).

Results and discussion

The work has involved the development of descriptive and mathematical models for groundwaters in relation to rock domains, fracture domains and deformation zones. The groundwaters have been interpreted in relation to their *origin*, *evolution* and *composition*, which require close integration with geological, climatological and hydrogeological information. Past climate changes are one of the major driving forces for long-term hydrogeochemical changes (hundreds to thousands of years) and are, therefore, of fundamental importance for understanding the palaeohydrogeological, palaeohydrogeochemical and present evolution of groundwater in the Fennoscandian crystalline bedrock. In contrast, redox buffer capacity of the bedrock will minimise the effects on changes in alkalinity and redox at repository depths, therefore limiting the variations in pH and Eh significantly, regardless of major changes in groundwater composition.

The Forsmark 2.2 and 2.3 data have resulted in significant modifications to the version 2.1 site understanding. The many consistent temporal and spatial data support the description concerning the groundwater origin, most of the major end members and major hydrochemical processes. Integration with hydrogeology supports the palaeohydrogeological description of the site. Reaction modelling, different isotope ratios (Sr, S, C, B, Cl, O, H and the U-decay series), buffer capacity modelling and measurements of Eh, pH and microbe data, all support the process understanding. Matrix porewater compositions have now been well established and have contributed greatly to the present conceptualisation of the Forsmark area. Input from the fracture mineralogical studies have provided important support to the palaeohydrogeological and process understanding of the site. The confidence concerning the three-dimensional variability of processes and properties was improved due to the addition of both new data in previously drilled boreholes and from new boreholes in specific key areas.

Several groundwater types which are now present in the bedrock can be associated with past climatic events in the late Pleistocene, including inter-glaciations, glaciations, de-glaciations, and associated shore-level displacements in connection with marine/non-marine transgressions and regressions. Among these, the last glaciation and post glacial period is the most important for the groundwater development in the Fennoscandian Shield, especially in terms of land uplift and shore-level displacement and the development of the Baltic Basin. The description is not restricted to post glacial time since there is groundwater and porewater evidence that indicates a pre-Pleistocene warm-climate derived meteoric water component. The hydrochemistry of the Forsmark area cannot be explained without recognising this older (minimum 1.5 Ma) component. The present groundwaters therefore are a result of mixing and reactions over a long period of geological time. The interfaces between different water types are not sharp but reflect the variability in the structural-hydraulic properties.

Groundwaters in the uppermost 20 to 200 m of the bedrock display a wide chemical variability with chloride concentrations in the range 200 to 2,000 mg/L suggesting influence of both fresh meteoric water and brackish marine water (i.e. Baltic Sea water and Littorina Sea relicts). Furthermore, a sharp decrease in tritium content at about 150 m depth, as well as ^{14}C data, indicate that these shallow groundwaters have short residence times that are mostly in the order of a few hundred years to only a few decades.

At depths greater than approximately 200 m, the water composition is indicative of a brackish marine water with chloride concentrations in the range 2,000 to 6,000 mg/L and with a clear Littorina component, as indicated by concentrations of magnesium and the bromide to chloride ratio concentrations. This water type is recognised down to 600 to 700 m depth in the transmissive gently dipping fracture zones in the south-eastern part of the candidate area (hanging wall bedrock), whereas the penetration depth in the footwall bedrock (i.e. fracture domain FFM01, the target volume), where the frequency of water-conducting fractures is low, the penetration is restricted to around 300 m. Below these depths, the water composition indicates brackish to saline non-marine groundwaters (i.e. absence of Littorina influence), reflecting processes which have occurred prior to the intrusion of the Littorina Sea waters. These deep waters further show a depth increase in calcium which, compared with sodium, represents a well recognised trend and indicative for water/rock interactions that occur under low flow to stagnant groundwater conditions which increase with depth.

Analyses of the composition of rock matrix porewater also support the occurrence of low groundwater turnover in the footwall bedrock (i.e. fracture domain FFM01). Porewater from this location generally has lower chloride contents and is enriched in $\delta^{18}O$ compared to the fracture groundwaters, indicating a transient state between the porewater and groundwater down to at least 650 m depth. A signature with low chloride, low magnesium and enriched in $\delta^{18}O$ and $\delta^{2}H$ has been preserved far away from conducting fractures, suggesting that these porewaters have evolved from an earlier, very long lasting circulation of old dilute groundwaters in a few fractures. This is also consistent with the still prevailing transient state between this porewater and fracture groundwater from equivalent depths that, based on ^{36}Cl and ^{4}He dating, have

residence times of more than 1.5 Ma. Southeast of the target volume in the hanging wall bedrock, a situation close to steady-state is suggested between porewater and fracture groundwater down to about 200 m depth, reflecting the high frequency of water conducting, gently dipping deformation zones, and the rapid circulation of significant volumes of water in this area. At greater depth, the porewater has lower chloride contents than the fracture groundwater indicating a transient state down to about 650 m depth.

Transport of water volumes and mixing (both advection-dispersion and molecular diffusion) are major processes giving rise to present-day groundwater compositions. However, mixing also induces reactions and therefore the separation of these two processes is not only very challenging, but is also important for site understanding in order to indicate effects from past/present transport and reactions. Reactions involve interaction with the bedrock and fracture minerals, and in particular the alkalinity and redox buffering capacity of the bedrock is of key importance for groundwater composition and predicting future changes due to, for example, potential infiltration of dilute and oxidising waters.

Weathering and potential calcite dissolution under acidic conditions in the near-surface bedrock environment is promoted by the extensive presence of limestones in the overburden and controlled by biogenic input of carbon dioxide. This gives rise to pH values usually above 7, calcium concentrations mostly between 50 and 200 mg/L, and bicarbonate concentrations in the range 200 to 900 mg/L in the near-surface waters (down to about 20 m depth). Concentrations then decrease to very low values at greater depths. However, bicarbonate is relatively high in most of the brackish marine groundwaters hosted in the upper 600 m of the gently dipping fracture zones in the hanging wall bedrock segment, south-east of the target volume, whereas brackish non-marine groundwaters below 300 m in the footwall bedrock segment (i.e. fracture domain FFM01) have low bicarbonate contents.

The pH buffering capacity in the Forsmark groundwaters at depths greater than 100 m appears to be controlled by the calcite system, and modelling indicates that this water is in equilibrium with calcite. Investigations of fracture minerals show that calcite in fractures is abundant and that no extensive leaching has occurred in response to past glaciation/deglaciation events. These findings suggest that the buffering capacity against infiltrating dilute groundwater is sufficient, although no quantifications have been made.

According to data analyses and modelling of the redox system, reducing conditions currently prevail at depths greater than about 20 m. Most of the Eh values determined in brackish groundwaters (at depths between 110 and 646 m) seem to be controlled by the occurrence of an amorphous iron oxyhydroxide with higher solubility than a truly crystalline phase. This indicates that the iron system is disturbed, which also is supported by mineralogical investigations that have identified the presence of fine-grained amorphous to poorly crystalline phases now evolving towards more crystalline phases. At still greater depths the iron system seems to be limited by only crystalline iron hydroxides, mainly hematite. Despite the uncertainty of the measured data (e.g. due to sampling perturbations), the dissolved sulphide concentrations at shallow to

intermediate depths are systematically low, possibly due to the precipitation of amorphous Fe(II)-monosulphides, linked to the activity of sulphur-reducing bacteria (SRB). At depths greater than 600 m, the dissolved sulphide concentrations increase, which is consistent with the occurrence of SRB and with the active precipitation of Fe(II)-monosulphides.

The behaviour of uranium is a special case at Forsmark. Elevated concentrations have been detected in groundwaters associated with a Littorina component and the highest concentrations are found in waters in the gently dipping deformation zones in the hanging wall bedrock south-east of the target volume. There are indications that these elevated concentrations are related to easy dissolvable uranium fractions in fracture coatings in contact with these waters. Speciation-solubility calculations support this conclusion and indicate that the high uranium contents are the result of the control exerted by an amorphous (and very soluble) uranium phase present in the system, and weakly reducing Eh values which may allow uranium complexation and re-equilibrium depending on Eh and dissolved carbonate.

The presence of goethite (FeOOH) in some hydraulically active fractures and fracture zones (mainly within the major gently dipping deformation zone ZFMA2/ZFMF1) in the upper part of the bedrock indicates circulation of oxidising fluids during some period in the past (potentially Quaternary). However, the presence of pyrite in the same zones suggests that the circulation of oxidising fluids has been concentrated along channels in which different redox micro environments may have been formed. Furthermore, mobilisation as well as deposition of uranium in the upper 150 m of the bedrock is indicated by U-series decay analyses (USD) of fracture coatings.

The analyses of the current redox system at Forsmark have consistently indicated that sampling (or drilling-induced) perturbation may have altered the original redox conditions of the hydrochemical system. Examples include oxygen intrusion and precipitation of amorphous iron oxyhydroxides, as indicated by the colloidal composition (see below) and mineralogical determinations. Additionally, there could have been modification of the original Eh and/or alkalinity by drilling waters, and the increase in dissolved uranium contents or changes in sulphide contents could have been caused partly by one or more of these disturbances. Despite these potential disturbances, the buffer capacity of the system maintains a marked alkalinity and a noticeable reducing character. Concerning the potential redox buffering capacity of the fracture system, it is concluded that previous oxidising episodes have not been intense enough to exhaust the reducing capacity of fracture filling minerals, which are still present in the shallow system (for example chlorite and pyrite).

Analyses of gases dissolved in groundwater at Forsmark have shown that the gas content increases with depth, but the waters are far from being oversaturated by gas. The major gas components are nitrogen and helium. Methane has also been detected, but generally in small amounts (less than 0.2 mL/L). Currently, it is not known whether the methane is of biogenic or non-biogenic origin, or a mixture of both.

Colloid amounts in Forsmark groundwater are comparable to that found in other granitic environments. The colloids are composed mostly of aluminium, silica, iron and sulphur. Uranium associated to the colloids was found in boreholes KFM02A and KFM06A, in line with the high groundwater uranium concentrations found in these boreholes. The uranium content on the colloids is about 10% of the uranium concentration in the groundwater and colloidal transport is, therefore, the result but not the origin to the elevated uranium content in the groundwater.

There is generally a high confidence in the description and understanding of the current spatial distribution of groundwater composition, mainly due to the consistency between different analyses and modelling of the chemical data, but also due to the agreement with the hydrogeological understanding of the area. The existence of a near-surface redox reaction zone appears to be plausible, but this is still unclear from uncertainties in data interpretation. Nevertheless, the abundance of calcite suggests there is active buffering capacity on dilute groundwaters low in calcite. Furthermore, even though quantification of the bedrock buffering capacity is not yet achieved, general indications from the Forsmark area as a whole point to a bedrock which has a sufficiently large buffering capacity to maintain pH values in the range 7 to 8.5 and Eh values lower than -140 mV. One important remaining uncertainty concerns the increase in sulphide concentrations measured in the on-going monitoring programme. Initial drilling and pumping may have disturbed the system or may have facilitated sulphate reduction, but this issue remains to be resolved. The monitoring programme will also support the overal understanding of the long term behaviour of other groundwater parameters such as uranium, DOC and tritium.

Relevance of the above results for PA

The results and methods used for modelling within the SKB hydrochemistry and hydrogeological programme can be used in performance assessment (PA) and safety assessment (SA) by the following:

- Provide understanding of water movement and timescales for calculating the dose and validation of hydrogeological models.
- Water types can indicate the presence of hazardous species (e.g. HS, CH_4, U and high Cl) in areas with little or no sampling.
- Mixing models can be used within PA and SA to indicate changes of concentrations with time.
- Confirmation and calibration of processes of importance for PA and SA.
- Site understanding builds long-term confidence in the site.

The results and modelling methods used within the SKB hydrochemical and hydrogeological programmes can be used in site performance assessment (PA) and safety assessment (SA). The obtained data and process understanding can be used: 1) for input parameter values in calculating long-term repository safety, and 2) to understand the present undisturbed hydrogeochemical conditions and how these conditions will change in the future. Parameter values for safety analysis include pH, Eh, S, SO_4, HCO_3, HPO_4 and TDS (mainly cations), together with colloids, fulvic and

humic acids, other organics, bacteria and nitrogen. These values will be used to characterise the groundwater environment at, above and below repository depths. When the hydrogeochemical environment is characterised, this knowledge, together with an understanding of the past and present groundwater evolution, should provide the basis for predicting future changes.

Summary and Conclusions

The hydrogeological and hydrogeochemical characterisation of the Forsmark site have been achieved and issues relevant to key geochemical processes and understanding have been addressed. These results are directly relevant for site performance assessment not only at the present time, but importantly in predicting the future evolution of the site.
The specific aims were achieved:

- To document the hydrogeochemistry at the Forsmark site with focus on the development of conceptual models to describe and visualise the site.
- To provide relevant parameter values to be used for safety assessment calculations.
- To provide the hydrogeochemical basis for the modelling work by other SKB modelling teams, in particular hydrogeology.
- To take account of the feedback from the safety assessment work that bears relevance to the hydrogeochemical modelling work.

References

Laaksoharju, M., Smellie, J., Tullborg, E-L., Gimeno, M., Molinero, J., Gurban, I., Hallbeck, L., (2008a): Hydrogeochemical Evaluation and Modelling Performed within the Site Investigation Programme. Appl. Geochem. No 23. Issue 7, July 2008.

Laaksoharju, M., Smellie, J., Tullborg, E-L., Gimeno, M., Hallbeck, L., Molinero, J. and Waber, N., (2008b): Bedrock hydrogeochemistry Forsmark, Site descriptive modelling, SDM-Site Forsmark. SKB R-08-47

Laaksoharju M, Smellie J, Tullborg E-L, Molinero J, Gimeno M and Buckau G. (2007a): Results from the groundwater hydrogeochemical investigation program in Sweden, in: 2nd Annual Workshop Proceedings of the Integrated Project "Fundamental Processes of Radionuclide Migration", SKB Technical Report TR-07-05, pp 123 - 129.

Laaksoharju M, Smellie J, Tullborg E-L, Gimeno M, J.B. Gómez, L.F. Auqué, Molinero J, Gurban I, Hallbeck L and Gunnar B. (2007b): Hydrogeochemical methodology for constructing site descriptive models within the Swedish site investigation programme. Contibution to the WRI-12 conference in Kunming, China 2007.

SKB R-05-18: Preliminary site description, Forsmark area – version 1.2. SKB R-Report (R-05-18), SKB, Stockholm, Sweden.

SKB R-06-38: Site descriptive modelling Forsmark stage 2.1. Feedback for completion of the site investigation including input from safety assessment and repository engineering.

SKB R-05-17: Hydrogeochemical evaluation. Preliminary site description, Forsmak area – Version 1.2, Report SKB R-05-17, Svensk Kärnbränslehantering AB, March 2005.

SKB R-06-69: Hydrogeochemical evaluation of the Forsmark site, modelling stage 2.1 - issue report SKB R-06-69.

DYNAMIC STUDY OF BENTONITE COLLOID RETENTION IN A SMOOTH GRANITE FRACTURE UNDER UNFAVORABLE ELECTROSTATIC CONDITIONS

N. Albarran*, T. Missana, U. Alonso, M. García-Gutiérrez, T. Lopez-Torrubia

CIEMAT, Departamento de Medioambiente
Avenida Complutense, 22 – 28040 MADRID (Spain)
Phone: +34-913466185, Fax:+34-913466542

*Correspongin author: nairoby.albarran@ciemat.es

Abstract

The study of the main mechanisms affecting bentonite colloid transport/retention in a crystalline medium under low water flow rates is an important task to understand their role in radionuclide migration. As roughness effects have been reported to be relevant in bentonite retention under unfavorable electrostatic conditions, a smooth artificial granite fracture was used to analyze in detail the effects of water velocity on colloid recovery.
Even when electrostatic conditions were unfavorable for colloid attachment to rock surfaces, colloids were observed to be retained in the fracture. Retention increased when the water flow rate decreased indicating the importance of the hydrodynamic conditions.

Introduction

In the frame of performance assessment of a deep geological repository (DGR), it is necessary to study all the processes that can affect radionuclide (RN) migration after an eventual canister failure. In particular, the contribution of colloids that could be generated from the engineered barrier of the repository is a process under analysis.
Transport experiments in a granite fractured column coming from the FEBEX site located at the GTS (Grimsel Test Site, Switzerland) were carried out with bentonite colloids (100 ppm) under low water flow rates, trying to mimic the conditions present in a DGR. Experiments were performed at low ionic strength and alkaline pH, as these conditions ensures colloid stability.
In these conditions, the granite surface is negatively charged as well as bentonite colloids and, in principle, electrostatic repulsion is expected. However, Alonso et al., 2008. (this volume) in static experiments, observed that under these conditions, colloids can be still retained over the surface, probably due to physico-chemical heterogeneity effects.

The main aim of this work is to study the bentonite colloid (retention) but under dynamic conditions, also in the unfavourable case for colloid/rock electrostatic interactions. The roughness effects are minimised, by using an artificial polished granite

fracture. Nonetheless, the effects of water velocity on colloid retention are also analysed trying to approach the lower flow rate, as in the real case.

Materials and methods

Bentonite colloids were produced from a bentonite coming from the Cortijo de Archidona deposit (Almeria, Spain), FEBEX bentonite, that has a high smectite content (93±2%). The colloidal fraction (< 0.5 μm) was obtained after converting it in a homoionic Na-form.
Transport of colloids in the fracture was studied using suspensions prepared at pH 9.7 in $NaClO_4$ $5 \cdot 10^{-4}$ M and with concentration of 100 ppm.
Figure 1 (left) shows the image by field emission scanning electron microscopy (FESEM), of bentonite colloids prepared in laboratory.

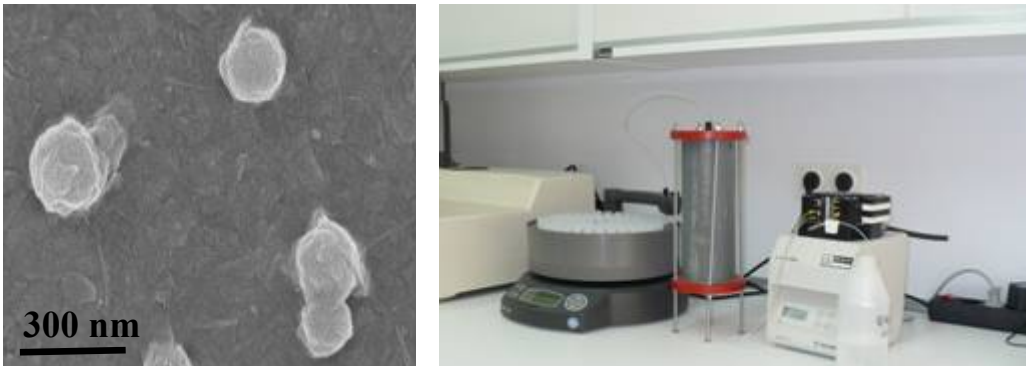

Figure 1: *Left: FESEM image of bentonite clay colloids as prepared in laboratory. Right: Experimental set-up used in column experiments.*

Column transport experiments were carried out using a granite core from the Grimsel Test Site (GTS, Switzerland) with a longitudinal fracture artificially produced. The core comes from the borehole FUN01 recently drilled at the FEBEX gallery at the GTS (Huertas et al., 2000).

For the hydrodynamic characterization of the column, previous to colloid migration tests, the transport of tritiated water (HTO) was studied using a water flow rate of Q = 0.5 $mL \cdot min^{-1}$. The HTO initial concentration was C_0 = 134000 $\mu Ci \cdot mL^{-1}$. This tracer is used because it presents negligible interactions with the solids, it is no-sorbing (conservative) and thus its transport behavior represents that of the water. The activity of HTO was measured by liquid scintillation counting with a TR-2700 Packard counter.
To perform transport experiments, the tracer (0.5 mL) or the colloidal suspension (2 mL) were injected as a "pulse" at the bottom of the column with a peristaltic pump. Before starting the experiment, the stability of the flow rate was controlled. Experimental set-up with the granite column is showed in Figure 1 (right).
Transport experiments were carried out varying the flow rates (from 0.02 to 1.16 $mL \cdot min^{-1}$). The eluted water was periodically collected, at the end of the column with a fraction collector in previously weighted polyethylene tubes. The concentration of bentonite particles in a given sample was measured by Photon Correlation Spectroscopy (PCS) using calibration curves (*counts vs. bentonite colloid concentration*) (Missana et

al., 2003). Breakthrough curves are expressed as the ratio between the measured concentration in the eluted fraction and the initial one (C/C_0) as a function of time or eluted volume.

Results and discussion

Previous to colloid transport experiments, the behavior of the conservative HTO in the Grimsel column was studied. According to the position of the peak obtained in the HTO breakthrough curve, the dynamic porosity (or pore volume) of the system was determined to be 10.0 ± 0.5 mL. The peak height is close to 17 % of initial tracer concentration. The recovery of HTO in this experiment is approximately 100 %, as expected for a conservative tracer, due to its negligible interactions with the solid.

Figure 2 shows the breakthrough curve of bentonite colloids in the Grimsel fractured core. Figure 2a shows the breakthrough curves of bentonite colloids at three different flow rates (1.11, 0.16 and 0.02 mL·min^{-1}) and Figure 2b shows the fraction of bentonite colloids recovered at those flow rates.

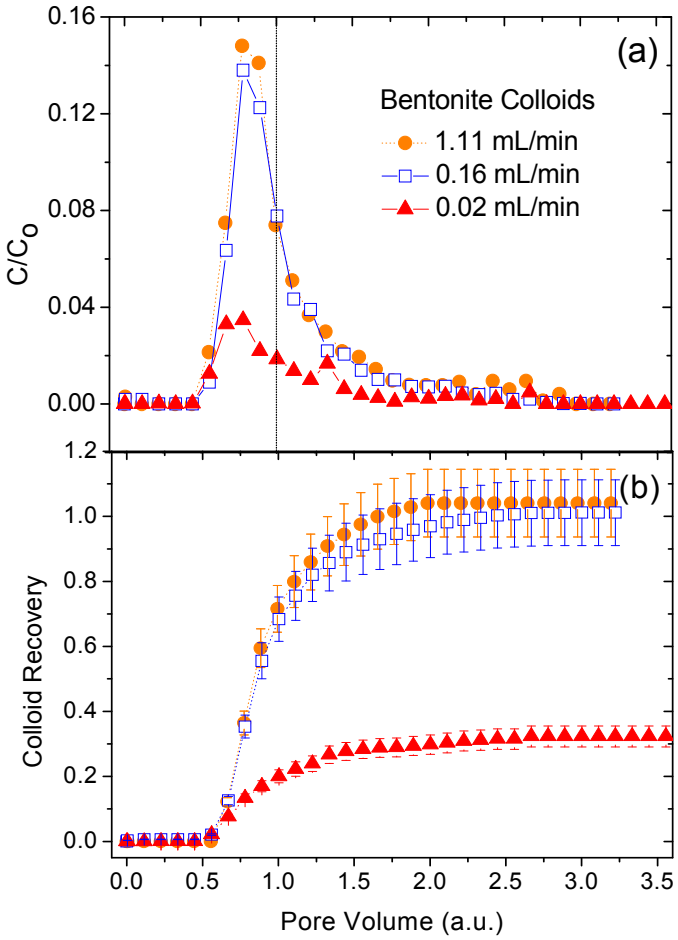

Figure 2: *a) Bentonite colloid breakthrough curves at different flow rates. b) Fraction of colloids recovered.*

The peak of the breakthrough curves of colloids appears at approximately 0.8 units of pore volume, a position slightly anticipated in respect to the conservative tracer HTO, dashed line in the graph (Figure 2a), indicating that colloids in this system may travel slightly faster than water, as was previously observed at the GTS (Möri et al., 2003). Anionic exclusion is probably the physical phenomena that explains this slightly anticipated position (Small et al., 1976).

However, the height of the peaks decreases as the flow rate decreases, indicating that retention in the fracture takes place. Higher residence times encourage somewhat stronger colloid-fracture surface interactions (Missana et al., 2006).
Figure 3 summarises the flow rate dependence of the recovery for bentonite colloids. In these experiments, the maximum recovery for bentonite colloids was obtained at the higher flow rate investigated (1.1 mL·min^{-1}) and was 100 %, similar to that of the conservative tracer. However, in spite of the unfavorable electrostatic conditions, at lower water flow rates, bentonite colloids were retained in the fracture, indicating a strong filtration of the clay colloids in the system. This is an important observation for the analysis of colloid effects in radionuclide transport in a waste repository.

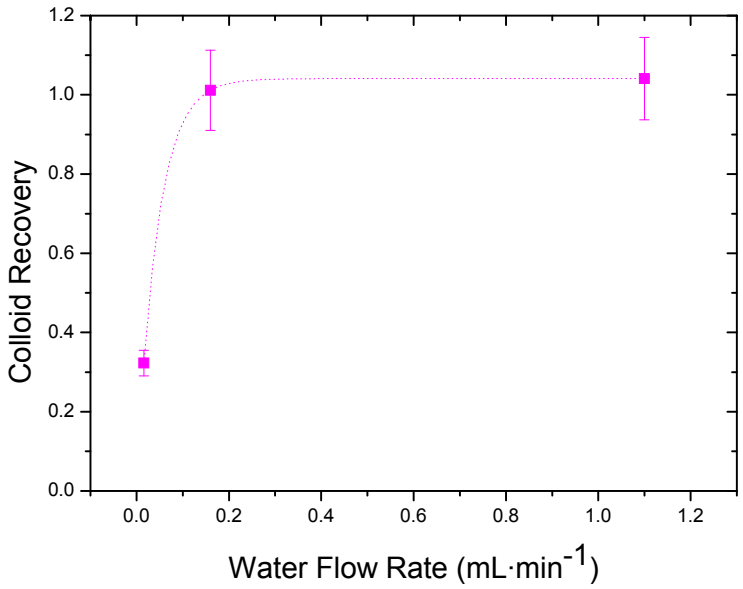

Figure 3: *Dependence on the colloid recovery as a function of the water flow rate.*

Migration studies presented here, were performed in columns with an artificially cut longitudinal fracture in which the roughness is minimized in respect to the "real" case.

Previous studies of bentonite colloid migration in a natural longitudinal fracture (Missana et al., 2008) with similar hydrodynamic characteristics that the one used in this work , also indicated a clear dependence of the recovery with flow rate: the higher the flow rate, the higher the colloid recovery, confirming that the flow rate is a critical

parameter in bentonite colloid transport. The bentonite colloid recovery obtained in a natural rough fracture (Missana et al., 2008), under similar conditions to that used in the present study ($I=1\cdot10^{-3}$ M, pH=9.7, flow rate 0.2 $mL\cdot min^{-1}$, pore volume 11 mL and bentonite colloid concentration = 100 ppm), was even smaller than that showed in Figure 2b. In fact, it was lower than 10 %.

Figure 4 shows data from Missana et al., 2008. If we compare the recovery of bentonite colloids in the Missana et al., 2008 work with the present one (red point , FUNMIG column), it is clear that roughness effects must play an additional important role in colloid filtration in a granite fracture. In fact, for natural fracture at similar concentration (100 ppm) and flow rate conditions the colloid recovery is less than 20%. For this reason it would be important to complete these studies with a characterization in depth of the granite fracture surface and the measurement of roughness that will be performed when dynamic studies will be finalized.

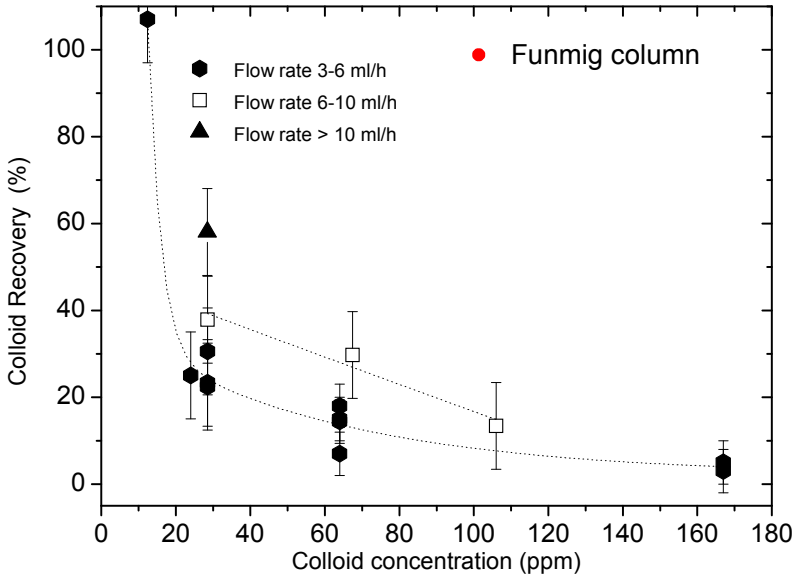

Figure 4: *Colloid recovery as a function of the colloid concentration at different flow rates.*

The nature and morphology of clay colloids may be important in their filtration behavior. Clay is a plastic material that can suffer higher friction in a surface above all when water flow rate is low and surface roughness is low. It would be of interest to study additionally the behavior of colloid of different composition and size.
If RNs would be adsorbed onto colloids generated from bentonite barrier, their transport in the environment would be affected by their presence. In the ‘‘real” repository site, if bentonite colloids are present and cannot be washed away from fractures they might cause plugging of the flow path as pointed out by Sen and Khilar (2006).

Conclusions

Bentonite colloid transport experiments in a granite fracture were performed to analyze the effects of the water velocity on colloid retention in the fracture.

The analysis made in this study lead to the conclusion that, even under dynamic conditions, retention / filtration processes were observed in spite of unfavorable electrostatic for colloid-rock attachment. When the water flow rate is low enough, surface defects, roughness and physico-chemical heterogeneities are playing a role on colloid retention.

In particular, the roughness of the surface plays an important role in enhancing colloid retention as we could deduce by the comparison with results obtained under similar hydrodynamic conditions, but in a natural fracture.

Acknowledgment

This study was partially supported by the EU within the FUNMIG (Fundamental Processes of Radionuclide Migration) project (Ref. FP6-516514) and by the Spanish Ministry MEC (PROMICOL Project; CGL 2005-01482/BTE).

References

Alonso U, Missana T, García-Gutiérrez M, Patelli A, Ceccato D, Albarran N, Lopez-Torrubia T, Rigato V. Mingarro M Colloid attachment to the granite surface under "unfavorable" conditions, (2008) CIEMAT technical report 4rd. Annual Workshop Proceedings 6TH EC FP - FUNMIG IP.

Huertas F, Fuentes-Santillana J.L, Jullien F, Rivas P, Linares J, Fariña P, Ghoreychi M, Jockwer N, Kickmaier W, Martínez M.A, Samper J, Alonso E, Elorza F.J, 2000 Full scale engineered barriers experiment for a deep geological repository for high-level radioactive waste in crystalline host rock., EC Final REPORT EUR 19147.

Missana T, Alonso U, Turrero M.J, (2003) Generation and stability of bentonite colloids at the bentonite /granite interface of a deep geological radioactive waste repository, Journal of Contaminant Hydrology, v. 61, p. 17-31.

Missana T, Alonso U, García-Gutiérrez M, Mingarro M, (2008) Role of colloids on the migration of europium and plutonium in a granite fracture, Applied Geochemistry, v. 23, p. 1484-1497.

Missana T, García-Gutiérrez M, Alonso U, Mingarro M, (2006) On radionuclide retention mechanisms in fractured geologic media, Journal of Iberian Geology, v. 32, p. 55-77.

Möri A, Alexander W.R, Geckeis H, Hauser W, Schäfer T, Eikenberg J, Fierz T, Degueldre C, Missana T, (2003) The colloid and radionuclide retardation experiment at the Grimsel Test Site: influence of bentonite colloids on radionuclide migration in a fractured rock, Colloids and Surfaces A: Physicochemical and Engineering Aspects, v. 217, p. 33-47.

Sen T.K, Khilar K.C, (2006) Review on subsurface colloids and colloid-associated contaminant transport in saturated porous media, Adv. Colloid. Interface Sc 119, p. 71–96.

Small H, Saunders F.L, J.Solc, (1976) Hydrodinamic Chromatography: a new approach to particle size analysis, Advance in colloid and interface science 6, p. 237-266.

TOPICAL SESSION

4TH TOPICAL SESSION: "FUNMIG AND THE SAFETY CASE"

Bernhard Schwyn
National Cooperative for the Disposal of Radioactive Waste (Nagra), Switzerland

Introduction

All research and development activities performed in the IP FUNMIG orient towards the application of their results in future safety cases. A mutual understanding between the providers of scientific information and the end-user of the latter facilitates a purposive research. To promote the communication between performance assessors and research oriented partners the first Topical Session was, among other topics, dedicated to the presentation of the various European repository concepts and the implementation of far field processes in recent safety cases (Schwyn et al., 2006). To close the circle the 4th Topical Session was again dedicated to the communication between performance assessors and researchers, now discussing the outcome of FUNMIG in respect of its implications for future safety cases. A detailed evaluation of the FUNMIG results towards its use in safety cases is presented in Nagra (2009)

Programme of the Topical Session:

- Universal not host rock specific talk "Implications of FUNMIG for the Safety Case" by J. Schneider, Nagra (see presentation, below)
- Argillaceous rock specific talk "FUNMIG research results on radionuclide migration in clay-rich host formations: potential (likely) uses in future safety cases" by S. Altmann, Andra
- Talk on "Use of research Data to support a Safety Case" by C. Tweed, NDA (see presentation, below)
- Talk on "Regulatory Perspective on FUNMIG Work: Summary of Presentation to the Fourth FUNMIG Workshop" by B. Sagar, CNWRA (see presentation, below)
- Round Table Discussion summarized in the following section

Round Table Discussion

The discussion was organized by assigning to the panel members adequate roles according to the four interacting groups involved in a safety case as proposed by Schwyn et al. (2006):

- The **management group**, responsible for overall management of repository planning.

The role was formally assign to the chairman of the round table discussion:

- B. Schwyn, Nagra

- The **science and technology group**, responsible for the scientific and technical basis of the safety case.

The role was assigned to the RTDC leaders:

- T. Missana, CIEMAT; U. Noseck, GRS; P. Reiller, CEA; T. Schäfer, FZK

- The **performance assessment group**, responsible for the development of a system concept, the safety concept and the approach to safety assessment, as well as the carrying out of the safety assessment and the compilation of the safety case.

The role was assigned to representatives of Waste Management Organisations and other persons involved in the development of safety cases (performance assessors):

- S. Altmann, Andra; J. L. Cormenzana, Enresa; J. Mönig, GRS; C. Tweed, NDA

- The **bias audit group**, responsible for ensuring that the scientific basis for safety assessment is complete, fully documented and exploited in an unbiased manner in safety assessment.

The role was assigned to regulators and persons co-working with regulators:

- F. Altorfer, HSK (now ENSI); B. Sagar, SWRI; D. Pelegrini, IRSN

In the discussion the **scientists** challenged the appraisal of the FUNMIG results by the Waste Management Organisations documented in Nagra (2009). The **performance assessors** defined the reasoning behind their assessment of the FUNMIG results towards achieved improvements. FUNMIG tasks were strictly assessed from a point of view of benefits for future safety cases for the individual European disposal concepts. **Performance assessors** are not in a position to judge the scientific quality of the work carried out within FUNMIG. The **scientists** asked whether performance assessors should be more open-minded about new findings.

As highlights achieved within FUNMIG, progress made in understanding colloid formation and behaviour, results from redox studies, and the development of up scaling tools for fractured rock were mentioned among other topics by the **scientists**.

According to statements by the **performance assessors**, benefits derived from the outcome of FUNMIG depend on the stage of the particular national programmes. Countries with defined host rock types profit the most from the corresponding rock specific RTDC while countries with not yet defined host rock type like the UK derive more advantage of the rock unspecific RTDCs 1 and 2. Future projects, however, will tend to more rock or site specific investigations thus getting more difficult to combine research on migration properties of different host rock types under one umbrella.

In the **regulator's** view the outcomes of FUNMIG clearly added a lot to the state of knowledge on migration of radionuclides through host rock. However one has to keep in mind that this is only one, usually not the most important issue with regard to the assessment of the repository long-term safety. On the question whether the FUNMIG scope of investigations was balanced, the **regulators** replied that it is the job of the

implementer to set research priorities, although **regulators** may bring in additional issues to be included in the safety considerations. **Waste Management Organisations** usually do not balance their research programme but rather optimise it in respect of reducing uncertainties. The development of a disposal programme is a learning process and research priorities are usually adapted after each safety case exercise.

The question was raised how close the **regulator** should co-work with the **implementer** without compromising his independency. A **regulator** stated that a close contact with the **implementer** and his experts is essential for the review of the **implementer's** safety cases and does not hamper the formation of the **regulator's** mind. Such a co-work is also appropriate because the implementer usually has much more resources available; nevertheless, an independent research programme of the regulator is indicated or even necessary to develop own expertise.

Presentation:

Implications of FUNMIG for the Safety Case

Jürg Schneider
National Cooperative for the Disposal of Radioactive Waste (Nagra), Switzerland

Introduction

The Aim of the presentation was to discuss the implications of FUNMIG for the safety case, based on a brief review of the focus and products of FUNMIG on one hand and on the purpose, the nature and the elements of a safety case on the other hand.

FUNMIG: Focus and products

The bulk of the work performed within FUNMIG was to study a large number of processes in great detail. Each of the 113 FUNMIG tasks is described in a concise way in a so-called Task Abstract Form (TAF) of a prescribed maximum length of one page containing the following elements:

- Title
- Motivation and aim
- Type of work
- Involved participants
- State of knowledge before FUNMIG
- Main results (abstract)
- Achievements for the safety case
- References

The safety case: Purpose, nature, elements

Figure 1 serves to illustrate the key purposes of the safety case, which are: (i) to periodically assess the strategy for repository implementation at major milestones; i.e. to assess the quality of the repository system and the quality of the associated scientific-technical understanding, (ii) to support licence applications (e.g. for construction, operation and closure) and (iii) to provide a platform for informed discussion with all stakeholders.

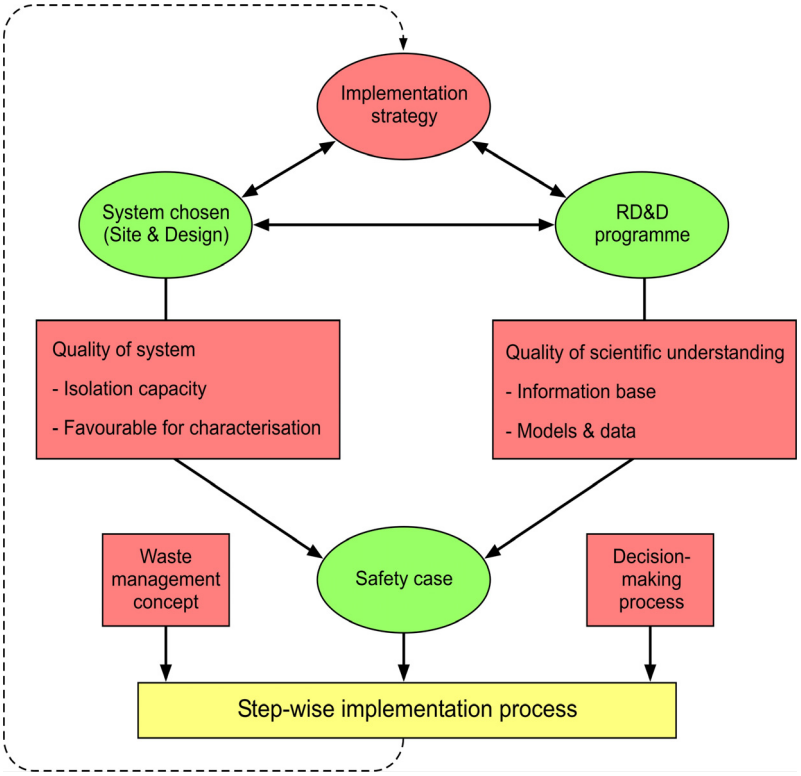

Figure 1: *The safety case: Important elements of decision-making for the step-wise and iterative repository implementation process (taken from Nagra, 2002)*

The nature of the safety case is well captured in two quotations taken from two recent NEA documents:

1. "The English word "case" can be interpreted in a legal sense, as if a case for repository safety were being prepared to be brought to trial. In such a trial, all relevant information for determining the safety or lack of safety of the proposed system would be brought to the attention of judges or juries, or both." (NEA, 2008)

2. "A safety case is the synthesis of evidence, analyses and arguments that quantify and substantiate a claim that the repository will be safe after closure and beyond the time when active control of the facility can be relied on." ("Safety Case Brochure", NEA, 2004)

The elements of a safety case are, according to the Safety Case Brochure:

- Statement of purpose and context
- Safety strategy
  - Management strategy
  - Siting and design strategy
  - Assessment strategy (→ safety concept, treatment of uncertainties, ...)

- Assessment basis[1]
  - Description of the disposal system (repository and its geological setting)
  - Scientific and technical data and understanding
  - Assessment methods, models, computer codes and databases
  - Evidence and arguments to support the quality and reliability of its components
- Evidence, analyses and arguments
  - Numerical analyses required to quantify repository performance and for comparison with dose / risk criteria
  - Use of multiple lines of evidence
  - Complementary safety arguments
- Synthesis

The safety case: Where does FUNMIG come in?

Next, it is shown to which of the elements of a safety case indicated above FUNMIG may contribute, and how. These elements are:

- Safety concept
- Treatment of uncertainties
- Scientific and technical data and understanding
- Assessment methods, models, computer codes and databases
- Evidence and arguments to support the quality and reliability of the disposal system and of the associated scientific and technical understanding

In the following a few examples are given how FUNMIG may contribute to these elements.

Safety concept

Typical safety concepts are based on a barrier system with a series of passive barriers (including "functional" barriers such as the geological setting) which provide a number of safety functions. An "example set" of such safety functions is (based on Nagra, 2008):

- S1: Isolation of the waste from the human environment
- S2: Long-term stability of the barrier system
- S3: Containment of radionuclides
- S4: Delayed release of radionuclides
- S5: Radionuclide retention in the near field and in the geosphere
- S6: Low radionuclide release rates

[1] Collection of information and analysis tools supporting the safety assessment.

An assessment of the elements of the barrier system with regard to their contribution to providing these safety functions shows that e.g. the element "geological setting" provides the safety functions S1 and S2 and the element "host rock" provides the safety functions S5 and S6. In order to provide the required safety functions, the elements of the barrier system must possess a number of safety-relevant properties, which are characterised by a number of features, events and processes (FEPs). In our example one set of important safety-relevant properties of the element "host rock" are its radionuclide retention properties, which are partly determined by the FEPs "ion exchange" and "surface complexation", both of which were studied extensively within FUNMIG.

Treatment of uncertainties

The treatment of uncertainties in a safety case is often guided by principles, which may include:

- Identification of key safety-relevant uncertainties (considering that not all uncertainties are important or even relevant) through expert judgement guided by sensitivity analyses, safety and system analyses
- Avoidance of important uncertainties by siting / design
- Mitigation of the effects of important uncertainties by siting / design
- Remaining uncertainties are (i) considered in the analyses for the safety case for the milestone at hand to illustrate their consequences and (ii) reduced if feasible within an implementer's RD&D programme in view of the subsequent milestones; this is often partly done within, e.g., EU projects such as FUNMIG, within bi- or multilateral research agreements, etc.

Scientific and technical data and understanding / assessment methods, models, computer codes and databases

The improvement of the scientific and technical data and understanding and, thereby, of the databases used in performance assessment, are at the core of FUNMIG activities.

Evidence and arguments to support the quality and reliability of the disposal system and of the associated scientific and technical understanding

The quality of the work done within FUNMIG is assured by, e.g., the promotion, by FUNMIG, of a "synthesis view" by the researchers ("how do my results fit in with the work done elsewhere?"), by the publication of results in peer-reviewed journals and by the presentation and discussion of results at international conferences.

Implications of FUNMIG for the Safety Case

A large body of high-quality work has been performed within FUNMIG, as evidenced by the large number of FEPs studied in great detail within 113 FUNMIG tasks. The

question then is whether all this work will have any implications for future safety cases. In order to answer that question, it is useful to consider the likely geosphere-related information needs of future safety cases. In many cases these will be related to site and host rock specific information based on field investigations, URL experiments and other sources, the latter two of which were to some extent addressed within FUNMIG. Under what conditions will the associated FUNMIG results be used in future safety cases? There are two conditions that have to be fulfilled. The performance assessors compiling future safety cases (i) have to be aware of the FUNMIG work, and (ii) they have to be convinced of its adequacy and quality.

By means of host rock specific "Task Evaluation Tables" (TETs) the end-users of that work (i.e. the performance assessors) were asked to evaluate the importance of these FEPs or Tasks. For each Task (and, via FEP mapping, associated FEPs) they were asked to indicate the importance of improvements for the safety case and, towards the end of the FUNMIG project, to indicate achieved improvements within the FUNMIG project. This process ensures that condition (i) above is fulfilled. That condition (ii) above may be fulfilled to a large extent was discussed under the heading "quality of the work done within FUNMIG" further above.

The link between FUNMIG and future safety cases is illustrated in Figure 2. The link is via the performance assessors, a large fraction of whom participated in FUNMIG (Figure 3). It is very likely that a large fraction of the same performance assessors will also be involved in compiling future safety cases. The box "Enforcing co-operation" (between FUNMIG scientists and performance assessors) comprises several elements, including an adequate structure of the FUNMIG Project with RTDC 6[2] as an "integrator", with clearly defined roles of the different groups.

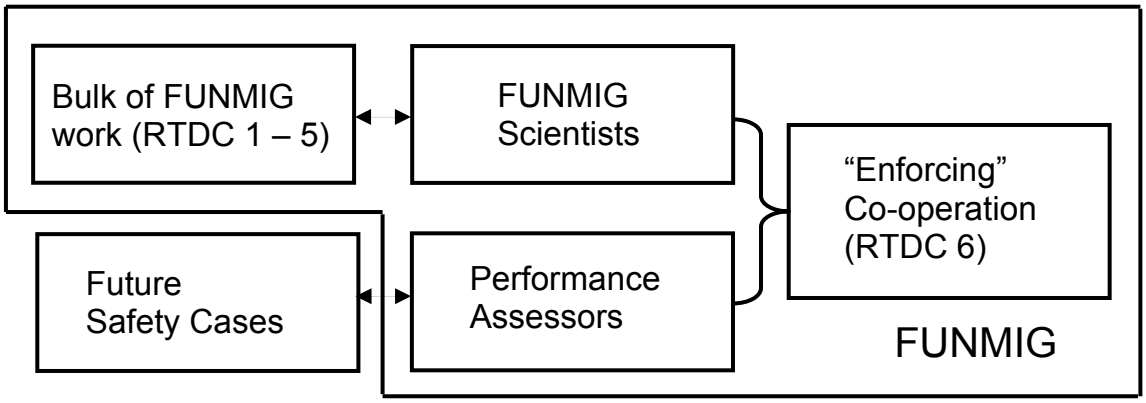

***Figure 2**: The link between FUNMIG and future safety cases*

[2] Integration of processes and their abstraction to PA

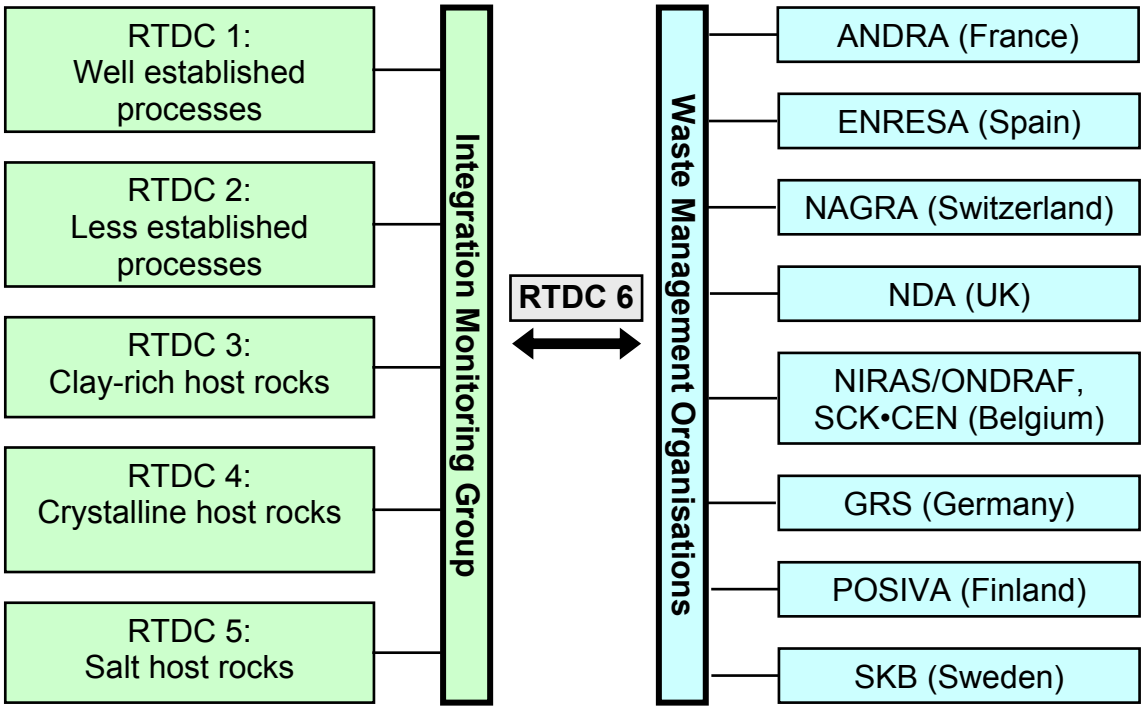

Figure 3: *Link between "Science" and "Performance Assessment" and participating waste management organisations (represented by performance assessors)*

Conclusions

In summary, it is likely that some of the FUNMIG results will be used in some of the future safety cases. The extent to which this will happen is strongly host rock, country, and development stage specific. One important aspect in every safety case is the co-operation between scientists and performance assessors. In this regard, FUNMIG was particularly successful, thanks to an adequate structure of the FUNMIG Project and the "integrating"role played by RTDC6.

Presentation:

Use of research Data to support a Safety Case

Cherry Tweed
Nuclear Decommissioning Authority (NDA). UK

The aim of the presentation was to illustrate how the NDA, the organisation charged with implementing geological disposal for the long-term management of UK's higher activity radioactive waste, makes use of research and development such as that performed as part of FUNMIG, to support a safety case.

A safety case typically relies on a combination of safety functions, e.g.

- low dissolution rates of wasteforms
- low solubilities of radionuclides
- retention of dissolved radionuclides in the engineered and natural system
- low rates of groundwater movement.

The role of research is to provide sufficient understanding of the physical and chemical processes expected to take place in the facility and its environment, to provide confidence in the safety arguments (NDA, 2008). This is illustrated schematically in Figure 1 below (NEA, 2004). The work in FUNMIG has been particularly concerned with developing understanding of the contribution of the natural barrier to radionuclide retention.

One contribution to the safety case is a calculation often referred to as a performance or safety assessment in which the radiation dose as a function of time in the future is calculated, as illustrated schematically in Figure 2 below.

In order to be able to undertake a performance assessment it is necessary to know not only the 'best estimate' of the properties of all the materials considered, but also an estimate of the possible range of uncertainty associated with such values.

In a geological disposal system there are a number of different areas in which uncertainty may influence a performance assessment:

- uncertainty over future states of the system
- data uncertainty, including limitations on the accuracy of making measurements and how representative the measurements are
- model uncertainty
- uncertainty about human behaviour.

In some cases it may be possible to bound the uncertainty and demonstrate that the bounding case(s) give acceptable safety, or it may be possible to argue that the probability of a parameter taking some value is so low that it can be ignored. However, it may be necessary to quantify the uncertainties in more detail. Typically this is done by considering the probabilities of a parameter taking various values. This is called a 'probabilistic approach' and the representation of the different probabilities associated with differing values of a parameter is called a 'probability distribution function (PDF)'. A probability distribution may be thought of as a plot of the probability (or 'degree of belief') that a parameter can take specified values. The range of values that a parameter can take are almost always limited by extreme upper and lower bounds beyond which values for the parameter are not possible or are extremely unlikely. The probability of such values is taken as zero.

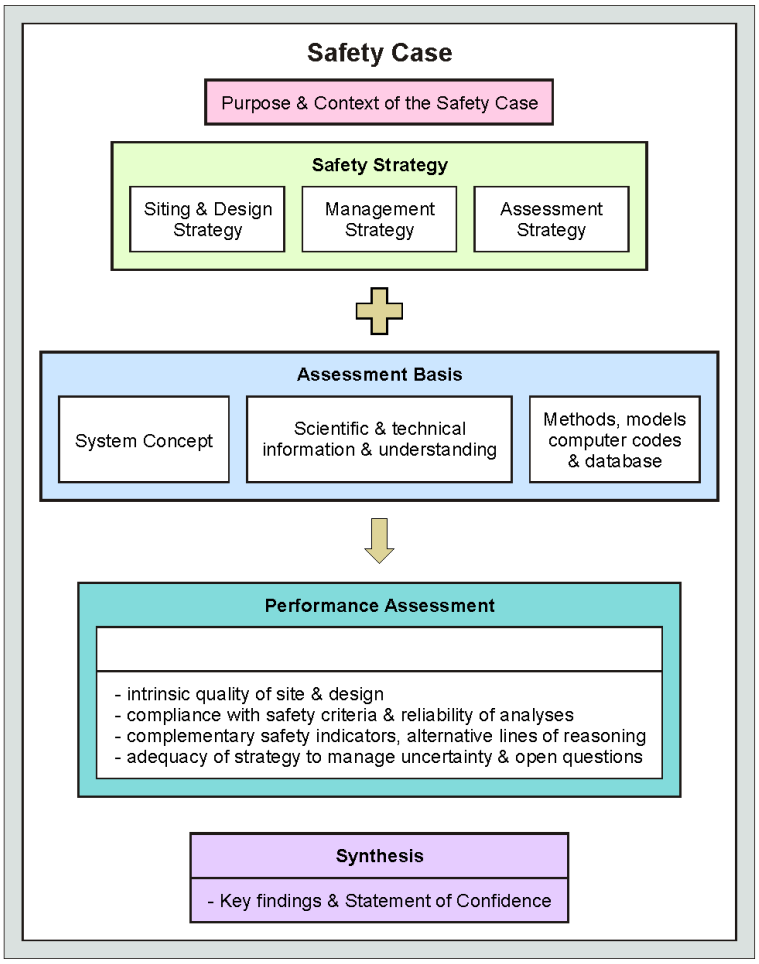

***Figure 1**: The Role of R&D in the Safety Case*

With the uncertainty quantified as PDFs, a probabilistic assessment can be carried out using Monte-Carlo methods. In such an assessment, a computer model is run many times (each run is called a realisation) with different sets of parameter values. In each realisation, the values of the parameters are chosen at random from the PDFs representing the range of possible values. This is known as a 'probabilistic safety

assessment', or PSA, approach. It ensures that wide ranges of possible parameter values are considered within a performance assessment. Statistical analysis of the results of a PSA can be used to explore the sensitivity of the performance measure e.g. risk to the uncertain model parameters.

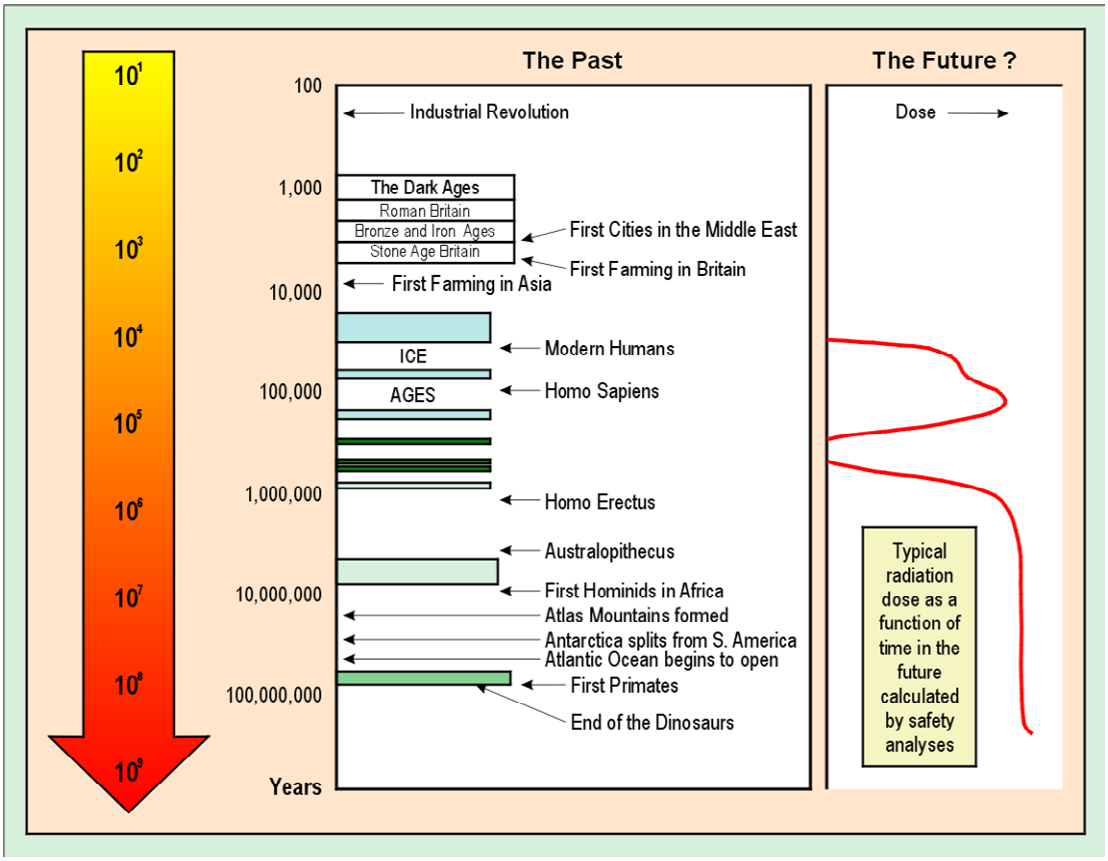

Figure 2: *Schematic Illustration of the output of a Performance Assessment Calculation*

In practice, it is often not possible to obtain sufficient data to determine the precise form of the probability distribution and so experts are asked to provide their judgement in determining the form of the probability distribution. It has been shown that probability distributions that are precise, reliable and accurate can be obtained by elicitation from groups of experts provided that a formal structured approach is adopted (Nirex, 2006).

There has been considerable research interest in this topic and there is an extensive literature on elicitation for a wide range of applications (see for example Morgan and Henrion, 1990). These have shown that in order to elicit probability distributions a structured methodology is essential to limit human bias. Provided that such an approach is followed the elicited probability distributions can be precise, reliable and accurate (Phillips, 1987; Spetzler and Stael von Holstein, 1975). A number of approaches to elicitation have been developed. These differ in the number of experts involved and whether they should work in isolation or as part of a group. The method adopted by Nirex is based on 'group consensus elicitation' in which a group of experts

is tasked with coming to a consensus as to the probability distribution of the uncertain quantity (Phillips, 1999).

In the 1990s, Nirex used the elicitation process to obtain probability distributions for about 200 parameters. More recently, experts in decision analysis have reviewed the whole process and concluded that elicitation was still the credible approach, and that group elicitation was preferred, although expensive.

To illustrate the elicitation process, an example has been selected which refers to the selection of data ranges for Np(IV) and Np(V) sorption onto natural minerals (Jackson and Hunter 2007). It forms part of a project carried out in the UK to select representative ranges of sorption data to be used for 'generic' performance assessment, where data appropriate to a particular site or geological formation are not available. Figure 3 shows the range of data for sorption of Np(IV) and Np(V) obtained during an extensive literature search and distributed to the expert elicitation group for their consideration. Documentation of relevant data forms an important part of the elicitation process as it helps to minimise bias.

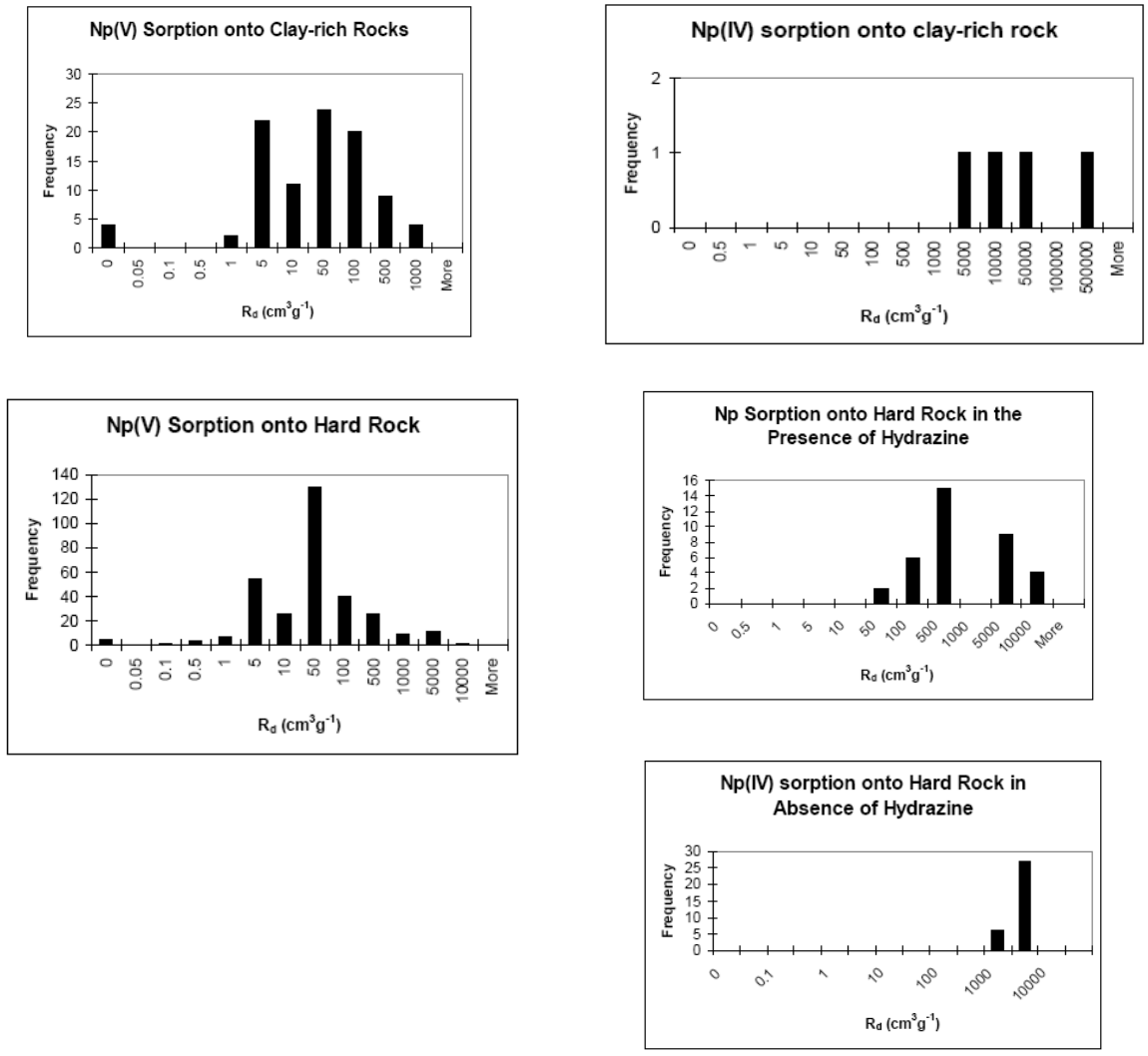

Figure 3: *Range of Literature Values for Np sorption onto various rock types.*

The available measurements do not constitute a representative sample for the geochemical conditions of interest. For example, there are many more measurements for some rock types than others; the pH range is not uniformly sampled; in some of the experiments, the quantity measured is not quite the same as the quantity defined to be of interest (e.g. because the aqueous phase was not as carefully determined); and the experiments are of varying quality (e.g. the solubility limit may have been exceeded, so that the measured values would be determined by precipitation as well as sorption). All of the above needs to be taken into account, which was done in the structured data elicitation session.

The elicited ranges for Np(IV) and Np(V) sorption to be used under the appropriate geological conditions are shown in Figure 4 below. Comparison between the recommended ranges and the original data demonstrates that the experts have considered the data but used their expert opinion to evaluate the relevance and accuracy of the various measurements. An important consideration in making this judgement is an understanding of the various processes and mechanisms occurring in the experiments used to measure the data and expected in a geological disposal facility to which the data will be applied.

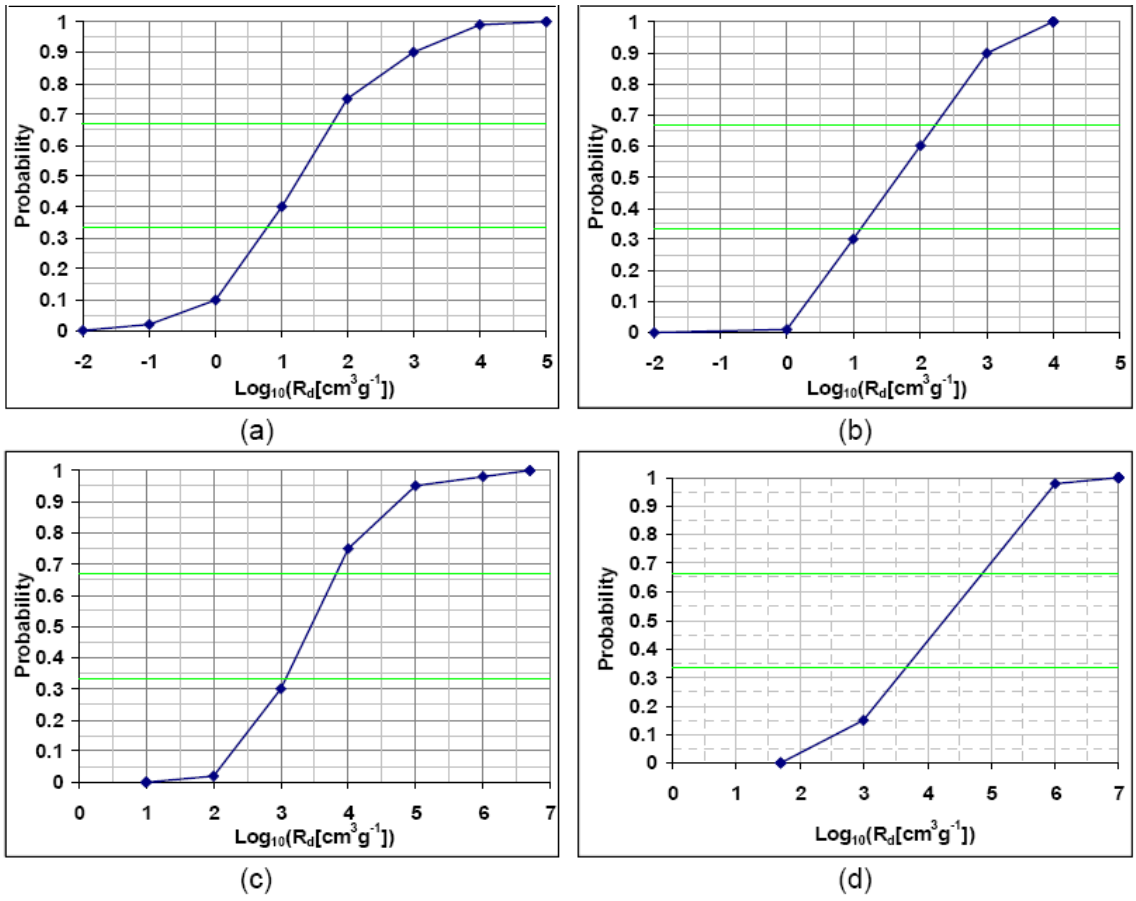

Figure 4: *Elicited cumulative distribution functions for R_d for the sorption of neptunium under the stated conditions (a) Np(V) to sandstones/hard rock, (b) Np(V) to clay-rich rocks, (c) Np(IV) to sandstones/hard rocks, (d) Np(IV) to clay-rich rocks.*

The work in FUNMIG has been particularly important in enhancing the knowledge base on radionuclide migration that is available to support a safety case. It forms an important input to the selection of parameters to be used in performance assessments in the UK.

The numerical values must be supported by a sound understanding of the relevant physical and chemical processes. FUNMIG has also made significant advances in this understanding.

Presentation:

Regulatory Perspective on FUNMIG Work: Summary of Presentation to the Fourth FUNMIG Workshop

Budhi Sagar
Center for Nuclear Waste Regulatory Analyses, USA

Large integrated research projects such as the European Commission-funded Fundamental Processes of Radionuclide Migration (FUNMIG) project add to the knowledge essential for implementing a safe repository concept that can be useful to all stakeholders, including the regulator.

The design, construction, safe operation, and final closure of the repository are the responsibility of the implementer. The implementer has to demonstrate in its safety case, presented to all stakeholders but particularly to the regulator, that the proposed concept can be safely built and operated and continue to protect public health and the environment for a long time. It is the regulator's responsibility to set protection and safety standards, and evaluate the safety case and determine whether the proposed concept will indeed meet the safety standards (Figure 1). Regulators also have authority to inspect facilities and enforce license requirements. Safety standards and regulations must be transparent, must be able to be implemented with current methods, and must be based on the current knowledge. While the regulator conducts some independent scientific/engineering investigations, more generally he/she depends on a knowledge base generated by various stakeholders, research organizations including academic institutions, and particularly the implementing organizations. Knowledge created through FUNMIG fits into this spectrum. The confidence levels in the safety case generally increase with increase in knowledge, although it is not uncommon to see an occasional dip in the confidence when difficult problems are encountered as depicted in Figure 2.

Because of the large space and time scales involved, the safety case usually is based on models and other congruent arguments; there is not a physical test that can be conducted. In this sense, an absolute proof of safety is not feasible and generally not required by the regulator. The regulator, however, does expect the implementer to demonstrate sufficient understanding of important features, processes, and events affecting safety to instill confidence in the space-time extrapolation conducted through the use of models. The public expects the safety case to be transparent, scientifically based, and not unnecessarily complex. On the other hand, the public also expects (Figure 3) the regulator to have the capability to independently evaluate the safety case and be able to clearly and openly present its findings.

FUNMIG-generated publications will remain an important source of information on the state-of-the-art with respect to migration processes as depicted in Figure 4. FUNMIG researchers focused on four important migration processes: retention, colloidal transport, matrix diffusion, and fracture characterization. The research involved fundamental experimental and theoretical work from the pore scale to the

repository scale. Both the implementer and the regulator will be greatly interested in the researchers' attempt to explicitly establish a link between their research and its potential use in safety assessment. This step involved resolving difficult scaling issues that can provide a relationship between measurements at small scales in the laboratory and data measured in the field at much larger scales.

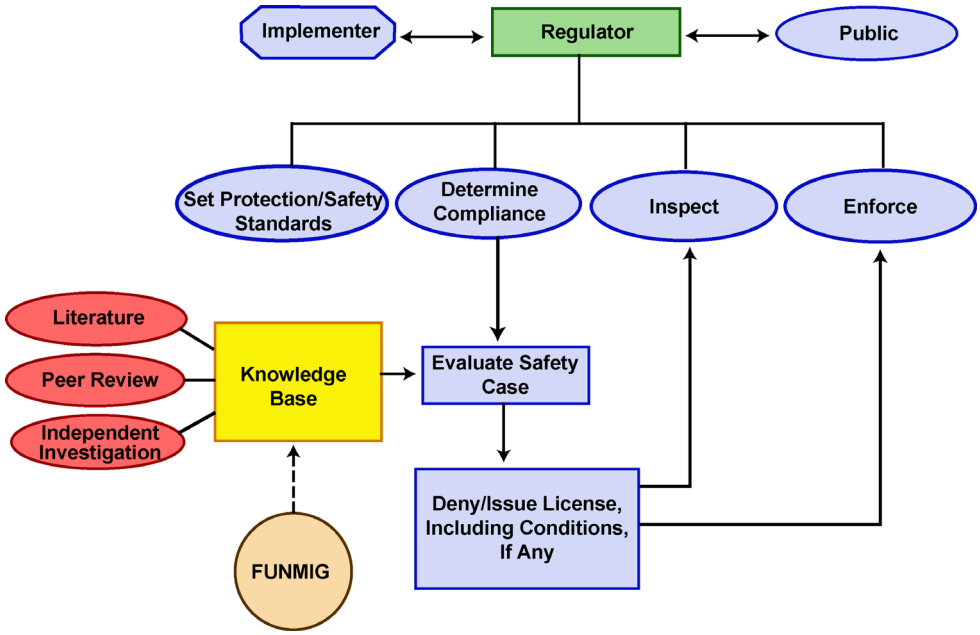

Figure 1: *Role of Regulator*

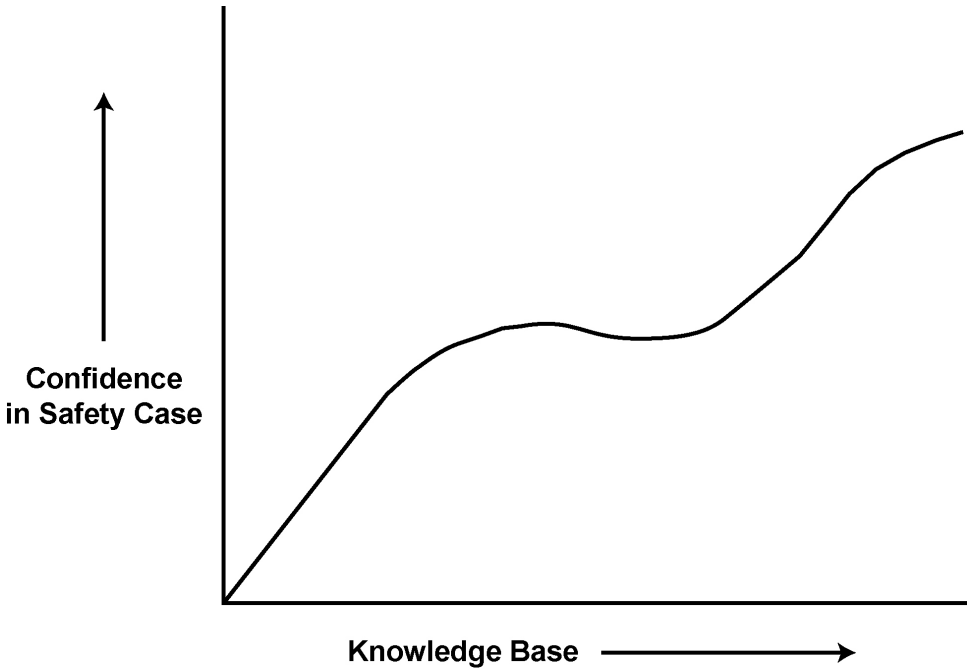

Figure 2: *Evolution of Confidence in Safety Case*

Overall, the regulators, even though they are not direct active participants in the project, will benefit from the enhanced knowledge base from FUNMIG.

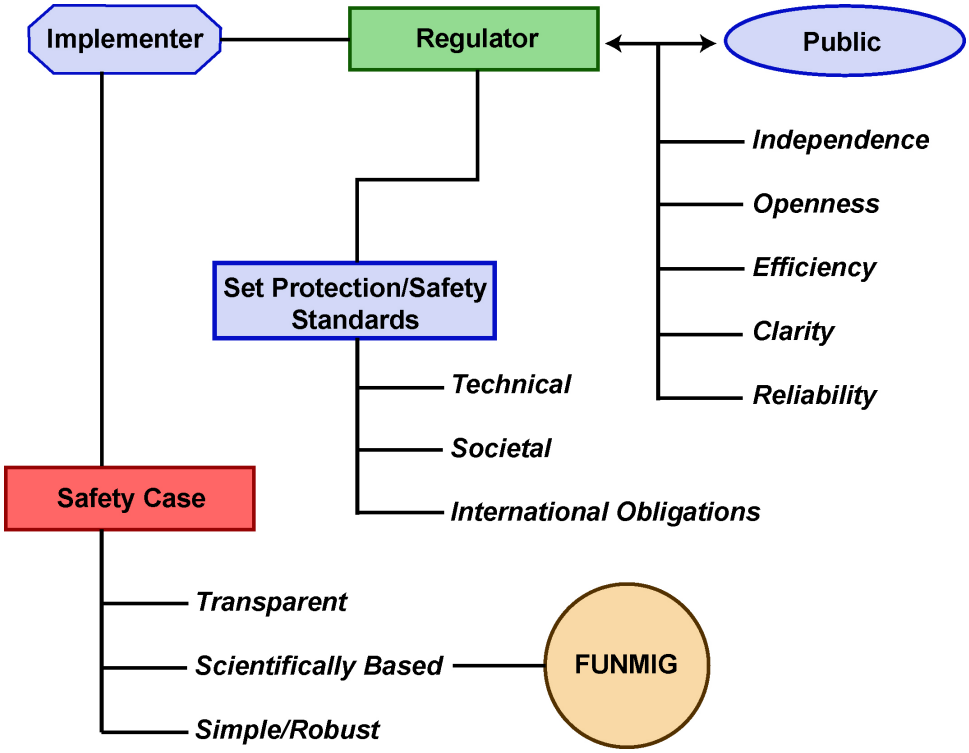

***Figure 3**: Stakeholder Expectations*

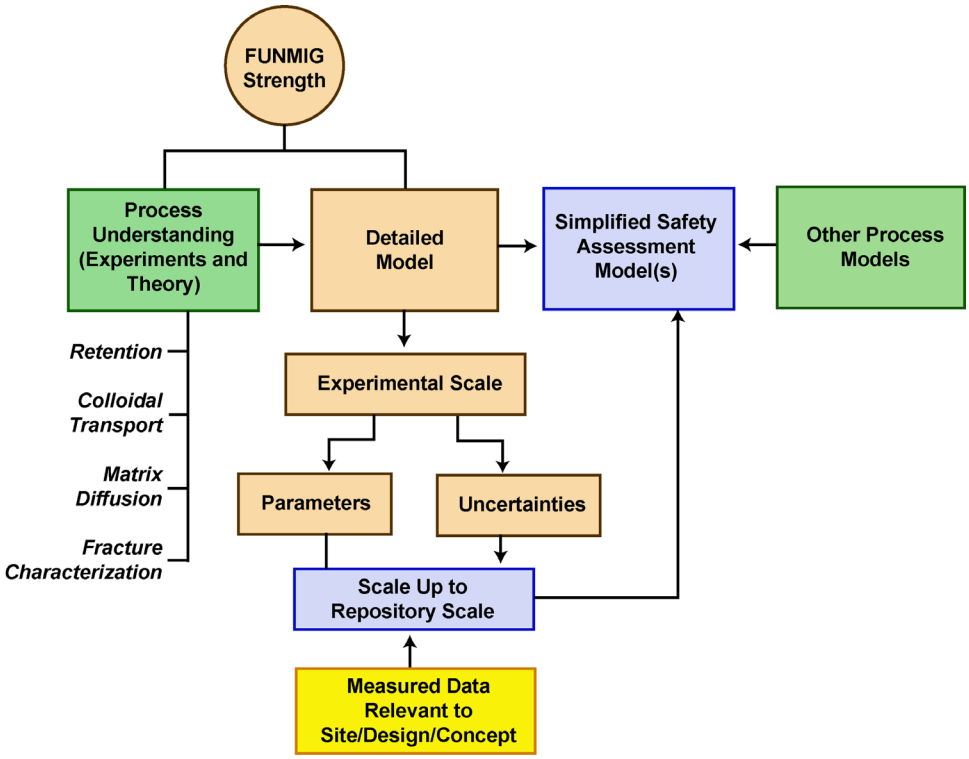

***Figure 4:** FUNMIG Contributions to Knowledge Base*

References

Jackson C.P. and Hunter F.M.I (2007): Formal Structured Data Elicitation of Neptunium Sorption Distribution Coefficients for Sandstones/hard rock and clay-rich rocks, SA/ENV-0852 Issue 2.

Morgan M.G. and Henrion M. (1990): Uncertainty: A guide to Dealing with Uncertainty in Quantitative Risk and Policy Analysis, Cambridge University Press.

Nagra (2002): Project Opalinus Clay: Safety Report: Demonstration of disposal feasibility for spent fuel, vitrified high-level waste and long-lived intermediate-level waste (Entsorgungsnachweis). Nagra Technical Report 02-05. Nagra, Wettingen.

Nagra (2008): Vorschlag geologischer Standortgebiete für das SMA- und das HAA-Lager. Begründung der Abfallzuteilung, der Barrierensysteme und der Anforderungen an die Geologie. Bericht zur Sicherheit und technischen Machbarkeit. Nagra Technical Report 08-05. Nagra, Wettingen.

Nagra (2009): Fundamental Processes of Radionuclide Migration: Topics and processes dealt with in the IP FUNMIG and their treatment in the Safety Case of geologic repositories for radioactive waste. Nagra Technical Report 09-01. Nagra, Wettingen, (in preparation).

NDA (2008): Radioactive Waste Management Directorate Proposed Research and Development Strategy, NDA, May 2008

NEA (2004): Post-closure safety case for geological repositories, nature and purpose. OECD / NEA, Paris.

NEA (2008): Safety cases for deep geological disposal of radioactive waste: Where do we stand? Symposium proceedings Paris, France, 23-25 January 2007. OECD/NEA, Paris.

Nirex (2006): A Procedure for data elicitation in support of performance assessments Nirex Report N/132.

Phillips L.D. (1999): Group elicitation of probability distributions: Are many heads better than one?. In J. Shanteau, B. Mellers, D. Schum (editors) Decision Science and Technology: Reflections on the Contributions of Ward Edwards. Kluwer Academic Publishers, Norwell MA, 313-330.

Phillips L.D. (1987): On the adequacy of judgemental forecasts. In: G. Wright and P. Ayton (editors) Judgemental Forecasting. Chichester, John Wiley.

Schwyn, B., Schneider, J., Zuidema, P. (2006): Scientific knowledge base of processes/topics and its implementation in performance assessment from the point of view of waste management organizations. pp 241 - 248 in Reiller, P., Buckau, G., Kienzler, B., Duro, L., Martell, M. (eds.): 1st Annual workshop proceedings of integrated project fundamental processes of radionuclide migration, IP FUNMIG, CEA report R-6122, Saclay, France.

Spetzler C.S. and Stael von Holstein C-A.S. (1975): Probability encoding in decision analysis, Management Science, 22, 340-358.